The Flux-MMF Diagram Technique and Its Applications in Analysis and Comparative Evaluation of Electrical Machines

Rajesh Pranay Deodhar

A Thesis
Submitted to
the Department of Electronics and Electrical Engineering
of
the University of Glasgow
for the Degree of
Doctor of Philosophy

October 1996

Abstract

The thesis describes a new technique, called the flux-MMF diagram technique, for analysis and comparative evaluation of electrical machines. The technique has evolved from the principle of virtual work, and the ψ-i diagram, used commonly in designing switched reluctance machines and relays. Several applications of this technique are demonstrated in the thesis, supported by experimental validation. These are, the prediction of electromagnetic and cogging torque ripple, modelling of the effect of skew on torque and torque ripple, modelling of the variation of torque constant due to saturation, and comparative evaluation of different types of electrical machines.

The thesis shows that the technique can be applied successfully in analysis of a wide variety of electrical machines. These include conventional machines such as the DC commutator, PM brushless AC, Interior PM, and the synchronous reluctance machine; as well as non-conventional machines such as the switched reluctance, PM brushless DC, and the doubly-salient PM machine.

The technique has been implemented in a finite-element software, with the help of a link program which links the FE software with the dimensioning or sizing software, such as PC-BDC, produced by the SPEED Laboratory. The link program serves as a vital means of shortening the time it takes to analyse a new design in an FE software, by several orders of magnitude.

The thesis also describes a new brushless doubly-salient permanent-magnet machine, called the flux-reversal machine. The design and fabrication process, and the experimental results are presented for a prototype single-phase, high-speed flux-reversal generator. The performance analysis of the prototype based on the flux-MMF diagram technique is included, and this validates its capability in analysing new and non-conventional machines, which cannot be analysed using the classical means.

Table of Contents

Acknowledgements

First and foremost, I would like to thank my supervisor Prof. T. J. E. Miller for his inspiring guidance and support throughout my PhD studies. A special thanks to Dr. David Staton, Prof. Ion Boldea and Dr. Tom Jahns for providing ideas and motivation through many helpful discussions. Thanks to Dr. André Pittet, my supervisor for the Master's dissertation, for encouraging me to do a PhD.

I would like to acknowledge the support provided in various forms by the Committee of Vice-Chancellors and Principles (CVCP), the University of Glasgow, the SPEED Consortium, the Department of Electronics and Electrical Engineering, and the J. N. Tata Endowment.

Thanks to all my colleagues, former and present, in the SPEED Laboratory, for their valuable support. Especially Peter Miller and Jimmy Kelly in hardware and experimental set-ups, Malcolm McGilp in software, Svante Andersson and Dennis Kom in testing and fabrication, and Saffron Alsford in administration. I would like to thank my seniors, especially Dr. Wen Soong, Dr. Mary Tolikas and Dr. Bala Srinivasan for inspiring me through their own achievements.

Thanks to all my friends in Glasgow for their help and understanding. Finally and most importantly, I would like to thank my parents, my family in India and Kenya, and my fiancée, Anagha, for believing in me and sharing my dreams.

List of Figures

List of Tables

List of Symbols

W	Magnetic energy	[J]
i	Instantaneous current	[A]
λ, ψ	Instantaneous flux-linkage	[V-s]
W'	Magnetic coenergy	[J]
T_e	Instantaneous electromagnetic torque	[Nm]
T_{eav}	Average electromagnetic torque	[Nm]
m	Number of phases	
N_r	Number of rotor poles	
N_{ph}	Number of phases	
MMF	Magnetomotive force	[A-t]
e	Error in calculated coenergy	[J]
$\mathbf{F}$	Lorentz force vector	[N]
Q	Electric charge	[C]
$\mathbf{E}$	Electric field vector	[V/m]
$\mathbf{v}$	Velocity vector	[m/s]
$\mathbf{B}$	Magnetic field vector	[T]
F	Lorentz force (scalar)	[N]
B	Magnetic field (scalar)	[T]
l	Length of conductor	[m]
f_n	Normal component of Maxwell stress	[N/m^2]

μ_0	Permeability of free space	[H/m]
B_n	Normal component of flux-density	[T]
B_t	Tangential component of flux density	[T]
f_t	Tangential component of Maxwell stress	[N/m^2]
T_c	Instantaneous cogging torque	[Nm]
l_a	Active length of conductor	[m]
Q_s	Number of stator slots	
b_0	Slot width	[m]
B_{rb1}	Flux density at one side of the stator tooth	[T]
B_{rb2}	Flux density at the other side of the stator tooth	[T]
r_t	Radius of the circular fringing path	[m]
D	Machine outer diameter	[m]
ξ	Harmonic index	
S	Least common multiple of the number of stator slots	
γ	Current angle, skew angle	[deg or rad]
k_s	Skew angle	[deg or rad]
Λ	Magnetic permeance	[Wb/A-t]
Φ,ϕ	Magnetic flux	[Wb]
l_m	Length of magnet	[m]
A_m	Area of magnet	[m^2]
μ_{rec}	Recoil permeability	
μ_r	Relative permeability	

B_r	Remanent flux density	[T]
A	Vector potential	[Wb/m]
n	Number of magnet segments	
p	Number of pole pairs	
I	Peak current, current phasor magnitude	[A]
ω	Angular velocity	[rad/s]
t	Time	[s]
v	Instantaneous voltage	[V]
V	Peak voltage, voltage phasor magnitude	[V]
K_f	Fringing coefficient	
Φ_{ph}	Flux linking a phase	[Wb]
Φ_m	Magnet flux	[Wb]
B_m	Magnet flux density	[T]
g	Length of airgap	[m]
E	Generated EMF	[V]
L	Phase inductance	[H]
Z	Phase impedance	[Ω]
R	Phase resistance	[Ω]

1 Introduction

1.1 Background

"It is humbling to realise how much scope for innovation remains in the field of motors and drives, even a century and a half after Faraday.[1]*"*

—T. J. E. Miller

This expression really sums up the inspiration behind the piece of research described in this thesis. Since Faraday discovered the principle of electromagnetic induction in 1831 [1], the field of electrical machines and drives has indeed come a long way. But even then, there remains immense scope in making fundamental contributions to many aspects of engineering design and analysis of existing machines and in inventing new types of machines. Especially in view of recent developments in ever higher-speed computing, faster numerical techniques, better ferromagnetic, insulation and permanent-magnet materials, and power-electronic components. The *flux-MMF diagram technique* (FMDT) and its utilisation in analysis of conventional machines as well as the *flux-reversal machine* (FRM)—a new type of brushless doubly-salient permanent-magnet machine—are a few such contributions to this end, presented in this thesis.

While the original idea, which led to the development of the FMDT came from Prof. Martyn Harris of the University of Southampton many years ago, the recent invention of the FRM is credited to Prof. Ion Boldea of the Polytechnic Institute of Timisoara, Romania. The developments on the FMDT have continued in the SPEED

[1]From the preface of the book titled 'Brushless Permanent-Magnet and Reluctance Motor Drives,' Oxford Science Publications, 1989.

Laboratory since 1992, while work on the FRM has started recently and gained momentum during Prof. Boldea's visiting fellowship here in the Summer of 1995.

Dr. David Staton and Dr. Wen Soong, both formerly with the SPEED Laboratory, developed the FMDT to some extent when they made an attempt, for the first time, to compare the torque producing mechanism in switched and synchronous reluctance machines using the ψ-i diagram as a common basis of analysis [47]. It was shown that while the ψ-i diagram for a switched reluctance machine is roughly triangular in shape and restricted to the first quadrant; for a synchronous reluctance machine, it is elliptical in shape and encompasses all four quadrants.

This was followed up by extending the technique to include different types of AC, DC, PM and Reluctance machines [48]. The term 'FMDT' was introduced here for the first time. The capabilities of this technique were further expanded by using it to analyse vital performance aspects of an electrical machine such as the electromagnetic and cogging torque ripple, the effect of saturation and armature reaction on torque constant, and the effect of skew on torque ripple [49]–[52].

1.2 Why FMDT?

Electric machines are classified in many ways depending on various factors such as nature of electric supply (AC or DC), mode of operation (synchronous or asynchronous), geometry (internal or external rotor, slotted or slotless stator), nature of rotation (smooth or stepped), nature of saliency (non-salient, singly-salient or doubly-salient), mode of excitation (single or double excitation) etc. Different machine types belong to different classes and there is a clear distinction between the methods of design and analysis for each one of them.

With the rapid advances of technology in the fields of power electronics, microcontrollers and permanent-magnet materials, performance of the relatively new machine types such as switched reluctance and brushless DC is improving dramatically. At the same time, performance of the conventional machine types such as induction and synchronous is constantly being enhanced. The attempts at comparing different machine types typically involve systematically tabulating a wide range of design and performance parameters and appraising each in turn as illustrated, for example, in [4].

However, such attempts are only partially successful as they are limited to considering only the output parameters and they do not take account of fundamental differences which exist in operational characteristics of various machine types. Thus, there is no single or unified method which can be applied to design, analysis and comparative evaluation of different machine types. The so called 'generalised theory of electrical machines', which has long been established, is based on the dq-axis transformation; whereby a synchronous machine is 'transformed' into a DC machine so that both machine types can be analysed using essentially the same kind of treatment.

The generalised theory works on certain basic assumptions regarding the geometry and the nature of excitation of an electric machine. For example, one of the pre-conditions in applying it is that either the stator or the rotor surface must be ideally smooth. While this condition is satisfied by some of the conventional machine types, it clearly leaves out certain recently developed machine types such as steppers, switched reluctance and brushless DC. Another restriction is that it can only be applied to machines which have sinusoidally distributed windings, i.e. spatial MMF. Again that leaves out many of the modern inverter-driven, non-sinusoidally excited machines. In short, this theory does not and cannot deal with machines having double saliency or machines having non-sinusoidally distributed windings.

In these circumstances, clearly there is a need for a generalised method of design and analysis of electrical machines which would encompass all machine types and which would enable real performance comparisons to be made at the design stage itself rather than at the output performance stage. The FMDT fulfils this need as it is based on the principle of virtual work; which is universally applicable to all types of electrical machines, and indeed, to all types of electromechanical energy conversion devices. And when the FMDT is implemented using one of the modern numerical techniques, such as finite-element analysis (FEA), it is not constrained by any assumptions regarding linearity, geometry, saliency or mode of excitation.

1.3 Literature Review

To the best of author's knowledge, the flux-MMF diagram technique in its present form, its implementation using FE analysis, and its practical applications as demonstrated in this thesis have not been treated in any previously published literature. Nevertheless, in the past, there have been allusions of various kind to the basic idea of the flux-MMF diagram itself.

Harris and Miller [4] have mentioned it in relation to comparing torque producing mechanism in switched reluctance and induction motors. Jenkins et al. [5] have proposed it in the context of torque calculations in the stepper motors. They have shown that the so-called 'coil flux/coil MMF diagram' yields better results as compared to the 'tooth flux/tooth MMF diagram' for a saturated machine. More recently, the technique has gained prominence in the form of the ψ-i diagram, used commonly in calculating average and instantaneous torque in switched reluctance motors [3], [57]. Indeed, as explained later on in this chapter, the ψ-i diagram forms the very basis of the flux-MMF diagram.

As far as methods of analysing various performance aspects of an electrical machine are concerned; extensive literature is available on such topics as prediction of electromagnetic and cogging torque ripple, effect of skew on torque ripple and effect of saturation on torque constant. The literature related to each one of these topics has been reviewed individually in each chapter.

1.4 Thesis Overview

1.4.1 Original Contribution

The original contribution of this thesis can be summarised as follows.

- The concept of the *flux-MMF diagram technique* is introduced. Although essentially an improved implementation of the principle of virtual work, it is shown that the FMDT, coupled with the FE analysis, makes it much more powerful and applicable to a wide range of problems.

- A *link program*, developed to interface the FE software with the SPEED software, is described. Such a link program between the dimensioning or sizing software such as PC-BDC, and the specialist electromagnetic analysis software such as OPERA-2d, is a vital means of shortening the time it takes to analyse a motor design accurately. By making the link program efficient and robust, and by incorporating in it the *art of mesh-building*, the time taken for the whole process has been reduced from several weeks to a few hours.

- An original analysis of various performance aspects of electrical machines, based on the FMDT, is presented. This forms the main body of the thesis. Experimental validation, substantiating this analysis, is included where appropriate. The analysis

is performed primarily on permanent-magnet machines covering the following performance aspects.

1. Electromagnetic torque ripple.
2. Cogging torque ripple.
3. Effect of skew on torque ripple.
4. Effect of saturation and armature reaction on torque constant.
5. Comparative evaluation of different machine types.

These aspects are of paramount importance in designing an electrical machine for a particular application. Although analytical means have been developed over the years which are specific to a type of machine and to its particular aspect under consideration; the FMDT, for the first time, provides a unified and comprehensive means of analysis and comparative evaluation of electric machines.

- A new type of brushless doubly-salient permanent-magnet machine—the flux-reversal machine—is introduced. Its principle of operation is explained, and it is compared with other machine types in its class. The suitability of the FMDT as an analytical tool, applied to an unconventional machine such as the FRM, is demonstrated.

- The first prototype flux-reversal machine, developed as a single-phase high-speed generator, is described. A detailed treatment on its design, performance analysis, fabrication process, and test results is included.

- Finally, some novel multi-phase configurations for the flux-reversal machine are proposed, which can seriously contend with other high-performance brushless PM machines in its class.

1.4.2 Thesis Structure

Fig. 1.1 gives an outline of the thesis structure. The rest of this chapter is concerned with presenting evolution of the flux-MMF diagram, details of its construction and description of the link program between the finite-element and the SPEED software.

The next five chapters, from Chapter 2 to Chapter 6, describe specific applications of the FMDT, supported by experimental validation where appropriate. These applications are; prediction of electromagnetic torque ripple, prediction of cogging torque ripple, modelling of the effect of skew on torque ripple, modelling of the effect of saturation on torque constant, and comparative evaluation of electrical machines.

Chapter 7 is concerned with the FRM. Its principle of operation, comparison with other machine types in its class, the 'proof-of-principle' prototype design, analysis, fabrication, and experimental results are presented in this chapter.

Finally, overall conclusions are drawn and some possibilities regarding future work are discussed in Chapter 8.

The flux-MMF Diagram Technique and Its Applications in Analysis and Comparative Evaluation of Electrical Machines

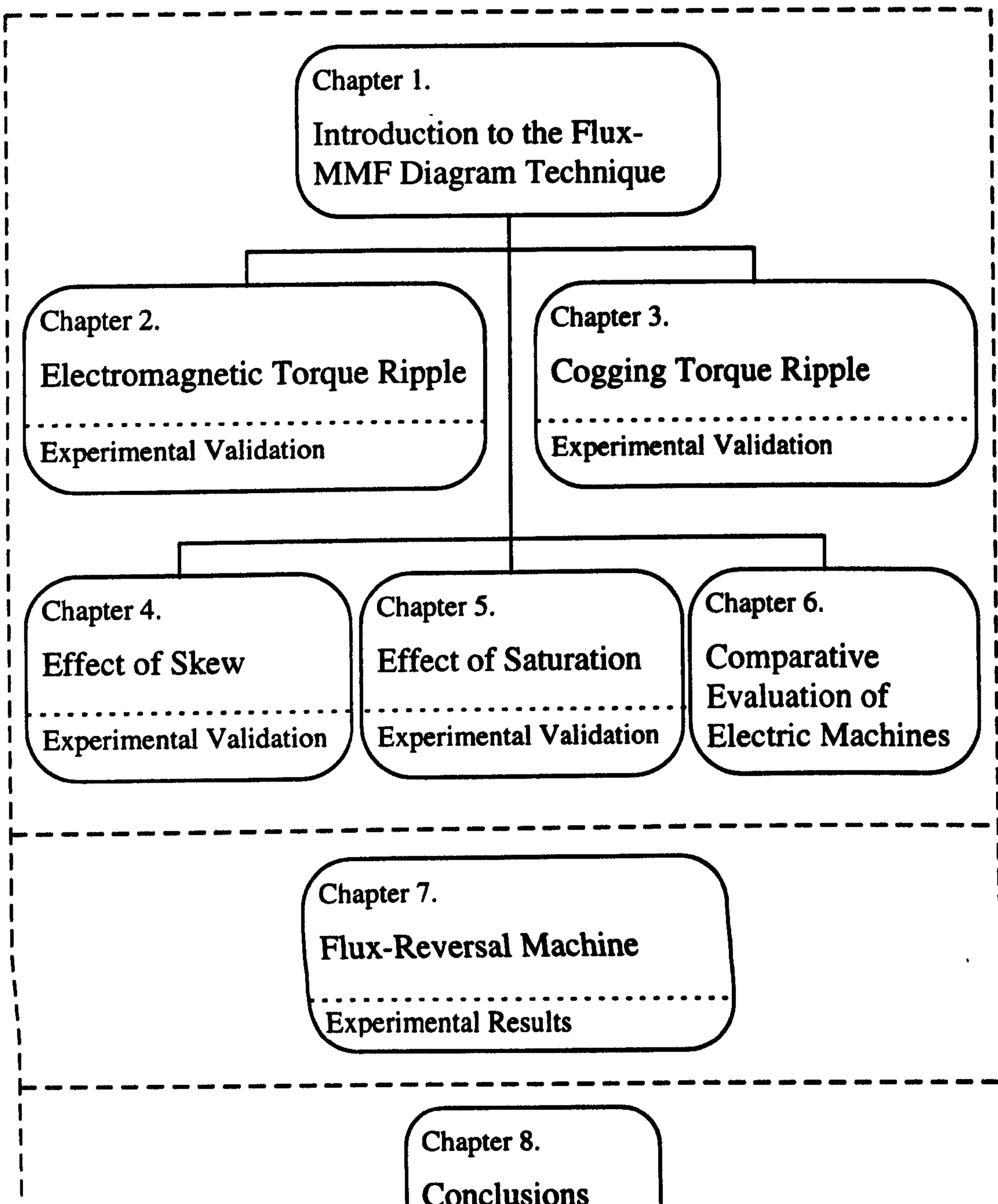

Figure 1.1. Overview of the thesis structure.

1.5 Flux-MMF Diagram Evolution

The flux-MMF diagram has its origin in the ψ-i diagram, used commonly in design and analysis of switched reluctance machines and relays [57], which is in turn based upon the principle of virtual work. The following account explores this chain of evolution in detail.

1.5.1 Defining Terms

To begin with, certain terms, pertaining to the FMDT, are defined which are used throughout this thesis.

Magnetisation Curve: The variation of total flux-linkage (including self and mutual components) of a coil, winding or a phase with respect to the current flowing through it, for a particular position of the movable part in an electromechanical system. Note that this is a universal definition applicable to all types of electromechanical devices such as relays, solenoids, actuators and motors.

ψ-i (Flux-MMF) Trajectory: The dynamic locus of change in total flux-linkage (flux)—including self and mutual components—of a coil, winding or a phase with respect to change in position of the movable part in an electromechanical system, for a given current (MMF) excitation.[2]

ψ-i (Flux-MMF) Diagram: A combined graphical representation of the magnetisation curves and the ψ-i (flux-MMF) trajectories for a coil, winding or a phase in an electromechanical device.

---

[2] The equivalence between the pairs of terms 'flux-linkage and current' and 'flux and MMF' is explained in Section **1.5.4**.

Electromagnetic torque ripple: The variation of instantaneous electromagnetic torque with rotor position for a particular value of load current in an electrical machine. It includes both the DC (average) and the AC (ripple) torque components.

Cogging torque ripple: The variation of instantaneous no-load or open-circuit torque with rotor position in an electrical machine. It includes only the AC (ripple) torque component, as the average component is always zero.

Total torque ripple: The variation of instantaneous total torque (including the electromagnetic and the cogging torque) with rotor position for a particular value of load current in an electrical machine. It includes both the DC (average) and the AC (ripple) components.

1.5.2 Principle of Virtual Work

Since the principle of virtual work forms the very basis of the electromechanical energy conversion process, it has been treated in almost every text-book on electrical machines. Some of the most notable and comprehensive treatments can be found in [55], [59] and [60]. Fig. 1.2(a) shows the magnetisation curve for any device capable of storing magnetic energy such as an inductor, an electromagnet, a transformer coil or a motor winding.

If the device has no moving parts, such as an inductor or a transformer coil, and if the effect of hysterisis is neglected; there can only be a single magnetisation curve, where flux-linkage is expressed solely as a function of current. On the other hand, if the device has a moving part, such as a relay, solenoid, actuator or an electric motor; then it is capable of electromechanical energy conversion and there can be a number of magnetisation curves corresponding to a range of displacement values for the moving part (see Fig. 1.2(b)). In this case, flux-linkage is expressed as a function of both current and displacement.

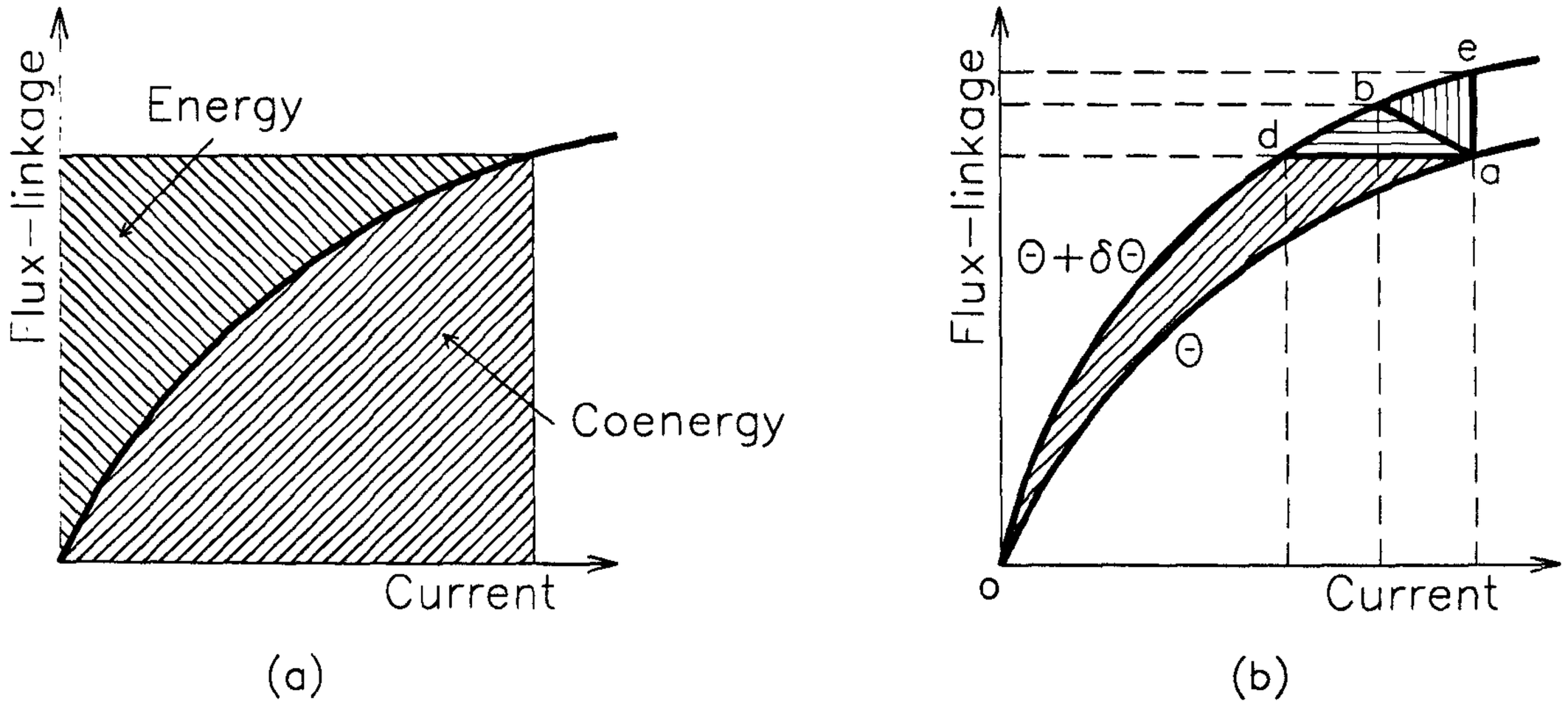

Figure 1.2. Illustration of the principle of virtual work.

Consider an electric motor, in which the magnetisation curve for any one phase, at a particular rotor position, θ, can be represented by Fig. 1.2(a). By definition, the area enclosed between the magnetisation curve and the ψ-axis represents *magnetic energy* given by,

$$W = \int i(\lambda, \theta)\, d\lambda \tag{1.1}$$

Alternately, the area enclosed between the magnetisation curve and the i-axis is defined as *magnetic coenergy* given by,

$$W' = \int \lambda(i, \theta)\, di \tag{1.2}$$

Unlike *energy* which is a physical quantity, *coenergy* is a mathematical abstraction. But it is a useful quantity as it simplifies the mathematics involved in calculating electromagnetic forces and torques.

Now, consider an infinitesimally small rotor displacement, $\delta\theta$, such that the rotor is at a different position, $\theta+\delta\theta$, from the one earlier at θ. The magnetisation curve corresponding to the new position is shown in Fig. 1.2(b). The torque acting on the

rotor can be expressed in terms of either the rate of change of energy or coenergy with respect to displacement [60].

$$T_e = -\left.\frac{\partial W(\lambda,\theta)}{\partial\theta}\right|_{\lambda=const.} \tag{1.3}$$

$$T_e = +\left.\frac{\partial W'(i,\theta)}{\partial\theta}\right|_{i=const.} \tag{1.4}$$

This method of determining forces or torques acting on any movable part of an electromechanical system, by means of evaluating the change in energy balance due to an infinitesimally small imaginary or virtual displacement, is known as the *principle of virtual work*. When applying this principle, three important factors need to be considered.

- The condition of holding either i or λ constant, shown in (1.3) and (1.4) respectively, is a purely mathematical constraint imposed by the selection of independent co-ordinates and has nothing to do with actual electrical terminal constraints [60]. In other words, the equations are valid regardless of whether i or λ are held constant or not during the motor operation.

- In (1.3), ∂W indicates the change in energy due to a displacement of $\partial\theta$ at constant flux-linkage, which is area *oado* in Fig. 1.2(b). While in (1.4), $\partial W'$ indicates the change in coenergy due to a displacement of $\partial\theta$ at constant current, which is area *oaeo* in Fig. 1.2(b). However, in the limiting case of an infinitesimally small rotor displacement, both areas *oado* and *oaeo* approach the same value, since area *ade* which is the difference between areas *oado* and *oaeo*, represents a second-order effect and becomes negligible in the limit as $\partial\theta\rightarrow 0$. Thus, for a small enough displacement, either (1.3) or (1.4) can be applied for any two arbitrary operating points *a* and *b* in Fig. 1.2(b).

- Although the torque itself is independent of the path taken between points *a* and *b* for a differential displacement of $\partial\theta$, the mechanical work done does depend upon the flux-linkage vs. current locus between points *a* and *b* [60].

The procedure of applying the principle of virtual work to a switched reluctance machine to generate a ψ-i diagram, and calculating the instantaneous as well as average torque from it, is explained next.

1.5.3 ψ-i Diagram for a Switched Reluctance Machine

A typical ψ-i diagram for a switched reluctance machine is shown in Fig. 1.3. It shows how flux-linkage for a particular phase varies with current flowing in that phase for different rotor positions between the unaligned and the aligned positions [57]. Fig. 1.3 is nothing but an extension of Fig 1.2(b) and hence the instantaneous torque at a particular rotor position can be calculated using (1.4). Since the torque developed in a switched reluctance machine is independent of the direction of current flow in any particular phase, the ψ-i trajectories are restricted to the first quadrant. W' in Fig. 1.3 represents the net change in coenergy over one *stroke*, where one *stroke* is defined as the displacement between the aligned and the unaligned position. Then, the average torque developed over one revolution is given by,

$$T_{eav} = \frac{mN_r W'}{2\pi} \tag{1.5}$$

Where,

T_{eav} is the average electromagnetic torque.

m is the number of phases.

N_r is the number of rotor poles.

W' is the change in coenergy over one stroke.

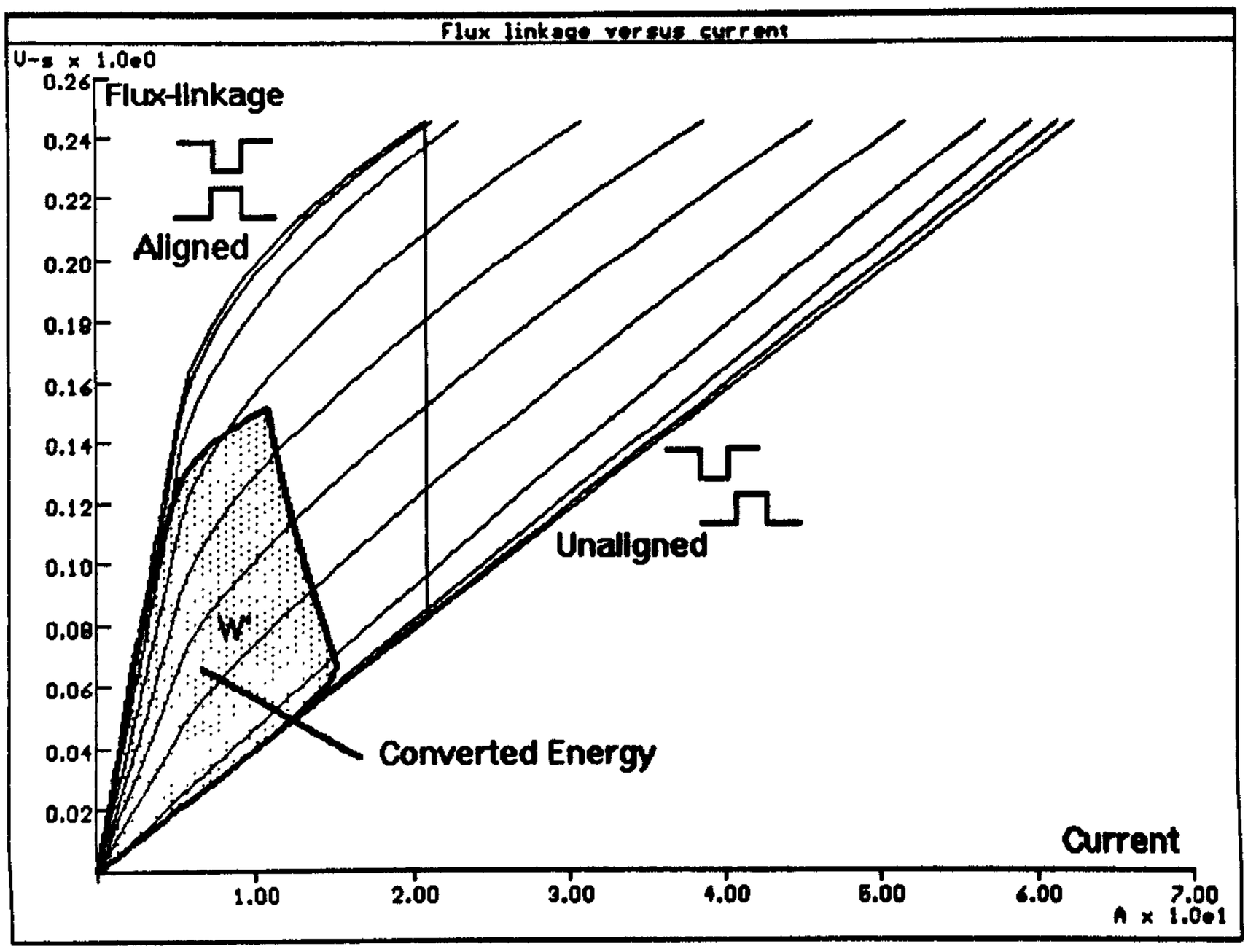

Figure 1.3. A typical ψ-i diagram for a switched reluctance machine.

The procedure of translating a ψ-i diagram into a flux-MMF diagram, in order to make it applicable to a wide variety of machine types, is explained next.

1.5.4 Flux-MMF Diagram : A Generalised ψ-i Diagram

If the flux-linkage and current values are respectively divided and multiplied by N_{ph}, the series number of turns per phase, the ψ-axis becomes the *effective phase flux*-axis and the i-axis becomes the *phase MMF*-axis. These are similar to per-unit quantities. The quantity ψ/N_{ph} is not the actual flux in the machine but the *effective flux* which links the winding and thus produces torque. Thus, rigorously speaking, *effective phase flux* is really the *flux-linkage per unit turn*. But for the sake of compactness, hereafter, it is referred to as the *effective phase flux* or simply the *phase flux* and the diagram is then called the *flux-MMF diagram*.

The ψ-i diagram of Fig. 1.3, can also be constructed for a synchronous reluctance, PM brushless AC, PM brushless DC or any other type of machine. It turns out that the ψ-i trajectory is a closed loop with the shape of an ellipse for a sinewave excited machine and a parallelogram for a squarewave excited machine. The equivalence between the ψ-i and the flux-MMF diagram is illustrated in Fig. 1.4 for a sinewave excited machine. The figure shows that the net change in coenergy over the entire flux-MMF trajectory can either be calculated from the flux-MMF locus or the ψ-i locus, since both enclose the same area.

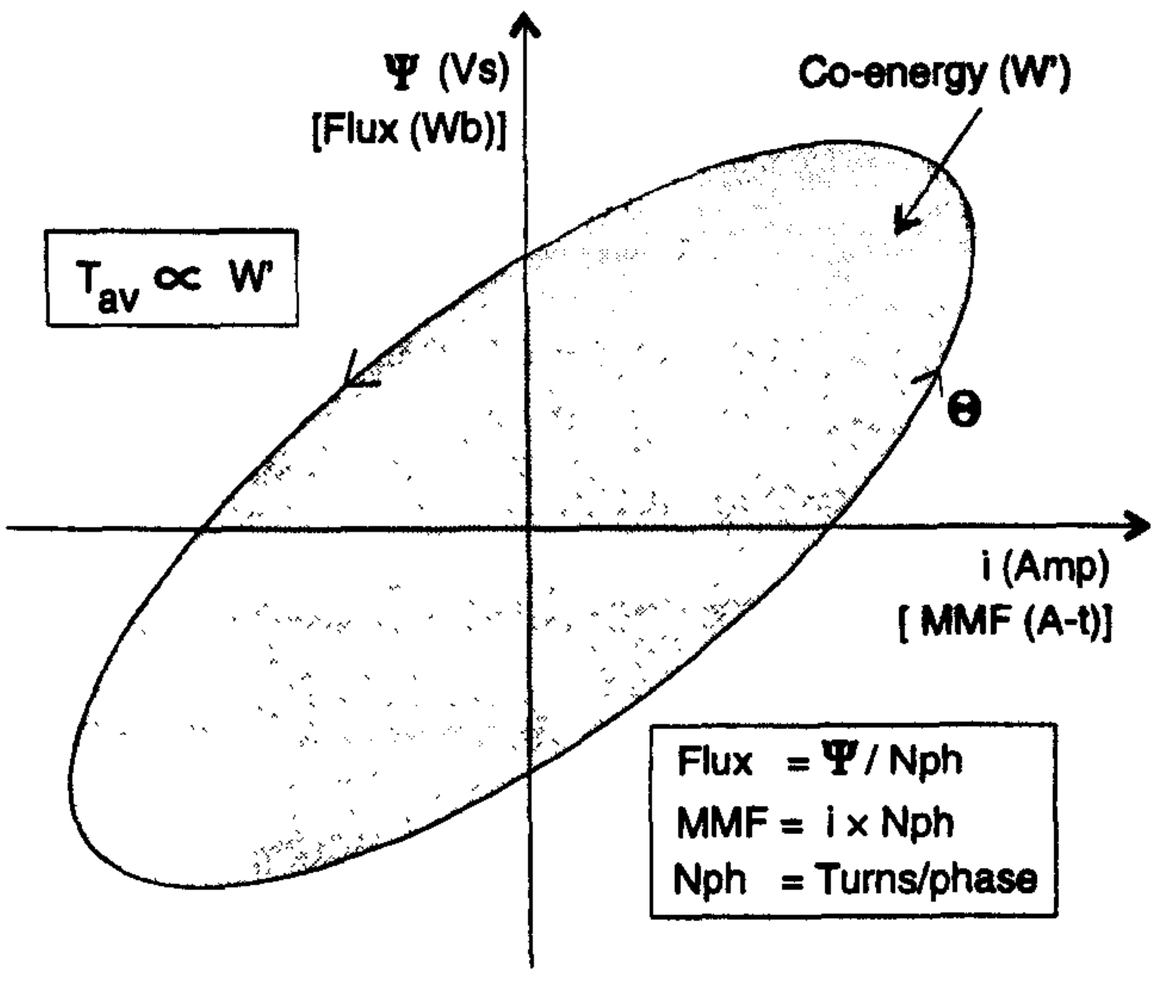

Figure 1.4. The equivalence between the ψ-i and the flux-MMF diagram.

The principal reason for translating a ψ-i diagram into a flux-MMF diagram is that it eliminates the arbitrariness of the number of turns used in a particular design. For example, two machines of comparable size and output power can have completely different numbers of turns depending upon factors such as required speed, working air-gap flux level and applied voltage. In such cases, regardless of the number of turns used in a particular design, the flux-MMF diagram facilitates direct comparison between two different designs of same machine type or even different machine types. Clearly, this is not possible with the ψ-i diagram. Chapter 6 illustrates this point

further as it deals with the comparative evaluation of a wide variety of machine types. This elimination of the number of turns, as a parameter that is not fundamental to the operation of the machine, was first pointed out by Harris et al. [6]. The flux-MMF diagrams illustrated throughout this thesis are based upon ideal sinewave or squarewave current excitation. However, it should be possible to construct the flux-MMF diagram for any given non-ideal current excitation. It must also be mentioned that because of the relatively large magnitude of MMF excitation encountered under normal operating conditions, the hysteresis effect has been safely neglected in obtaining the magnetisation curves.

1.6 Flux-MMF Diagram Construction

In this section, first, the constructional features of a typical flux-MMF diagram are illustrated. Then, an overview of the method of finite-element analysis is presented, with a detailed description of each of the three stages involved. Finally the process of constructing the flux-MMF diagram is explained using an example of a PM brushless AC motor. Fig. 1.5 shows the constructional details of a typical flux-MMF diagram for any one phase of a multi-phase PM brushless AC machine, followed by a list of its salient features.

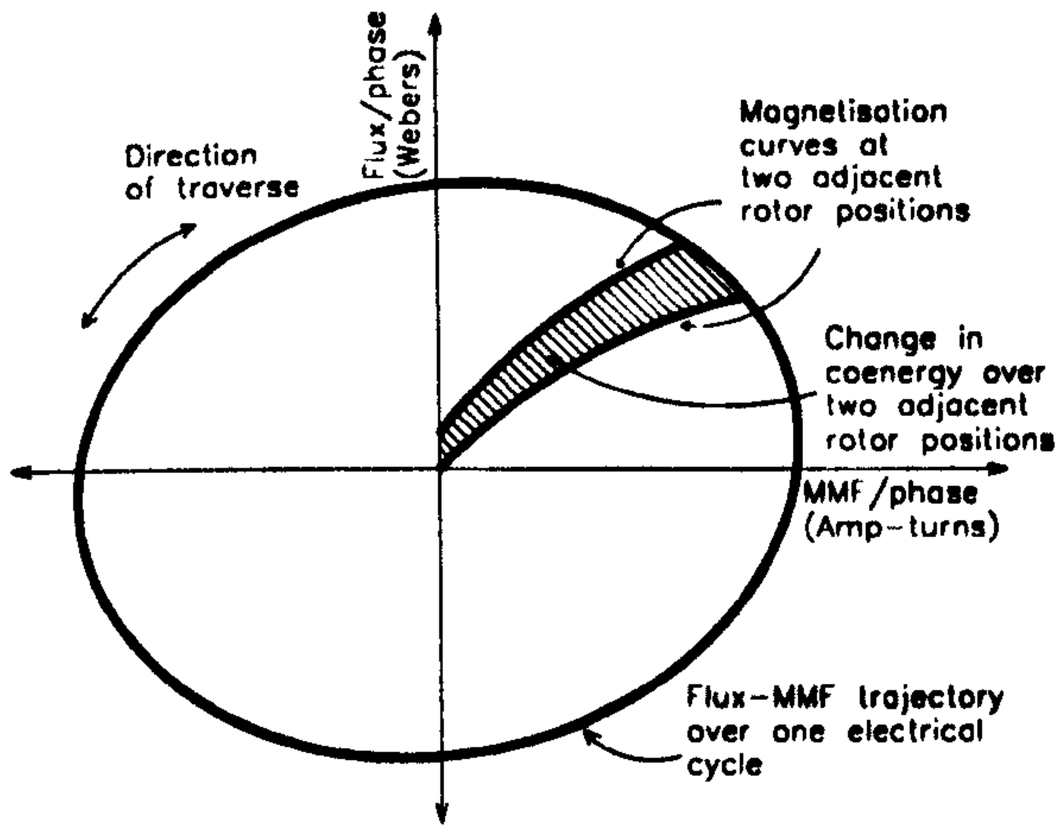

Figure 1.5. Flux-MMF diagram construction.

- The shape of a flux-MMF trajectory indicates the nature of excitation. The ideal shape for a sinewave machine is elliptical, while for a squarewave machine, it is rectangular.
- The average torque can be calculated from the area enclosed by a flux-MMF trajectory, while the instantaneous torque and torque ripple can be calculated from the incremental areas enclosed by the magnetisation curves at successive rotor positions.
- The extent of deviation of a flux-MMF trajectory from its ideal shape, and the extent of uneven spacing of the magnetisation curves, indicate the amount of torque ripple.
- The orientation of the major axis of a flux-MMF trajectory with respect to the MMF-axis indicates the kVA utilisation in squarewave excited machines and the power factor in sinewave excited machines.
- The electric and magnetic loadings and the resultant utilisation of copper and iron, in an electrical machine, are indicated graphically.

Each one of these features is further illustrated in the following chapters with the help of specific examples.

The current state-of-the-art of constructing a flux-MMF diagram involves carrying out a series of steps, each with the help of either a numerical based or a mathematical data processing software package. Fig. 1.6 gives an overview of different software packages utilised in the process. As is evident from this figure, each software performs a specialised function and the so-called 'link-program', which is an interface between the two software programs, is instrumental in making efficient utilisation of individual capabilities of each software. This is further illustrated in the subsequent discussion, where such a link program is described in detail.

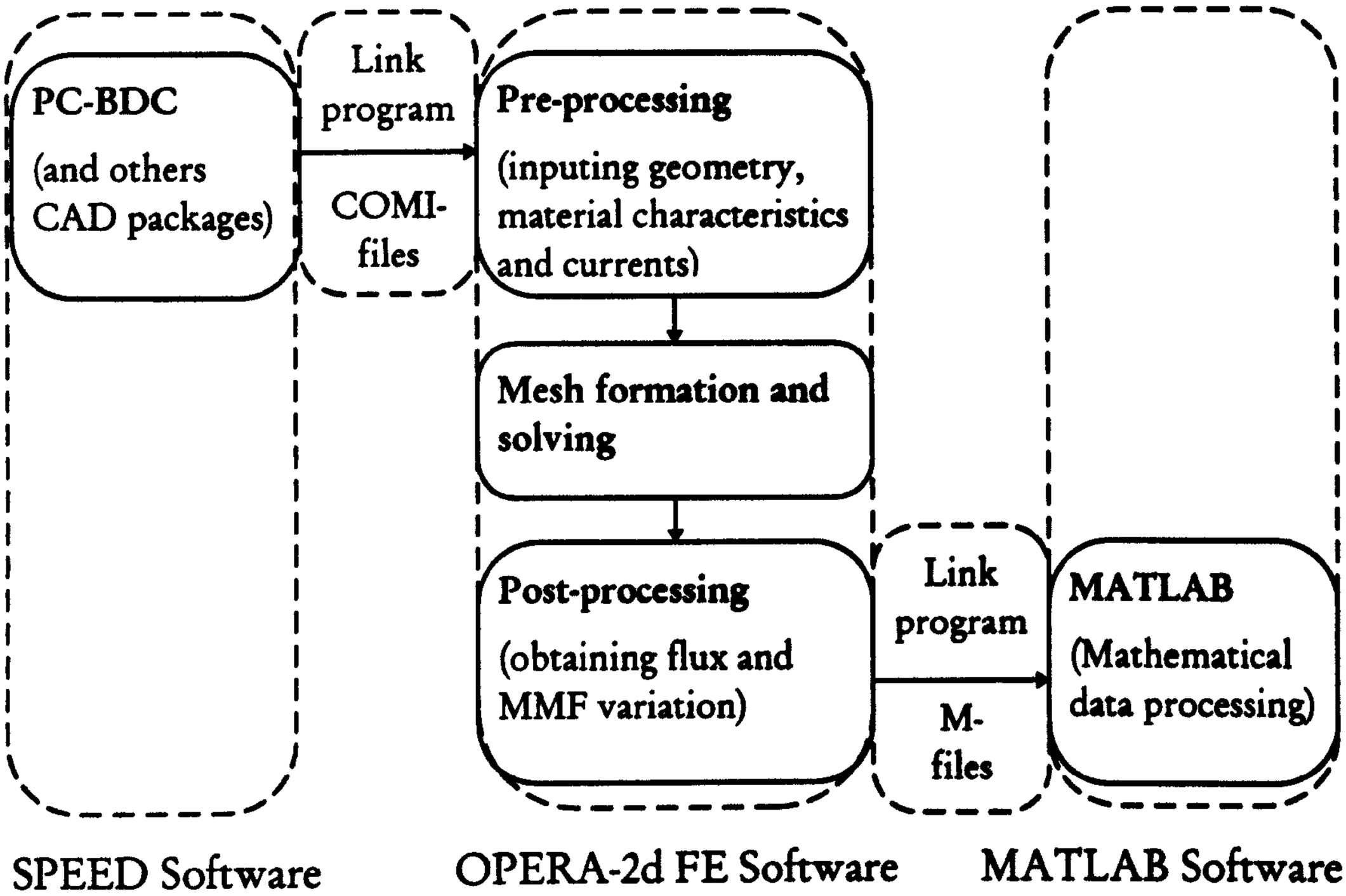

Figure 1.6. Overview of the software packages used in constructing a flux-MMF diagram.

1.6.1 Finite-Element Analysis : An Overview

In recent years, finite-element analysis has established itself as one of the leading numerical techniques for analysing electromagnetic and electromechanical energy conversion devices, because of its accuracy, rigour, robustness and powerful graphical user interface that usually comes along with it. A detailed treatment on modalities and inner workings of a typical finite-element software is considered beyond the scope here. Indeed, the idea is to merely use FE analysis as a tool and exploit many of its features in effectively implementing the flux-MMF diagram technique.

A wide variety of literature is available on the topic of FE analysis and one of the prominent ones is by Lowther and Silvester [66]. For the purpose of understanding, it is sufficient to say that the FE analysis, as applied to the analysis of electrical machines, can be performed in either 2-Dimensional or 3-Dimensional geometries; and in either case, it involves three main stages which are briefly explained as follows.

Pre-processing: This involves building the machine geometry made up of different material regions such as steel, conductors, airgap and magnets; through a user-friendly graphical interface. The appropriate non-linear B-H characteristics are then assigned to different material regions, current densities are assigned to conductor regions, where necessary, and magnetisation directions are assigned to magnet regions. Suitable boundary conditions are specified at the cross-section (or volume, in the case of 3-D analysis) boundaries such that minimal fraction of a machine need be modelled (for example, in many 2-D analyses, a fraction of the cross-section over a pole or a pole-pair is sufficient rather than the full-machine cross-section). The motor cross-section (volume) is then discretised into many smaller areas (volumes), called *finite-elements* of a particular shape; triangular (brick) being the most popular.

Field Solution: The spatial variation of magnetic (vector or scalar) potential throughout the motor cross-section (volume) is described by a non-linear partial differential equation derived from Maxwell's equations. Through the descretisation performed in *pre-processing*, this equation is transformed into a large number of simultaneous non-linear algebraic equations containing unknown node (a node is a vertex of a single finite-element) potentials. These equations are then solved using an iterative numerical procedure to obtain the node potentials.

Post-processing: Here, many useful output quantities such as flux, flux-density, inductance, torque, stored energy, and their spatial and temporal variation; are calculated from the magnetic node potentials. Again, this is done through a graphical interface, usually in common with the one used for pre-processing.

1.6.2 Pre-Processing : The Link Program

This is the first stage in the FE analysis. OPERA-2d—one of the many commercially available finite-element software packages developed by Vector Fields Ltd. [67]—has been used throughout this thesis to perform the required FE analysis. It has its own high-level programming language which can be used for both pre- and post-processing. The so called *link program*, which links the SPEED software with the pre-processing module of the FE software, is written in this language. The programs are stored in *comi-files* and the program listings are given in Appendix B. A few other links have also been developed subsequently in the SPEED Laboratory along similar lines. Some notable examples are the PC-SRD–MagNet link [68] and the PC-SRD–PC-OPERA link [69].

Fig. 1.7 is a flow-chart which elucidates the algorithm used in any generic link program. It typically receives input data from a SPEED software, such as PC-BDC or PC-SRD. This data consists of motor geometry details, material B-H characteristics, winding configuration, and current distribution. This data is then used in the pre-processing stage of the FE analysis, to build the required fraction of the motor cross-section. This is achieved by first creating the *building blocks* for the stator and the rotor. For the stator it is the cross-section over half a *slot* pitch, and for the rotor it is the cross-section over half a *pole* pitch. These building blocks are then simply mirrored and copied a number of times to create complete stator and rotor regions. The appropriate current densities are assigned in the conductor regions and the appropriate directions of magnetisation are assigned in the rotor magnet regions. The airgap regions are then created and the required boundary conditions are assigned, usually on the outer periphery of the entire cross-section modelled. Finally, the mesh is generated and stored, and the whole process is repeated as many times as necessary to create meshes at multiple rotor positions.

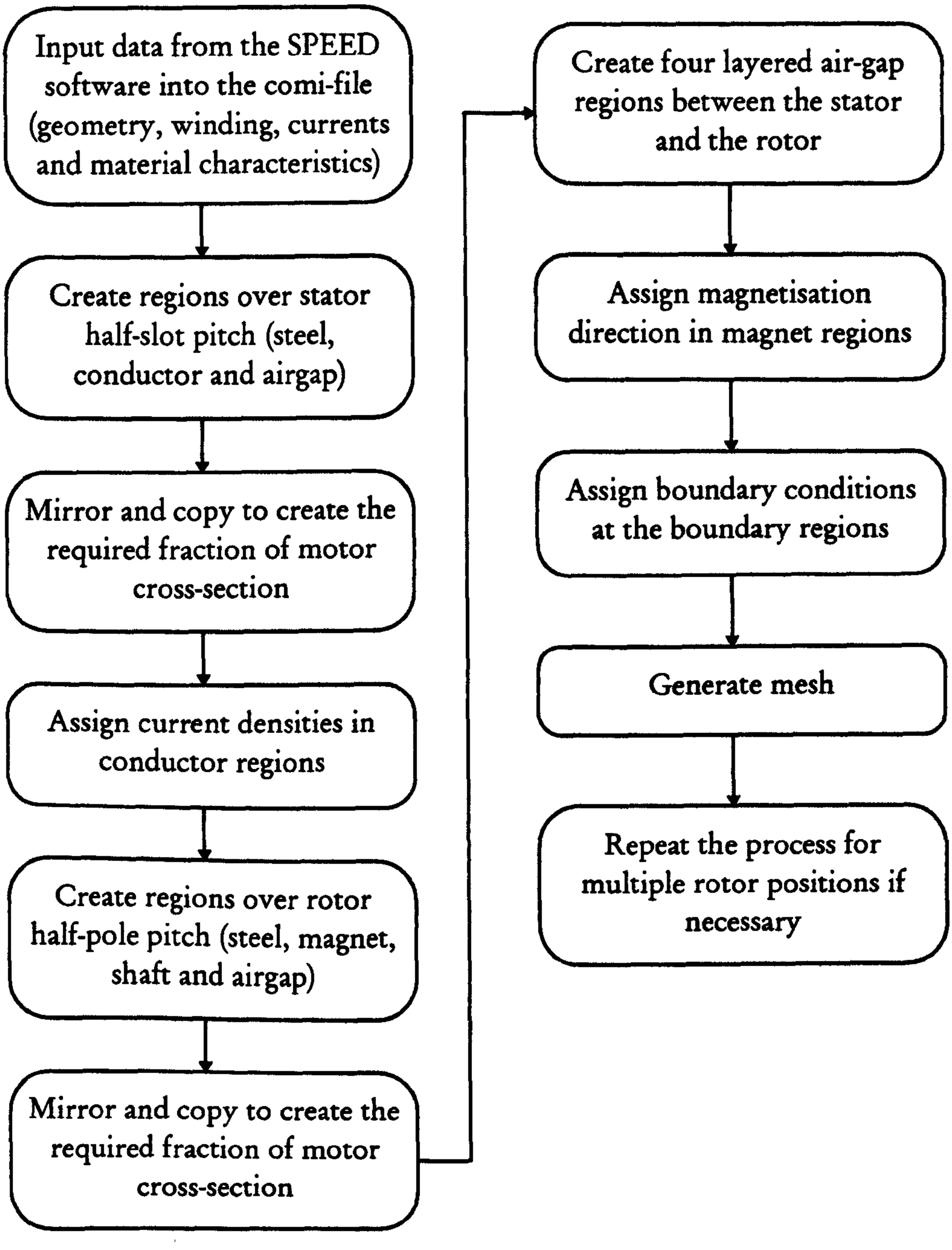

Figure 1.7. Pre-processing link program flow-chart.

The importance of getting the *right kind* of mesh density and distribution throughout the modelled motor cross-section cannot be overstated and there are two important considerations to it.

- The time taken to solve a particular finite-element problem is proportional to the *square* of the number of elements.
- The *global* accuracy is dependent upon the number of elements. Although *local* accuracies may vary depending upon a few other factors.

As far as the total number of finite-elements are concerned, a fine mesh (with a large number of elements) can generate accurate results but with excessively long solution times; whereas a coarse mesh (with a small number of elements) will have short solution times but may not give the required accuracy. Apart from the number of finite-elements, the *distribution* of these elements throughout the modelled motor cross-section is equally important. In general, the mesh needs to be dense in places where the flux-density gradient is high, for example near tooth tips and slot edges; and it needs to be sparse in places where the flux-density gradient is not so high, for example in stator and rotor yoke, and shaft.

An optimised mesh is a best compromise between the solution time and accuracy. It is here that the *art* of mesh-building, itself a combination of skill and experience, plays an important role. One of the significant contribution of the link program is the *automatic* incorporation of this expertise into the software such that it is almost transparent to the user. For example, the assignment of number of subdivisions along every region boundary (called a *face* in 2-D FE parlance), which essentially decides the resultant mesh density and distribution, is *built-in* within the program. This is an important feature, as it obviates the need for the user to spend a lot of time and learn all the necessary skills involved in building an optimised mesh.

1.6.3 Sliding Mesh Generation and Solution

This is the second stage in the FE analysis. In order to obtain variation of flux-linkage with current *and* rotor position, the exercise of building motor geometry and generating mesh is repeated for a series of incremental rotor positions. This is the last step in the flow-chart shown in Fig. 1.6. Once the meshes for all the required rotor positions are generated and stored, the next step is to create solutions for all the meshes at different current values (*scale factors* in FEA parlance).

Important parameters such as the maximum number of iterations to be performed, the extent of accuracy desired, and the scale factors at which the solutions need to be created, are specified in the form of a batch file. The solutions are finally created and stored by running this batch file under the given operating system. Of all the three stages involved in FE analysis, the solution stage needs maximum amount of computing resources in terms of solving time, memory usage and storage space.

The computing time and the storage space required for a particular solution directly depend upon the number of elements in an FE formulation. For example, Figs. 1.8 and 1.9, show the meshes generated at two different rotor positions for the motor of Fig. 1.11, over quarter of a cross-section. In terms of the number of elements and the number of nodes, the two meshes are identical, as they both have 3548 elements and 1826 nodes.

It is important to realise that the mesh itself does not alter in any way from one rotor position to the next. This is achieved through a process called the *sliding mesh generation*. As the term suggests, in this kind of problem formulation, the mesh literally *slides* along the face in the middle of the four airgap regions, shown in Fig. 1.10, as the rotor moves from one rotor position to the next. This means that the two airgap layers adjacent to the rotor surface move along with the rotor; while the two airgap layers adjacent to the stator surface remain stationary.

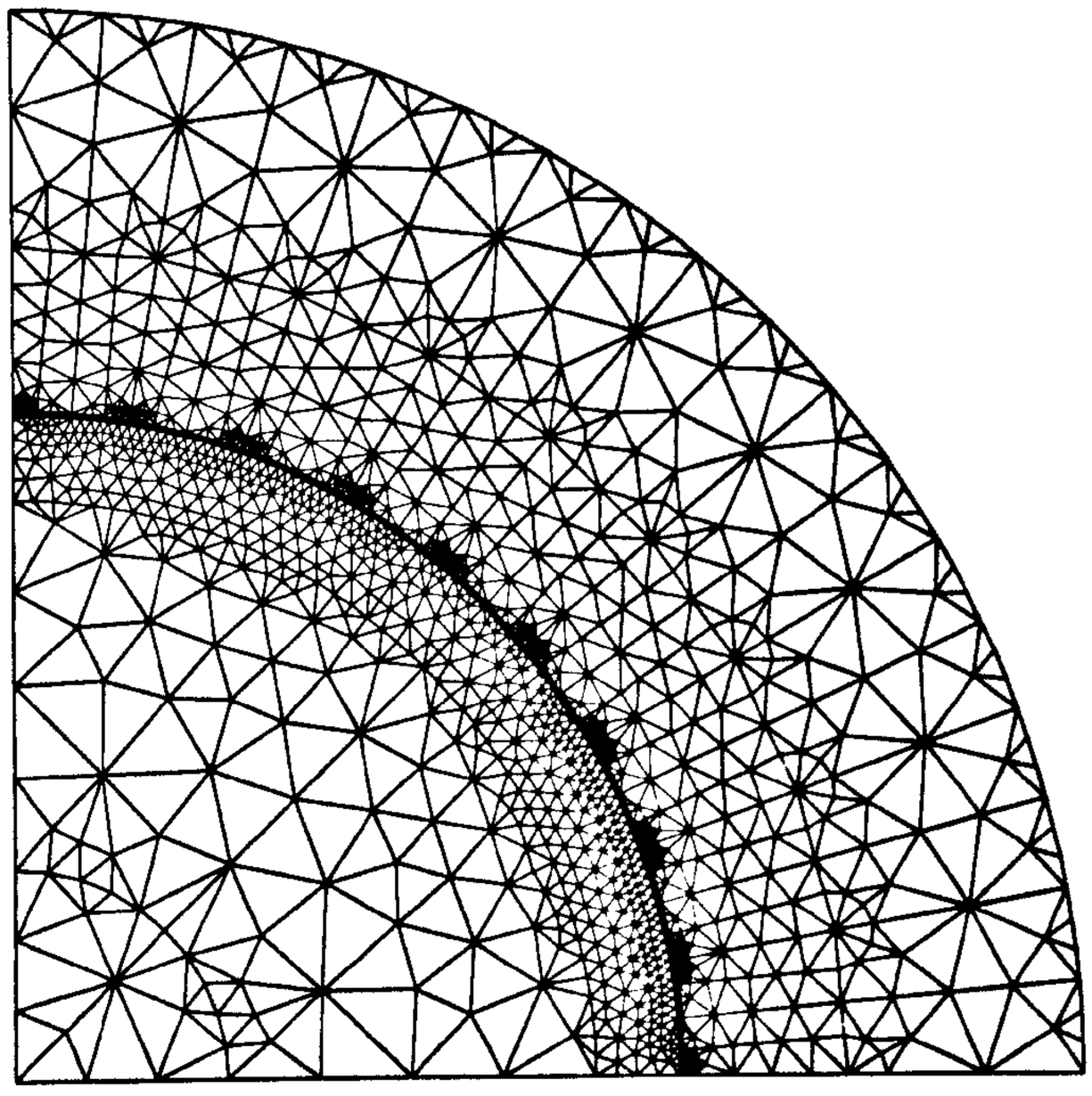

Figure 1.8. Finite-element mesh at 0° rotor position for a brushless PM machine.

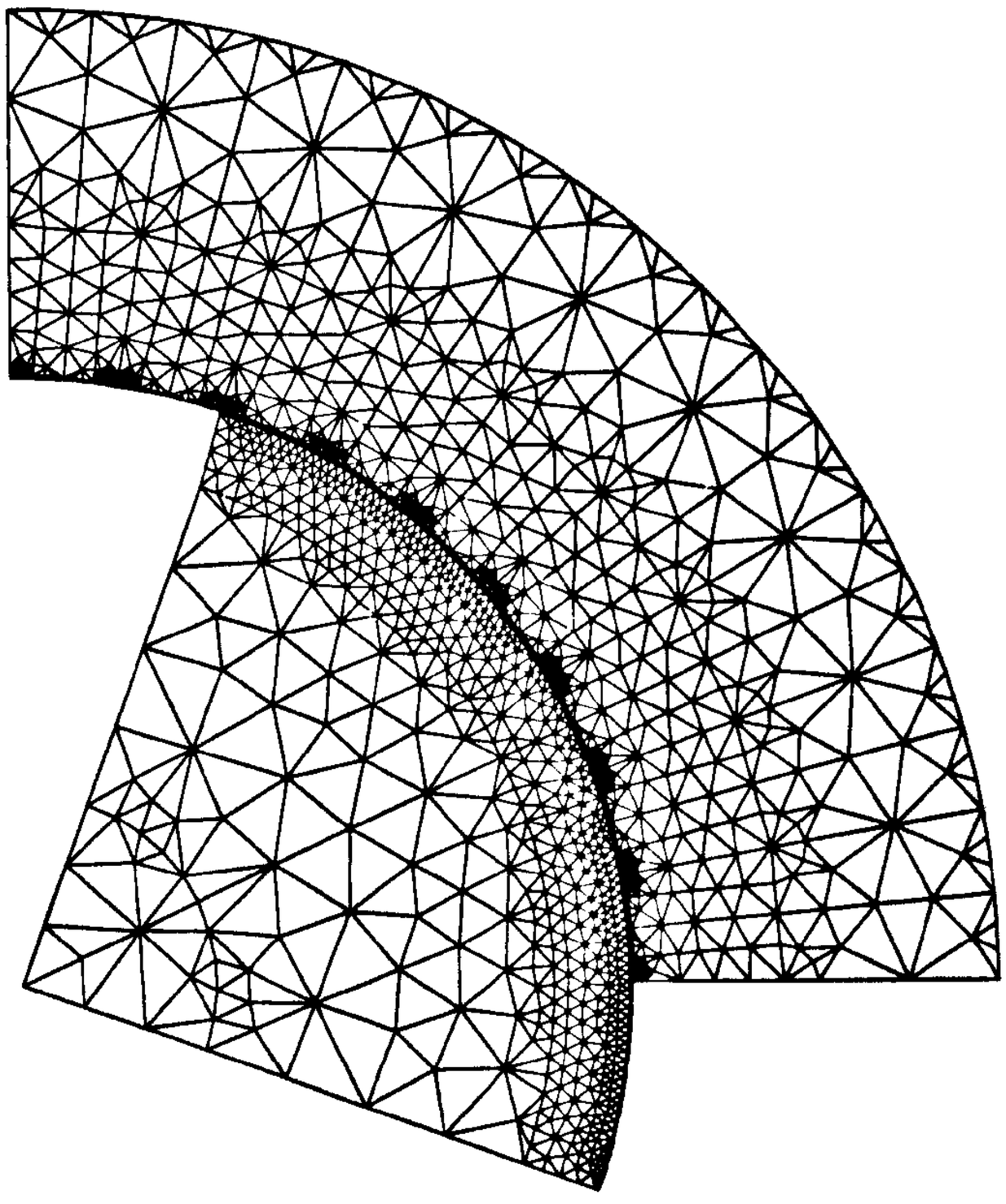

Figure 1.9. Finite-element mesh at 20° rotor position for the same brushless PM machine.

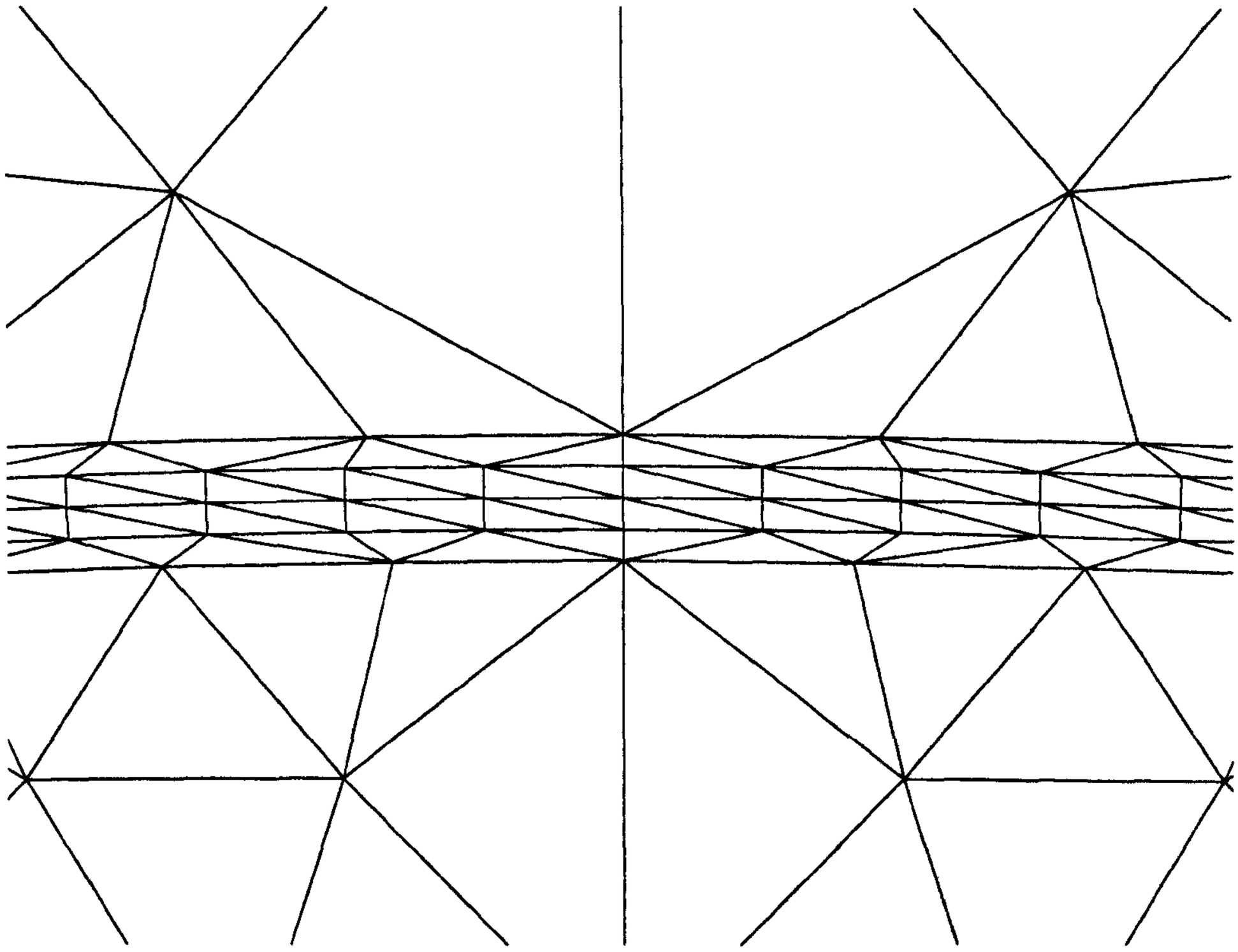

Figure 1.10. A magnified view of the finite-element mesh showing a four-layered airgap region.

In order that the mesh is *stitched* properly at all rotor positions, and that the nodes at the sliding interface are equally spaced, it is required that the minimum increment in rotor position is the same as the unit sub-division along the sliding face. For example, if a quarter of a motor cross-section (i.e. over 90°) is modelled, and if the number of sub-divisions along the sliding face is 90, then the minimum possible increment in rotor position is 1°. While this imposes a restriction on the resolution that can be achieved in rotor movement, it has two main advantages.

- The mesh generation times are reduced substantially.
- The global as well as local errors, to whatever extent they may be throughout the motor cross-section, are *maintained constant* at all rotor positions.

The second advantage is especially important as it helps in implementing the principle of virtual work with good amount of accuracy and confidence. This has also been pointed out in [66]. Briefly, it can be explained as follows.

Equation (1.6) gives the principle of virtual work, (1.4), in the form of numerical differentiation. This form has been used throughout the thesis for calculating torque in an electrical machine.

$$T_e = \frac{W'_2 - W'_1}{\theta_{12}} \tag{1.6}$$

Where,

T_e is the instantaneous electromagnetic torque

W'_1 is the coenergy at position 1.

W'_2 is the coenergy at position 2.

θ_{12} is the amount of displacement between positions 1 and 2.

Typically, the change in coenergy over a small displacement is only a very small fraction of the total coenergy at any one rotor position. This means that the *difference* in coenergy, the numerator of (1.6), turns out to be a very small number calculated from subtracting two almost equal and large numbers corresponding to coenergies at two rotor positions. Now, if the error inherent in calculating W'_1 is say, e_1 and similarly for W'_2 it is e_2, then the numerator of (1.6) is given by,

$$(W'_2 + e_2) - (W'_1 + e_1) = (W'_2 - W'_1) + (e_2 - e_1) \tag{1.7}$$

This shows that, whatever may be the errors in estimating coenergies at different rotor positions (e_1 and e_2), as long as they are of almost the same value and sign, the *difference* in coenergy is bound to be accurate. Thus, as mentioned earlier, the sliding mesh generation ensures that the errors involved in calculating coenergies at different rotor positions are maintained constant. It also reduces the solution times and helps in making efficient utilisation of computing resources. Both these advantages would be

lost if the meshes were to be different and generated individually for every rotor position.

1.6.4 Post-Processing

This is the third and the final stage of the FE analysis. Although many different quantities, as mentioned earlier, could be obtained through post-processing, with regard to the FMDT, the only quantity of interest is the variation of flux-linkage with current and rotor position. This is obtained by executing programs written in the same high-level programming language as used in pre-processing. The programs are stored in *comi-files* and the program listings are given in Appendix B.

Once the information on variation of flux-linkage with current and rotor position is obtained in the form of a matrix, it is processed using MATLAB [70], which is one of the many commercially available software packages for mathematical data processing. The programs are written in MATLAB's own programming language and stored in *m-files*. They are used to construct the flux-MMF diagram, calculate torque, and obtain other information such as the effect of skew and saturation on torque. The MATLAB program listings are given in Appendix C.

1.6.5 Using Symmetry

In an ideally symmetrical multi-phase electrical machine, the current waveforms and the winding configuration are identical for all the phases except that they are phase shifted in time and space respectively. This symmetry can be exploited in constructing flux-MMF diagram for any one phase, in such a way as to make an efficient utilisation of the finite-element method and minimise the computing resources needed. This is best explained with the help of an example.

Fig. 1.11 is the cross-section of a 3-phase, 4-pole, PM brushless AC machine. The details of its design are explained in Chapter 6, where it has been used for the comparative evaluation of several different types of electrical machines. Fig. 1.13 shows the flux-MMF diagram for any one phase of this machine, which has been constructed by executing the series of steps outlined in the foregoing discussion, including the FE analysis. Fig. 1.12 shows a typical flux-plot at no-load obtained from the FE analysis.

The flux-MMF diagram consists of six flux-MMF trajectories for six phase current values ranging from 0 to 20 A RMS. Each one of these flux-MMF trajectories represents the variation of phase flux with position plotted against the variation of phase MMF with position for a given phase current. Figs. 1.14 and 1.15 show these variations of the flux and MMF respectively. Roughly speaking, sine variation of MMF leads to a cosine variation of flux, and this is the reason why the flux-MMF trajectories are elliptical when the flux is plotted against the MMF.

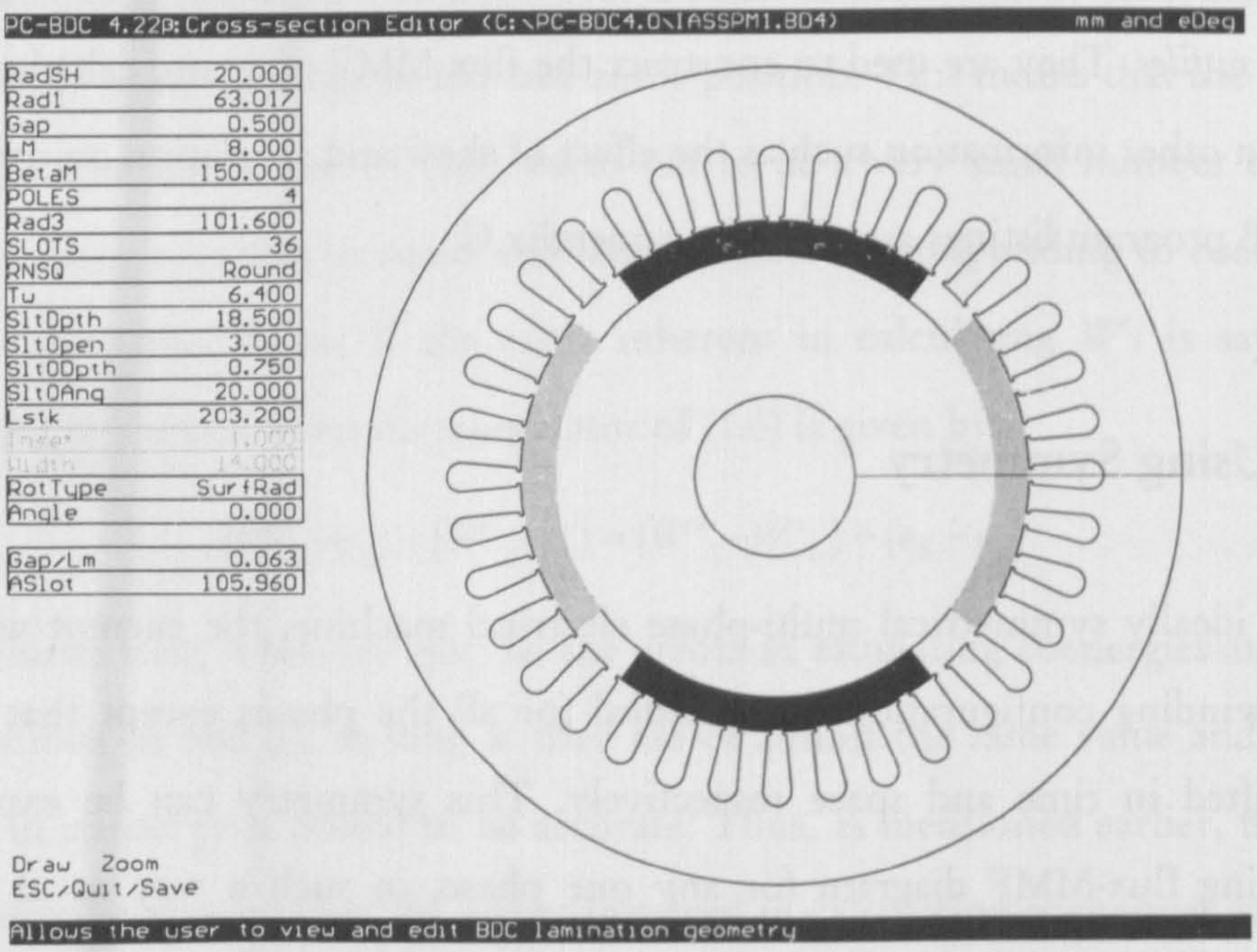

Figure 1.11. Cross-section of the 3-phase, 4-pole PM brushless AC motor.

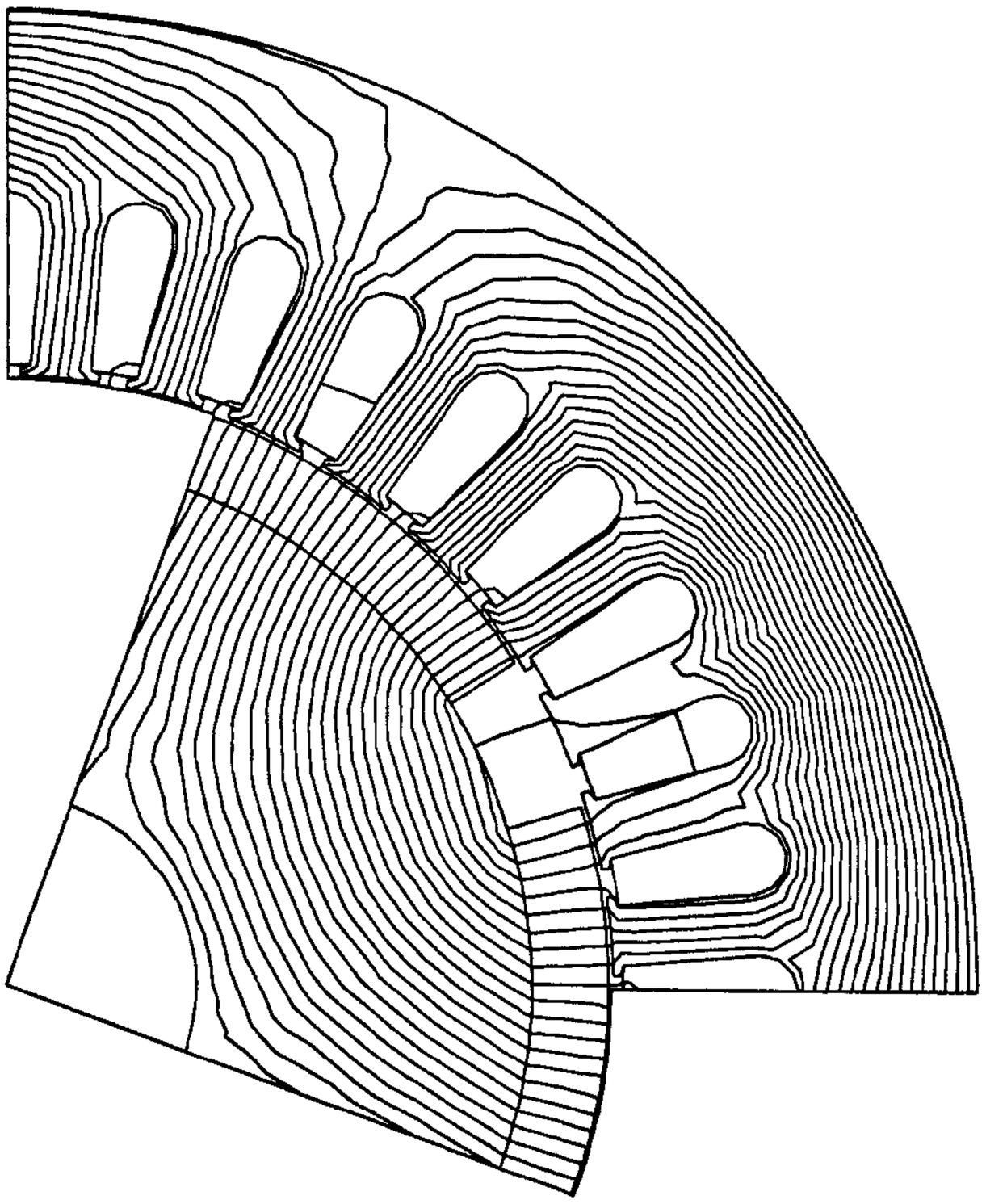

Figure 1.12. PM brushless AC motor flux-plot obtained from the FE analysis.

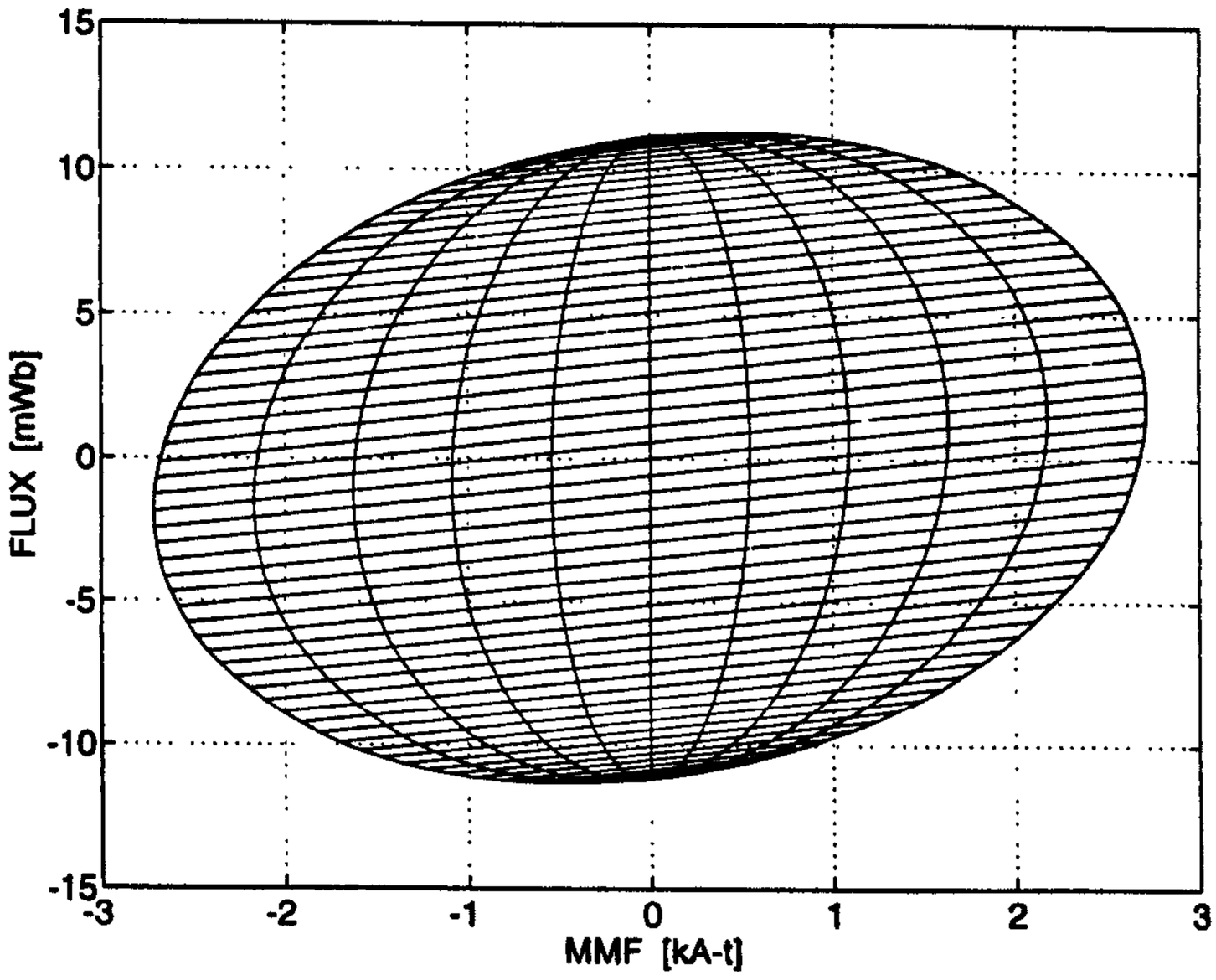

Figure 1.13. Flux-MMF diagram for any one phase of the PM brushless AC motor.

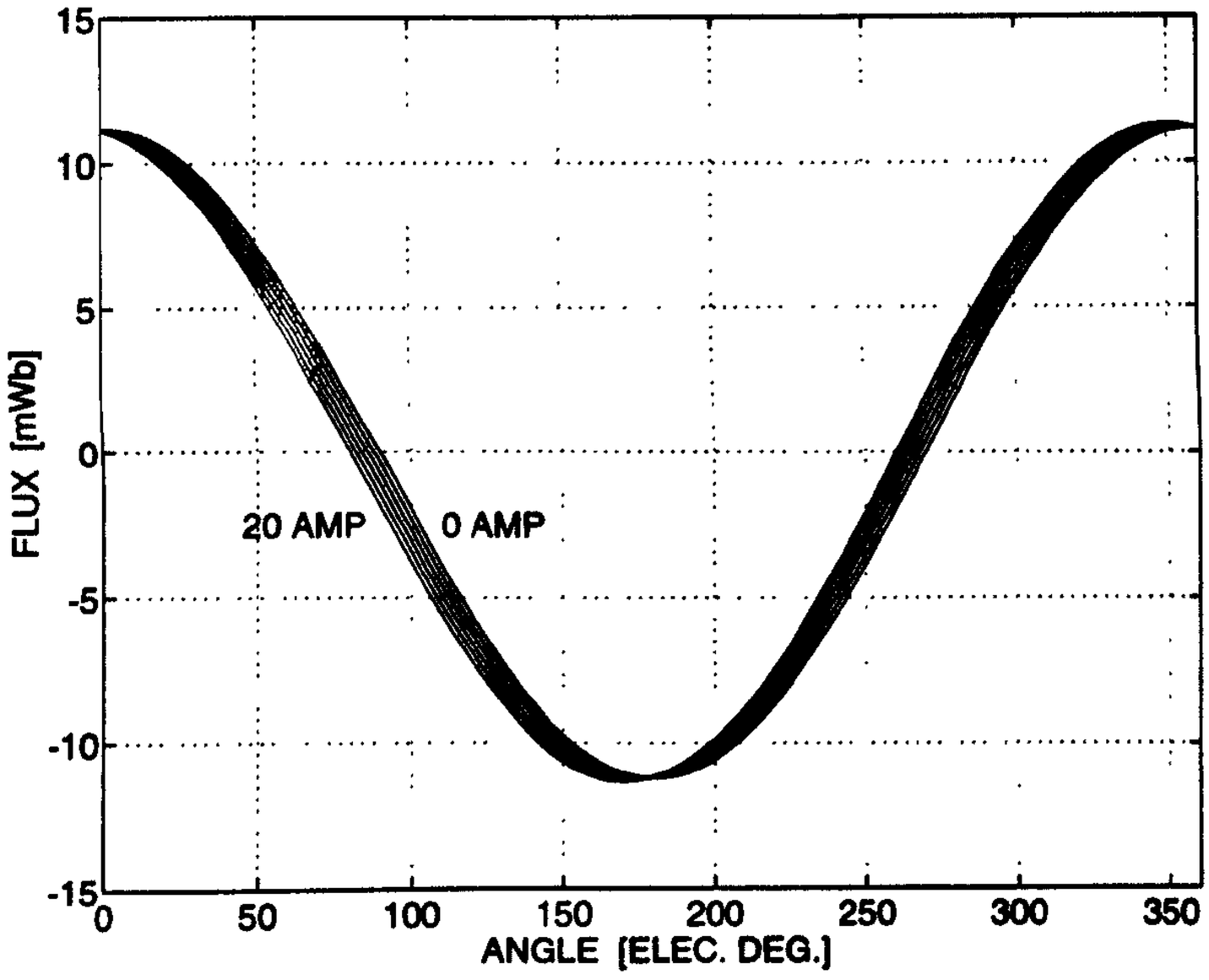

Figure 1.14. Variation of phase flux with position at increasing RMS phase currents.

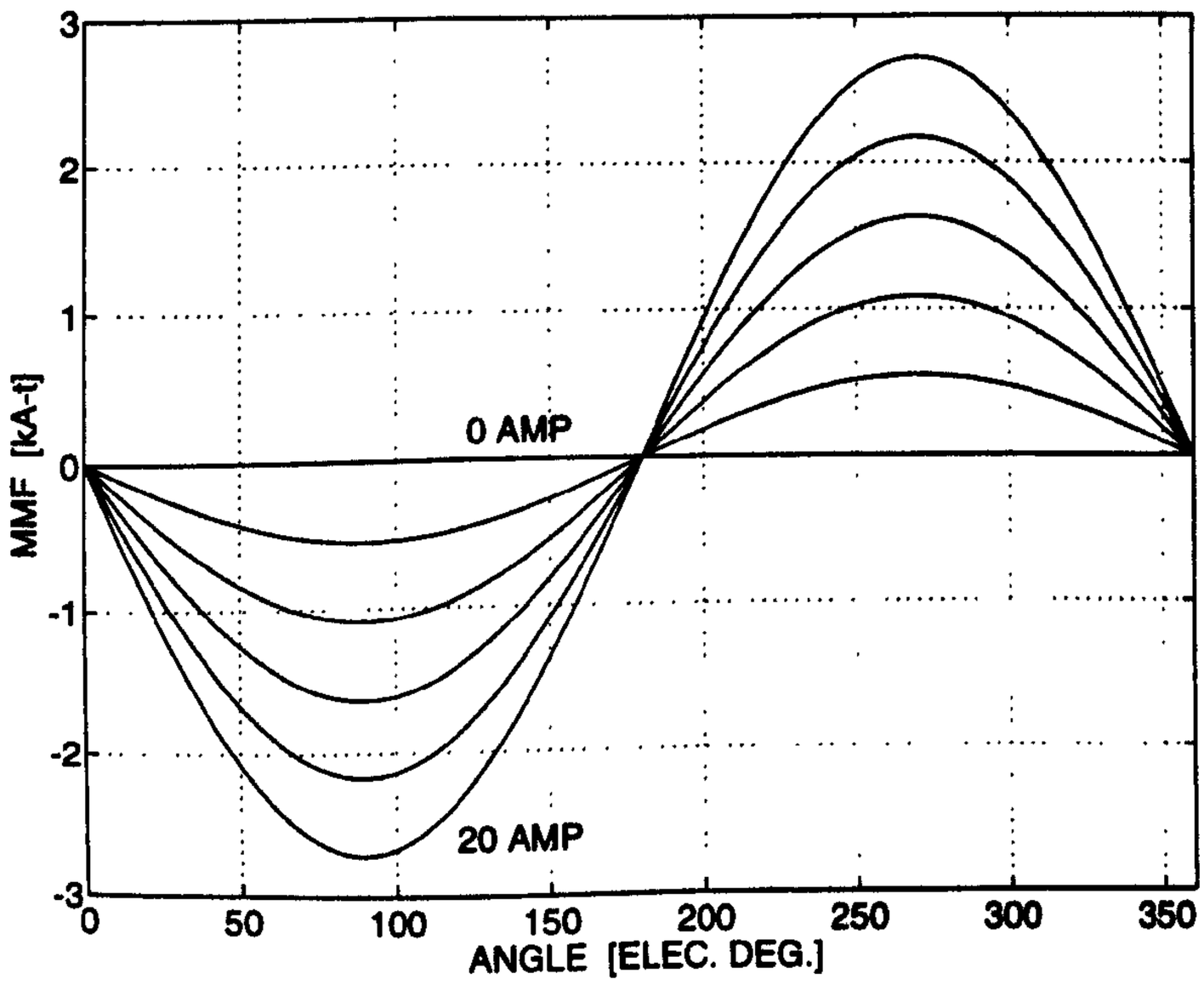

Figure 1.15. Variation of phase MMF with position at increasing RMS phase currents.

Fig. 1.13 also has magnetisation curves corresponding to 120 rotor positions over one electrical cycle (360° elec.). This gives an incremental spacing of 3° elec. (1.5°

mech.). Thus there are 6×120=720 data points in total, in the flux-MMF plane; and these points completely define the flux-MMF diagram. In the absence of any symmetry, the FE analysis would need 120 meshes at 120 rotor positions over one electrical cycle. These meshes would then need to be solved for 6 scale factors corresponding to six current values, needing 720 solutions in total, to construct the flux-MMF diagram of Fig. 1.13. However, by exploiting the symmetry which exists in a 3-phase sinewave current waveforms, the same diagram can be constructed using just 20 meshes and 6×20=120 solutions. This can be realised from Fig. 1.16 which shows the 3-phase current waveforms used in FE analysis.

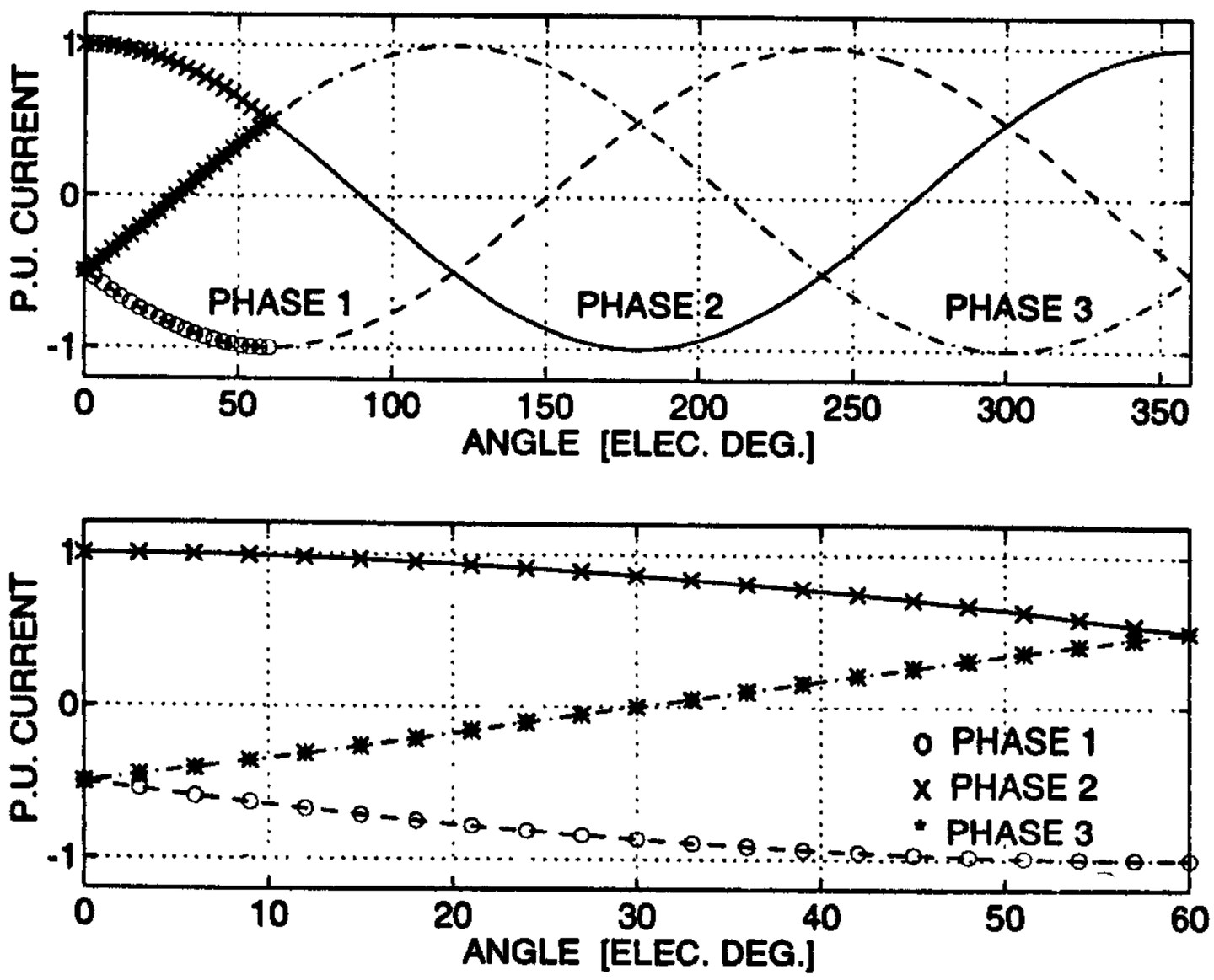

Figure 1.16. 3-phase current waveforms used in FE analysis. The top half shows waveforms over one electrical cycle while the bottom half shows the same over 1/6th of an electrical cycle.

The top half shows waveforms over one electrical cycle while the bottom half shows the same over 1/6th of a cycle. It can be seen from this figure, that the current waveform for any one particular phase over one electrical cycle can be reconstructed from the *components* of the 3-phase waveforms over 1/6th of a cycle. These

components are displayed in the bottom half of Fig. 1.16, which is a magnified view of the top half. The actual rotor positions, for which FE analysis is performed, are also shown in Fig. 1.16. These are 21 rotor positions over a total displacement of 60° elec. with an increment of 3° elec. Thus, by extracting the information, such as flux-linkage variation, over $1/6^{th}$ of an electrical cycle for all the three phases, the flux-linkage variation for any one particular phase over one cycle can be reconstructed.

Fig. 1.17 displays the constituent portions of the flux-MMF diagram of Fig. 1.13. These are constructed using the flux-linkage variation data for each of the three phases calculated over $1/6^{th}$ of an electrical cycle. The data points on the left, indicated by solid lines, are calculated from FE analysis; while those on the right, indicated by dotted lines, are simply derived from those on the left by using *mirror* symmetry.

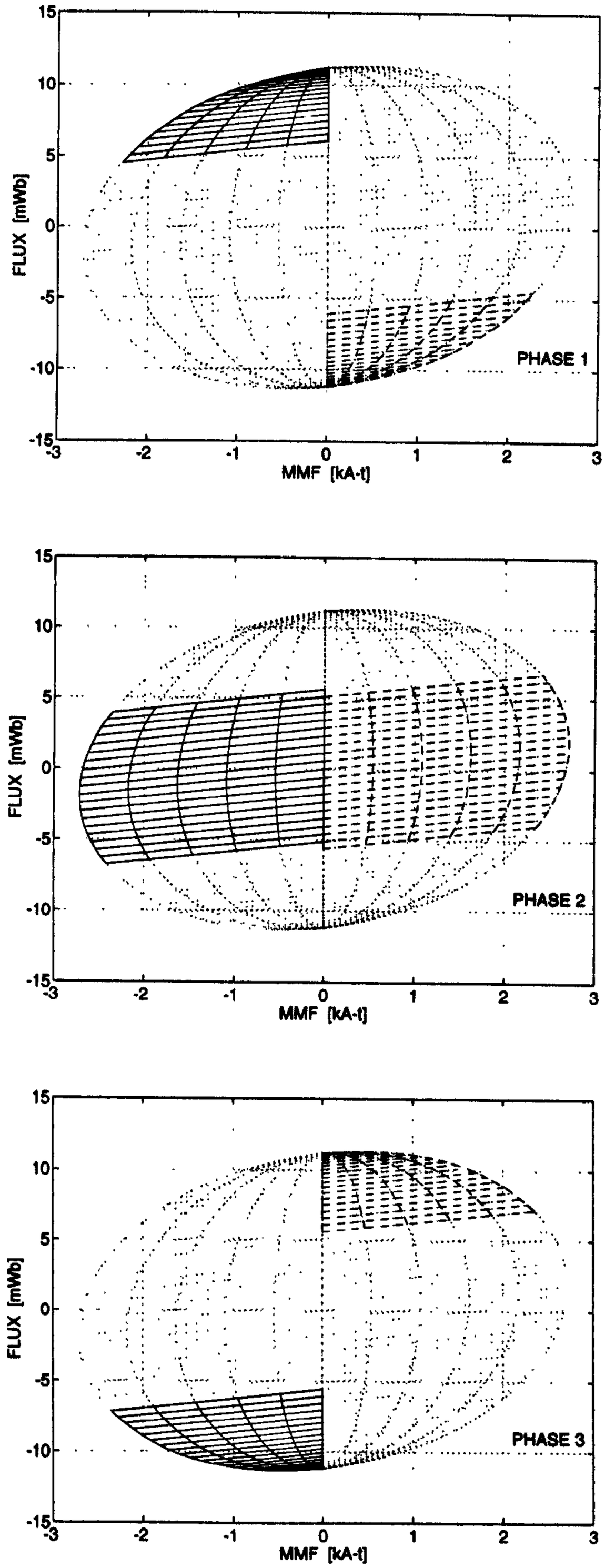

Figure 1.17. Constituent portions of the flux-MMF diagram of Fig. 1.13.

1.7 Chapter Summary

Chapter 1 has introduced the concept of the flux-MMF diagram. It has shown how the flux-MMF diagram has evolved from its more established and familiar forerunners such as the ψ-i diagram and the principle of virtual work. It elaborates on the process of constructing a flux-MMF diagram using the finite-element analysis, and brings out its salient features. It gives a brief overview of the steps involved in carrying out the FE analysis and includes the algorithm developed for the PC-BDC–OPERA FE link program. It shows how to use the symmetry that exists in a normal multi-phase machine, to minimise the computing resources needed for carrying out the FE analysis. The chapter also summarises the original contribution of the thesis and gives an outline of its structure.

2 Electromagnetic Torque Ripple

2.1 Introduction

Prediction of electromagnetic torque ripple is the most significant application of the flux-MMF diagram technique. While Chapter 1 has focused on the evolutionary and constructional aspects of the flux-MMF diagram, this chapter concentrates on applying the flux-MMF diagram to predict variation of instantaneous electromagnetic torque with rotor position and load current. The exact definitions for the terms *electromagnetic torque ripple* and *cogging torque ripple* are given in Chapter 1 and there is a clear distinction between the two.

While the term *electromagnetic torque* itself refers to the *main* torque generated in an electrical machine due to the interaction between magnetic field and electric current, the term *cogging torque* refers to the *auxiliary* or *parasitic* torque generated due to the interaction between magnetic field and a slotted armature, and it exists even when there is no electric current. Chapter 3 deals exclusively with cogging torque and its prediction using the flux-MMF diagram technique and in this chapter, attention is focused on electromagnetic torque.

The next section presents a literature review of the established techniques used for predicting torques and forces in any electromechanical device in general. Section 2.3 illustrates the procedure of predicting electromagnetic torque ripple with examples of PM brushless AC and DC motors. Section 2.4 describes an alternate method of doing the same using static torque characteristics. Experimental validation is presented where appropriate.

2.2 Literature Review

The topic of finite-element based force and torque calculations in electrical machines has been treated extensively in the published literature [8]–[20]. Three prominent methods are described.

2.2.1 Lorentz Force Method

The most general expression for the force acting on an electrically charged moving particle in the presence of an electric and a magnetic field is given by [7],

$$\mathbf{F} = Q\mathbf{E} + Q(\mathbf{v} \times \mathbf{B}) \tag{2.1}$$

where,

F is the Lorentz force vector.

Q is the electric charge on the moving particle.

E is the electric field vector.

v is the velocity vector for the moving particle.

B is the magnetic field vector.

This is known as the *Lorentz force* expression, so named after H. A. Lorentz. In an electrical machine, only the second term on the right hand side of (2.1) is considered; in which case, the expression reduces to a more simpler and familiar form given by,

$$F = Bil \sin\theta \tag{2.2}$$

where, F is the force on a linear current-carrying conductor of length l, carrying current i, placed in a uniform magnetic field B. Equation (2.2) is a scalar equation and relates only the magnitude of the quantities involved. However, the force vector **F** is perpendicular to both **I** and **B**, and θ in this case is the angle between **I** and **B**.

The Lorentz force method is often considered to be the most direct and reliable method for calculating force on a current-carrying conductor since it is based on experimental evidence [17]. It is most commonly applied in analytical formulations of electrical machines (rather than finite-element formulations) where a slotless armature is assumed with conductors uniformly distributed in the airgap. Physically, however, this is not the case for the great majority of machines. Also, this method is incapable of predicting such effects as cogging torque which are present even in the absence of any current [20].

2.2.2 Maxwell Stress Method

James Clerk Maxwell, in his *Treatise on Electricity and Magnetism* [2], proposed a system of stresses, expressed in terms of field quantities such that, by integrating the stresses along a closed path, C, surrounding a moving component, the total force on the component could be computed. The expressions for stresses are given as follows [11], [17].

$$f_n = \frac{1}{2\mu_0}(B_n^2 - B_t^2) \tag{2.3}$$

$$f_t = \frac{1}{\mu_0} B_n B_t \tag{2.4}$$

where f is the force per unit area and B is the flux-density. The subscripts n and t denote the components normal and tangential to the contour C respectively.

The Maxwell stress method is valid for computing force on non-linear as well as linear materials and for current-carrying as well as current-free regions. However, the use of (2.3) and (2.4) requires that the contour C be closed and situated entirely in linear material. This is by far the most popular method of force and torque calculation in finite-element formulations. Many of the recent studies on Maxwell

stress have either tried to extend and generalise this method [8]–[10], or reported the sources of possible errors in calculations and ways of improving accuracy by proper choice of the contour for integration [11]–[12], [17].

Carpenter [8] has given the first comprehensive account of the Maxwell stress method in recent years. Penman and Grieve [9] have proposed an extension of this method by applying it in conjunction with the dual-energy or complementary-energy approach. Chang et al. [10] have presented a modified form of this method by means of an area integration over the airgap region rather than the usual contour integration to improve accuracy and robustness of the method.

Tärnhuvud and Reichert [11], McFee and Lowther [12], and DeBortoli and Salon [17] have all discussed the accuracy problems and the sources of errors encountered in applying the Maxwell stress method. In some cases, they have also suggested possible means of alleviating such difficulties. The overall conclusions of these studies are:

1. The optimal path for integration can be constructed in one the following ways.

- A path joining the centroids of neighbouring elements
- A path crossing elements by joining the midpoints of two of their sides
- A path crossing perpendicular to each element boundary

2. Since only a small fraction of total number of finite-elements, those which are in the path of integration, are used in obtaining force; this tends to magnify the effect of local field errors. To address this problem, an average value of forces obtained from several paths can be taken, thereby increasing the number of elements contributing to the force computation.

2.2.3 Virtual Work Method

The *principle of virtual work* has been described in detail in Chapter 1, however, as far as implementation of this method using finite-element analysis is concerned, many

variations are possible [13]–[16], [86]. Indeed, as mentioned earlier, the flux-MMF diagram technique is just one such variation. Briefly, in this method, a numerical differentiation of coenergy with respect to position is performed at constant current to compute the resultant force. As against the Maxwell stress method where only one field solution is needed, this method requires at least two field solutions to compute the force and thus becomes computationally expensive.

To circumvent this difficulty, Coulomb and Meunier [13]–[14] have proposed a single-solution implementation of the virtual work method. In this approach, the movable portion is not displaced physically; instead, the so-called *virtual displacement factors*, v, are assigned to each and every node of the mesh, indicating their relative virtual displacement. All nodes within the movable portion have $v=1$ and all nodes within the fixed portion have $v=0$. Nodes within the space which is enclosed by the movable and the fixed portions (the airgap) are assigned values of v such that $0 \le v \le 1$, with higher values assigned to nodes nearer the movable portion. In this way, the computation of force is spread over the entire region modelled, lessening effects of local field inaccuracies. Freeman and Ashen [15], and Aronson and Brauer [16] have also proposed one-solution schemes for employing virtual work method, and these are essentially variations of the original scheme described above.

With regard to the two-solution implementation of the virtual work method, there are different ways of estimating system coenergy. The most commonly employed approach is to calculate coenergy associated with the entire system. Some others, for example De La Ree and Boules [86], have considered only the energy or coenergy associated with the airgap region arguing that the energy stored in the iron portions can be assumed to be negligible. This assumption, though simplifying the method, is also its limitation.

2.2.4 Comparative Evaluation

Many comparative studies of the three methods mentioned above have been performed [17]–[19]. The overall conclusions from these studies could be summarised as follows.

- In finite-element analysis in general, field estimation is more accurate than the force estimation obtained from it.
- Different methods of force and torque estimation do not always yield the same result and even if they do, there is no guarantee that the result obtained is the correct one.
- None of the three methods distinguishes itself as the most accurate, consistent, or reliable. All methods should be used with due consideration for the problem at hand, the amount of computational expense that can be afforded, and the possible sources of error.

It is worth mentioning at this point that the flux-MMF diagram technique can be distinguished from the other virtual work based methods, described above, in many different ways. Table 2.1 summarises these distinguishing characteristics.

Table 2.1. Distinction between the FMDT and the other virtual work based methods.

Coenergy Calculation	Other virtual work based methods	Flux-MMF diagram technique
What coenergy?	Either associated with the entire system or the airgap region	Either associated with the coil, phase or the permanent-magnet
How is it calculated?	Directly, from the FEA	Indirectly, from the flux-linkage variation with position and current
What about the accuracy of coenergy calculations at a particular position?	Affected by the local field inaccuracies encountered in the airgap regions	Does not involve airgap regions, hence not affected by those inaccuracies
What about the accuracy of 'change in coenergy with position' calculations?	Affected by the accuracy of coenergy estimation, if the mesh is different at every position	Unaffected by the accuracy of coenergy estimation, since the mesh is same at every position

2.3 Prediction of Electromagnetic Torque Ripple

Chapter 1 has dealt with the method of constructing the flux-MMF diagram for any one phase of an electrical machine. Having constructed such a diagram, this section deals with the method of predicting electromagnetic torque ripple from it.

2.3.1 PM Brushless AC Motor

Fig. 1.13 from Chapter 1, which shows the flux-MMF diagram for any one phase of a 3-phase PM brushless AC motor is repeated here in Fig. 2.1, with some additional legend for the purpose of explanation. By applying the principle of virtual work in the form of (1.6), as described in Chapter 1, it is possible to obtain instantaneous variation of phase torque with position at six phase current values between 0 and 20 A, as shown in Fig. 2.2. The variation shown is for one electrical cycle, since one traverse round the flux-MMF trajectory represents one electrical cycle. Each point on a phase torque ripple curve, at a particular value of phase current, is obtained by first calculating the area enclosed between magnetisation curves at two adjacent rotor positions. This area represents the change in coenergy. It is then simply divided by the amount of displacement between two adjacent rotor positions to give instantaneous torque.

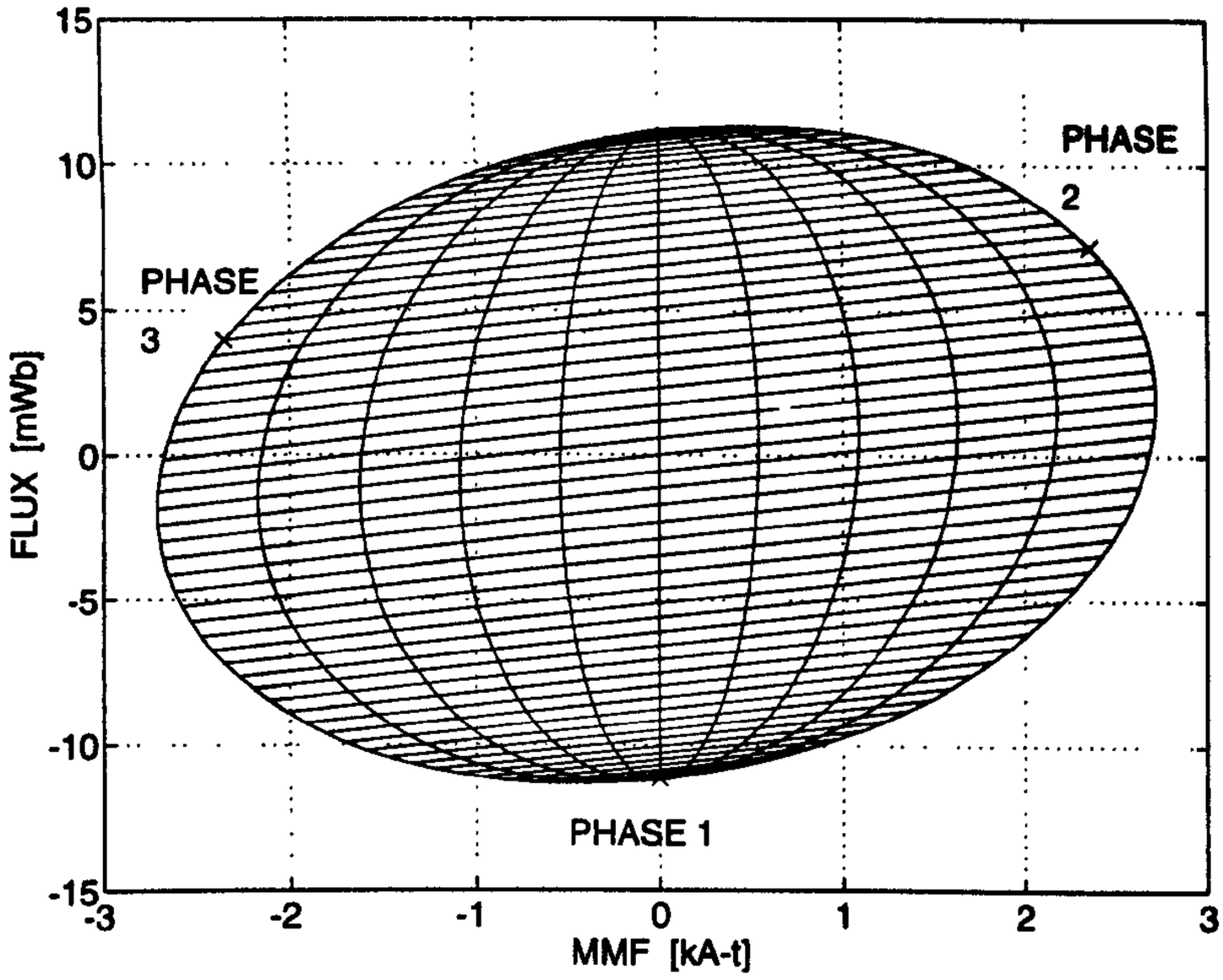

Figure 2.1. Flux-MMF diagram for any one phase of the 3-phase PM brushless AC motor at 0, 4, 8, 12, 16 and 20 A RMS phase currents. The '×' marks indicate operating point at a particular instant for the three phases at 20 A.

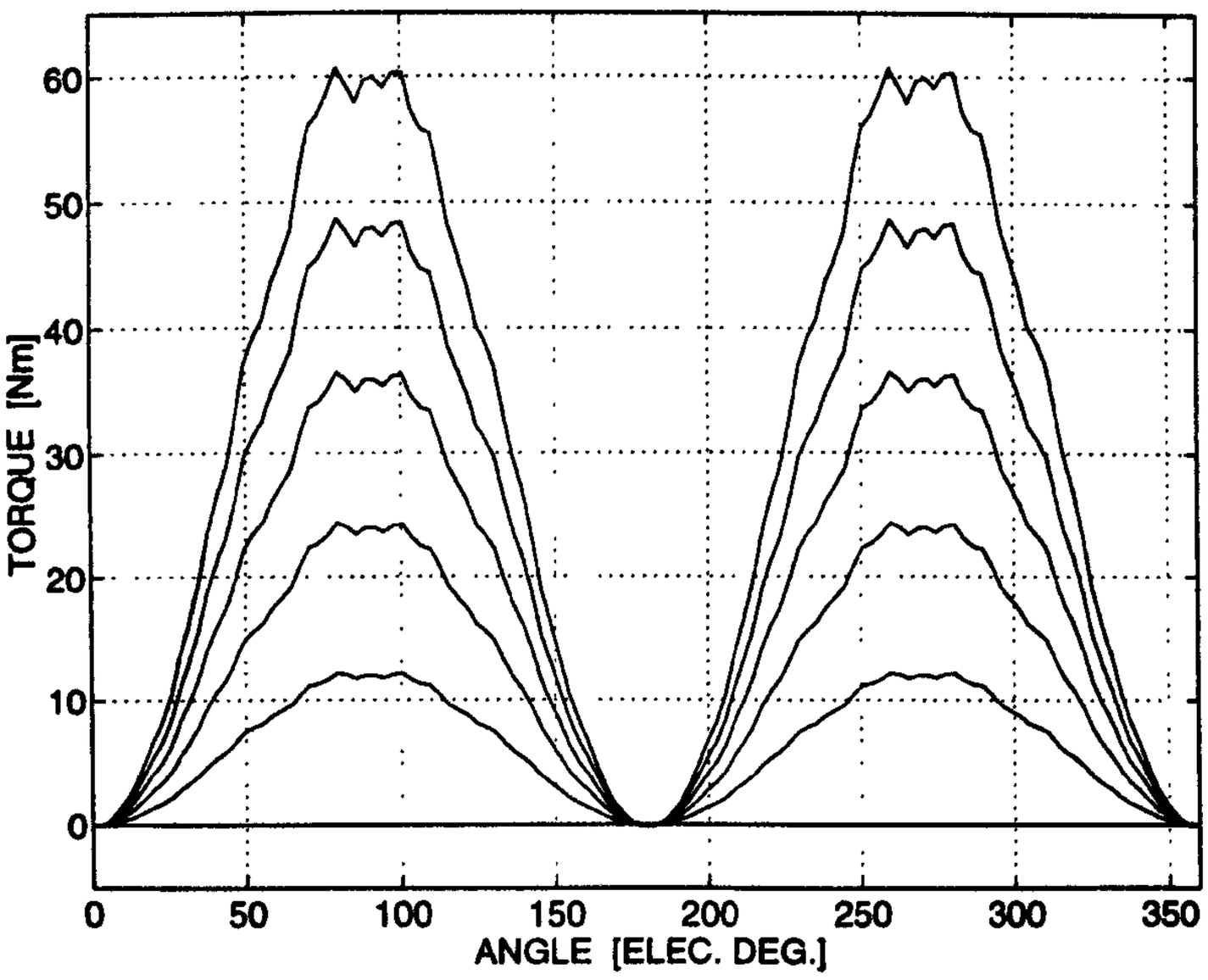

Figure 2.2. Instantaneous variation of phase torque with position for the PM brushless AC motor at 0, 4, 8, 12, 16 and 20 A RMS phase currents.

Having obtained the electromagnetic torque ripple curve for any one phase, the total torque ripple for the entire machine is obtained by simply adding torque contributions from every individual phase. Depending upon the number of phases, these contributions are phase shifted by an appropriate number of electrical degrees. This is shown in Fig. 2.3 where three identical phase torque ripple curves are phase shifted by 120° elec. (since it is a 3-phase machine) and added to obtain the total torque ripple at 20 A RMS phase current.

Note that for any one phase of an *ideal* 3-phase AC machine, when the generated EMF is in phase with the current, the phase torque curve will have the shape of the function $f(\theta)=\sin^2\theta$; since it is a product of two perfectly sinusoidal variations of generated EMF and current. When three such phase torque curves are phase shifted by 120° elec. and added, it can be shown mathematically that the result is a perfectly smooth total torque curve with no 'AC' component of torque ripple. This is shown in Fig. 2.4, which is same as Fig. 2.3, except that an ideal 3-phase machine is assumed.

In a *non-ideal* 3-phase AC machine, however, the presence of stator slotting and imperfectly sinusoidal winding distribution, gives rise to the 'AC' component of torque ripple. Thus, in a sense, the magnitude of the 'AC' component of torque ripple is an indication of the *extent of deviation* from an ideal 3-phase machine. For example, both Figs. 2.3 and 2.4 show an average total torque of 91.07 Nm but Fig. 2.3, which is for a non-ideal machine, shows a peak-to-peak ripple of 8.31%. Whereas Fig. 2.4, which is for an ideal machine, shows no ripple.

The '×' marks in Fig. 2.1 indicate the operating point at a particular instant for each phase on the outermost flux-MMF trajectory of 20 A, and the '×' marks in Fig. 2.3 indicate the corresponding calculated torque values at that instant, for each phase and for the entire machine. Finally, Fig. 2.5 shows the total electromagnetic torque ripple curves calculated in this manner at six phase current values between 0 and 20 A RMS.

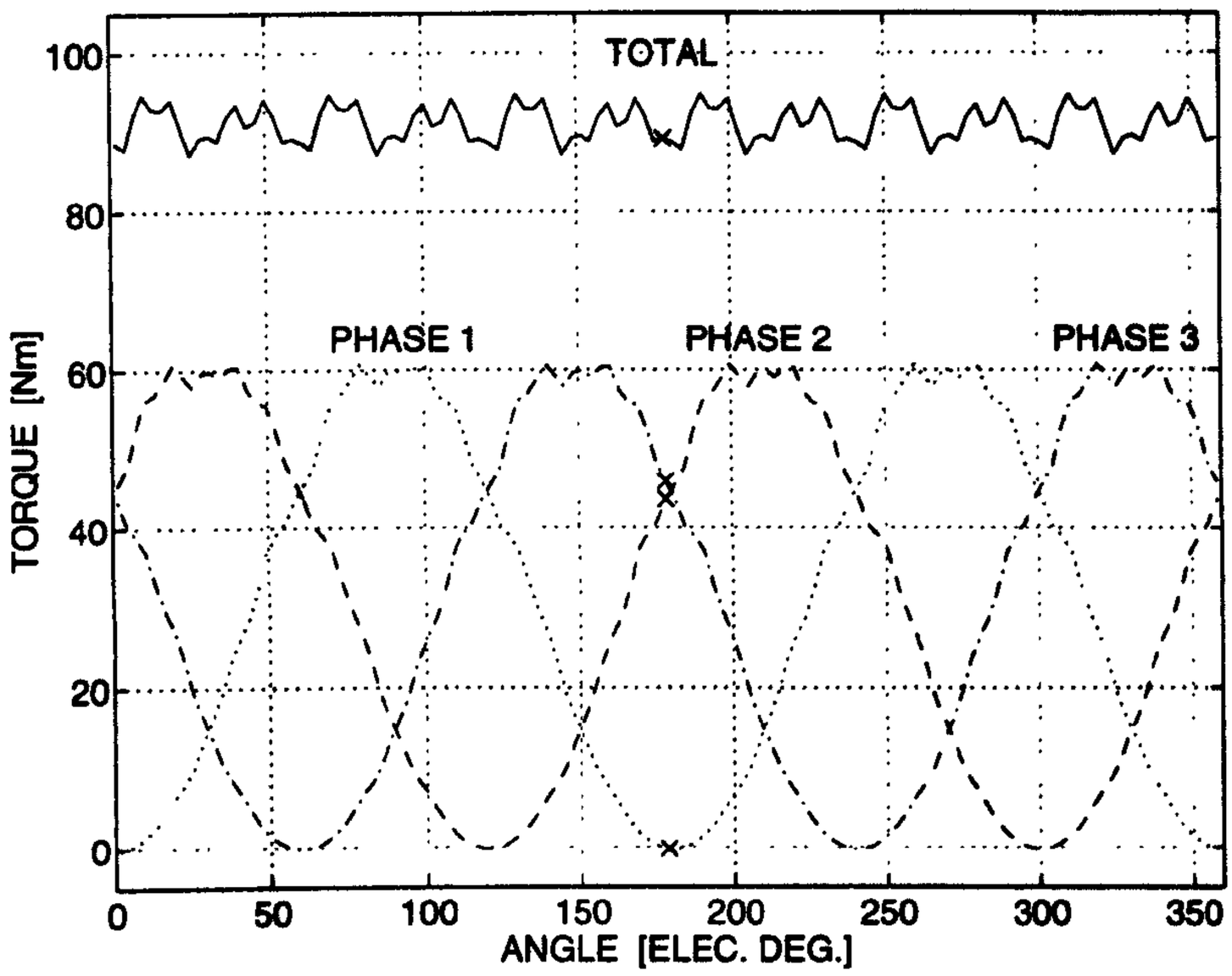

Figure 2.3. Total electromagnetic torque ripple for the non-ideal machine at 20 A RMS phase current.

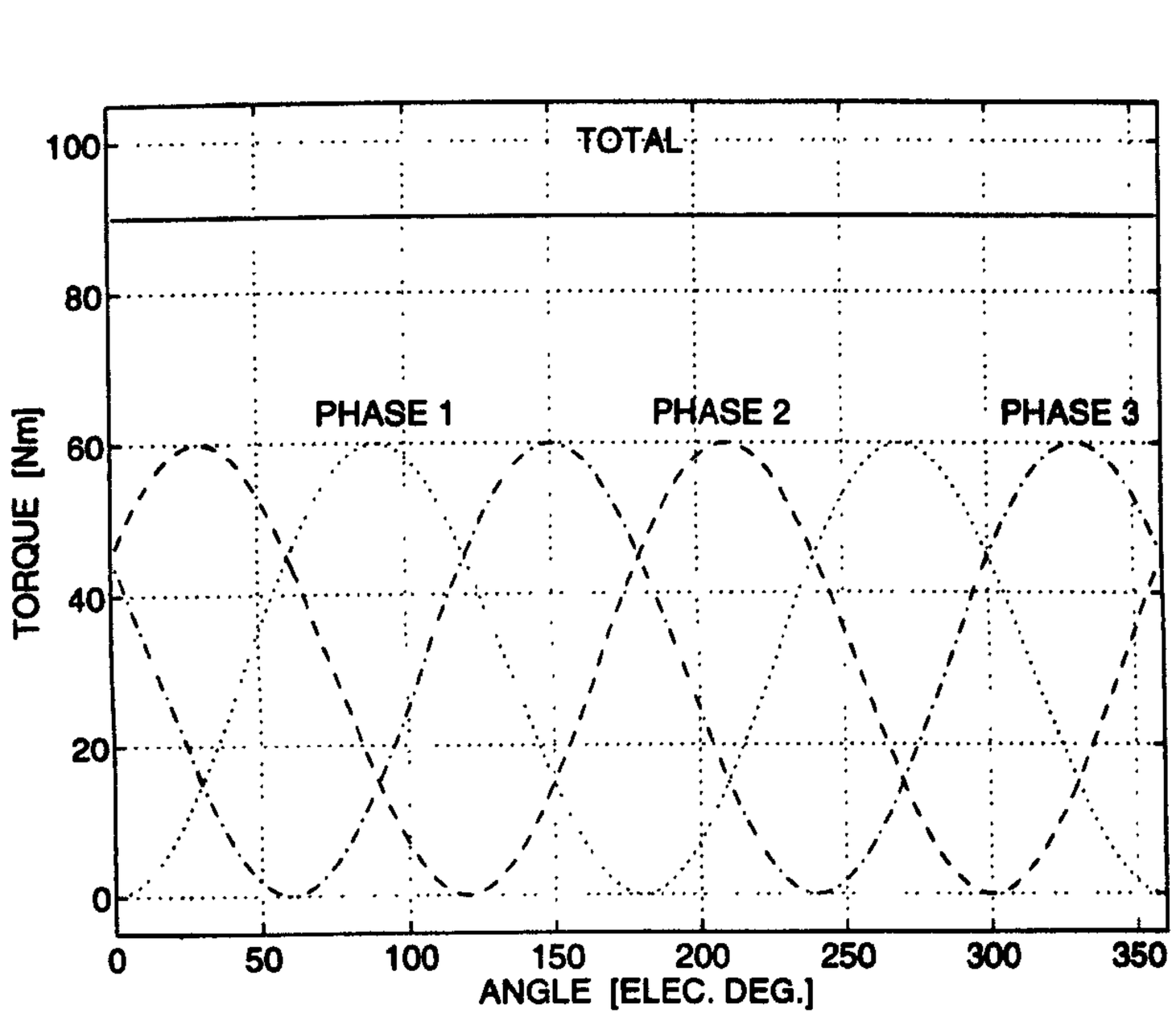

Figure 2.4. Total electromagnetic torque ripple for the ideal machine at 20 A RMS phase current.

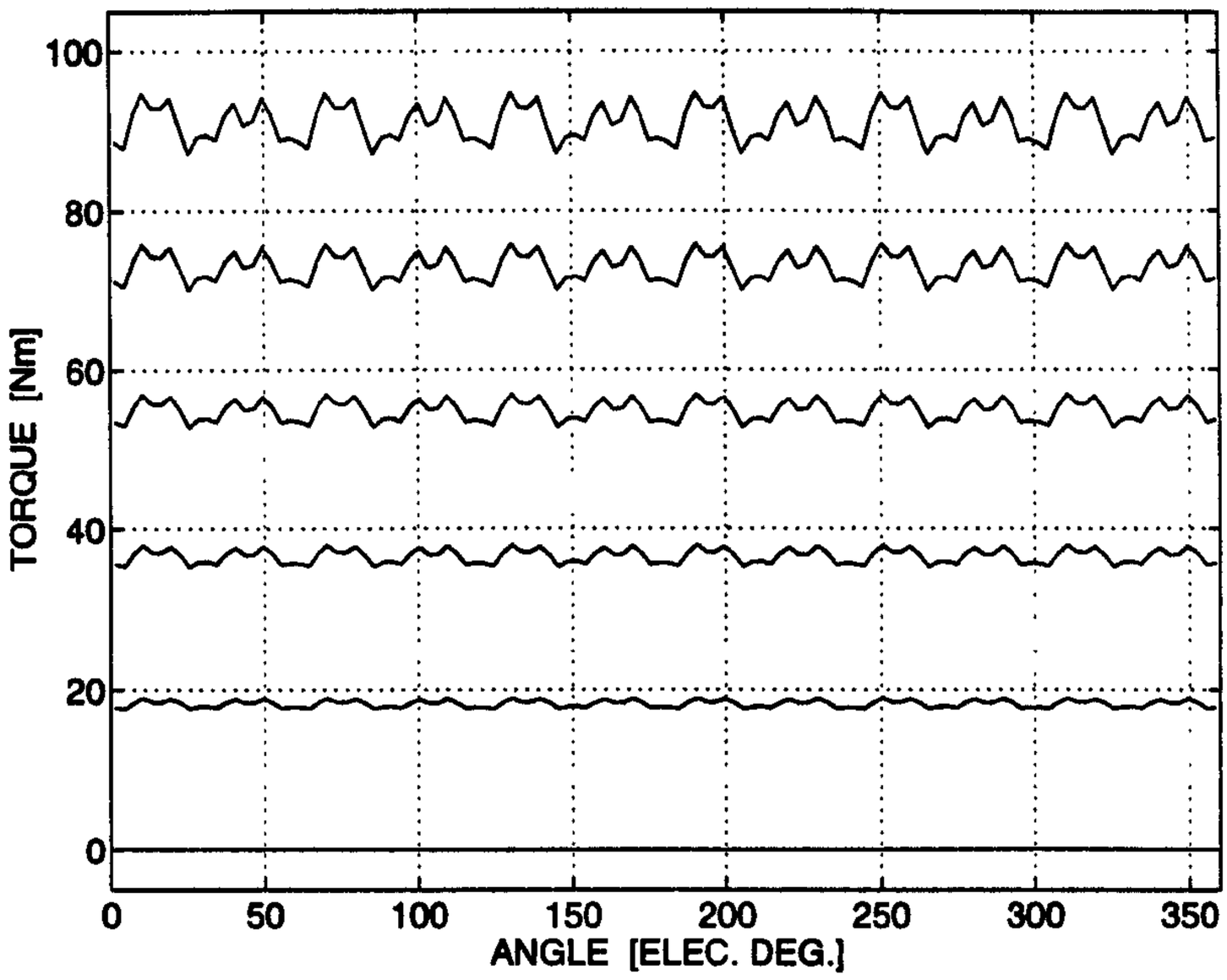

Figure 2.5. Total electromagnetic torque ripple for the non-ideal machine at 0, 4, 8, 12, 16 and 20 A RMS phase currents.

In general, the method described above holds good for machines which are symmetrical; where winding distribution, and current excitation for each phase are identical with a phase shift in space and time respectively. The method can also be used for a purpose-built non-symmetrical machine, where the flux-MMF diagram needs to be constructed and torque ripple calculated for each phase separately.

It is important to note that the calculation of total torque ripple using FMDT is a two step process. In the first step, the phase shifted individual phase torque contributions are added up to calculate the total electromagnetic torque ripple. This assumption of superposition is valid *even when the machine is saturated*; as long as the phase torque ripple is calculated using the phase flux-MMF diagram. In general, the condition of linearity is implied in applying superposition. However, in this case, the phase flux-linkage values used in constructing a flux-MMF diagram, include both the self and the mutual components. Thus, the effect of saturation, due to self as well as mutual coupling for any one phase, is already taken into account. This leads to a

phase torque ripple calculation which includes the effect of saturation and any non-linearities arising out of it. In the second step, the cogging torque ripple, if it is present in the machine, is calculated using the FMDT as explained in Chapter 3, and added up to the electromagnetic torque ripple to obtain the total torque ripple. However, unlike the first step, where mutual and saturation effects are always taken into account, the influence of load current is not taken into account in calculating cogging torque ripple. Thus, the assumption of superposition of electromagnetic and cogging torque ripple, although reasonably good, may only be valid as long as the machine is not severely overloaded or heavily saturated.

2.3.2 PM Brushless DC Motor

Fig. 2.6 shows the cross-section of a 3-phase ferrite-magnet brushless DC motor, FBL550A-A, manufactured by Oriental Motor Co. Its major design specifications are given in table 2.2.

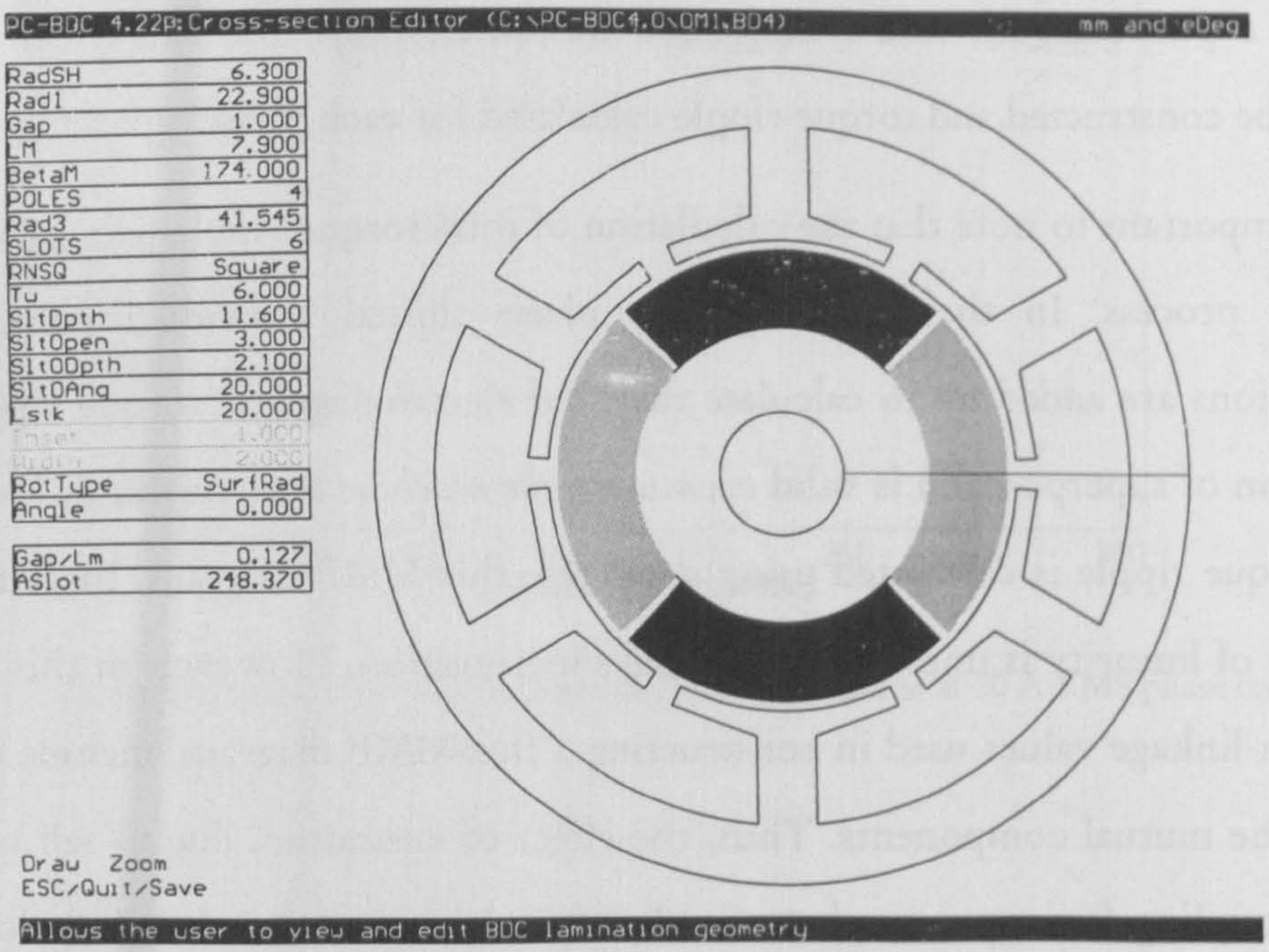

Figure 2.6. FBL550A-A PM brushless DC motor cross-section.

Table 2.2. Major design specifications for the FBL550A-A motor.

Number of phases	3
Number of rotor poles	4
Number of stator slots	6
Stator outer diameter	83.09 mm
Magnet type	FB3X, Ferrite
Remanent flux density	0.385 T
Winding Configuration	Wye connection
Turns per phase	400

The input phase MMF variation with position, used in constructing the flux-MMF diagram, and the resulting phase flux variation are shown in Figs. 2.7 and 2.8 respectively. In a PM brushless AC motor, the flux-MMF trajectories have the shape of an ellipse due to sinewave current excitation. Whereas in a PM brushless DC motor, the flux-MMF trajectories have the shape of a parallelogram, due to squarewave current excitation. The complete flux-MMF diagram is shown in Fig. 2.9.

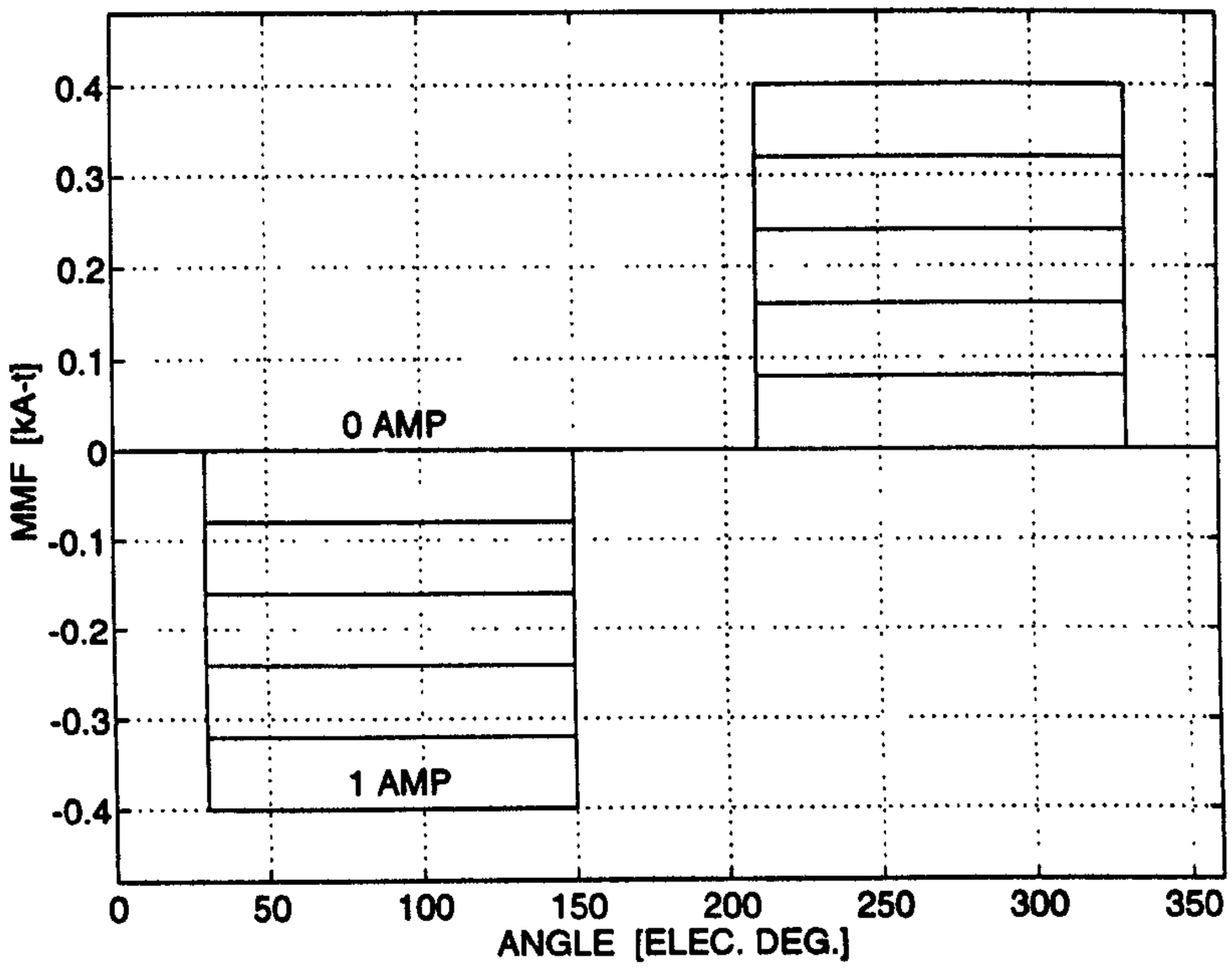

Figure 2.7. Variation of phase MMF with position at 0, 0.2, 0.4, 0.6, 0.8 and 1.0 A peak phase currents.

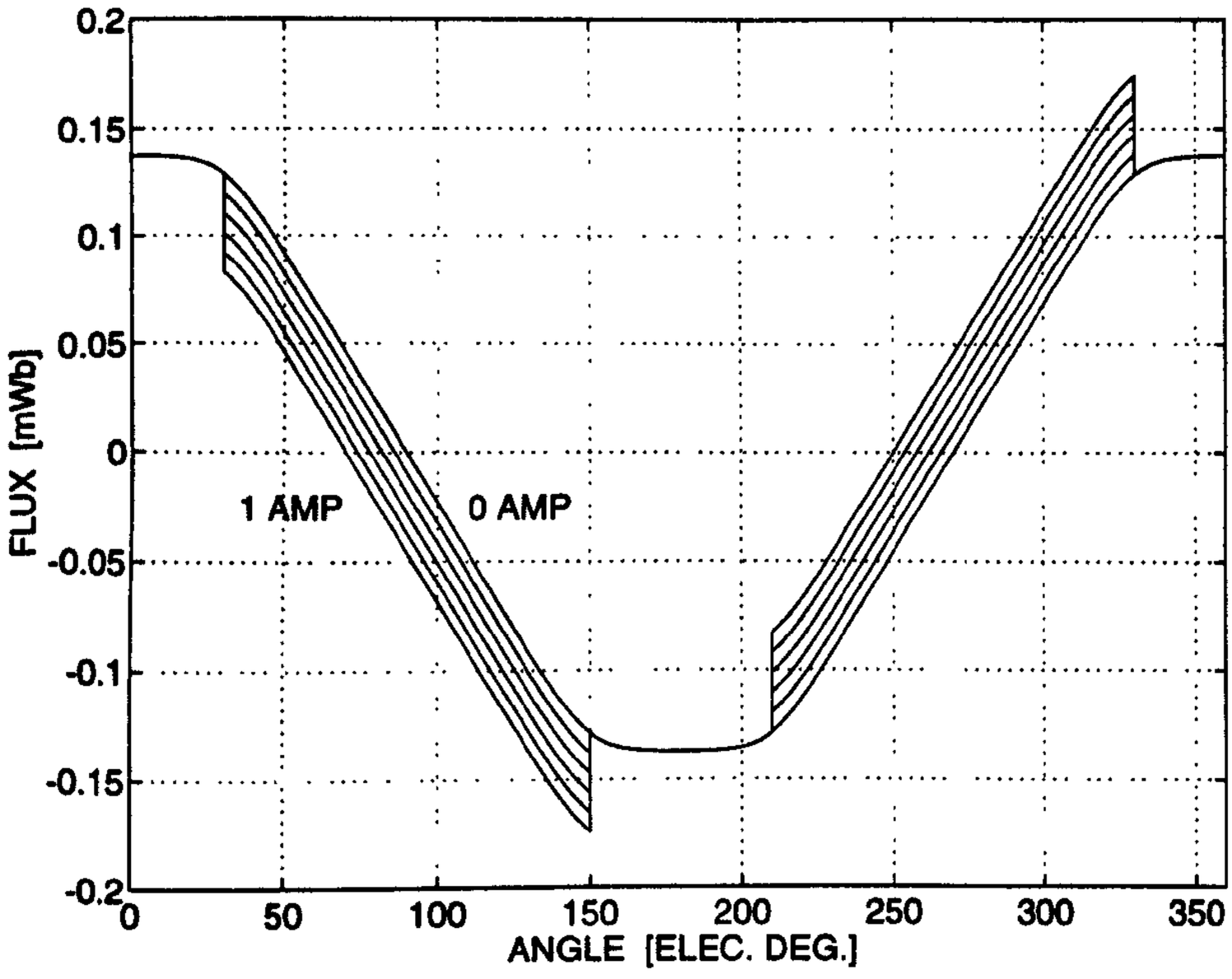

Figure 2.8. Variation of phase flux with position at 0, 0.2, 0.4, 0.6, 0.8 and 1.0 A peak phase currents.

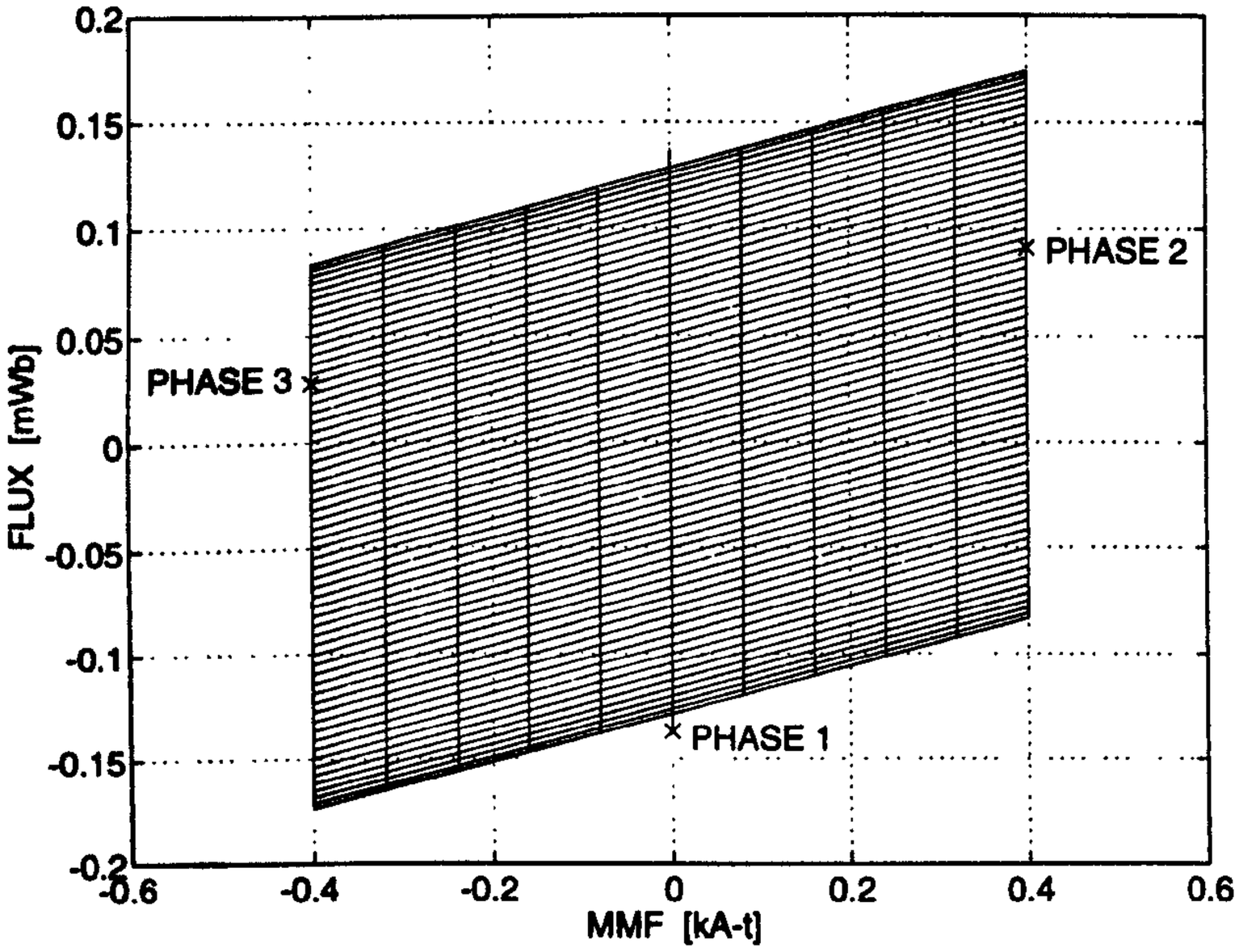

Figure 2.9. Flux-MMF diagram at 0, 0.2, 0.4, 0.6, 0.8 and 1.0 A peak phase currents. The 'x' marks indicate an operating point at a particular instant for the three phases at 1.0 A.

The phase torque ripple curves at six peak phase current values between 0 and 1 A, calculated using the flux-MMF diagram, are shown in Fig. 2.10. As in the case of PM brushless AC motor, the total electromagnetic torque ripple at a particular current, is obtained by adding torque contribution from each phase, shifted by 120° elec. This is shown in Fig. 2.11. Again, a comparison between an *ideal* and a *non-ideal* squarewave machine is an interesting one. Both Figs. 2.11 and 2.12 show an average total torque of 0.1965 Nm. However, Fig. 2.11, which is for a non-ideal machine, shows that the magnitude of the 'AC' component of torque ripple indicates the *extent of deviation* from an ideal 3-phase squarewave machine, due to stator slotting. In this case, the peak-to-peak ripple is 24.91%. Fig. 2.12 is for an ideal machine and it shows perfectly rectangular phase torque contributions, which are a product of ideally squarewave phase current and generated EMF waveforms and thus it shows no ripple.

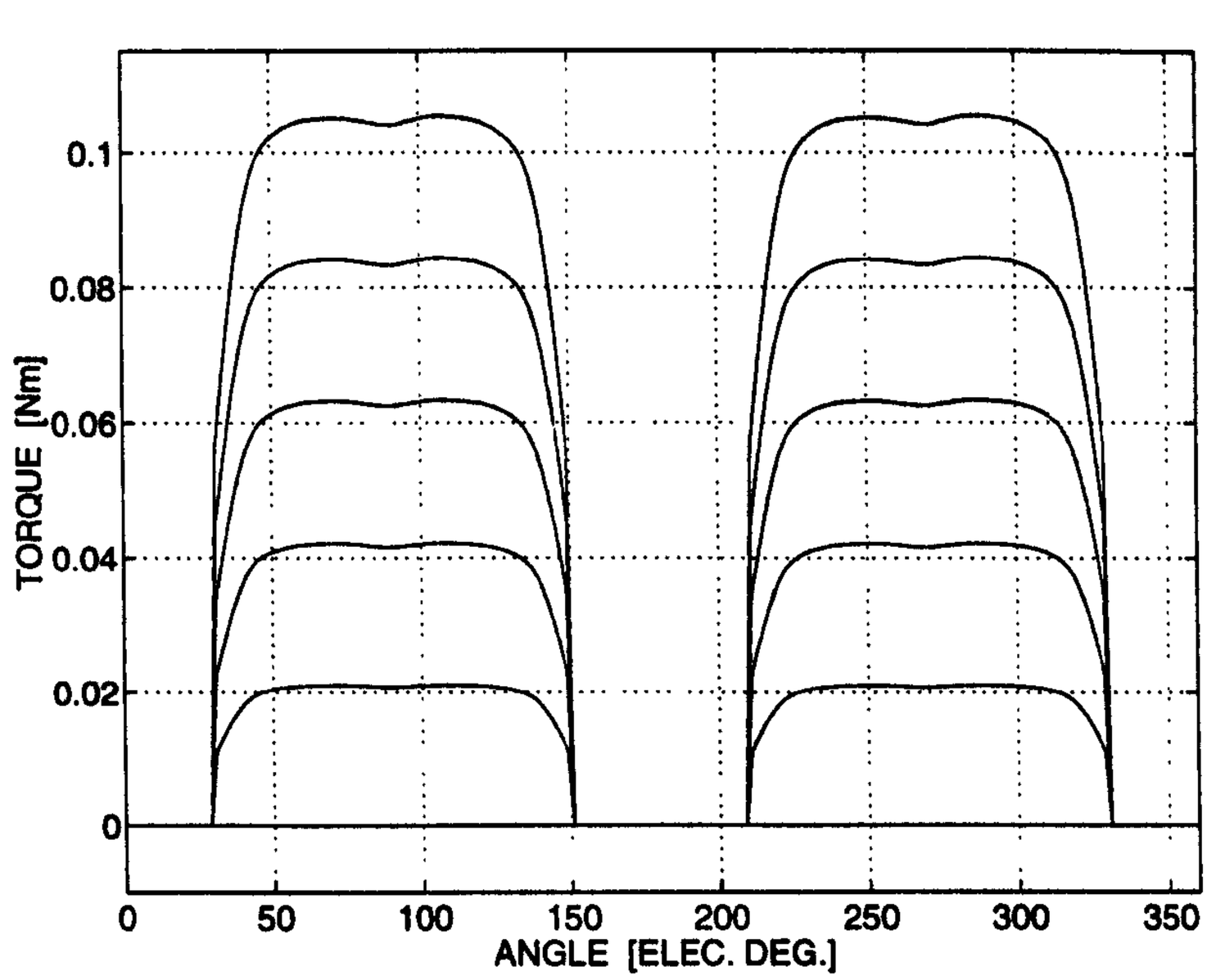

Figure 2.10. Variation of phase torque with position at 0, 0.2, 0.4, 0.6, 0.8 and 1.0 A peak phase currents.

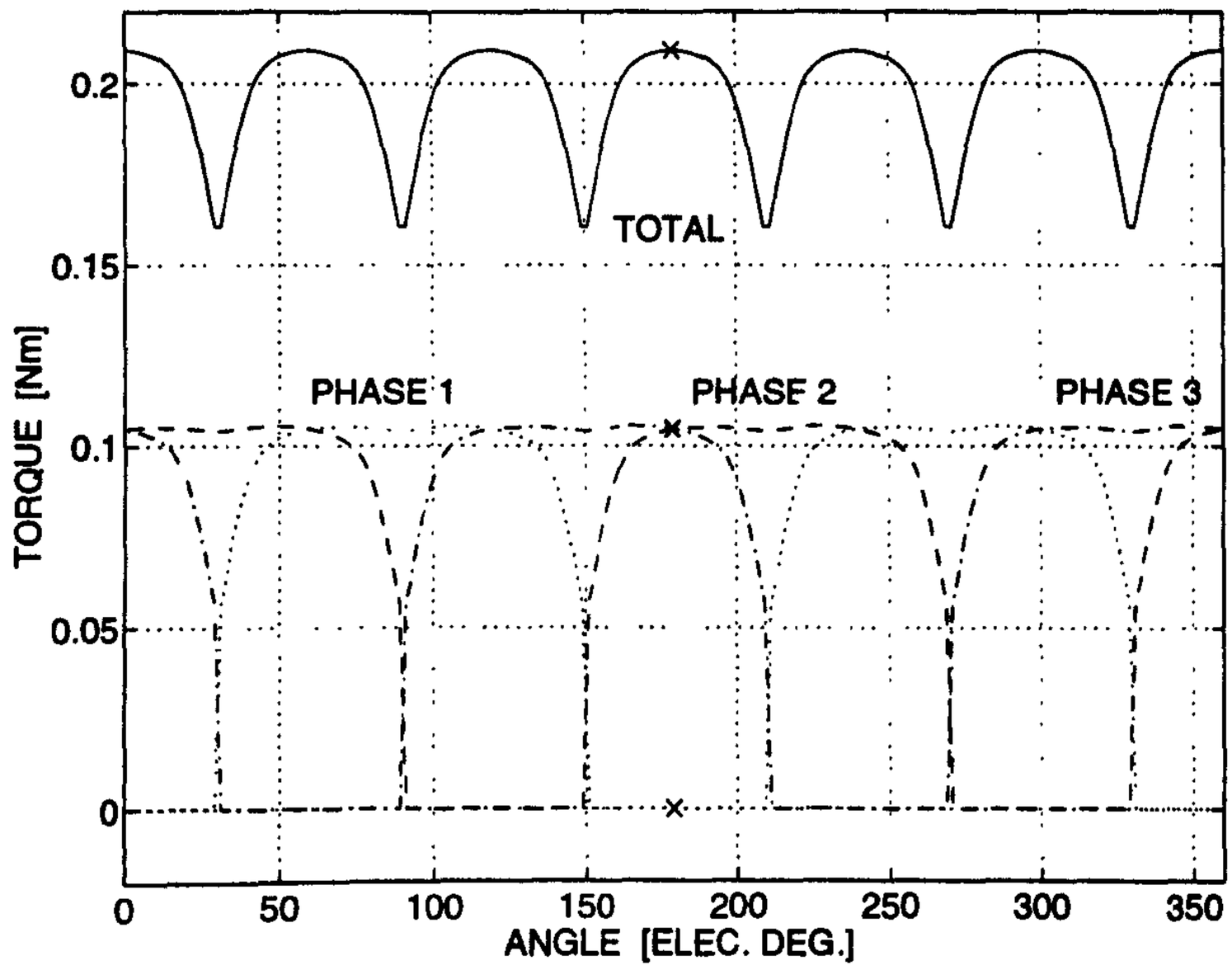

Figure 2.11. Total electromagnetic torque ripple for the non-ideal machine at 1.0 A peak phase current.

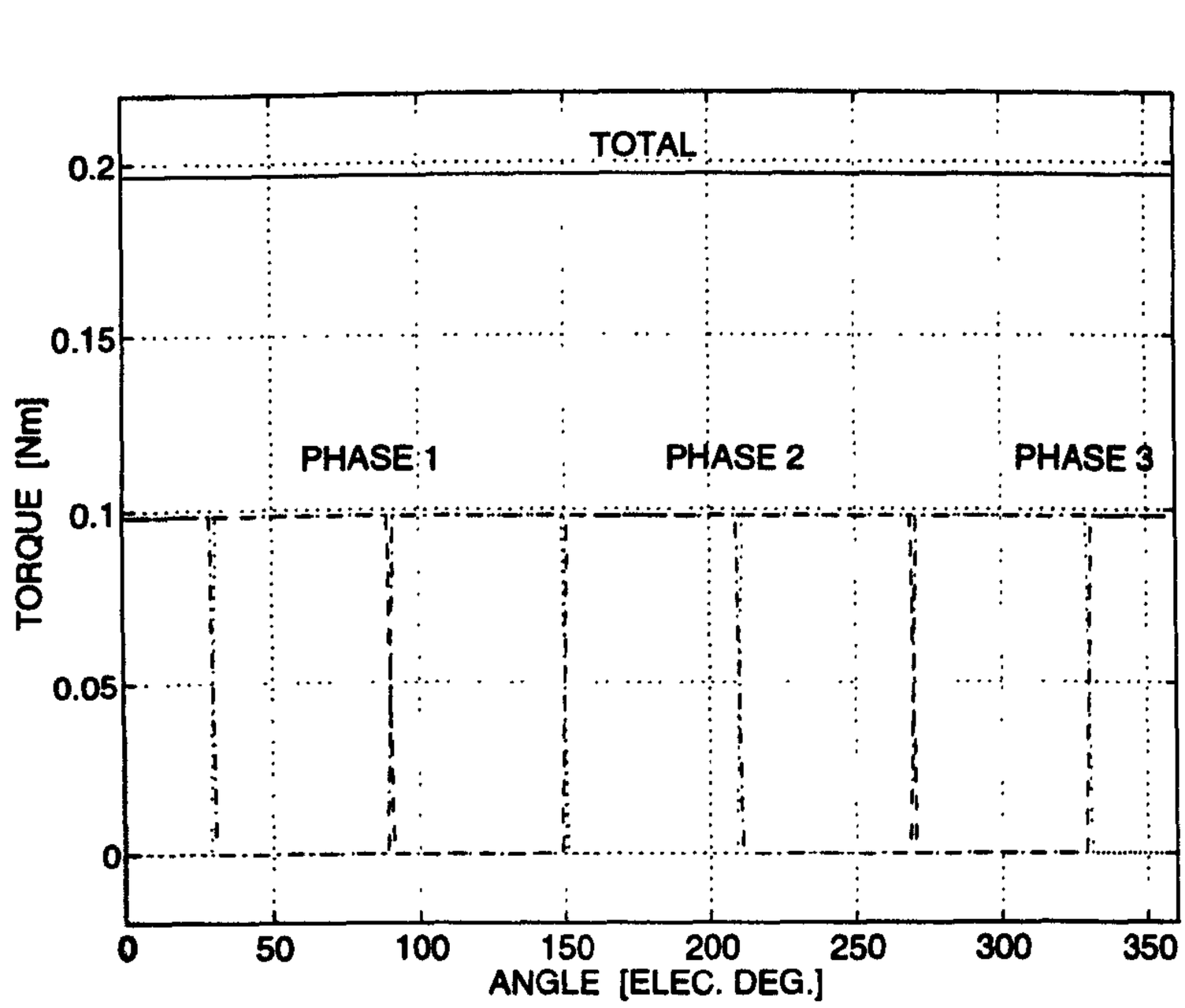

Figure 2.12. Total electromagnetic torque ripple for the ideal machine at 1.0 A peak phase current.

Finally, total electromagnetic ripple curves at six phase current values between 0 and 1 A, calculated in this manner, are shown in Fig. 2.13.

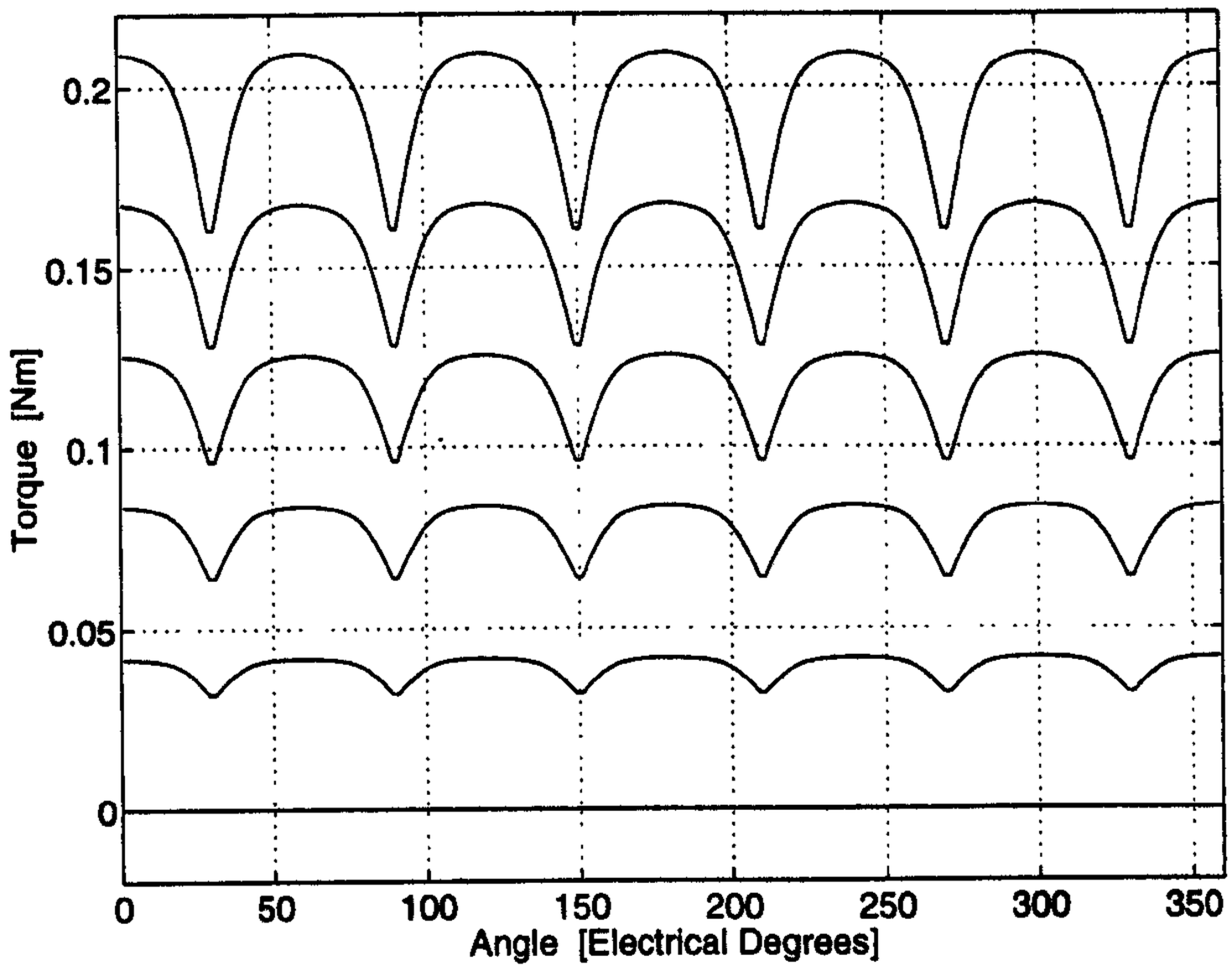

Figure 2.13. Total electromagnetic torque ripple curves at 0, 0.2, 0.4, 0.6, 0.8 and 1.0 A peak phase currents.

2.3.3 Static Torque Measurement Test Set-Up

In this section, the test set-up used for carrying out static torque measurements is described. Fig. 2.14 is a schematic drawing of the test set-up. It consists of a dividing head (model: ELLIOTT 3½" Universal Dividing Head), a high-precision Vibro-meter in-line torque transducer (model: TG–0.2/B, rated torque: 2 Nm, maximum torque: 5 Nm), a DC power supply, and the motor under test.

The dividing head is a special indexing device capable of providing controlled incremental motion in steps of varying resolution, which can be 'programmed' through settings on the front plate. The handle shown in the picture is operated manually. One revolution of this handle corresponds to a displacement of 9° of the main (in-line) shaft. One revolution can be further subdivided by using a dent-and-a-notch arrangement. The handle has a notch at the end which fits into one of the dents

shown as black dots in the picture. It can be adjusted or 'programmed' to take any of the nine concentric circular paths such that the desired resolution of displacement at the main shaft can be obtained.

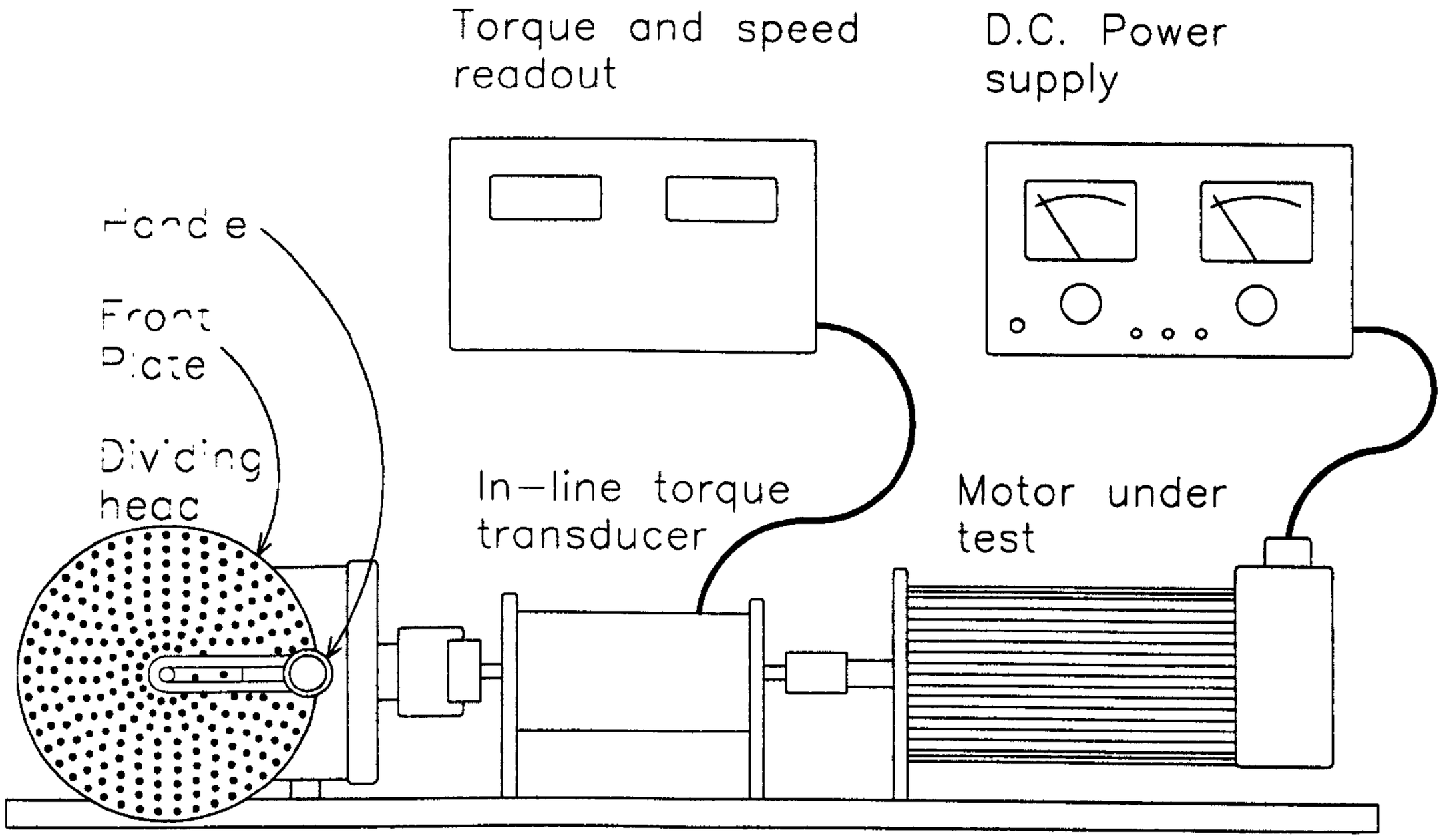

Figure 2.14. Experimental test set-up used for static torque measurements.

Each of the series of concentric circles marked on the plate, consists of a different number of dents starting with 15 on the innermost circle to 47 on the outermost. Thus the innermost circle provides a resolution of 0.60°, while the outermost circle provides a resolution of 0.19° for the displacement at the main shaft. Table 2.3 gives information on various possible resolutions which can be obtained using the dividing head.

Table 2.3. Displacement resolutions obtained from the dividing head.

Circular path	Number of Dents	Minimum resolution
1 (innermost)	15	0.60°
2	18	0.50°
3	20	0.45°
4	23	0.39°
5	27	0.33°
6	31	0.29°
7	37	0.24°
8	41	0.22°
9 (outermost)	47	0.19°

The motor under test is supplied with the required DC current excitation and then indexed in steps of desired resolution (typically 1° or smaller) over total displacement corresponding to either one full electrical cycle or a fraction of it. The winding connections are commutated manually at appropriate rotor positions to simulate the actual steady-state low-speed motor operation. Torque readings are obtained from the readout at every step.

The measurements are carried out twice, once in the clockwise direction and again in the counterclockwise direction, to take account of the 'friction torque' offset. The results are then averaged to eliminate the friction torque offset and to obtain resultant variation of instantaneous torque with position. The elimination of the friction torque offset is especially important at low torque levels, where it can form a substantial component of the measured torque and hence can introduce errors in the test results. This is demonstrated in Chapter 3, which deals with the prediction and measurement of low-level cogging torque. Finally, the process is repeated for a number of DC phase current values, to obtain variation of instantaneous torque with position as well as current.

2.3.4 Experimental Validation

In recent years, experimental validation for the low-speed torque ripple, predicted using the flux-MMF diagram technique, has been carried out in the SPEED Laboratory on a variety of machine types. Apart from the switched reluctance machine, for which the technique has already gained wide acceptance, the following machine types have been tested.

- Synchronous Reluctance Machine
  (Both the single-barrier and the axially-laminated types)
- PM brushless DC Machine
- PM Brushless AC Machine
- Flux-Reversal Machine

Synchronous Reluctance Machine: Staton et al. [47] have presented the flux-MMF diagrams, and the predicted as well as measured torque-ripple curves, for both the single-barrier and the axially-laminated types of synchronous reluctance machine. Fig. 2.15, for example, shows the flux-MMF diagram for a 7.5 kW axially-laminated synchronous reluctance motor built by Soong. The details on design, construction and test procedure for this motor can be found in [77]. Note that because of the absence of permanent-magnets in this machine, all the magnetisation curves start from the origin; like an SR machine, but unlike a PM machine where all the magnetisation curves start from different points on the MMF-axis (Figs. 2.1 and 2.9 for example).

The corresponding predicted and measured low-speed torque ripple curves are shown in Fig. 2.16. Since, there is no cogging in a pure reluctance machine, the total torque ripple curves are the same as the electromagnetic torque ripple curves. In a PM machine, however, because of the cogging torque, the two are different as shown next for a PM brushless DC motor.

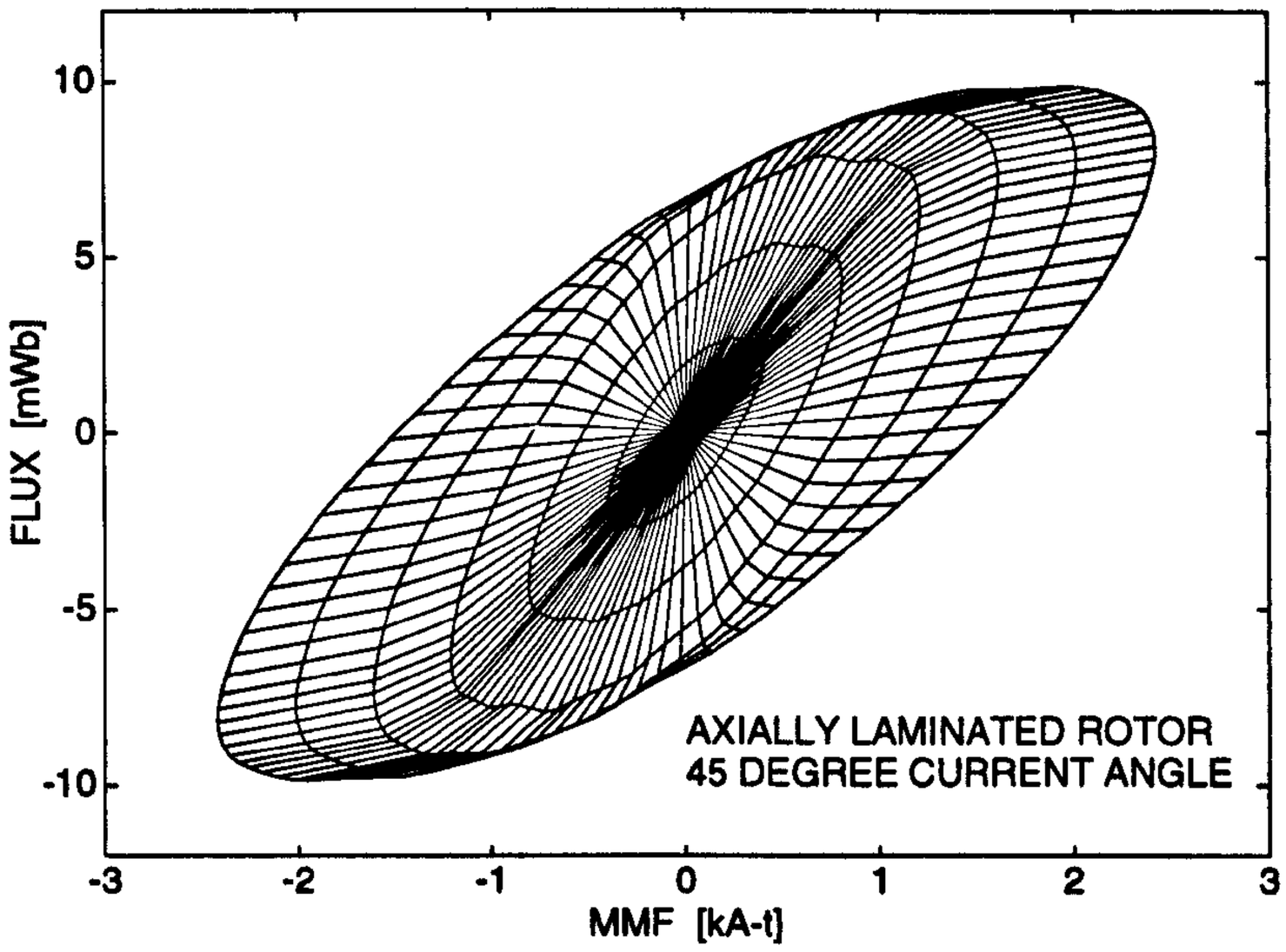

Figure 2.15. Flux-MMF diagram for the axially-laminated synchronous reluctance machine (*Reproduced from* [48] *courtesy of Dr. Dave Staton and Dr. Wen Soong*).

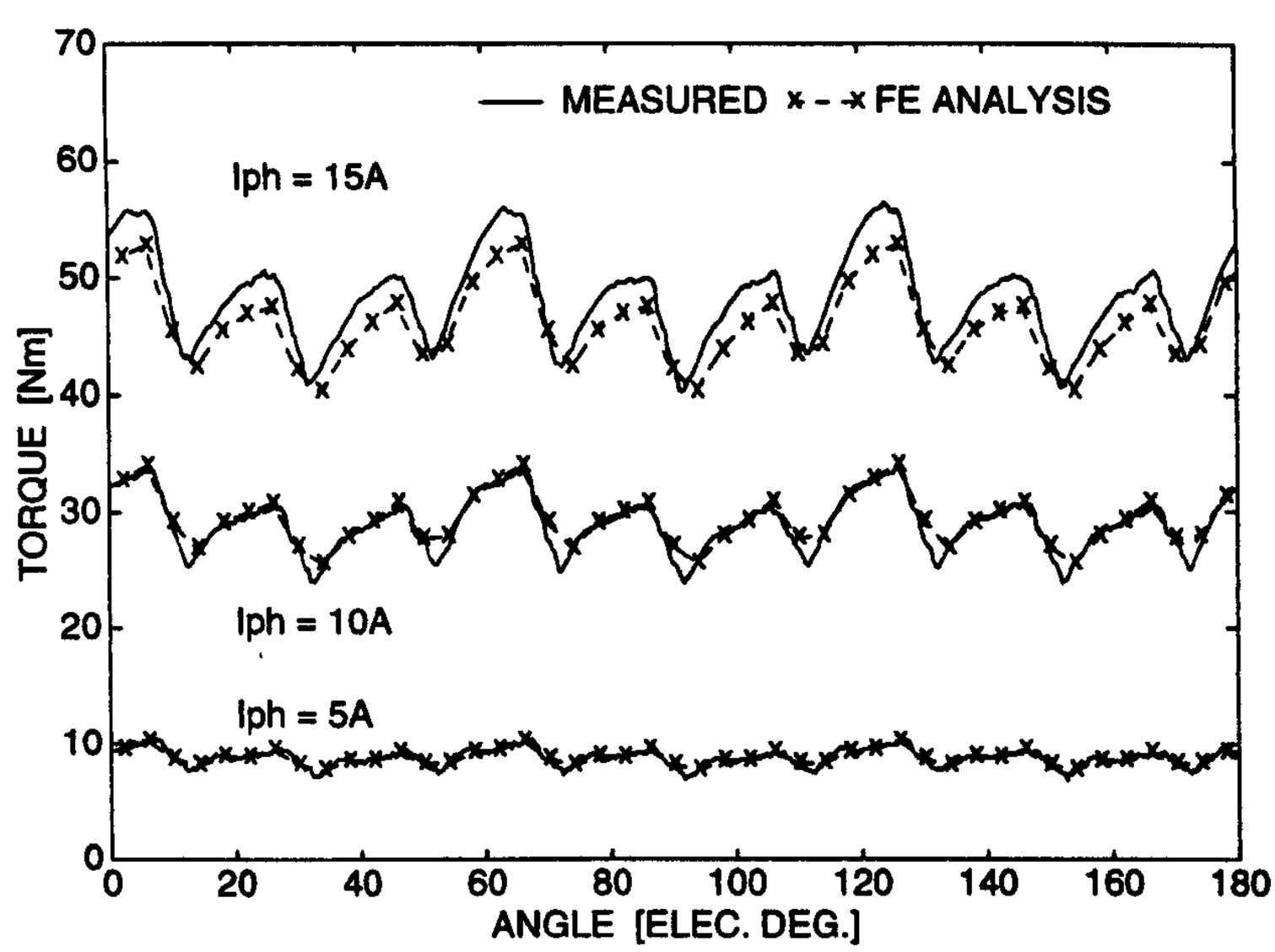

Figure 2.16. Predicted and measured low-speed torque ripple for the axially-laminated synchronous reluctance machine (*Reproduced from* [48] *courtesy of Dr. Dave Staton and Dr. Wen Soong*).

PM Brushless DC Machine: The FBL550A-A motor shown in Fig. 2.6 is used here for the purpose of experimental validation. Fig. 2.17 shows the predicted and the

measured total torque ripple curves at six peak phase currents between 0 and 1.0 A. A comparison between Figs. 2.13 and 2.17 brings out a few important points to be noted. While Fig. 2.13 shows purely electromagnetic torque ripple curves, in practice, the cogging torque ripple is always present along with it; and the resultant total torque ripple curves have a different shape and magnitude. Thus Fig. 2.17 validates only the total torque ripple curves. The cogging torque ripple curves have been calculated using the method described in Chapter 3 and superimposed upon the electromagnetic torque ripple curves. Although strictly speaking, the superposition may not hold good in the case of a saturated machine, it is a reasonably good assumption as indicated by the close agreement between the predicted and the measured torque ripple curves.

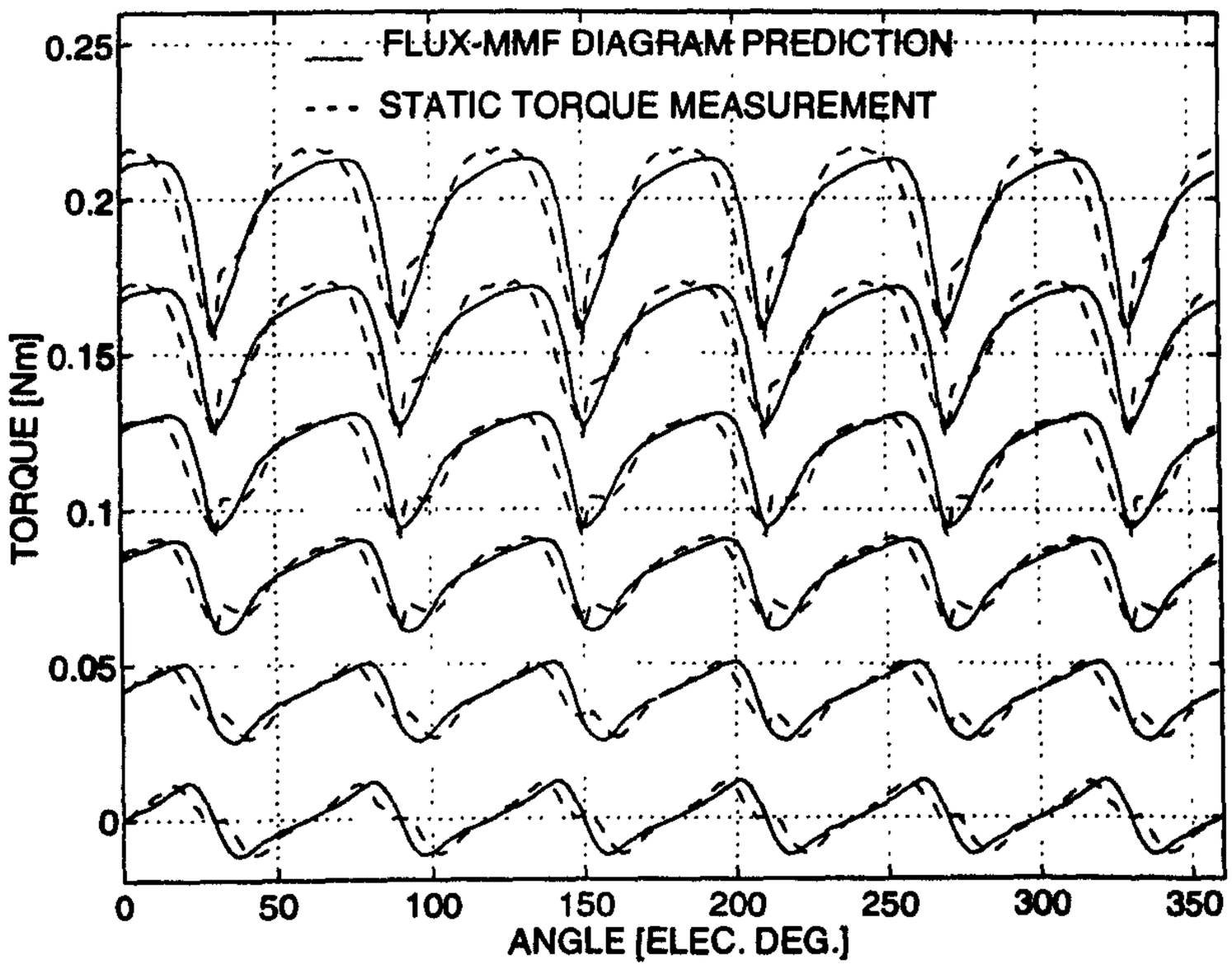

Figure 2.17. Predicted and measured total torque ripple in PM brushless DC motor at 0, 0.2, 0.4, 0.6, 0.8 and 1.0 A peak phase currents.

At 1.0 A of peak phase current, the FBL550A-A motor roughly operates at the full-load operating point. The motor has also been tested under severe overload with

up to 5.0 A of peak phase current. In this case, the motor is heavily saturated and this is reflected in the flux-MMF diagram shown in Fig. 2.18, which shows non-linear magnetisation curves. The spacing of the magnetisation curves is fairly uniform except in the vicinity of the commutation instants. Fig. 2.18 is in contrast to Fig 2.9 which shows linear magnetisation curves for the same motor without saturation. Fig. 2.19 shows the corresponding predicted and measured torque ripple curves. Finally, Table 2.4 summarises the torque ripple analysis for the FBL550A-A motor with and without saturation. Here, the torque ripple is calculated as the % ratio of peak-to-peak to average value. It shows that the torque ripple is very high at low currents (65% at 0.2 A), where the cogging torque ripple is dominant. It decreases sharply as current increases (37% at 0.4 A) and again increases slightly at severe overload currents (34% at 5.0 A).

Table 2.4. Torque ripple analysis for the PM brushless DC motor.

Without Saturation			With Saturation		
Current [A]	Torque [Nm]	Ripple [%]	Current [A]	Torque [Nm]	Ripple [%]
0.0	0	—	0.0	0	—
0.2	0.04	65	1.0	0.20	28
0.4	0.09	37	2.0	0.39	27
0.6	0.12	31	3.0	0.58	30
0.8	0.16	29	4.0	0.75	33
1.0	0.20	28	5.0	0.90	34

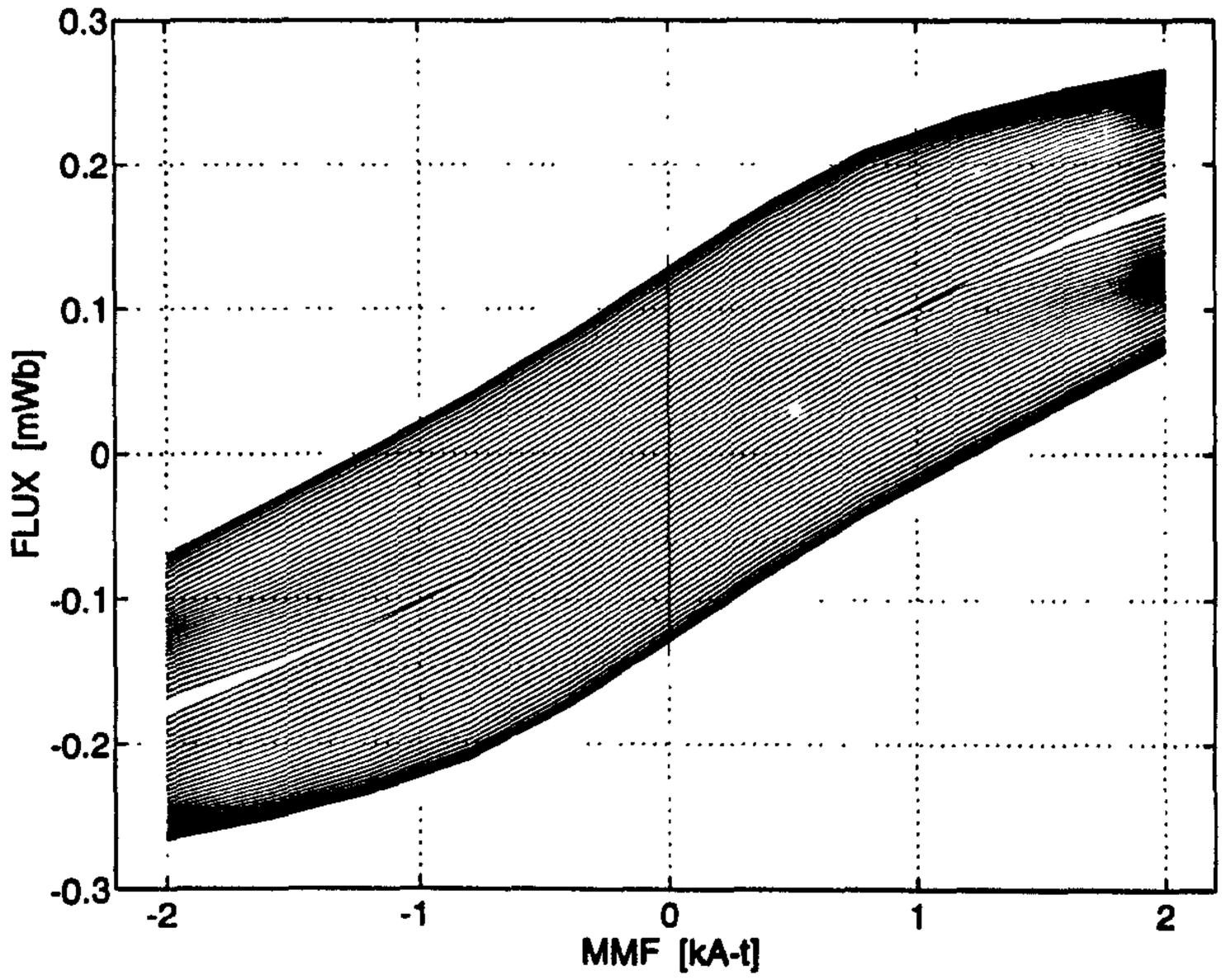

Figure 2.18. Flux-MMF diagram for the PM brushless DC motor under saturation at 0, 1, 2, 3, 4 and 5 A peak phase currents.

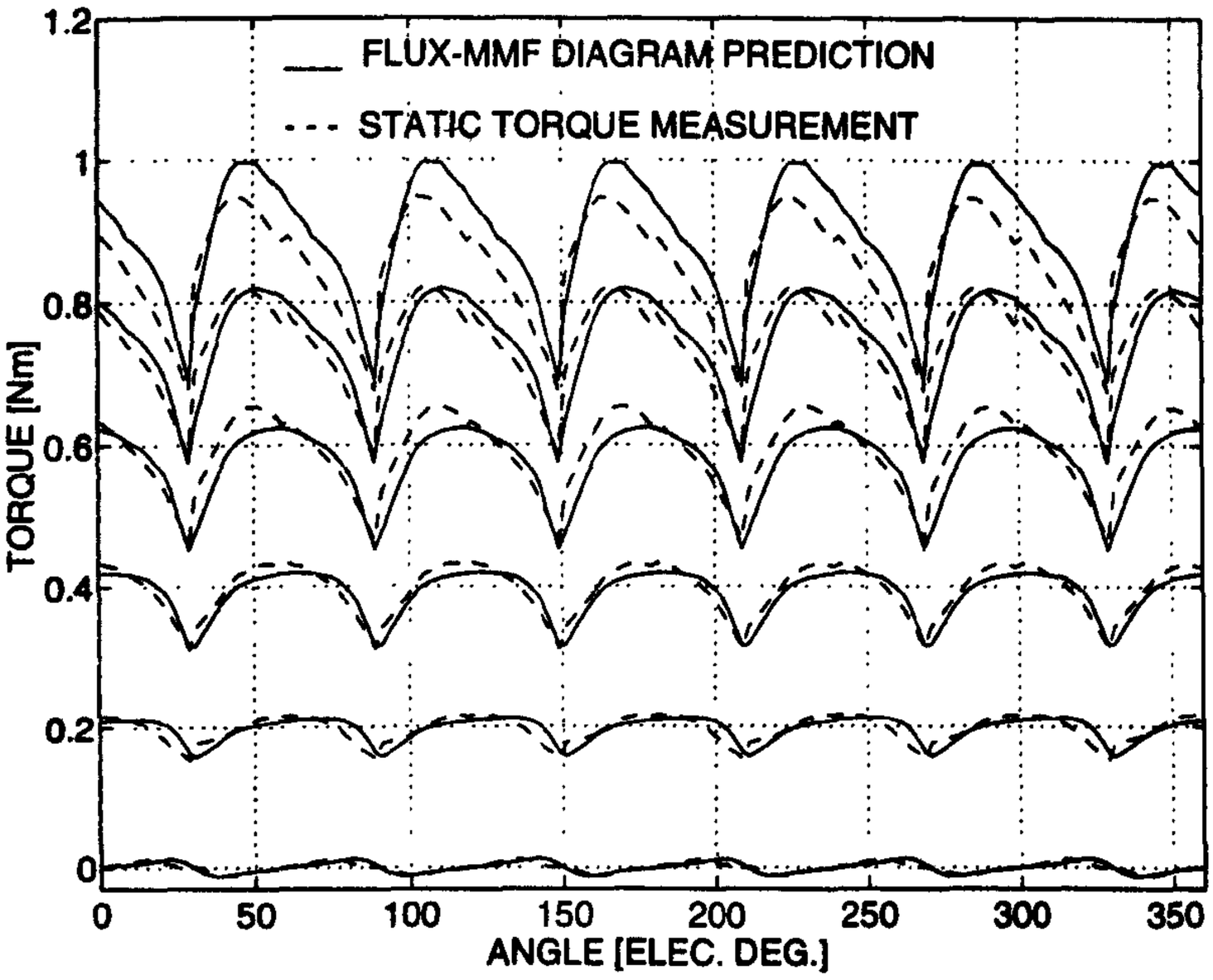

Figure 2.19. Predicted and measured total torque ripple for the PM brushless DC motor under saturation at 0, 1, 2, 3, 4 and 5 A peak phase currents.

2.3.5 Comparison with Maxwell Stress Method

Fig. 2.20 makes a comparison between total torque ripple curves, predicted using the FMDT and the Maxwell stress method, in FBL550A-A motor without saturation. Fig. 2.21 shows the same set of curves for the motor with saturation. Both figures show a close agreement between the results obtained using these two methods. The two methods, however, are implemented in entirely different ways in the FE analysis, as explained earlier on in this Chapter. The Maxwell stress method, in general, is considered to be the most reliable means of torque calculation using FE analysis. Thus Figs. 2.20 and 2.21 provide additional validation for the flux-MMF diagram technique; apart from Figs. 2.17 and 2.19, which provide the actual experimental validation.

Note, however, that the results obtained from the FMDT and the Maxwell stress method are based on the same FE formulations. In fact, the pre-processing, mesh generation, and solution stages performed, are exactly identical in both the cases. This means that both methods have used the same number nodes, elements, scale factors, and the same amount of computing resources. The only difference appears at the post-processing stage. In the case of FMDT, the torque is obtained indirectly from the FE solutions, by calculating the variation of phase flux-linkage with position and current. Whereas in the case of Maxwell stress method, the torque is obtained directly from the FE solutions, by using an in-built post-processing command which integrates the Maxwell stress tensor along a given path in the airgap region. Actually, four different torque values are obtained from four different airgap regions (Fig. 1.10 in Chapter 1), and the results are averaged to improve the accuracy and reliability of the torque estimate.

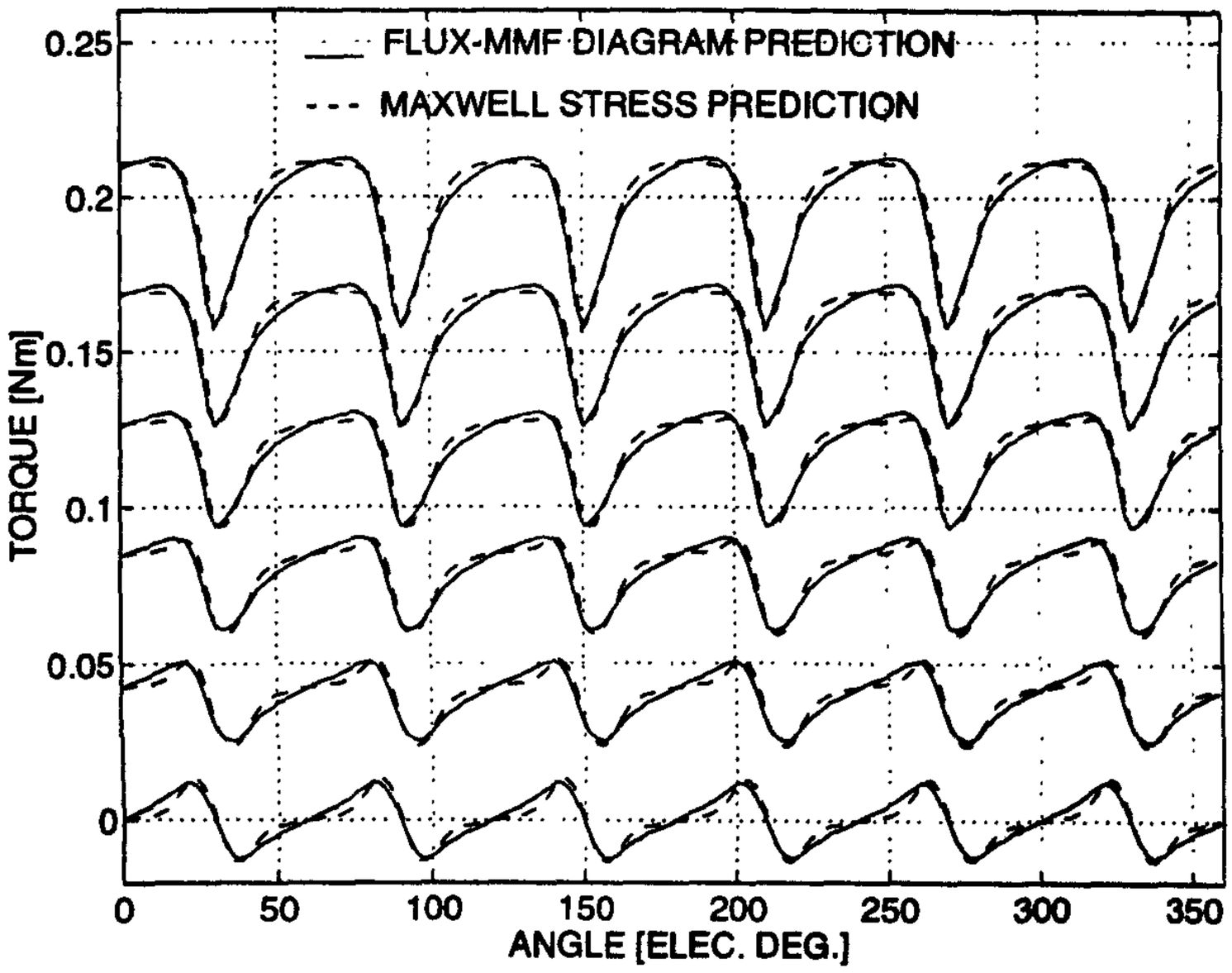

Figure 2.20. Comparison between the FMDT and the Maxwell stress method for the PM brushless DC motor without saturation. Total torque ripple curves shown at 0, 0.2, 0.4, 0.6, 0.8 and 1.0 A peak phase currents.

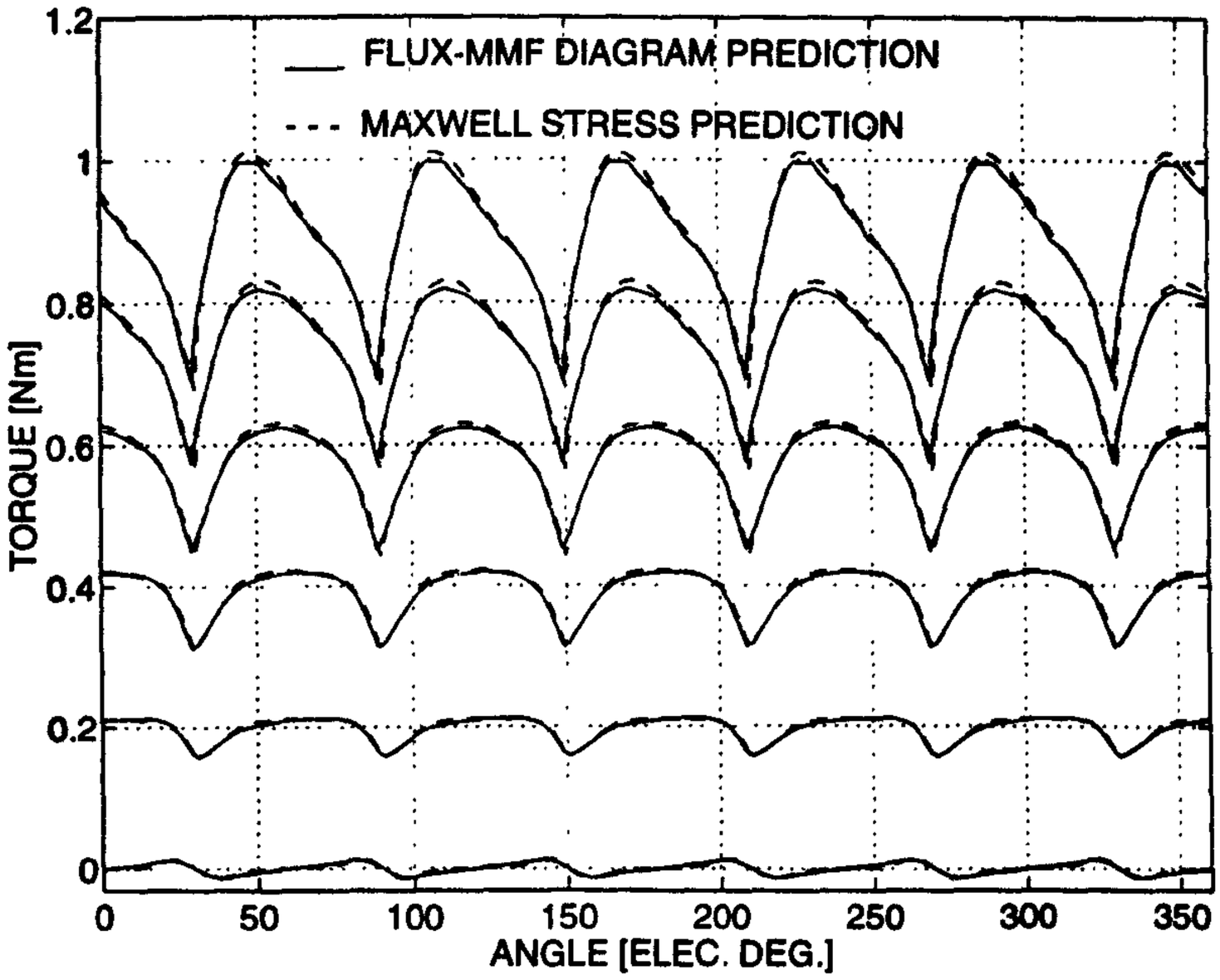

Figure 2.21. Comparison between the FMDT and the Maxwell stress method for the PM brushless DC motor with saturation. Total torque ripple curves shown at 0, 1, 2, 3, 4 and 5 A peak phase currents.

2.4 Prediction of Static Torque Characteristics

This chapter so far has dealt with the FMDT, as applied in predicting the electromagnetic torque ripple in brushless PM machines. The FMDT can also be applied in predicting the so-called *static torque characteristics* of a PM machine. The concept of static torque characteristics is employed commonly in the design and analysis of hybrid stepper motors [21] and switched reluctance motors [57]. It refers to the variation of instantaneous torque with position for a particular phase for a given DC current excitation.

Although the concept of static torque characteristics has some common ground with the concept of electromagnetic phase torque ripple, explained in the previous section, there are some important differences. These are explained and summarised at the end of this section where the two concepts are compared from the point of view of their usefulness in calculating the total electromagnetic torque ripple.

Next, the methodology of predicting static torque characteristics using the flux-MMF diagram, and calculating the total electromagnetic torque ripple from it, is explained. Experimental validation is also provided for a couple of PM brushless motors.

2.4.1 Methodology

Fig. 2.22 shows the flux-MMF diagram for any one phase of the FBL550A-A motor, considered earlier on. As compared to Fig. 2.9, the main difference here is that there is only one level of phase current excitation, fixed at 1.0 A, throughout one electrical cycle. This results in the flux-MMF trajectory which is simply a vertical straight line rather than a parallelogram.

As with any other flux-MMF diagram, the area enclosed between any two adjacent magnetisation curves gives the change in coenergy. This area, divided by the amount of rotor displacement, gives the instantaneous torque. The static torque characteristic for any one phase, calculated in this manner, can be phase shifted by the appropriate number of electrical degrees (120° for a 3-phase machine), to obtain the static torque characteristics for all the phases as shown in Fig. 2.23.

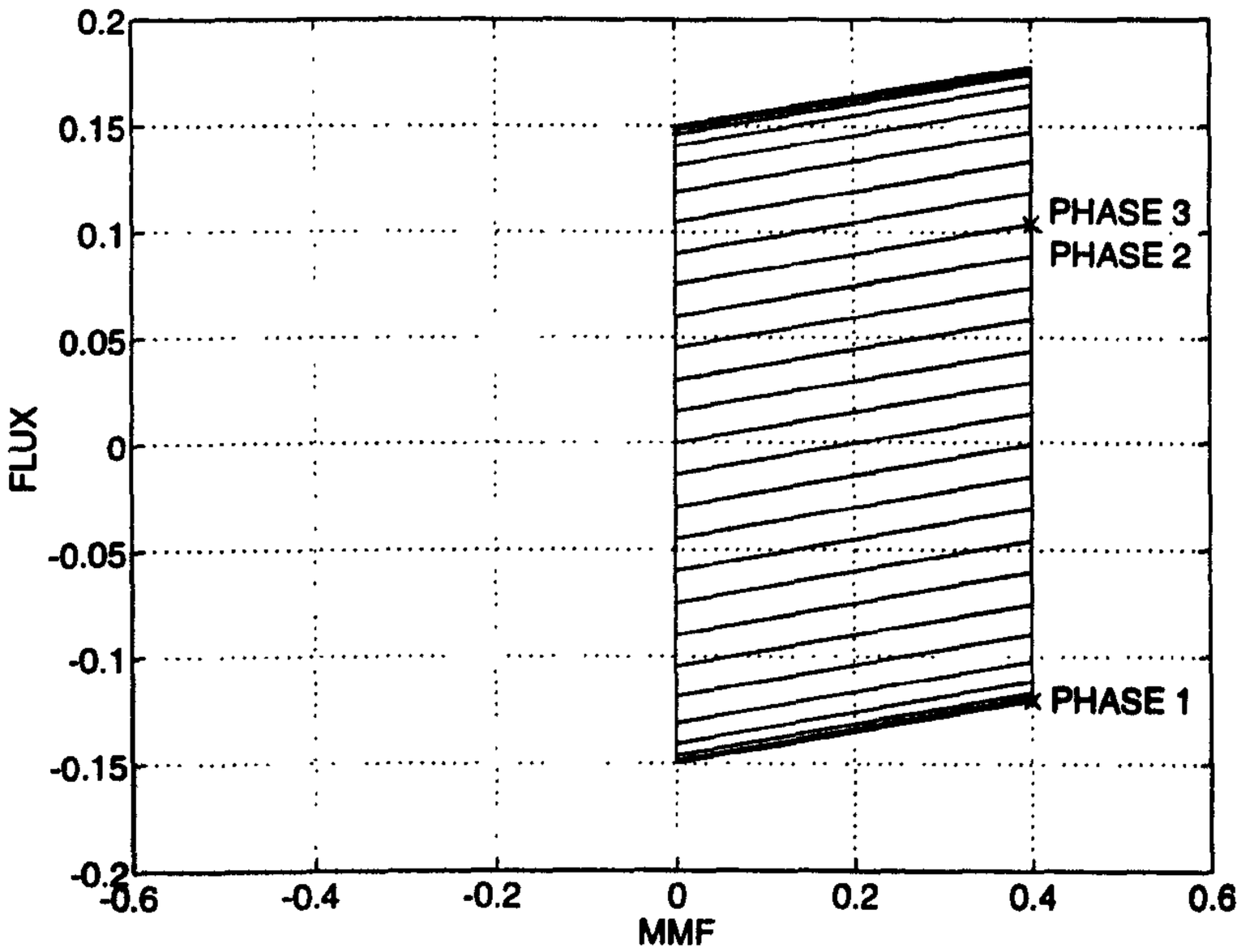

Figure 2.22. Flux-MMF diagram for any one phase of the PM brushless DC motor at 1.0 A fixed DC current.

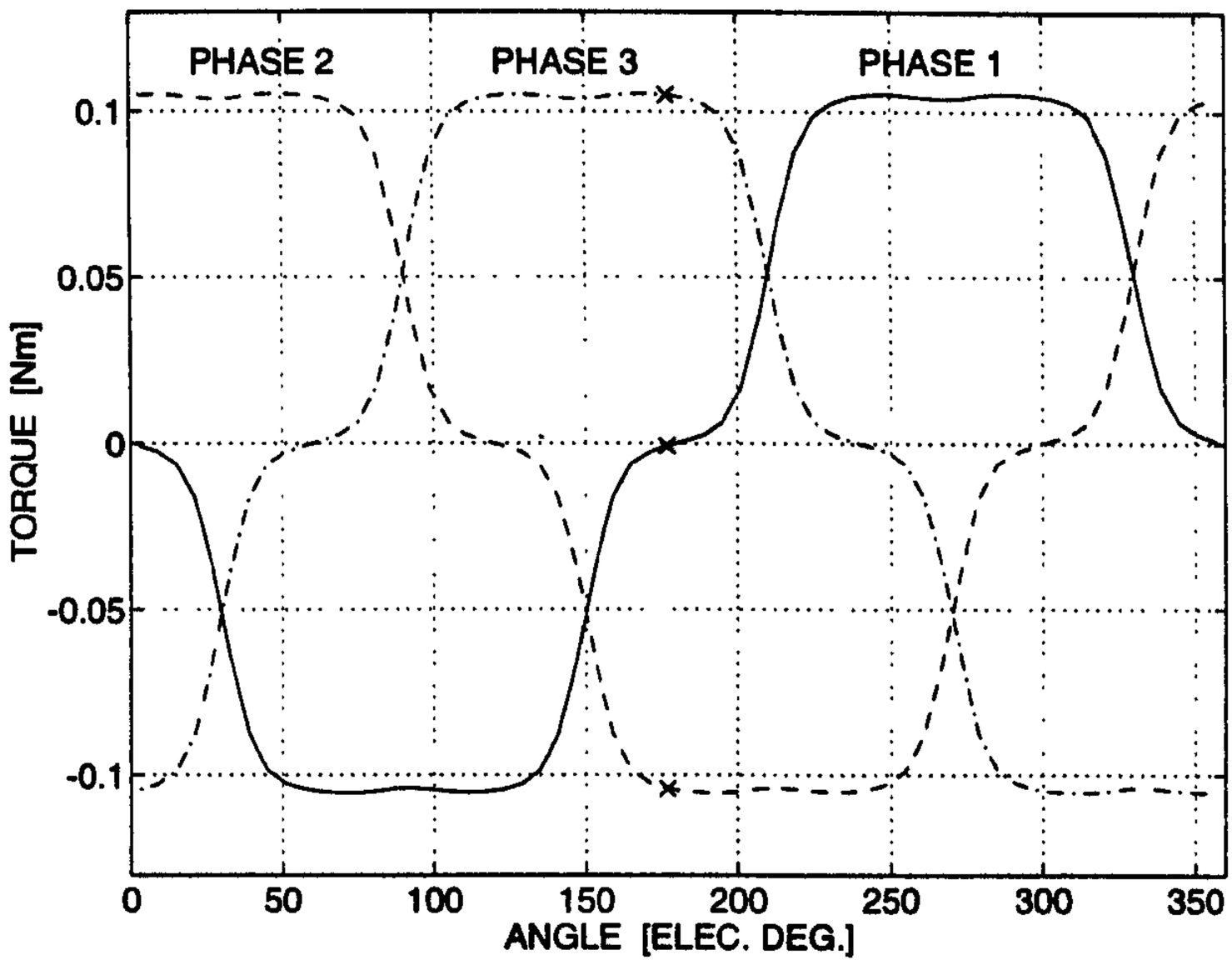

Figure 2.23. Static torque characteristics for all three phases of the PM brushless DC motor at 1.0 A fixed DC current.

These 3-phase static torque characteristics can be multiplied by any arbitrary shaped 3-phase current waveforms to obtain individual phase torque ripple curves. For example, Fig. 2.24 shows 3-phase squarewave current waveforms at 1.0 A peak current. These are multiplied by the respective static torque characteristics in Fig. 2.23 to obtain individual phase torque ripple curves as shown in Fig 2.25. These curves can then be simply added to obtain the total electromagnetic torque ripple, assuming that the principle of superposition holds good.

Fig. 2.25 is similar to Fig. 2.11. Both show the total electromagnetic torque ripple in FBL550A-A motor at 1.0 A, obtained by superimposing the individual phase torque curves. But there are a few differences. First, the individual phase torque curves are obtained using two different methods, described in the foregoing discussion. Secondly, the resolution in Fig. 2.25 is 3° mech., as against 1° mech. in Fig. 2.11. This results in the torque ripple shape being different in the two cases.

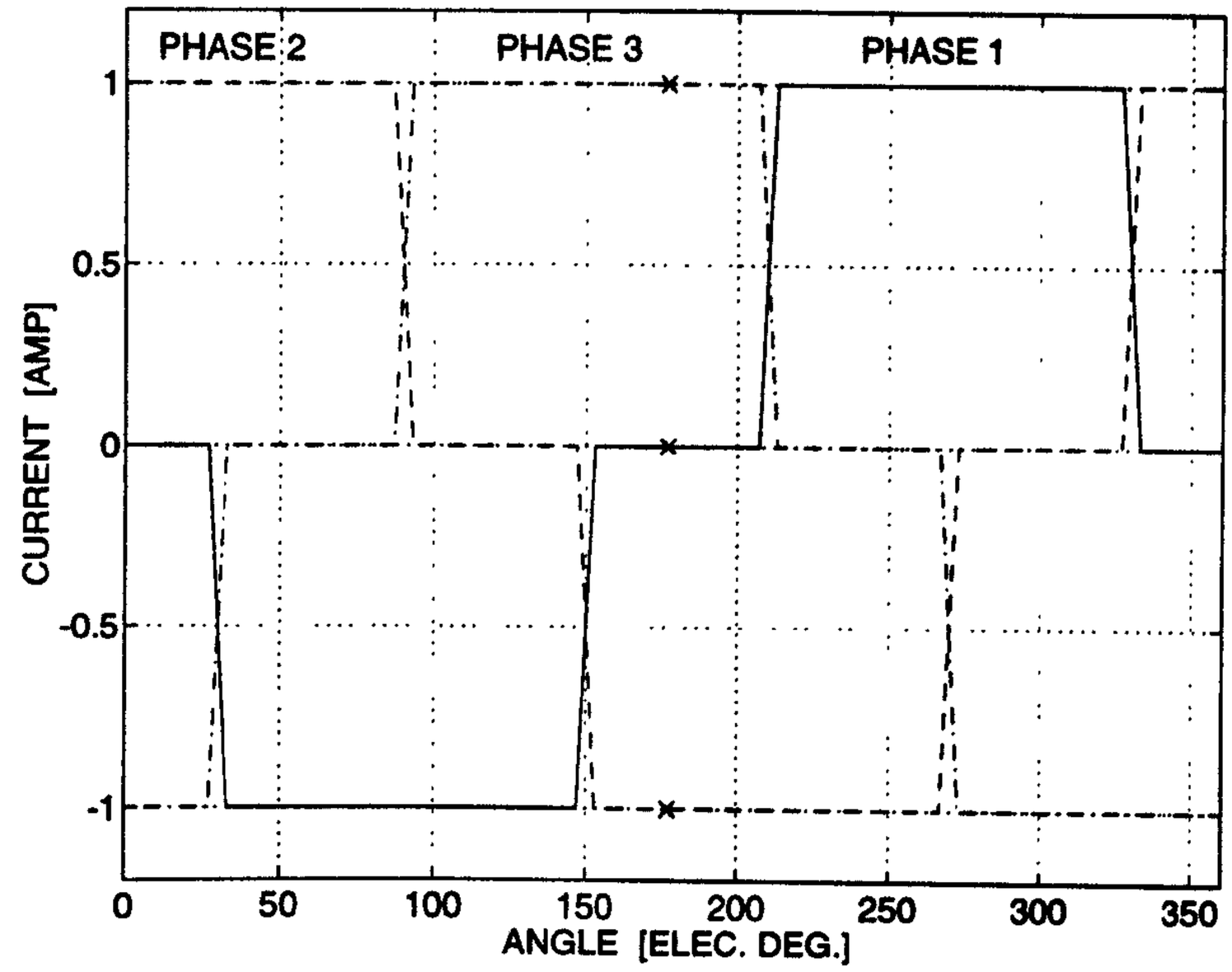

Figure 2.24. 3-phase squarewave current waveforms at 1.0 A peak phase current.

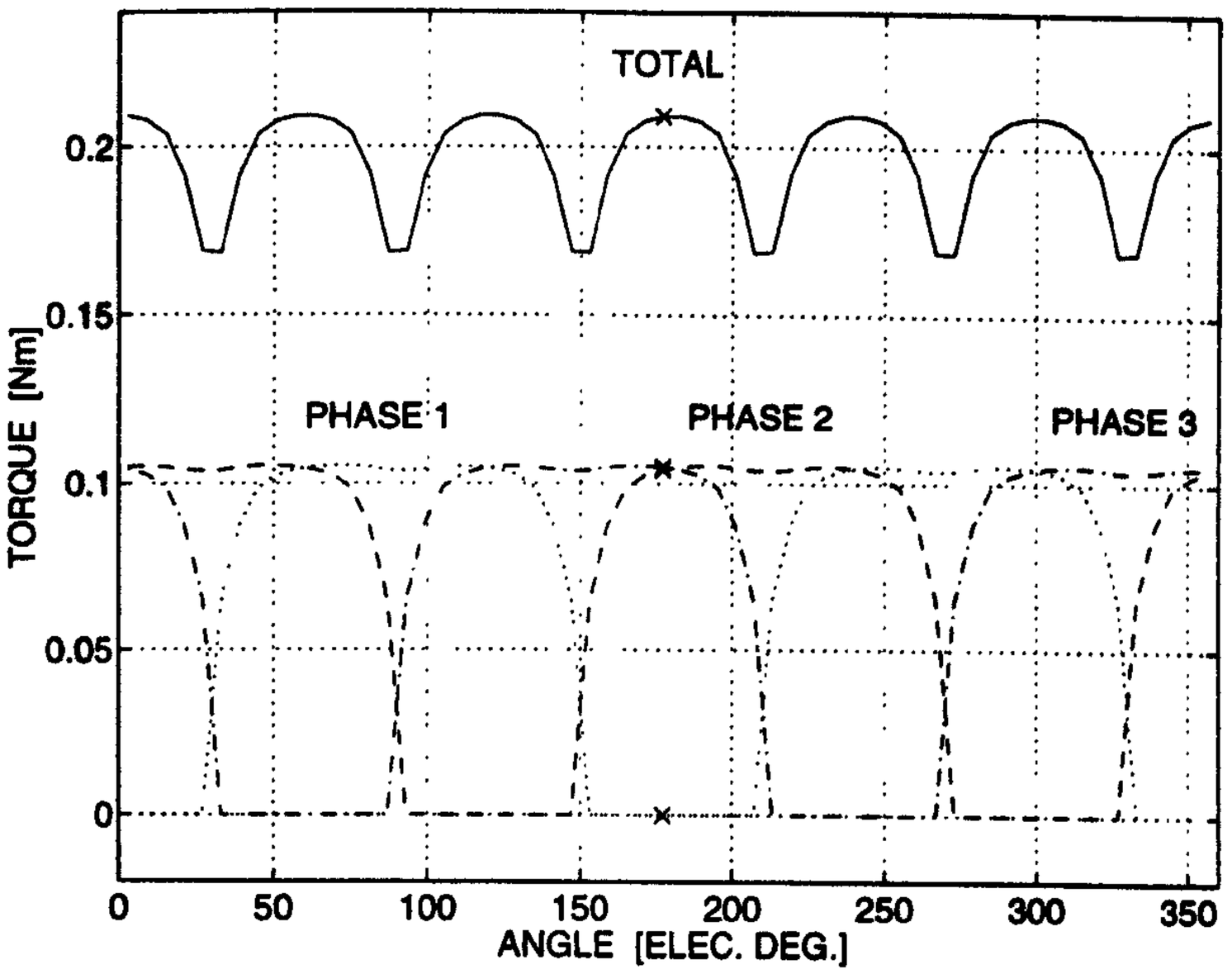

Figure 2.25. Electromagnetic torque ripple for each phase and for the entire machine at 1.0 A peak phase current.

2.4.2 Experimental Validation

The static torque characteristics of the FBL550A-A motor, shown in Fig. 2.23, are purely electromagnetic in nature. In order to validate these curves against experimental measurements, a combined or total static torque characteristic, made up of the electromagnetic and the cogging torque components needs to be obtained. Such characteristic is shown in Fig. 2.26. Here, the cogging torque ripple is obtained using the method described in Chapter 3, and superimposed on the electromagnetic torque ripple.

Fig. 2.27 compares the predicted and the measured static torque characteristics at 1.0 A DC phase current. A close agreement between the two curves shows that the principle of superposition can indeed be applied to obtain total torque ripple, from a combination of the electromagnetic and the cogging torque components, as long as the machine is not heavily saturated.

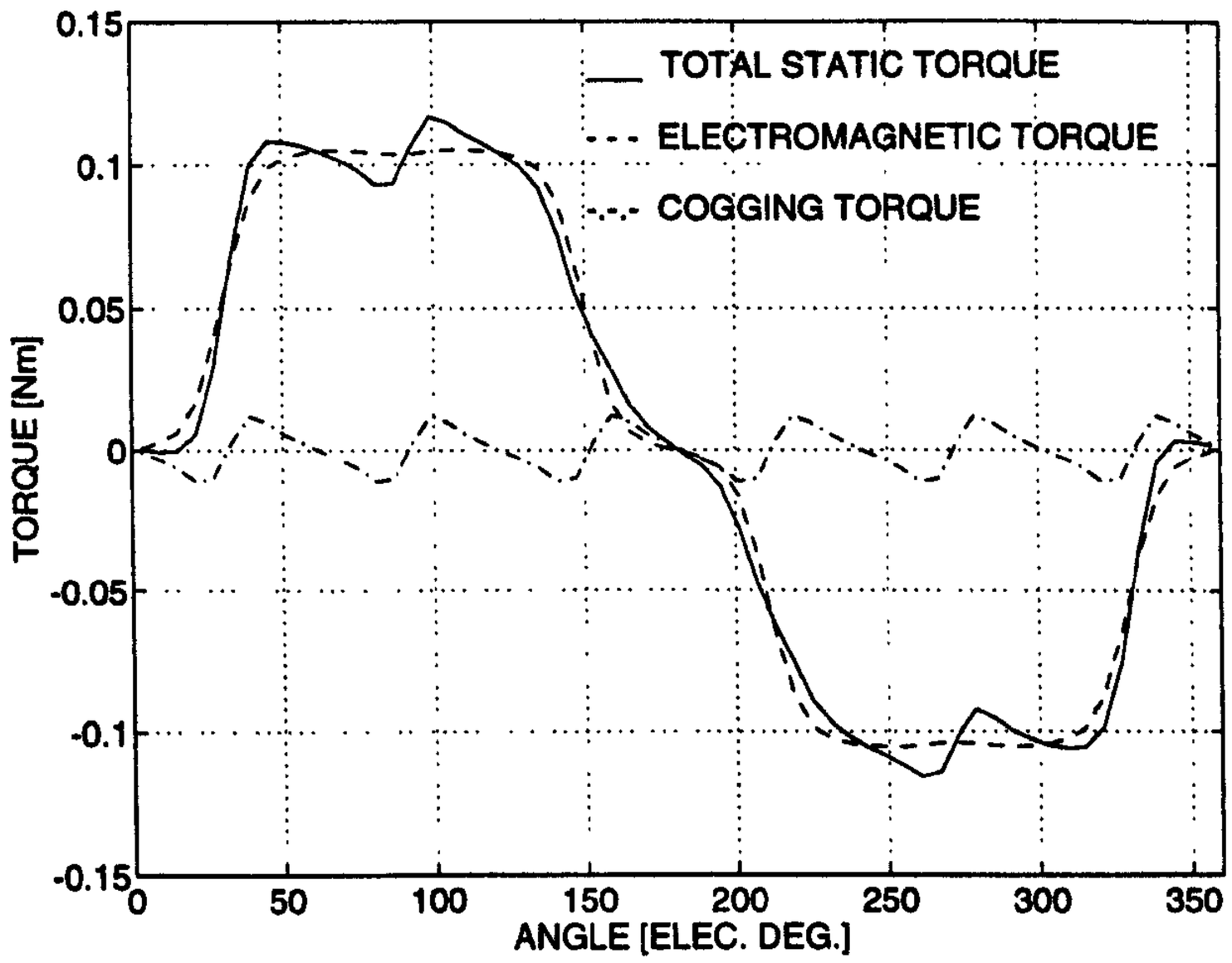

Figure 2.26. Total static torque characteristic for the PM brushless DC motor at 1.0 A DC phase current. Made up of the electromagnetic and the cogging torque components.

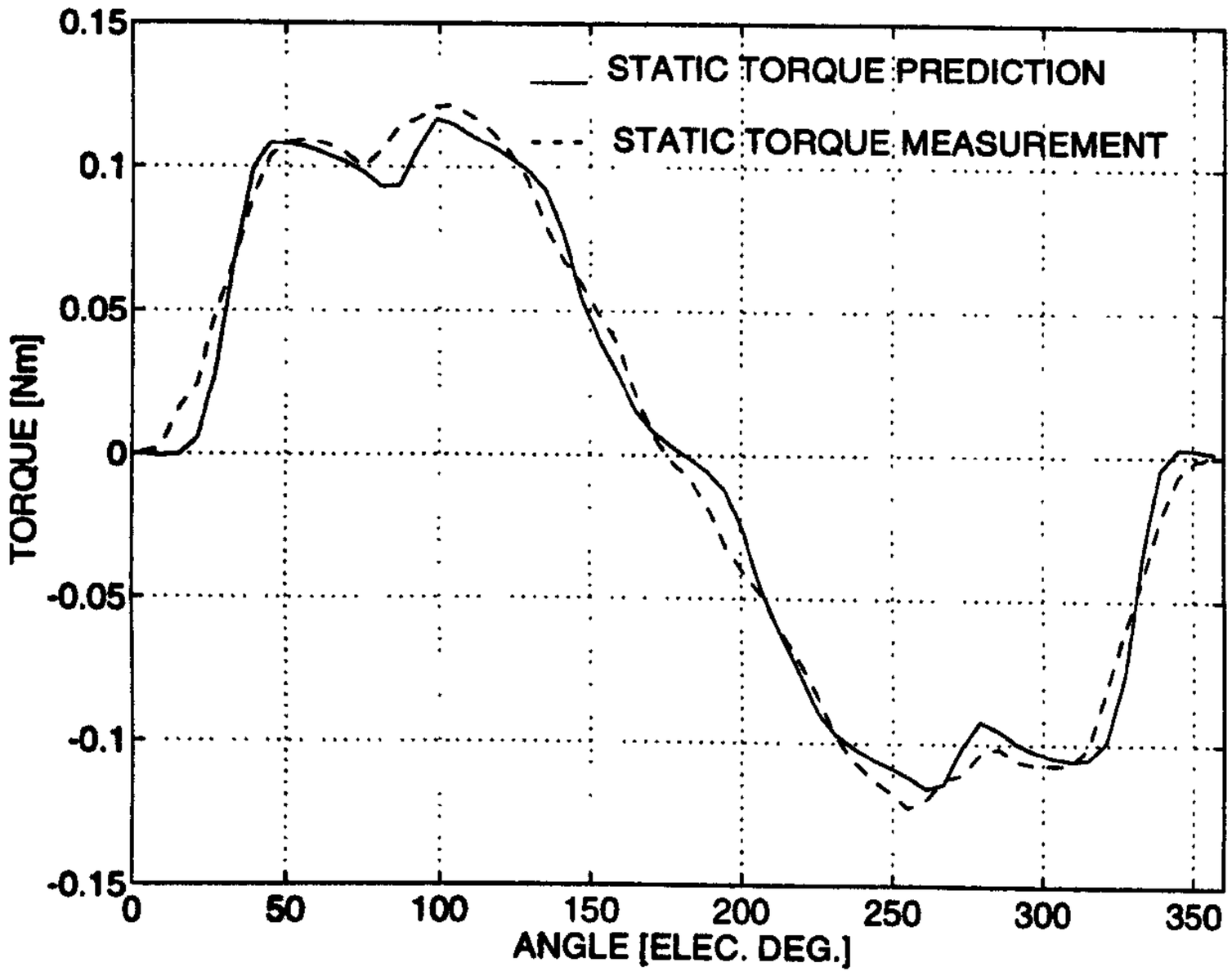

Figure 2.27. Predicted and measured static torque characteristics for the PM brushless DC motor at 1.0 A DC phase current.

Experimental validation is also provided for a PM brushless AC motor, BMR115C6-64S, manufactured by SEM Ltd. This is a 3-phase, 6-pole, 18-slot, rare-earth magnet motor. The detailed specifications with regard to the geometry and winding design can be found in Chapter 3 (Figs. 3.11 and 3.23, and Table 3.1).

Fig. 2.28 shows the combined or total static torque characteristic made up of the cogging and the electromagnetic torque components. Fig. 2.29 compares the predicted and the measured static torque characteristics at 1.0 A DC phase current. Note that, the PM brushless AC motor was designed with a stator skew of one slot pitch. Therefore, the effect of skew was incorporated in the predicted waveforms using the method described in Chapter 4. Because of the stator skew, the torque ripple magnitude in Fig. 2.29 is seen to be much smaller than the one shown in Fig. 2.27, which is for the PM brushless DC motor without skew.

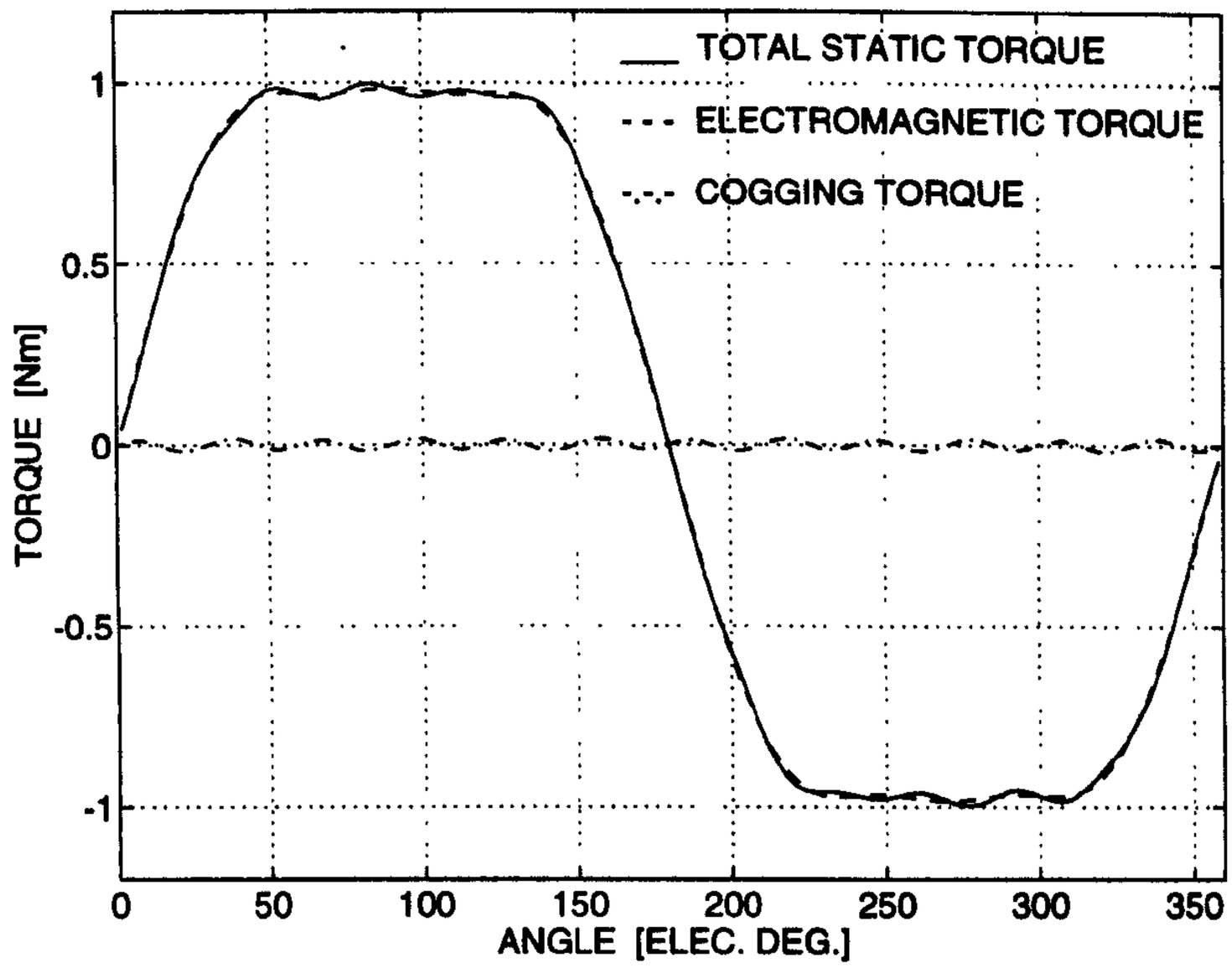

Figure 2.28. Total static torque characteristic for the PM brushless AC motor at 1.0 A DC phase current, made up of the electromagnetic and the cogging torque components.

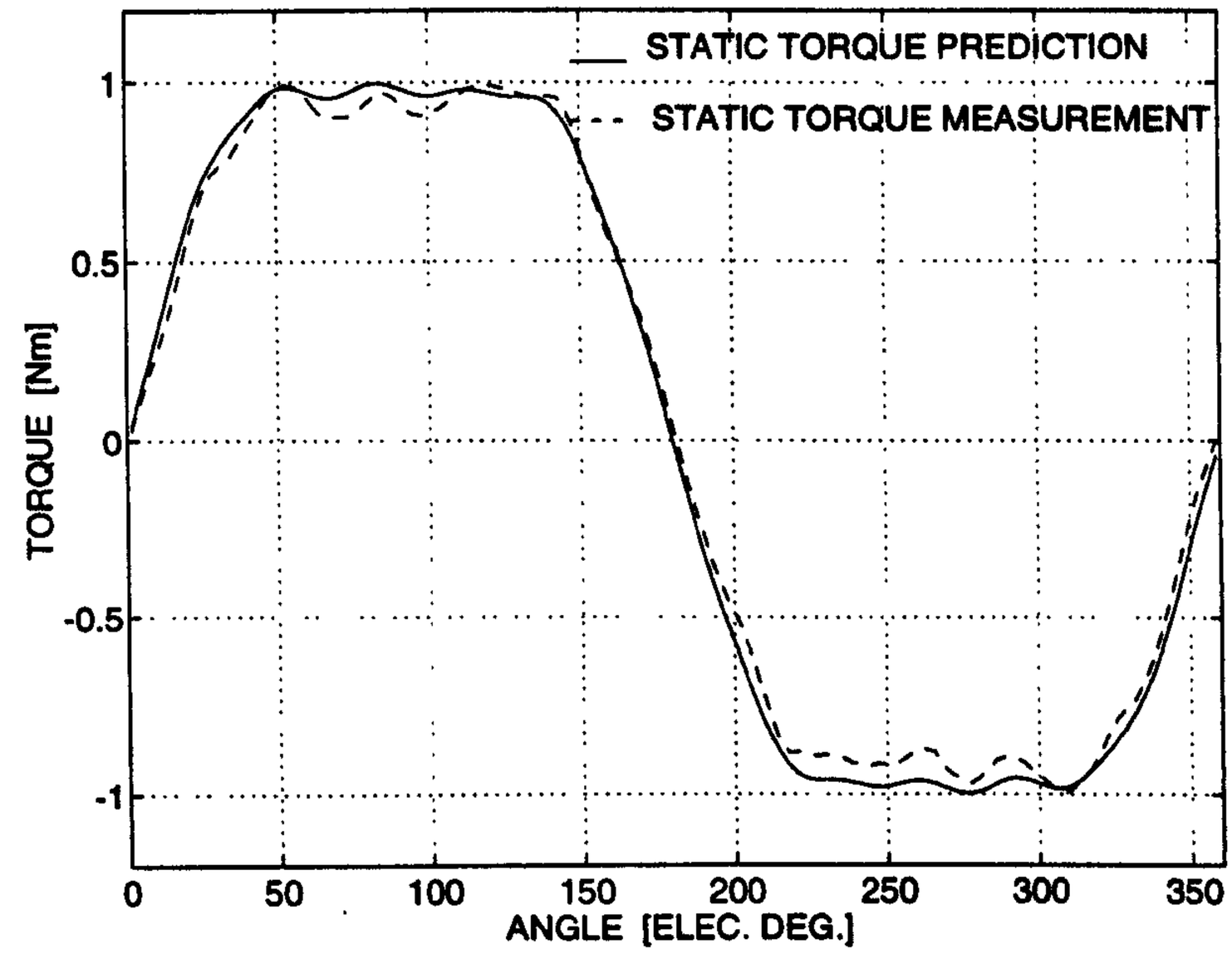

Figure 2.29. Predicted and measured static torque characteristics for the PM brushless AC motor at 1.0 A DC phase current.

2.4.3 Comparative Evaluation

The following two variations of the flux-MMF diagram technique for predicting the electromagnetic torque ripple are presented in this Chapter.

- Electromagnetic Phase Torque Ripple Method. This is presented in Section 2.3, where torque ripple curves for the individual phases are obtained directly from the phase flux-MMF diagram, constructed for the given current excitation (usually squarewave or sinewave). These are then suitably phase shifted and added to obtain the total torque ripple for the entire machine.

- Static Torque Characteristics Method. This is presented in Section 2.4, where first, static torque characteristics for the individual phases are obtained from the phase flux-MMF diagram, constructed for a fixed DC current excitation. These characteristics are then multiplied by the given current excitation (usually squarewave or sinewave) to obtain individual phase torque ripple curves. These curves are then suitably phase shifted and added to obtain the total torque ripple for the entire machine.

The advantages and disadvantages of the individual methods, and a comparative evaluation of the two methods will now be discussed.

Flexibility: The static torque characteristics method provides more flexibility in terms of calculating torque ripple for a variety of current excitation waveforms for the same motor. An example would be of help in explaining this point. The calculation of the total electromagnetic torque ripple in FBL550A-A motor, for squarewave current excitation, has been shown in a series of figures from Fig. 2.22 to Fig. 2.25. The same calculation can also be performed for any other arbitrary shaped current excitation, such as a sinewave current excitation. This is shown in Fig. 2.30, which shows 3-phase current waveforms at 1.0 A peak phase current. The phase currents are respectively

multiplied by the phase static torque characteristic shown in Fig. 2.23, to obtain the phase torque ripple curves and the total torque ripple, as shown in Fig. 2.31.

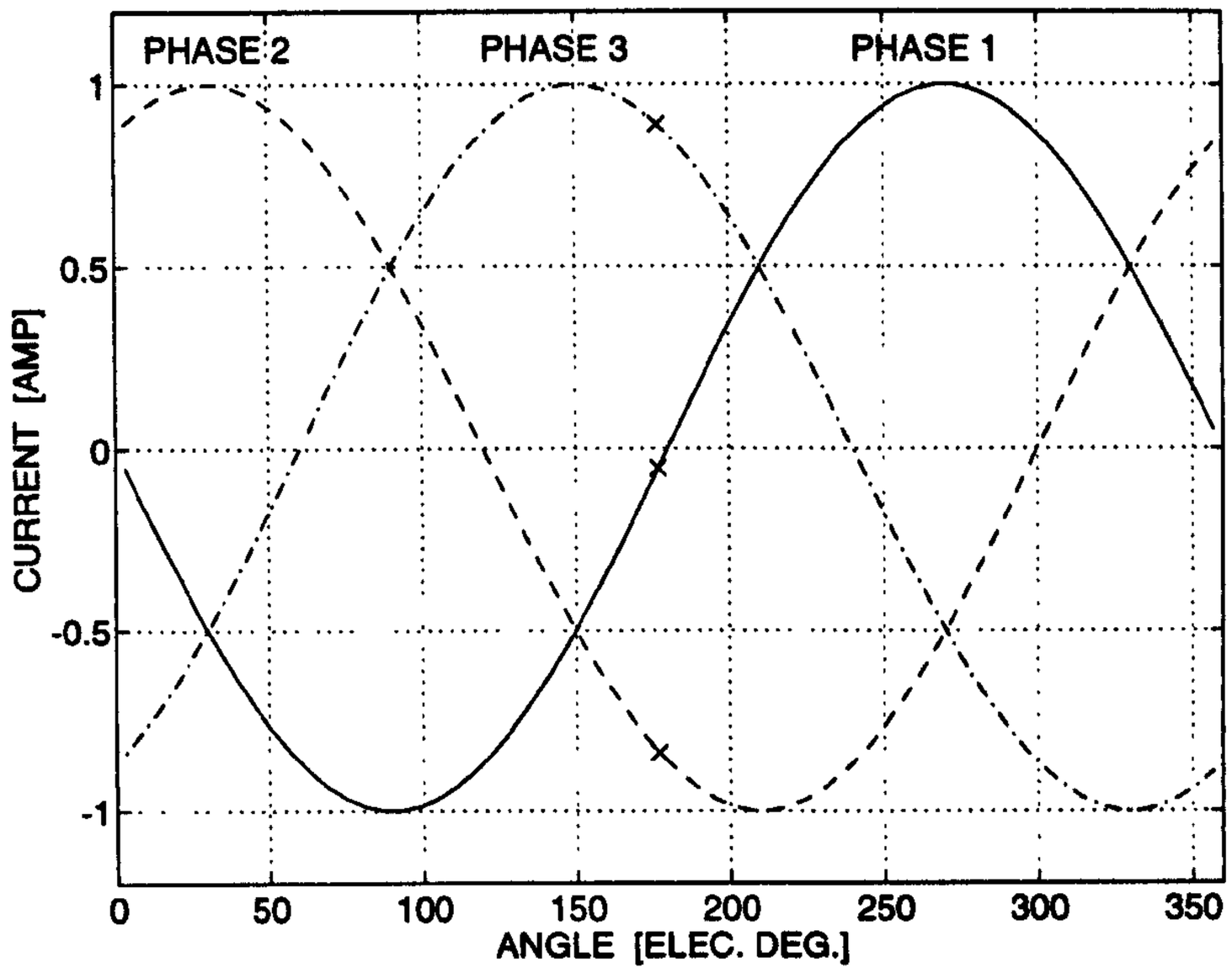

Figure 2.30. 3-phase sinewave current waveforms at 1.0 A peak phase current.

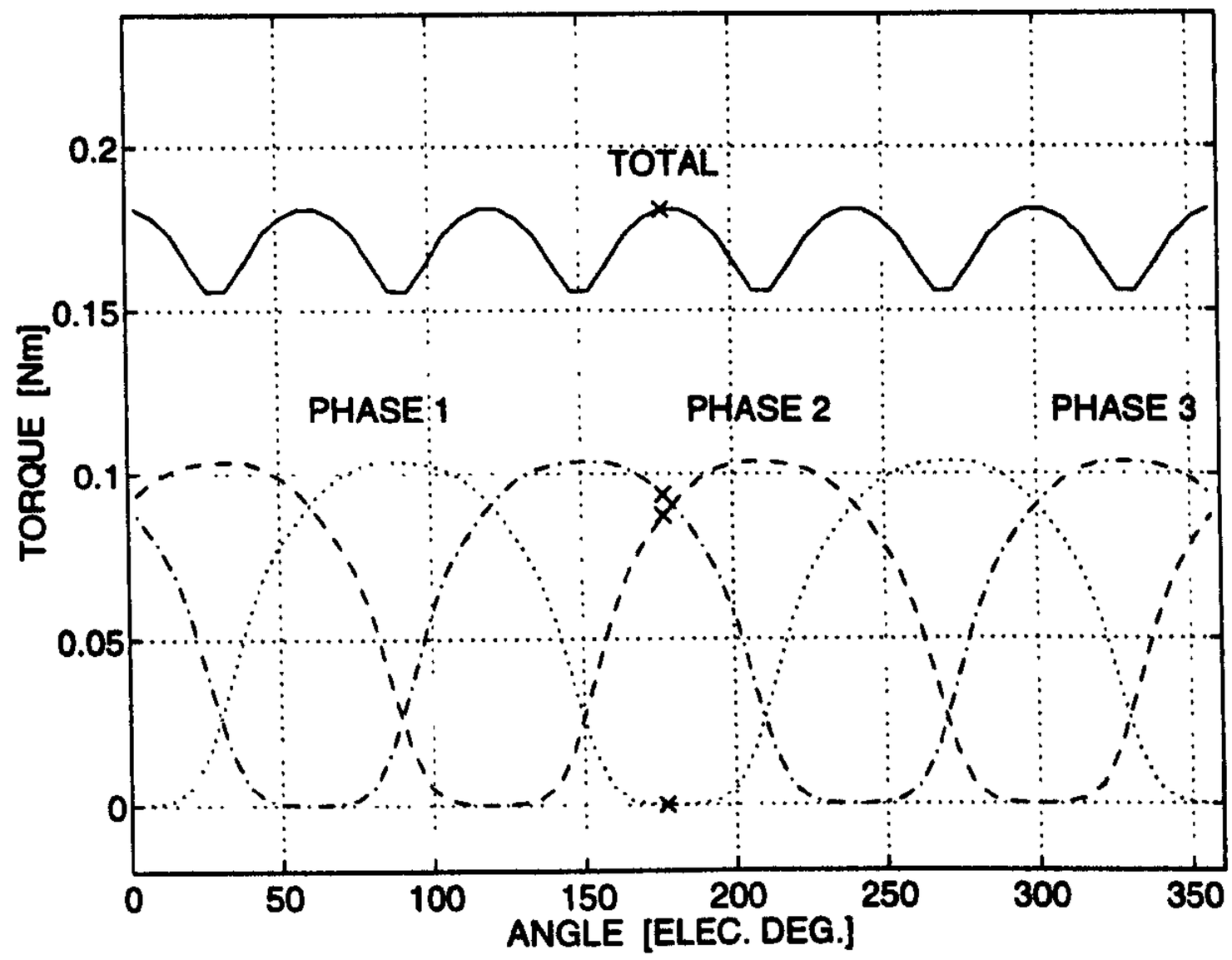

Figure 2.31. Electromagnetic torque ripple for the PM brushless DC motor with sinewave currents.

Since the static torque characteristics are independent of a particular shape of current waveform, they can be used to calculate the torque ripple for any given current excitation. The electromagnetic phase torque ripple method does not provide such flexibility as the phase torque curves are dependent upon the shape the phase current waveforms and hence the torque ripple can be calculated only for a particular current excitation.

Validity: While the Static torque characteristics method has the advantage of flexibility, it also has the disadvantage of restricted validity. In the electromagnetic phase torque ripple method, the torque values for a particular phase are calculated with all the phases excited. Thus, it takes account of *mutual effects*, which are due to the presence of currents in the other phases. Whereas in the static torque characteristic method, the torque values for a particular phase are calculated with only that phase excited. Thus, it does not take account of mutual effects.

In short, even though both the methods make use of the principle of superposition, the static torque characteristics method can only be used under *linear* conditions, when the machine is not saturated; whereas the electromagnetic phase torque ripple method can be used under *all* conditions, with or without saturation in the machine. Fig. 2.32 illustrates this point. It compares the measured torque ripple curves for the FBL550A-A motor, with those calculated using the two different FMDT based methods under unsaturated (at 1.0 A) as well as saturated (at 5.0 A) conditions. The figure demonstrates the fact that while the three curves show reasonable agreement at 1.0 A, the static torque characteristic method is not able to predict the drop in average torque due to saturation at 5.0 A.

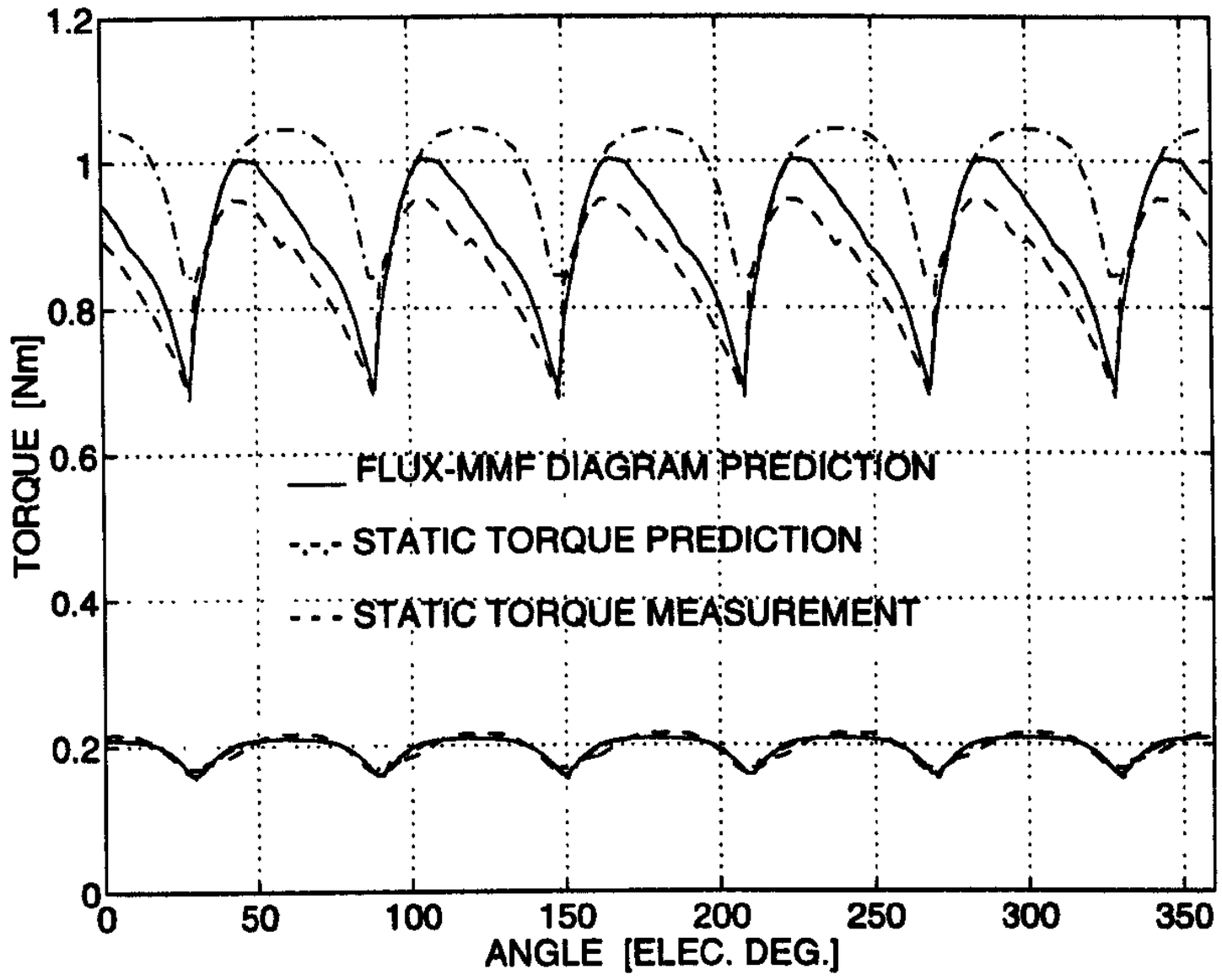

Figure 2.32. Comparison of the measured torque ripple curves for the FBL550A-A motor with those calculated using two different FMDT based methods, under unsaturated (at 1.0 A) as well as saturated (at 5.0 A) conditions.

Computing Resources: In terms of finite-element computational expense, there are advantages and disadvantages associated with both the methods.

In the electromagnetic phase torque ripple method, the advantage is that the rotor displacement modelled needs to be only over 1/6th of an electrical cycle for a 3-phase machine. The disadvantage is that the FE solutions are required for a number of scale factors in order to take account of the saturation.

In static torque characteristics method, the advantage is that the FE solutions are required only for one scale factor. The disadvantage is that the total rotor displacement modelled needs to be for at least half an electrical cycle.

For example, to construct the flux-MMF diagram of Fig. 2.9, 30 meshes were generated at 30 different rotor positions with 1° mech. increment, over $1/6^{th}$ of an electrical cycle. Each mesh was solved for 6 scale factors, totalling 30×6=180 solutions. Whereas to construct the flux-MMF diagram of Fig. 2.22, 90 meshes were

generated at 90 different rotor positions with 3° mech. increment, over half an electrical cycle. Each mesh was solved for 2 scale factors, totalling 90×2=180 solutions. Even though the total number of solutions happen to be the same in this particular case, the rotor displacement resolution has been compromised in calculating static torque characteristics as compared to the calculation of electromagnetic phase torque ripple (3 times coarser in Fig. 2.22 as compared to Fig. 2.9).

Comparative Evaluation Summary: Table 2.5. gives a summary of the discussion so far on comparative evaluation of the two methods of torque ripple calculation.

Table 2.5. A comparison between the two FMDT based methods of torque ripple calculation.

Static Torque Characteristic	Electromagnetic phase torque ripple
Calculated with a fixed DC current excitation in any one phase	Calculated with a given mode of current excitation in all the phases, typically either squarewave or sinewave
Does not take account of the mutual effects	Takes account of the mutual effects
Is always bipolar over one electrical cycle in a PM machine	Can either be bipolar or unipolar depending upon the current excitation
Can be used to derive the total electromagnetic torque ripple, only under linear or unsaturated conditions	Can be used to derive the total electromagnetic torque ripple, under all conditions (unsaturated and saturated)
The phase flux-MMF diagram is restricted to two quadrants either on the left or on the right of the flux-MMF plane	The phase flux-MMF diagram may encompass all the four quadrants depending upon the nature of current excitation
The flux-MMF trajectories are just vertical straight lines	The flux-MMF trajectories may have the shape of an ellipse, a parallelogram or any other shape depending upon the nature of current excitation
The magnetisation curves are always assumed to be linear	The magnetisation curves may be non-linear depending on the level of saturation

2.5 Chapter Summary

Chapter 2 has briefly reviewed the established methods of torque calculation in electrical machines using the finite-element analysis, and has described in detail, two different methods of predicting electromagnetic torque ripple using the flux-MMF diagram. The first method involves constructing a phase flux-MMF diagram for a given current excitation in all the phases and calculating the phase torque ripple curves from it. These curves are then phase shifted and simply superimposed to calculate the resultant electromagnetic torque ripple.

The second method involves constructing a phase flux-MMF diagram for a fixed DC current excitation in only one phase and calculating the phase static torque characteristics from it. These characteristics are then phase shifted and multiplied by the given current excitation. The resulting phase torque ripple curves are then superimposed to calculate the resultant electromagnetic torque ripple.

The advantages and disadvantages of both the methods are discussed and experimental validation is provided in both the cases. A comparison with the established Maxwell stress method of torque calculation shows that the FMDT provides results of comparable accuracy in predicting the electromagnetic torque ripple.

3 Cogging Torque Ripple

3.1 Introduction

At the outset, it is appropriate to define what exactly is meant by the term 'Cogging.' Hendershot and Miller [56] have given a fairly succinct, but at the same time comprehensive, definition for the term as—"cogging is the oscillatory torque caused by the tendency of the rotor to line up with the stator in a particular direction where the permeance of the magnetic circuit *seen* by the magnets is maximised". Cogging torque in permanent-magnet machines is gaining increasing importance along with the demand for high performance brushless PM machines. It is a vital design consideration in power steering, robotics, machine spindle, high-precision position control and indeed, any application where minimising torque ripple, vibration and noise is an essential requirement. In the ensuing analysis, the term 'cogging torque ripple,' which always refers to the instantaneous torque variation, is preferred over the terms such as 'cogging' and 'cogging torque,' which in some literature, refer only to the peak value.

In order to be able to develop alternate and improved techniques of reducing cogging torque, it is important to be able to predict it accurately for any given motor geometry and configuration. Most of the recent literature on cogging makes use of some form of analytical method, the Maxwell stress method or the stored energy method, often enhanced by finite-element analysis (FEA) [23]-[46]. The calculations involved in these methods can be cumbersome and often obscure the physical picture. Also, many cogging torque calculations are specific to a particular method of reducing cogging and it is difficult to generalise them. The flux-MMF diagram technique on the other hand, offers a fundamental basis of design evaluation and a clear physical insight

based on graphical interpretation of diagrams such as Figs. 2.9 and 3.5 [47]–[51]. The technique is well adapted for use with the FEA. It also satisfies the need for a universal technique of cogging torque prediction, which can be used with all the commonly employed methods of cogging torque minimisation.

The next section presents a literature review of the cogging torque calculation and minimisation techniques. Section 3.3 describes the method of predicting cogging toque ripple using the flux-MMF diagram. Section 3.4 analyses various methods of cogging torque minimisation using the flux-MMF diagram technique. Finally, experimental validation is provided in Section 3.5.

3.2 Review of Cogging Torque Calculation and Minimisation Techniques

3.2.1 Calculation Techniques

Extensive amount of literature is available describing a variety of cogging torque calculation techniques. Fig. 3.1 gives a summary of how the calculation techniques can be classified based on the methodology involved. They fall into two primary categories—analytical and numerical. Analytical approaches typically begin with calculation of magnetic flux density distribution along the machine's airgap [25], [26], [29], [32], [33], [41], [84], [86]. These calculations invariably require a series of simplifying approximations in order to make the problem more tractable, such as assumptions of infinite iron permeability [26] or zero flux density under the stator slots [25], [86]. Cogging torque is then derived from the flux density distribution by employing a variety of methods; some of which are discussed here as follows.

- Taking derivative of the associated stored energy [23], [26], [86] with respect to the displacement as in (3.1). While some analyses consider the stored energy over the entire volume [23], [26], others consider the stored energy only in the airgap [86].

$$T_c = \left.\frac{\partial W'}{\partial \theta}\right|_{i,\, MMF = constant} \tag{3.1}$$

- Zhu and Howe [26] have suggested a method of predicting cogging torque in radial field PM motors, based on the analytical calculation of airgap field distribution and summing of the net lateral magnetic force acting along the sides of the stator teeth. Equation (3.2) is an expression, based on this approach, for the net cogging torque developed at a given rotor position.

$$T_c = \sum_{k=1}^{Q_s} l_a \int_0^{b_0/2} \left(\frac{B_{rb1}^2 - B_{rb2}^2}{2\mu_0} \right) r_t \, dr_s \tag{3.2}$$

Where,

T_c is the net cogging torque.

l_a is the active length.

Q_s is the number of stator slots.

b_0 is the slot width (a simple rectangular slot is assumed).

B_{rb1} & B_{rb2} are the flux-density values on the two adjacent sides of a stator tooth.

r_t is the radius for the circular fringing flux path between a rotor pole and a stator tooth side.

This expression, however, makes some simplifying assumptions such as purely rectangular stator slots and infinitely permeable iron, which limit its applicability.

- Ackermann et al. [25] have given an analytical expression for cogging torque based on the rate of change of coenergy as in (3.3).

$$T_c = -\frac{\pi}{4} D l_a \sum_{\xi} \xi \, \frac{\sin(\xi \gamma l_a)}{\xi \gamma l_a} \Lambda_\xi \Phi_\xi \sin(\xi \theta) \tag{3.3}$$

Where,

D	is the machine outer diameter.
l_a	is the stack length.
$\xi = cS,\ c = 1, 2, ..., S$	is the least common multiple of the number of slots.
$\mathrm{Sin}(\xi\gamma l_a)/(\xi\gamma l_a)$	is a factor which determines the influence of skewing.
Λ_ξ	is the ξ^{th} space harmonic of the permeance.
Φ_ξ	is the ξ^{th} space harmonic of the magnetic flux distribution.
θ	is the angle of rotation.

This expression, again, makes an assumption of infinite iron permeability and hence does not take account of saturation.

One of the earliest attempt of analysing cogging torque using the modern numerical methods was made by Wagner [34]. He applied (3.1) to a developed form of one pole pitch of a brushless DC torque motor to calculate cogging torque. Among the variety of modern numerical techniques available for cogging torque calculation, finite-element analysis is by far the most popular approach [34]–[40], [87]. However, closer examination indicates that there are many variations in how FEA is used. Although the majority of reported studies have used well-established 2-dimensional FEA techniques, more recent work has applied 3-dimensional formulations in efforts to model the influence of machine end effects and structure skewing more accurately [24], [91]. Cogging torque is typically extracted from the FEA results using one of the following approaches;

- The energy method by which the torque is calculated from differences in the stored energy at incremental angular positions [85], [87] as in (3.1)
- Hamdi et al. [36] have recently suggested a different implementation of the principle of virtual work in finite-elements by defining 'mean' and 'difference' potentials from the normal vector potentials and using these potentials to calculate the difference in stored energy. They have claimed that this approach circumvents the problem of extracting a small amount of difference from two similarly large quantities; in this case, the stored energies at successive rotor positions.

- Direct torque calculation by integrating the resulting Maxwell stress tensor over the machine's airgap surface [37], [38], [39], [85].

Reported results suggest that no one of these cogging torque calculation methods can be judged superior to the others under all conditions. Although the FEA-based techniques offer opportunities for more precise field calculations than the analytical approaches based on simplifying assumptions, the FEA results are also subject to errors introduced by mesh generation problems or inadequate models of the iron and magnet characteristics [25]. Given the complicated machine geometries and associated non-linearities in material properties, there is a general trade-off between calculation complexity and required torque prediction accuracy which must be judged on a case to case basis.

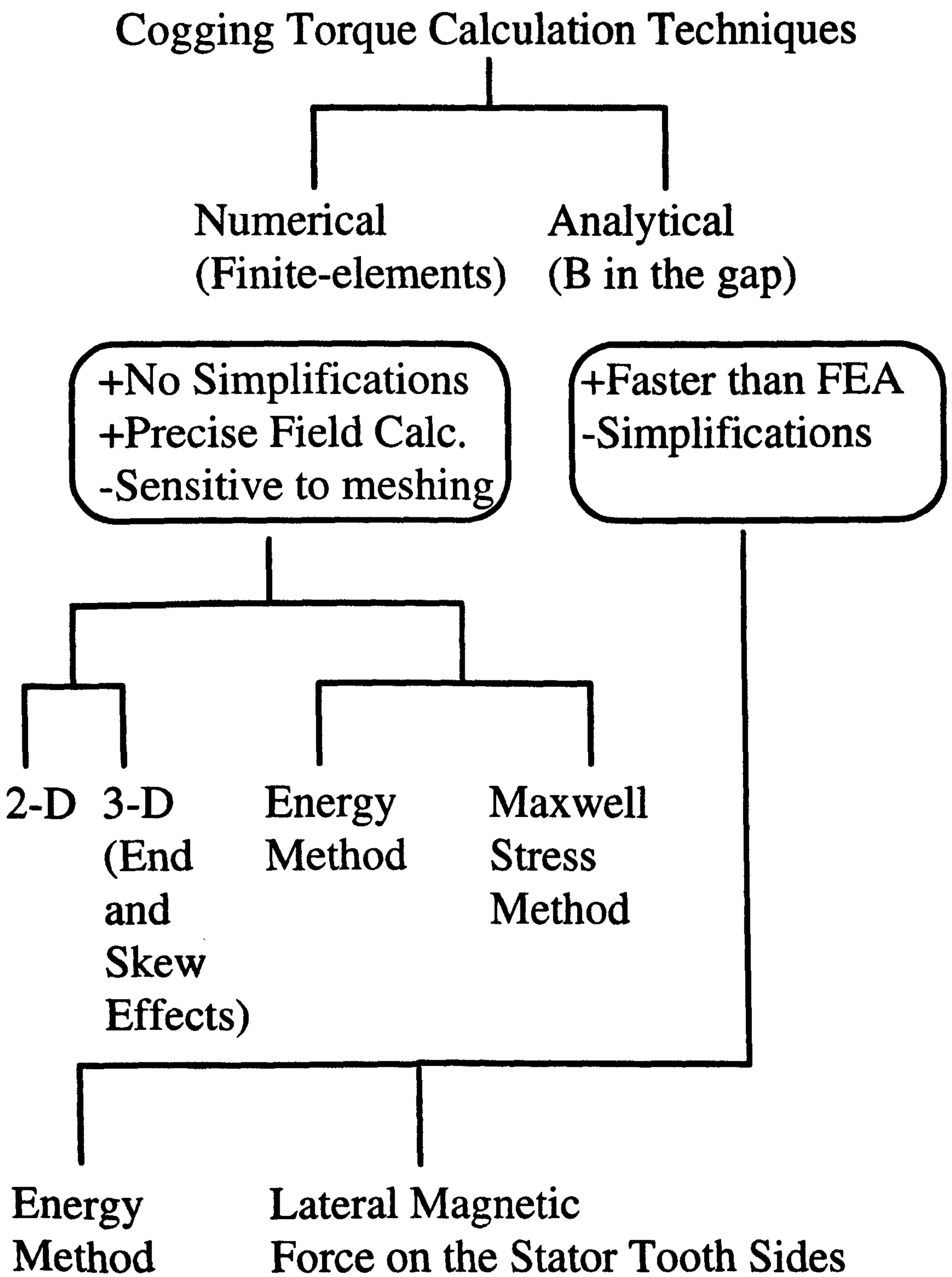

Figure 3.1. A summary of the cogging torque calculation techniques. A '+' sign indicates an advantage while a '-' sign indicates a disadvantage.

3.2.2 Minimisation Techniques

A wide variety of techniques for minimising cogging torque is documented in the literature for both sinusoidal and trapezoidal permanent-magnet machines. Fig. 3.2 gives a summary of the classification of these techniques. A comprehensive list of minimisation techniques is also given in [56]. The majority of this work has been carried out during the past decade coincident with the growing interest in brushless PM machines for high-performance applications. However, many of these techniques trace their origins to the same fundamental methods developed years earlier for minimising torque ripple in conventional AC and DC machines.

One of the most effective of these familiar techniques for cogging torque minimisation is stator slot skewing. Several studies have demonstrated that skewing the stator slots by one stator tooth pitch can reduce the cogging torque to very low levels [29], [43], [84], [85], [86]. If stator skewing poses unacceptable manufacturability problems, the alternative approach of skewing the rotor magnetic field distribution via either skewed rotor magnets (or magnetisation) [43], [82] or skewed mounting of discrete magnet segments on the rotor [84] has been demonstrated to yield similar cogging torque reductions. Since the airgap magnetic permeance variations caused by stator slots are such an important factor in cogging torque generation, a variety of additional techniques have been suggested for minimising these variations or at least favourably modifying their harmonic spectra. One of the more obvious of these approaches is minimisation of the stator slot openings [25], [26], [29], [85], [88], which has the undesirable effect of complicating the stator construction. Taking this approach a step further, slotless stator configurations have been adopted in some special applications where total elimination of cogging torque is required [40], [41].

Other techniques seek to reduce cogging torque production by pushing the harmonic components in the spatial airgap permeance distribution to higher frequencies by either adding dummy slots [45] or dummy teeth [46] to the stator

laminations. Alternatively, this frequency spectrum can be beneficially modified to reduce cogging torque either by shifting the angular positions of individual stator slots [26] or by adopting a fractional number of slots per pole design [29], [39], [43]. However, the impact of such techniques on both the average torque and torque ripple when the windings are excited must be carefully considered.

The tight interrelationship between the cogging torque ripple and the electromagnetic torque ripple is particularly apparent in trapezoidal PM machines where conflicts often arise during attempts to reduce both components simultaneously. Since trapezoidal machines favour concentrated stator windings in order to minimise electromagnetic torque ripple, skewing of the stator slots to reduce the cogging torque has the undesired effect of increasing the total torque ripple [86].

As a result of this trade-off, alternative approaches for reducing the cogging torque in trapezoidal machines have been investigated with unskewed stators. For example, optimal ratios of magnet arc width to pole pitch have been identified for minimising cogging torque, combined with a strategy of shifting alternate magnet arcs by one-half stator slot pitch in multi-pole-pair designs [38], [84], [87]. However, the effectiveness of these techniques is dependent on maintaining accurate mechanical tolerances on the physical dimensions and magnetisation of the rotor magnets. Other rotor-based techniques which have been proposed for reducing cogging torque include shaping of the rotor magnet segments [85] and addition of a thin magnetic retaining ring [35].

All of the cogging torque minimisation techniques reviewed in this section involve modifications of the machine design. If circumstances make it impractical to reduce cogging and/or electromagnetic torque ripple sufficiently in the basic machine design, a separate set of control based techniques have been developed to compensate these parasitic torque components by modifying the current excitation waveforms [27], [30], [44].

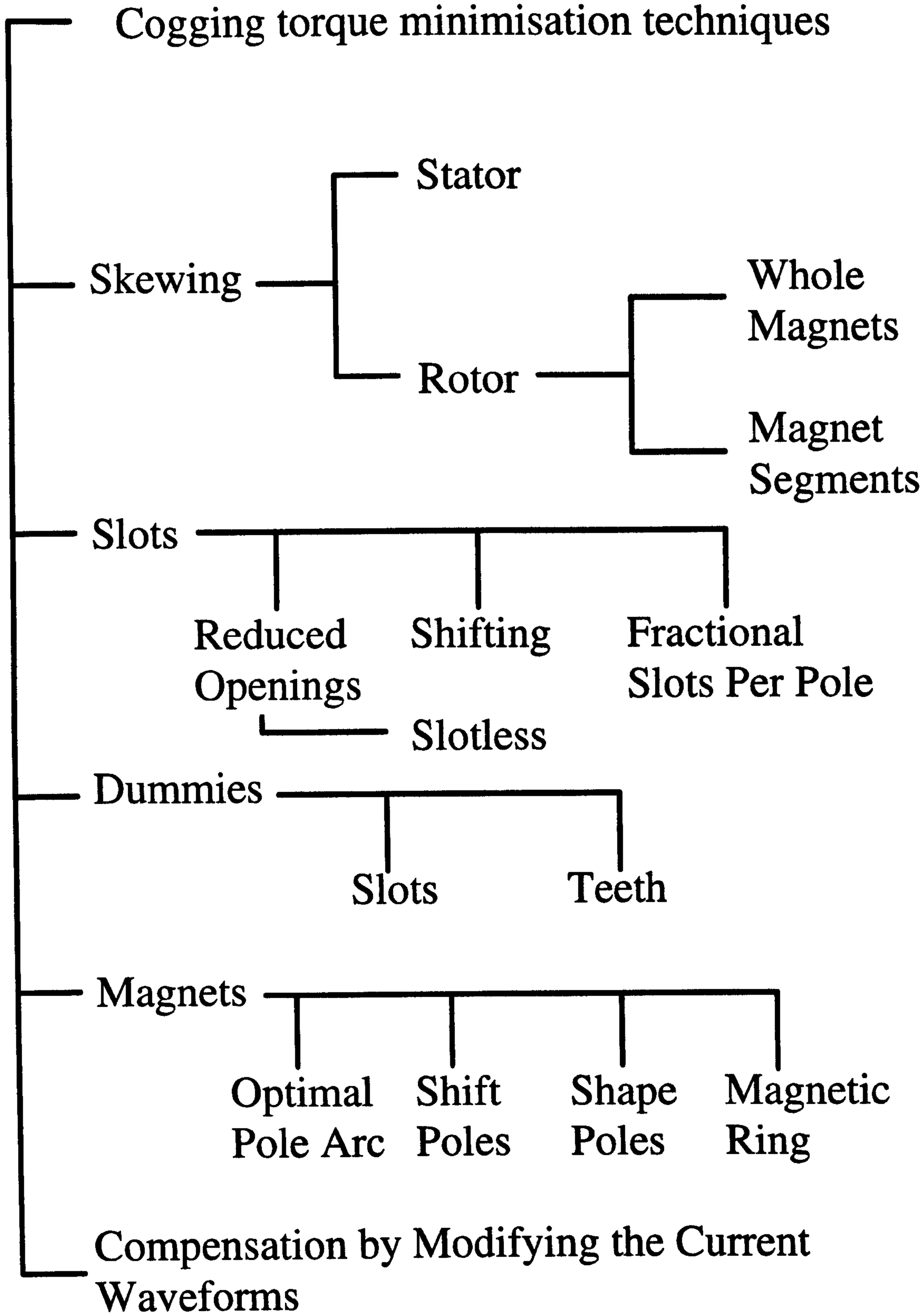

Figure 3.2. A summary of the classification for the cogging torque minimisation techniques.

3.3 Prediction of Cogging Torque Ripple using the Flux-MMF Diagram

3.3.1 Flux-MMF Diagram for a Phase

Chapters 1 and 2 have discussed how to construct a flux-MMF diagram for any one phase of an electrical machine, and how to predict electromagnetic torque ripple from it. However, it is important to realise that the flux-MMF diagram for a phase does not and cannot, by itself, predict the cogging torque ripple.

To understand this, consider any phase flux-MMF diagram for a PM machine shown in Figs. 1.13, 2.1 or 2.9, from Chapters 1 and 2. Although, they are of different shapes and are constructed for different machines, they all have one feature in common. At zero phase current, they all show flux-MMF trajectories which are simply vertical lines on the MMF=0 axis. In general, at any non-zero phase current, the flux-MMF trajectory encloses a finite area which is proportional to the phase current and indicates the average torque generated at that current. But at zero current, the trajectory is just a vertical line which does not enclose any area and hence does not predict any torque. This confirms the fact that cogging torque ripple, by itself, is independent of any current excitation. This can be observed in Figs. 2.5 and 2.13. Both show purely electromagnetic torque ripple curves for different machines at different currents, but both show zero torque ripple at zero current.

Thus it can be recognised that with the conventional way of constructing the flux-MMF diagram for any one phase, it is not possible to predict cogging torque in a permanent-magnet motor. Since the phenomenon of cogging depends only on the interaction of the permanent-magnets with the stator slotting, it is independent of the nature of current excitation and distribution of conductors in any one phase.

In order to circumvent this problem, it is proposed that rather than plotting the flux-MMF diagram for *any one phase*, the flux-MMF diagram can be plotted for a permanent-magnet corresponding to *any one pole*, so that the cogging torque can be predicted by applying the principle of virtual work. The next section describes this methodology in detail.

3.3.2 Flux-MMF Diagram for a Permanent-Magnet

Fig. 3.3 shows the sketch of a typical flux-MMF diagram for a permanent-magnet corresponding to any one pole of a PM motor. It is constructed using a combination of data on the flux and MMF variation with respect to rotor position for a single pole, obtained from the FE analysis; and the demagnetisation characteristic of the permanent-magnet.

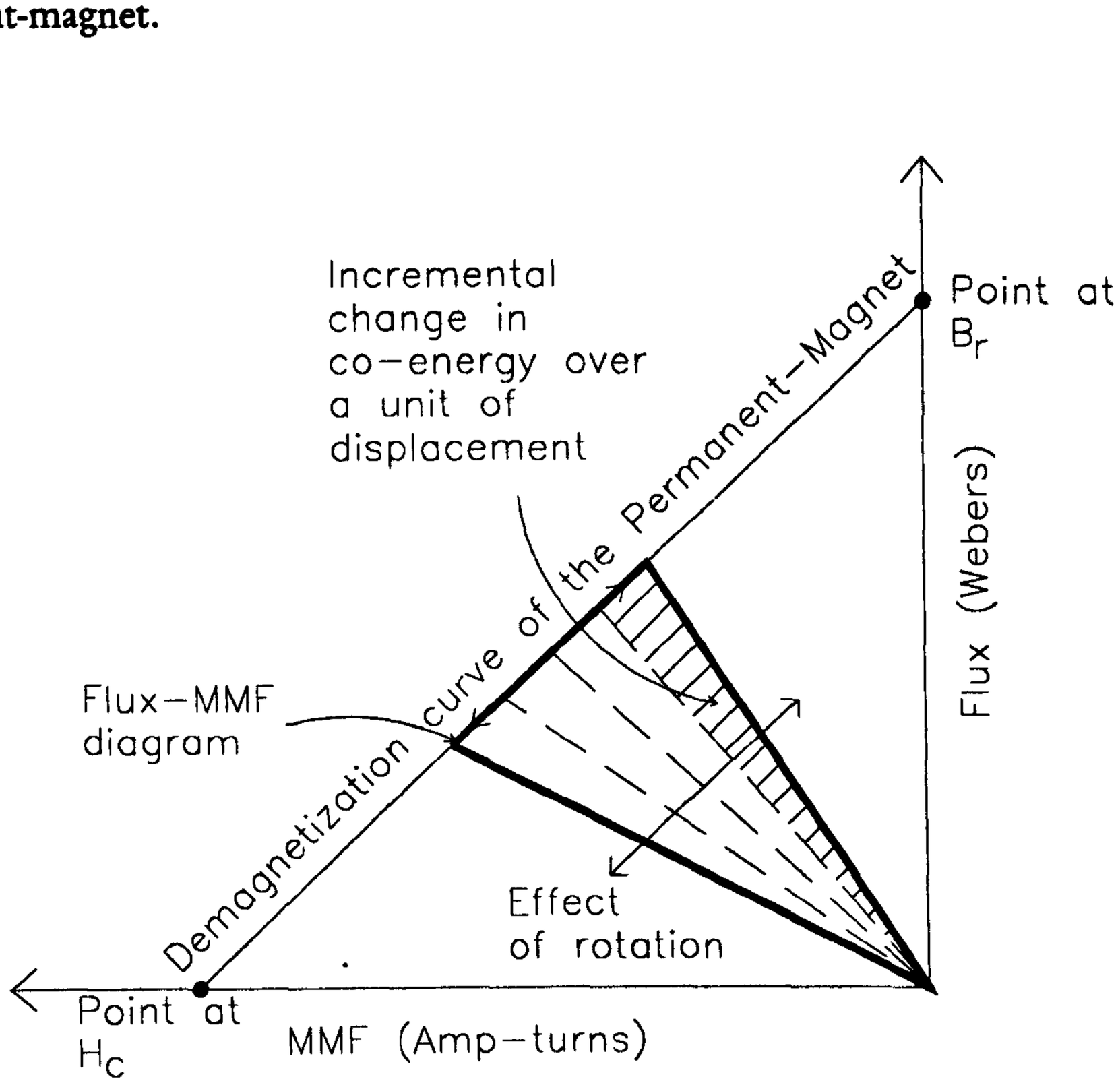

Figure 3.3. Flux-MMF diagram for a permanent-magnet corresponding to any one pole.

Just as in the case of a conventional flux-MMF diagram (for a phase), finite-element solutions are generated at incremental rotor positions over one cogging torque cycle. Using these solutions, values of total flux emanating from the permanent-magnet for a single pole are obtained at each rotor position. Fig 3.4 explains how flux is calculated simply as a difference of vector potentials at the two edges of the permanent-magnet.

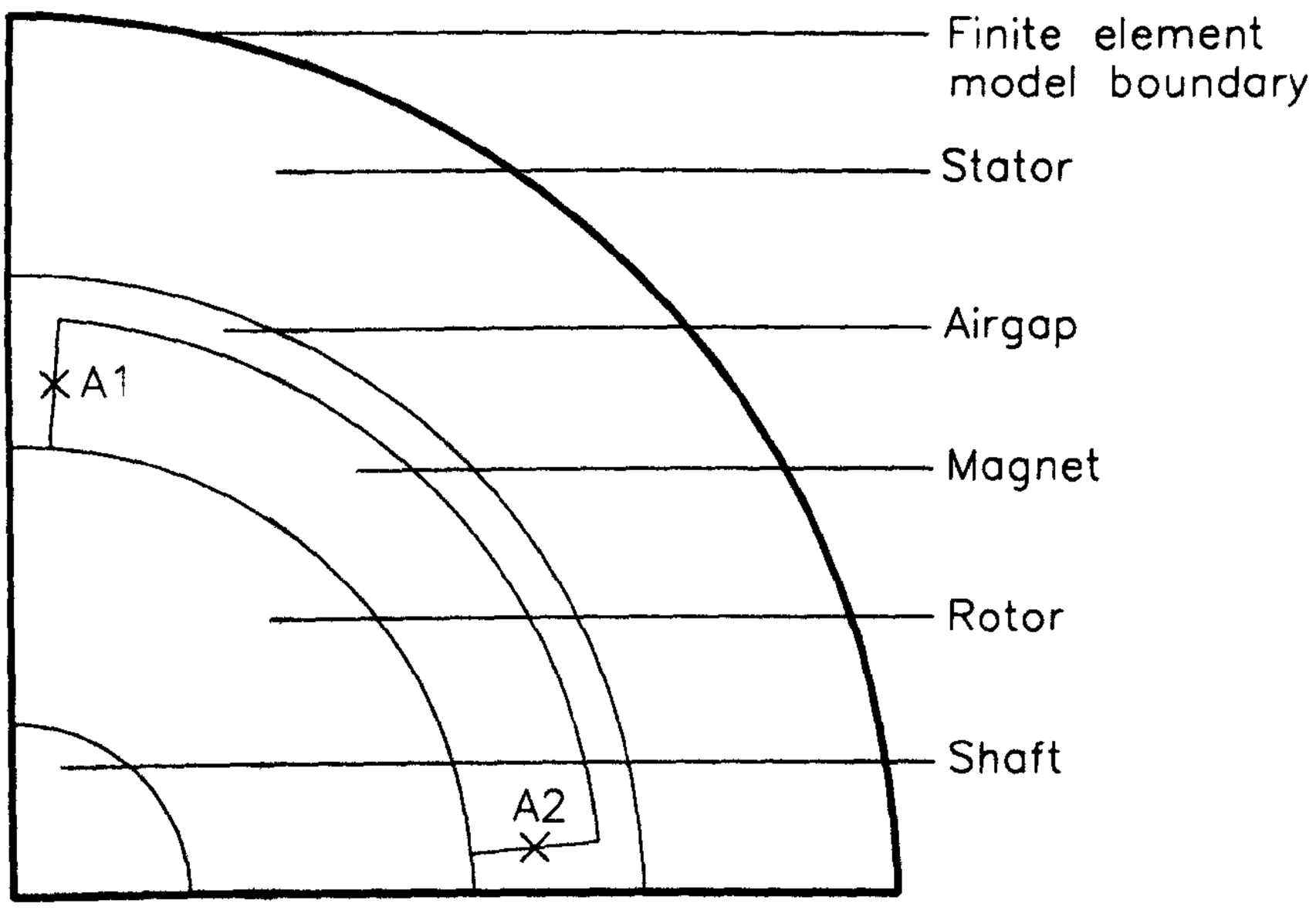

Figure 3.4. Calculation of the flux emanating from a permanent-magnet.

The corresponding MMF values are obtained using the demagnetisation characteristic expressed in the form of (3.4).

$$MMF = \frac{l_m}{\mu_0 \mu_r}\left(\frac{\varphi}{A_m} - B_r\right) \tag{3.4}$$

Variation of flux is then plotted against the variation of MMF over one cogging torque cycle superimposed on the demagnetisation characteristic. This represents the flux-MMF diagram for a permanent-magnet corresponding to any one pole—a triangle

in dark solid lines in Fig. 3.3. Note that an average working point on the demagnetisation characteristic is defined with the flux and MMF values calculated at every rotor position. Any localised variations in this working point within the magnet are assumed to be small and hence neglected. Also, the so called *load-lines* at each incremental rotor position, shown by the dotted lines in Fig. 3.3, are assumed to be linear. This is adequate in most cases except when there is high saturation in stator tooth tips or when the magnet working point is pushed beyond the *knee-point* due to the extremely high load currents, in which case, the load-lines may be non-linear [61].

It is interesting to note that the flux-MMF diagram for a permanent-magnet is, in a way, similar to the ψ-i diagram for a switched reluctance motor or a relay. While the PM diagram is plotted in the second quadrant, the SR diagram is usually plotted in the first quadrant and both can take account of linear as well as non-linear magnetisation curves. Once the flux-MMF diagram for any one pole is obtained, predicting cogging torque becomes an easy matter of calculating *instantaneous* torque for each incremental rotor position using the rate of change of coenergy with displacement as in (3.1). Even when no current is flowing, (3.1) can still be applied by replacing i with *MMF* of the permanent-magnet. Finally, total cogging torque is obtained by simply adding together the cogging torque contribution from each individual pole.

The methodology is now explained with the help of a specific example. Fig. 3.5 is the actual flux-MMF diagram for a permanent-magnet corresponding to any one pole for the FBL550A-A motor shown in Fig. 2.6. The variation of flux and MMF with respect to the rotor position, which is used to plot Fig. 3.5, is shown in Fig. 3.6. Fig. 3.7 is same as Fig. 3.6 but plotted with respect to absolute zero on the ordinate, to bring out the fact that this variation is indeed very small. This is the reason why the flux-MMF diagram appears to be a single dotted line in the top half of Fig. 3.5. But in reality it is made up of a number of load lines all starting from the origin and giving an overall shape of a triangle as shown in Fig. 3.3. This is also shown in the bottom

half of Fig. 3.5. Fig 3.8 Shows the cogging torque ripple predicted for the FBL550A-A motor using the flux-MMF diagram of Fig. 3.5.

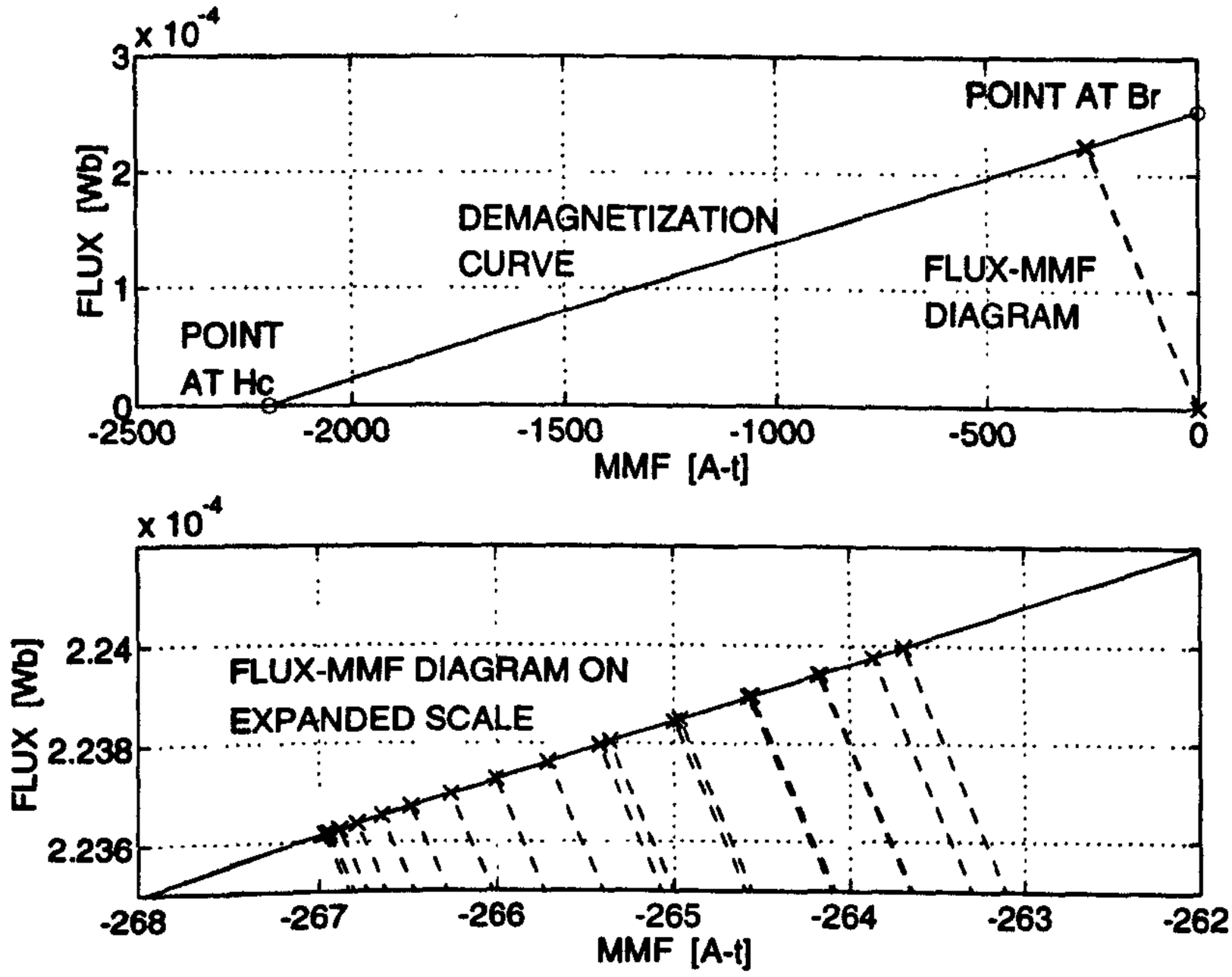

Figure 3.5. Flux-MMF diagram for a permanent-magnet corresponding to a single North pole of the OM FBL550A-A motor. Figure at the top is the actual flux-MMF diagram showing very small areas enclosed by dotted load lines at successive rotor positions, while figure at the bottom shows the same on an expanded scale.

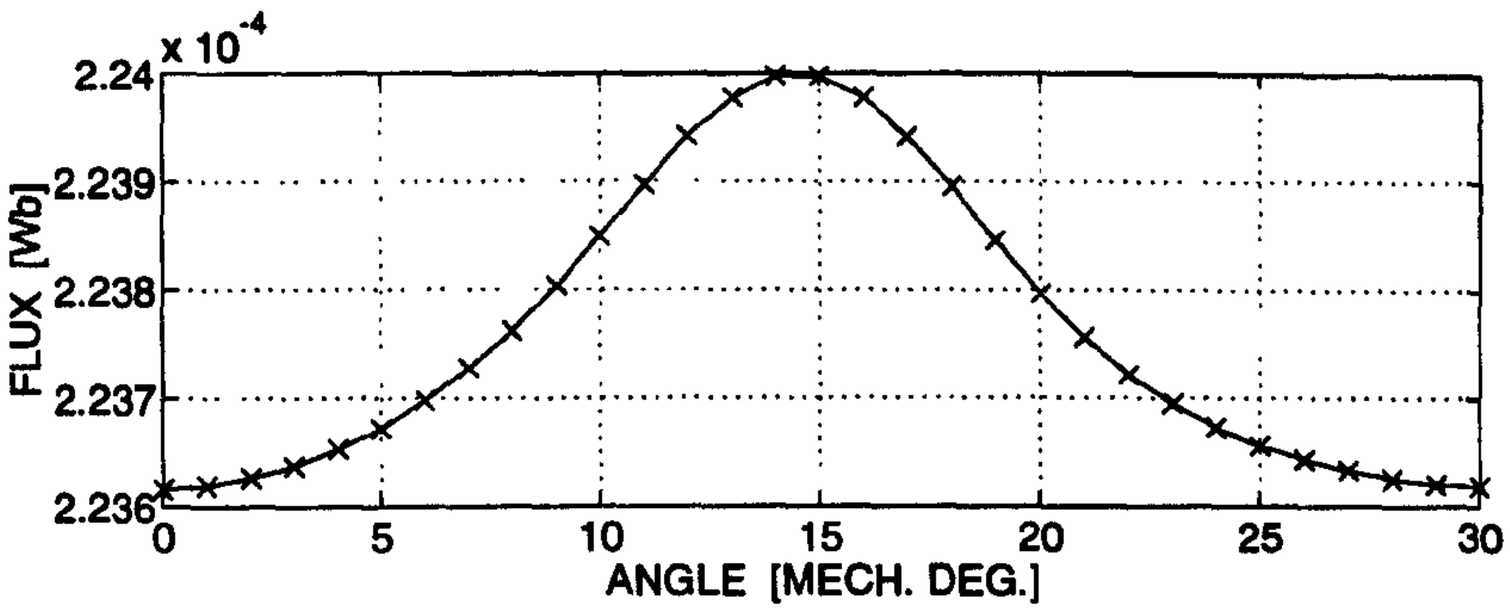

Figure 3.6. Flux and MMF variation with respect to the rotor position for a single pole over a cogging torque cycle used to construct the flux-MMF diagram shown in Fig. 3.5.

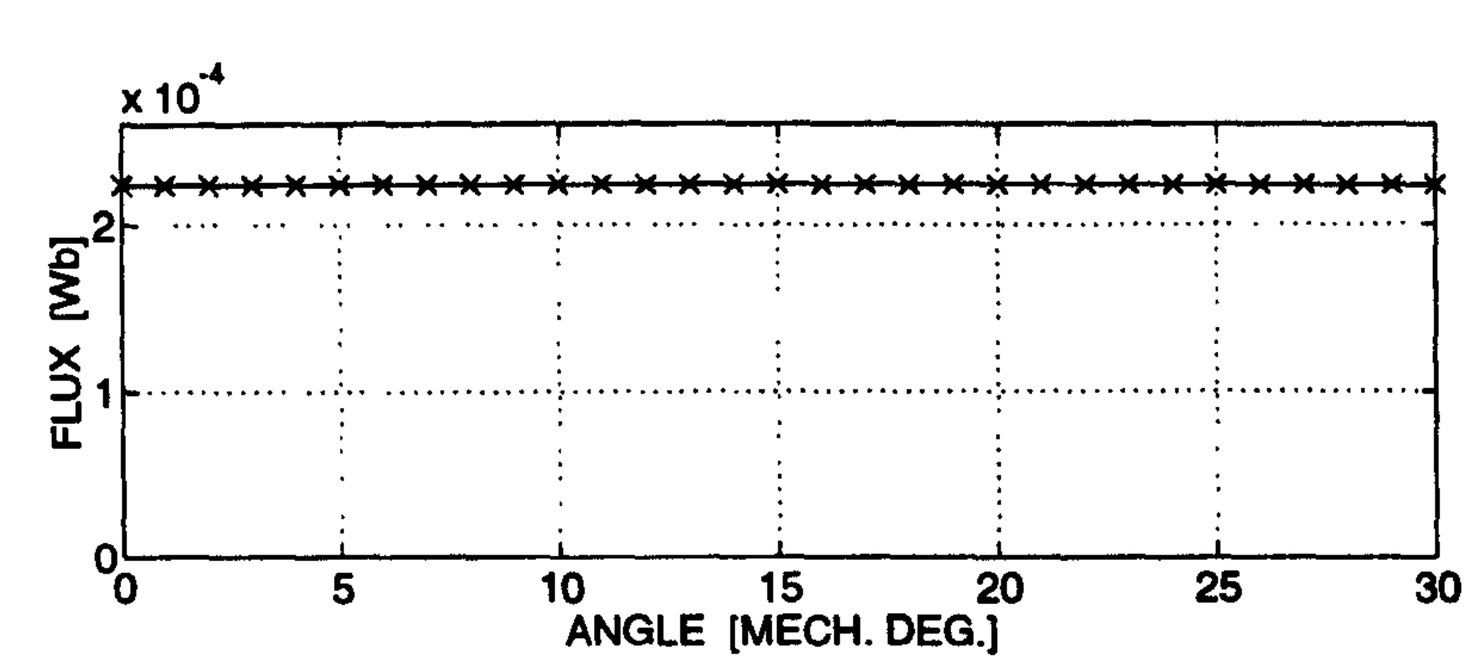

Figure 3.7. Same as Fig. 3.6 but plotted with respect to absolute zero on the ordinate, showing that the flux and MMF variation is indeed very small.

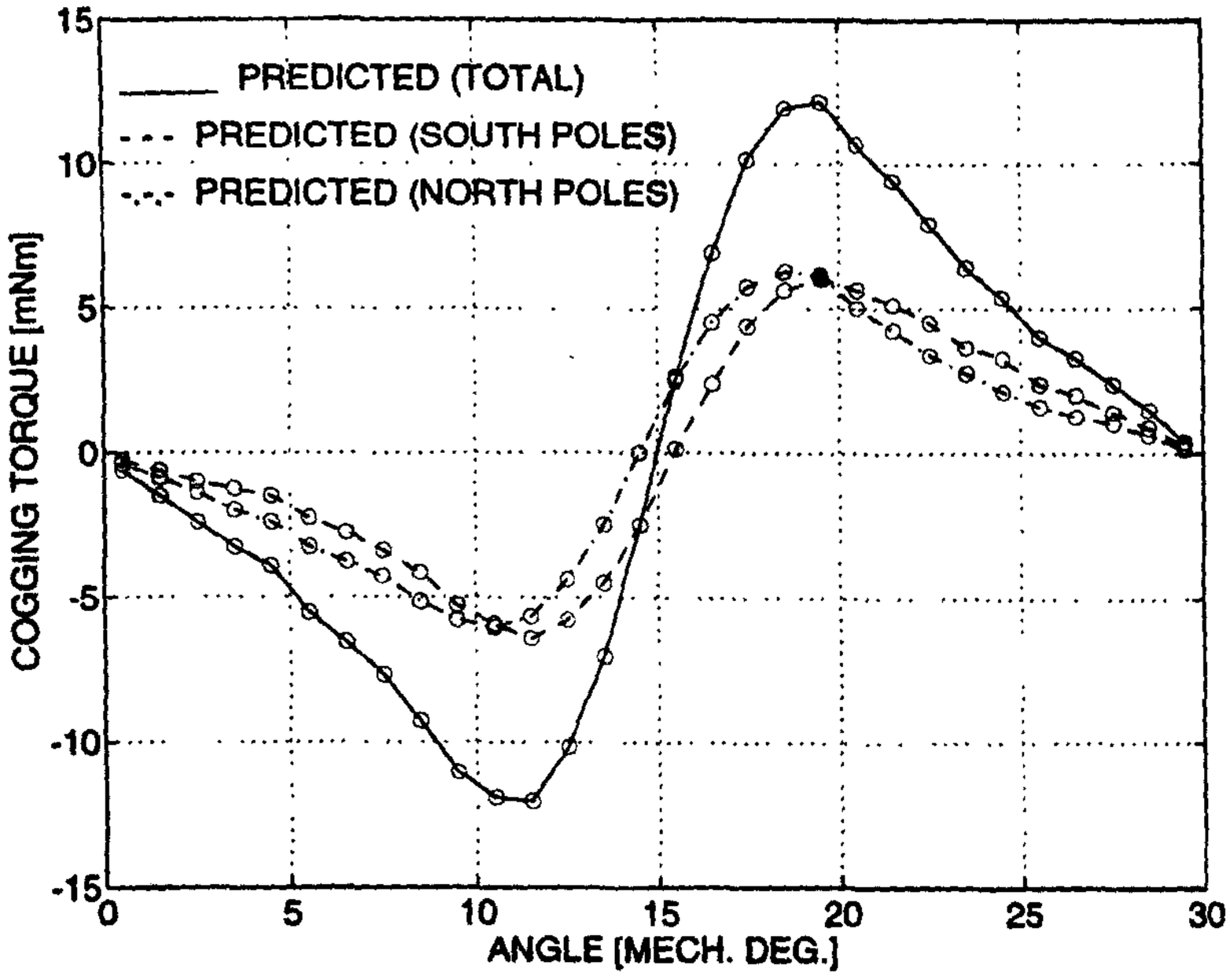

Figure 3.8. Predicted cogging torque ripple for the OM FBL550A-A motor. Different ripple curves for the pairs of North and South pole are also shown.

It is to be noted that in Fig. 3.8, total predicted cogging torque ripple is made up of two different cogging torque ripple curves corresponding to the pairs of North and South pole and these two curves are mirror images of each other. The reason can be seen clearly from Fig. 2.6. At any given rotor position, while one pair of poles with same polarity is facing teeth, the other pair is facing slots; which means that the two pairs are subjected to different magnetic circuits. When the flux-MMF diagrams are plotted for each pair, they are different from each other, giving rise to cogging torque ripple curves which are consequently different from each other. This phenomenon is peculiar to motors with fractional number of slots per pole. In motors with integral number of slots per pole, each pole is subjected to an identical magnetic circuit and the flux-MMF diagram is exactly the same for all poles.

3.4 Analysis of Cogging Torque Minimisation Techniques using the FMDT

3.4.1 Skewing

This is the most common method applied for reducing cogging torque in permanent-magnet motors. The flux-MMF diagram is adept at taking account of fractional as well as integral slot pitch skew [51]. A detailed analysis of this method is given in chapter 4.

3.4.2 Varying the Magnet Arc

Varying the magnet arc has a significant effect on the magnitude and shape of the cogging torque ripple. As an example, BMF115C6-T, a ferrite-magnet brushless DC motor, manufactured by SEM Ltd., is considered. The cross-section picture of this motor is shown in Fig. 4.7 in Chapter 4. A flux plot for this motor over two half poles obtained from the finite-element analysis is shown in Fig. 3.9. The motor has full (180° elec.) magnet arcs as seen in Fig. 3.9. Fig. 3.10 shows the effect of varying the magnet arc on cogging torque ripple analysed using the flux-MMF diagram. For this particular design, if the magnet arc is reduced, the peak cogging torque is also reduced, only up to a certain value of magnet arc (130° elec.) beyond which it starts to increase again (125°, 120° and 100° elec.). From this kind of analysis, it is possible to calculate the *optimum* magnet arc for which cogging torque will be minimum for a given motor geometry.

It is important to note that changing the magnet arc will affect both cogging and electromagnetic torque ripple in completely different ways. While cogging torque depends only on the interaction between the magnets and the stator slots,

electromagnetic torque ripple depends, among many other factors, on the shape of the generated EMF which in turn depends upon the magnet arc. It is unlikely that a particular value of magnet arc will minimise both kinds of torque ripple at the same time. In most cases, a compromise has to be made in order to minimise the total torque ripple.

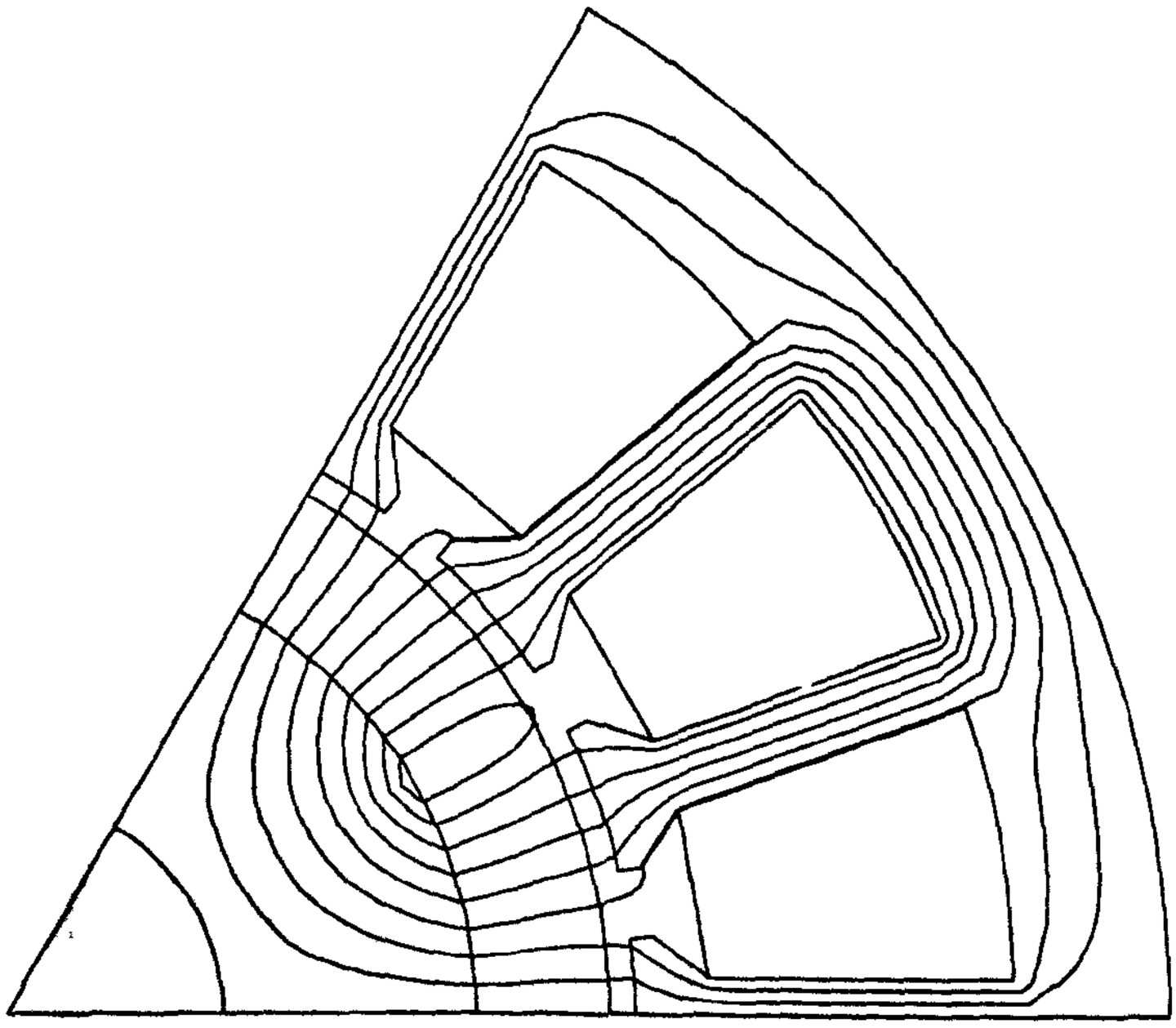

Figure 3.9. Flux plot over two half poles for the SEM BMF115C6-T motor.

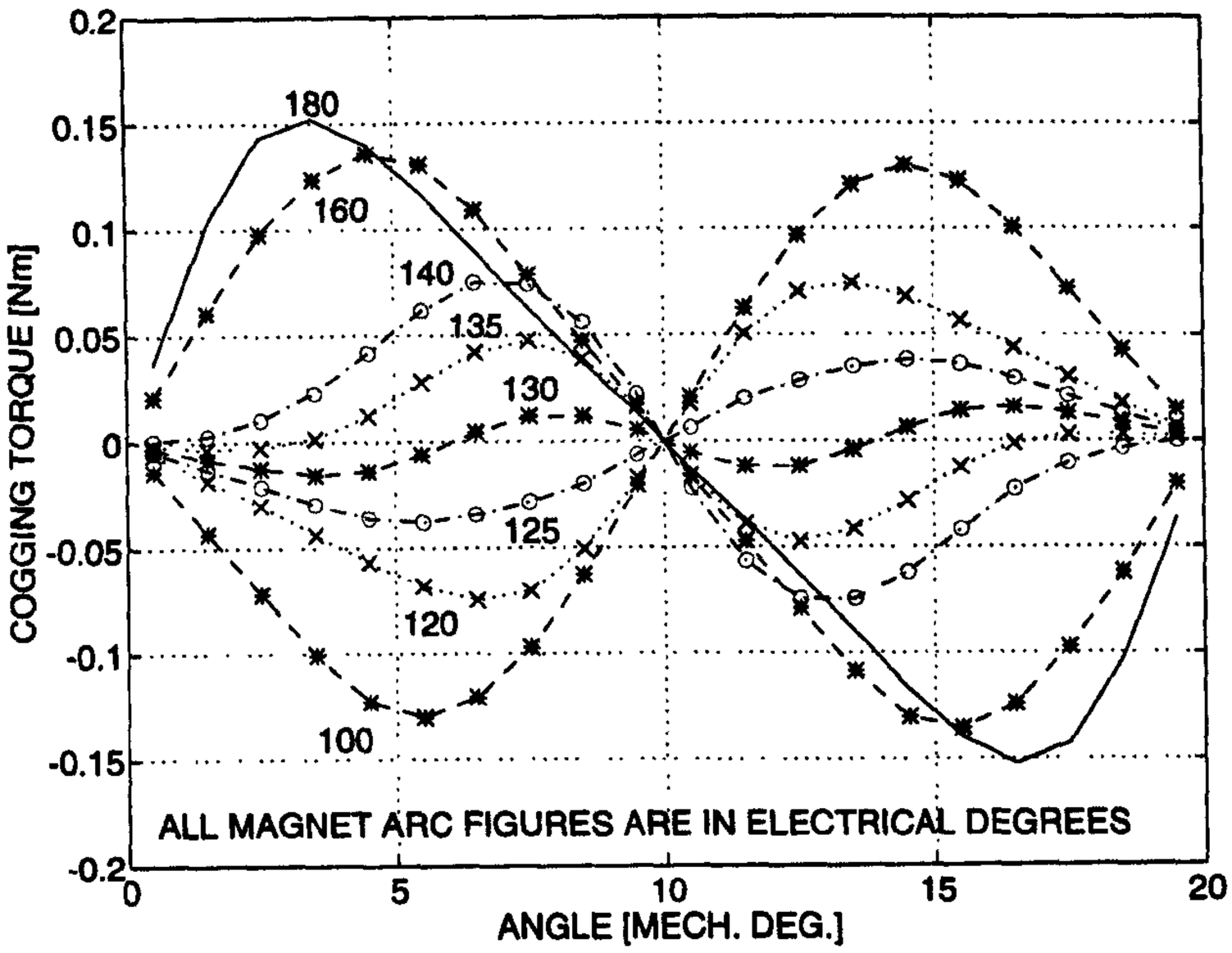

Figure 3.10. Cogging torque ripple at different magnet arcs for the SEM BMF115C6-T motor.

3.4.3 Bifurcated Teeth

This method and some minor variations of it, are documented in detail in [45], [46]. In this method, small sized dummy slots, which do not carry any winding, are added at the tooth tip such that every tooth is sub-divided into a number of smaller teeth and the number of slots *seen* by the magnets is effectively increased. This reduces the period (increases the frequency) of a cogging torque cycle and simultaneously reduces the peak cogging torque value. Hanselman [31] has shown that the peak cogging torque is directly proportional to the net variation in magnetic permeance with respect to the rotor position, which readily explains the fact that adding dummy slots or teeth to the stator, reduces the net permeance variation leading to reduction in peak cogging torque. Figs. 3.11 and 3.12 are flux plots over two half poles for the SEM BMR115C6-64S rare-earth magnet sinewave brushless AC motor, with and without bifurcated teeth respectively. Fig. 3.13 compares cogging torque ripple in

both the cases. It can be observed that bifurcated teeth halve the period (double the frequency) and simultaneously reduce the peak cogging torque by about 50%. The same effect is observed, as expected, in the flux and MMF variation with respect to the rotor position over a cogging torque cycle shown in Fig. 4.18 in Chapter 4.

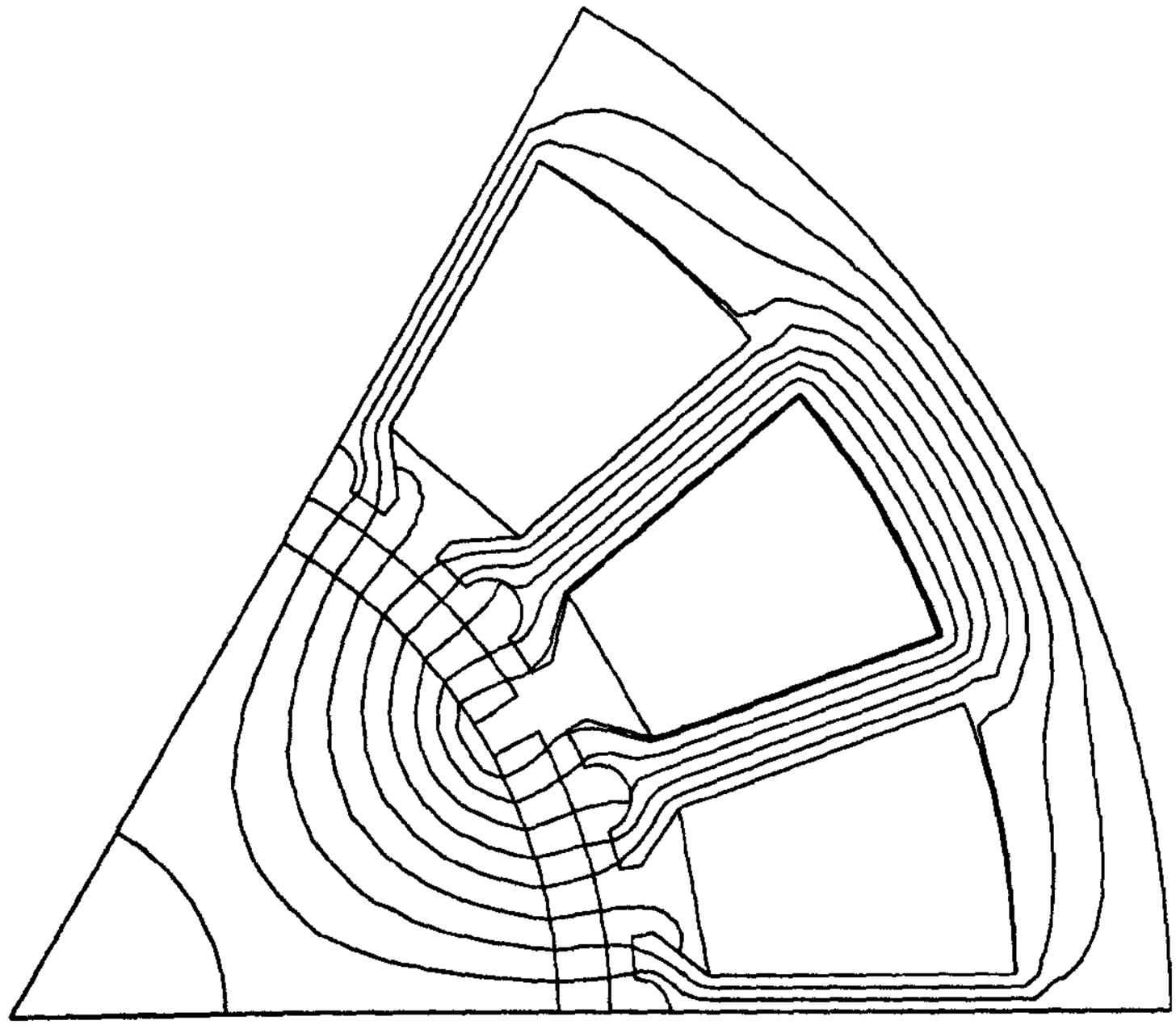

Figure 3.11. Flux plot over two half poles for the SEM BMR115C6-64S motor showing bifurcated stator teeth.

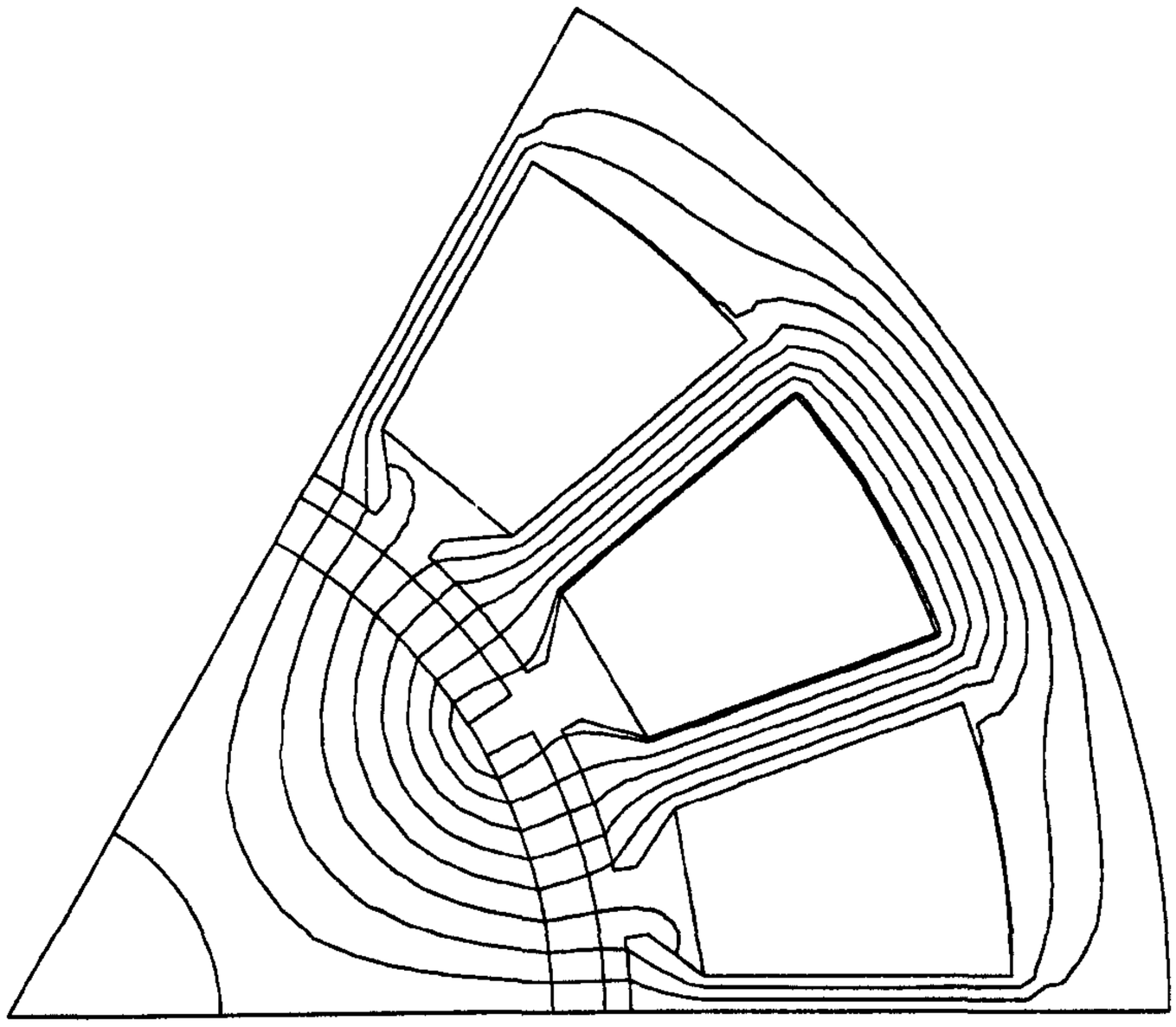

Figure 3.12. Flux plot over two half poles for the SEM BMR115C6-64S motor showing normal stator teeth.

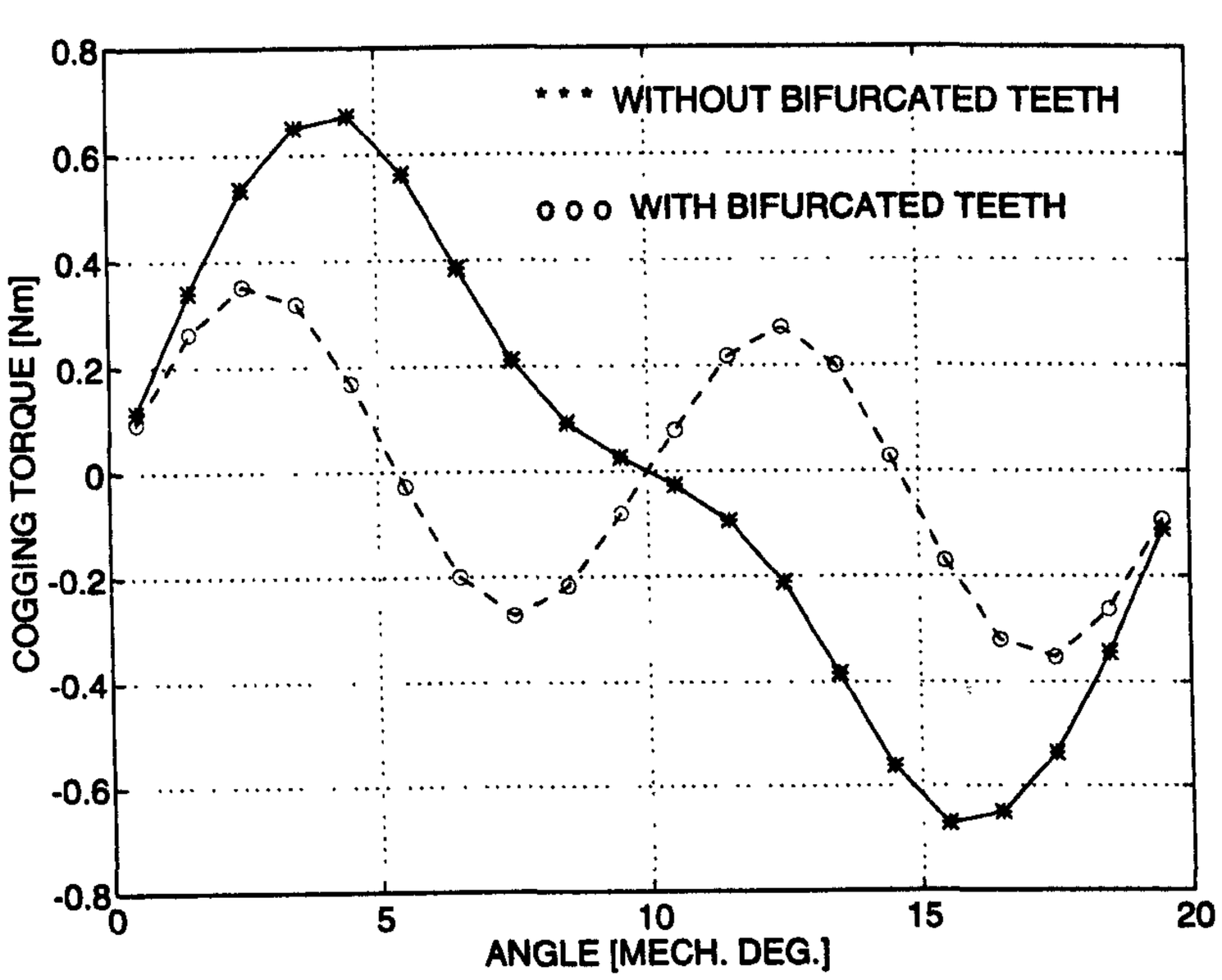

Figure 3.13. Comparison of cogging torque ripple for the SEM BMR115C6-64S motor with and without bifurcated teeth.

3.4.4 Varying the Magnetisation of Magnets

Just like varying the magnet *arc*, varying the *magnetisation* (radial or parallel) of magnets has an effect on the shape and magnitude of cogging torque ripple. This can be illustrated with an example. Figs. 3.14 and 3.15 are flux plots over half a motor cross-section for the OM FBL550A-A motor, showing radial and parallel magnetisation respectively. Fig. 3.16 compares cogging torque ripple in the two cases. It can be seen that parallel magnetisation of magnets leads to about 20% less peak cogging torque as compared to the radial magnetisation. However, this also has an effect on the electromagnetic torque ripple and hence the resulting reduction in the total torque ripple will not necessarily be the same.

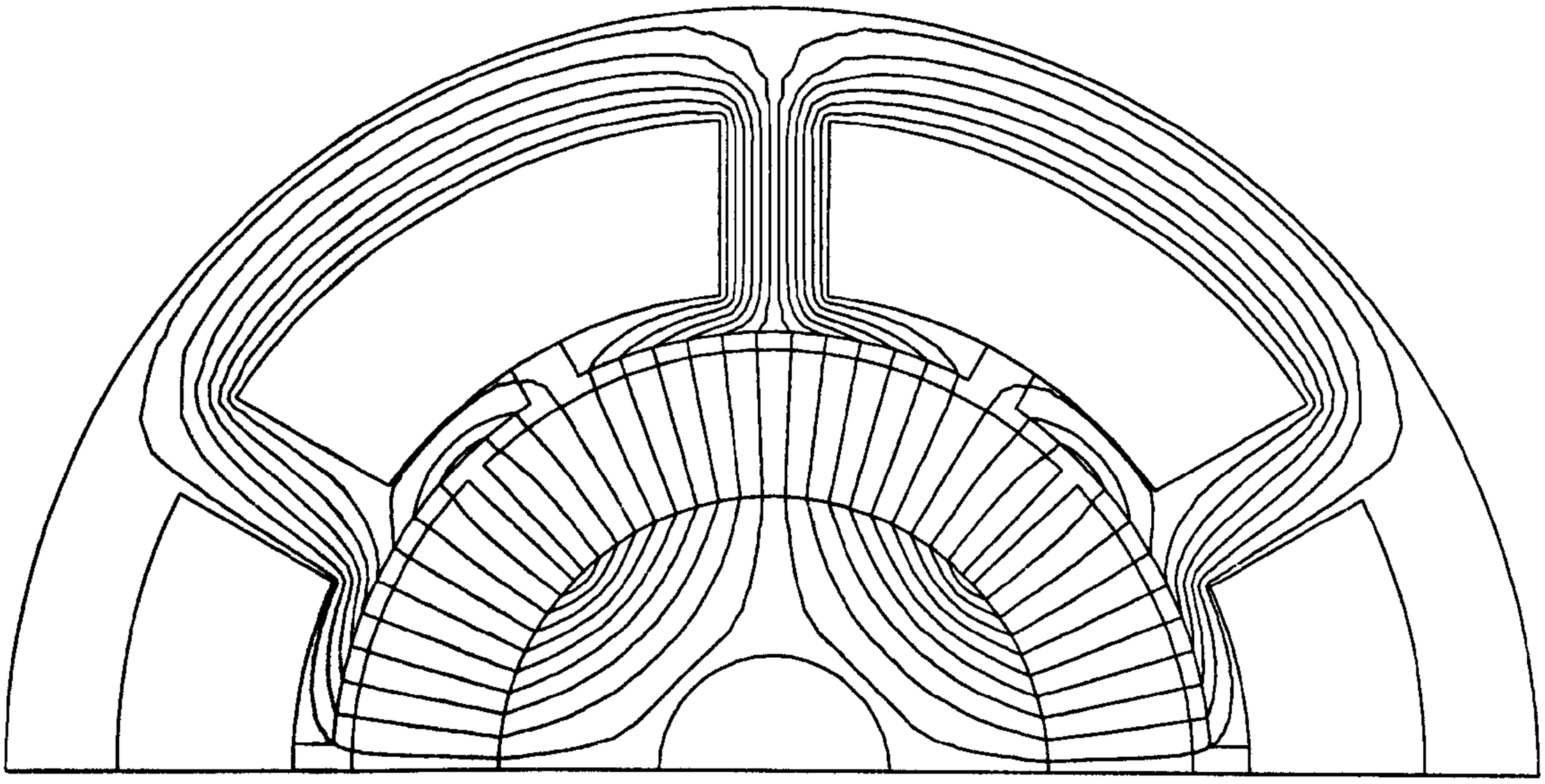

Figure 3.14. Flux plot over half a motor cross-section for the OM FBL550A-A motor displaying radial magnetisation of magnets.

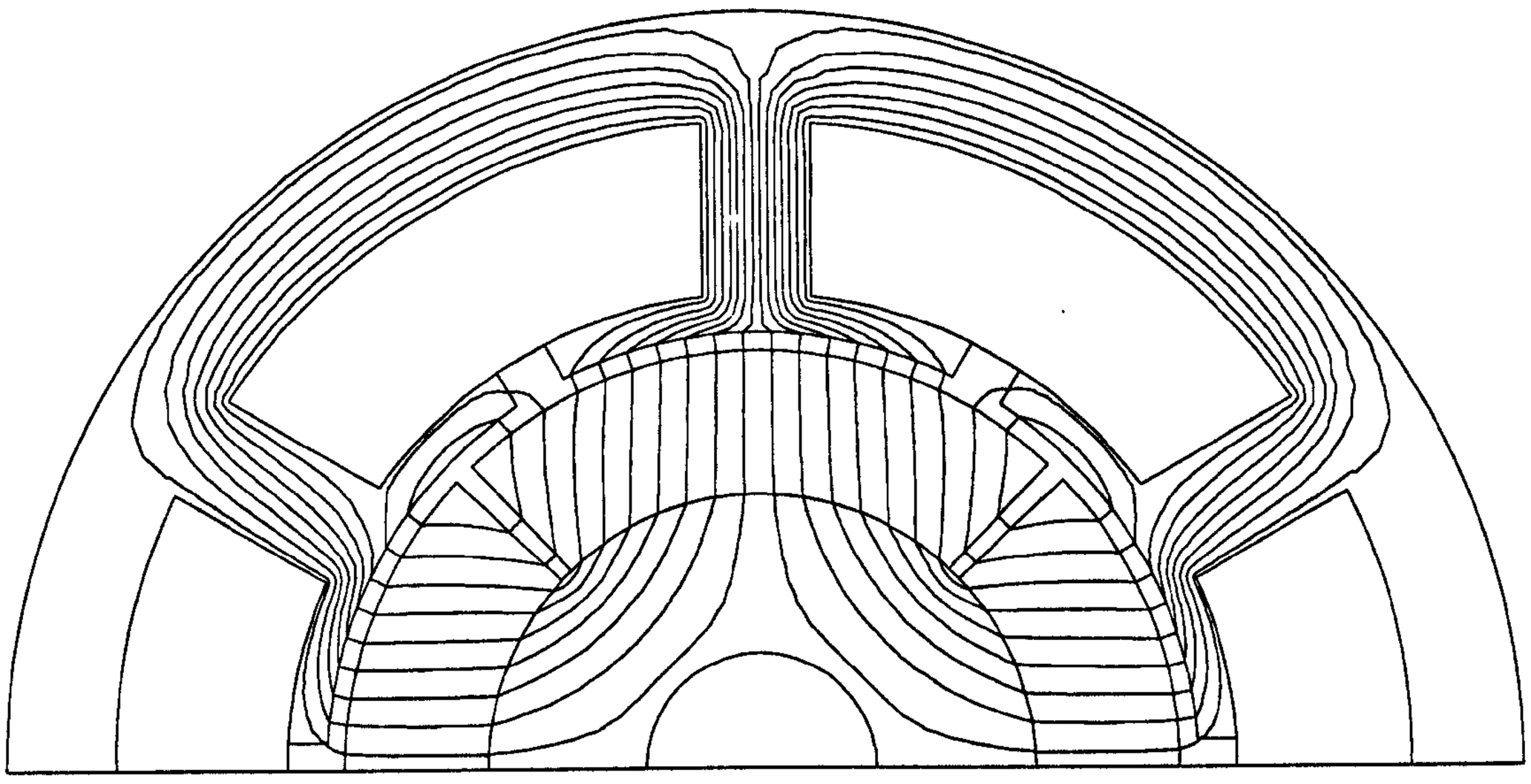

Figure 3.15. Flux plot over half a motor cross-section for the OM FBL550A-A motor displaying parallel magnetisation of magnets.

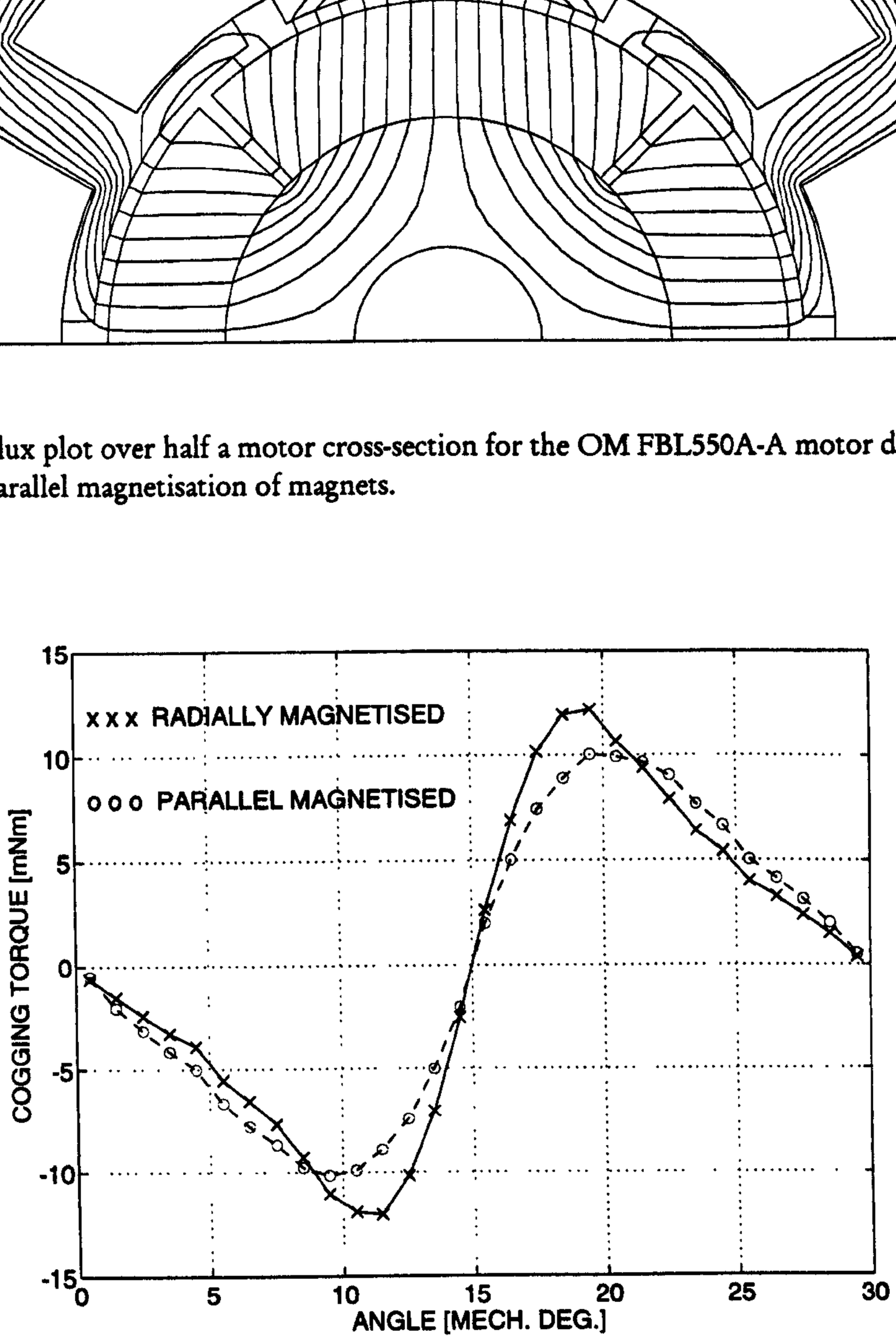

Figure 3.16. Comparison of cogging torque ripple curves between radial and parallel magnetised magnets for the OM FBL550A-A motor.

3.4.5 Using Fractional Slots Per Pole Design

A 9-slot, 8-pole, rare-earth magnet brushless PM motor manufactured by Hathaway Corp. is used here for the purpose of illustration. Fig. 3.17 shows the motor cross-section and Fig. 3.18 shows the flux-plot at no-load.

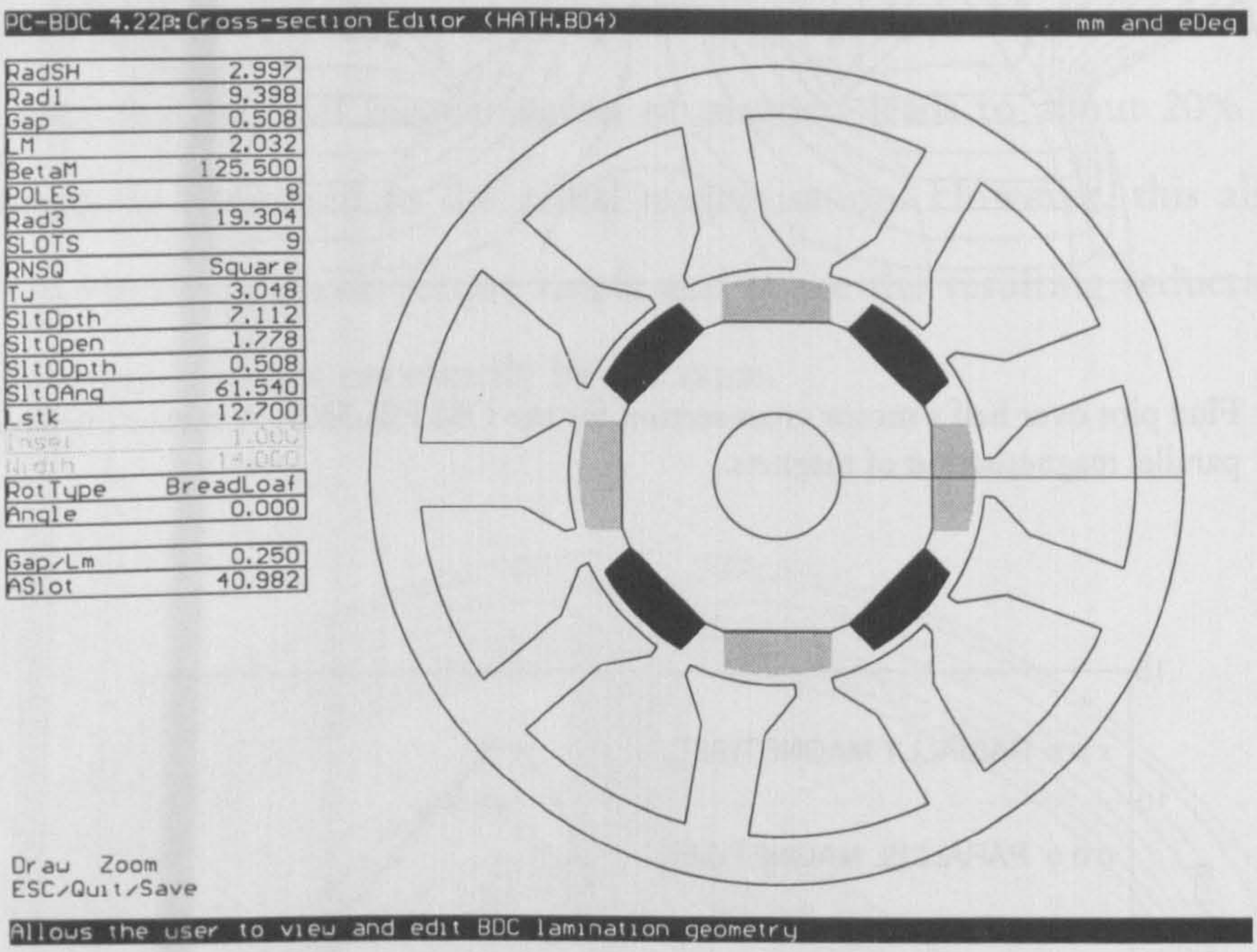

Figure 3.17. 9-slot, 8-pole Hathaway motor cross-section.

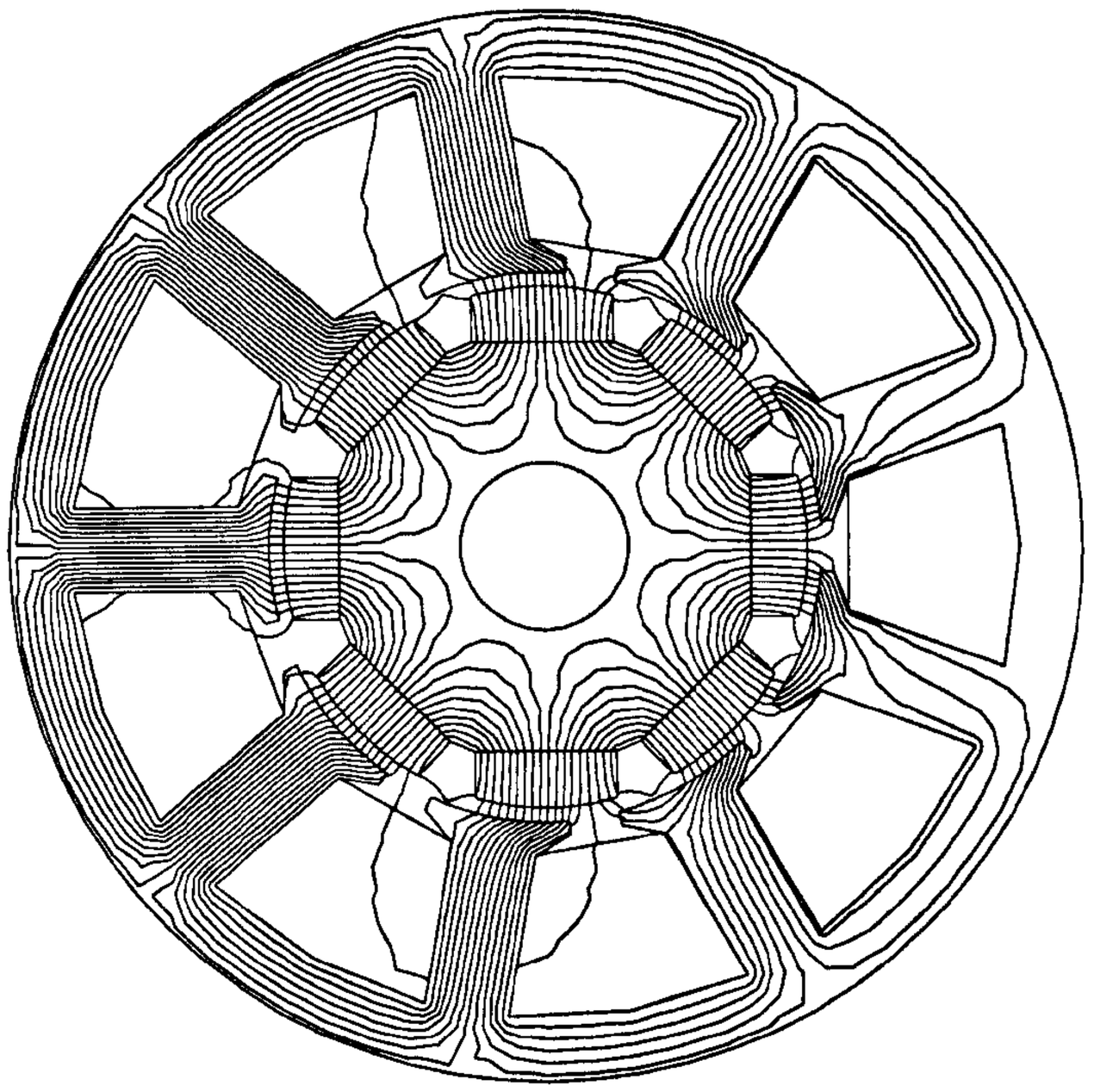

Figure 3.18. Hathaway motor flux-plot at no-load.

The cogging torque contribution from each individual pole, calculated using the flux-MMF diagram, is shown in Fig. 3.19. Since the machine has 9 slots, the cogging torque period for each individual pole is 40° mech. with a peak value of about 0.008 Nm. Fig. 3.20 shows the cogging torque contributions from the South and the North poles and the total cogging torque for the entire machine. It can be seen that the cogging torque contributions from 4 poles of either polarity have a period of 10° mech. with a peak value of about 0.001 Nm which is eight times lower as compared to the one for individual poles. Further, the two cogging torque curves corresponding to either polarity are in phase opposition and hence cancel out. The resulting total cogging torque for the entire machine has a period of 5° mech. with a peak value of about 0.0002 Nm which is forty times lower as compared to the one for individual poles.

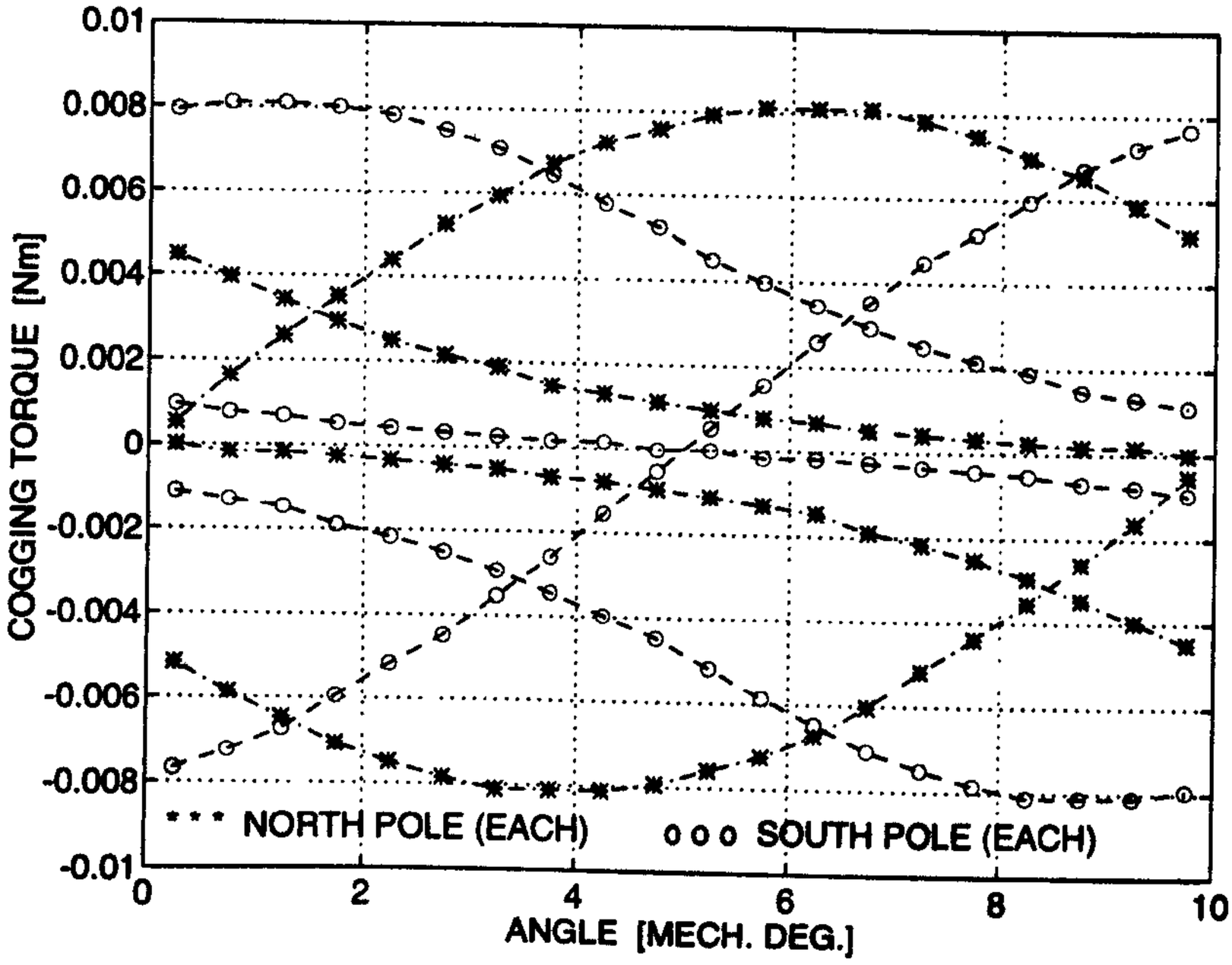

Figure 3.19. Cogging torque contribution from each individual pole.

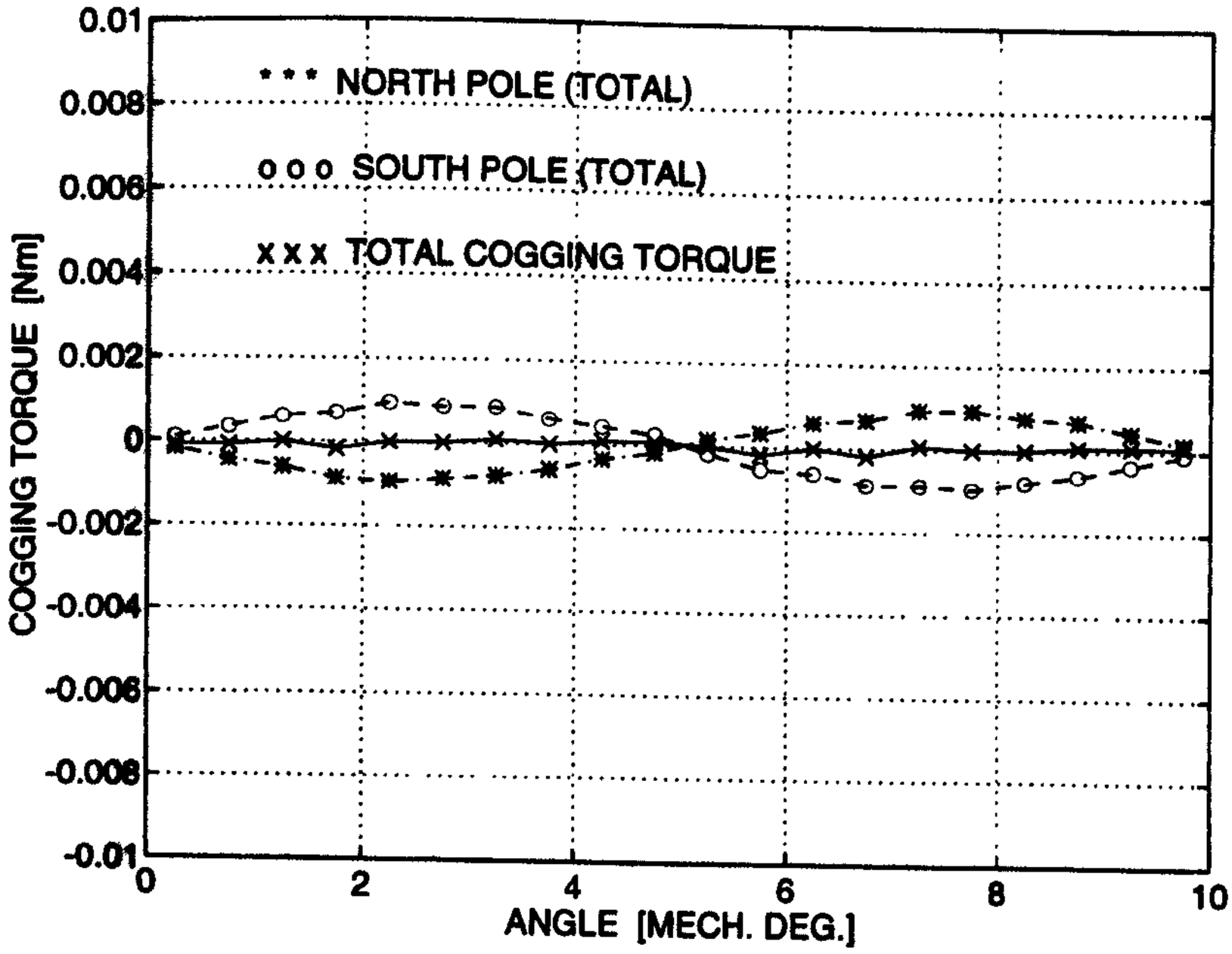

Figure 3.20. Cogging torque contribution from the South and the North poles and the total cogging torque for the entire machine.

It must be mentioned, that although in theory it is possible to obtain very small cogging torque with fractional slots per pole designs, such designs are very sensitive to certain manufacturing imperfections such as rotor eccentricity. Thus, in practice even a small amount of uneven airgap can lead to manifold increase in cogging torque. However, it is possible to model the effect of rotor eccentricity on cogging torque using the flux-MMF diagram technique.

3.4.6 Other Methods

Apart from the above mentioned commonly employed techniques of cogging torque minimisation, there are a few other techniques described earlier in this Chapter. Some of these other techniques will now be considered briefly. The method of shifting alternate magnet poles by one-half stator slot pitch in multi-pole-pair designs and the method of varying the radial air-gap length around the full circumference of a machine; can both be analysed using the flux-MMF diagram technique. In such cases however, the full machine, rather than just the cross-section over a pole or a pole pair, needs to be modelled using the FEA. Flux-MMF diagram needs to be obtained for each pole individually, as each pole is subjected to a different magnetic circuit at any given rotor position. The total cogging torque ripple can still be obtained by superimposing contributions from each individual pole.

3.5 Experimental Validation

In this section, experimental validation is provided by comparing the predicted and the measured cogging torque results for three different types of brushless PM motors. The test set-up used is described in Chapter 1, Section 2.3.3. The only difference being that the DC excitation shown in Fig. 2.14, is removed in cogging

torque measurements. The measurements were carried out twice, in clockwise as well as counterclockwise direction and the results were averaged to obtain resultant cogging torque ripple. The reason for averaging can be seen from Fig. 3.21. It shows that a small component of *friction torque* gets added to the measured torque values in either direction in the form of a fixed offset. This friction torque offset needs to be eliminated from the readings to obtain true cogging torque variation. Since friction always opposes the direction of motion, the friction torque offset value has roughly equal magnitude but opposite sign in either direction and it gets cancelled out as a result of averaging.

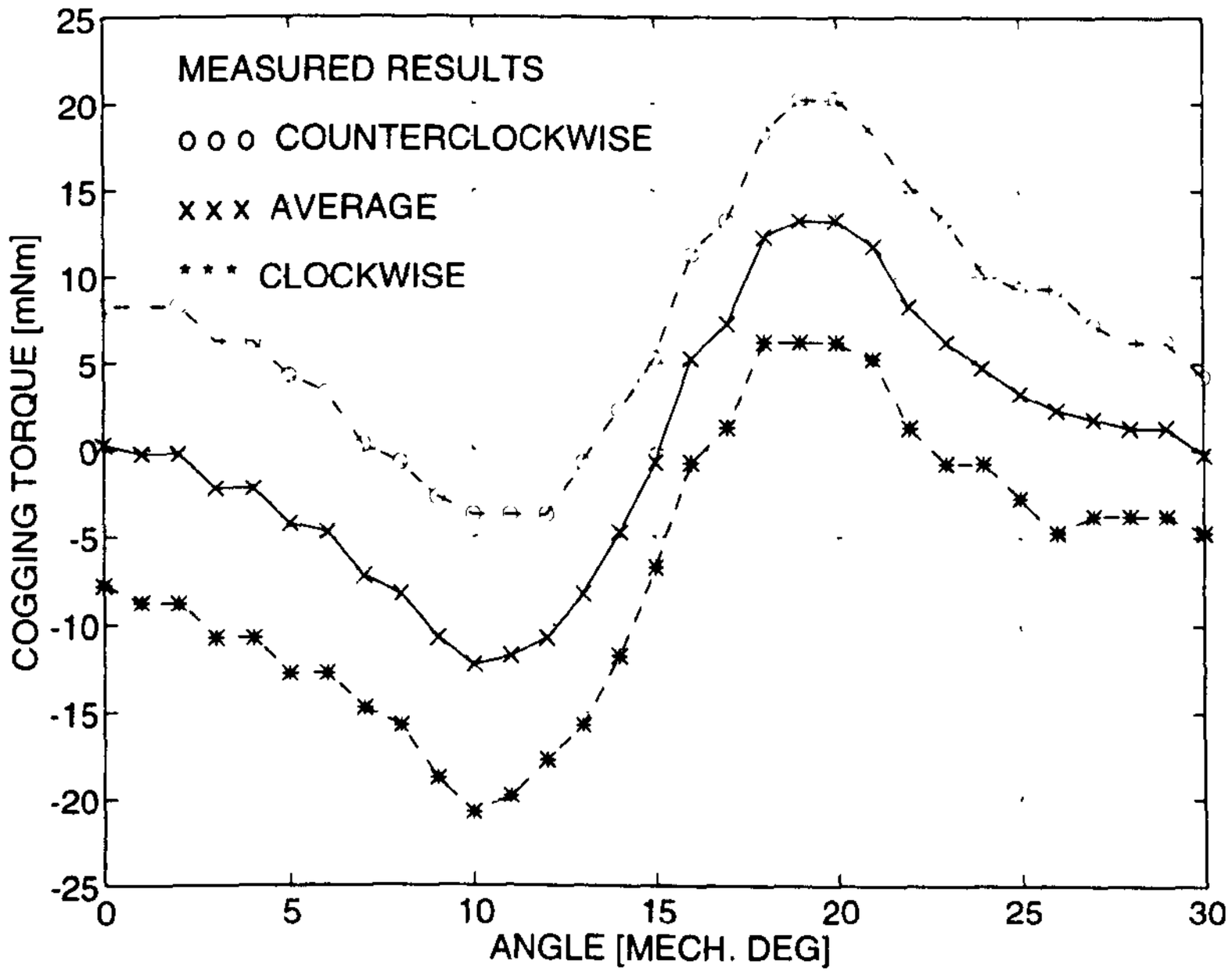

Figure 3.21. Cogging torque measurements on the OM FBL550A-A motor, showing friction torque offset of roughly equal magnitude but opposite sign in either direction.

3.5.1 Fractional Slots Per Pole Motor

Cogging torque measurements were carried out on the FBL550A-A motor. This motor is described in detail in Chapter 2. Its cross-section picture and design specifications can be found in Fig. 2.6 and Table 2.2.

Flux-MMF diagram for a single pole of this motor was constructed using the methodology described earlier in this Chapter. Being a fractional slots per pole motor, it has two sets of flux-MMF diagram and resulting cogging torque ripple, slightly differing from each other, for the pairs of South and North pole respectively. Fig 3.6 is the actual flux and MMF variation with respect to the rotor position for a single pole over one cogging torque cycle obtained using FEA and Fig 3.5 is the flux-MMF diagram, both corresponding to a North pole. A comparison between predicted and measured cogging torque ripple is given in Fig. 3.22 and it shows a good agreement between the two.

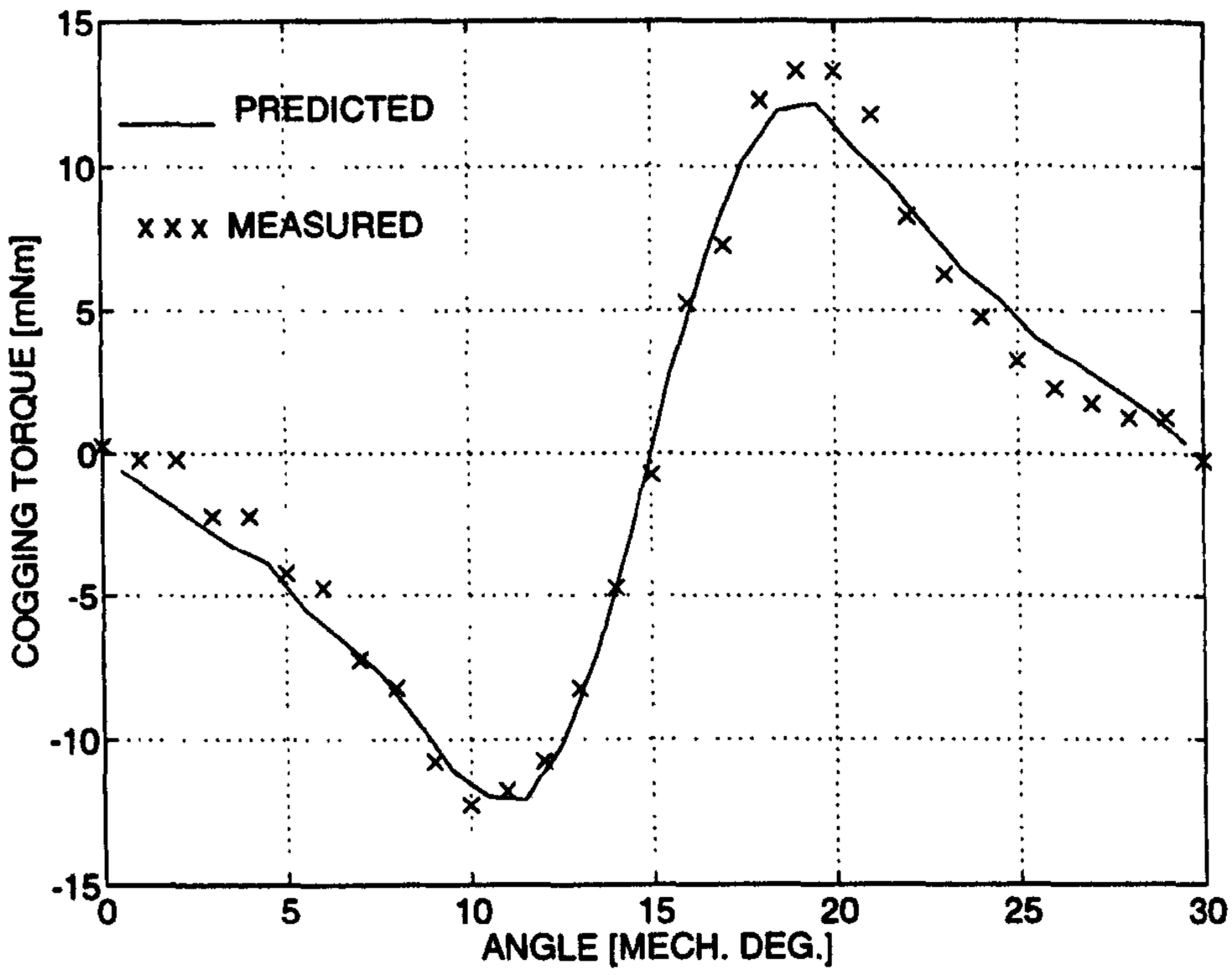

Figure 3.22. A comparison between predicted and measured cogging torque ripple for the OM FBL550A-A motor.

3.5.2 Integral Slots Per Pole Motor

A rare-earth magnet brushless AC motor, BMR115C6-64S, manufactured by SEM Ltd., was used for the purpose of validation. While the production model of this machine has bifurcated teeth and a skew of one slot-pitch; the actual analysis and measurements were performed on a one-off stator, which had no bifurcated teeth and had no skew, since the cogging torque is most pronounced under these conditions. The stator was custom made by SEM Ltd. for the SPEED Laboratory. Fig. 3.23 shows the motor cross-section and Table 3.1 gives the major design specifications.

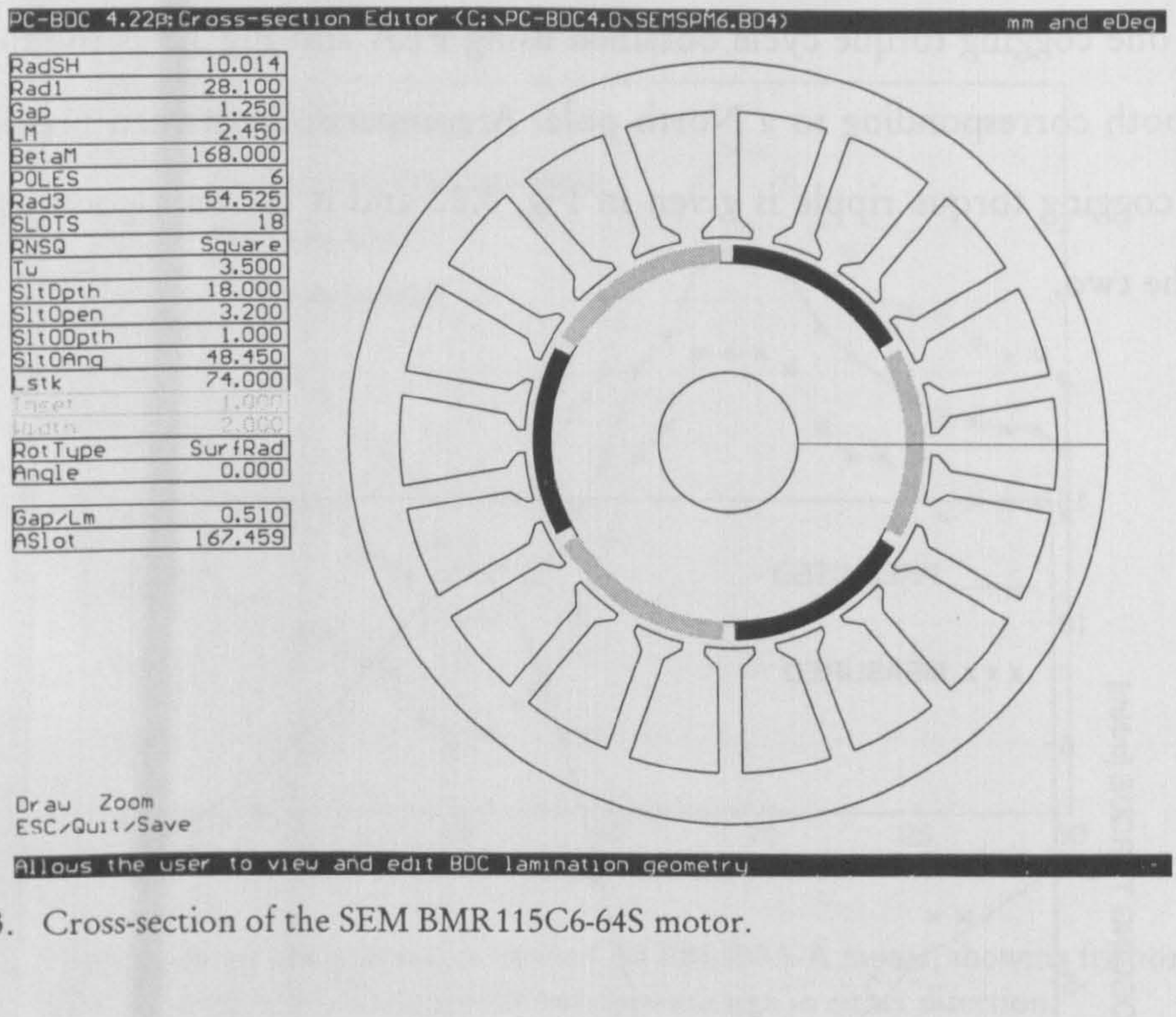

Figure 3.23. Cross-section of the SEM BMR115C6-64S motor.

Table 3.1. Major design specifications for the BMR115C6-64S motor.

Number of phases	3
Number of rotor poles	6
Number of stator slots	18
Stator outer diameter	109.06 mm
Magnet type	SmCos
Remanent flux density	0.85 T
Winding configuration	3 Wye in parallel
Turns per coil	170

Fig. 3.24 shows the actual flux and MMF variation for a single pole over one cogging torque cycle obtained using FEA. Fig. 3.25 is the flux-MMF diagram for a single pole and Fig. 3.26 is a comparison between predicted and measured cogging torque ripple. Although there is a reasonable agreement between the two peak cogging torque values, there are some localised discrepancies in ripple shape which could be attributed to the fact that each magnet pole is segmented into four rectangular blocks in manufacturing whereas it is modelled as a continuous arc in the FEA. In the particular motor which was used for testing, a close examination of the rotor after disassembly revealed uneven spacing of individual magnet blocks, which explains the uneven cogging torque ripple shape.

Figs. 3.5 and 3.25 make an interesting comparison. While 3.5 is for the OM motor which uses ferrite magnets (B_r = 0.375 T), Fig. 3.25 is for the SEM motor which uses rare-earth magnets (B_r = 0.85 T). Since the length of magnet and the magnetic circuit are different in the two cases, the average operating point for the SEM motor is further down the demagnetisation curve as compared to the OM motor (Permeance Coefficient, PC of 1.96 for the SEM motor as against 7.90 for the OM motor). Also, the SEM motor operates at a higher level of flux and MMF with a bigger net variation, leading to an increased amount of cogging, as expected.

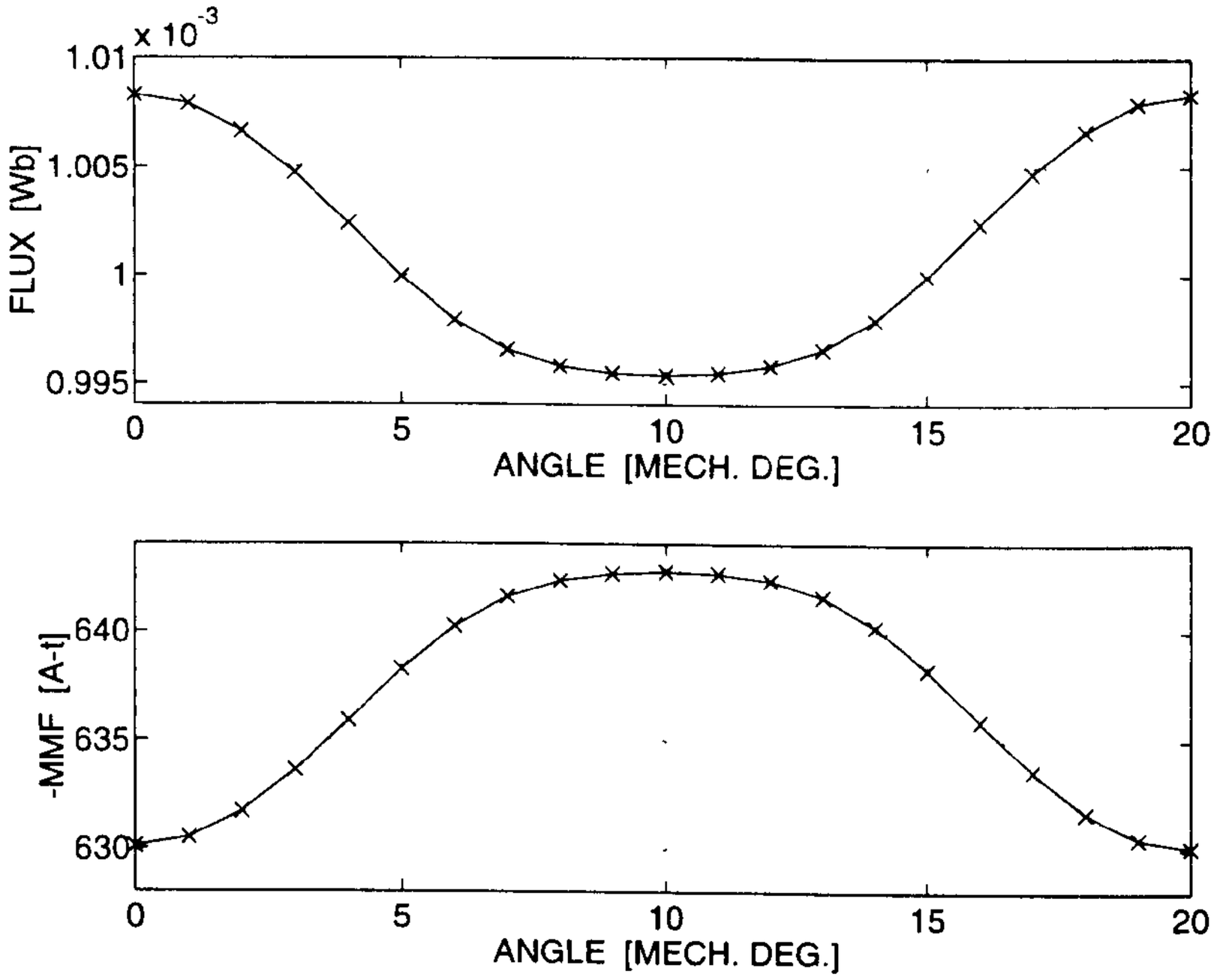

Figure 3.24. Actual flux and MMF variation with respect to the rotor position for a single pole of the BMR115C6-64S motor over one cogging torque cycle.

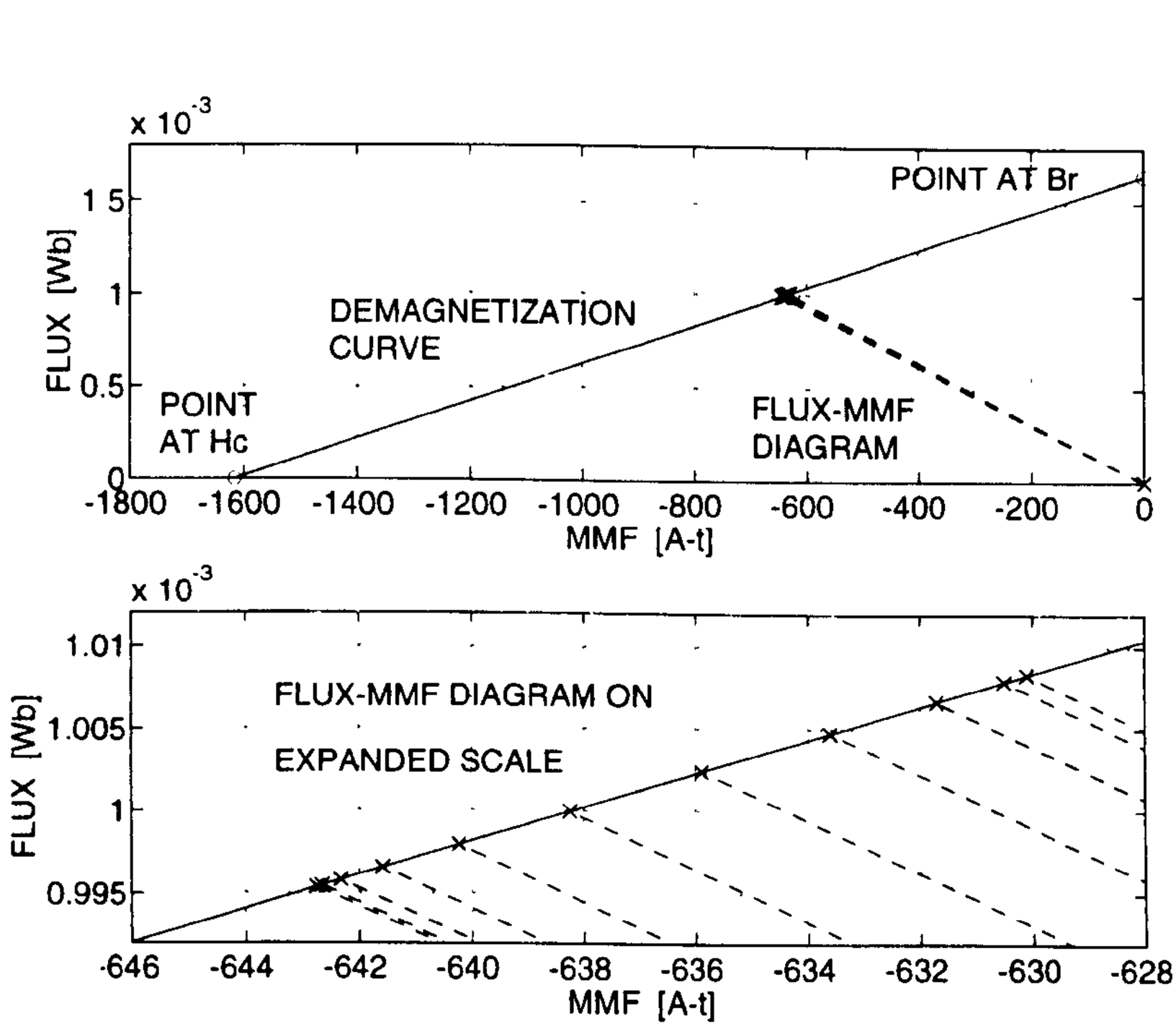

Figure 3.25. Flux-MMF diagram for a single pole of the BMR115C6-64S motor.

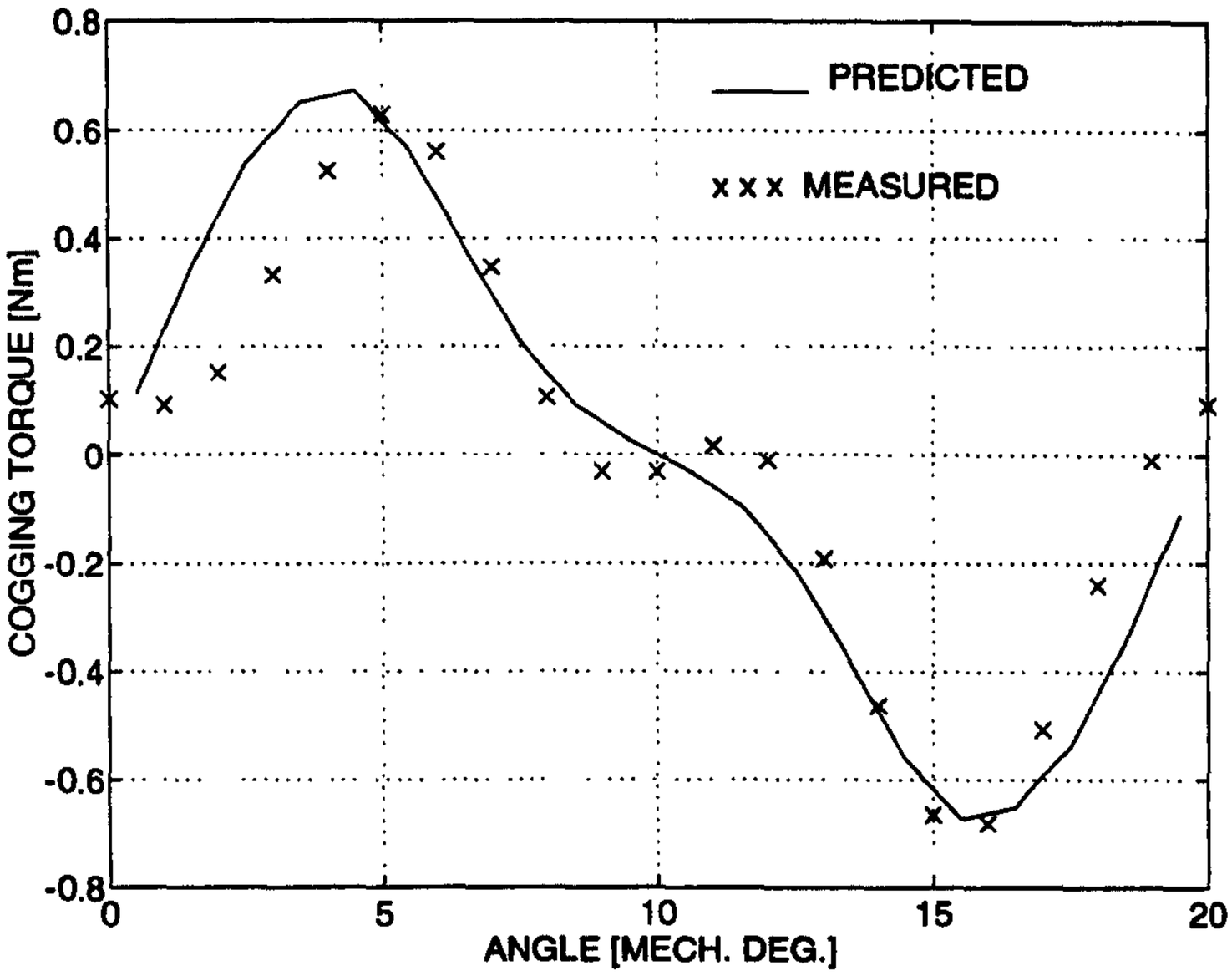

Figure 3.26. The predicted and the measured cogging torque ripple for the BMR115C6-64S motor.

3.5.3 Interior Permanent-Magnet Motor

While the first two validation examples were surface PM motors, here, an interior permanent-magnet (IPM) motor, manufactured by DANFOSS A/S, is considered. The cross-section picture is shown in Fig. 3.27 and Table 3.2 provides the major design specifications for the motor.

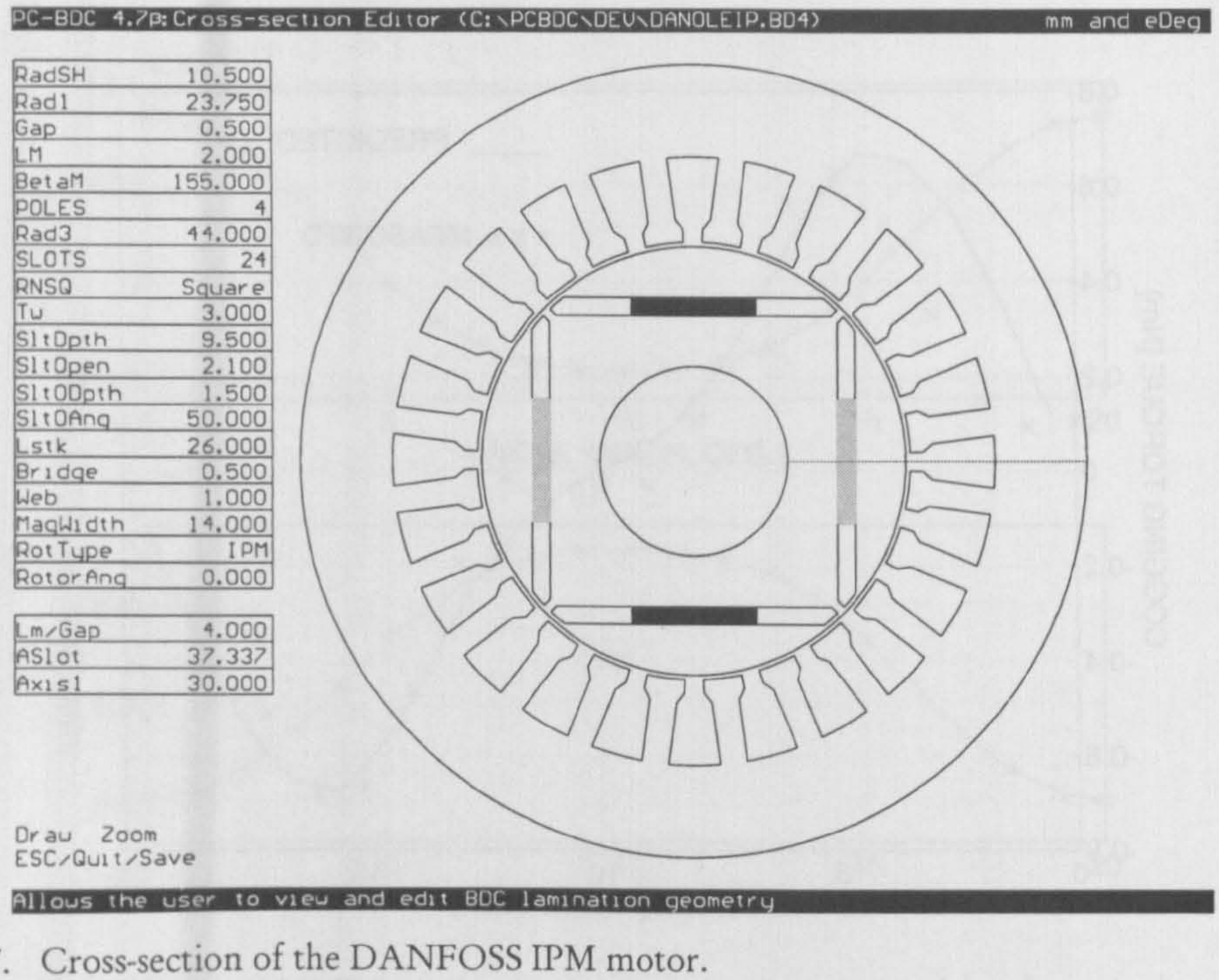

Figure 3.27. Cross-section of the DANFOSS IPM motor.

Table 3.2. Major design Specifications for the DANFOSS IPM motor.

Number of phases	3
Number of rotor poles	4
Number of stator slots	24
Stator outer diameter	88.00 mm
Magnet type	NdFeB
Remanent flux density	1.15 T
Winding configuration	Wye connection
Turns per phase	62

Fig. 3.28 shows the actual flux and MMF variation with respect to the rotor position for a single pole over one cogging torque cycle obtained using FEA. Fig. 3.29 is the flux-MMF diagram for a single pole and Fig. 3.30 is a comparison between predicted and measured cogging torque ripple.

Again, a comparison between Figs. 3.29 and 3.25 brings out some interesting observations. While both SEM and DANFOSS motors use rare-earth magnets, the DANFOSS motor, having interior permanent-magnets, has a much lower net variation of flux and MMF and hence lower cogging torque as compared to the SEM

motor which has surface permanent-magnets. For the same reason, the average operating point is also different in the two cases, being further down the demagnetisation curve for the SEM motor as compared to the DANFOSS motor (PC of 1.96 for the SEM motor as against 4.00 for the DANFOSS motor).

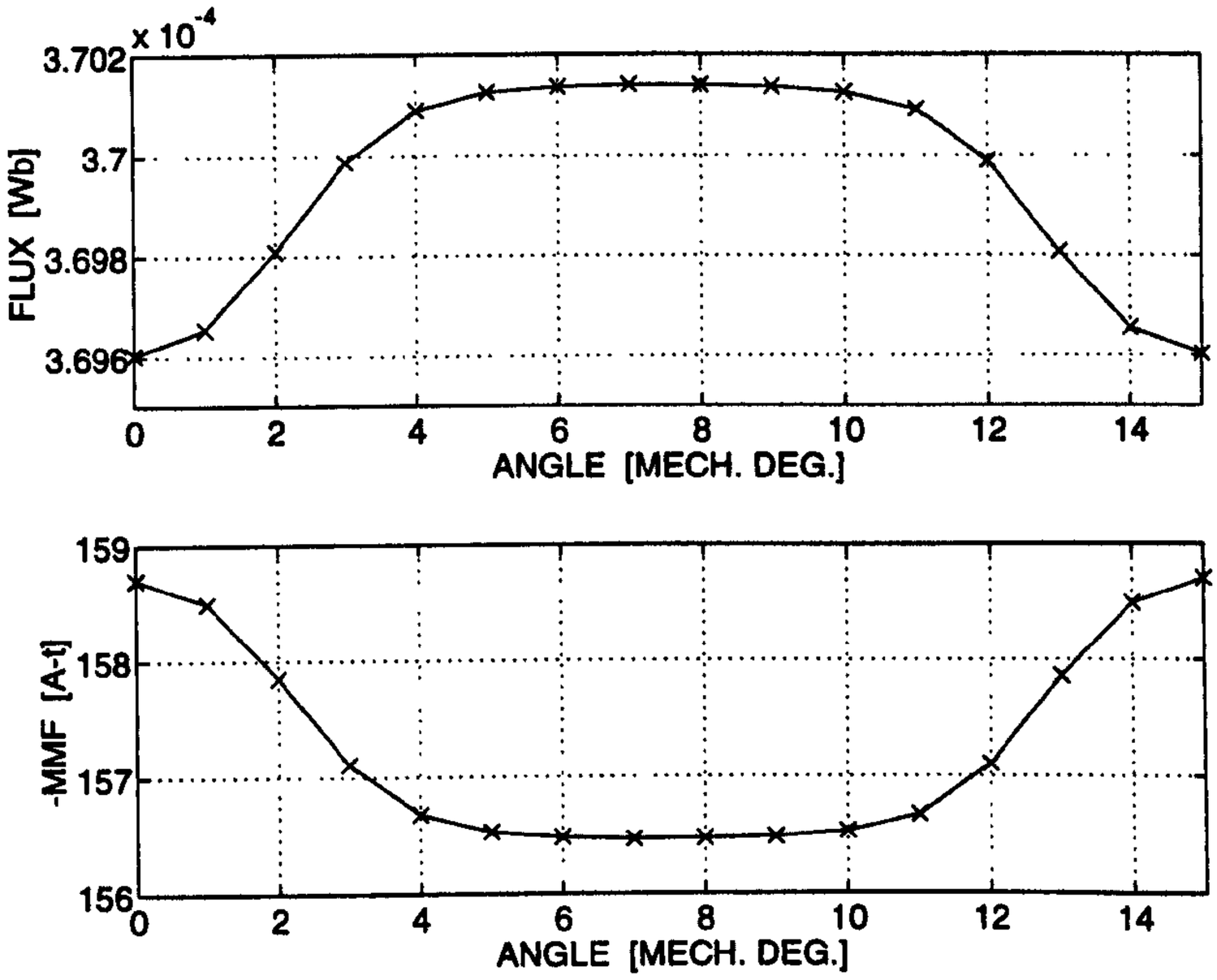

Figure 3.28. Actual flux and MMF variation with respect to the rotor position for a single pole of the DANFOSS IPM motor over one cogging torque cycle.

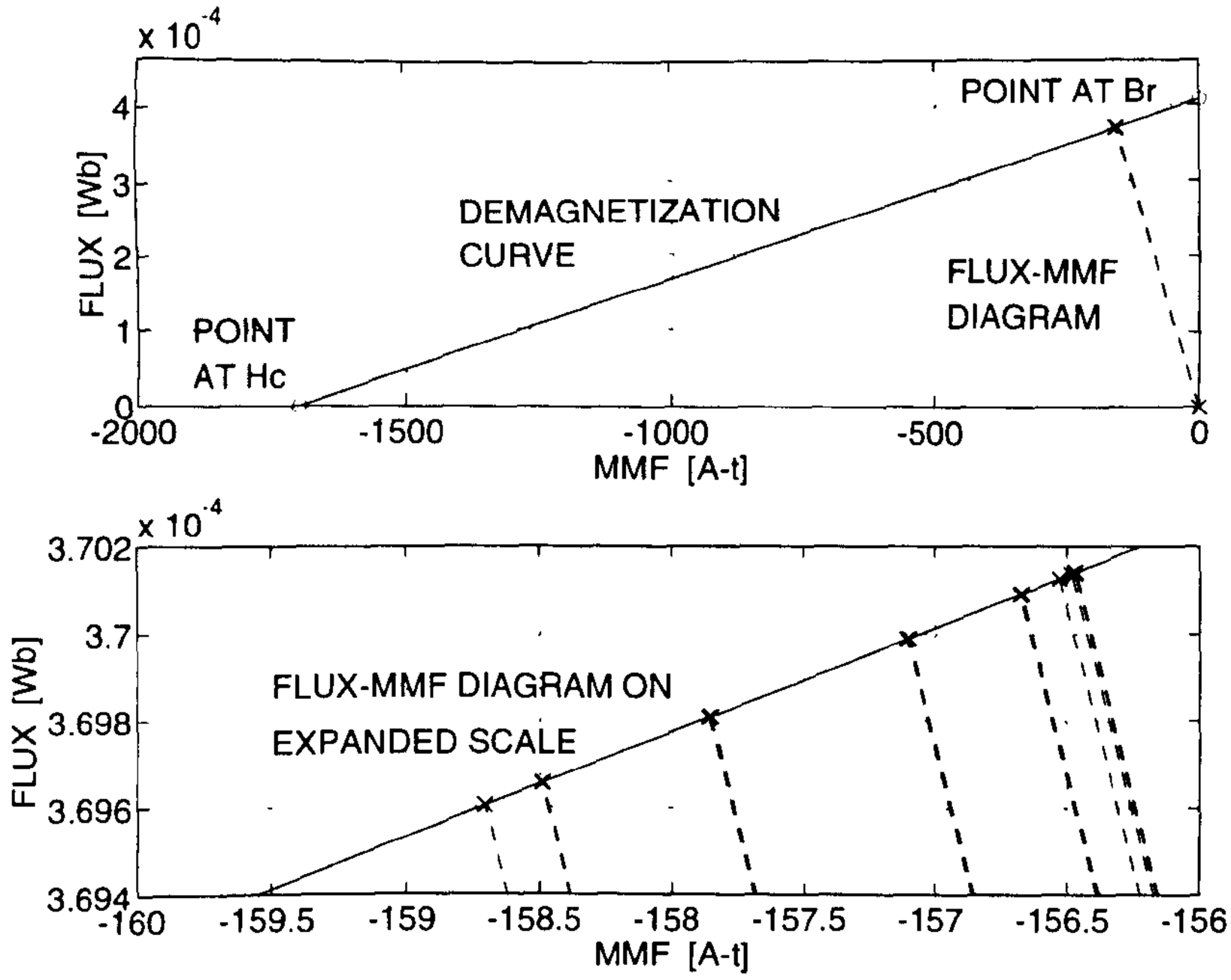

Figure 3.29. Flux-MMF diagram for a single pole of the DANFOSS IPM motor.

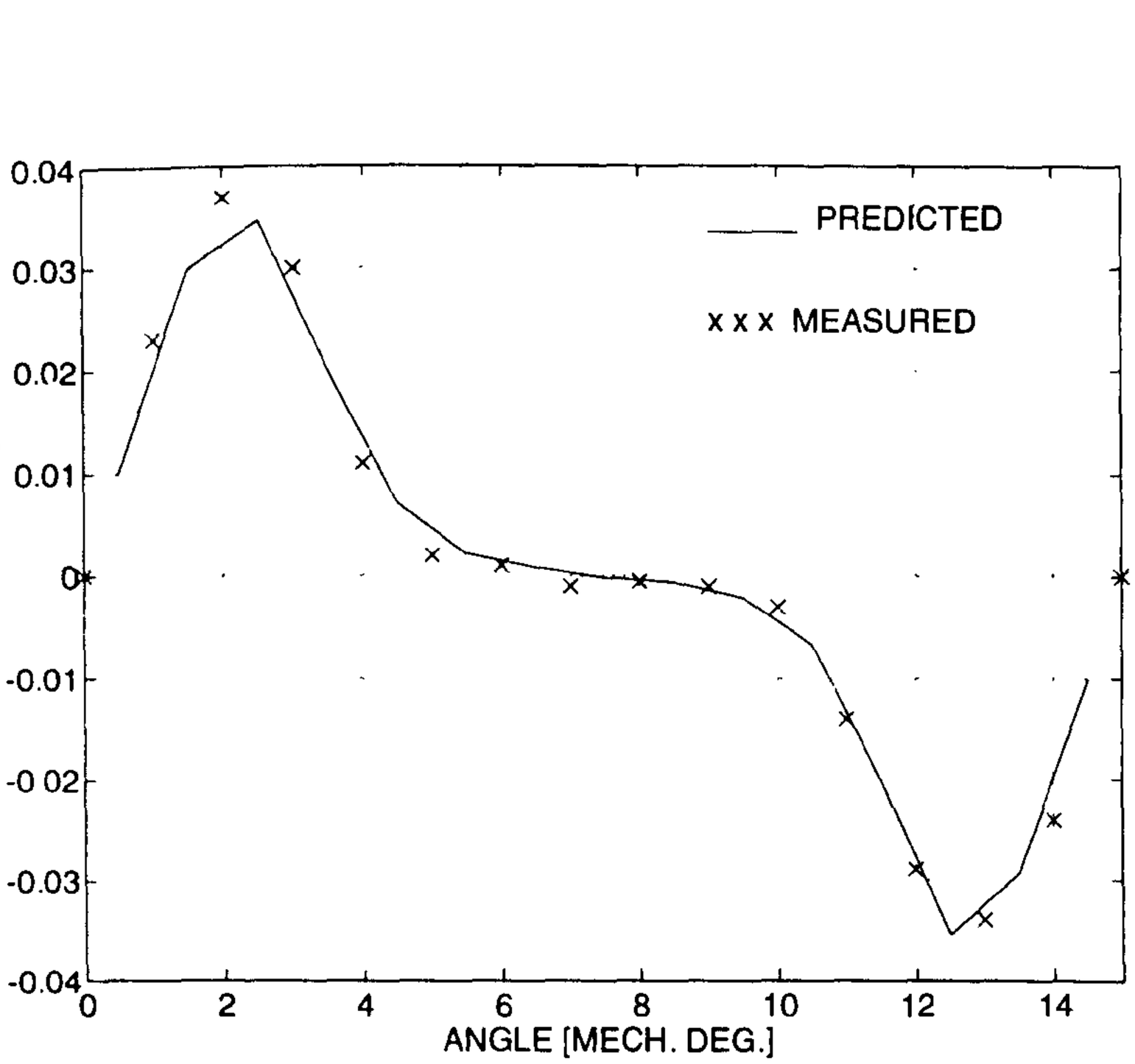

Figure 3.30. Comparison between predicted and measured cogging torque ripple for the DANFOSS IPM motor (*Measured results courtesy of DANFOSS A/S*).

Table 3.3 summarises some important points on the comparison between the cogging torque and the flux-MMF diagram for different motors considered so far.

Table 3.3. Summary of comparison between the three motors used in validation.

Design parameter	OM SPM motor	SEM SPM motor	DANFOSS IPM motor
Magnets used	Ferrite	$SmCo_5$	NdFeB
B_r	0.375 T	0.85 T	1.15 T
μ_{rec}	1.27	1.025	1.049
Average Permeance Coefficient	7.90	1.96	4.00
Δflux over one cogging cycle	0.381×10^{-6} Wb	12.932×10^{-6} Wb	0.537×10^{-6} Wb
ΔMMF over one cogging cycle	3.277 A-t	12.655 A-t	2.238 A-t
Peak cogging torque	0.013 Nm	0.671 Nm	0.035 Nm

3.6 Chapter Summary

Chapter 3 has reviewed the existing methods of cogging torque calculation and minimisation techniques, and has described the method of predicting cogging torque ripple in permanent-magnet machines, using the flux-MMF diagram technique. It has been shown that in a conventional phase flux-MMF diagram, the flux-MMF trajectory at no-load is simply a straight line which does not enclose any area and hence cannot predict any torque.

A new method of constructing the flux-MMF diagram for a permanent-magnet rather than a phase, has been proposed. Such a flux-MMF diagram is shown to be composed of the demagnetisation characteristics of the permanent-magnet and the load-lines at incremental rotor positions over a cogging torque cycle. The applications of the FMDT in analysing various cogging torque minimisation techniques have been demonstrated along with the experimental validation of the technique on a variety of permanent-magnet machines.

4 Modelling of Skew

4.1 Introduction

In permanent-magnet motors, skewing of either the stator or the rotor is usually incorporated in order to reduce the torque ripple as well as noise and vibration arising out of it. While both essentially have the same electromagnetic effect on the machine operation, the choice is greatly dictated by the manufacturability of a particular design. The stator skewing is generally continuous in nature and it involves assembling a stack of loose stator laminations with a simple axial twist before windings are placed in its slots. Alternately, in some cases, the windings are placed in the slots first and then the stator is skewed. While this gives a smooth and continuous back-EMF and torque ripple characteristics, it complicates the coil winding process which is usually automatic.

The rotor skewing can either be continuous or discretised in nature. Continuous rotor skewing involves either placing the pre-magnetised magnet poles in a skewed fashion or magnetising the magnet poles in a skewed manner after assembly. Discrete rotor skewing involves making up a complete magnet pole from a number of discrete magnet segments placed along the axis (see for example Fig. 4.2). While rotor skewing keeps the stator manufacturing simple, it has its own difficulties with respect to maintaining accurate manufacturing tolerances. Different implementations of skew discussed above, and their respective advantages and disadvantages are summarised in Fig. 4.1.

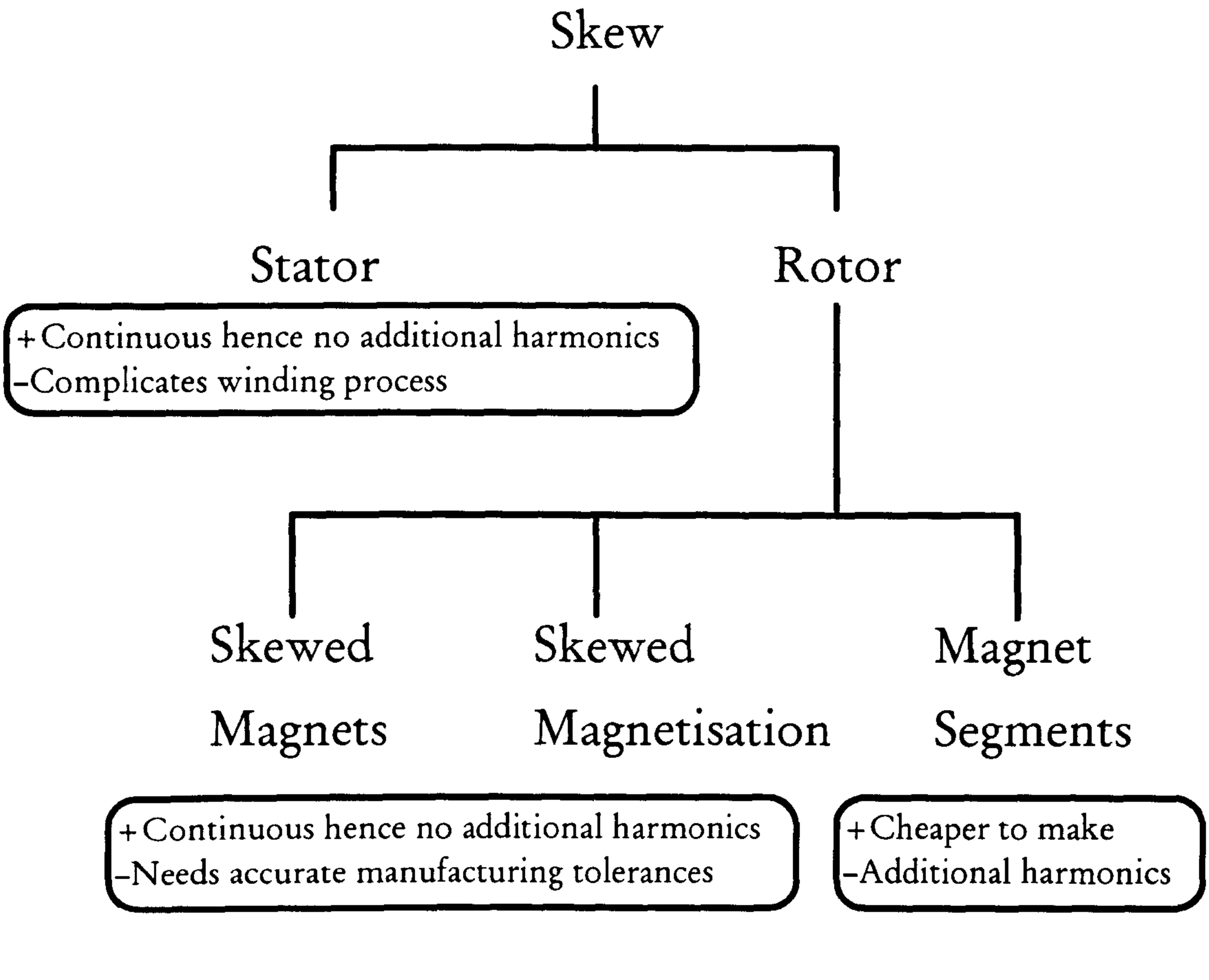

Figure 4.1. Summary of different possible implementations of skew. A '+' sign indicates an advantage while a '–' sign indicates a disadvantage.

This chapter is concerned with modelling of skew using the flux-MMF diagram. The principal advantage of this technique is that, once the diagram is constructed, the effect of skew on torque ripple can be analysed quickly with minimal amount of computation. Although one slot pitch is a fairly common value for the skew factor in permanent-magnet machines, different values can be considered, by constructing a flux-MMF diagram and calculating torque ripple in each case, before finalising on a particular value.

The next section gives a brief literature review of some of the prominent work performed on the topic of skewing and its effect on torque ripple. Section 4.3 explains how skew can be represented in a flux-MMF diagram. Sections 4.4 and 4.5 respectively examine the effect of skew on the electromagnetic and the cogging torque

ripple with the help of specific examples. An interior permanent-magnet motor is considered in Section 4.4, as it shows pronounced electromagnetic torque ripple; while a ferrite-magnet surface PM motor is considered in Section 4.5. Finally, experimental validation on a rare-earth surface PM motor is presented in section 4.6.

4.2 Literature Review

Analytical as well as finite-element based methods have been developed to investigate the effect of skew on machine performance [82]-[93]. Analytical methods usually involve formulation of expressions for airgap permeances, MMF and flux density distribution. Quantities such as back-EMF and cogging torque are then derived from these expressions such that the effect of skew on torque ripple can be taken into account [82], [83], [88]. Finite-element based methods make use of either the 2-D or the 3-D analysis. In the case of 2-D analysis, multiple finite-element meshes may be required at different positions along the axis [89], [93]; while in the case of 3-D analysis, a single finite-element mesh may be sufficient to incorporate the effect of skew at a particular rotor position [91], [92].

In general, skewing has the effect of reducing the higher-order back-EMF harmonics, producing more sinusoidal back-EMF waveforms [84]. While in PM brushless AC machines, this reduces the torque ripple, in PM brushless DC machines, this smoothes the trapezoidal back-EMF waveform and hence may slightly increase the torque ripple [86]. Skewing usually leads to an increase in leakage reactances and stray losses and a decrease in average torque. Although a skew of one slot pitch is most commonly employed, in machines with low slot numbers, skewing by one slot pitch may result in substantial reduction in average torque. Hence skewing is restricted to machines with moderate number of slots per pole per phase [90]. Skewing also generates a small amount of axial thrust on bearings which may degrade

the bearing life and overall performance. Thus, in spite of being a simple and effective technique of reducing torque ripple, a few specialised applications cannot make use of skewing and some other techniques must be used in such cases.

4.3 Representation of Skew in the Flux-MMF Diagram

To understand how skew is represented in a flux-MMF diagram, consider any point on a flux-MMF trajectory which corresponds to an instantaneous value of flux for a particular rotor position of a machine with skew. Fig. 4.2 shows a developed view of skewed rotor magnet segments against the stator slots.

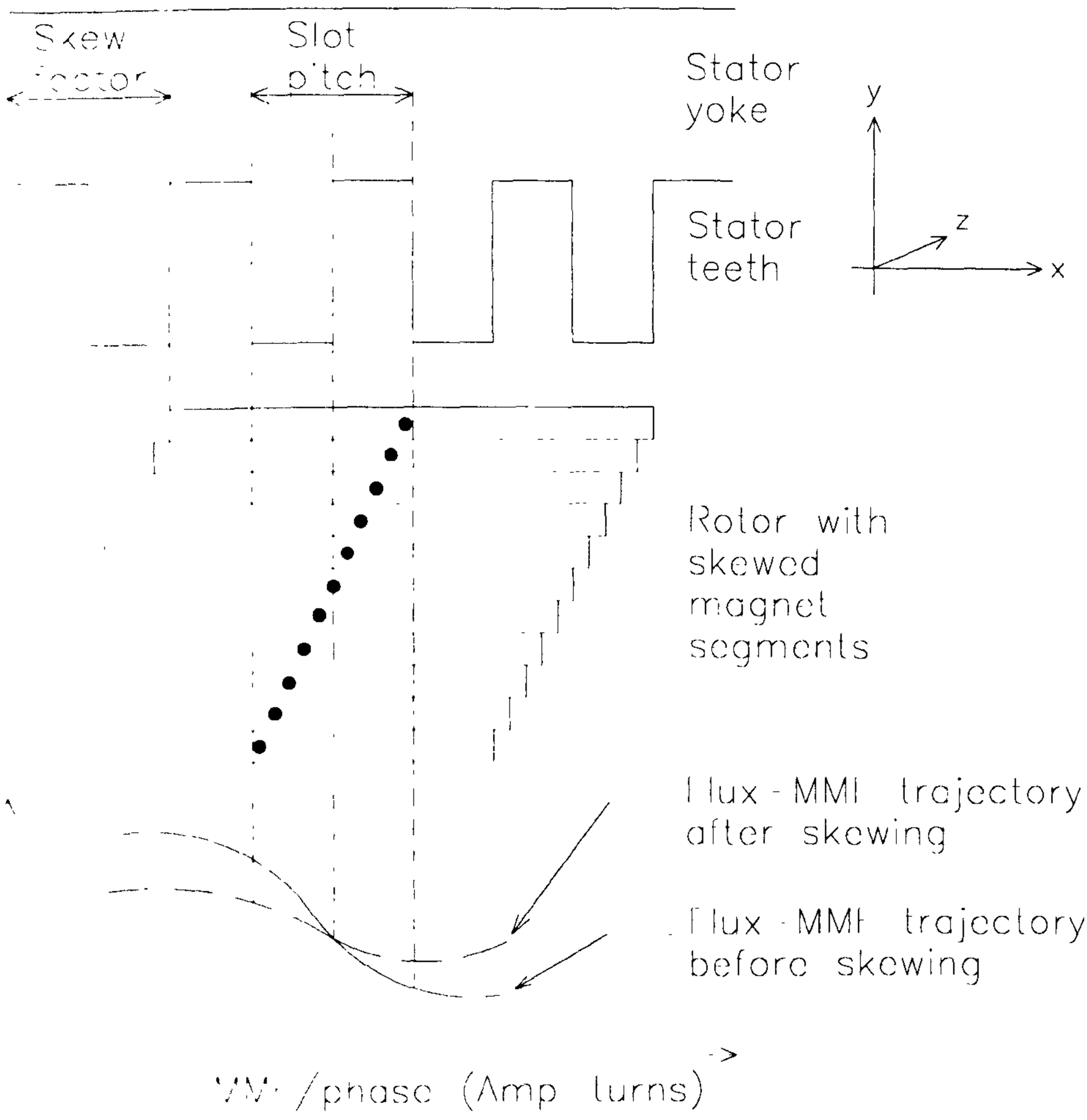

Figure 4.2. Effect of skew on the flux-MMF trajectory.

In practice, the magnets need not be segmented. Even if the rotor (or the stator) is skewed continuously, sections of varying magnet discretisation can be considered to develop the theory. It can be deduced from Fig. 4.2 that flux at a particular rotor position for the machine with skew is an *average* of flux values at successive rotor positions over the skew angle for the machine without skew. Mathematically, this averaging can be represented as in (4.1).

$$\phi_{av} = \frac{\sum_{i=1}^{n} \phi_i}{n} \tag{4.1}$$

Where,

φ_{av} is the average flux at a particular rotor position.

n is the number of magnet segments along the axial length.

φ_i represent instantaneous flux values at successive rotor positions with an incremental angle of $\theta_i = k_s/n$, k_s being the skew factor in degrees.

The number of magnet segments, n, is either known for a segmented magnet rotor, or chosen, if a continuously skewed magnet is discretised. Torque ripple curves can now be obtained from the *skewed* flux-MMF diagram as explained in Chapter 2, and thus torque ripple magnitude can be calculated as a function of skew.

4.4 Electromagnetic Torque Ripple : Effect of Skew

Fig. 4.3 shows cross-section of a rare-earth interior permanent-magnet brushless AC motor, also known as *spoke type* motor. Although not realised practically, this is a reasonably optimised design based on a commercially available 3-phase induction motor stator. The motor was designed for the purpose of comparative evaluation of electrical machines and the design procedure is explained in detail in Chapter 6.

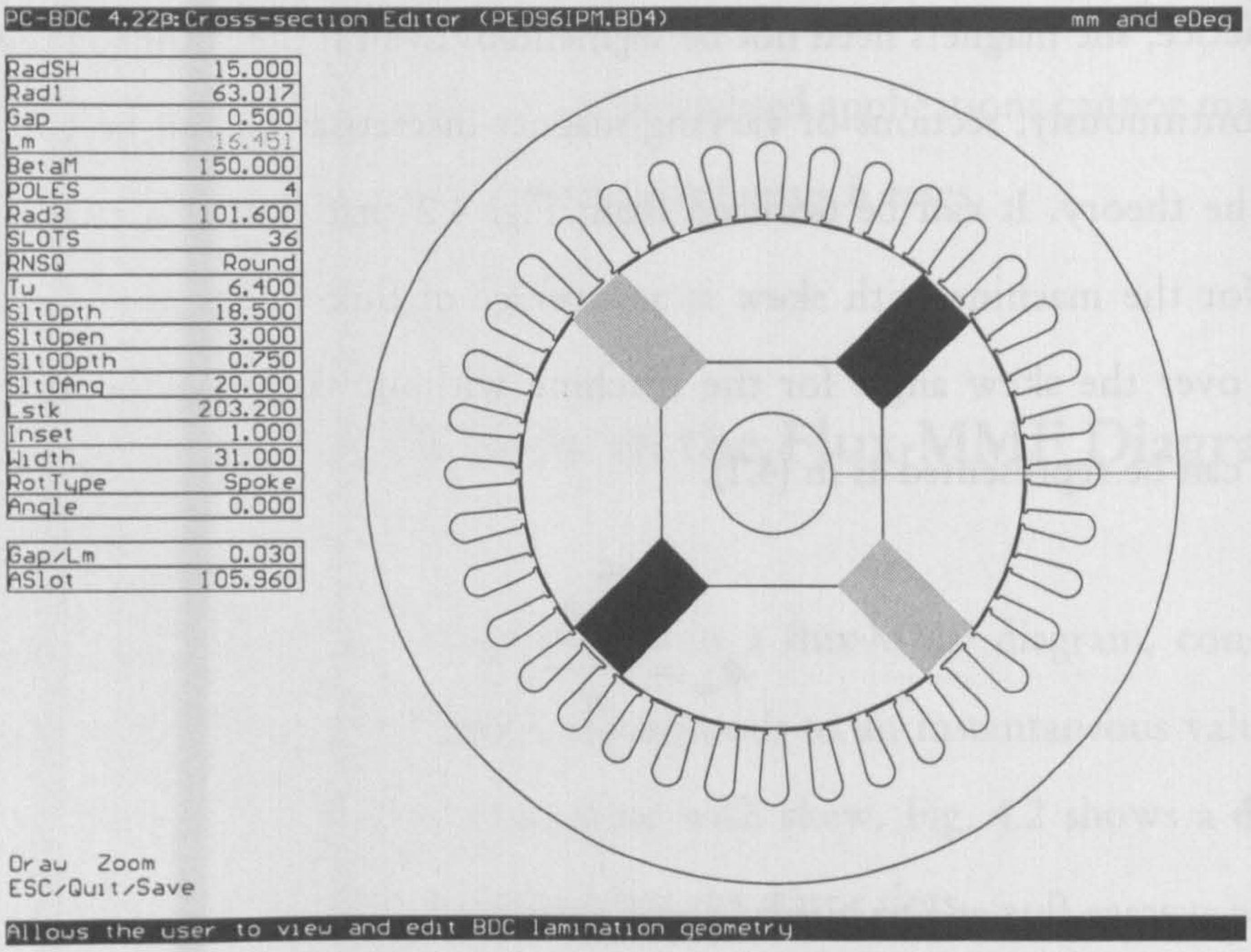

Figure 4.3. Cross-section of the spoke type motor.

Flux-MMF diagram for the spoke type motor without skew is shown in Fig. 4.4. The deviation from the ideal elliptical shape and highly irregular spacing of the magnetisation curves indicate a large amount of electromagnetic torque ripple as shown in Fig. 4.6. Since this is a salient pole machine, the torque ripple is a combination of mutual and reluctance torque components and both are taken into account in Fig. 4.6. Fig. 4.5 is the flux-MMF diagram for the same motor with a skew of one slot pitch. Graphical comparison between Figs. 4.4 and 4.5 shows that the effect of skew on the flux-MMF diagram is of two kinds.

- The spacing of the magnetisation curves in Fig. 4.5 is more regular than in Fig. 4.4.
- The shape of the flux-MMF trajectories is closer to ideal elliptical shape in Fig. 4.5 than in Fig. 4.4.

Both these effects lead to a reduction in electromagnetic torque ripple as shown in Fig. 4.6.

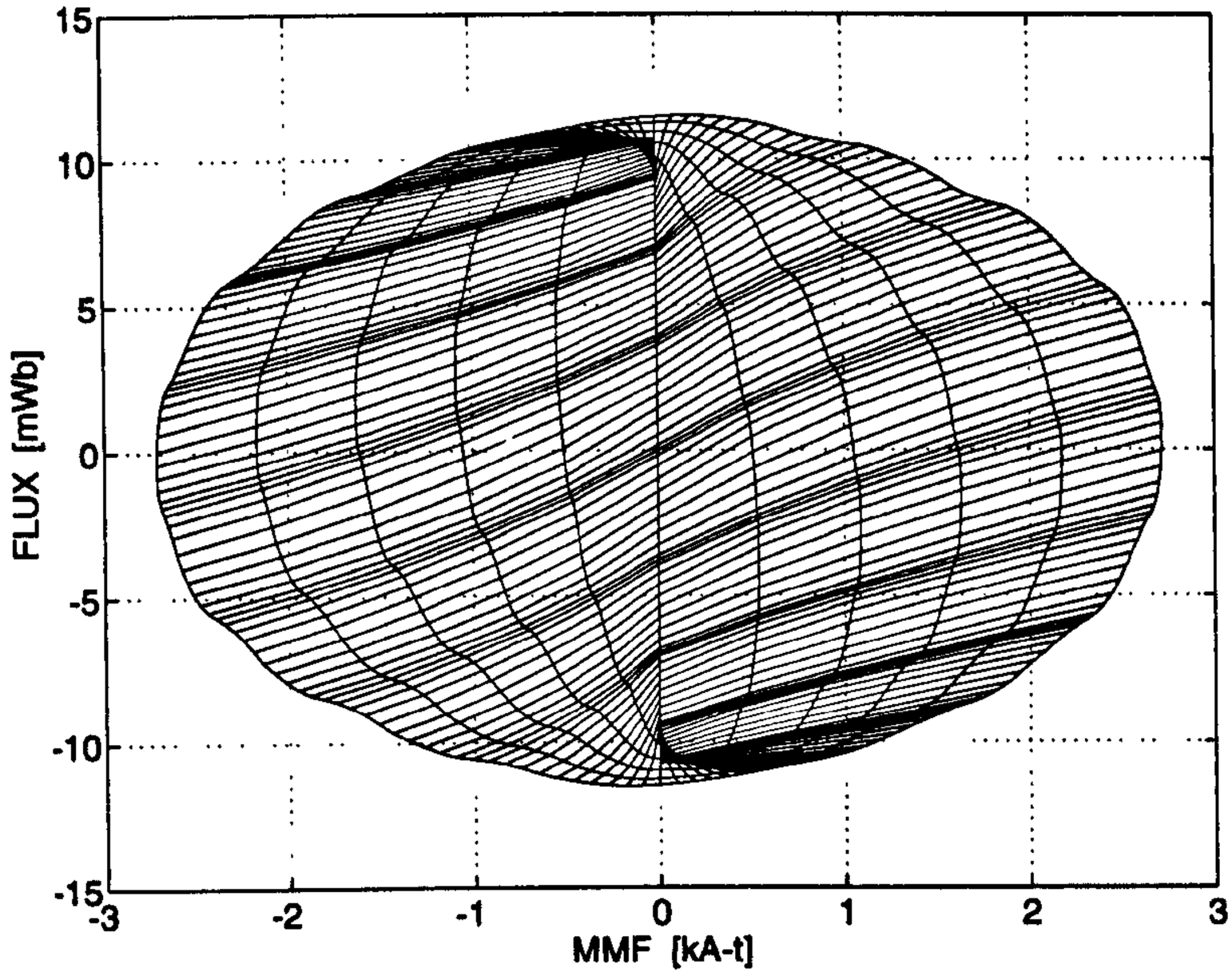

Figure 4.4. Flux-MMF diagram for the spoke type motor without skew at 0, 4, 8, 12, 16 and 20 A RMS phase currents.

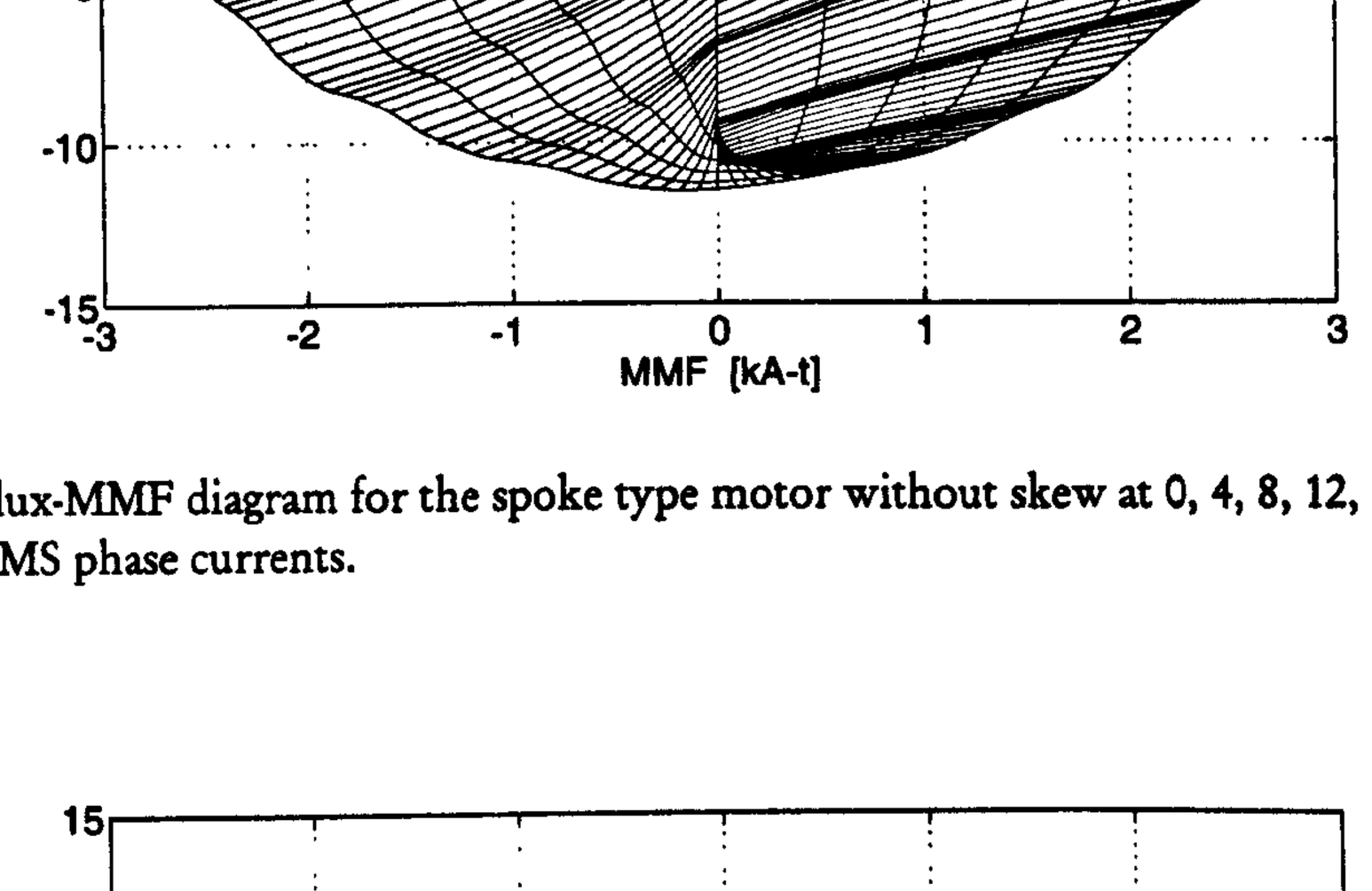

Figure 4.5. Flux-MMF diagram for the spoke type motor with a skew of one slot pitch at 0, 4, 8, 12, 16 and 20 A RMS phase currents.

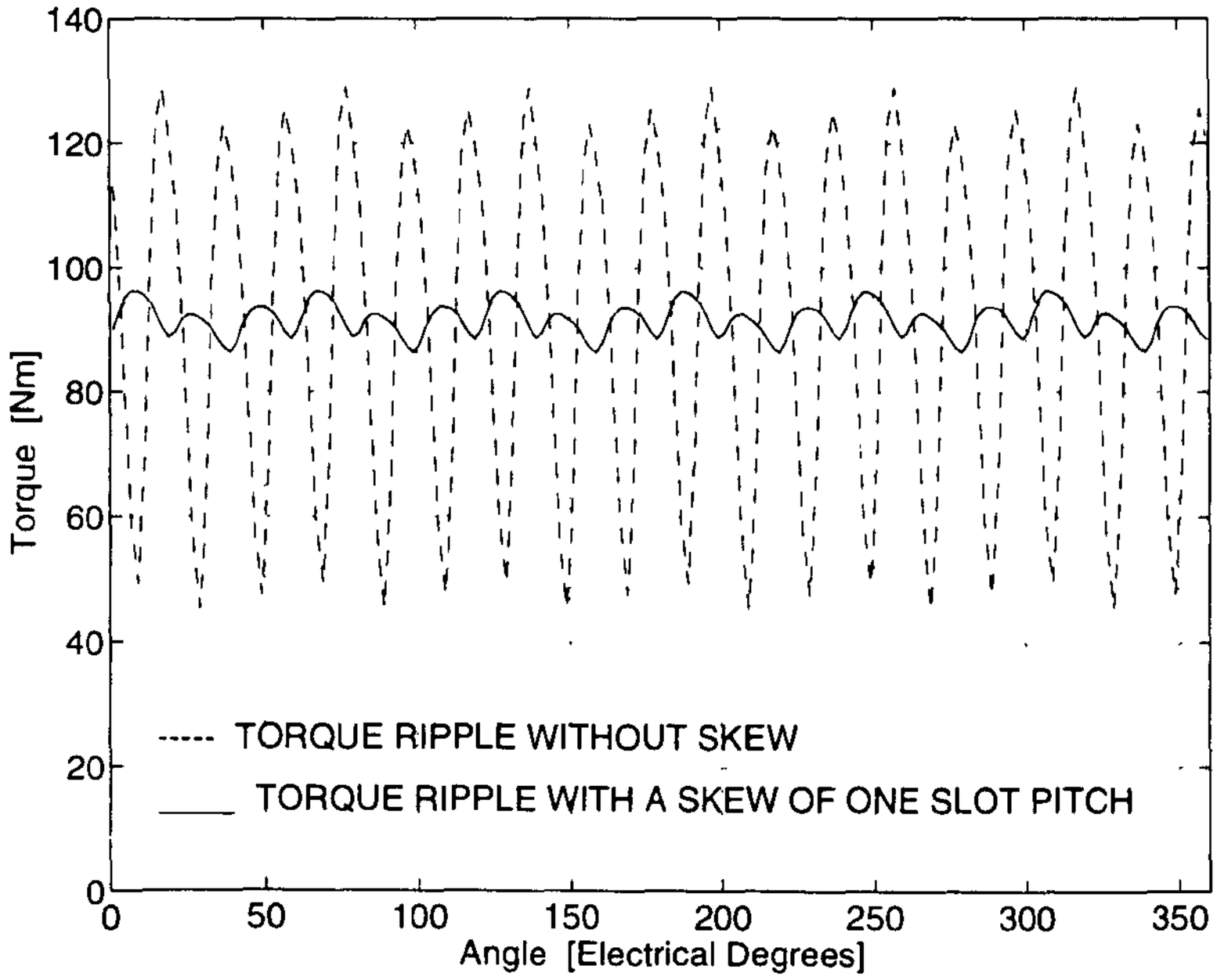

Figure 4.6. Electromagnetic torque ripple for the spoke type motor, without skew and with a skew of one slot pitch at 20 A RMS phase current.

4.5 Cogging Torque Ripple : Effect of Skew

The technique of predicting cogging torque ripple using the flux-MMF diagram has been described in Chapter 3. Briefly, it has been shown in Chapters 2 and 3 that the flux-MMF diagram for any one phase of a machine can only predict electromagnetic torque ripple at a certain non-zero load current. Since the flux-MMF diagram is merely a vertical line at zero current, it does not enclose an area and hence does not predict any torque. In order to be able to predict cogging torque ripple which is present even at zero current, the flux-MMF diagram is plotted for a permanent-magnet corresponding to *any one pole* rather than for *any one phase* of an electrical machine. The cogging torque ripple is then predicted by applying the principle of virtual work. The calculation of cogging torque ripple and the effect of skew on it will now be illustrated with the help of an example.

Fig 4.7 shows the cross-section of a ferrite-magnet brushless DC motor, BMF115C6-T, manufactured by SEM Ltd.

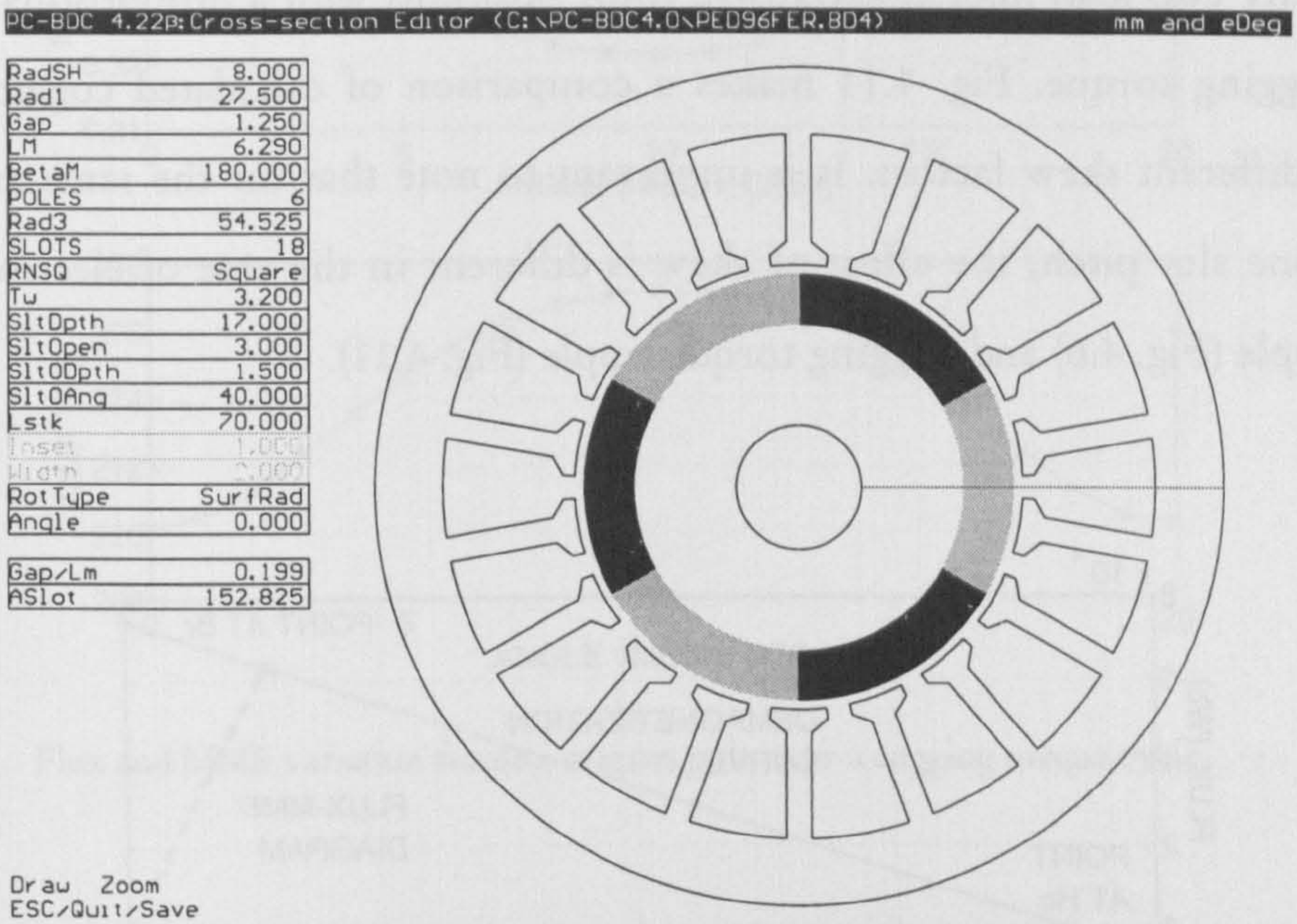

Figure 4.7. Cross-section of the SEM BMF115C6-T ferrite-magnet brushless DC motor.

Fig. 4.8 is the flux-MMF diagram for a permanent-magnet corresponding to any one pole, obtained using FEA. Note that in the FE model, each rotor pole was assumed to have a uniform radial magnetisation over the entire pole arc of 60°. In practice, however, the effective pole arc is bound to be slightly less than 60° due to a small neutral zone between any two adjacent poles. Fig. 4.9 shows that the calculated variation of flux and MMF in the permanent-magnet over a cogging torque cycle is very small. This is also reflected in the flux-MMF diagram shown in the top half of Fig. 4.8. The bottom half of Fig. 4.8 shows the same flux-MMF diagram on an expanded scale to indicate the areas enclosed by the average load lines at successive rotor positions. These areas indicate incremental change in coenergy over a unit of rotor displacement and the cogging torque is then calculated by applying the principle of virtual work. The effect of skew on the flux-MMF diagram of Fig. 4.8 is

demonstrated in Fig. 4.10. The flux-MMF diagram with skew was constructed from the one without skew, using the same method as described in Section 4.4. It shows that a skew of one slot pitch leads to a substantial reduction in the areas enclosed between any two load lines at successive rotor positions with a proportional decrease in the cogging torque. Fig. 4.11 makes a comparison of calculated cogging torque ripple at different skew factors. It is important to note that for the same amount of skew of one slot pitch, the effect of skew is different in the case of electromagnetic torque ripple (Fig. 4.6) and cogging torque ripple (Fig. 4.11).

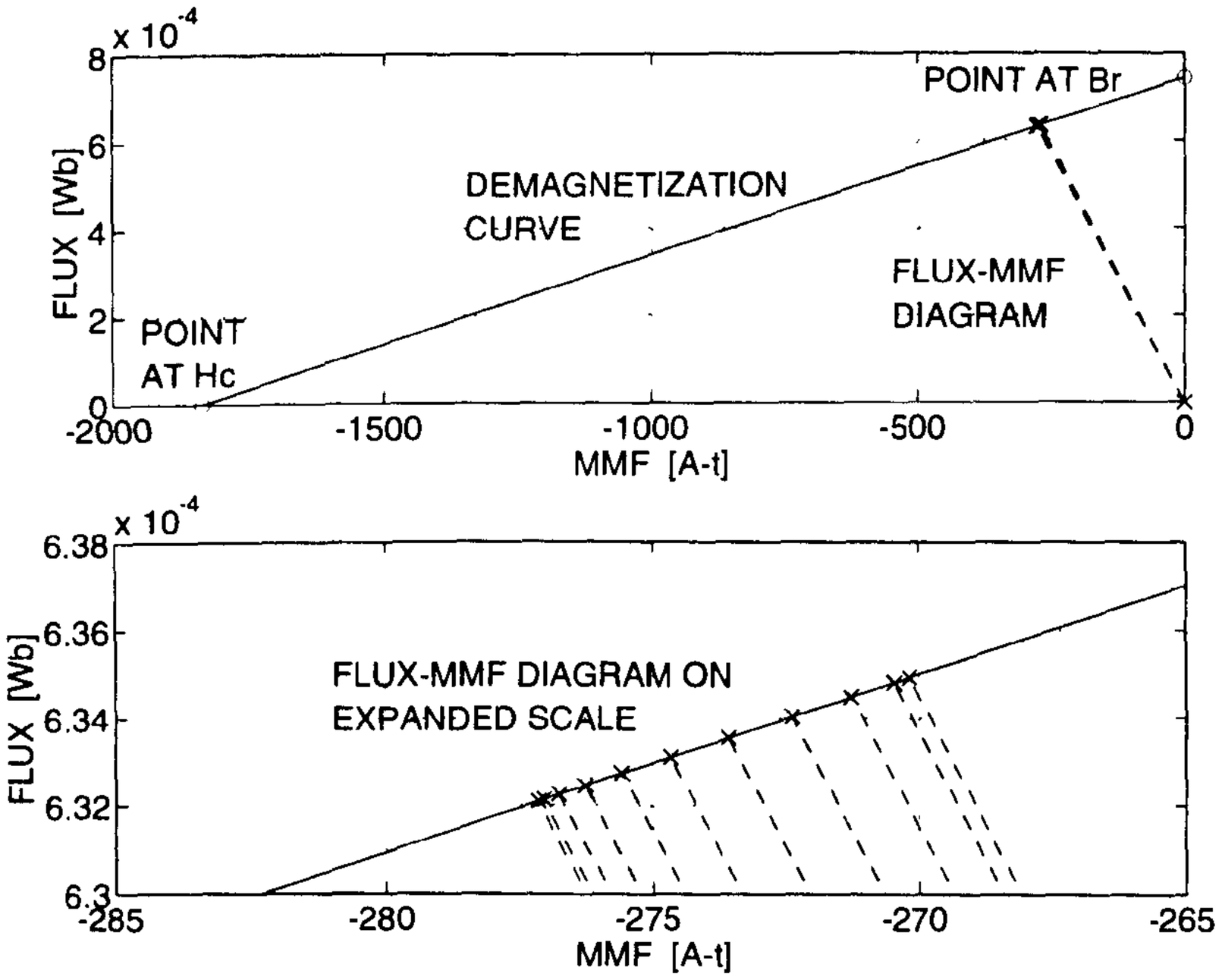

Figure 4.8. Flux-MMF diagram for one magnet pole of SEM ferrite-magnet motor. Figure at the top shows very small areas enclosed by dotted load lines at successive rotor positions. Figure at the bottom shows the same on an expanded scale.

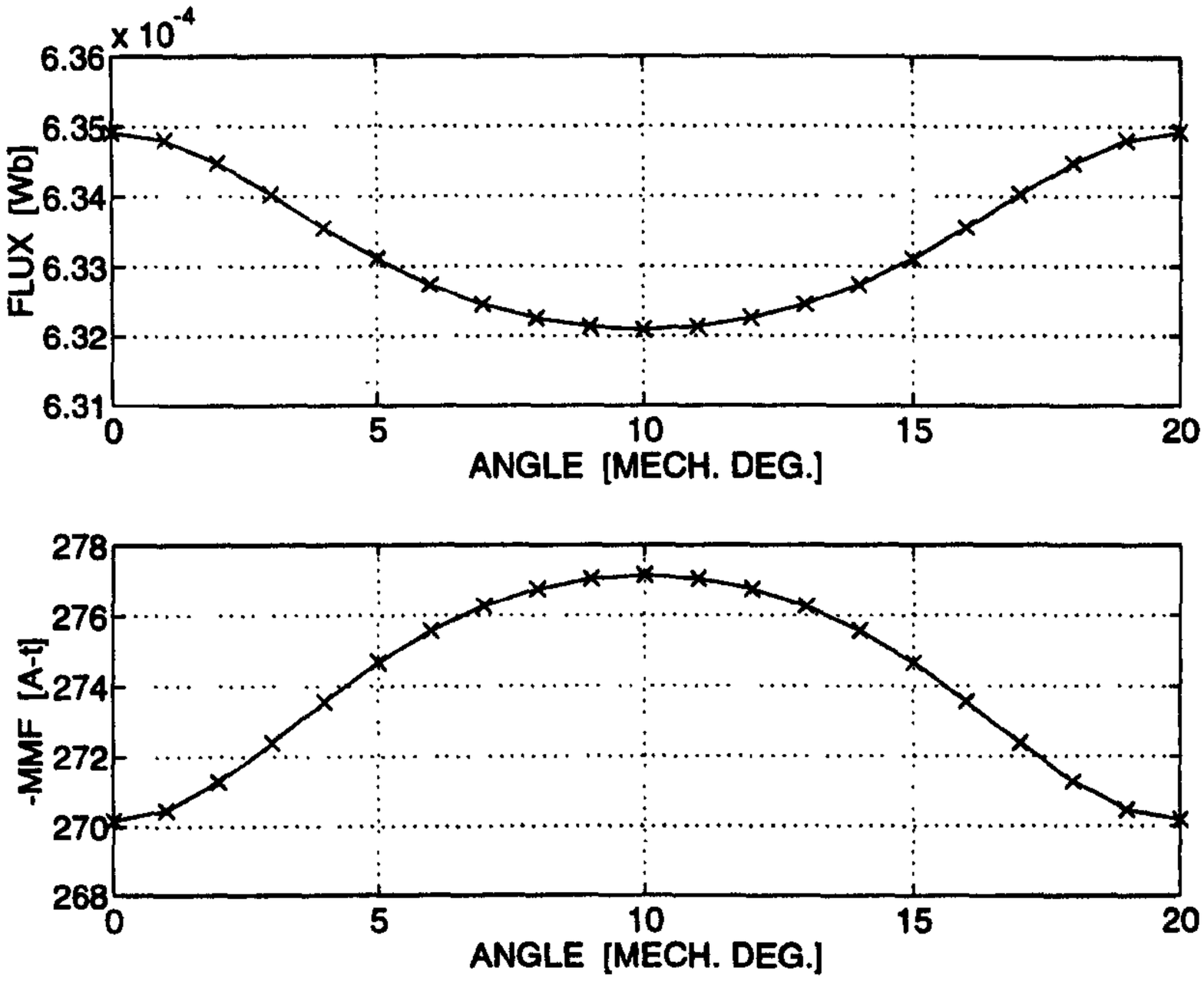

Figure 4.9. Flux and MMF variation for one magnet pole over a cogging torque cycle.

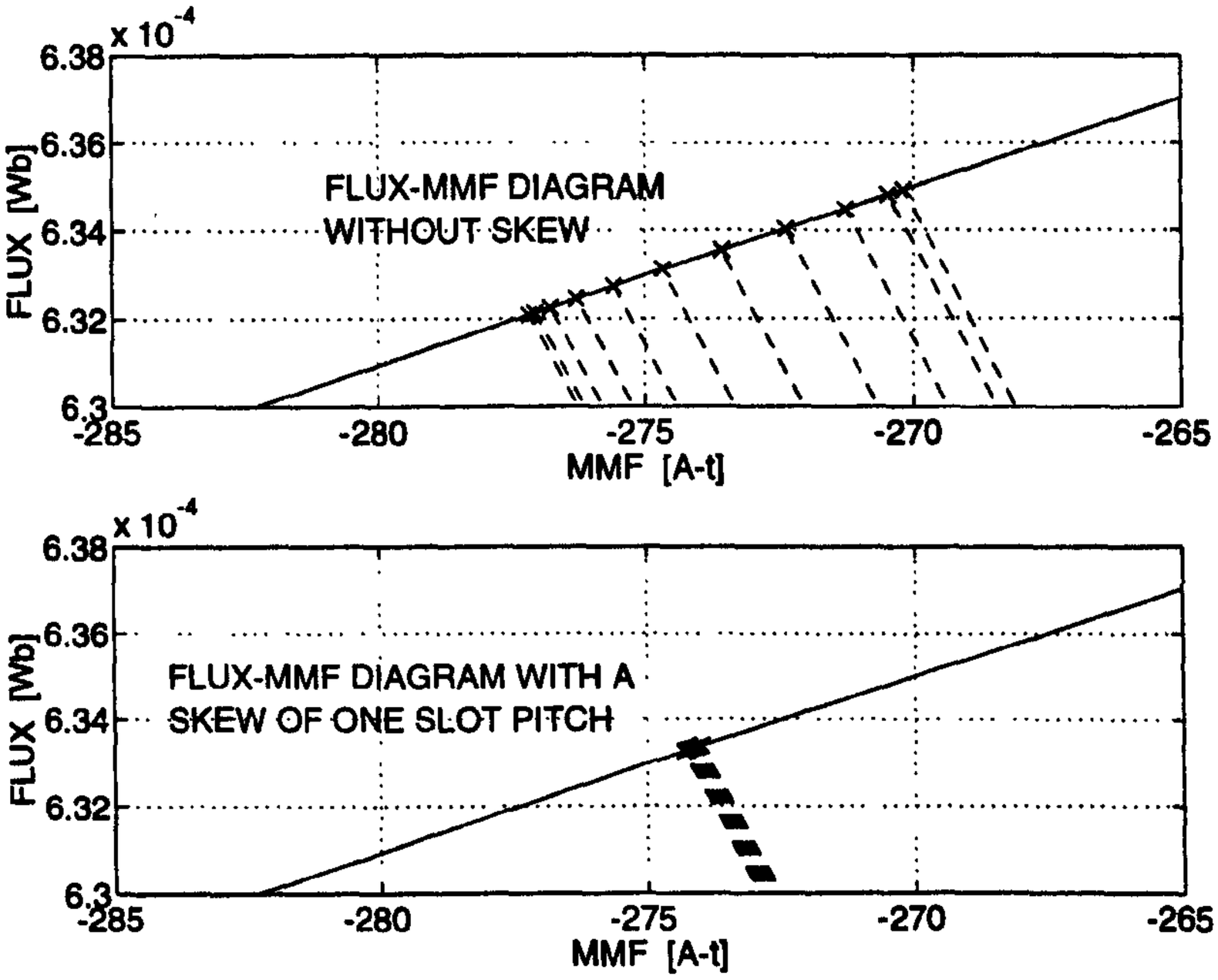

Figure 4.10. Effect of skew on the flux-MMF diagram for one magnet pole.

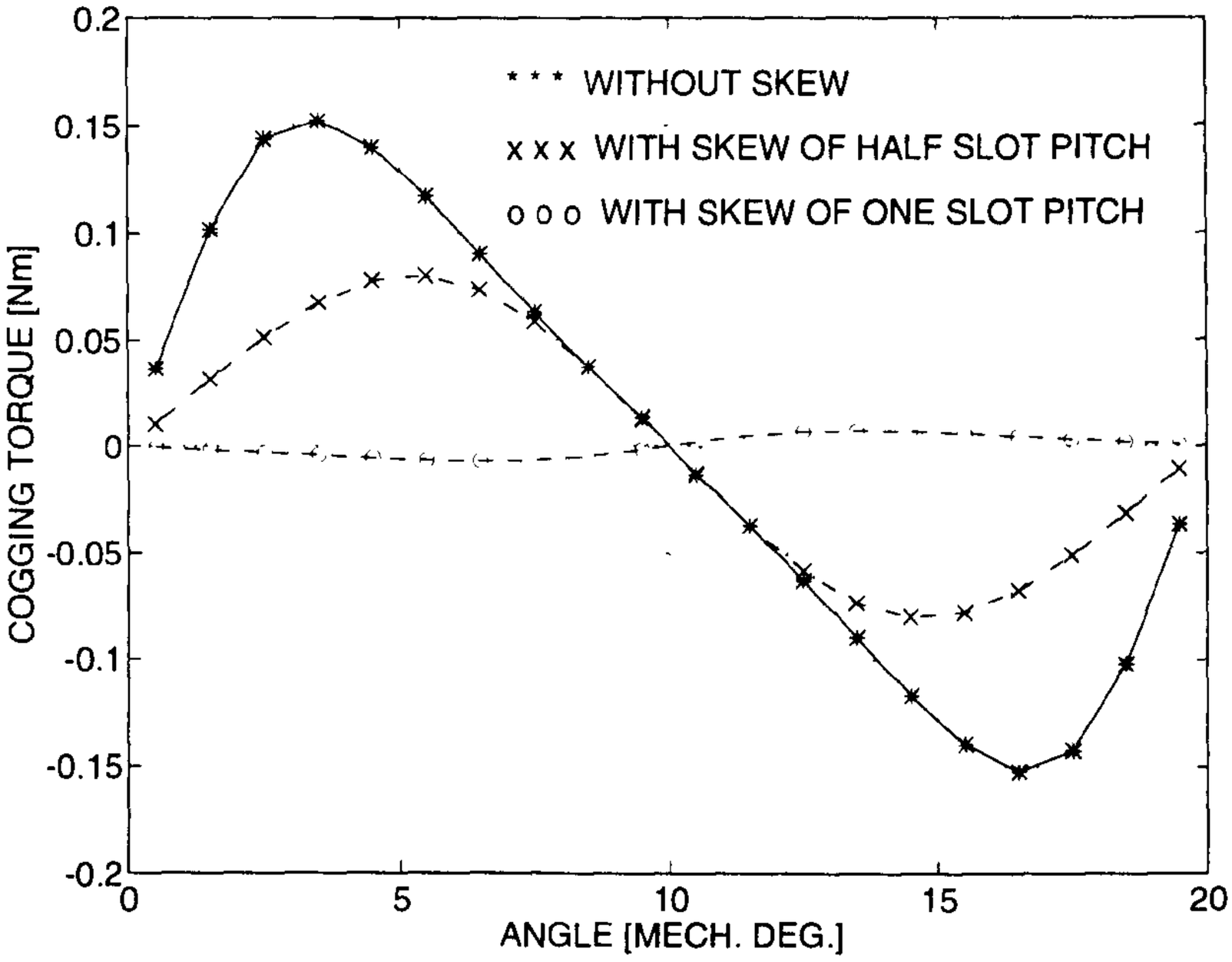

Figure 4.11. Effect of skew on cogging torque ripple for the ferrite-magnet SEM motor.

4.6 Experimental Validation

Experimental validation is provided by comparing the predicted and the measured low speed total torque ripple curves for a rare-earth magnet brushless AC motor, BMR115C6-64S, manufactured by SEM Ltd. The motor has bifurcated stator teeth to reduce cogging torque ripple. A detailed analysis of the effect of bifurcated teeth on cogging torque ripple in this motor is presented in Chapter 3. The cross-section diagram is shown in Fig. 3.23 while a typical flux plot at no-load, obtained using FE analysis, is shown in Fig. 3.11.

4.6.1 Electromagnetic Torque Ripple Calculation

Figs. 4.12 and 4.13 show the flux-MMF diagrams for one phase of the rare-earth magnet SEM motor with and without skew respectively.

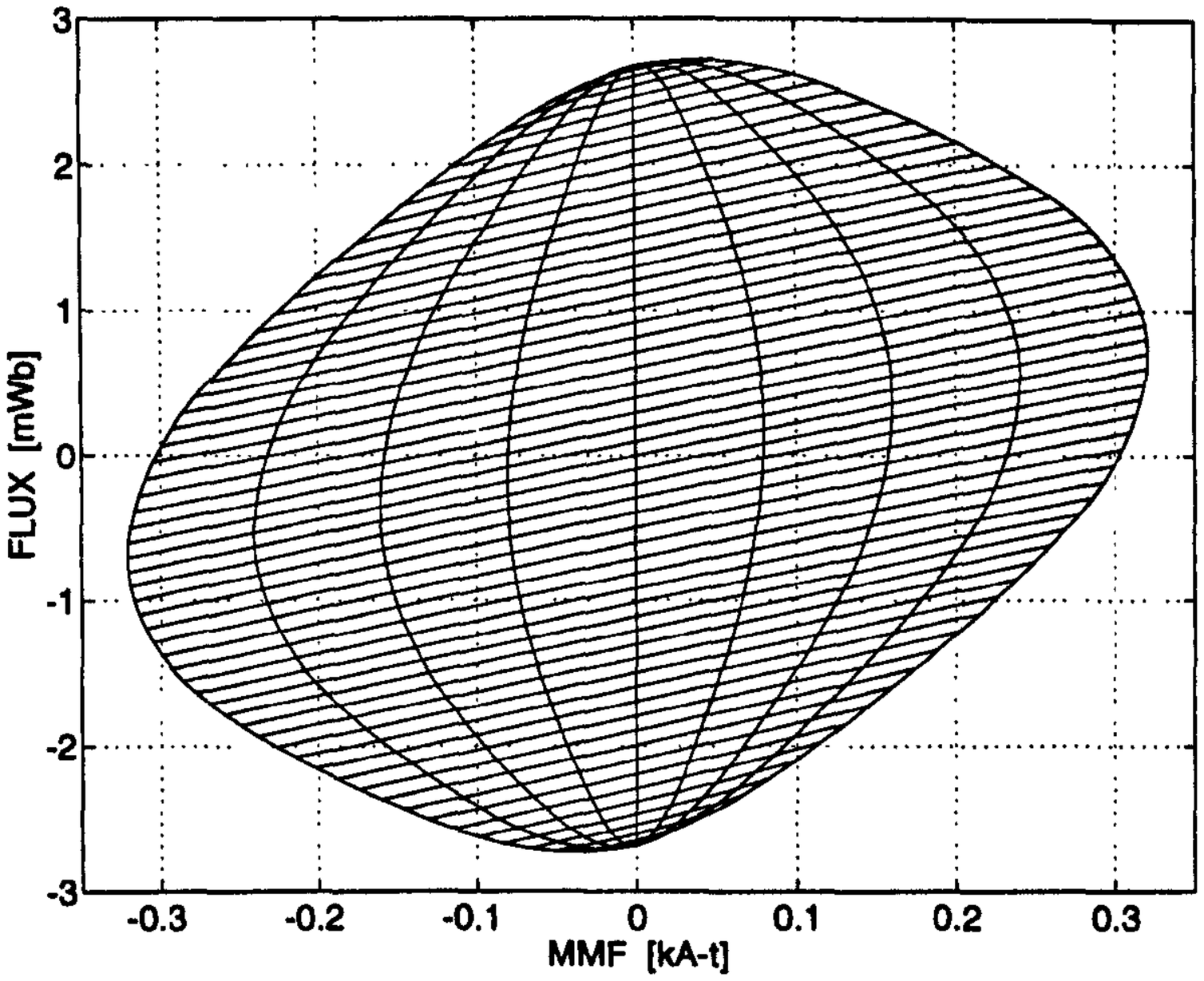

Figure 4.12. Flux-MMF diagram for the rare-earth magnet SEM motor without skew at 0, 1, 2, 3 and 4 A RMS phase currents.

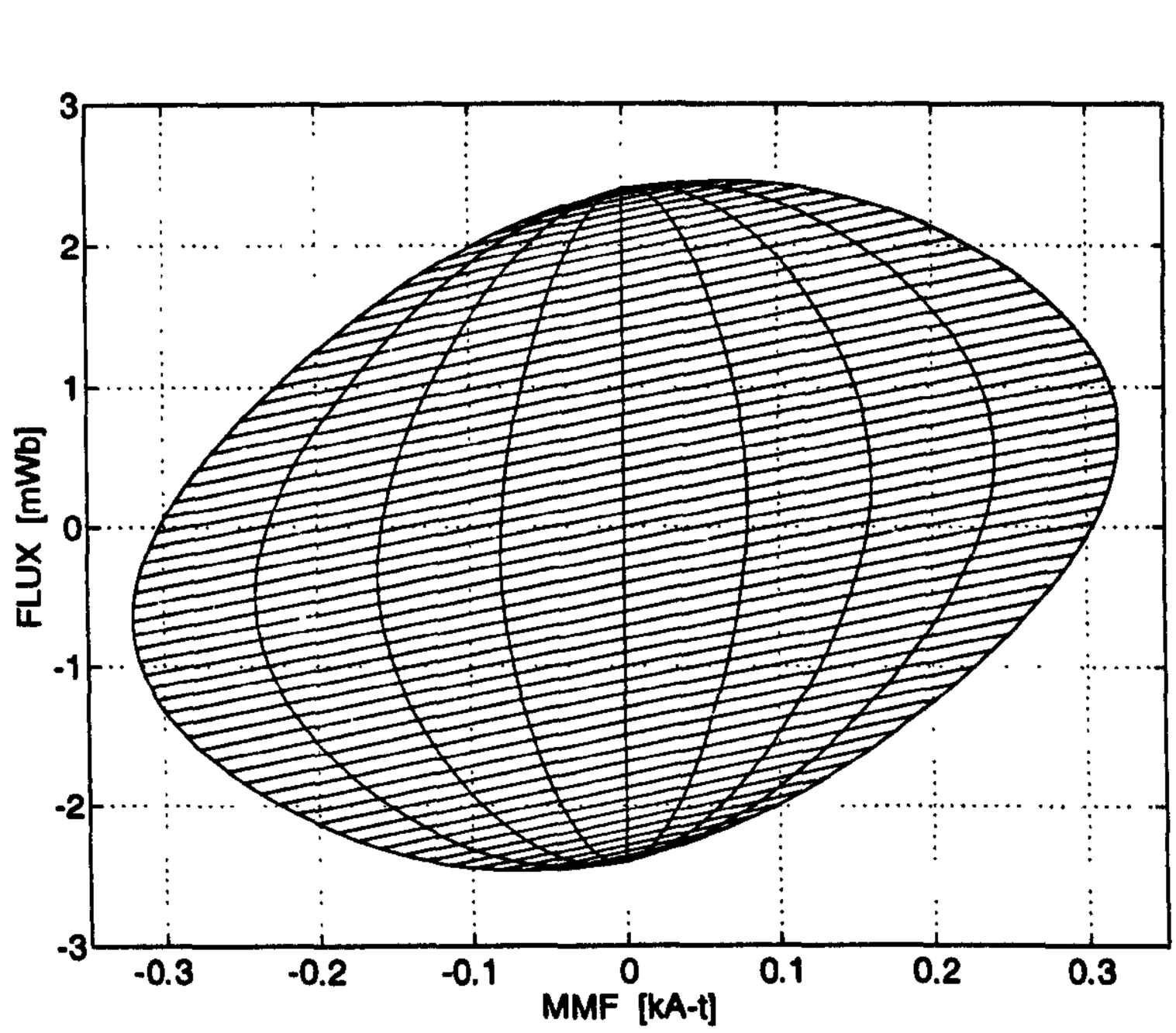

Figure 4.13. Flux-MMF diagram for the rare-earth magnet SEM motor with a skew of one slot pitch at 0, 1, 2, 3 and 4 A RMS phase currents.

Fig. 4.14 makes a direct comparison between the two cases for the flux-MMF trajectories at 4 A. It shows that the shape of the diagram is closer to the ideal elliptical shape for the motor with skew, indicating a reduced torque ripple. However, there is a price to be paid for this gain in terms of a slight reduction in average torque, again as indicated by the smaller area enclosed by the diagram for the motor with skew. Table 4.1 further illustrates this point with the help of some quantitative analysis of the total torque ripple in the two cases.

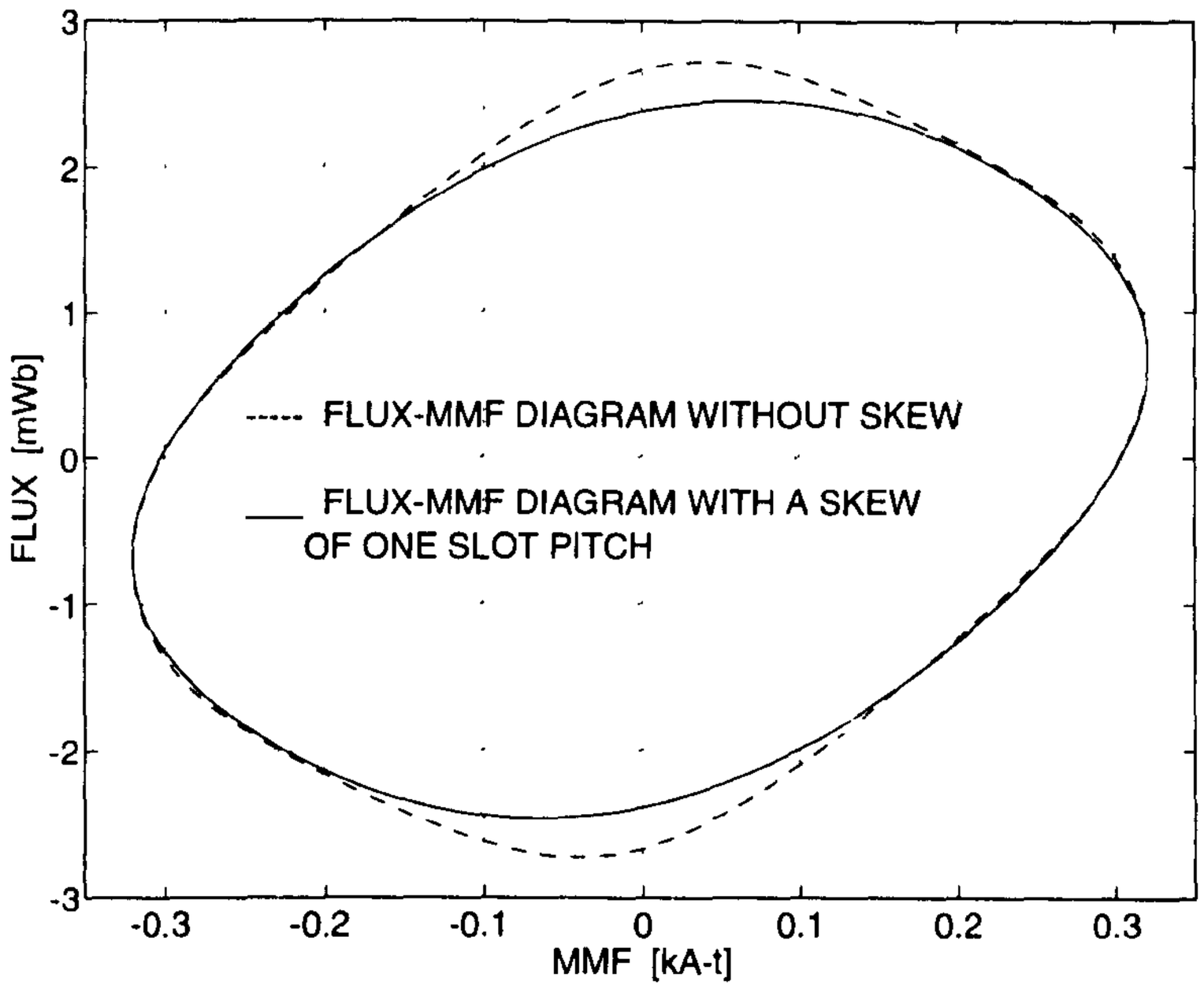

Figure 4.14. Comparison between the flux-MMF trajectories at 4 A RMS phase current, with and without skew.

Fig 4.15 shows the effect of skew on the electromagnetic torque ripple calculated for one phase. It shows that in the case of motor with skew, even with a regular spacing of magnetisation curves, as shown in Fig. 4.13, there is some amount of torque ripple present due to deviation from the ideal elliptical shape of the flux-MMF trajectories. Fig. 4.16 compares the electromagnetic torque ripple in the two cases, with and without skew.

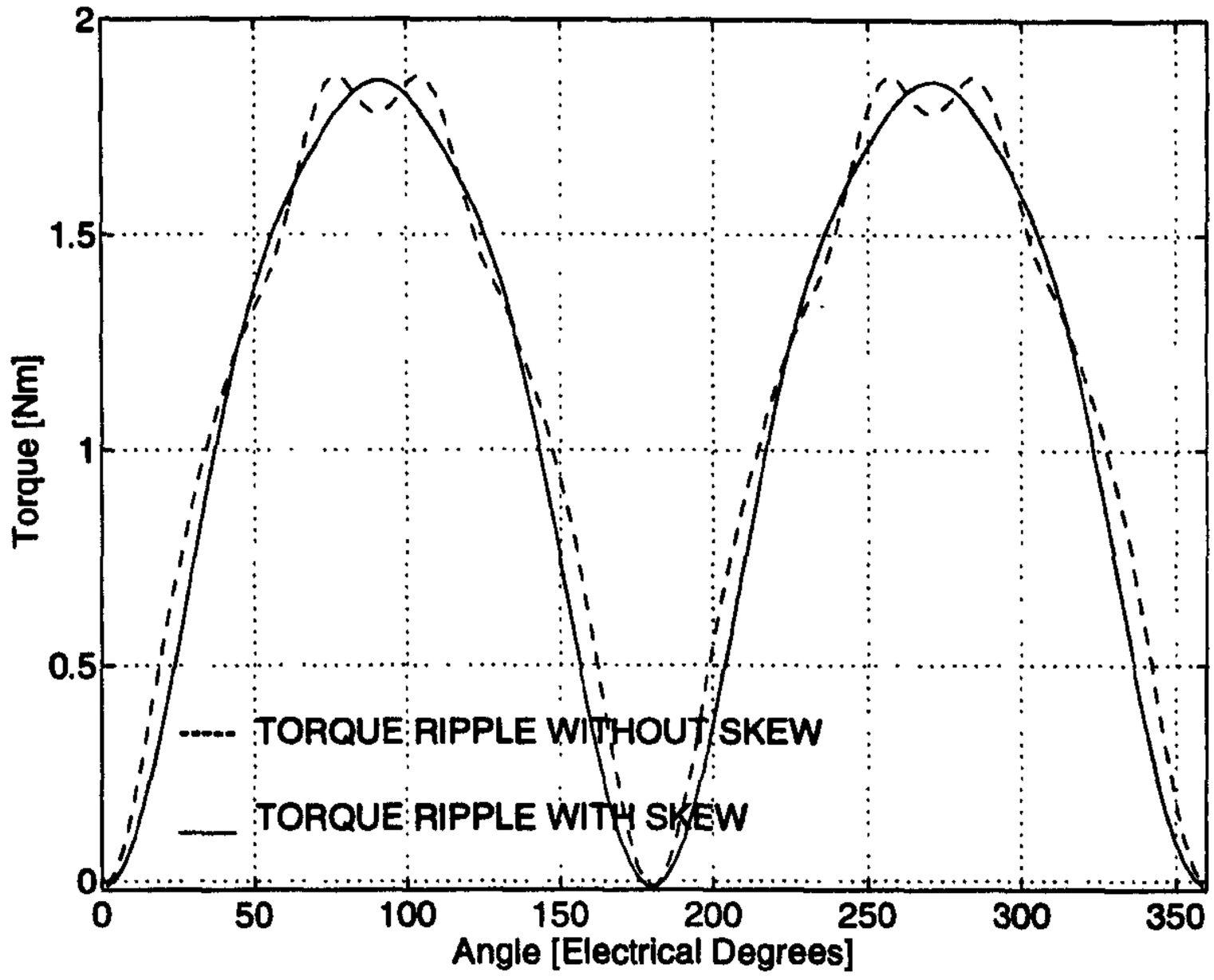

Figure 4.15. Comparison between the phase electromagnetic torque ripple for at 4 A RMS current, with and without skew.

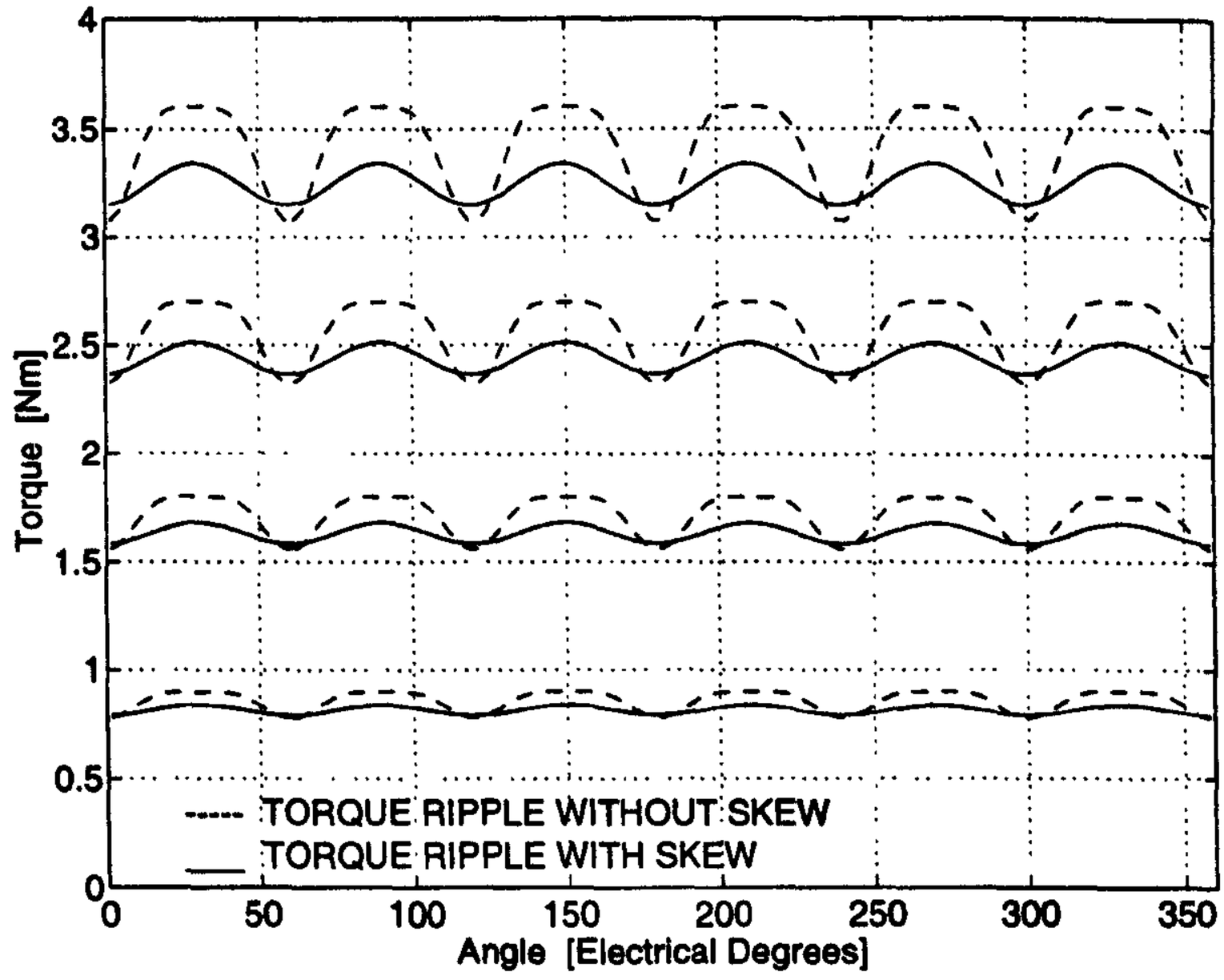

Figure 4.16. Comparison between the total electromagnetic torque ripple at 1, 2, 3 and 4 A RMS phase currents, with and without skew.

A comparison between Figs. 4.6 and 4.16 brings out the difference in electromagnetic torque ripple between a salient pole machine (Fig. 4.3) and a non-salient pole machine (Fig. 3.23). Both Figs. 4.6 and 4.16 have six ripple cycles per electrical cycle, but in the case of Fig. 4.6 an additional high frequency ripple of eighteen ripple cycles per electric cycle is superimposed owing to the salient pole nature of the machine.

4.6.2 Cogging Torque Ripple Calculation

Flux-MMF diagram for a magnet pole of the rare-earth magnet SEM motor without skew is plotted in Fig. 4.17. The corresponding flux and MMF variation is shown in Fig. 4.18.

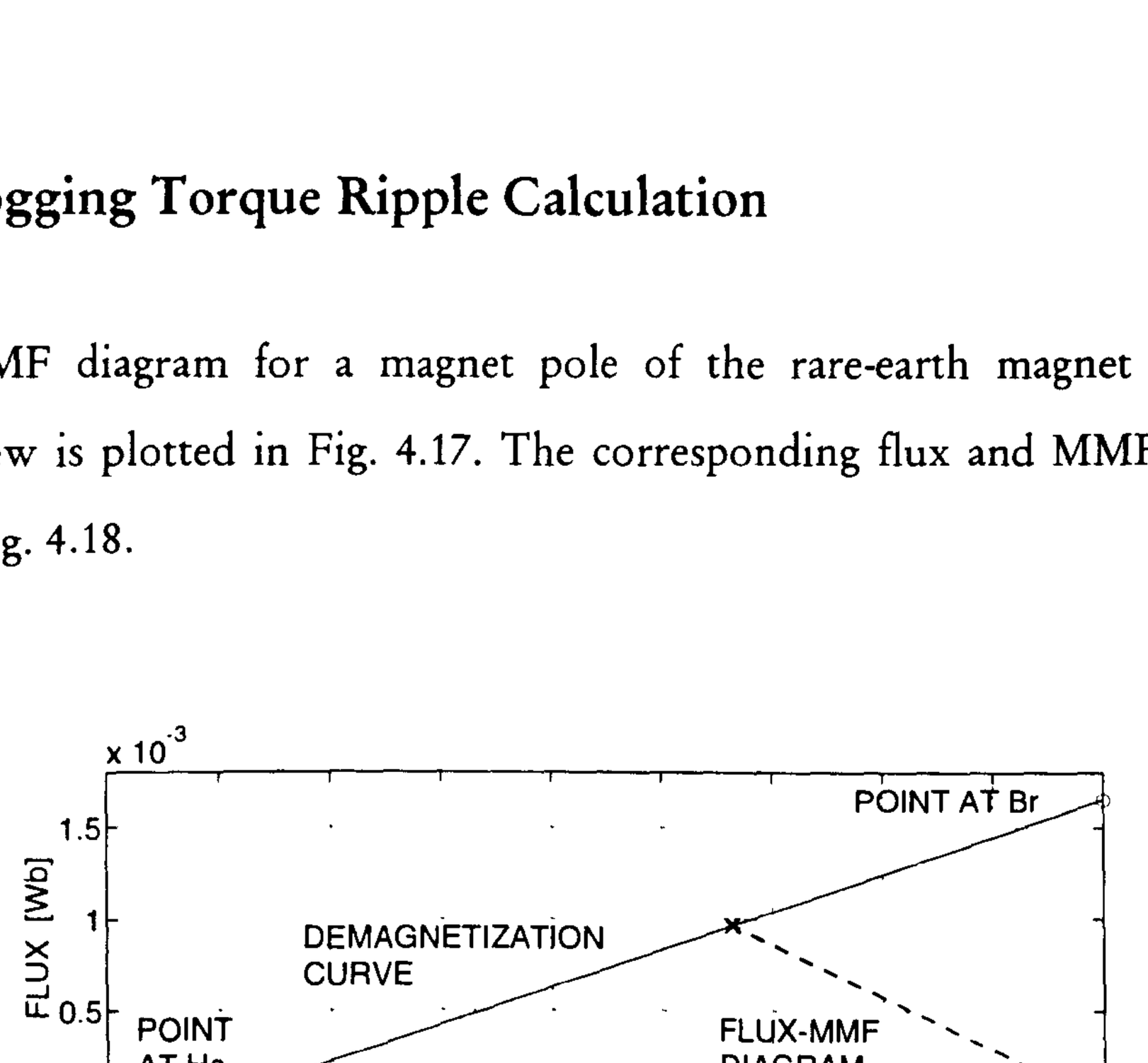

Figure 4.17. Flux-MMF diagram for a magnet pole of the rare-earth magnet SEM motor. Figure at the top shows very small areas enclosed by dotted load lines at successive rotor positions. Figure at the bottom shows the same on an expanded scale.

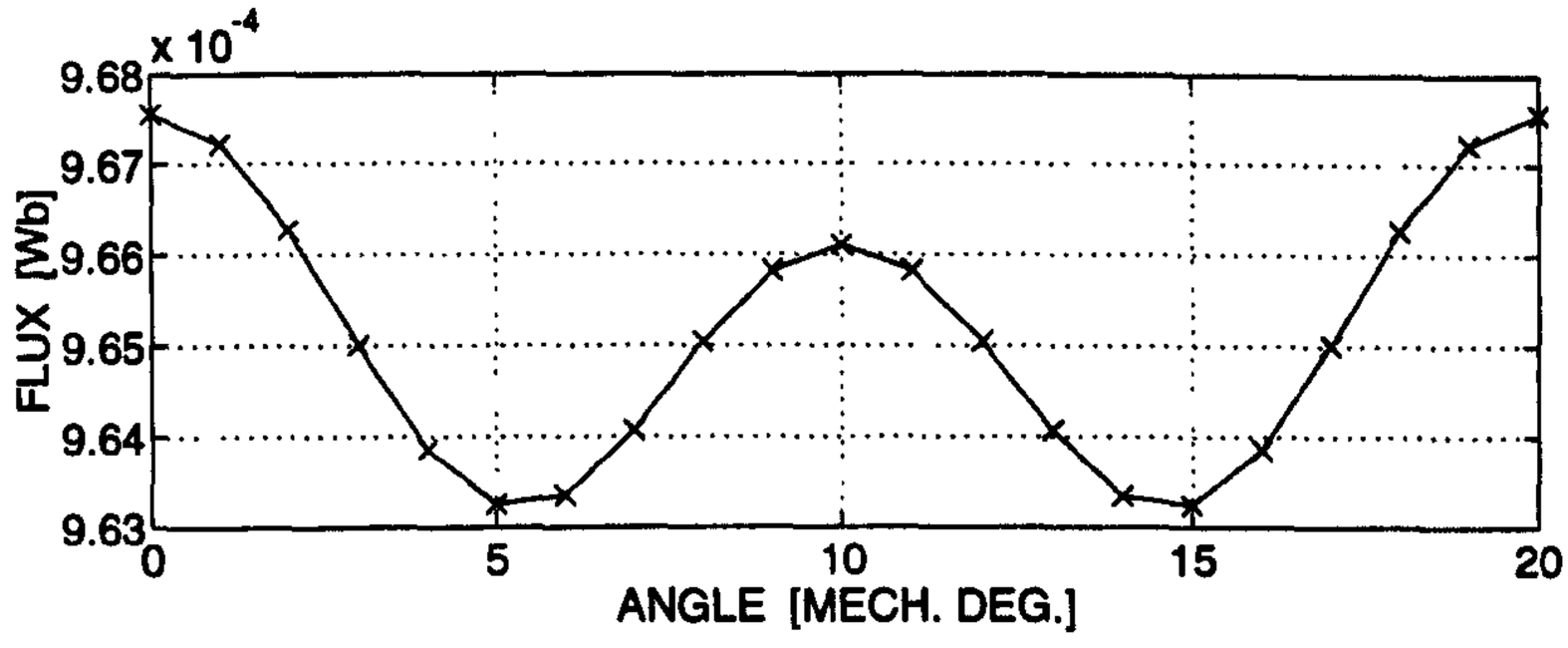

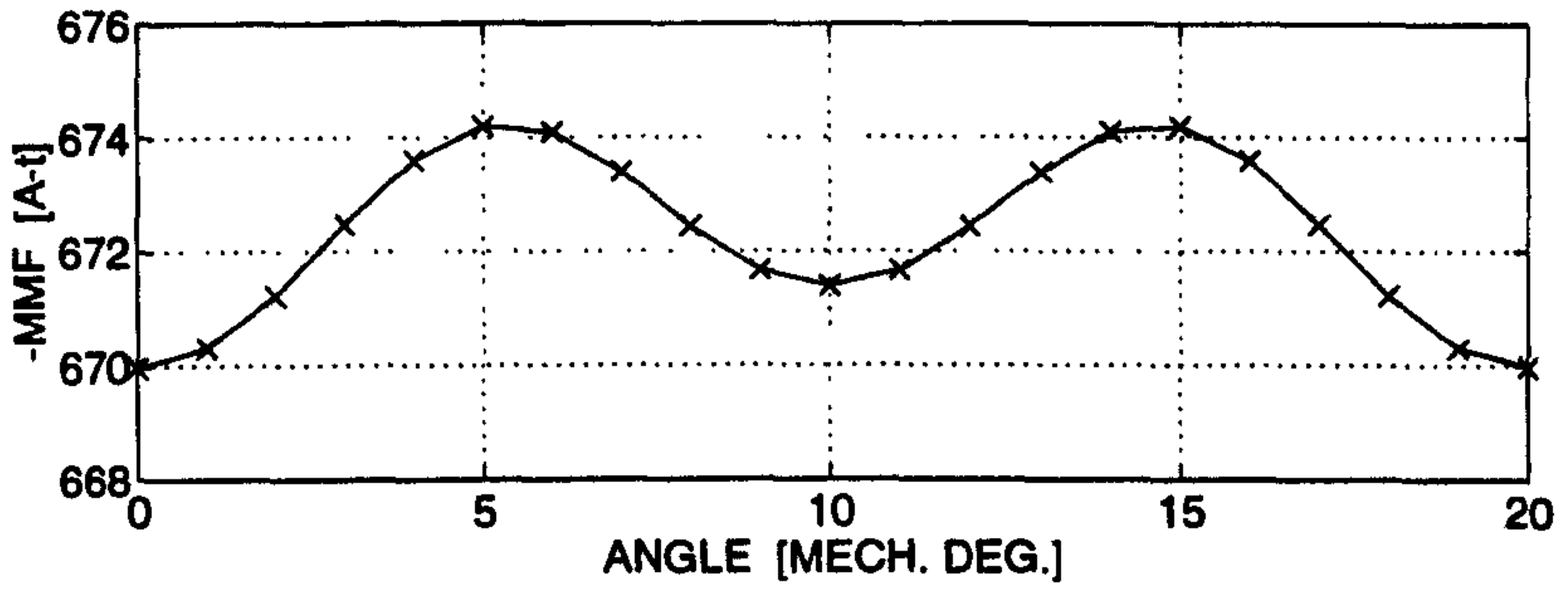

Figure 4.18. Flux and MMF variation in a magnet pole over a cogging torque cycle. Used to construct the flux-MMF diagram shown in Fig. 4.17.

The effect of skew of one slot pitch on the flux-MMF diagram and the resulting cogging torque ripple is shown in Figs. 4.19 and 4.20 respectively. A comparison between Figs. 4.9 and 4.18 shows that bifurcated teeth cause an additional ripple of double the frequency (12 cycles per electrical cycle) to be superimposed on the original slot ripple (6 cycles per electrical cycle). At the same time, bifurcated teeth also cause a reduction in the net variation of flux and MMF in the permanent-magnet which leads to a net reduction in cogging torque ripple.

Figs. 4.8 and 4.17 also make an interesting comparison. While Fig. 4.8 is for a ferrite magnet (B_r=0.39 T), Fig. 4.17 is for a rare-earth magnet (B_r=0.85 T). Since the length of magnet is different in the two cases (l_m=6.29 mm in Fig. 4.7 against l_m=2.45 mm in Fig. 3.23) for the same stator lamination geometry, the operating point for the rare-earth magnet motor is further down the Demagnetisation curve as compared to the ferrite magnet motor. Also, the bottom halves of Figs. 4.8 and 4.17 show that the

rare-earth magnets operate at a higher level of flux and MMF as compared to the ferrite magnets, as expected.

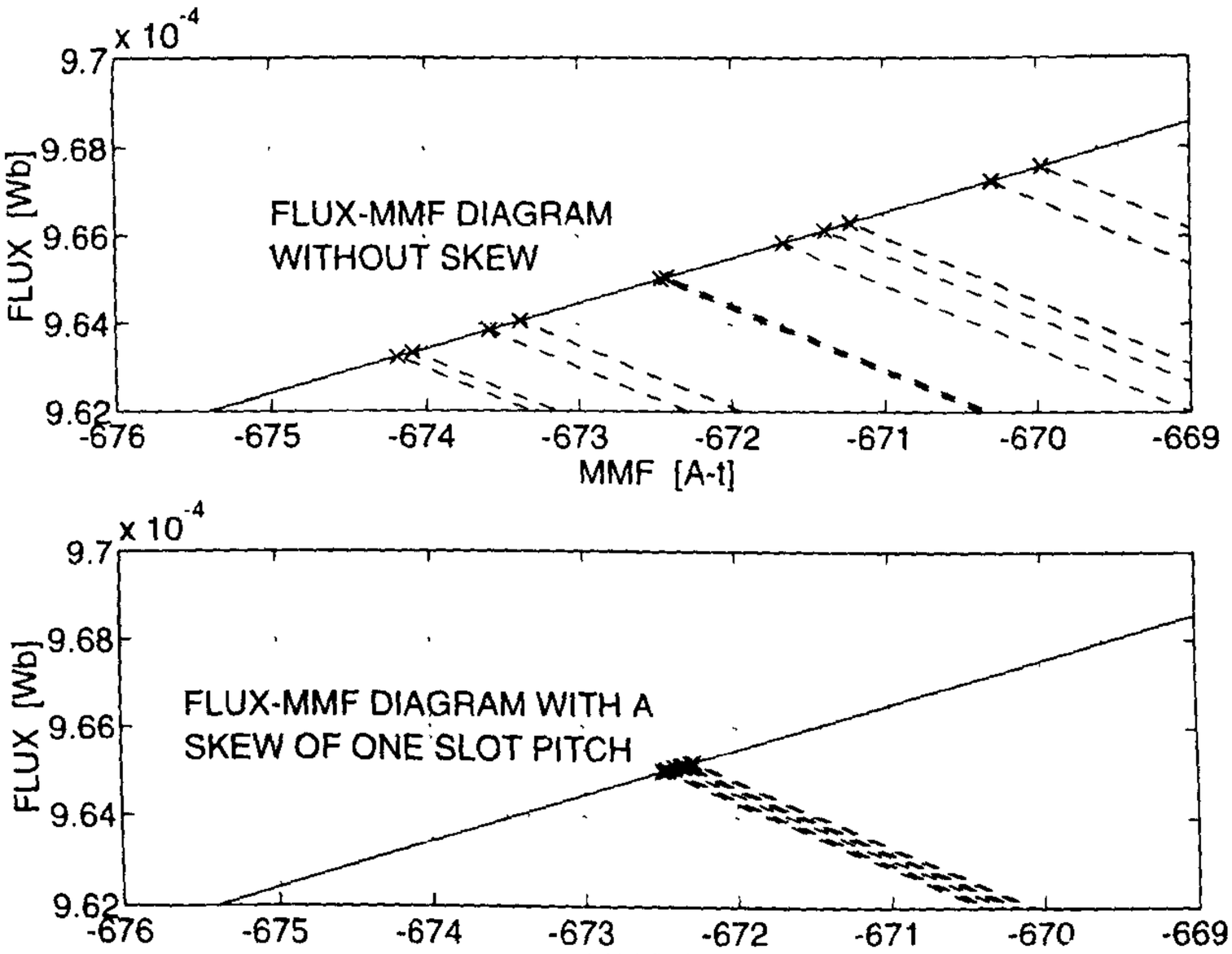

Figure 4.19. Effect of skew on the flux-MMF diagram of Fig. 4.17.

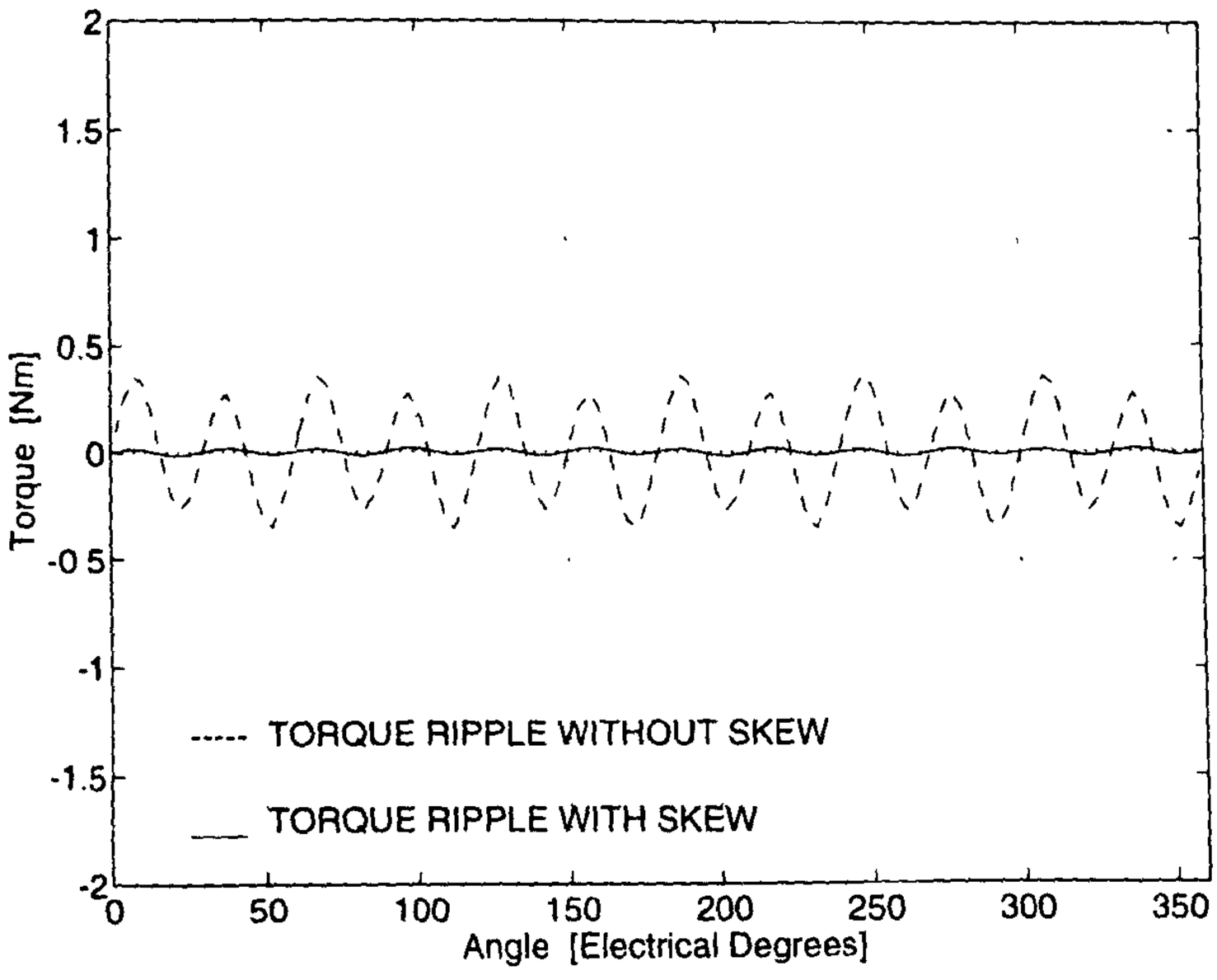

Figure 4.20. Effect of skew on cogging torque ripple of the rare-earth magnet SEM motor.

4.6.3 Total Torque Ripple Calculation and Measurements

Fig. 4.21 shows the effect of skew on the calculated total torque ripple and Table 4.1 gives a quantitative analysis of the same.

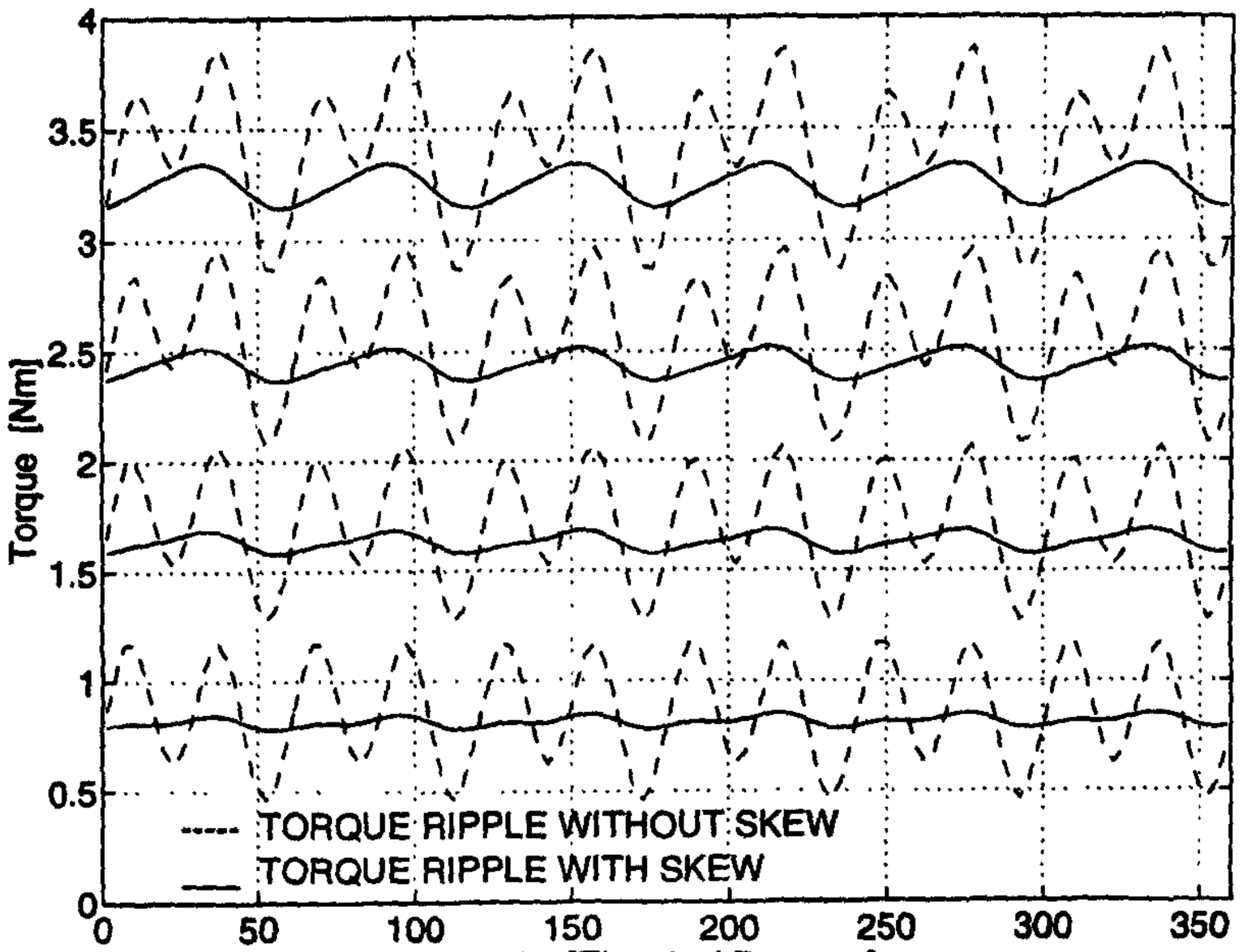

Figure 4.21. Comparison of calculated total torque ripple with and without skew at 1, 2, 3 and 4 A RMS phase currents.

Table 4.1. Quantitative analysis of the effect of skew. Shown with respect to Fig 4.21.

RMS Phase current	T_{RIPPLE}[a] without skew	T_{RIPPLE}[a] with skew	T_{AV} without skew	T_{AV} with skew	% drop in T_{AV} due to skew
1 A	82.6 %	8.1 %	0.86 Nm	0.82 Nm	5 %
2 A	46.3 %	6.7 %	1.72 Nm	1.63 Nm	5 %
3 A	34.5 %	6.2 %	2.57 Nm	2.44 Nm	5 %
4 A	29.1 %	6.0 %	3.41 Nm	3.24 Nm	5 %

[a] T_{RIPPLE} is expressed as a % ratio of peak-to-peak to average torque

The total torque ripple is calculated as a summation of the electromagnetic (Fig. 4.16) and the cogging (Fig. 4.20) torque ripple. Table 4.1 shows that while the extent

of minimisation of torque ripple decreases with increasing load current, the percentage drop in average torque remains the same for all values of load current.

For the purpose of experimental validation, low-speed dynamic torque measurements were carried out using the precision dynamometer built in the SPEED Laboratory [62]. The original objective was to validate torque ripple curves for a particular machine in both the cases—with and without skew. However, for the rare-earth magnet SEM motor, which is a commercially available design, it was not possible to obtain a one-off custom-made prototype without skew; and hence measurements were carried out only on the machine with a skew of one slot pitch. The dynamic test set-up is illustrated in Fig. 4.22.

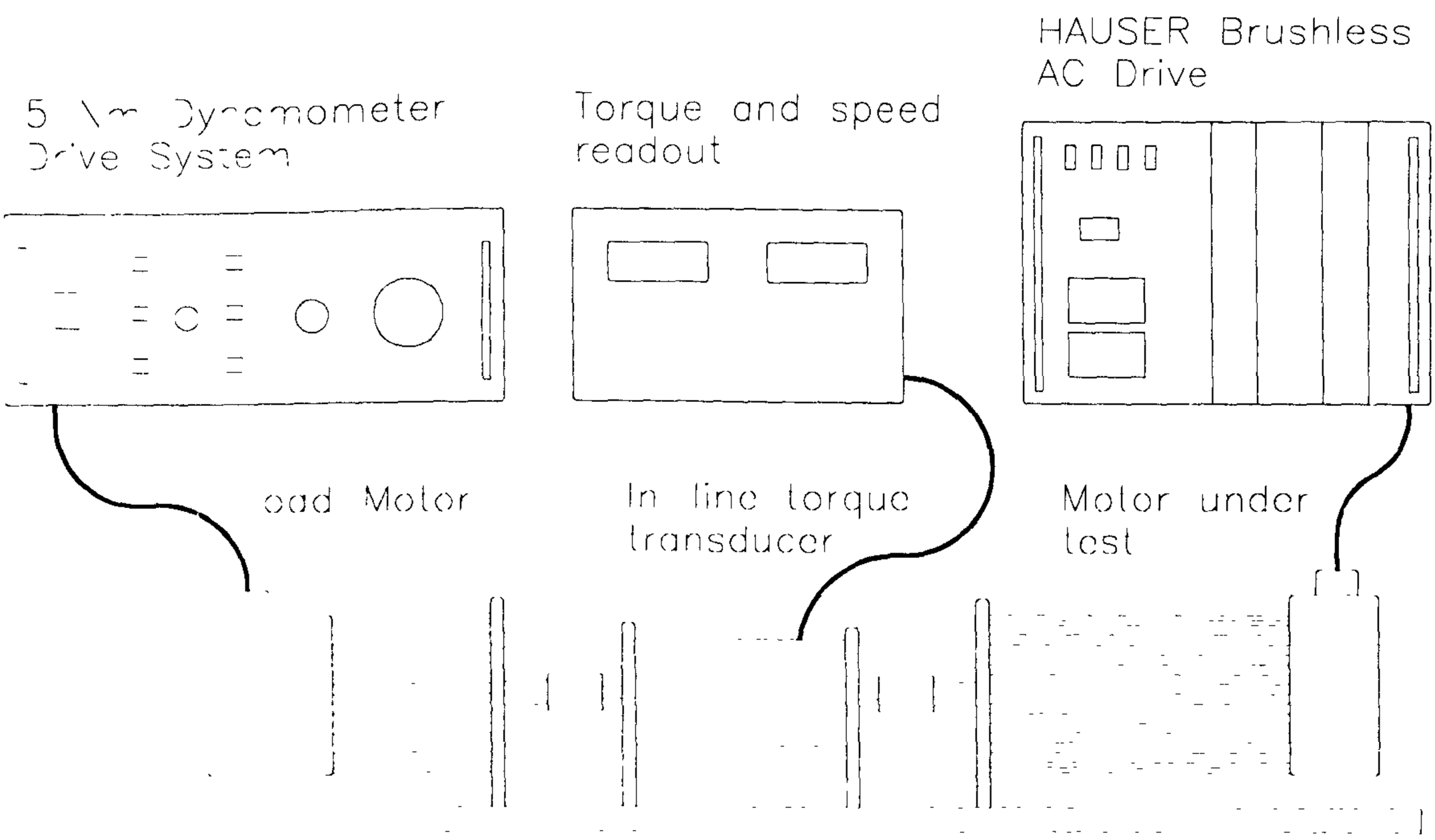

Figure 4.22. Dynamic torque measurement test set-up.

It consists of a load motor (Electro-Craft S-4030, 1 kW brushless sinewave AC motor), an in-line torque transducer (Vibro-Meter, TG-0.5/BP, rated 5 Nm), and the motor under test. The load motor was driven by a 5 Nm dynamometer drive system which is based on a motor compatible Electro-Craft BRU-200 DM-20 sinewave drive

[63]. The rare-earth magnet SEM motor was driven by HAUSER 3000-S sinewave drive [64]. Both drives were capable of four-quadrant operation. The load motor drive was operated in constant-speed, generating mode while the test motor drive was operated in constant-torque, motoring mode. The torque ripple waveforms were captured using the Nicolet 500 data acquisition system [65]. Note that the load motor torque ripple was at least an order of magnitude smaller than the test motor torque ripple. Fig. 4.23 compares the calculated and the measured total torque ripple.

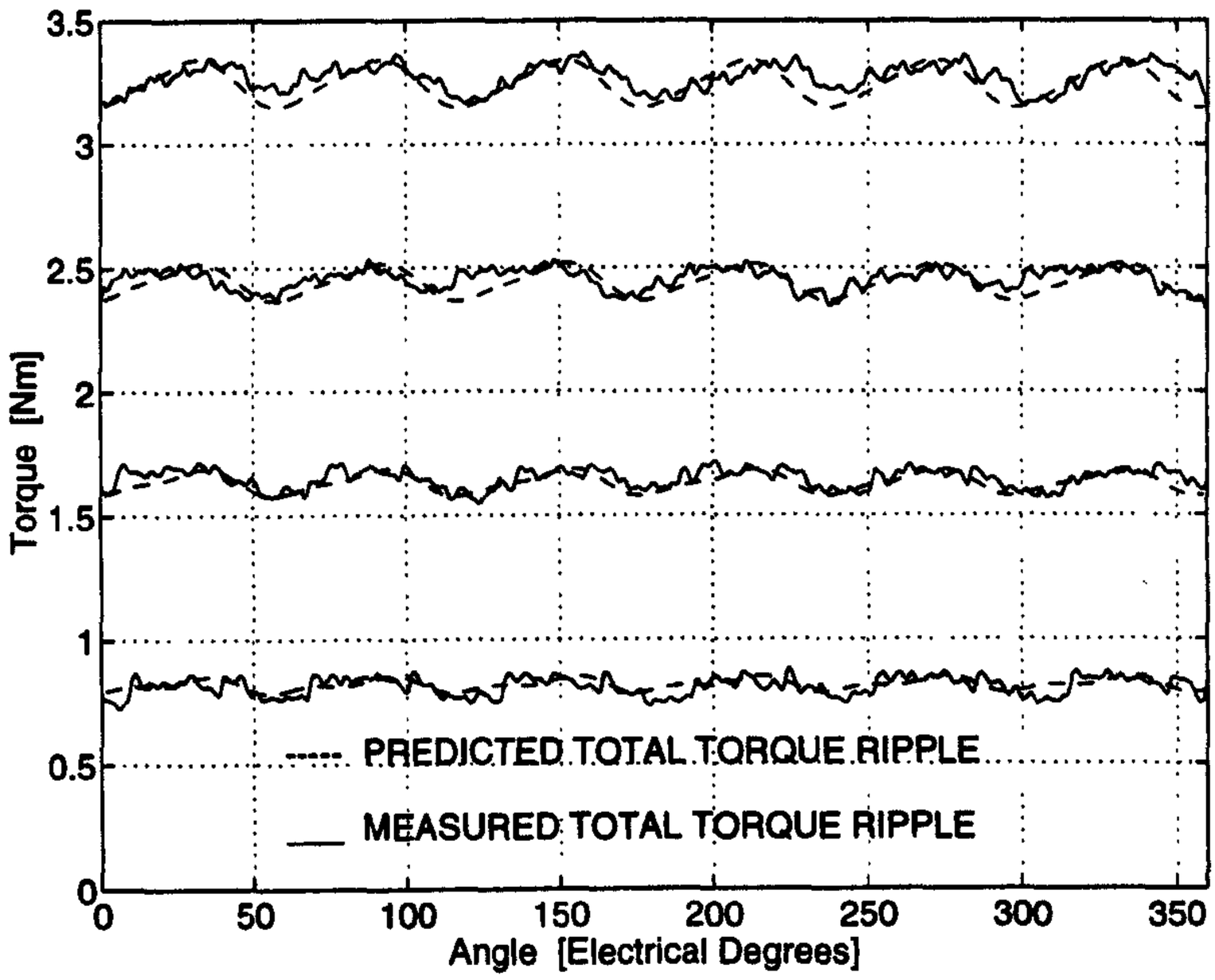

Figure 4.23. Comparison between calculated and measured total torque ripple for the rare-earth magnet SEM motor with a skew of one slot pitch at 1, 2, 3 and 4 A RMS phase currents.

Both the calculated and the measured waveforms show a 6 × electrical cycle frequency ripple which is of interest here. The measured waveforms also show a high-frequency ripple due to PWM chopping of sinewave currents in the actual drive. This is not seen in the calculated waveforms as ideal sinewave currents were assumed in the FE analysis. Since the assumption of ideal sinewave currents in FE analysis is strictly valid at low speeds, the measurements were performed at a low speed of 200 rpm.

4.7 Chapter Summary

Chapter 4 has briefly reviewed the earlier work on the topic of skewing and has dealt with modelling of the effect of skew on torque ripple using the flux-MMF diagram technique. A simple method of constructing the flux-MMF diagram for a machine with skew, from the flux-MMF diagram for a machine without skew, has been described. The effect of skew on the flux-MMF diagram has been illustrated graphically and analysed separately for the cogging and the electromagnetic torque ripple. Although it is well known that skewing minimises torque ripple, the chapter has quantified the difference in the extent of minimisation between the cogging and the electromagnetic torque ripple.

Experimental validation has been provided on a PM brushless AC motor, by first predicting the total torque ripple curves from the electromagnetic and the cogging torque ripple curves; and then comparing these curves against the measured low-speed torque ripple curves. A close agreement between the two sets of curves has validated not only the flux-MMF diagram technique and its ability to take account of skew, but also the method of superpositioning the electromagnetic and the cogging torque ripple to obtain the total torque ripple in a permanent-magnet machine.

5 Variation of Torque Constant

5.1 Introduction

Flux-MMF diagram, coupled with the finite-element analysis, provides an elegant way of analysing the effects of magnetic saturation in electrical machines. One such important effect—the variation of torque constant—is treated in this chapter through analysis of brushless squarewave and sinewave permanent-magnet machines using the flux-MMF diagram. It is commonly known that the inherent non-linear B-H characteristics of electrical steel and permanent-magnet materials affect the performance of an electrical machine in a significant way. In general, at low excitation levels, an electrical machine is said to operate in an unsaturated or linear region of B-H characteristics; while at high excitation levels, it is said to operate in a saturated or non-linear region of B-H characteristics.

In most of the non-FE based analytical treatments on electrical machines, the effect of saturation is either completely ignored, simplifying the underlying theory but restricting its applicability, or approximated in some way avoiding undue complexity. The finite-element analysis, on the other hand, provides a suitable means for taking account of magnetic saturation accurately [66]. This chapter illustrates how to utilise this ability of the finite-element analysis in a practicable manner through the technique of flux-MMF diagram. The next section provides a brief literature review of some of the work performed related to the variation of torque constant in electrical machines. Section 5.3 revisits *armature reaction*, a topic commonly encountered in dealing with commutator DC machines, but of equal significance in brushless PM machines. Finally, Sections 5.4 and 5.5 analyse the variation of torque constant in a PM brushless DC and a PM brushless AC machine respectively.

5.2 Literature Review

The classical literature, such as Fitzgerald and Kingsley [55] or Liwschitz-Garik and Whipple [71], on commutator DC machines and its operational characteristics, give a lucid account of the phenomenon of armature reaction. Although its presence is acknowledged in brushless PM machines, it has received little attention in terms of detailed analysis. In any case, armature reaction coupled with the magnetic saturation is the principal reason behind net reduction in airgap flux and consequent variation of torque constant with increasing load.

Recently, Demerdash et al. [72] have studied the effect of overload on parameters and performance of rare-earth magnet brushless DC motors. They reported that for momentary overloads as high as 4.5 p.u., magnet flux reductions of 29% and 42% of the no-load flux were obtained in the samarium-cobalt and strontium-ferrite PM machines, respectively. They then analysed the effect of this reduction on line-to-line armature inductances and back EMF. The effect on average torque or torque constant, however, was not reported. Sebastian and Slemon [73] produced an experimental evidence of variation of average torque with stator current at high overloads of up to 6.0 p.u. in a neodymium-iron-boron PM brushless motor. In this particular design, the effect of saturation on torque per ampere was found to be small and hence the characteristics were termed as "approximately linear". In a similar study of stall torque in a samarium-cobalt PM machine, Shah et al. [74] reported a reduction in p.u. stall torque with increasing armature current.

This chapter concentrates on prediction of average low-speed torque in brushless PM machines under linear as well as saturated conditions, leading up to the prediction and experimental validation of variation of torque constant with armature current.

5.3 Armature Reaction Revisited

The term *armature reaction* refers to the effect of magnetic field set up by the armature (or load) current on the net airgap flux density distribution set up by the permanent-magnets or field winding alone. The effect is of two types; cross-magnetisation and de-magnetisation. Usually, in PM commutator DC motors, the brushes are positioned in such a way that the armature field is in quadrature with the field set up by the permanent-magnets and in this case, only the cross-magnetising effect is present. But if the brushes are shifted away from this position in either direction, a combination of cross-magnetising and de-magnetising effect is present [71], [75]. Because of saturation, both effects cause a net reduction in airgap flux leading to the variation in torque constant with armature current. Clearly, the effect of armature reaction becomes more significant with increasing saturation. The two types of armature reaction effects, which are also present in brushless PM motors, are explained with the help of a specific example as follows.

Fig. 5.1 shows a cross-section sketch over two half poles of the BMR115C6-64S motor manufactured by SEM Ltd. This particular motor design has been considered before in Chapters 3 and 4 in relation to the analysis of cogging and effect of skew respectively. Fig. 5.1(a) shows the armature current excitation which gives a purely cross-magnetising effect while Fig. 5.1(b) shows the same for a purely de-magnetising effect of armature reaction. Finite-element analysis was performed in both the cases and the results are presented in the next two sub-sections.

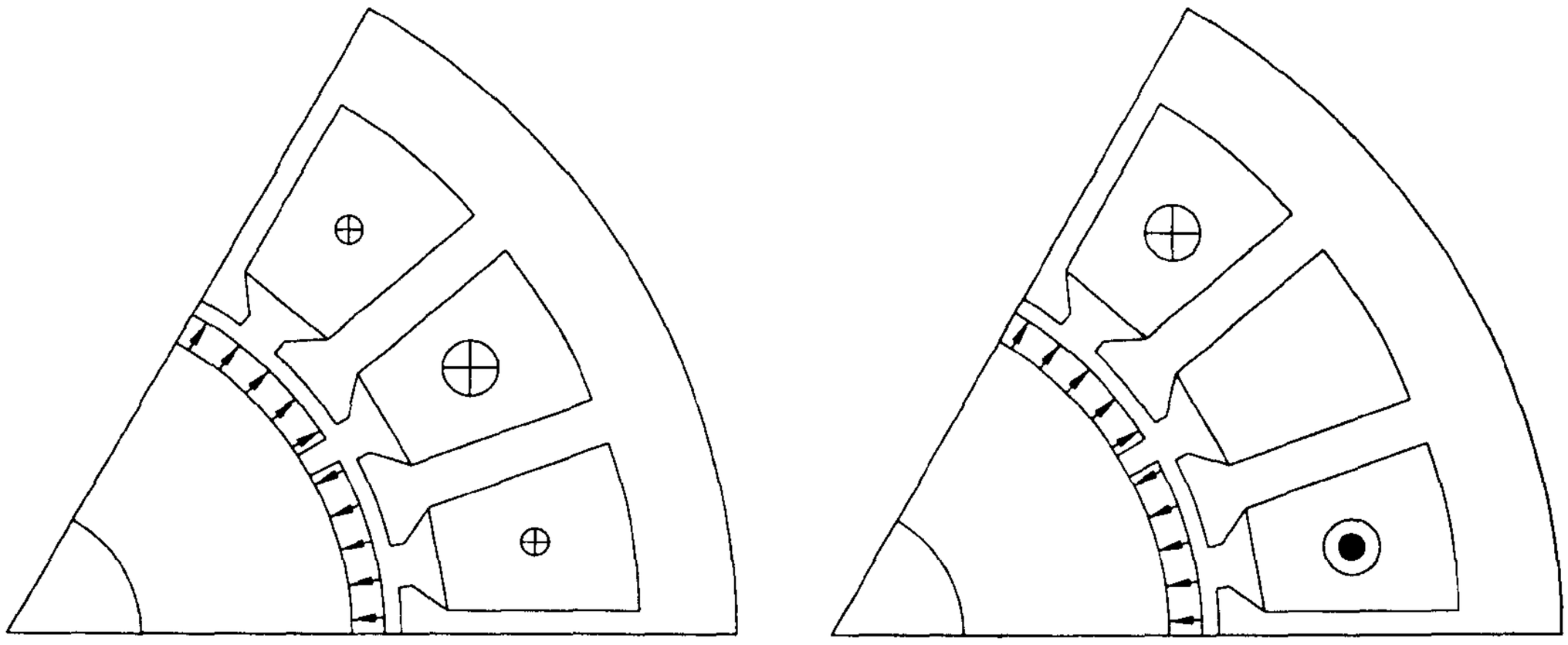

(a) (b)

Figure 5.1. Current excitation in the SEM motor. (a) Cross-magnetising effect. (b) De-magnetising effect.

5.3.1 Cross-Magnetising Effect of Armature Reaction

Fig. 5.2(a) is the flux-plot at no-load which shows the flux distribution throughout the motor cross-section due to permanent-magnets alone. Fig. 5.2(b) shows the effect of armature field, set up by the armature current of Fig. 5.1(a), on magnet field. Note that the armature MMF axis is in quadrature with the magnet MMF axis, which is the normal default operating condition in brushless as well as commutator DC motors.

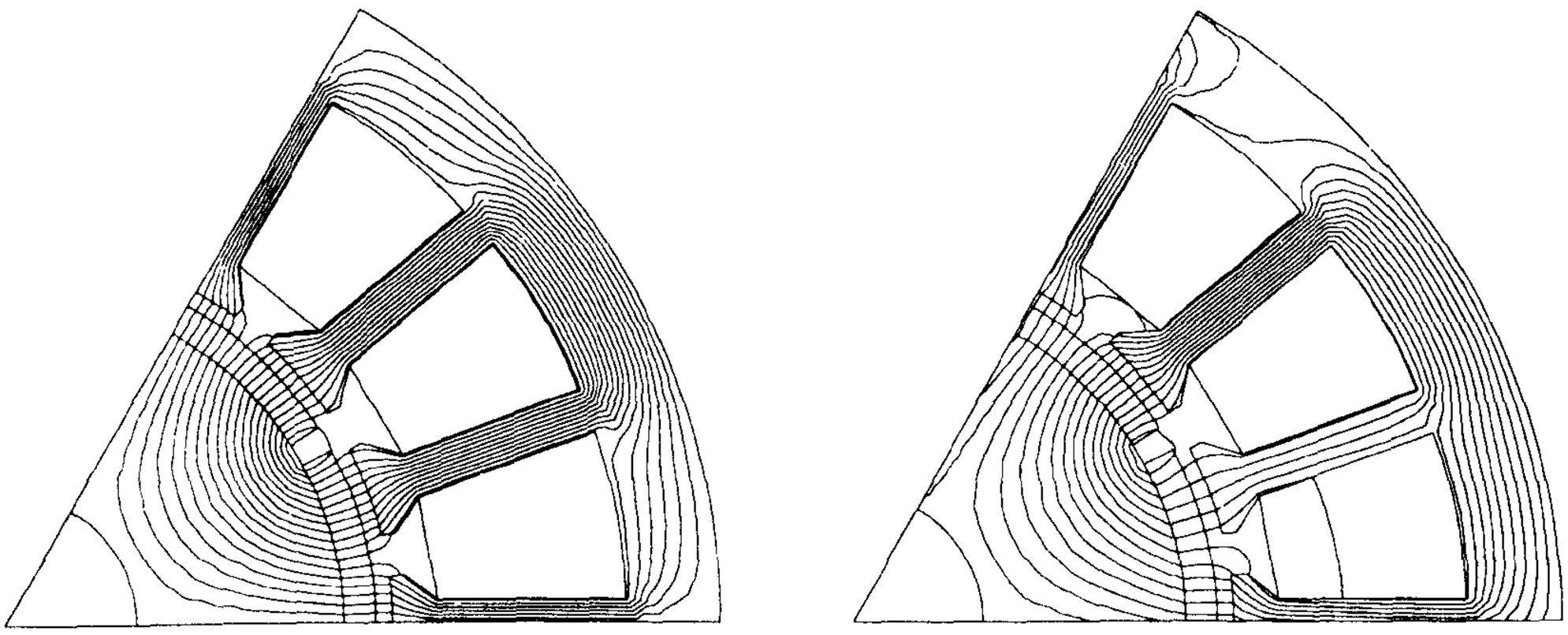

(a) (b)

Figure 5.2. Cross-magnetising effect of armature reaction. (a) No-load flux distribution. (b) Effect of armature field on magnet field.

The main difference in Fig. 5.2(b) from that of (a) is flux strengthening at the leading pole tip and flux weakening at the trailing pole tip (for counterclockwise direction of rotation). Due to saturation, flux strengthening at one end of the pole is not as strong as flux weakening at the other end, leading to the net reduction in airgap flux. This can also be seen from Fig. 5.3, which plots the airgap flux-density distribution over one pole for increasing values of armature current. This is the cross-magnetising effect of armature reaction.

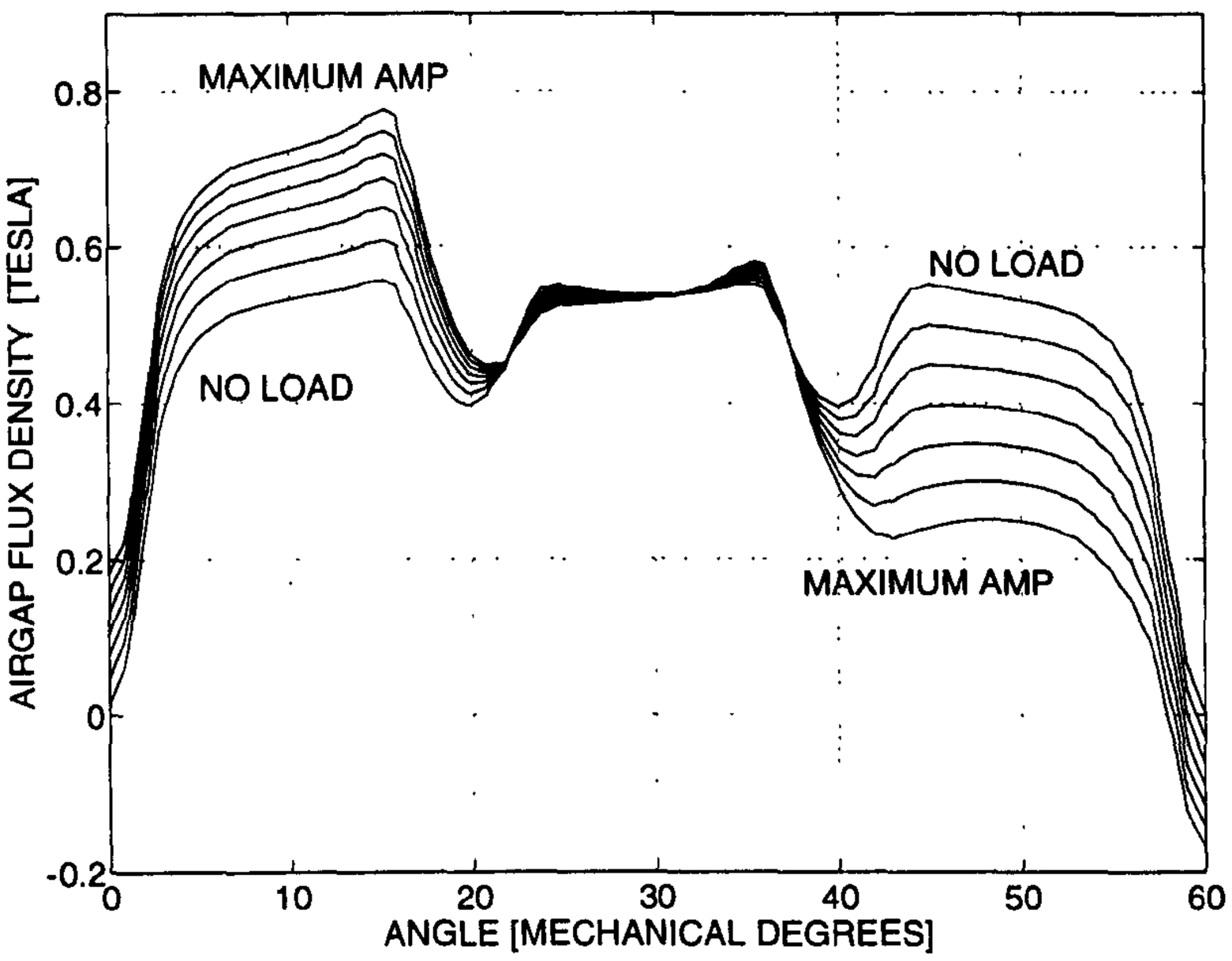

Figure 5.3. Variation in cross-magnetising armature reaction with saturation.

5.3.2 De-Magnetising Effect of Armature Reaction

The de-magnetising effect is most prominent when the armature MMF axis is aligned with the magnet MMF axis, as shown in Fig. 5.1(b). This condition, though, is rarely observed under normal operating conditions. It occurs mostly under fault conditions such as short-circuit, locked-rotor or 180° commutation error. Fig. 5.4(a)

shows the flux distribution due to permanent-magnets alone and Fig. 5.4(b) shows the effect of armature field on magnet field.

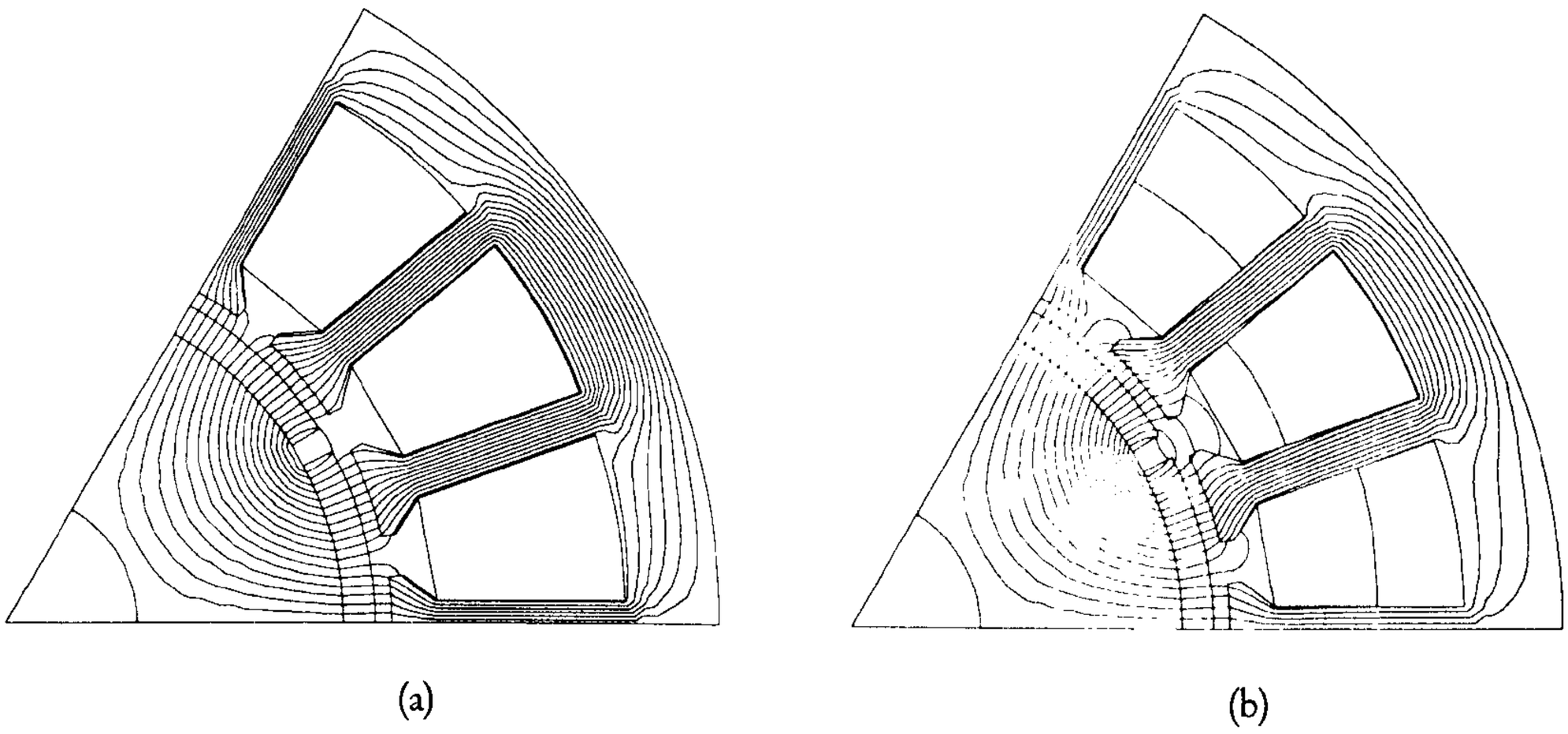

(a) (b)

Figure 5.4. De-magnetising effect of armature reaction. (a) No-load flux distribution. (b) Effect of armature field on magnet field.

Here, unlike the cross-magnetising effect, flux strengthening takes place at the either end of a pole while flux weakening takes place in the middle of a pole. Again, due to saturation, the flux weakening is stronger than flux strengthening giving an overall reduction in airgap flux. This is also seen in Fig. 5.5 where flux-density distribution is plotted over one pole for increasing values of armature current. This is the de-magnetising effect of armature reaction.

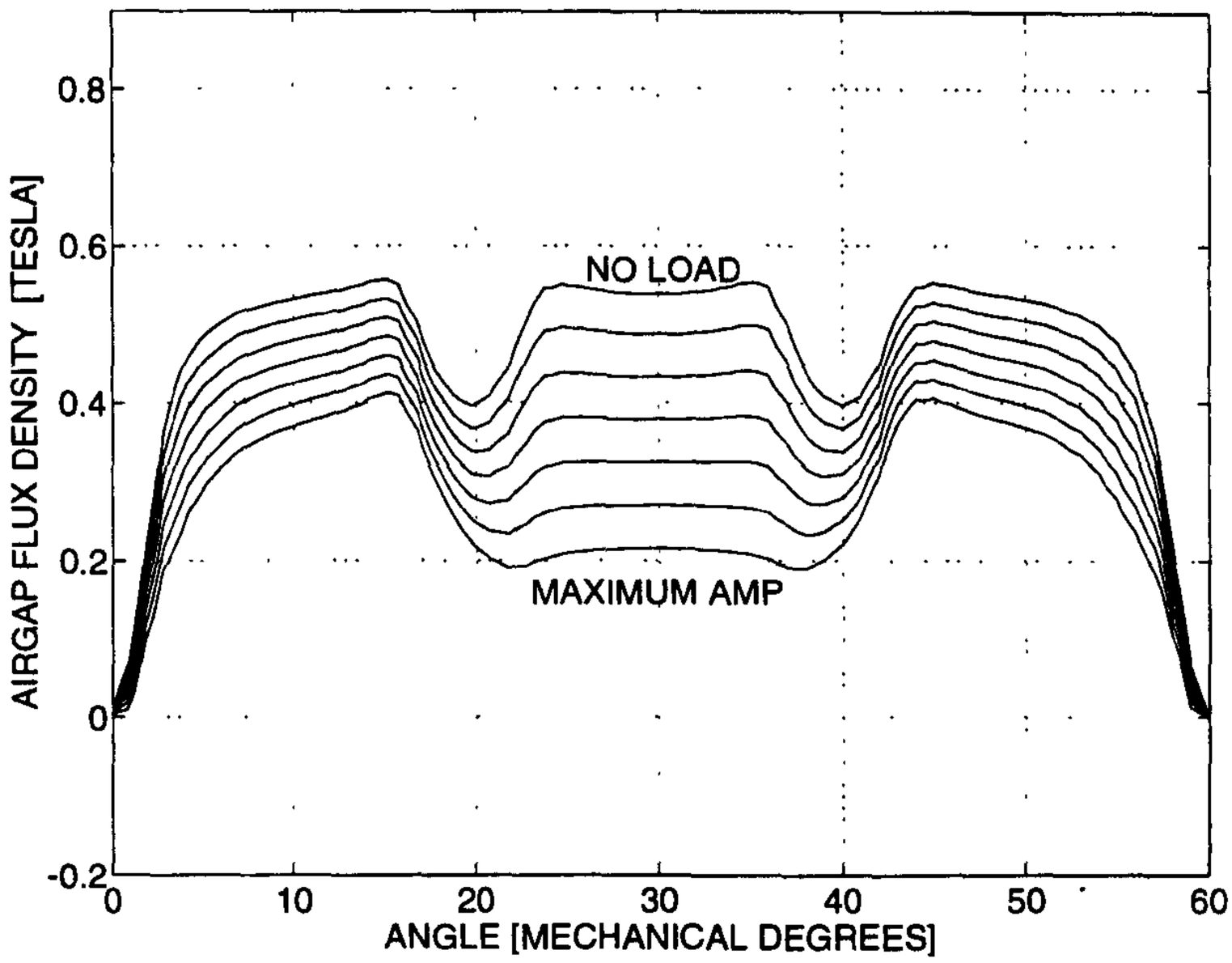

Figure 5.5. Variation in de-magnetising armature reaction with saturation.

5.4 Squarewave Brushless DC Motor

A 3-phase, 6-slot, 4-pole ferrite-magnet squarewave brushless DC motor FBL550A-A, manufactured by Oriental Motor Co., is used here for the purpose of analysis. This motor has already been described in Chapters 2 and 3 in relation to the prediction of electromagnetic and cogging torque ripple respectively. Figs. 2.6 and 3.14 show the motor cross-section and a typical no-load flux-plot respectively. In the following treatment, the same motor is analysed under unsaturated and saturated conditions to bring out the effect of saturation on torque constant.

5.4.1 Unsaturated Machine

Fig. 5.6 shows the flux-MMF trajectories obtained using finite-element analysis for six peak phase current values over a range of 0 to 1 A. The methodology of constructing the flux-MMF diagram using FE analysis has been explained in detail in Chapter 2. Note that 1 A is roughly the full-load peak phase current for this machine. Fig. 5.6 is same as Fig. 2.9 except that the magnetisation curves at incremental rotor positions are not shown. Since this chapter is concerned with average torque rather than instantaneous torque or torque ripple for a given current excitation, all flux-MMF diagrams shown in this chapter consist only of the flux-MMF trajectories and the magnetisation curves are omitted for the sake of clarity. Also, cogging torque, which does not make any useful contribution to the average torque, has not been considered in this chapter.

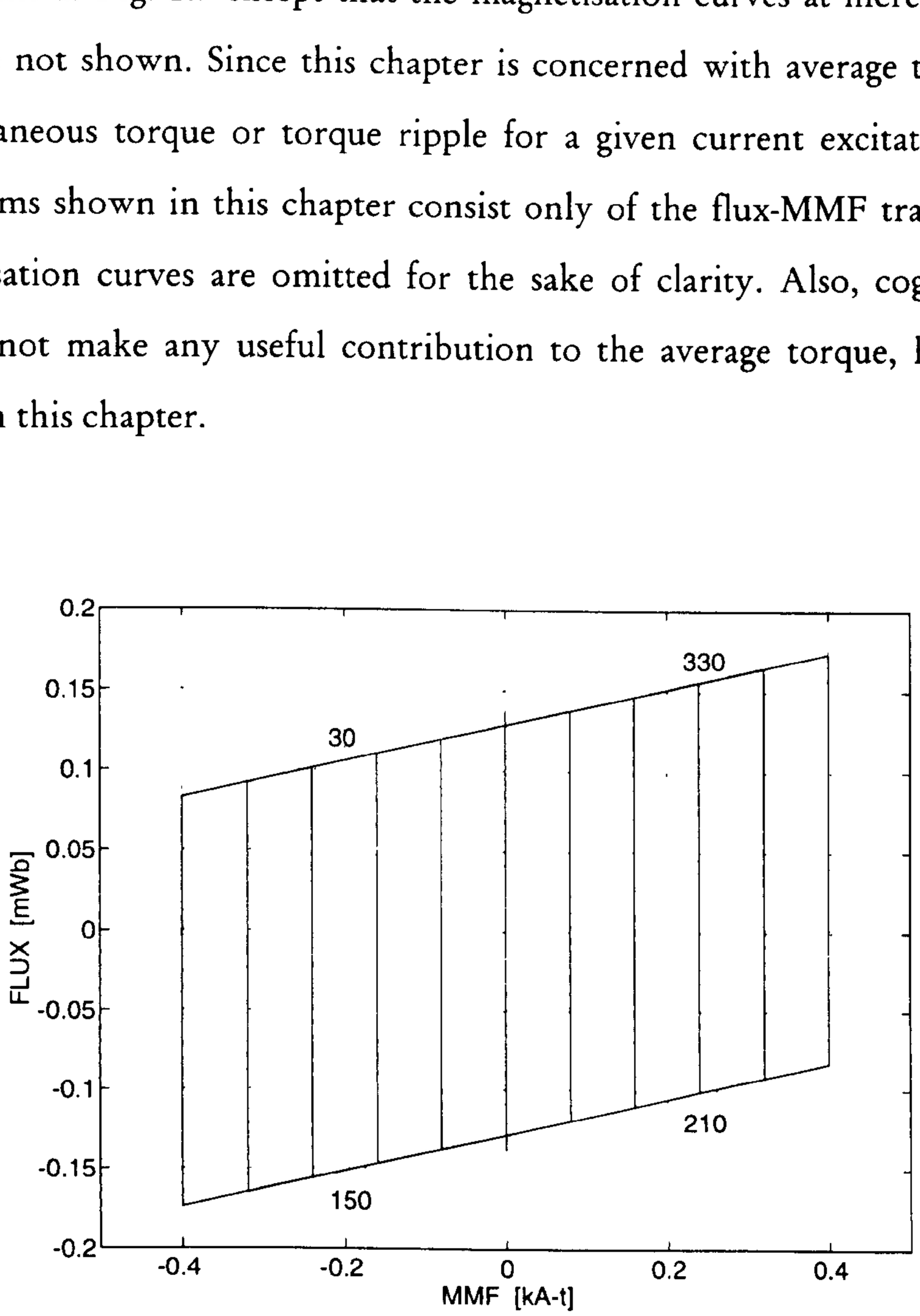

Figure 5.6. Flux-MMF trajectories for the unsaturated OM motor at 0, 0.2, 0.4, 0.6, 0.8 and 1.0 A peak phase currents.

The average electromagnetic torque can be calculated from the flux-MMF diagram using two different methods.

1. The method of total area. Where the average electromagnetic torque is calculated using (5.1).

$$T_{eav} = \frac{mpW'}{2\pi} \tag{5.1}$$

Where,

Te_{av} is the average electromagnetic torque over an electrical cycle.

m is the number of phases.

p is the number of pole-pairs.

W' is the total area enclosed by the flux-MMF trajectory.

This method makes use of the total area enclosed by a flux-MMF trajectory over an electrical cycle.

2. The method of incremental areas. The average electromagnetic torque can also be calculated from the torque ripple waveforms, shown in Fig. 2.11 in Chapter 2, simply as an average of instantaneous values over an electrical cycle. These instantaneous torque values are in turn calculated from the incremental areas enclosed by the magnetisation curves at successive rotor positions, as explained in Chapter 2.

It is important to note that while for sinewave excited machines, the two methods give the same result numerically, that is not the case for squarewave excited machines due to the phenomenon of commutation. This is explained in detail later on at the end of this section. Table 5.1 makes a comparison between the two methods of torque calculation mentioned above for the unsaturated squarewave excited machine.

Table 5.1. Comparison between two different methods of torque calculation.

Peak phase current (A)	T_{av} from incremental areas (Nm)	T_{av} from total area (Nm)
0.00	0.0000	0.0000
0.20	0.0393	0.0393
0.40	0.0786	0.0786
0.60	0.1179	0.1179
0.80	0.1572	0.1572
1.00	0.1965	0.1964

The comparison above shows that the two methods give almost the same result in an unsaturated machine and hence either of them can be used for calculating average torque. In the next section, however, it is shown that this is not the case for a saturated machine and that some additional FE analysis is required in order to model the flux-MMF trajectories at the instant of commutation.

5.4.2 Saturated Machine

Fig. 5.7 shows the flux-MMF trajectories at six peak phase current values over a range of 0 to 5 A. Note that in this case the machine is heavily saturated with a maximum current of 5 times the full-load value. Such load currents are not usually encountered under normal operating conditions. However, under short-duty severe overload or transient conditions, load currents as high as 5 p.u. can be encountered.

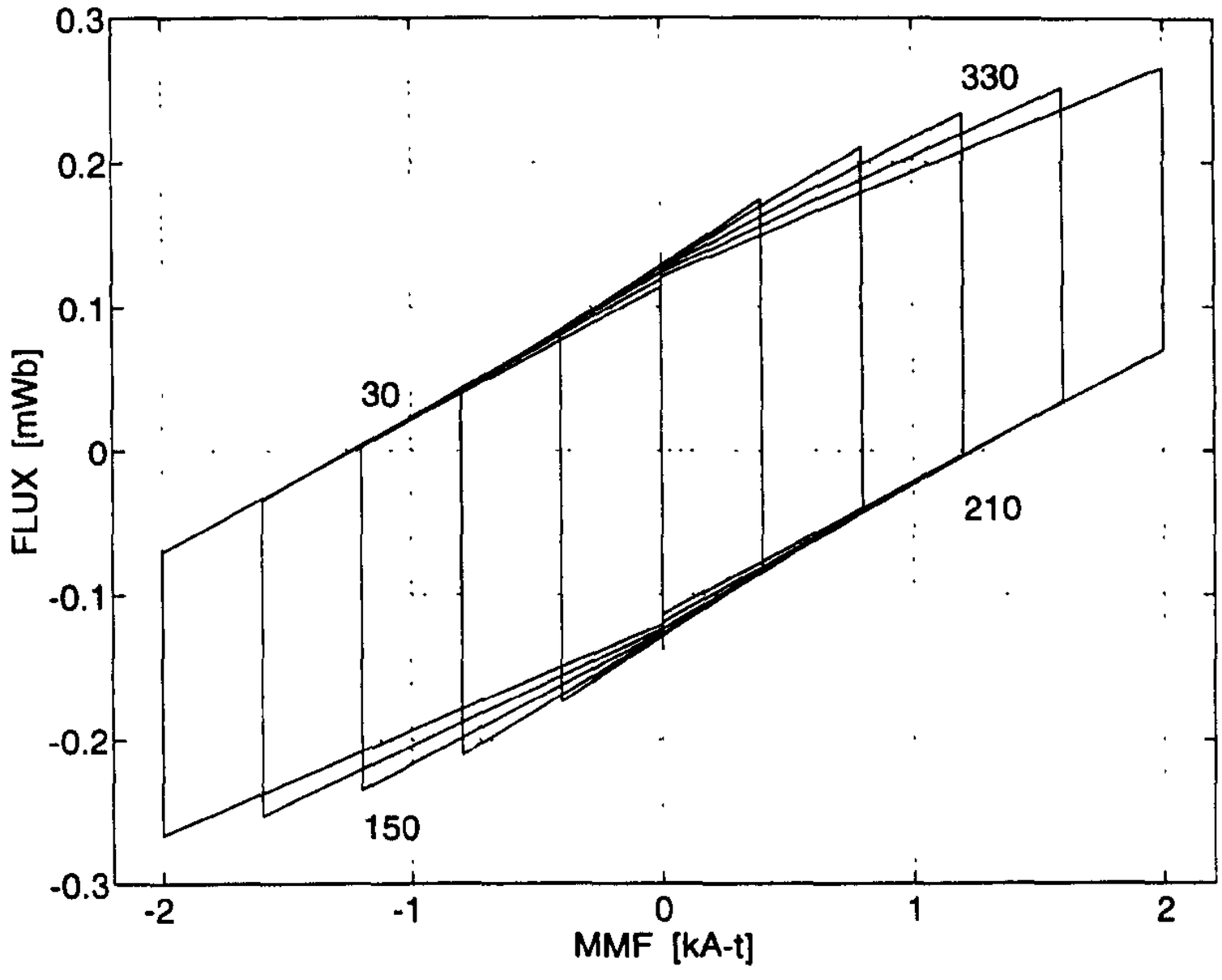

Figure 5.7. Flux-MMF trajectories for the saturated OM motor at 0, 1, 2, 3, 4 and 5 A peak phase currents.

Comparison between Figs. 5.6 and 5.7 gives a graphical indication of the effect of saturation by way of change in the shape of flux-MMF trajectories. However, the average torque calculations made using the method of total area, based on (5.1), are different from the calculations made using the method of incremental areas, as shown in Table 5.2. The next sub-section provides an explanation for this difference and describes the additional FE analysis required to model the effect of commutation.

5.4.3 Commutation in a Saturated Squarewave Machine

In squarewave brushless DC motors, unlike sinewave brushless AC motors, phase currents are electronically *commutated* or switched on and off abruptly at regular intervals. The commutation of phase currents leads to the so-called *discontinuities* in the flux-MMF trajectories as seen in Figs 5.6 and 5.7. The presence of such

discontinuities is the principal reason behind the difference in average torque results obtained using the two methods mentioned earlier.

To begin with, at the instant of commutation, phase currents are switched from zero to full value (and vice versa) directly without taking any values in between. This is termed as *two-point commutation* which translates into a *straight line* at the instant of commutation on the flux-MMF trajectory. In Figs. 5.6 and 5.7 for example, two-point commutation is employed at the four instants of commutation as indicated by their respective angles in electrical degrees. Phase current waveform for the two-point commutation is depicted in the top portion of Fig. 5.8.

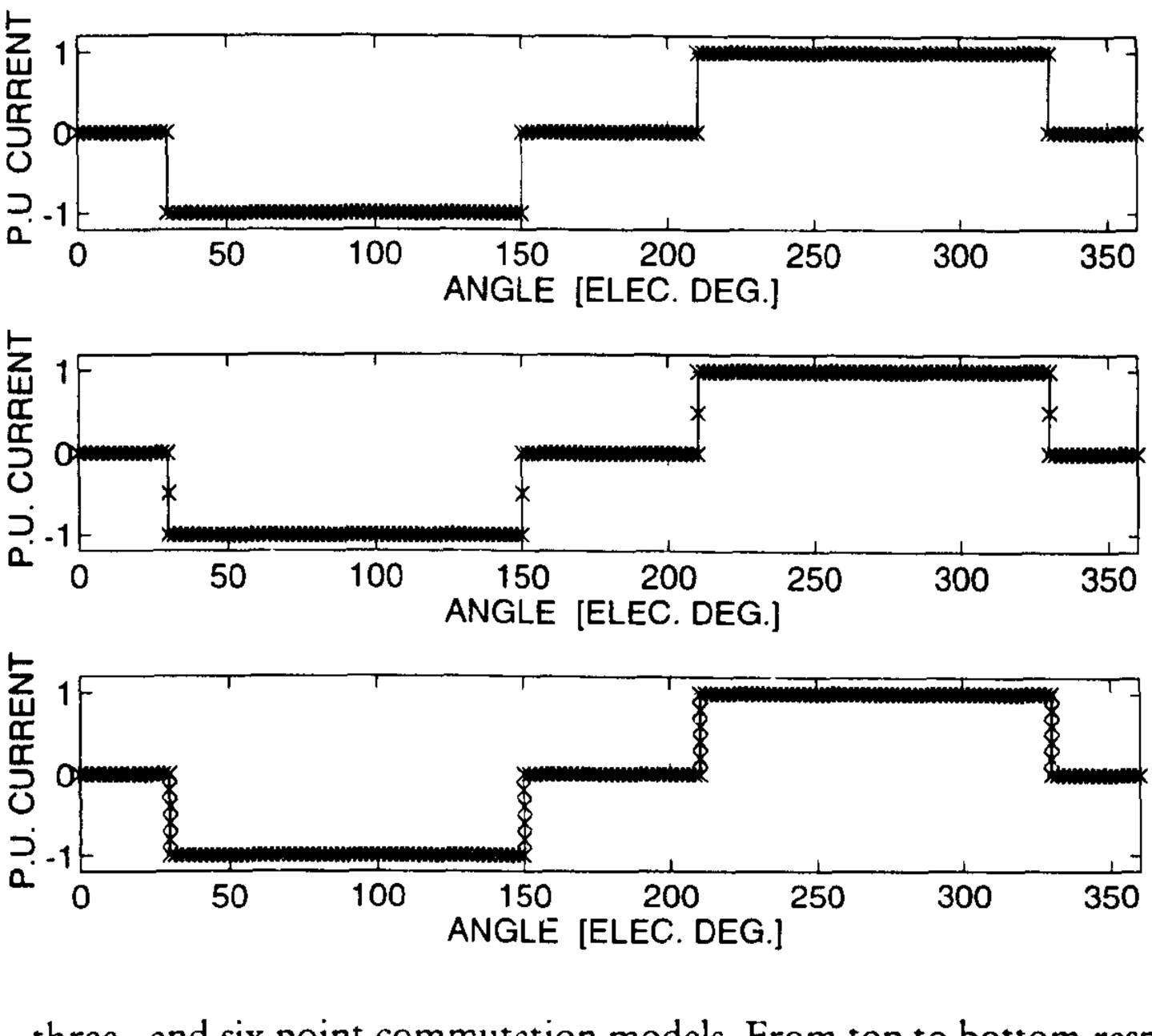

Figure 5.8. Two-, three-, and six-point commutation models. From top to bottom respectively.

For an unsaturated machine, two-point commutation model is adequate since the magnetisation curves themselves are *straight lines* and so, the total area calculated from the flux-MMF trajectories and the one calculated from the magnetisation curves, are nearly equal as indicated in Table 5.1. In the case of saturated machine, however, the magnetisation curves are non-linear (see Fig. 2.18 in Chapter 2) and accordingly, the

two-point commutation model needs to be improved upon to take account of the effect of saturation on commutation.

Phase current waveform for the *three-point commutation* model is depicted in the middle portion of Fig. 5.8. The flux-MMF trajectories obtained using this model are shown in Fig. 5.9, which is same as Fig. 5.7, except that at the four instants of commutation, the phase current is switched from zero to full value (and vice versa) by taking a third value half-way in between. This makes for a better agreement between the average torque calculations made using the method of total area and the method of incremental areas as shown in Table 5.2.

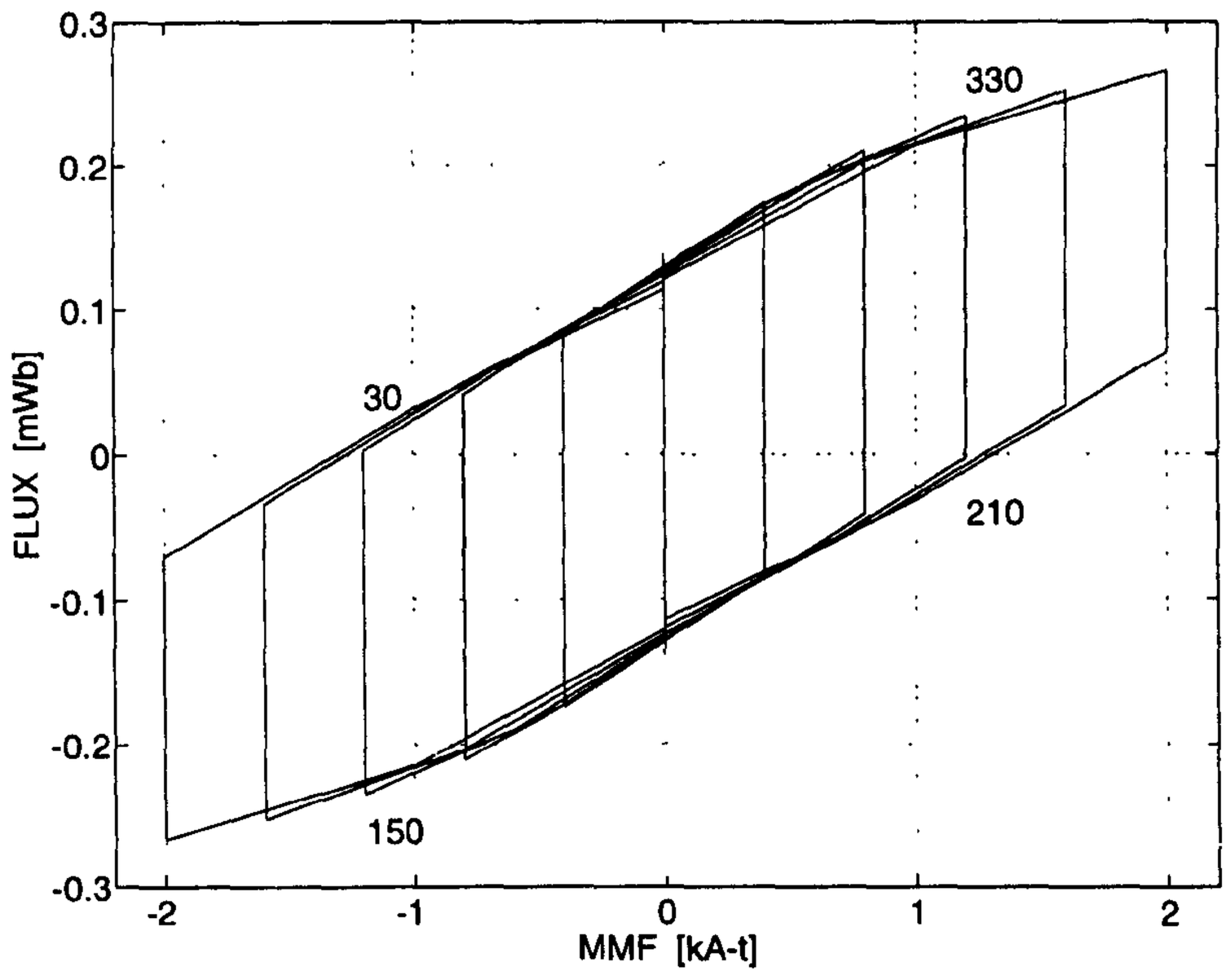

Figure 5.9. Flux-MMF trajectories using the three-point commutation model.

Further improvement to the modelling of flux-MMF trajectories at the instant of commutation can be made by using a *six-point commutation* model. The phase current waveform corresponding to this model is shown in the bottom portion of Fig. 5.8. Flux-MMF trajectories obtained using the six-point commutation model are shown in Fig. 5.10.

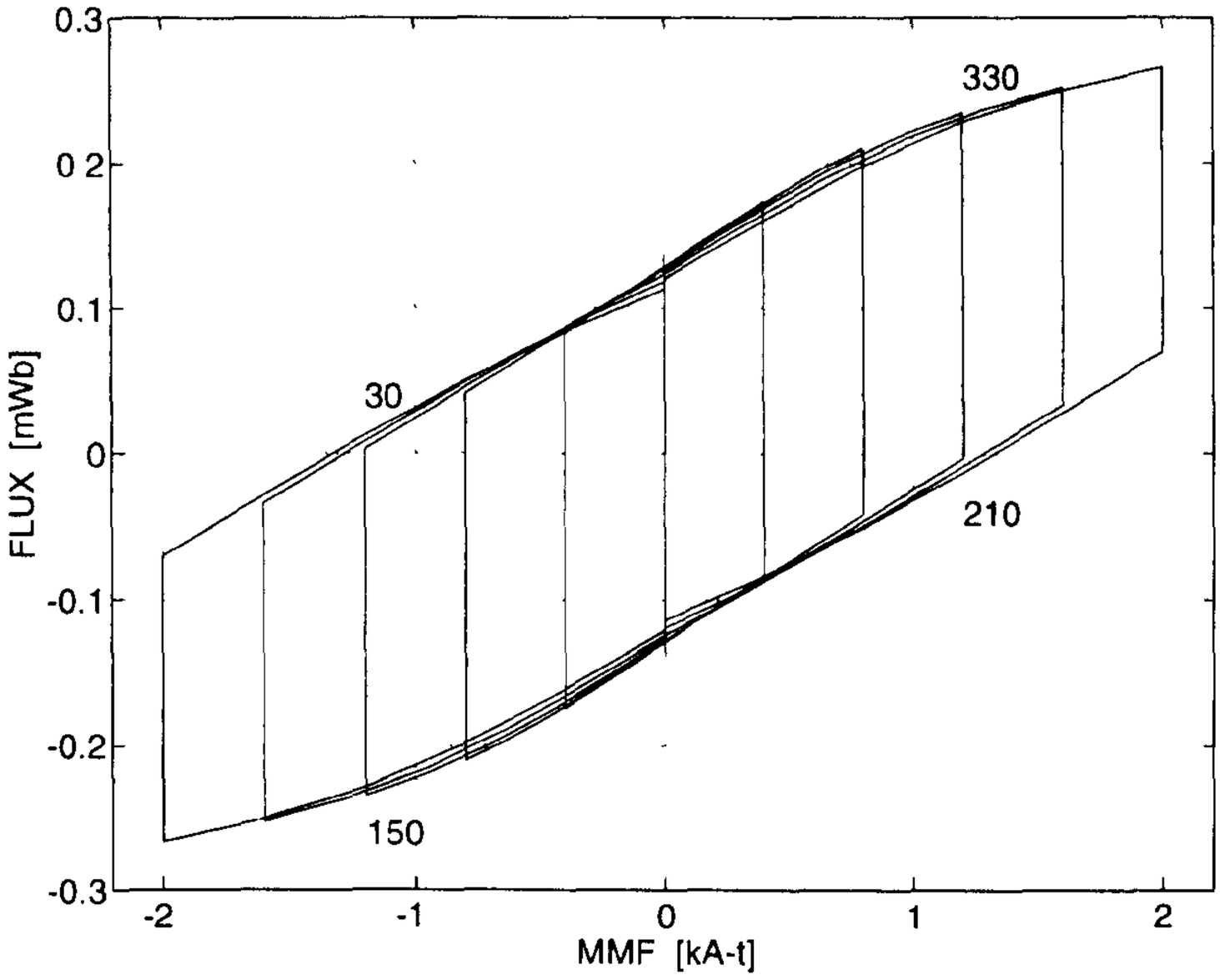

Figure 5.10. Flux-MMF trajectories using the six-point commutation model.

Table 5.2 compares the average torque values calculated using different commutation models. It clearly shows that for a saturated machine, average torque calculation can be improved upon by taking more number of points along the flux-MMF trajectories at the instants of commutation. In the limiting case, when the discretisation is infinitesimally small or the number of points are very large, both the magnetisation curves and the flux-MMF trajectories will be continuous curves rather than being composed of piecewise linear components.

Table 5.2. Comparison between different methods of torque calculation.

Peak phase current (A)	T_{av} from incremental areas (Nm)	T_{av} from total area. Two-point commutation. (Nm)	T_{av} from total area. Three-point commutation. (Nm)	T_{av} from total area. Six-point commutation. (Nm)
0.0	0.0000	0.0000	0.0000	0.0000
1.0	0.1964	0.1964	0.1965	0.1965
2.0	0.3905	0.3870	0.3901	0.3911
3.0	0.5758	0.5585	0.5727	0.5765
4.0	0.7455	0.7046	0.7382	0.7458
5.0	0.8951	0.8212	0.8814	0.8945

5.4.4 Experimental Validation

The average torque values calculated in the previous sections for the unsaturated as well as saturated machine are validated experimentally in this section. It is to be noted that since ideal squarewave phase current waveforms have been used in performing finite-element analysis, the results obtained—predicted as well as measured—are strictly valid at low speeds only. The test set-up used for performing static torque measurements has been described in detail in Chapter 2. Fig. 5.11 is the torque per ampere characteristic for the unsaturated OM motor. As expected, the characteristic is almost linear which means that there is no variation of torque constant with load current.

Fig. 5.12 is the torque per ampere characteristic for the saturated OM motor. The deviation from the ideal characteristic shows that the torque constant decreases with increasing saturation and load current. Fig. 5.13 plots the variation of torque constant and Table 5.3 gives an idea of percentage reduction in torque constant. It shows that the torque constant starts to decrease at full-load current with a reduction of 1.78%. This is due to onset of saturation in certain parts of the machine and especially in tooth tips. The percentage drop increases with increasing saturation and load current. Note that the torque constant here is simply defined as the ratio of average torque

over peak phase current. Various other definitions of torque constant in brushless PM machines are possible and these are discussed in [76].

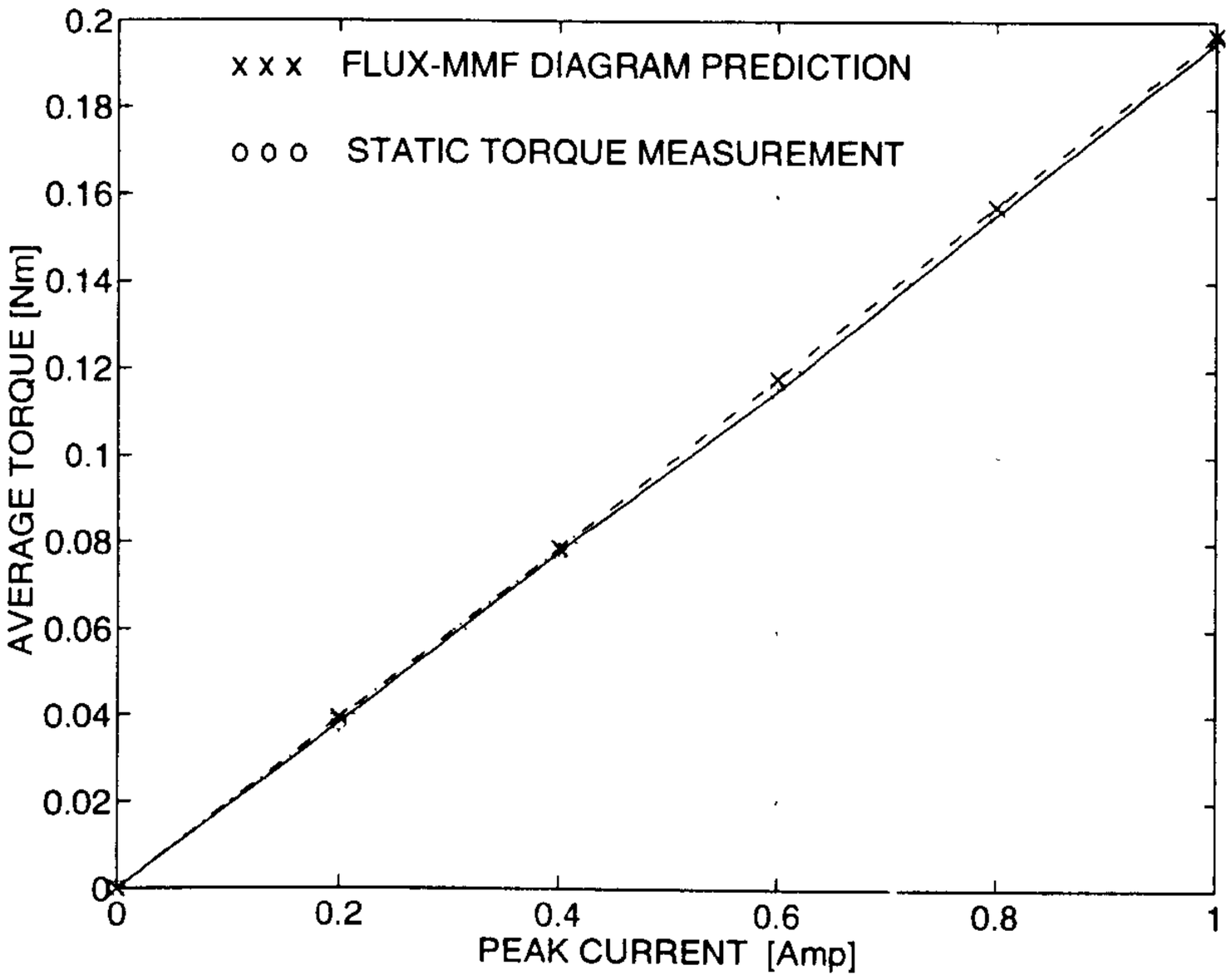

Figure 5.11. Torque per ampere characteristic for the unsaturated OM motor.

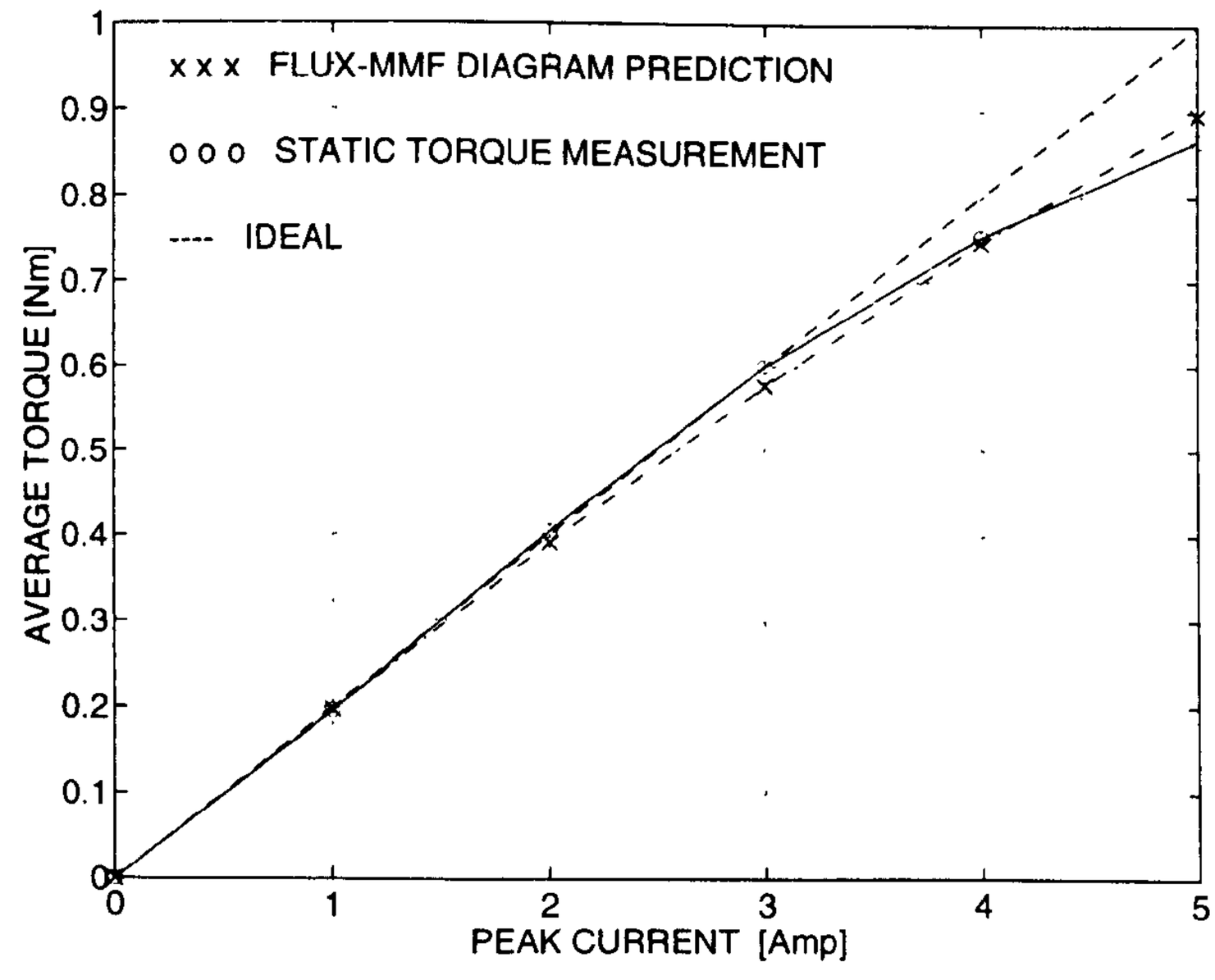

Figure 5.12. Torque per ampere characteristic for the saturated OM motor.

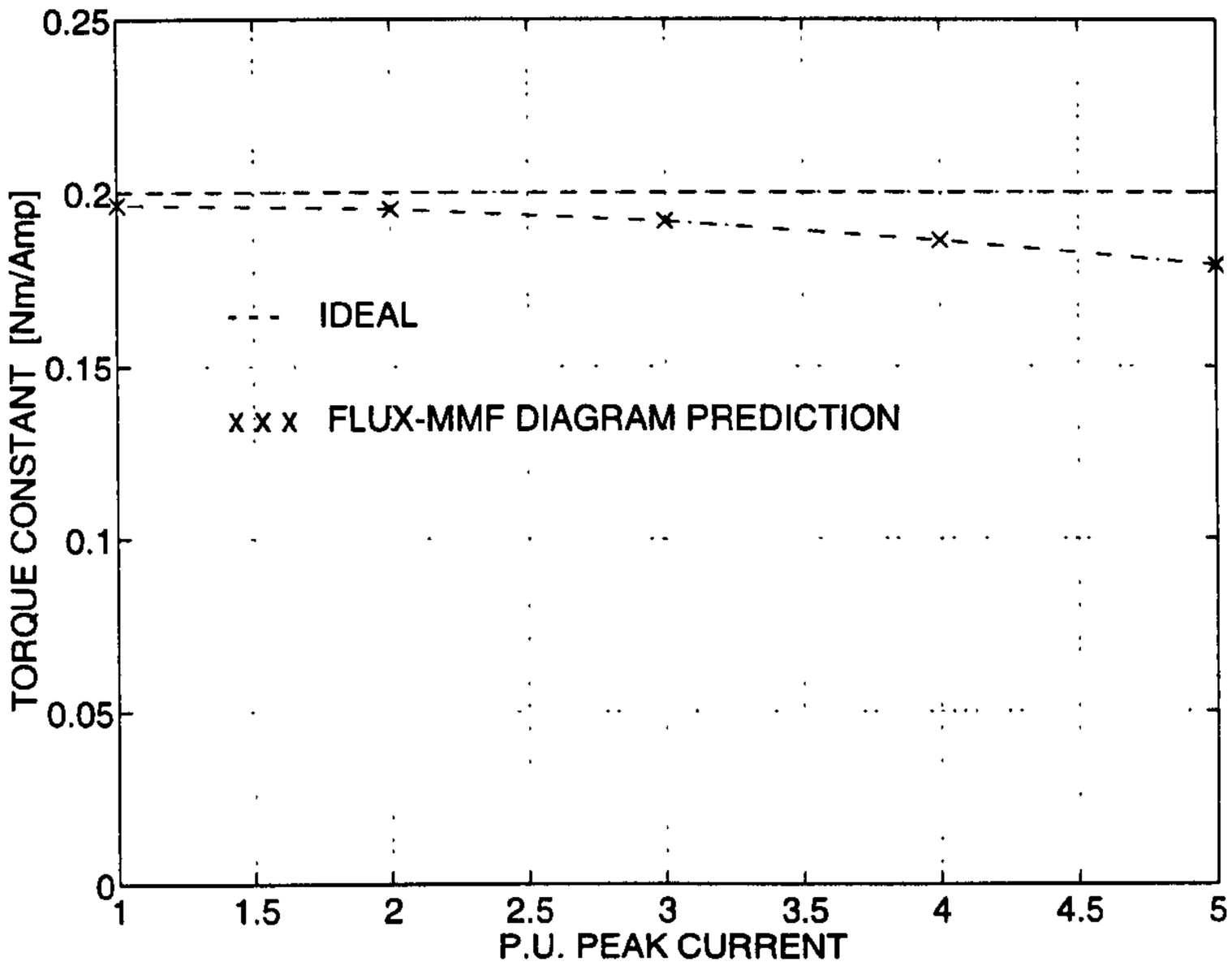

Figure 5.13. Variation of torque constant for the saturated OM motor.

Table 5.3. Percentage reduction in torque constant for the saturated OM motor.

% full-load current	Torque constant (Nm/A)	% drop in torque constant
100	0.1964	1.78
200	0.1952	2.39
300	0.1919	4.04
400	0.1864	6.82
500	0.1790	10.49

5.5 Sinewave Brushless AC Motor

The sinewave brushless AC motor considered here is a combination of the BMF115C6-T motor stator and the BMR115C6-64S motor rotor, both manufactured by SEM Ltd. The cross-section picture and a typical no-load flux plot, for the BMR116C6-64S motor, are shown in Figs. 3.23 and 3.11 in Chapter 3; and for the BMF115C6-T motor, are shown in Fig. 4.7 in Chapter 4 and Fig. 3.9 in Chapter 3,

respectively. Just as in the case of squarewave brushless DC motor, analysis is presented for the unsaturated as well as saturated machine.

5.5.1 Unsaturated Machine

Fig. 5.14 shows the flux-MMF trajectories at seven RMS phase currents over a range of 0 to 6 A. Note that full-load phase current for this machine is 6 A. The flux-MMF trajectories are elliptical in shape since the currents are sinusoidal.

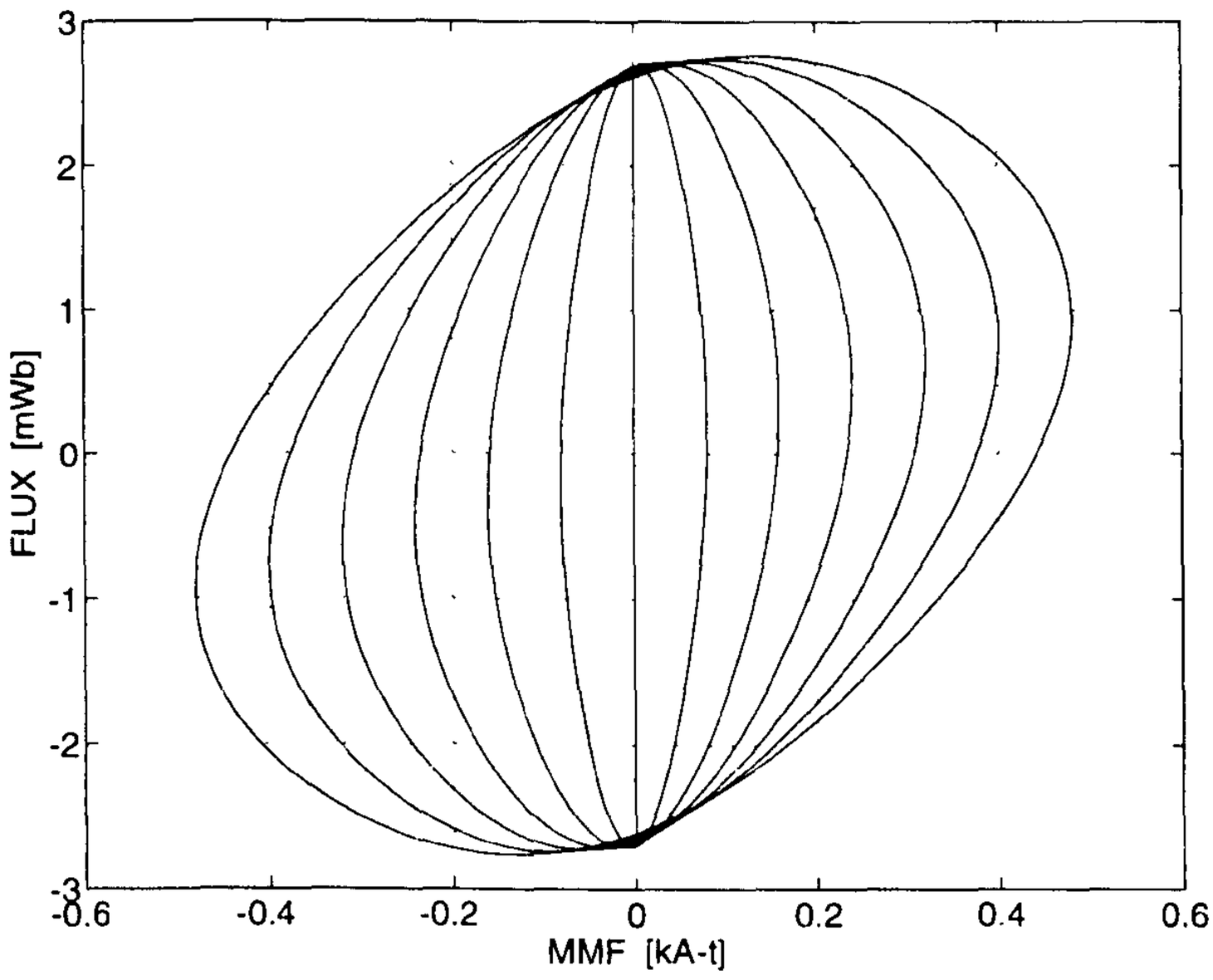

Figure 5.14. Flux-MMF trajectories for the unsaturated SEM motor at 0, 1, 2, 3, 4, 5 and 6 A RMS phase currents.

5.5.2 Saturated Machine

Fig. 5.15 shows the flux-MMF trajectories at seven RMS phase currents over a range of 0 to 12 A. Note that 12 A corresponds to twice the full-load current. The

effect of saturation is represented graphically by way of change in the shape of flux-MMF trajectories with increasing current. Unlike the squarewave excited machine, where maximum overload of five times the full-load current was considered, the maximum overload in this case was limited to twice the full-load current due to limitations of the static torque test set-up.

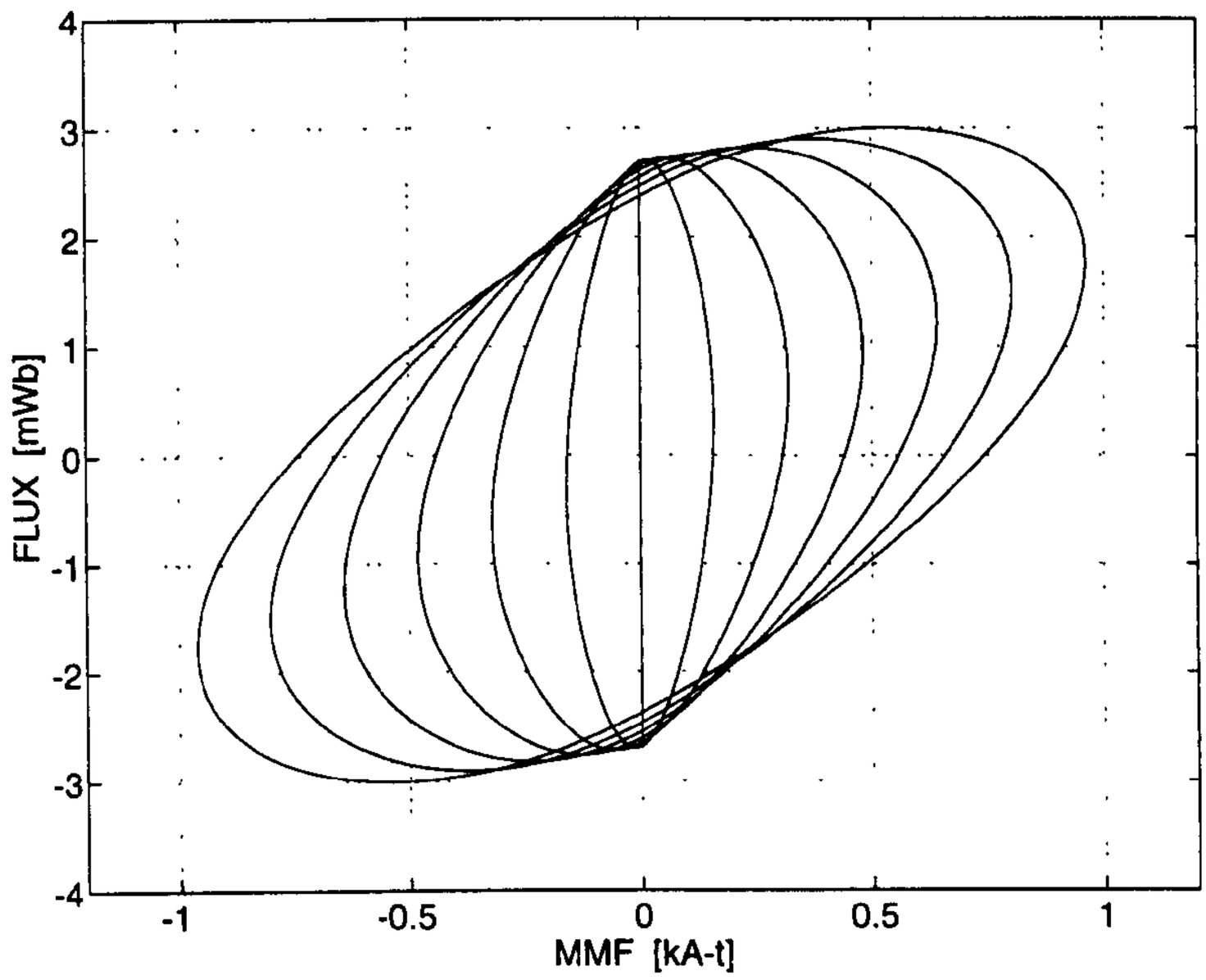

Figure 5.15. Flux-MMF diagram for the saturated SEM motor at 0, 2, 4, 6, 8, 10 and 12 A RMS phase currents.

5.5.3 Experimental Validation

Torque calculation in a sinewave excited machine is less complicated as compared to a squarewave excited machine. In a squarewave excited machine, there are commutating phase currents, reflected in plotting the flux-MMF trajectories but not the magnetisation curves. Thus, the two methods of calculating average torque mentioned earlier, give numerically different results, although the two results

converge to a single value in the limiting case. Whereas in a sinewave excited machine, there are no discontinuities due to commutation of phase currents and the two methods always give identical results.

Just as in the case of squarewave excited OM motor, ideal sinewave currents are assumed in performing finite-element analysis and hence average torque values, predicted as well as measured, are strictly valid at low speeds. Fig. 5.16 compares the predicted torque per ampere characteristic with the static torque measurements. The characteristic is linear, indicating no change in torque constant for an unsaturated SEM motor.

Figure 5.16. Torque per ampere characteristic for the unsaturated SEM motor.

Fig. 5.17 is a comparison between predicted and measured torque per ampere characteristic for the saturated SEM motor. The deviation from the ideal characteristic shows that the torque constant decreases with increasing saturation and load current. Fig. 5.18 plots the variation of torque constant and Table 5.4 gives an idea of percentage reduction in torque constant. It shows that the torque constant

starts to decrease at full-load current with a reduction of 1.78%. This is due to onset of saturation in certain parts of the machine and especially in tooth tips. The percentage drop increases with increasing saturation and load current. Note that the torque constant here is defined as the ratio of average torque over RMS phase current.

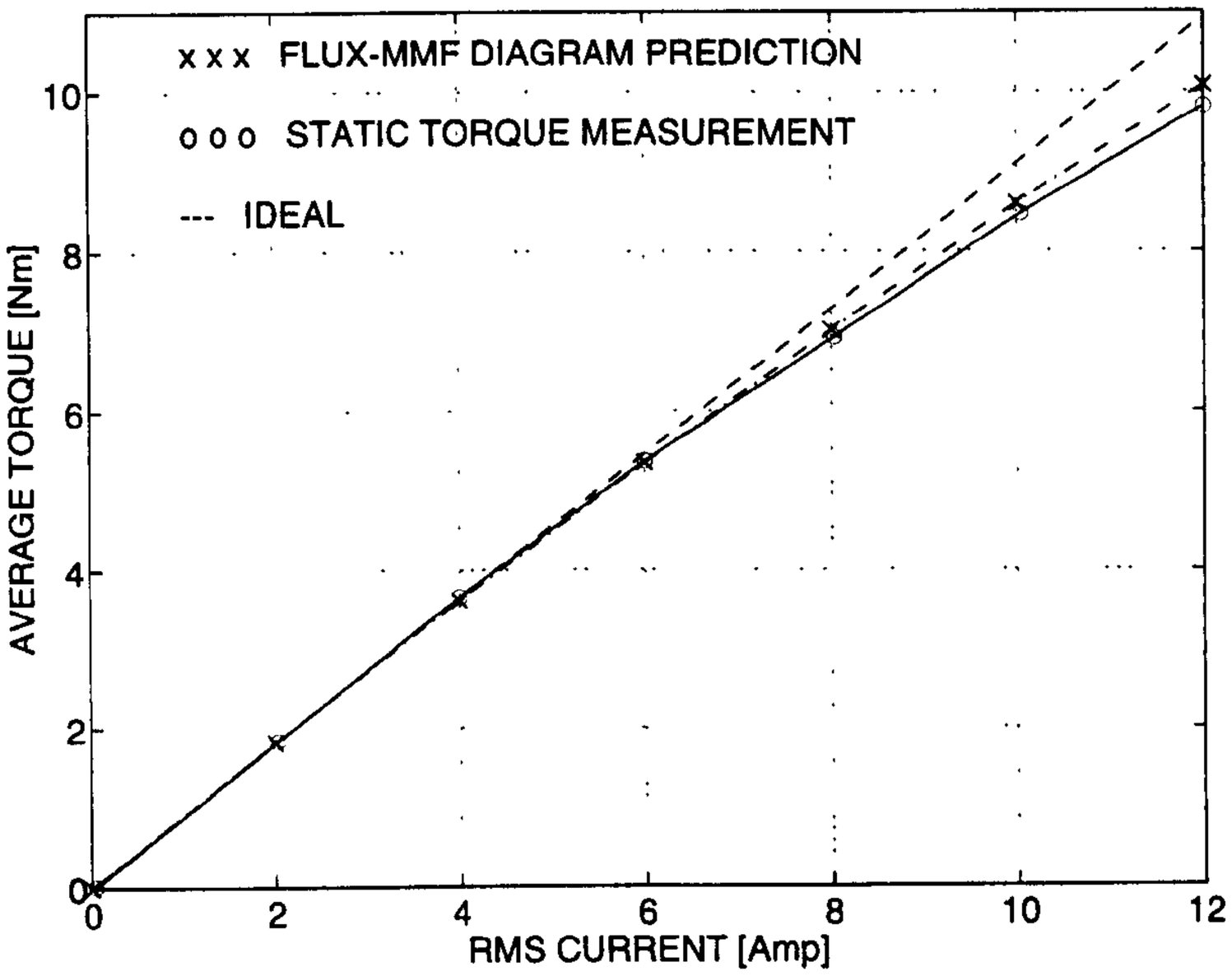

Figure 5.17. Torque per ampere characteristic for the saturated SEM motor.

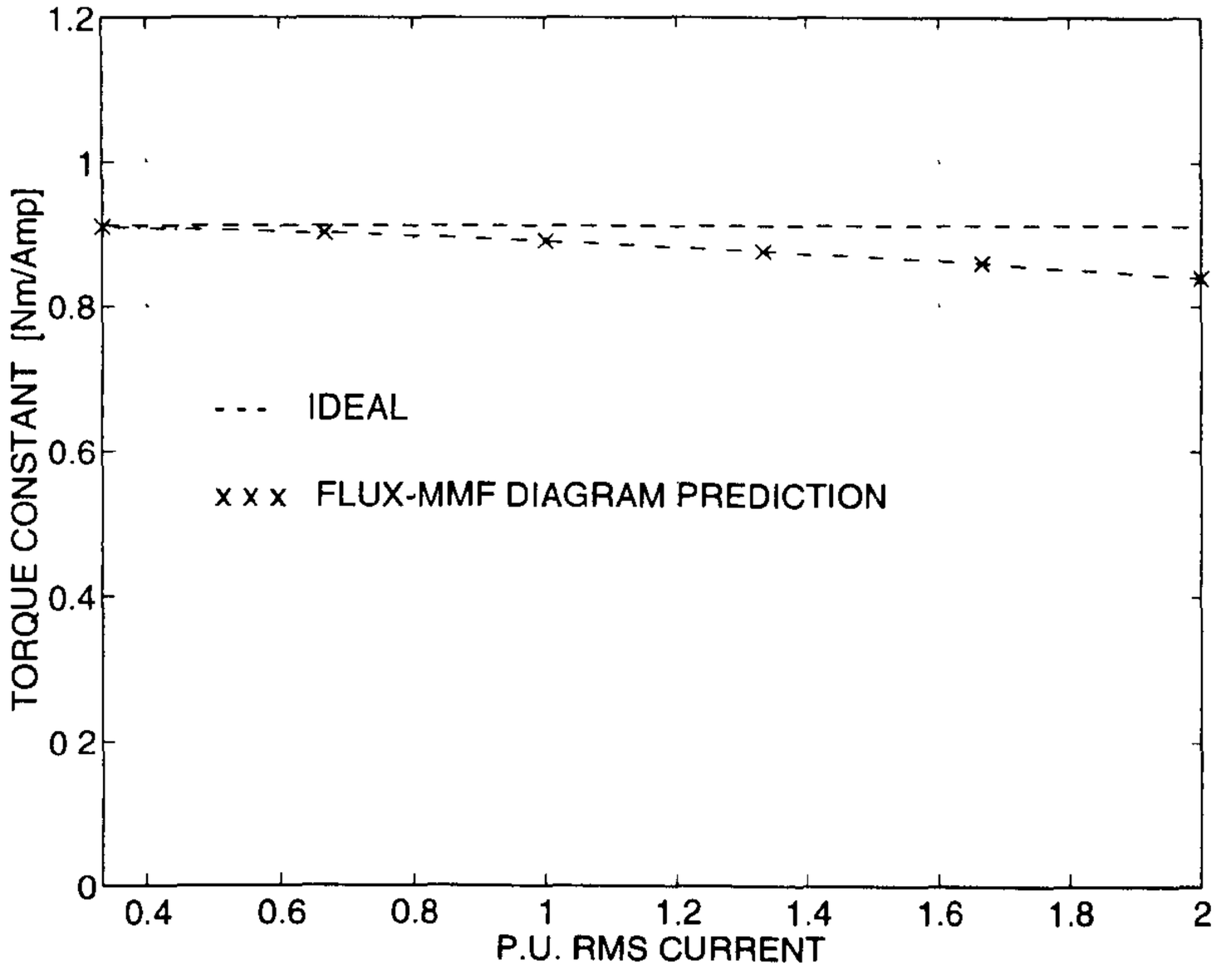

Figure 5.18. Variation of torque constant for the saturated SEM motor.

Table 5.4. Percentage reduction in torque constant for the saturated SEM motor.

% full-load current	Torque constant (Nm/A)	% drop in torque constant
33.33	0.9105	0.23
66.67	0.9028	1.08
100.00	0.8916	2.30
133.33	0.8771	3.90
166.67	0.8597	5.79
200.00	0.8399	7.97

5.6 Chapter Summary

Chapter 5 has shown that the flux-MMF diagram provides a valuable means of modelling the saturation effects in electrical machines. One such important effect—the variation of torque constant with armature current—has been presented for two types of permanent-magnet machines, the brushless DC and the brushless AC. This problem is not easy to deal with using classical methods of magnetic circuit analysis.

Although such methods have been developed for DC commutator motors [71], the brushless PM motor is not amenable to them because of the nature of the supply current waveforms, the small number of phases and the time-variation of the total magnetic flux distribution.

For both, the brushless AC and the brushless DC machine, the average torque values over a range of increasing currents have been calculated using the flux-MMF diagram technique. The calculations have been performed under two conditions; the unsaturated machine (for currents ranging from no-load up to full-load value) and the saturated machine (for currents ranging from no-load up to a certain overload of the order of 2 to 5 times the full-load current).

Both the brushless DC and the brushless AC machines have shown almost linear torque per ampere characteristics up to the full-load current value. But for the overload current values, both the machines have shown a non-linear torque per ampere characteristics. The torque per ampere characteristic curves have been validated against experimental measurements. In addition, the chapter has also briefly dealt with the method of modelling commutation in a saturated PM brushless DC machine.

6 Comparative Evaluation of Electrical Machines

6.1 Introduction

The principal objective of the work described in this chapter is to demonstrate the usefulness of the flux-MMF diagram in comparative evaluation of different types of electrical machines. The issue of comparing capabilities of different machine types and assessing their respective strengths and limitations has always been of interest. Lately, it has received much attention in the light renewed interest in switched reluctance machines. Such comparisons typically involve either theoretical considerations such as output equations or practical considerations such as output performance. However, it is widely acknowledged that a true comparison should involve much more than considering output equations or performance. In [4], for example, Harris and Miller state that "comparison of machine types through their output equations alone is insufficient; the exercise of assessment is multi-criteria in nature." The flux-MMF diagram technique takes the process beyond considering design and output parameters and enables real performance comparisons to be made by providing a universal basis of evaluation regardless of factors such as geometry, saliency, presence or absence of permanent-magnets and presence or absence of rotor excitation.

Historically, different types of electrical machines have developed over different periods of time and have followed different routes of evolution [77]. Although the principles governing the process of electromechanical energy conversion are known to be common to all types of electrical machines; their operational characteristics are still perceived to be radically different and much of the effort in comparing different

machine types is hampered by these differences. The flux-MMF diagram technique makes a contribution to this end by presenting a unified treatment of torque producing mechanism in different machine types in a practicable manner which can be implemented using finite-element analysis.

The next section presents a brief literature review of some of the recent work performed on comparing different machine types. To establish the whole process of comparing different machine types using the flux-MMF diagram, seven common types of electric motors are considered. These are; induction, synchronous reluctance, switched reluctance, PM brushless AC, PM brushless DC, interior PM and PMDC commutator motor. The individual designs are reasonably optimised by using a combination of SPEED software, such as PC-BDC and PC-SRD, and finite-element analysis. In order to make the comparisons as fair as possible, common design constraints are used and these are explained in Section 6.3. Section 6.4 describes design for each motor type in detail and illustrates respective flux-MMF diagrams and electromagnetic torque ripple curves derived from them. Section 6.5 demonstrates both, qualitative as well as quantitative, types of comparisons made between different machine types based on the flux-MMF diagram.

6.2 Literature Review

6.2.1 Conventional Means of Comparison

As described in the previous section, the conventional means of comparing different machine types are well explored and they are typically based on evaluating the D^2L-sizing equation and certain output performance parameters such as efficiency, torque-to-inertia ratio or power-to-weight ratio. Some notable treatments on this topic are given in [3], [4] and [22]. Lawrenson et al. [3], while providing the first

comprehensive treatment on switched reluctance machines, compared them favourably against the standard induction motors of equivalent ratings, then available, under certain specific operating conditions. Further, these comparisons were mainly restricted to and based upon parameters such as efficiency, output power and variable speed range. A much more rigorous comparison was given in [4], where a wide range of design and performance parameters for some commercial designs of SRMs and IMs were systematically tabulated and appraised in turn. Lipo and Li [22] have recently, presented a comparison between several different types of machines based on the D^2L-sizing equation. Although comprehensive in nature, D in this case is taken as D_i, the stator inner diameter, and it does not necessarily give any indication of overall volume or weight of a machine thus restricting the usefulness of the analysis.

6.2.2 Flux-MMF Diagram based Comparison

Research conducted at the SPEED Laboratory in recent years on comparative evaluation of electric machines using the FMDT has been described in [47], [48] and [53]. Staton et al. [47], made an effort for the first time to compare the torque producing mechanism in switched and synchronous reluctance motors using the ψ-i diagram as a common basis of analysis. The approach was later on extended and applied to PM brushless AC, brushless DC and DC commutator machines [48]; and to flux-reversal machine (FRM) [53]. The FRM and its qualitative assessment vis-à-vis other machines in its class are described in detail in Chapter 7. Other researchers have also made use of the ψ-i diagram to make similar comparisons. Notably, when Liao et al. [54] proposed a new doubly-salient permanent-magnet machine, they used the ψ-i diagram to help explain its principle of operation and compare its performance with the switched reluctance machine.

6.3 Design Constraints

Designs of the seven motor types described in the next section are all based upon a standard D132 frame 4-pole, 11 kW induction motor, manufactured by Brook Crompton Ltd. The major design constraints are listed in Table 6.1.

Table 6.1. Design Constraints.

Parameter	Constraint
Stator Outer Diameter	203.2 mm
Stack Length	203.2 mm
Air-gap	000.5 mm
Slot-fill	40 %
Total Copper Loss (@ 115 °C)	634 W

These constraints are based upon the following considerations.

- All motors, except the switched reluctance, to use the same stator lamination as the D132 frame induction motor. The lamination has 36 round-bottom slots and a yoke depth of 19.6 mm.
- All motors, including switched reluctance, to have the same electromagnetic volume i.e. the same stator outer diameter and stack length.
- All motors to have the same air-gap, slot-fill and total copper loss at 115 °C.
- Friction, windage and iron losses are not to be considered, so that the comparisons made are strictly valid at low speed of the order of 150 to 200 rpm.

In the interest of simplicity, only the electromagnetic torque is calculated and compared and cogging torque, if any, is not considered. This is for two reasons; first, the attention is solely focused here on average torque producing capabilities of different machines and the phenomenon of cogging contributes no useful average torque. Secondly, cogging torque can always be minimised by using such well established techniques as skewing. Note also that the flux-MMF diagrams for the

induction and the switched reluctance machine have been obtained using analytical approximations while the flux-MMF diagrams for the rest of the machines have been obtained using the finite-element analysis.

6.4 Motors Used in the Comparison

6.4.1 Induction Motor (IM)

This is a standard D132 frame induction motor, shown in Fig. 6.1, capable of 11kW when operated from a 50Hz sinusoidal supply. It is derated to 7.5kW for operation from a variable speed supply (10:1 speed ratio) with a constant torque (50 Nm). The total copper loss at 7.5kW is 634W (stator copper loss of 426W and rotor copper loss of 208W).

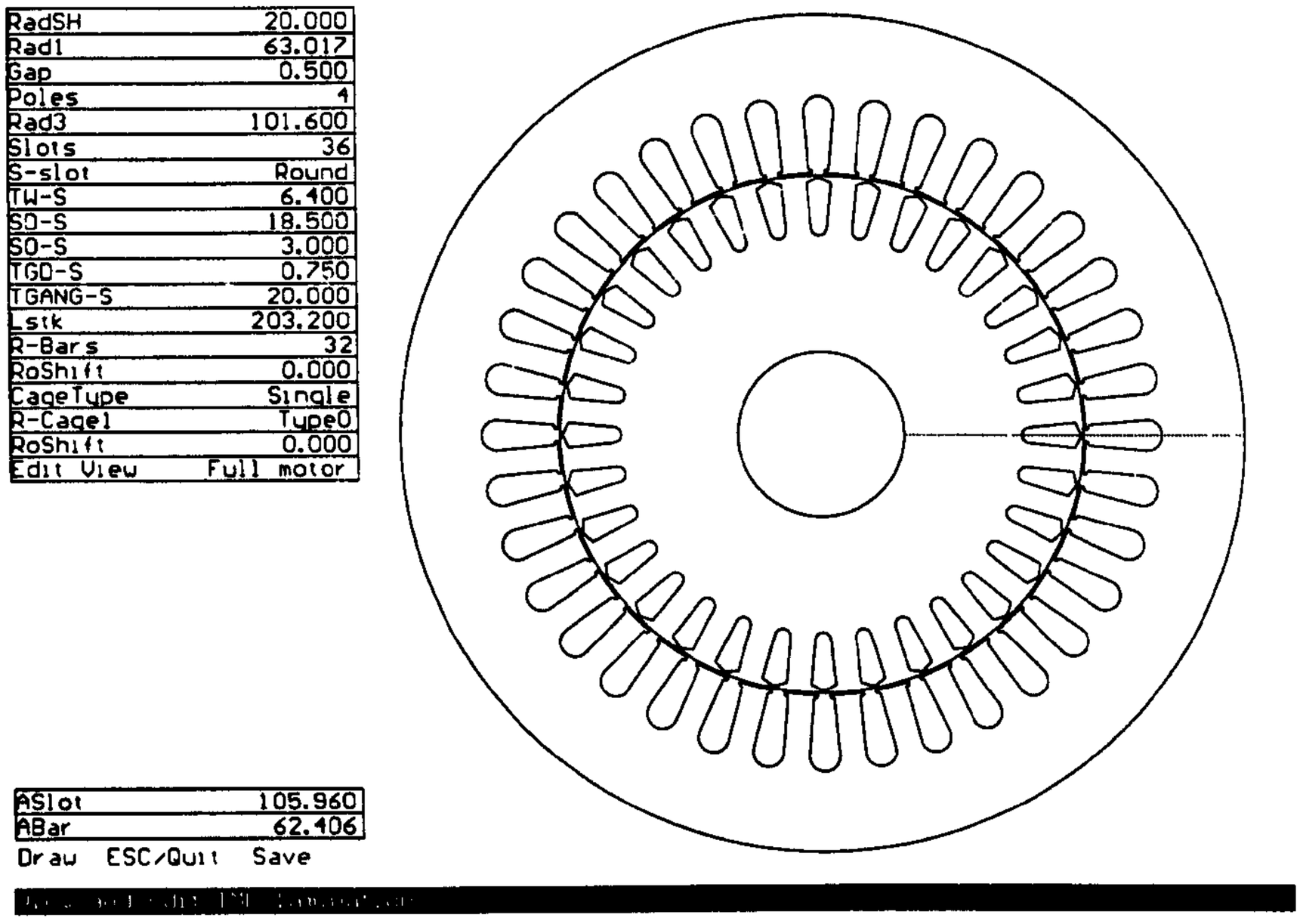

Figure 6.1. D132 frame induction motor cross-section.

The flux-MMF diagram for the IM is derived analytically, only for the full-load operating point (15 A RMS), using simple equations for instantaneous current, voltage and flux-linkage; rather than using finite-element analysis, which can be too complicated and time-consuming due to the asynchronous nature of the IM. This means that there is only one flux-MMF trajectory at full-load current and there are no magnetisation curves calculated at successive rotor positions.

The instantaneous phase current, voltage and flux-linkage for an IM are given by the following three equations;

$$i = I\cos(\omega t - \phi) \tag{6.1}$$

$$v = V\cos(\omega t) \tag{6.2}$$

$$\lambda = \int v\,dt = \frac{V}{\omega}\sin(\omega t) \tag{6.3}$$

Where,

i, v, λ are the instantaneous current, voltage and flux-linkage respectively.

I, V are the peak current and voltage respectively.

ω, ϕ are the steady-state speed and power-factor angle respectively.

The flux-MMF trajectory for the IM at full-load is shown in Fig. 6.9.

6.4.2 Synchronous Reluctance Motor (SYNCHREL)

A 7.5kW axially-laminated synchronous reluctance motor is used in the comparison since it has been shown that this construction gives the maximum saliency ratio [77], [79]. This motor has been described briefly in Chapter 2, and in detail in [77]. Figs. 2.15 and 2.16 from Chapter 2 show the flux-MMF diagram and the torque ripple curves respectively. The stator and winding type are the same as used in the induction motor.

6.4.3 Switched Reluctance Motor (SRM)

A 6:4 SRM was designed using PC-SRD and its cross-section is shown in Fig. 6.2.

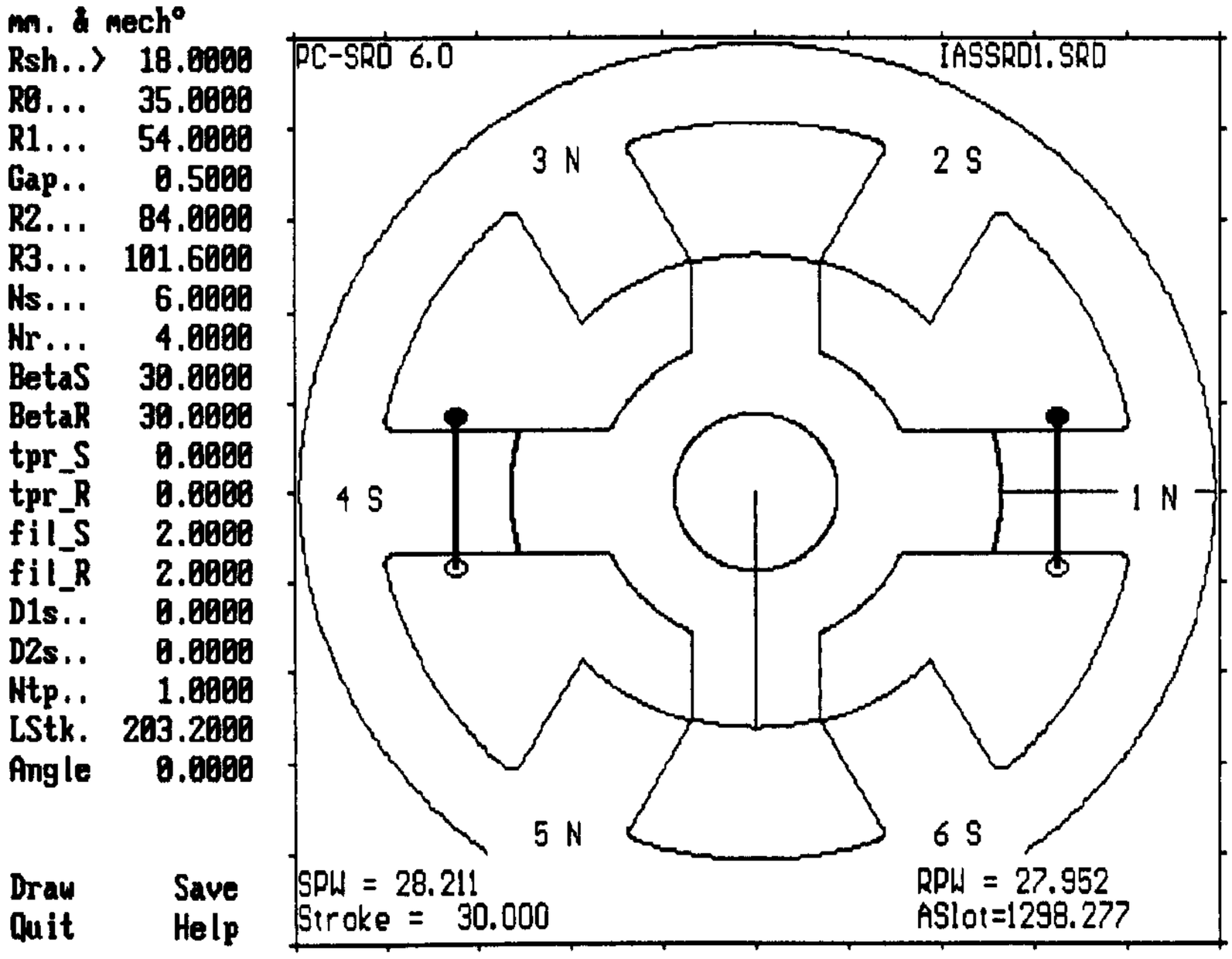

Figure 6.2. SRM cross-section.

A 6:4 topology was chosen since it has the same number of phases and energy conversion strokes per revolution as the other brushless motors used in this comparison. Figs. 6.3 and 6.4 show the ψ-i diagram and the torque ripple curves respectively. It must be noted that the torque ripple curves were obtained using the magnetisation curves generated in PC-SRD, which are based upon analytical approximations. A more rigorous calculation of magnetisation curves, obtained from the finite-element analysis and based on the actual phase current waveforms, is bound to produce torque ripple curves which are more uniform and closer to the actual motor operation.

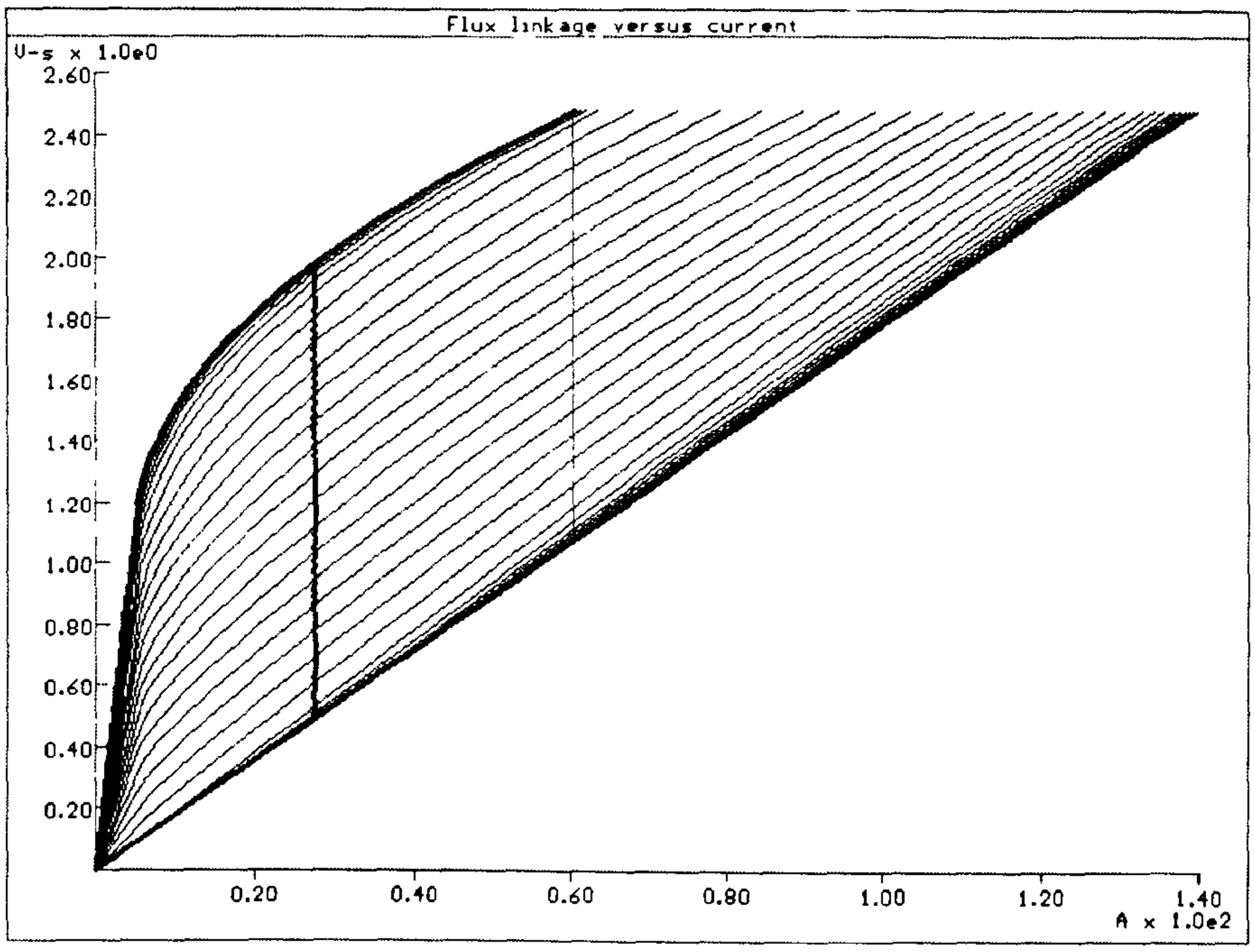

Figure 6.3. SRM ψ-i diagram.

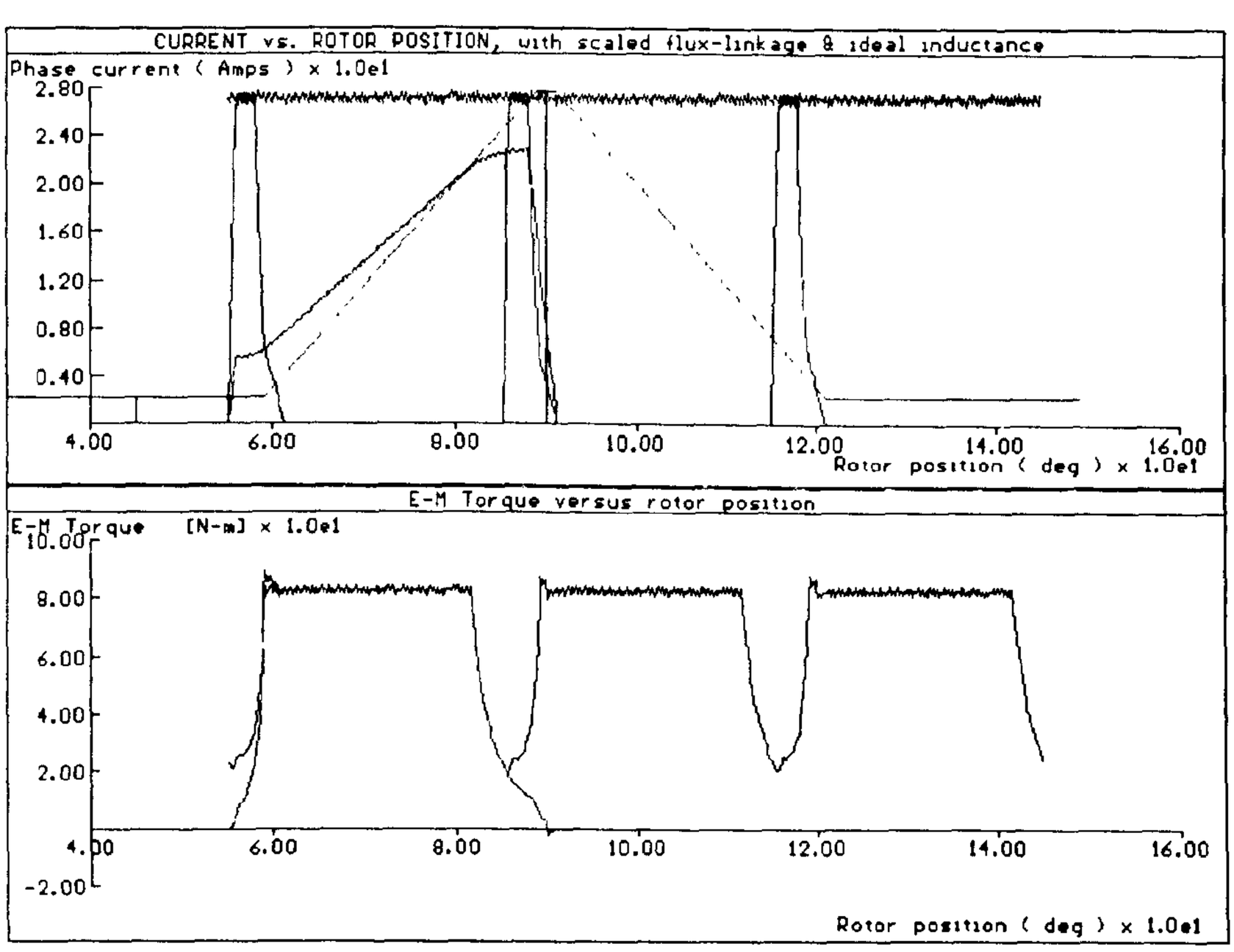

Figure 6.4. SRM phase current and torque ripple waveforms at 150 rpm, generated using PC-SRD.

6.4.4 Surface Permanent-Magnet Brushless AC Motor (SPM-AC)

The surface permanent-magnet brushless AC motor, designed using PC-BDC, has been described in Chapter 1 and Fig. 1.11 shows the motor cross-section. It has rare-earth magnets with a remanence of 1.1 T to give flux-density levels comparable to those in the IM. The magnet arc and distributed winding configuration were designed to give a sinusoidal back-EMF. Fig. 1.13 in Chapter 1 shows the flux-MMF diagram with magnetisation curves at 6 currents ranging from no-load to full-load.

The flux-MMF trajectories, which are the dynamic loci of the operating point, are nearly elliptical. The magnetisation curves are nearly straight lines because the flux-linkage is set by the magnets and is virtually independent of the current. Slight irregularities in the otherwise regular spacing of the magnetisation curves indicate a small amount of torque ripple due to slotting as shown in Fig. 2.3 in Chapter 2. A typical flux plot at full-load (20 A RMS phase current), obtained using FE analysis, is shown in Fig. 1.12.

6.4.5 Surface Permanent-Magnet Brushless DC Motor (SPM-DC)

Two surface permanent-magnet brushless DC motors were designed to operate with 120° elec. squarewave line currents.

1. SPM-DC1: with a 150° elec. magnet arc. This uses the same geometry and magnets as the SPM-AC motor, with a concentrated winding to give a flat-top back-EMF waveform.

2. SPM-DC2: with a 170° elec. magnet arc. This motor is exactly the same as SPM-DC1 except that it uses a larger magnet arc to reduce the torque ripple.

Fig. 6.5 is the flux-MMF diagram for the SPM-DC1 motor. The diagram has a nearly ideal rectangular shape and regular spacing of the magnetisation curves, with a

small amount of torque ripple that is further reduced in the SPM-DC2 design as shown in Fig. 6.13.

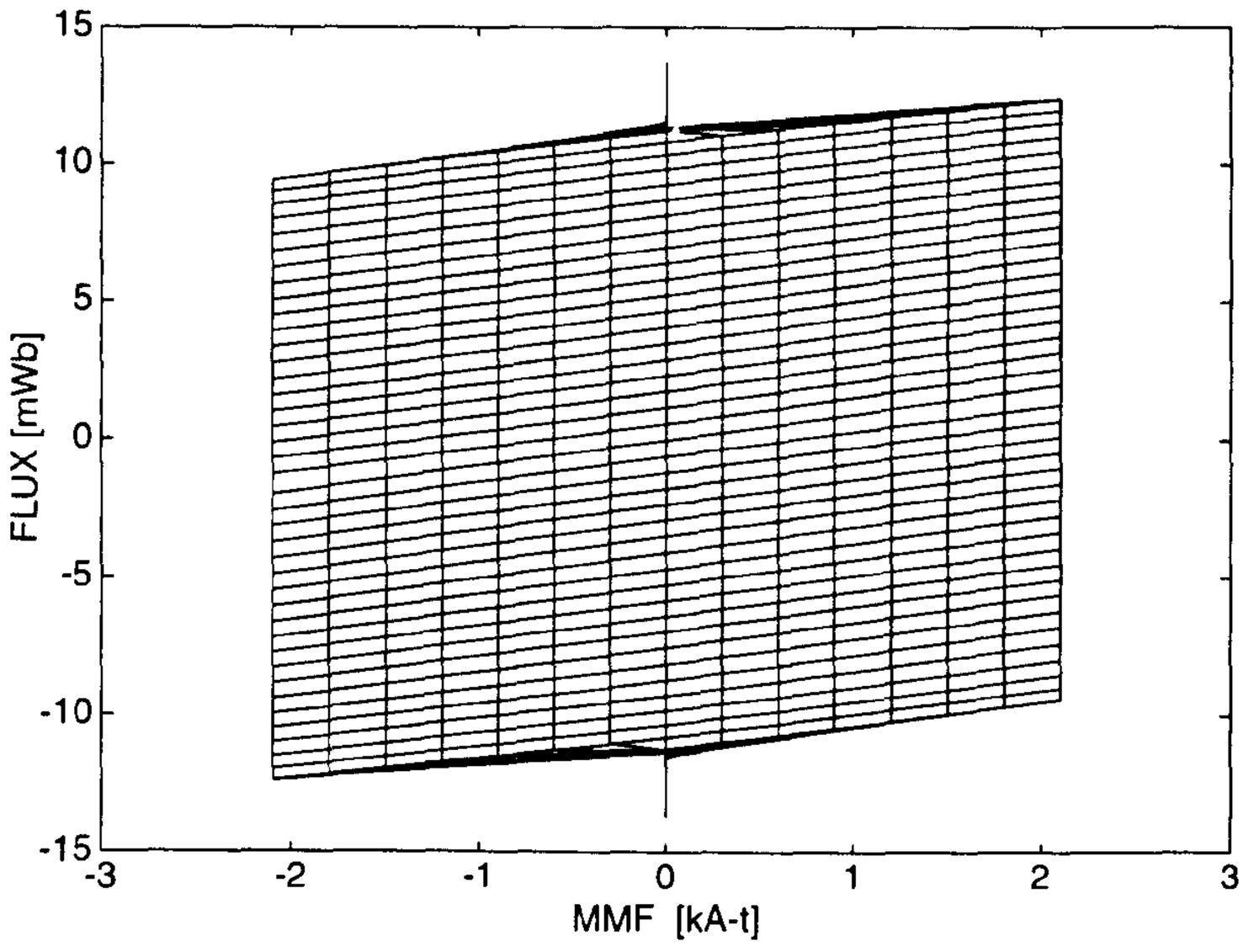

Figure 6.5. SPM-DC1 flux-MMF diagram at 0, 5, 10, 15, 20, 25, 30, 35 A RMS phase currents.

6.4.6 Interior Permanent-Magnet Motor (IPM)

The interior permanent-magnet (IPM) motor, also designed using PC-BDC, has been described in Chapter 4. Figs. 4.3, 4.4 and 4.6 show the motor cross-section, the flux-MMF diagram, and the torque ripple curves respectively. It was designed to operate from a sinusoidal supply and uses the same winding as the SPM-AC motor. The current angle, γ, was chosen to be 30° elec. for maximum torque per ampere operation.

6.4.7 Permanent-Magnet DC Commutator Motor (PMDC)

The permanent-magnet DC commutator motor (PMDC), used in the comparison, is shown in Fig. 6.6.

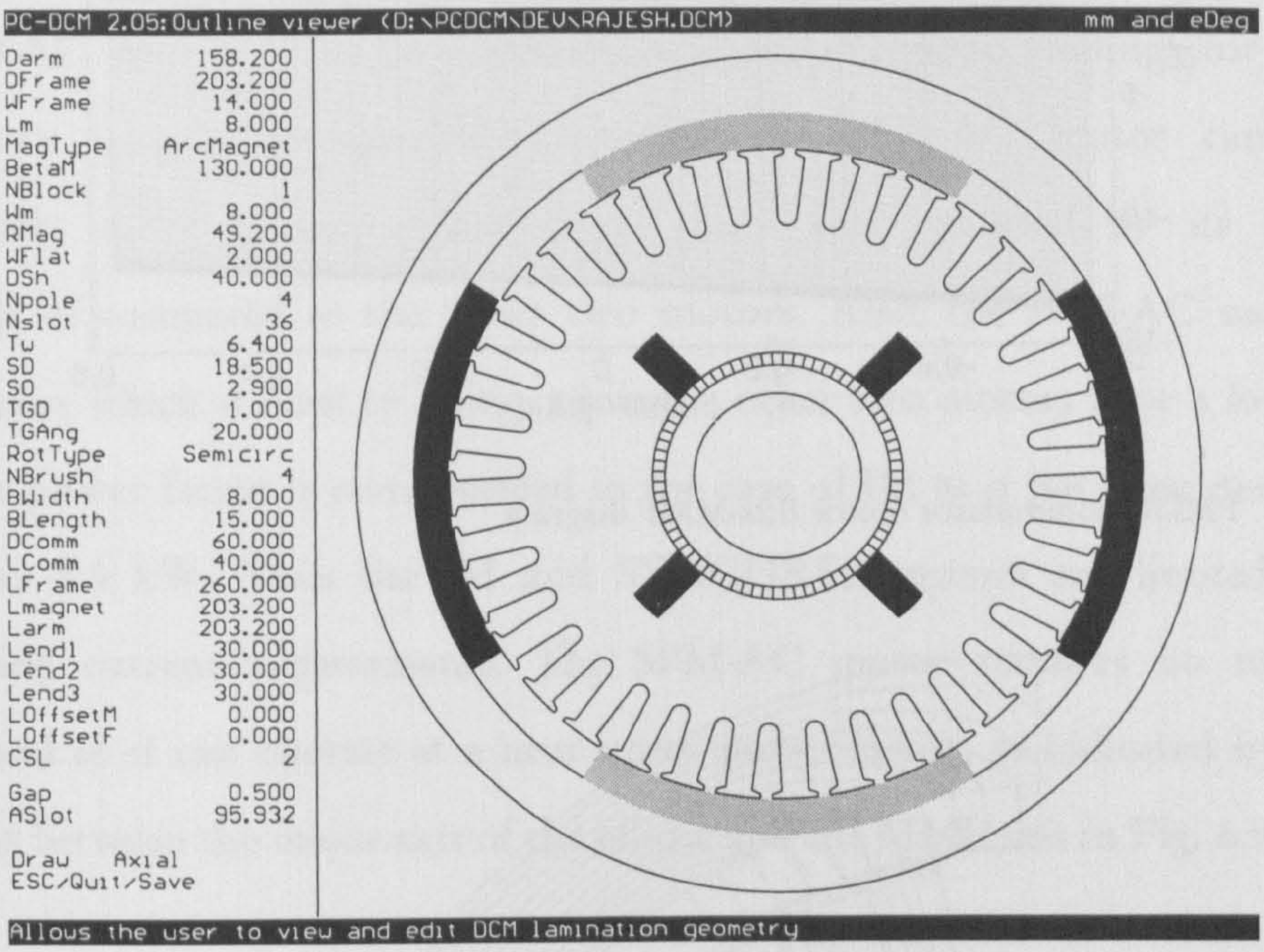

Figure 6.6. PMDC commutator motor cross-section.

It was designed using the PC-DCM software [81]. It has the same numbers of slots and poles as the SPM-DC motor, resulting in a '9 phase' motor. The magnet has a remanence of 0.75 T. This is less than the 1.1 T used in the SPM-DC motor but is required to increase the copper space, owing to the flux-concentrating nature of PMDC commutator motors. The flux-MMF diagram is shown in Fig. 6.7 and the predicted torque ripple in Fig. 6.16. A typical full-load flux plot taken from the finite-element analysis is shown in Fig. 6.8.

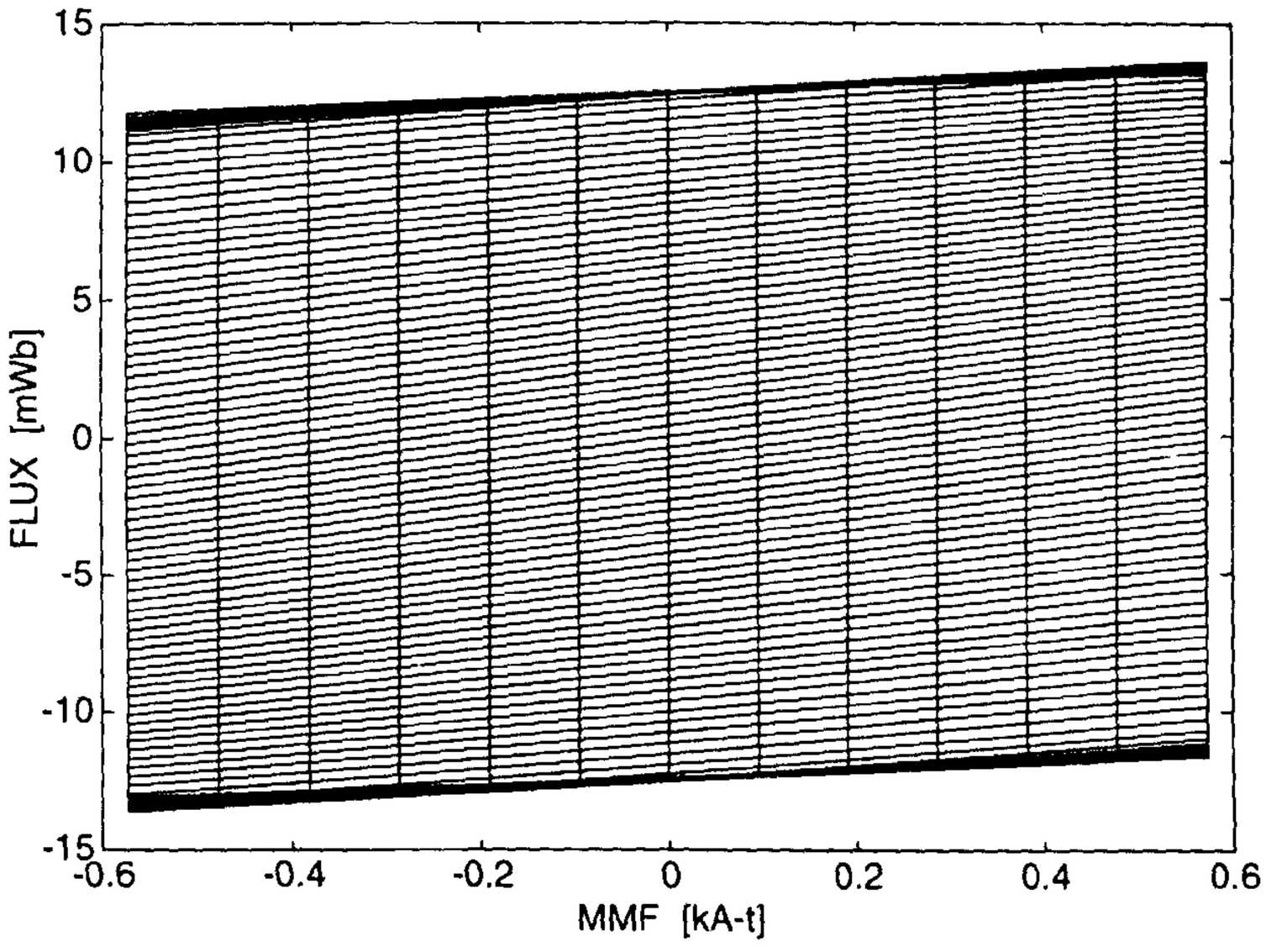

Figure 6.7. PMDC commutator motor flux-MMF diagram.

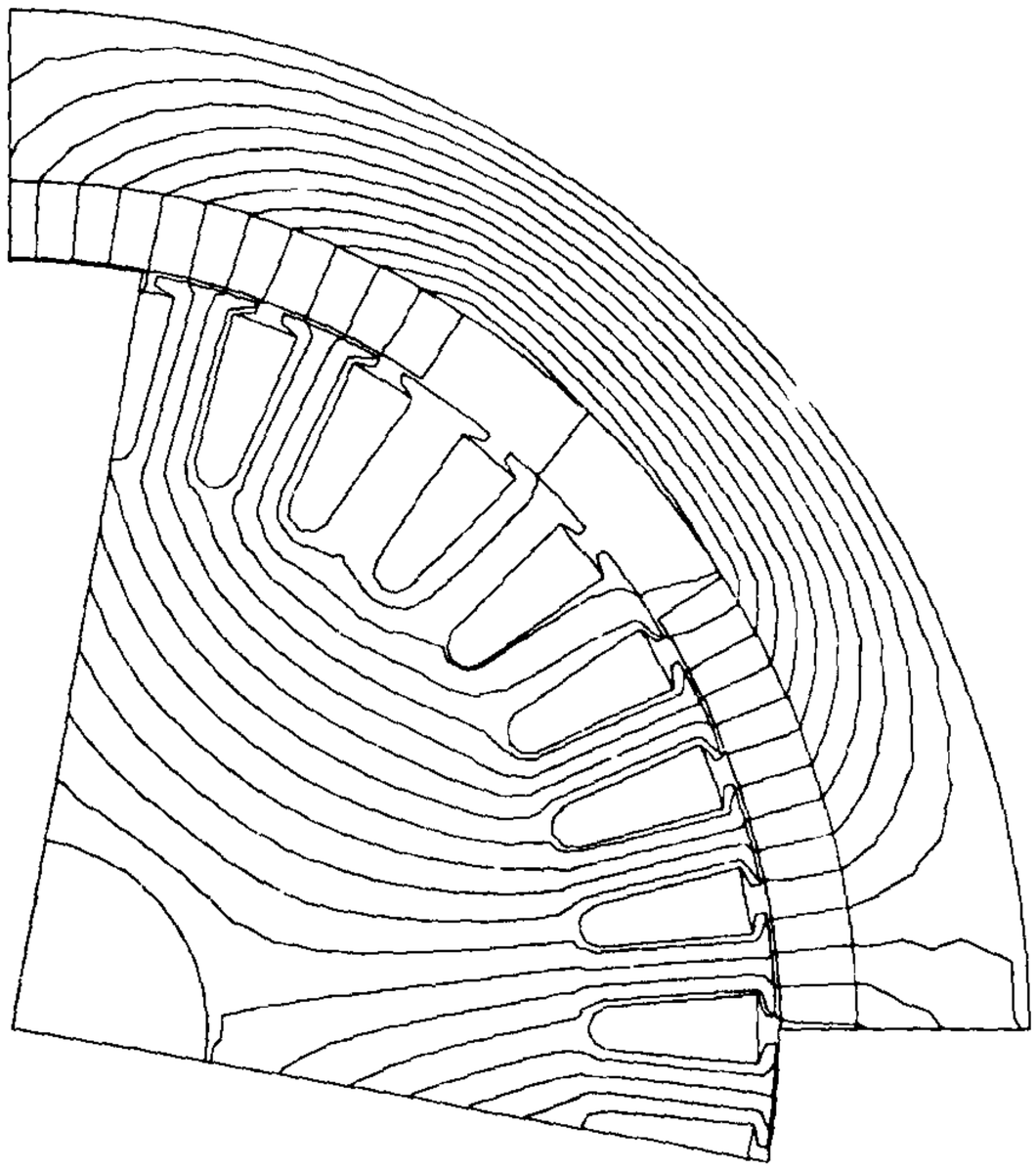

Figure 6.8. PMDC commutator motor flux-plot at full-load.

6.5 Comparisons Based on the Flux-MMF Diagram

6.5.1 IM, SYNCHREL and SPM-AC Motors

Fig. 6.9 compares the flux-MMF trajectories at full-load for the IM, SYNCHREL and SPM-AC motors. The maximum electric and magnetic loadings for the three motors are roughly comparable. However, the SPM-AC motor can generate substantially more torque, indicated by more area enclosed by its flux-MMF trajectory, as compared to the other two motors. Also, the SPM-AC motor has a power-factor which is close to unity, while the other two motors have a lower value. The poor power factor is compounded in the case of IM as it has been derated from 11 kW to 7.5 kW. Thus the IM and SYNCHREL motors are limited by their magnetising current requirements. The SPM-AC motor requires no magnetising current and so it can operate at a near unity power-factor, as indicated by the near alignment between the major axis of the ellipse and the MMF axis in Fig. 6.9.

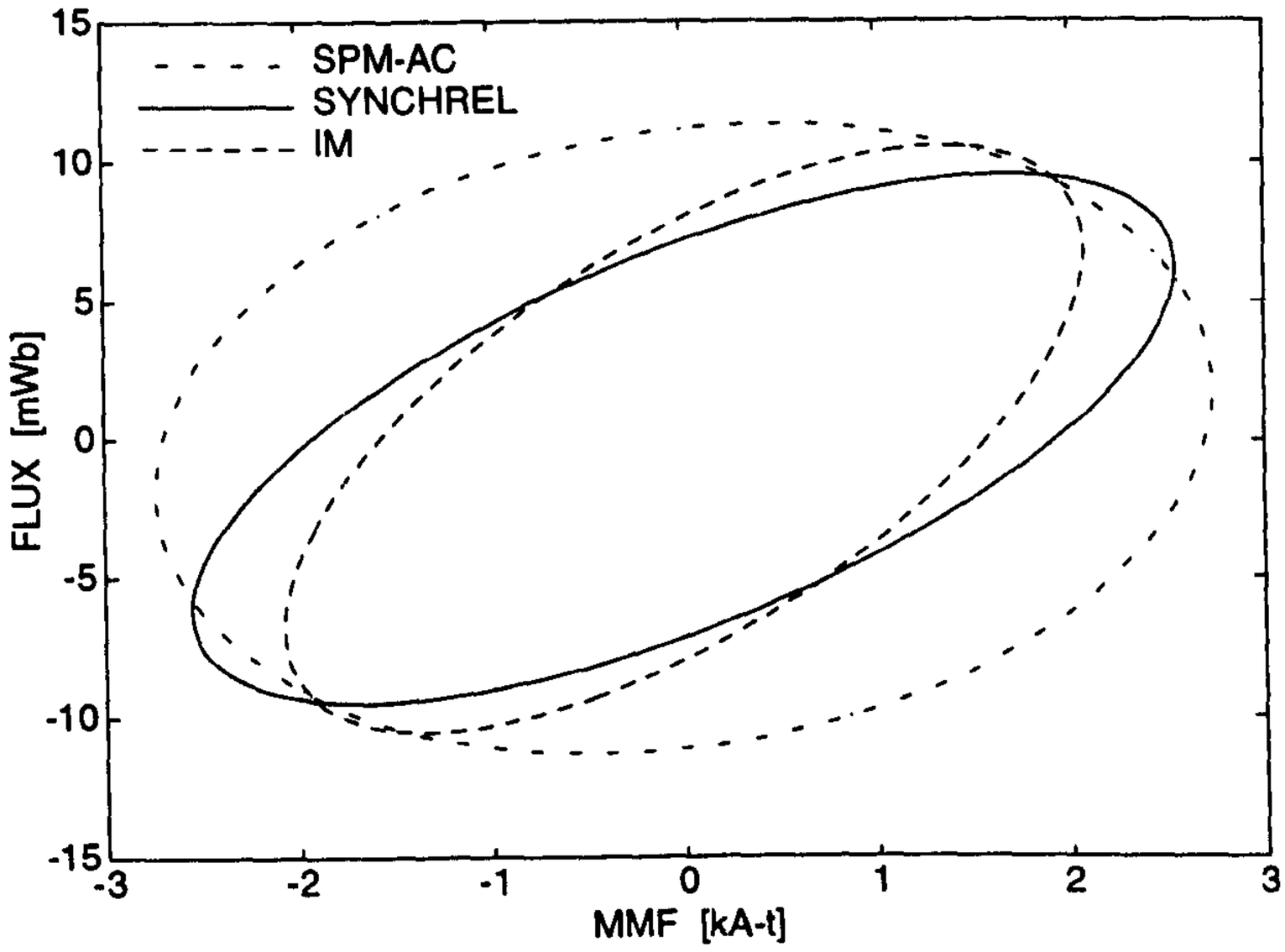

Figure 6.9. Comparison between the IM, SYNCHREL and SPM-AC motors at full-load.

6.5.2 SRM and SYNCHREL Motors

Fig. 6.10 compares the flux-MMF trajectories at full-load for the SRM and SYNCHREL motors. The SRM shows a similar flux level but a much higher MMF as compared to the SYNCHREL motor. The SRM average full-load torque is not dramatically better than SYNCHREL as the SRM flux-MMF trajectory is limited to the first quadrant in the flux-MMF plane while the SYNCHREL (as well as all other AC motors) benefits from mutual flux-linkage and its flux-MMF trajectory extends into all four quadrants.

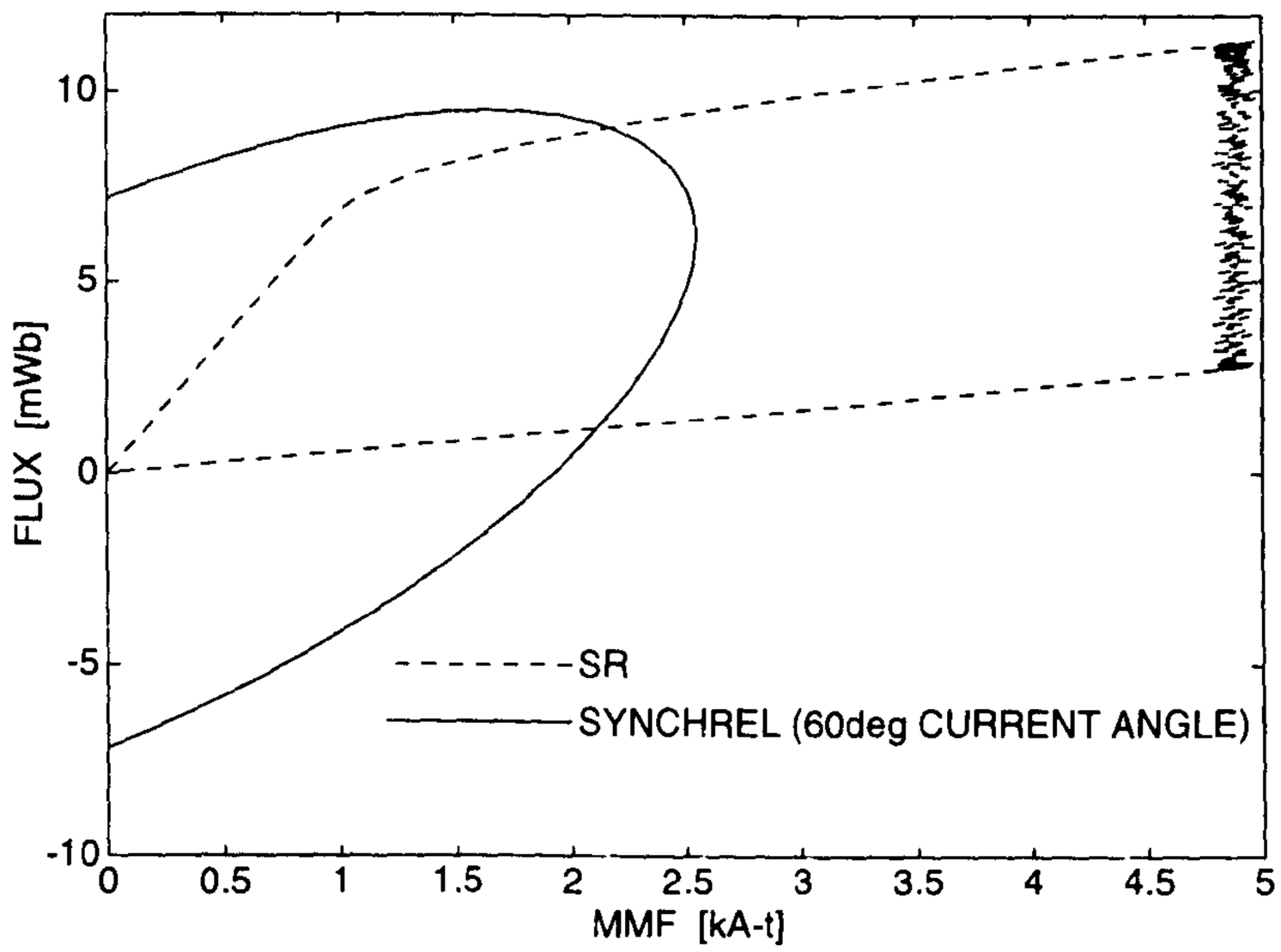

Figure 6.10. Comparison between the SRM and SYNCHREL motors at full-load.

6.5.3 SPM-AC and SPM-DC Motors

Fig. 6.11 compares the flux-MMF trajectories at full-load for the SPM-AC and SPM-DC1 motors. Both enclose almost the same area in the flux-MMF plane and

hence have about the same average full-load torque as shown in Fig. 6.12. However, the torque ripple is less in the SPM-AC motor. It is to be noted that the peak current rating of the inverter is higher for the SPM-AC motor with its sinusoidal drive. Whereas the peak flux in the SPM-DC1 motor is larger, even when both the motors have the same geometry and magnets. This is because the SPM-DC1 winding is concentrated rather than distributed.

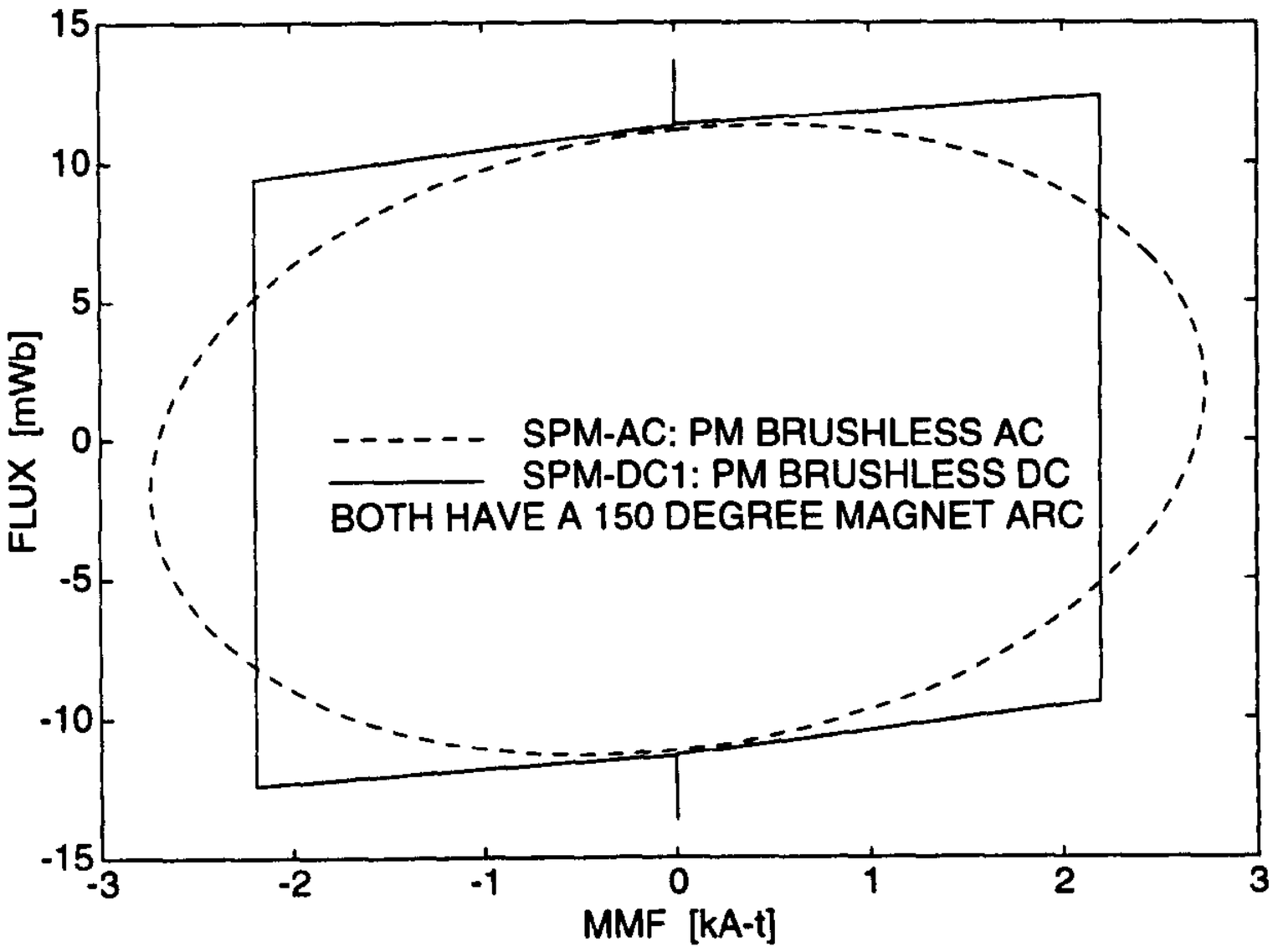

Figure 6.11. Comparison between the SPM-AC and SPM-DC1 motors at full-load.

Fig. 6.13 compares the full-load torque ripple between the SPM-DC1 and SPM-DC2 motors and it shows that the SPM-DC2 motor has a torque ripple comparable with that of the SPM-AC motor. While both the SPM-AC and SPM-DC1 motors use 150° elec. magnet arc, the SPM-DC2 motor uses 170° elec. magnet arc to reduce the torque ripple. This, however, does not take account of imperfect commutation and its effect on torque ripple at higher speeds.

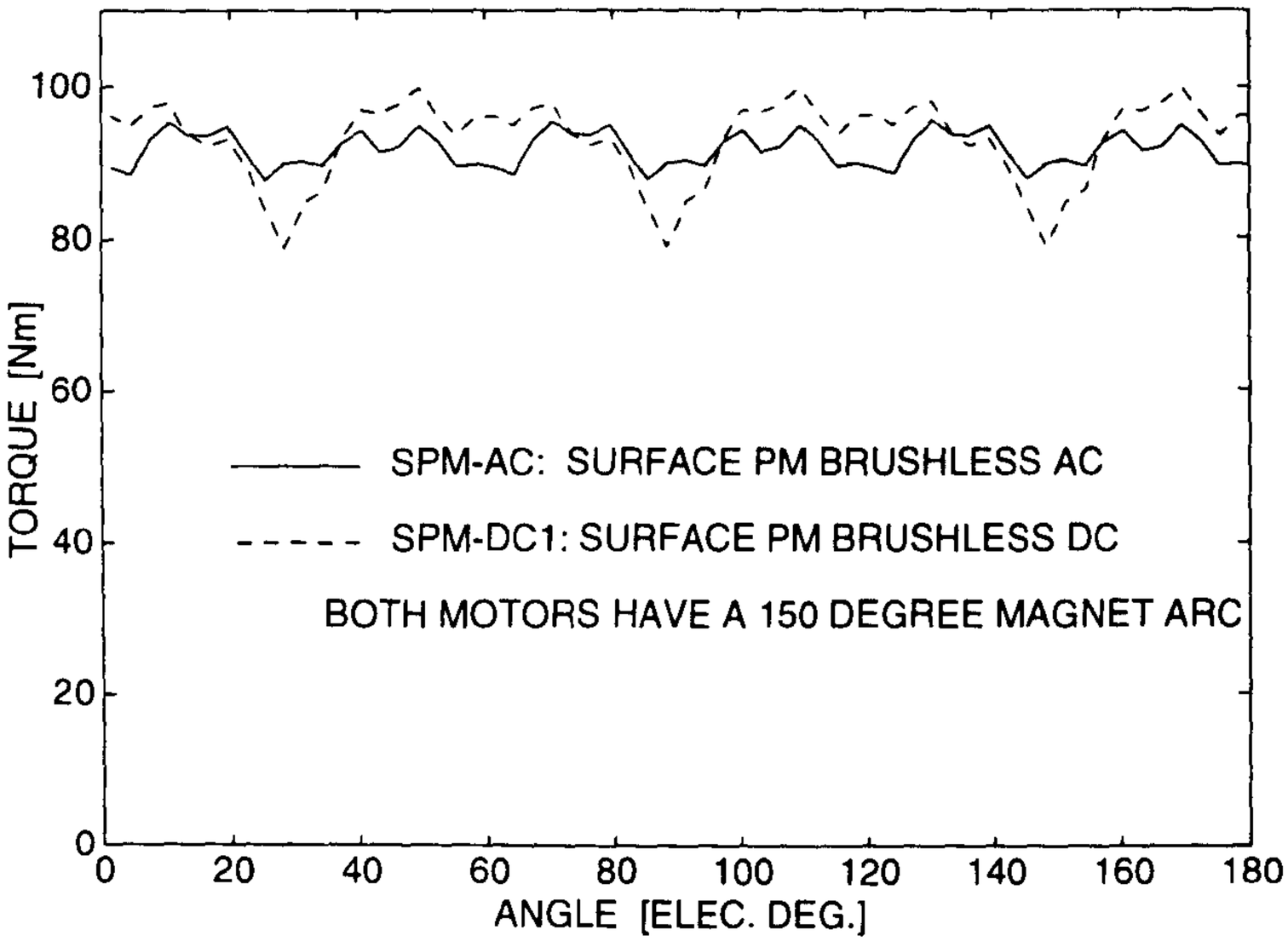

Figure 6.12. Comparison between the SPM-AC and SPM-DC1 motors. Torque ripple waveforms are at full-load currents of 20 and 35 A RMS respectively.

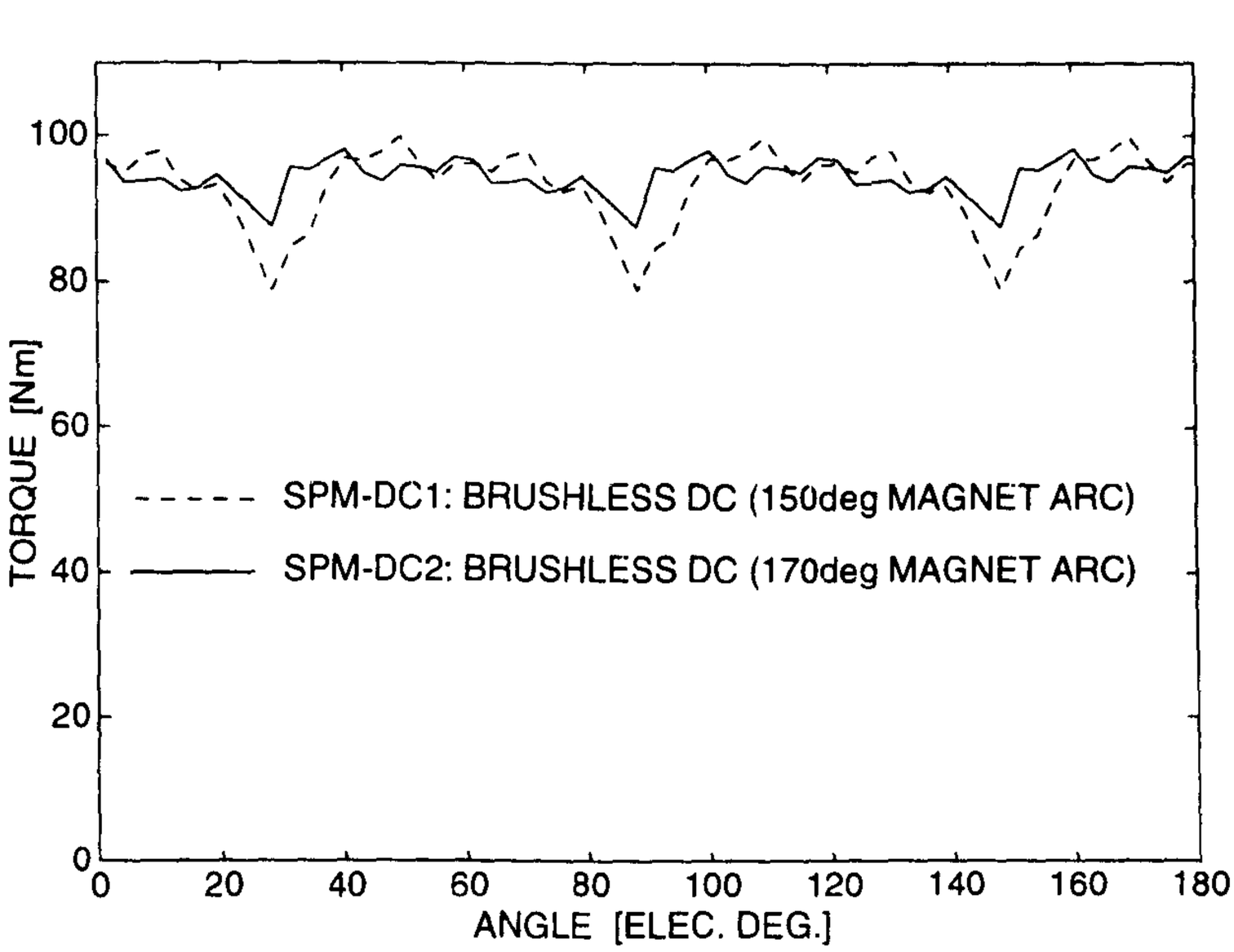

Figure 6.13. Comparison between SPM-DC1 and SPM-DC2 motors. Torque ripple waveforms are at full-load currents of 35 A RMS.

6.5.4 SPM-AC and IPM Motors

The IPM motor has almost the same average full-load torque as the SPM-AC motor. This can be deduced from the equivalent areas enclosed by their respective flux-MMF trajectories shown in Fig. 6.14. However, the torque ripple is much larger for the IPM motor as seen in Fig. 6.15. This is due to the uneven spacing of the magnetisation curves as well as the deviation from the ideal elliptical shape for the flux-MMF trajectories as shown in Fig. 4.4 in Chapter 4. The high torque ripple is mainly due to harmonics in the airgap permeance caused by slotting, and the salient pole nature of the machine. The IPM motor with γ=30 has a better power factor than with γ=0, as indicated by the orientation of the ellipses in Fig. 6.14.

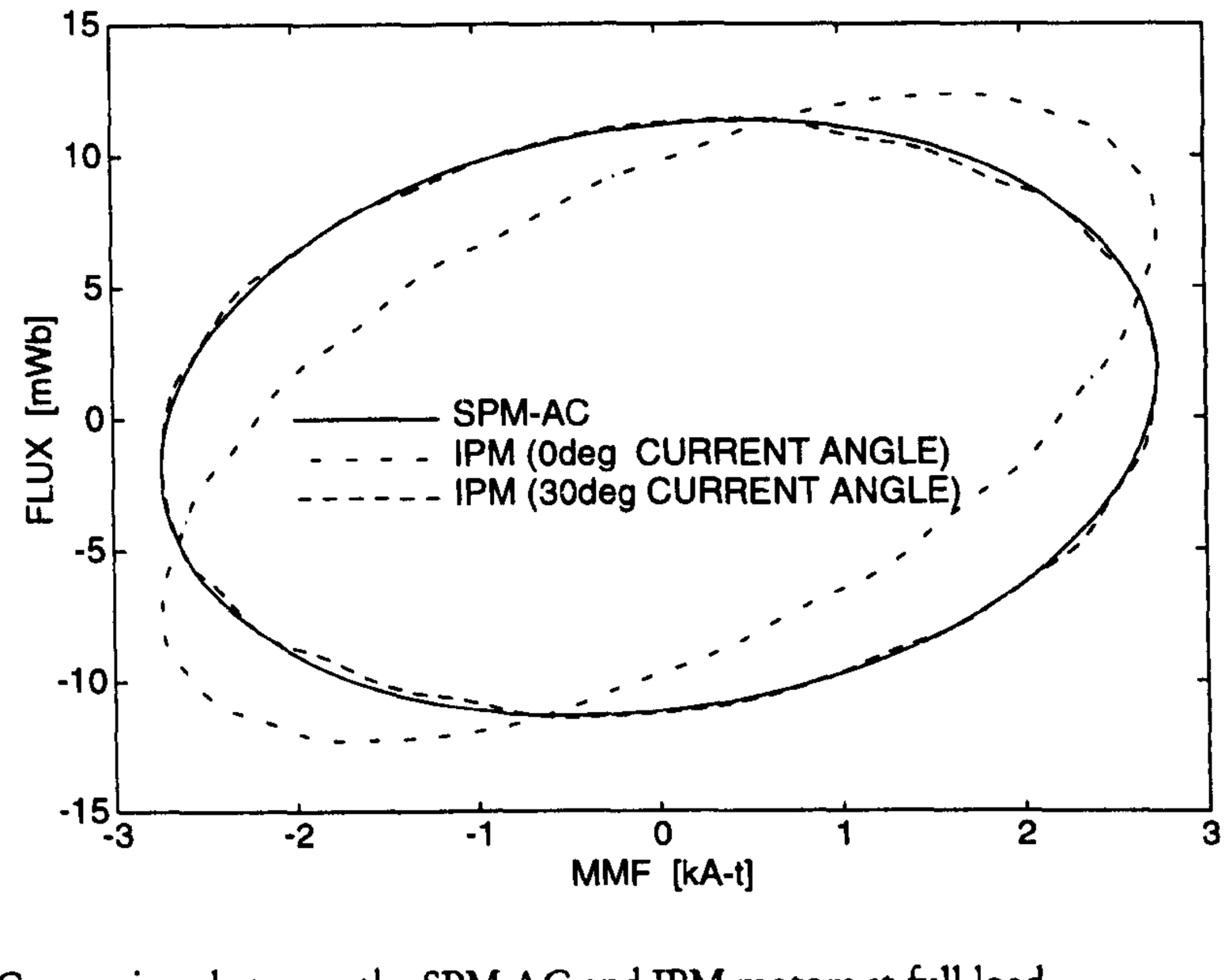

Figure 6.14. Comparison between the SPM-AC and IPM motors at full-load.

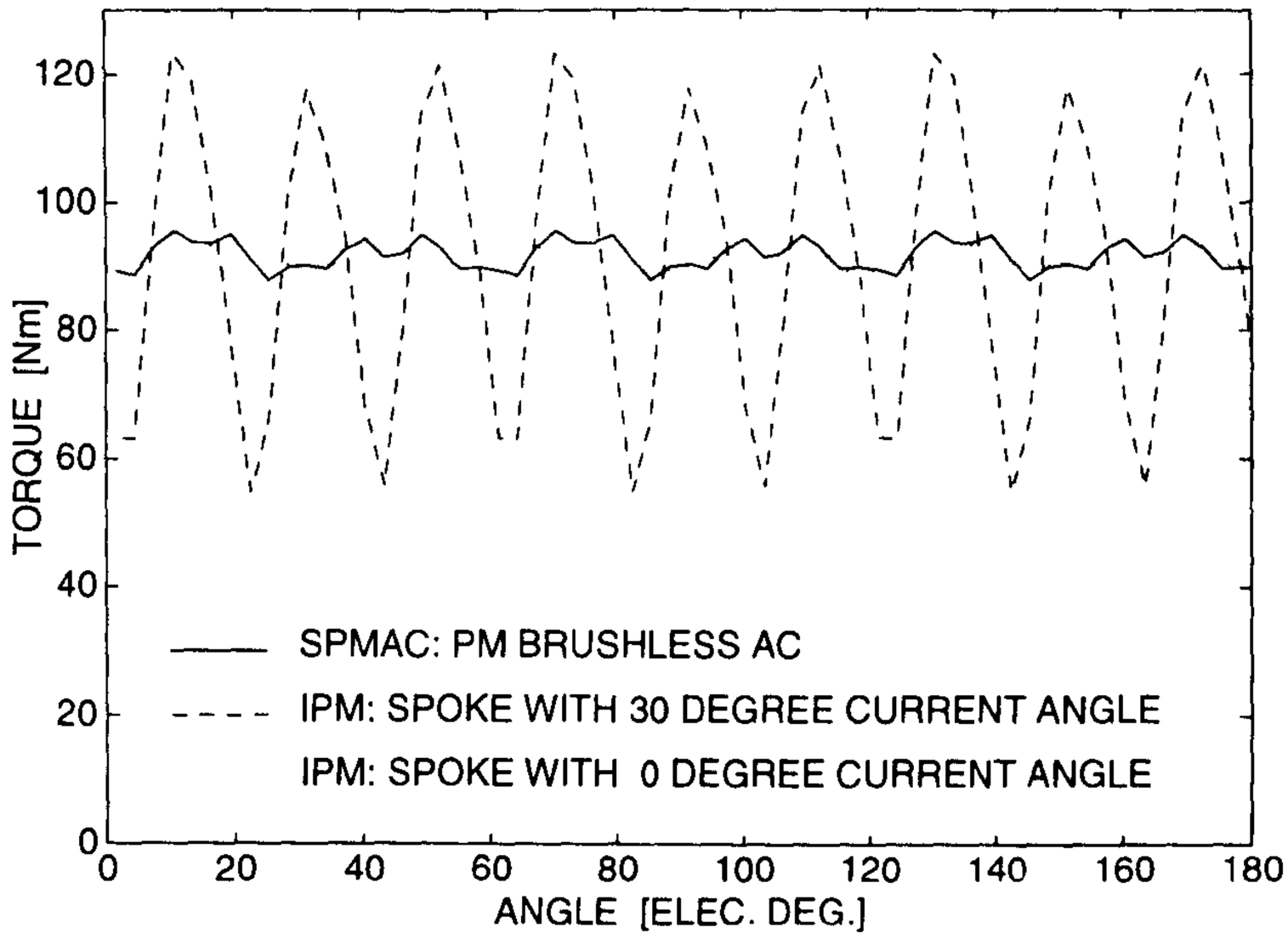

Figure 6.15. Comparison between the SPM-AC and IPM motors. Torque ripple waveforms are at full-load current of 20 A RMS.

6.5.5 SPM-DC2 and PMDC Motors

The comparison between the SPM-DC2 and PMDC motors is complicated by the fact that they have different number of phases. This results in a low peak phase MMF in the PMDC motor. Even if the phase ratio (9/3) is used to scale MMFs, the PMDC motor has a smaller MMF. This is mainly due to the fact that the SPM-DC2 motor has its slots on the outside of the motor and has a greater winding cross-section area. Fig. 6.16 compares the torque ripple at full-load between the SPM-DC2 and PMDC motors. In practice, the PMDC motor may need to be derated with respect to the other motors because most of the losses are generated in the armature which is not as easily cooled as when it is on the outside of the motor.

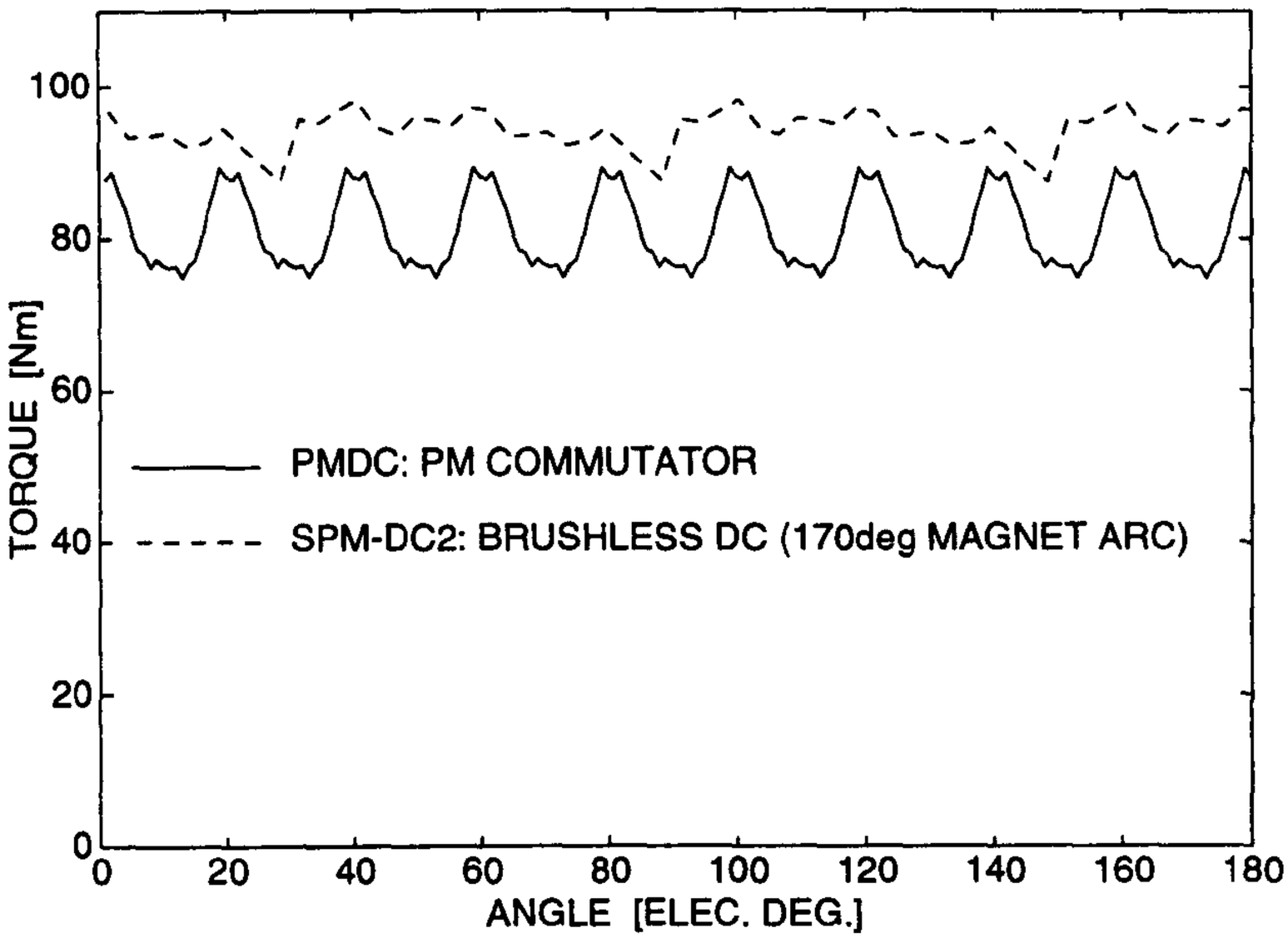

Figure 6.16. Comparison between the SPM-DC2 and PMDC motors. Torque ripple waveforms are at full-load currents of 35 and 23 A RMS respectively.

6.5.6 All Motors

Table 6.2 lists four important performance parameters at full-load for each motor type namely the average torque, torque ripple (expressed as the ratio of peak-to-peak to mean), peak phase MMF and peak phase flux. Figs. 6.17 to 6.20 make a graphical comparison based on each one of these four parameters. Note that no torque ripple data is available for the induction motor since its flux-MMF diagram has been calculated using analytical expressions rather than the finite-element analysis.

Table 6.2. Comparison between seven motor types.

Motor Type	T_{av} (Nm)	T_{ripple} (%)	MMF (kA-t)	Flux (mWb)
IM	49.7	—	2.07	10.53
SYNCHREL	54.8	25	2.55	9.50
SRM	63.4	75	4.98	11.33
SPM-AC	91.7	8	2.74	11.32
SPM-DC2	94.2	11	2.19	13.98
IPM (γ=30)	91.3	75	2.74	11.62
PMDC	81.1	18	1.74[a]	13.62

[a]The peak phase MMF for the PMDC motor has been multiplied by 3 as it is a '9-phase' motor (all other motors are 3-phase).

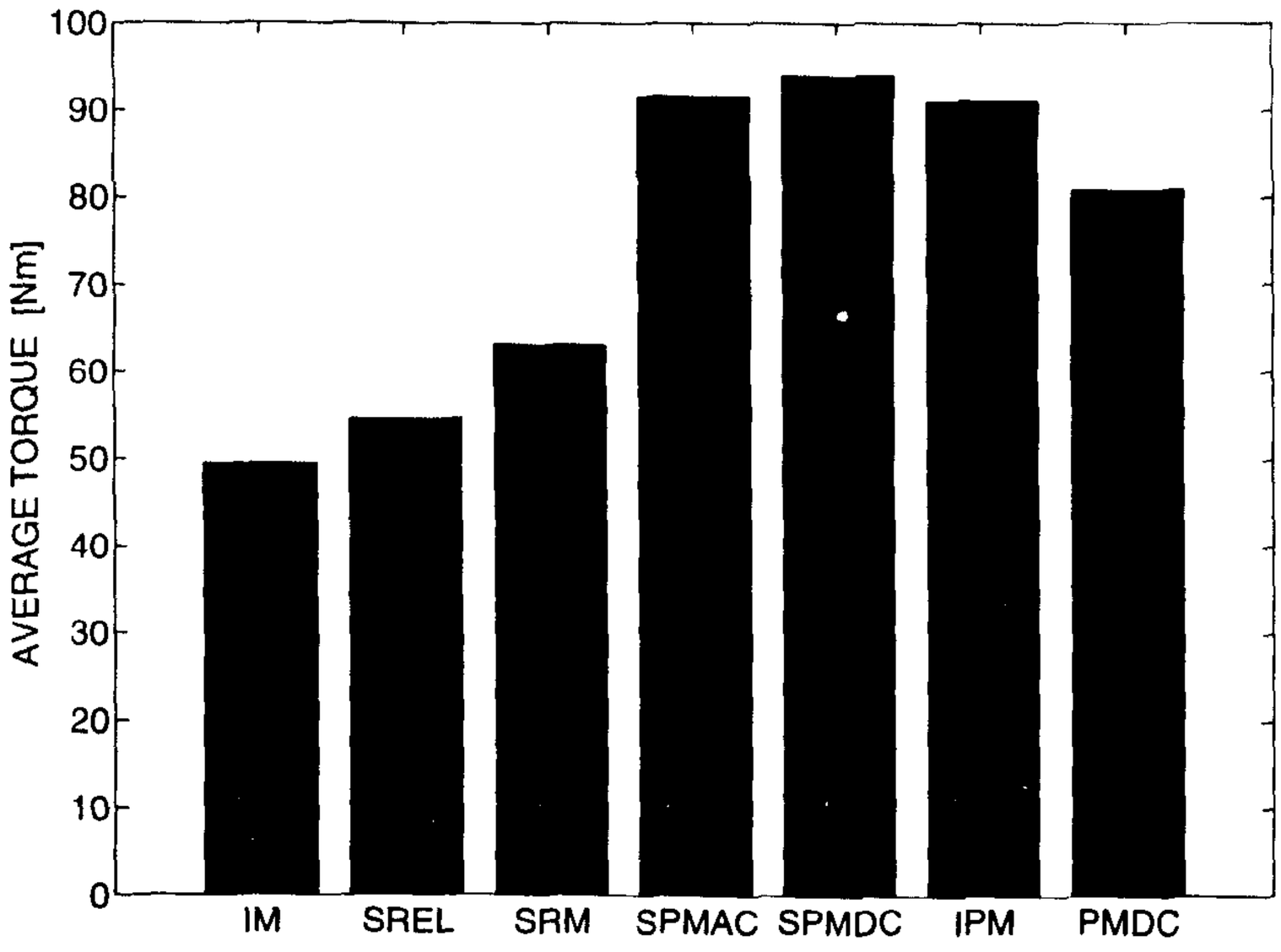

Figure 6.17. Comparison based on average torque.

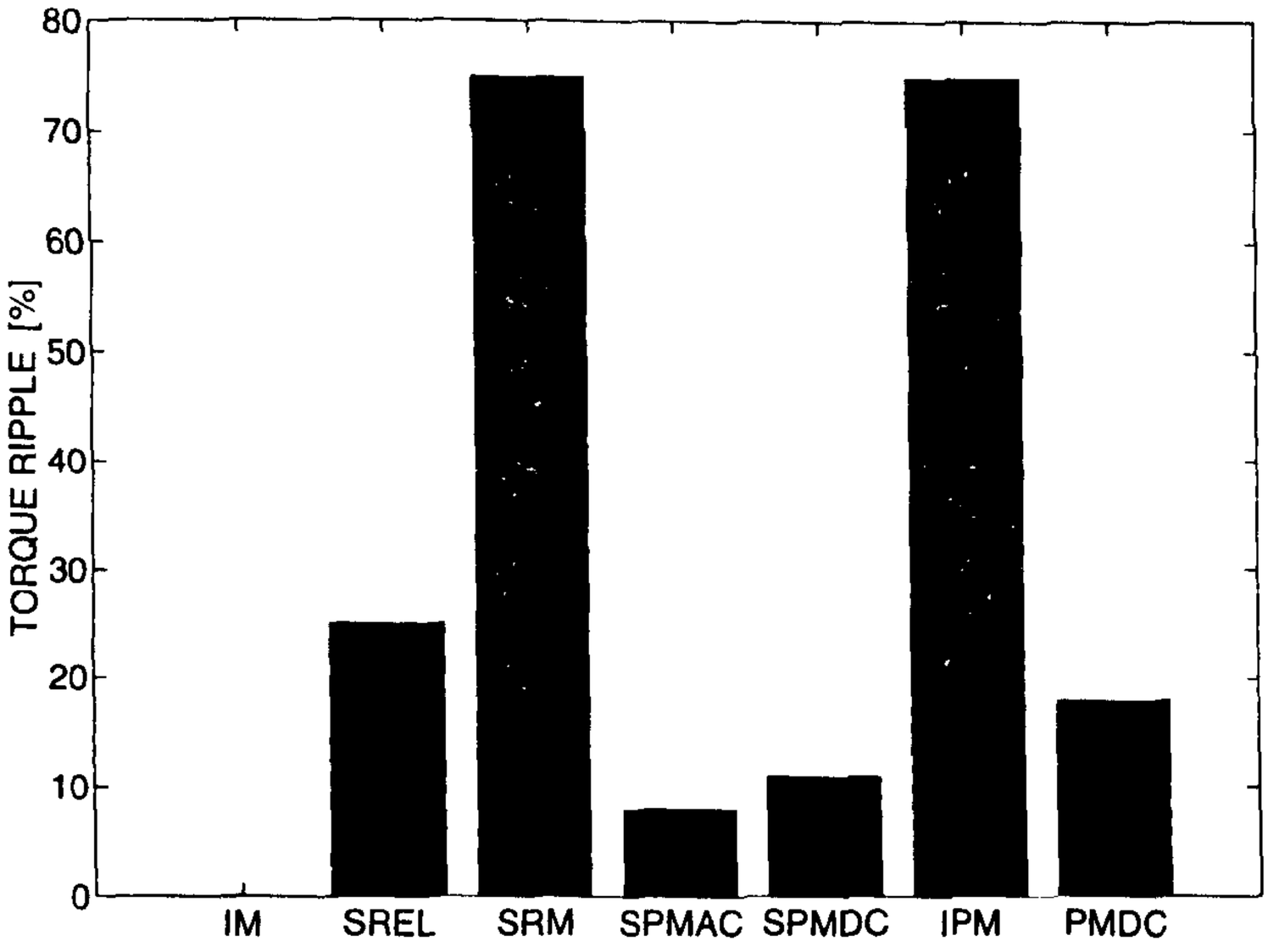

Figure 6.18. Comparison based on torque ripple. All machines are unskewed. The torque ripple levels can be reduced by employing the appropriate amount of skew.

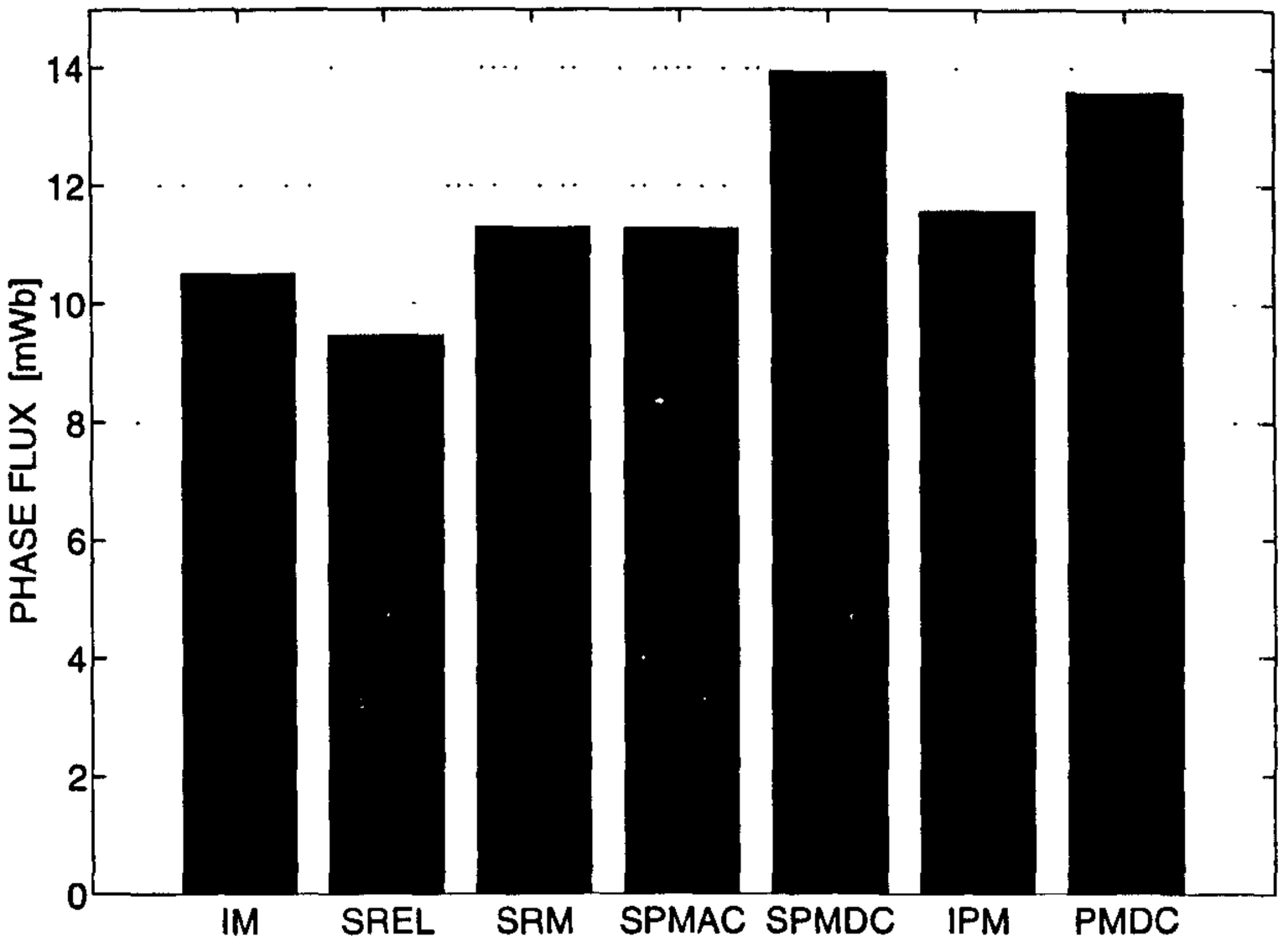

Figure 6.19. Comparison based on peak phase flux.

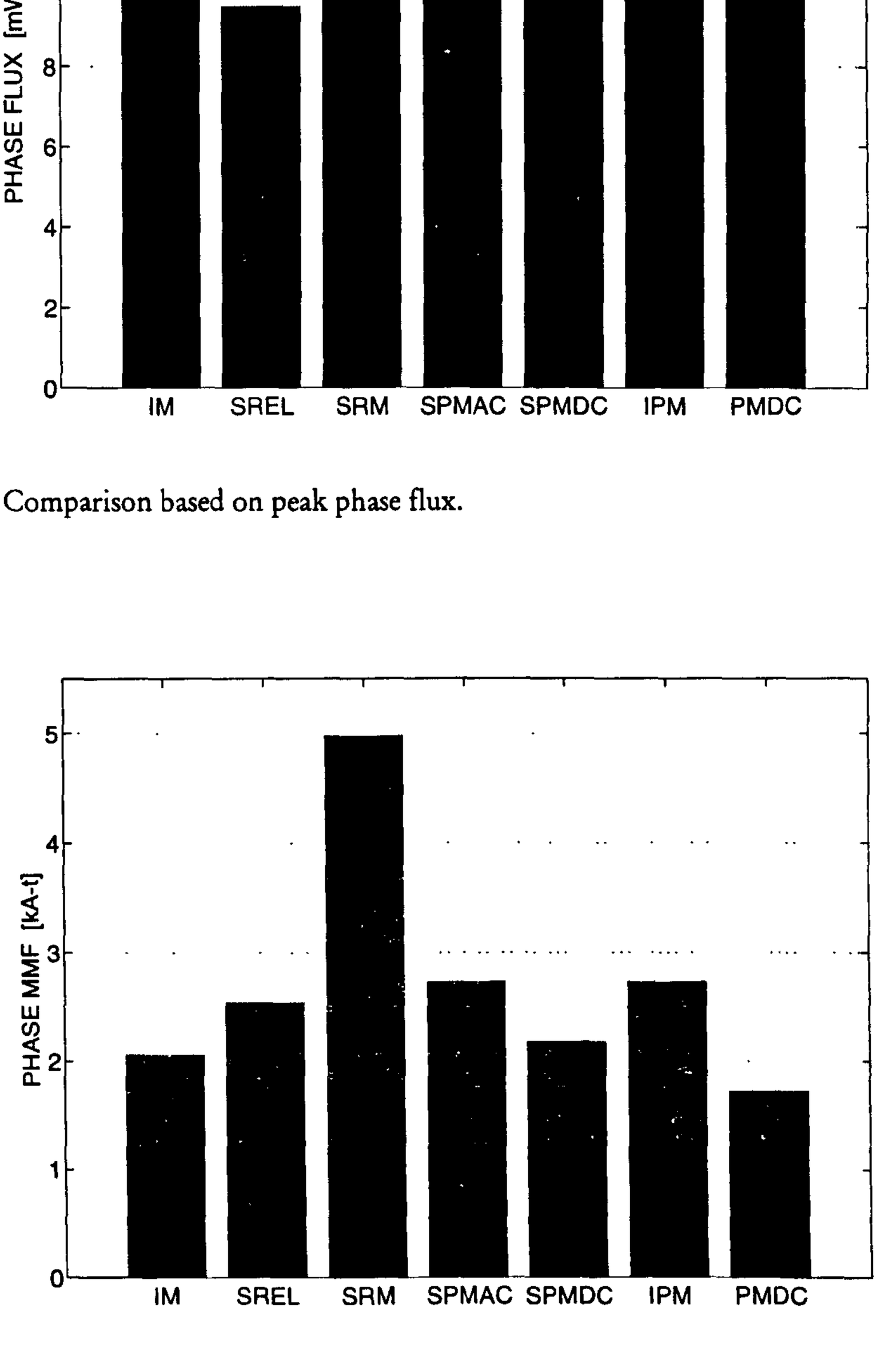

Figure 6.20. Comparison based on peak phase MMF.

For the given design and operational constraints, the SPM-DC2 motor shows the maximum average torque, while the SRM and IPM motors show the highest torque

ripple; although no attempt has been made to reduce it in their respective designs. With refinements in the SRM design and operation, and with the optimum current angle, γ, for the IPM motor operation, both motors are bound to show improvement in their torque ripple performance.

The SPM-DC2 motor shows the maximum phase flux, while the SRM shows the maximum phase MMF. This follows directly from the fact that the SRM flux-MMF trajectory lies entirely in the first quadrant of the flux-MMF plane and hence for a given phase flux, it has to have a much higher phase MMF to obtain a comparable level of average torque as other motors.

6.6 Chapter Summary

Chapter 6 has demonstrated the capability of the flux-MMF diagram technique in comparative evaluation of different types of electrical machines. It has been shown that any two or more numbers of electrical machine designs of either the same machine type, or of different machine types, can be compared using the flux-MMF diagram as a common means of graphical representation. The comparison can be made on the basis of a variety of criteria such as, the operational characteristics, average torque, torque ripple, electric and magnetic loadings, and the power factor or the power effectiveness.

The process of comparative evaluation has been illustrated by considering seven different motor types which have been designed using a common set of design constraints. The designs have been reasonably optimised using a combination of the SPEED CAD software and the FE analysis. The flux-MMF diagrams have been constructed for each motor type, and they have been used to make comparisons and draw specific conclusions about the operational characteristics of each of the machine types.

7 Flux-Reversal Machine

7.1 Introduction

This chapter has the twin objectives of describing a new brushless doubly-salient permanent-magnet machine, called the *flux-reversal machine*, and establishing the capabilities of the flux-MMF diagram technique in analysing such a non-conventional machine, which cannot be analysed using classical means of dq-axis transformation. As pointed out in Chapter 1, the dq-axis transformation can only be applied in machines which have sinusoidally distributed MMF, and have either the stator or the rotor or both non-salient. It cannot be applied in analysing the switched reluctance or the squarewave brushless DC machines, which do not satisfy these conditions. Such machines are characterised by either non-sinusoidal MMF distribution or double-saliency or both. The flux-reversal machine (FRM), proposed by Boldea et al. [96], is a new addition to such class of machines.

The impetus for developing the flux-reversal machine came from the research carried out on the switched reluctance machine (SRM), which has grown significantly in recent years. While the SRM has some advantages such as simple construction, fault tolerance and mechanical robustness; it also has certain limitations such as excitation penalty, control complexity, and an inherent propensity towards high torque-ripple, noise and vibration. The idea of overcoming these limitations, while retaining the advantages, has prompted many research explorations in incorporating permanent-magnets into the basic SRM structure. One of the new topologies proposed recently is the doubly-salient permanent-magnet machine (DSPMM) [54], which essentially has the same construction as an SRM, but with high energy magnets placed in the stator back iron. The flux-reversal machine has been proposed with the same objective of

combining the advantages of the SRM and the permanent-magnet machine (PMM) into one machine.

While the FRM is not the first doubly-salient PM machine to have stationary magnets combined with a simple unexcited variable reluctance rotor, it appears to be the first to have bipolar flux *and* MMF variation with rotor position. It also appears that the FRM has a naturally low inductance and therefore a low electrical time constant. These features, combined with its simple construction and low rotor inertia appear to make the FRM attractive as a low-cost, high-speed generator. This is important in the context of current attempts in the automotive industry to deal with certain limitations of the standard claw-pole alternator, such as limited efficiency and limited ability to respond quickly to sudden load changes. These problems become more severe as vehicle electrical loads continue to increase [94]–[95].

The work described in this chapter forms a part of the major research program on flux-reversal machine at the SPEED Laboratory. An overview of the various activities carried out by different people within this program is given in Fig. 7.1. The program was initiated with the following three objectives.

- To construct a 'proof-of-principle' prototype flux-reversal generator, verify its principle of operation and demonstrate its performance capabilities.
- To build a simple electronic controller to obtain a regulated DC output voltage from the variable AC generated voltage over a wide speed range.
- To develop a software program—PC-FRM—to serve as a quick and simple means of 'sizing' a machine combined with the high speed of calculations and the ability to evaluate a wide range of design options.

The next section explains the principle of operation of the FRM and the *flux-reversing nature* of the machine. Section 7.3 makes a qualitative comparison between the FRM and the other brushless machines in its class, based on the flux-MMF diagram. Section 7.4 discusses certain alternate configurations of the FRM. The design

of a prototype 2/3 configuration, single-phase flux-reversal generator (FRG), and its analysis based on the FMDT, is presented in Section 7.5. The construction of the prototype generator and the associated electronic voltage controller is described in Section 7.6. Finally, detailed static and dynamic test results are given in Section 7.7.

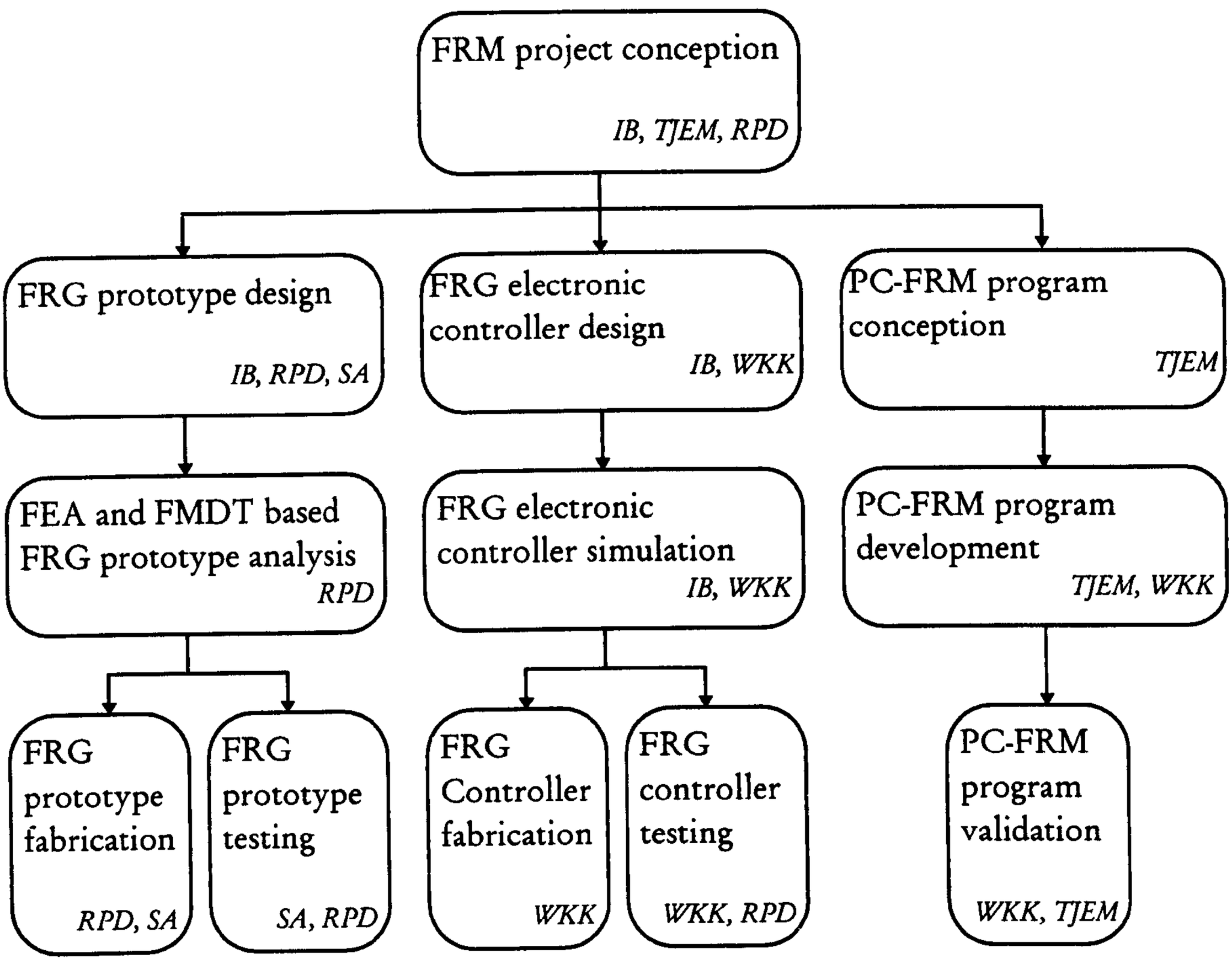

Figure 7.1. An overview of the research program on flux-reversal machine at the SPEED Laboratory.

7.2 Principle of Operation

Fig. 7.2 shows the basic constructional features of the prototype flux-reversal generator. It has a two pole stator and a three pole rotor, both of salient nature. Two arc magnets of opposite polarity are placed adjacent to each other on each stator pole face. The phase winding consists of concentrated coils would around each stator tooth, just as in the case of a switched reluctance machine.

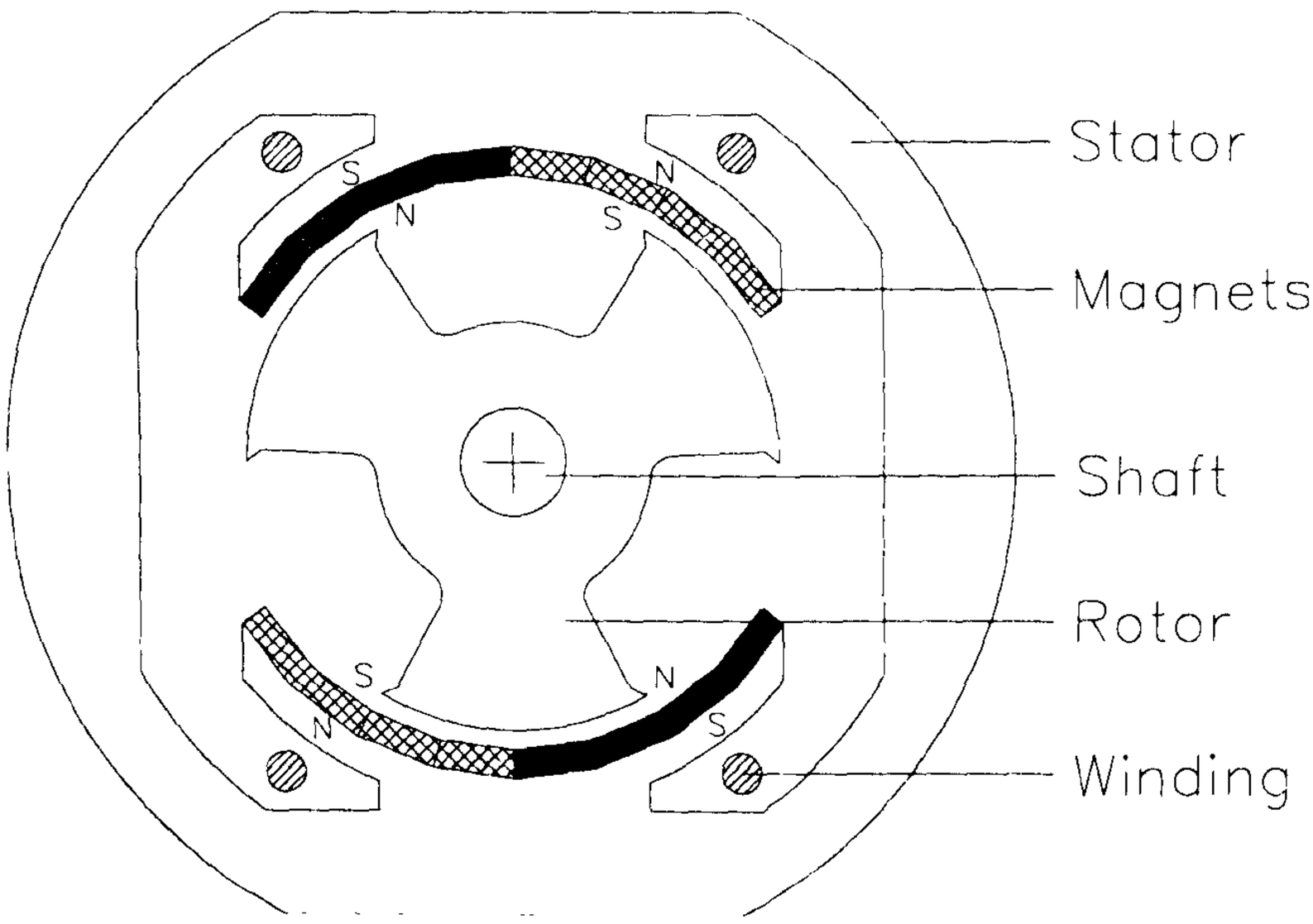

Figure 7.2. The single-phase, 2/3 configuration flux-reversal generator prototype.

Fig. 7.3 is a series of pictures, showing the changes in flux and current in the machine, at four incremental rotor positions over a stroke or an electrical cycle, which is 120° mech. in this particular case. The term 'stroke' derives itself from the switched reluctance terminology, while the term 'electrical cycle' comes from the PM synchronous terminology. Both the terms are equally valid in this case, as an FRM is a combination of the two topologies. The corresponding variation of the phase flux and MMF with rotor position over two electrical cycles, is shown in Fig. 7.4.

The phase flux variation is bipolar (ideally a triangular wave), leading to a flat-topped or trapezoidal generated EMF waveform, and the current is alternating current (ideally squarewave). The *flux reversing nature* of the machine can clearly be seen from Figs. 7.3 and 7.4. The phase flux reverses sign for every electrical cycle of rotor displacement (i.e., one rotor pole-pitch).

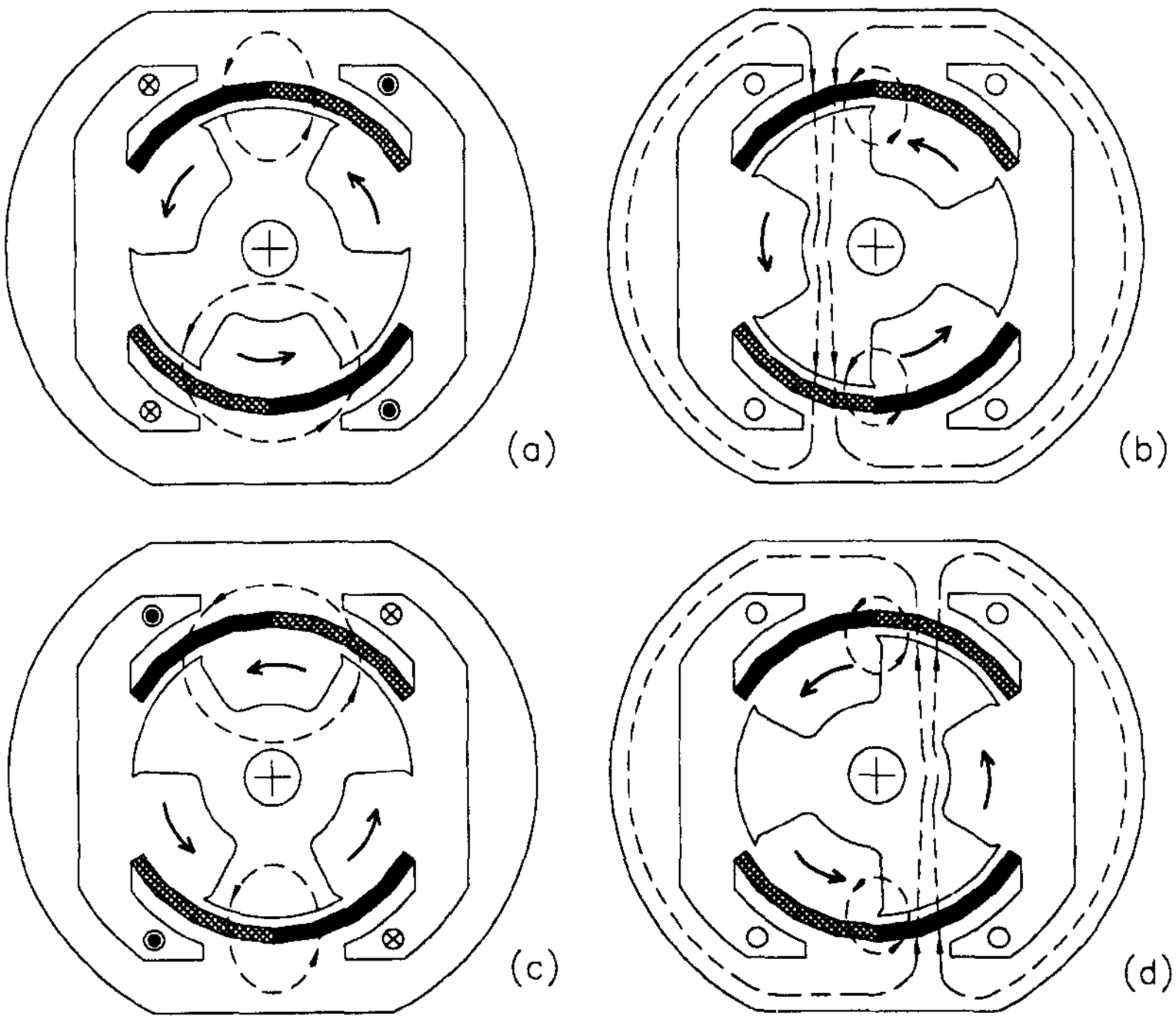

Figure 7.3. The principle of operation of the flux-reversal machine.

The principle of operation of the flux-reversal machine can be explained with the help of Figs. 7.3 and 7.4. In Fig 7.3, (a) is an equilibrium position, where the flux set up by the magnets circulates entirely within each stator pole and there is no flux in the stator back-iron. No flux links the coils in this position (point (a) in Fig. 7.4). In (b), the rotor is displaced by 30° counter-clockwise, so that the rotor poles overlap one or other of the magnets. The flux now passes through the coils and the back-iron and the phase flux is maximum at this position (point (b) in Fig. 7.4). In (c), the rotor is at a second equilibrium position, displaced from the first one by 60°, where again there is no flux in the stator back-iron and no flux linking the coils (point (c) in Fig.

7.4). A further displacement of 30° in the counter-clockwise direction leads to the position shown in (d), where phase flux is maximum in the direction opposite to the one shown in (b) (point (d) in Fig. 7.4). The linear bipolar variation of phase flux leads to a squarewave generated EMF. Applying Faraday's law, it can be seen from Fig. 7.3 that the EMF is maximum at (a), negative maximum at (c) and zero at (b) and (d). Based on the foregoing discussion, the following conclusions can be drawn regarding the operation of an FRM:

- Like the PMM, the FRM works on the principle of variable flux-linkage inducing an EMF that interacts with an alternating armature current.
- Although the field excitation is provided by the permanent-magnets, the flux-linkage of the armature windings is modulated by the variation of magnetic circuit reluctance as the rotor rotates, in such a way that a bipolar EMF is induced without rotating magnets.

7.3 Flux-MMF Diagram Based Comparison

In order to be able to evaluate the capabilities of the FRM, it is important to compare its torque producing mechanism and operational characteristics with other types of brushless machines in its class. In this section, such a comparison is made between the SRM, the DSPMM, the brushless DC machine (BLDCM) and the FRM, using the flux-MMF diagram. Fig. 7.4 shows the ideal variation of phase flux and MMF with rotor position for four types of brushless machines used in the comparison. Fig. 7.5 shows the flux-MMF diagram for each machine type plotted using the variation of phase flux and MMF shown in Fig. 7.4. Note that the same amount of net phase flux and MMF variation over a stroke or an electrical cycle is assumed in each case.

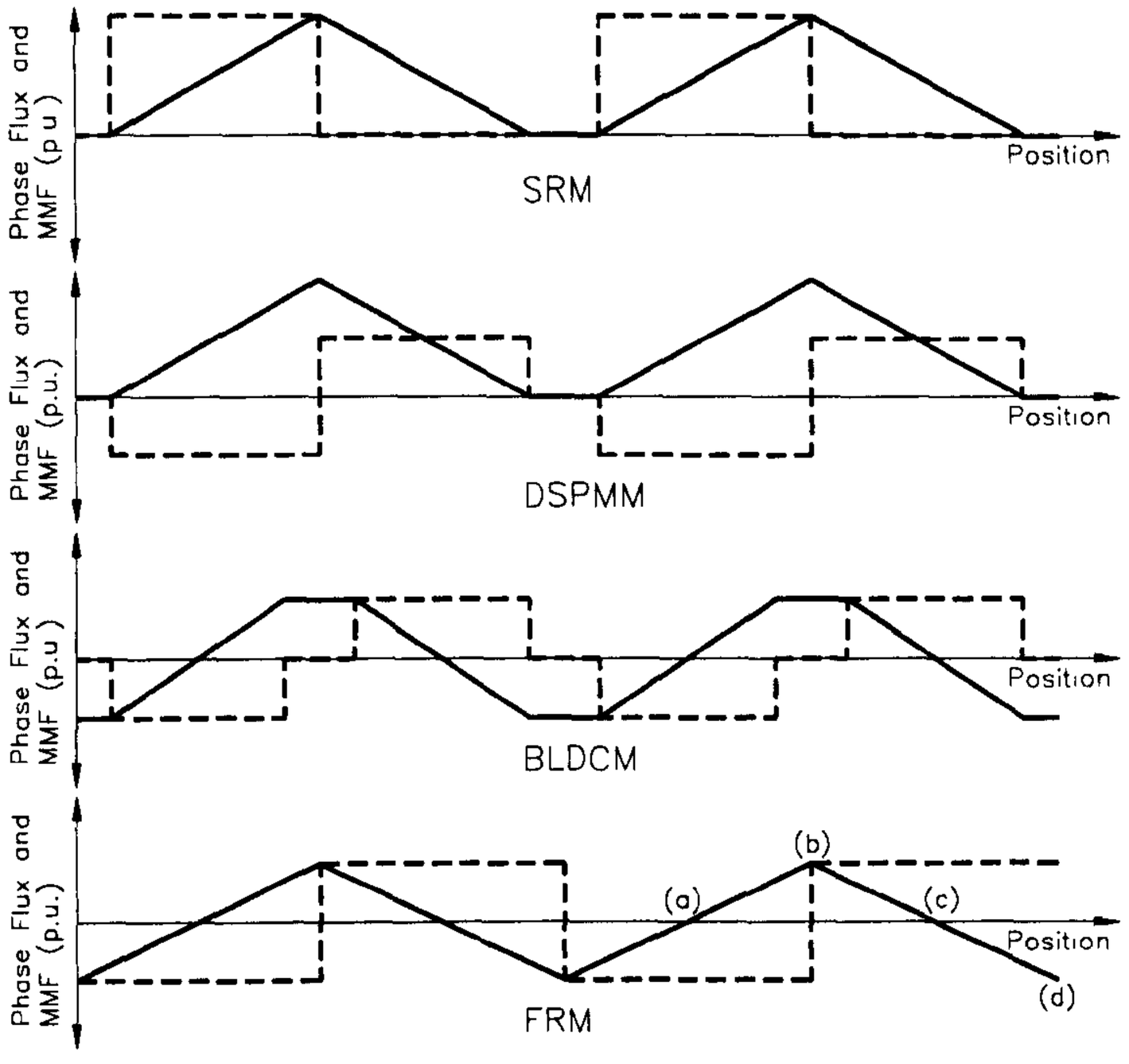

Figure 7.4. The ideal variation of phase flux (solid line) and MMF (dotted line) with position for different types of brushless machines.

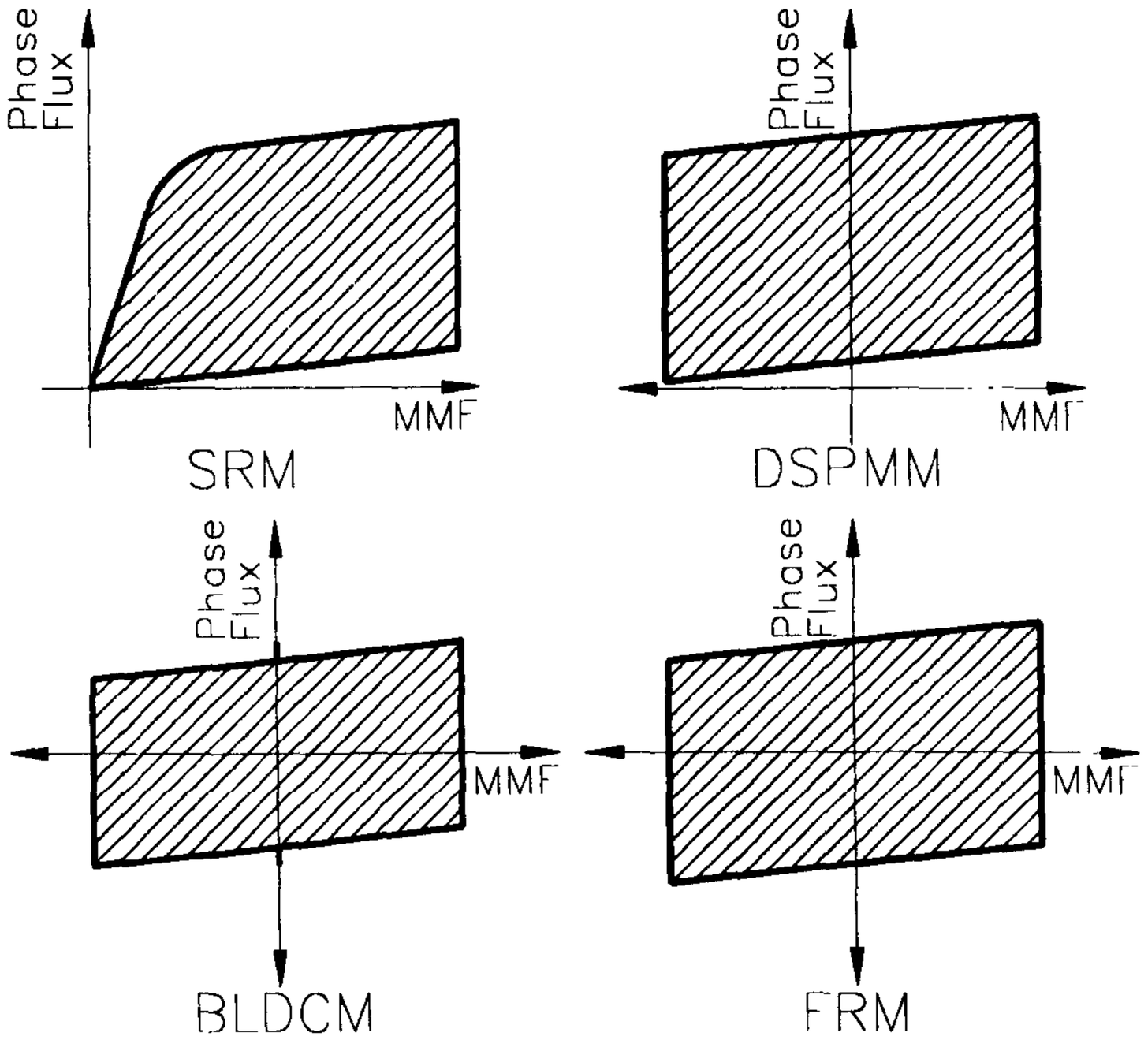

Figure 7.5. Comparison between the SRM, the DSPMM, the BLDCM and the FRM, using the flux-MMF diagram.

The following points can be noted on the comparative evaluation of each of the four machine types:

- The SRM has unipolar phase flux *and* MMF variation while the DSPMM has unipolar phase flux variation and bipolar MMF variation. The BLDCM and the FRM, both have bipolar phase flux *and* MMF variation.
- In the case of SRM, the energy conversion loop is limited to the first quadrant, while in the case of DSPMM, it is limited to the first two quadrants. In the case of BLDCM and FRM, it covers all four quadrants in the flux-MMF plane.

These and some other points with regard to the construction and the operational characteristics, are summarised in Table 7.1.

Table 7.1. Comparison between the FRM and the other three brushless machines.

Design Issue	SRM	DSPMM	BLDCM	FRM
Phase flux variation	Unipolar	Unipolar	Bipolar	Bipolar
MMF variation	Unipolar	Bipolar	Bipolar	Bipolar
Energy conversion loop	First quadrant only	First and second quadrant	All four quadrants	All four quadrants
PMs	No PMs	PMs in stator back iron	PMs on the rotor	PMs on the stator tooth faces
High speed capability	Limited by time constant	Limited by time constant	Limited by PM mountings	Limited by time constant
Rotor inertia	Low	Low	High or medium	Low

7.4 FRM Configurations

Although the FRM shown in Fig. 7.2 is a single-phase 2/3 configuration, many other configurations are possible with regard to the number of phases, and the numbers of stator and rotor poles. Some of these variations are illustrated in this section. Fig. 7.6 shows the same configuration as Fig. 7.2 captured in the PC-FRM

cross-section editor. PC-FRM is a preliminary CAD program for designing FRMs and the associated drive electronics, developed in the SPEED Laboratory. It is based on the highly successful SPEED software, the PC-BDC, used for designing brushless PM motors and drives, and it uses the same graphical user interface and file-handling routines as PC-BDC. The PC-FRM has a 'dynamic analysis' option which carries out design calculations and generates an 'output design sheet' containing a detailed list of design parameters, just as in the case of PC-BDC. A sample of the output waveforms generated using PC-FRM, for the FRM of Fig. 7.6, is shown in Fig. 7.7.

A single-phase 2/3 configuration has some advantages, such as a low device count for the power electronics controller and a low frequency of flux-reversals per revolution. It also has certain limitations such as an unbalanced magnetic circuit and a high level of noise and vibration arising out of it. In the light of these advantages and disadvantages, it is interesting to consider some other FRM configurations such as a two-phase 4/6 and a three-phase 6/8, shown in Figs. 7.8 and 7.9, respectively.

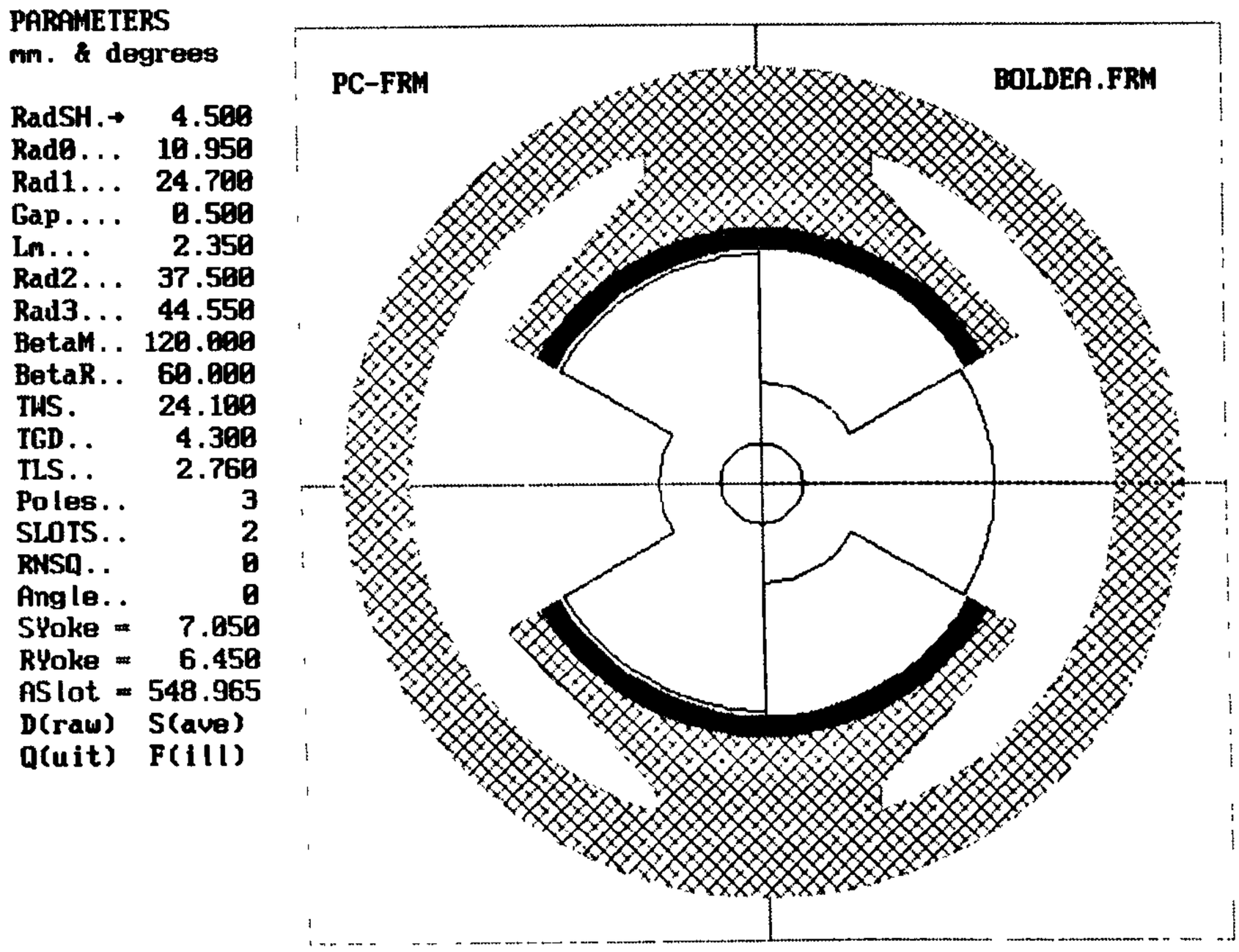

Figure 7.6. The PC-FRM cross-section editor showing a 2/3 single-phase configuration.

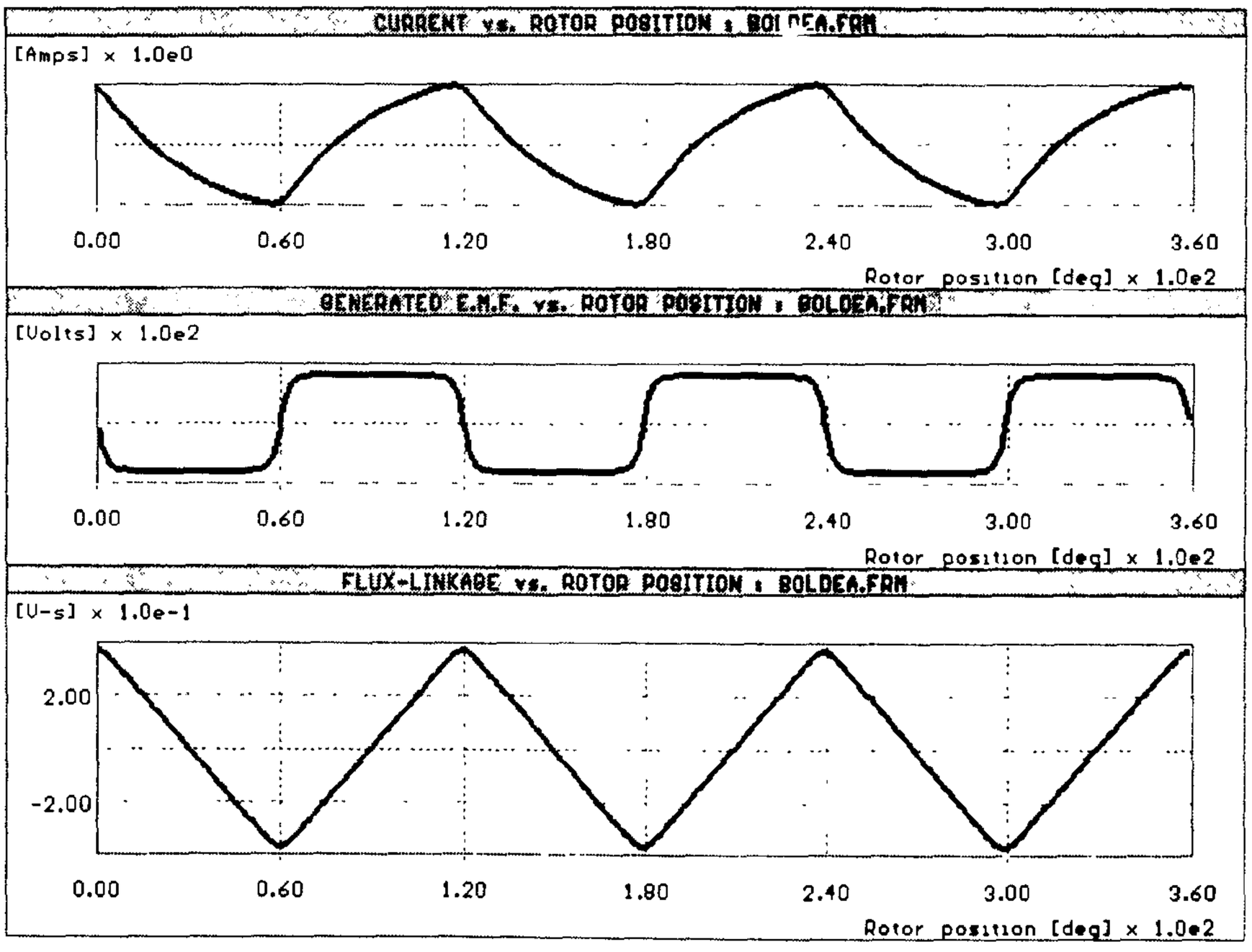

Figure 7.7. The output waveforms generated in PC-FRM for the FRM of Fig. 7.6.

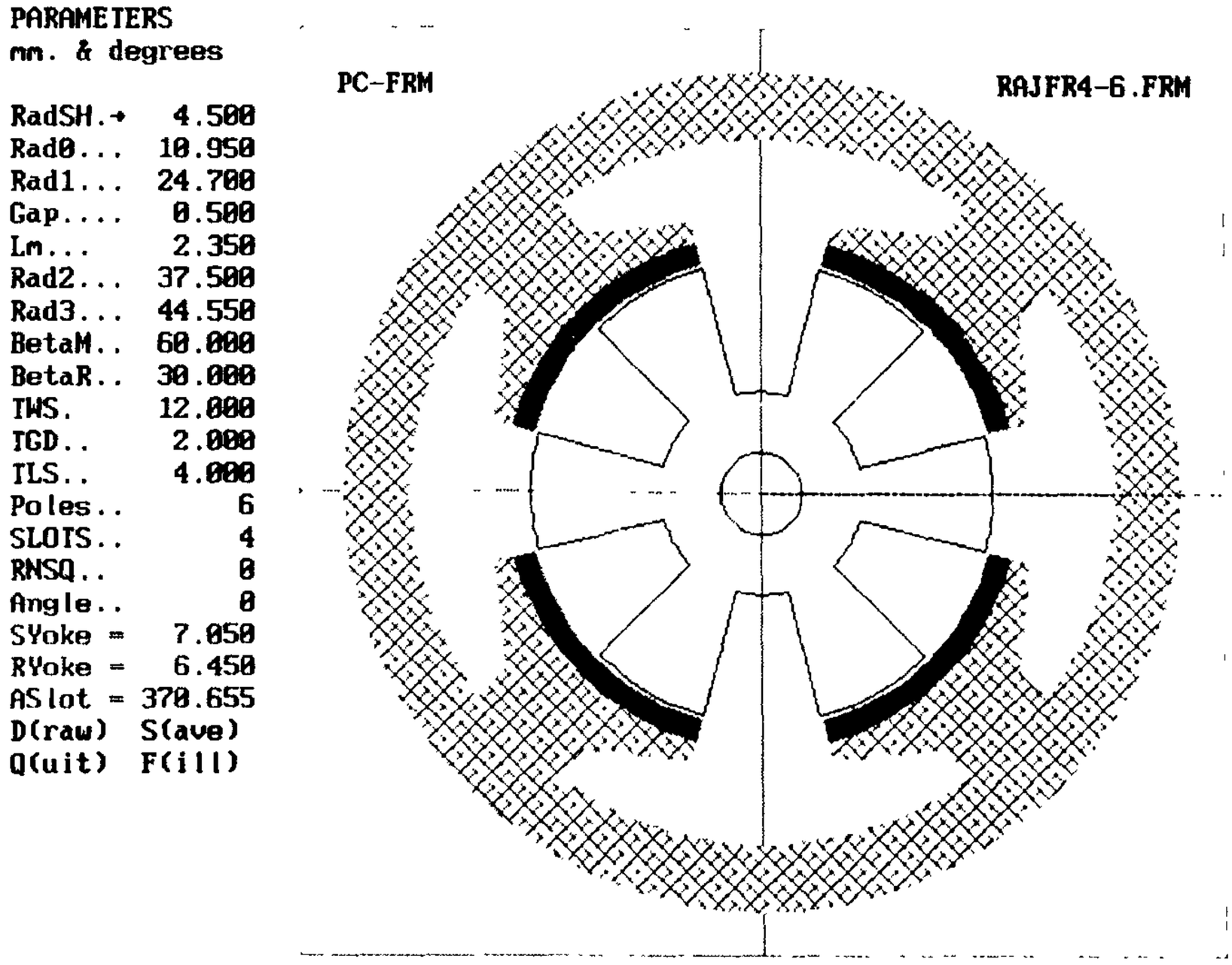

Figure 7.8. A 4/6 two-phase flux-reversal machine configuration.

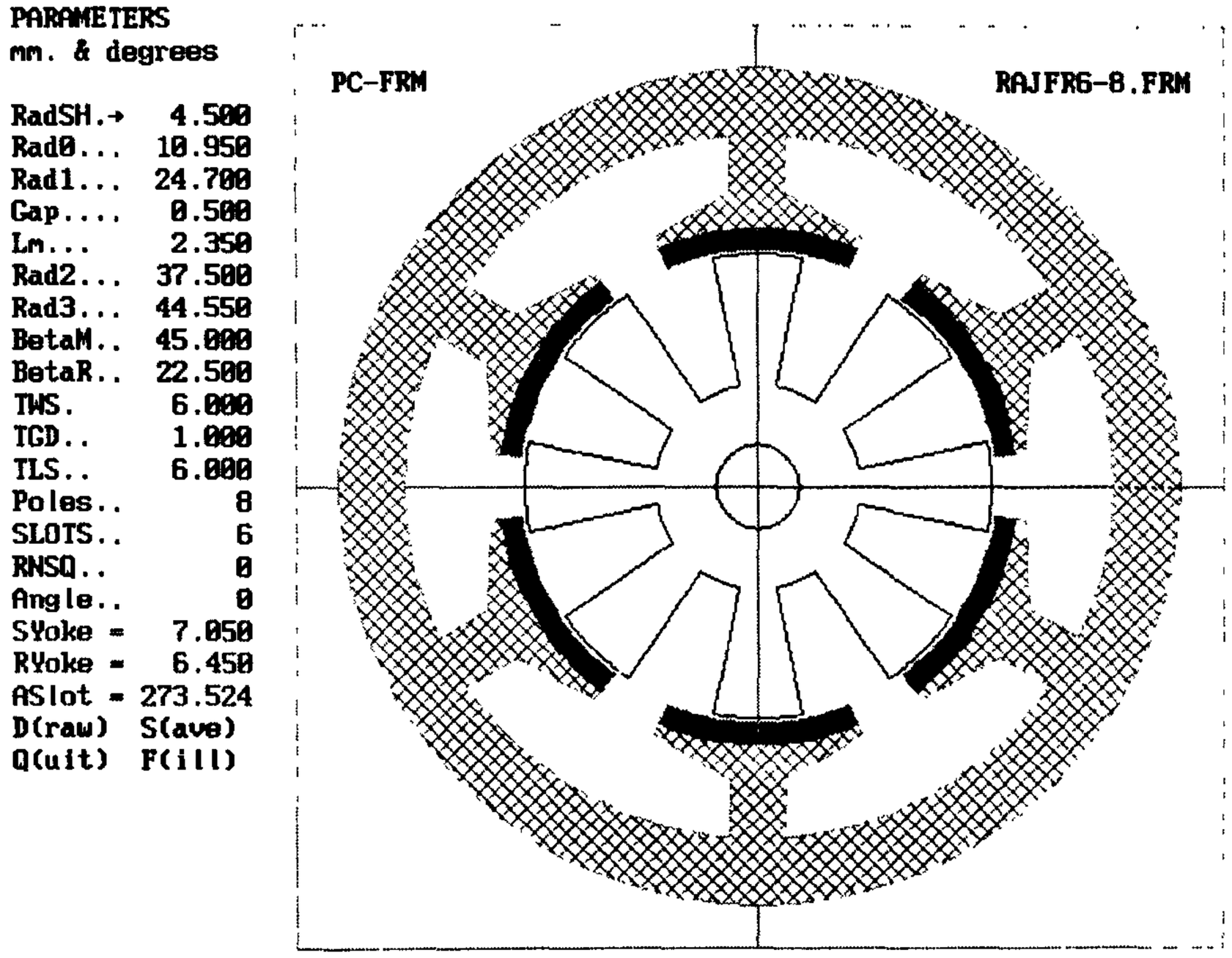

Figure 7.9. A 6/8 three-phase flux-reversal machine configuration.

The disadvantage in the case of multi-phase configurations is that they need a higher number of devices for the power electronic controller as compared to a single-phase configuration. On the other hand, they have a balanced magnetic circuit leading to a lower level of cogging torque, noise and vibration. While the single-phase configuration is better suited for generator application, the multi-phase configurations are better suited for motor applications.

7.5 FRG Design and Analysis

7.5.1 FRG Design

The principal objective was to design and construct a 'proof-of-principle' prototype flux-reversal machine to see if any of its apparent advantages were of practical value. It was decided to build a single-phase 2/3 configuration, low-cost,

high-speed, flux-reversal generator with a simple electronic voltage controller. Fig. 7.2 shows the stator and the rotor lamination geometry details.

The stator design was based on an existing two-pole universal motor stator. The original design had a smooth round stator bore. To accommodate the magnet poles made up of block magnets, it was necessary to modify the stator tooth faces by giving slight cuts to create a series of flat surfaces. The rotor design was optimised using a combination of finite-element and analytical methods, to create a new three-pole variable reluctance rotor. The magnets used were Samarium-Cobalt block magnets (B_r = 0.85 T) with four blocks making up a single pole arc of 60°, as shown in Fig. 7.2. The air-gap was designed to be 0.5 mm to obtain a reasonable permeance coefficient of 4.9. It was decided to use the same end-shields as those from the existing universal motor. A new shaft was designed to suit the FRG rotor and the end-shields. The mechanical drawings for the FRG components are enclosed in Appendix D.

An important parameter in designing flux-reversal machines is the fringing coefficient, K_f, which is the ratio of maximum flux linking a stator phase to magnet flux (7.1). An accurate estimate of K_f was needed in designing the prototype and hence FEA was used to obtain a value of K_f = 0.45.

$$K_f = \frac{\Phi_{ph}}{\Phi_m} = \frac{\Phi_{ph}}{A_m B_m} = \frac{\Phi_{ph}}{A_m B_r / 1+(g\mu_{rec}/l_m)} \tag{7.1}$$

The number of turns per phase, N_{ph}, was obtained using (7.2), which is derived specifically for the 2/3 configuration from the Faraday's law assuming a linear variation of phase flux with rotor position.

$$E = -\omega N_{ph} \frac{d\Phi_{ph}}{d\theta} = -\omega N_{ph} \frac{2K_f \Phi_m}{\pi / 3} \tag{7.2}$$

A simple electronic voltage controller was designed to rectify and regulate the generated AC voltage, to obtain a constant DC output voltage over a wide speed range. Certain design specifications, such as the generator speed and voltage range,

and the output DC voltage value, were based on the existing automotive generator specifications. Table 7.2 gives a summary of the important FRG design specifications. Further details on the FRG prototype design procedure are given in [97].

Table 7.2. Prototype FRG design specifications.

Stator lamination material	Newcor800, 0.65 mm thick
Rotor lamination material	Losil 400/50, 0.5 mm thick
Magnet material	$SmCo_5$
Length of magnet	2.45 mm
Magnet B_r	0.85 T
Stator outer diameter	89.10 mm
Stator lamination inner diameter	55.30 mm
Stator bore diameter	50.40 mm
Length of air-gap	00.50 mm
Stack Length	40.00 mm
Rotor outer diameter	49.40 mm
Rotor pole length	13.75 mm
Number of turns per pole	224
Copper wire gauge	AWG 23
Generator speed range	900 to 9000 rpm
Generated peak AC voltage range	30 to 300 Volts
Output DC voltage of the controller	14 Volts

7.5.2 FRG Analysis Using the FMDT

The Flux-MMF Diagram Technique was used to analyse the prototype FRG performance in terms of the following characteristics.

- Electromagnetic torque ripple
- Cogging torque ripple
- Phase inductance
- Phase flux variation
- Generated EMF

Fig. 7.10 shows the prototype FRG flux-plot at no-load, obtained from the finite-element analysis. Based on the procedure described in Chapters 1 and 2, the flux-

MMF diagram for the phase was constructed as shown in Fig. 7.11, and the electromagnetic torque ripple was predicted from it as shown in Fig. 7.21.

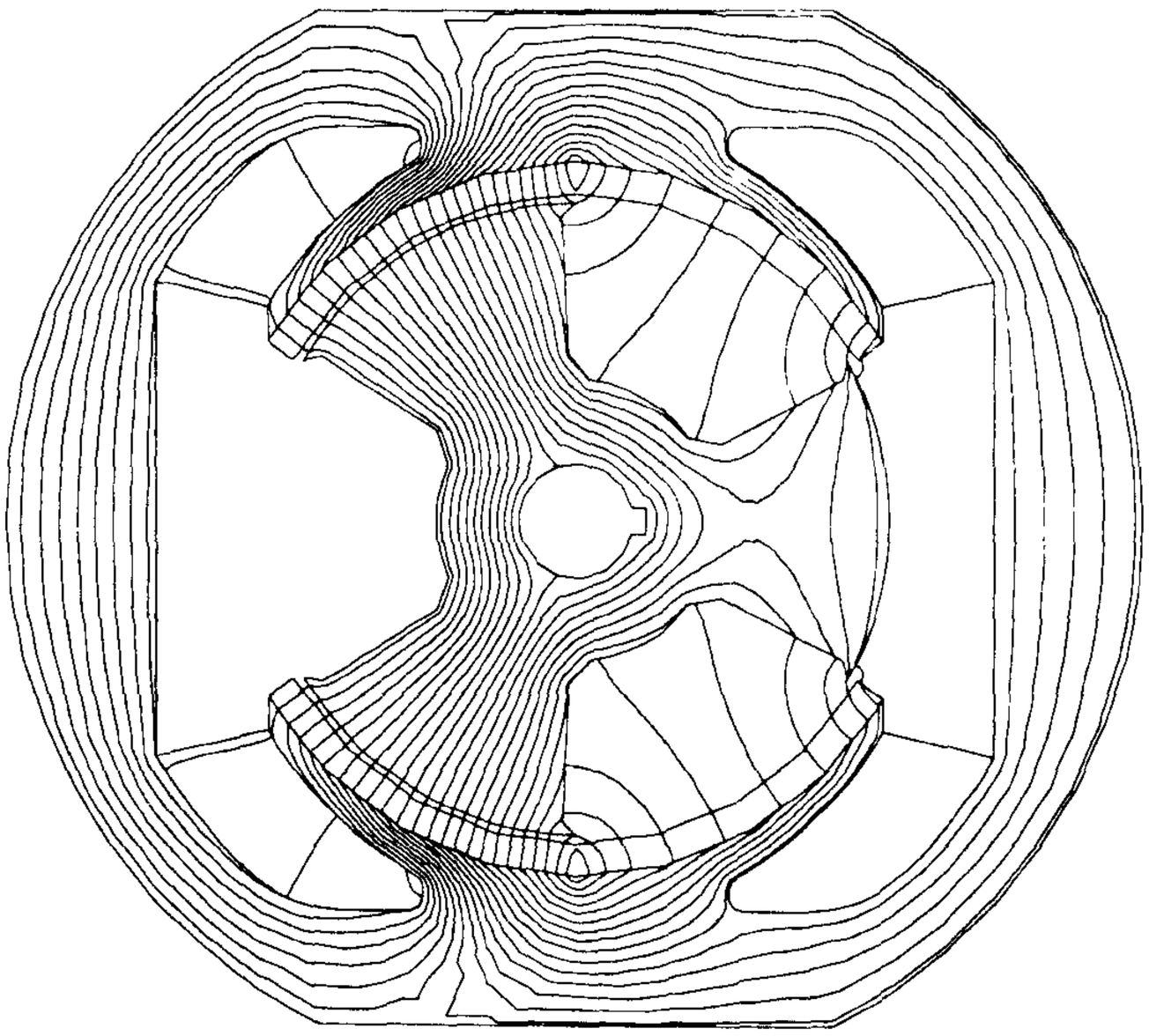

Figure 7.10. The prototype FRG flux-plot at no-load.

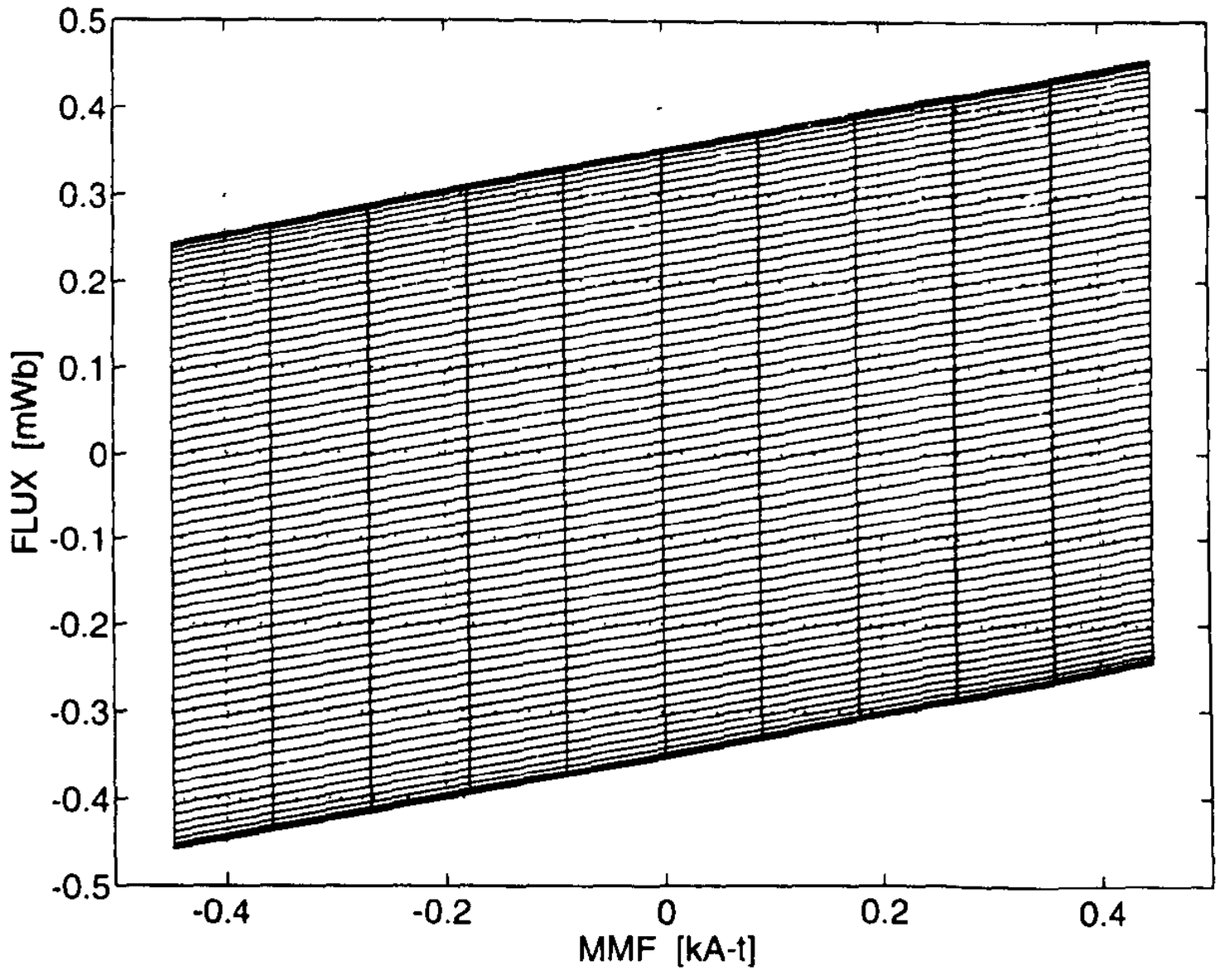

Figure 7.11. The phase flux-MMF diagram for the prototype FRG at 0, 0.2, 0.4, 0.6, 0.8 and 1.0 A peak currents .

The flux-MMF diagram and the phase torque characteristics of a single-phase FRM are very similar to those of a PM brushless DC motor as shown in Chapter 2, Figs. 2.9 and 2.10 respectively. This confirms the fact that the FRM, in its multi-phase configuration, can be a brushless PM motor.

The cogging torque ripple was predicted by using the method described in Chapter 3. Since this is a fractional slot-per-pole machine with no symmetry involved, it was necessary to obtain the flux and MMF variation for each of the four magnet poles over a cogging torque period. This is shown in Fig. 7.12. The flux-MMF diagram for one of the poles (pole1) is shown in Fig. 7.13. The total cogging torque ripple obtained from the contribution of each pole is shown in Fig. 7.14. It is interesting to note that while the cogging torque period for each pole contribution is 120°, the resultant cogging torque period is only 60°.

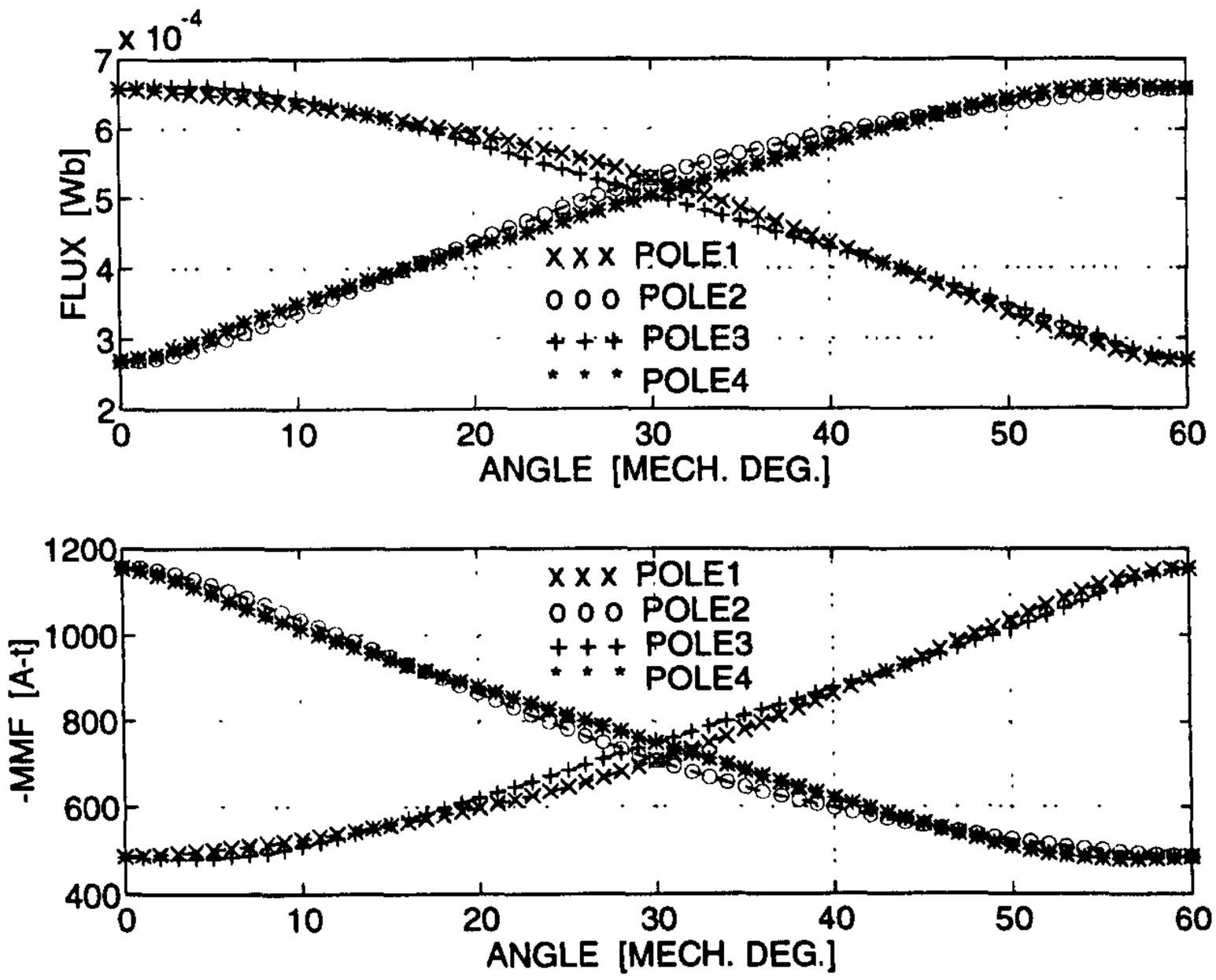

Figure 7.12. The flux and MMF variation for each magnet pole. The poles are numbered clockwise from the top left-hand corner in Fig 7.2.

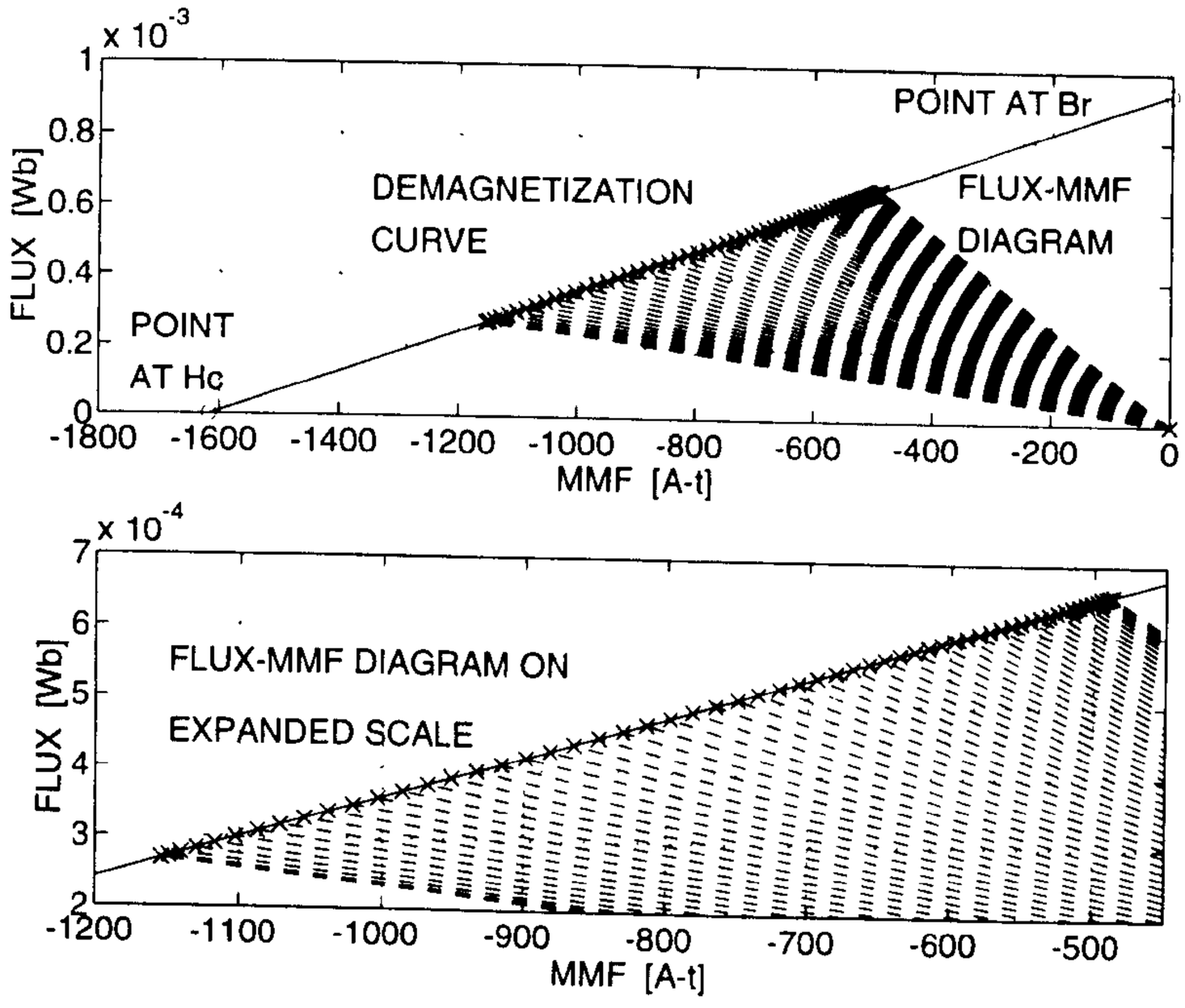

Figure 7.13. Flux-MMF diagram for one magnet pole. The top half shows the flux-MMF diagram for pole1 of the prototype FRG. The bottom half shows the same on an expanded scale.

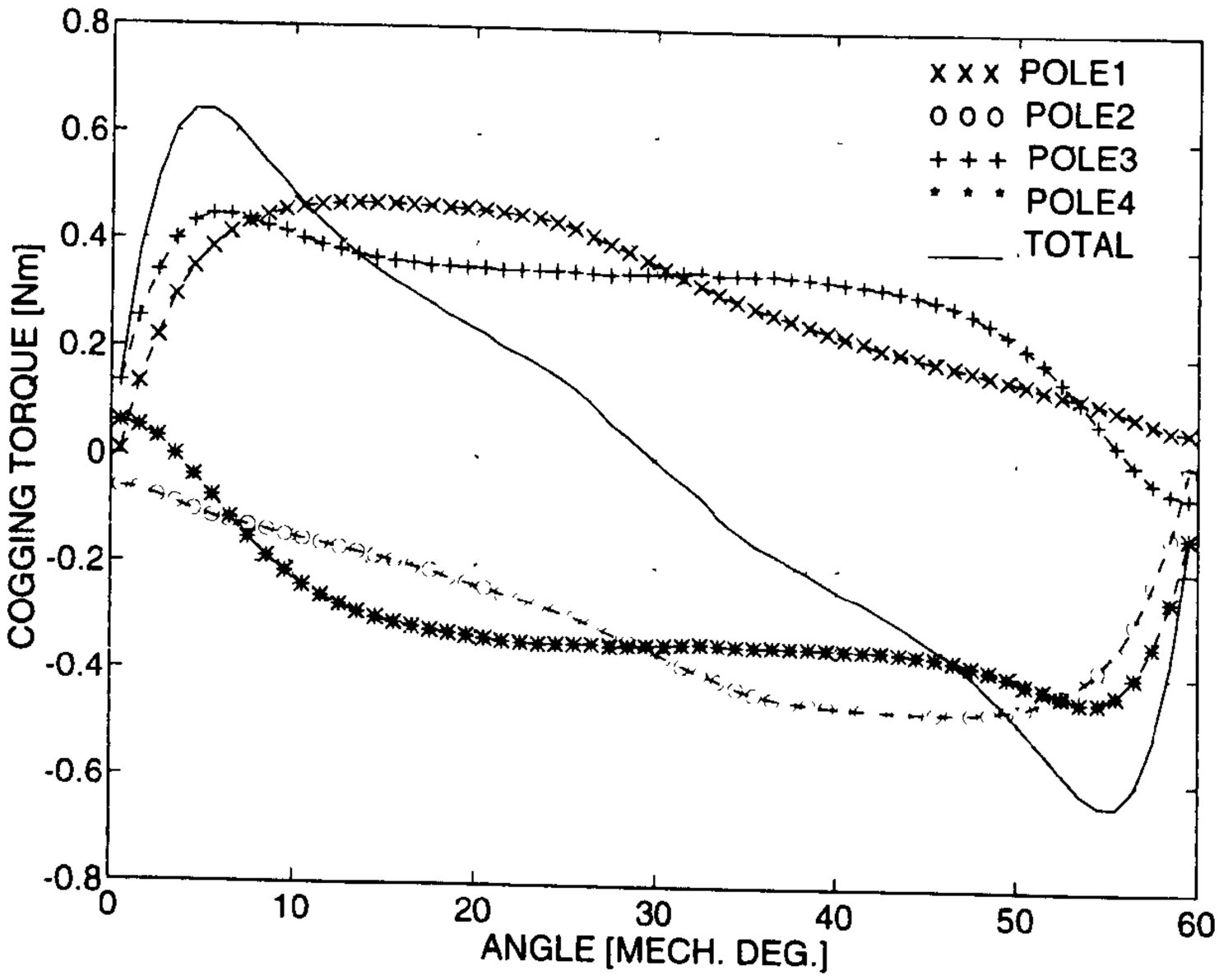

Figure 7.14. The predicted cogging torque ripple for each magnet pole and for the entire machine.

In an electrical machine, in general, the phase inductance is a function of rotor position and phase current. For a given rotor position, the incremental inductance is defined as the ratio of incremental change in phase flux-linkage caused by the incremental change in phase current.

$$L = \frac{\delta\psi}{\delta i} \tag{7.3}$$

Using this definition, the variation of phase inductance with rotor position and phase current can be obtained from the flux-MMF diagram. This is done simply by calculating the incremental slopes of the magnetisation curves at each rotor position at different current values. This is shown in Fig. 7.24, which is obtained from the flux-MMF diagram of Fig. 7.11.

Similarly, by applying (7.2), the variation of phase flux and generated EMF with rotor position can be predicted from the flux-MMF diagram. This is shown in Figs. 7.25 and 7.26 respectively.

7.6 FRG Construction

7.6.1 Prototype Fabrication

The FRG stator was built from an existing universal motor stator. The universal motor was a lawn-mower motor manufactured by Black & Decker Ltd. It was necessary to use the wire EDM process to cut the stator and the rotor laminations, in order to produce a superior surface finish and to maintain accurate tolerances. Fine cuts were given on the stator tooth faces to obtain an array of flat surfaces so as to accommodate the block magnets. Fine cuts were also given at the tooth edges to obtain an accurate pole arc of 120°. The variable reluctance rotor laminations were

cut from a stack of lamination material, and the rotor was assembled by mounting the stack on a mild steel shaft with an suitable nut and washer arrangement.

Assembling the stator and the magnets together turned out to be the most critical process. The magnets used were block magnets made of sintered Samarium-Cobalt material, manufactured by Swift-Levick Magnets Ltd. Each magnet pole was made up of four blocks and these were glued onto flat surfaces created on the stator tooth faces, using Locktite 326 anaerobic superglue. Since this was done manually, there were some imperfections in the relative placement of magnet blocks. This resulted in some distortion in the flux distribution as reflected in the experimental measurements shown in Section 7.7.

The 10-turn search coils, used for sensing flux, and the main stator coils, were wound on each stator pole in that order. The main coil on each stator pole was made up of two coils, as shown in Fig. 7.15. This flexibility was incorporated in order to obtain different voltage and current ratings for the same rotational speed by connecting these coils in a combination of series or parallel connections. Fine-wire thermocouples were mounted on the winding, magnet and stator back-iron surfaces to measure temperature rise in different parts of the machine.

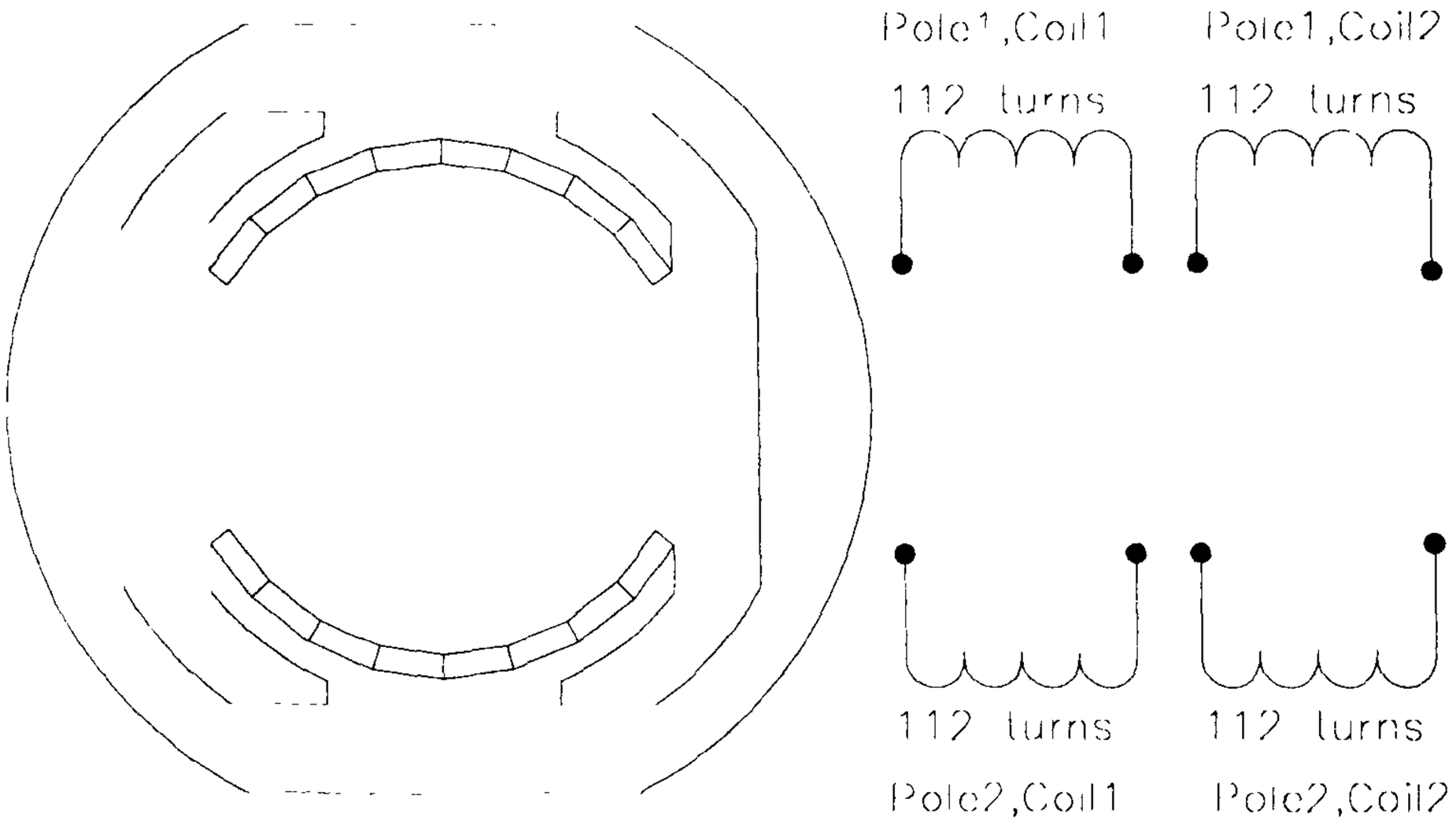

Figure 7.15. Flux-reversal generator prototype coil list.

The next four figures from Fig. 7.16 to Fig. 7.19 show the photographs for various components and sub-assemblies of the prototype FRG.

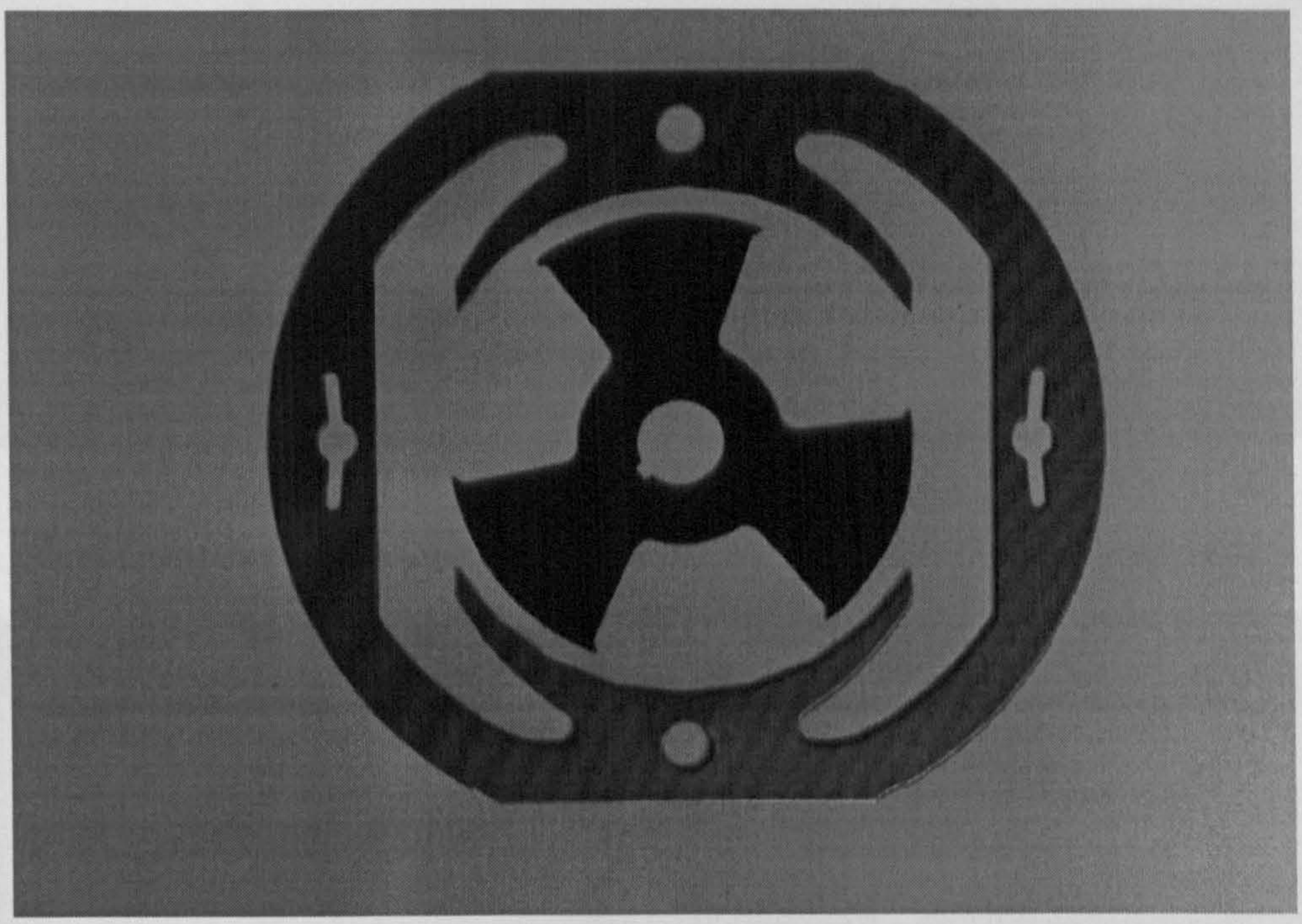

Figure 7.16. Prototype FRG stator and rotor lamination.

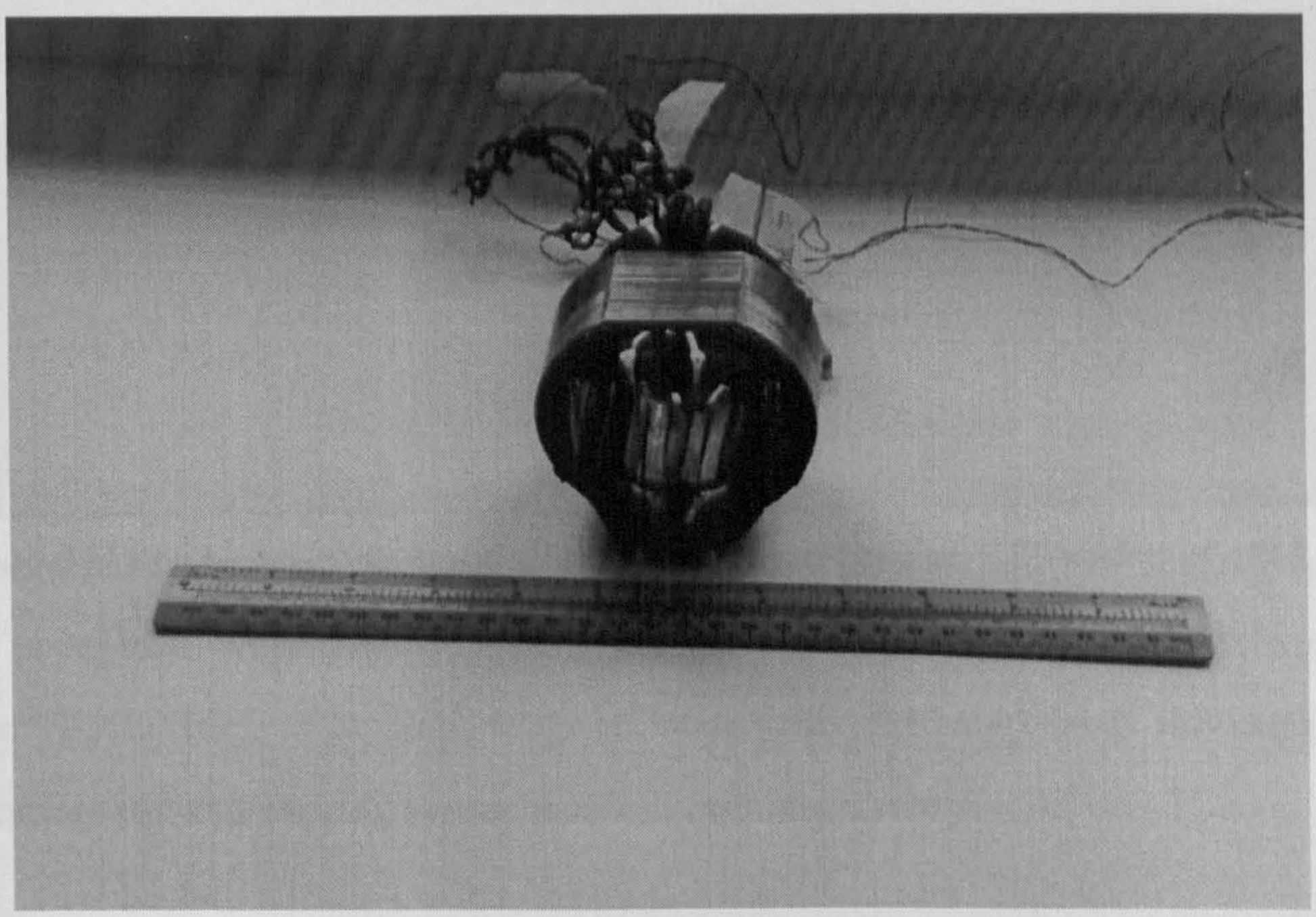

Figure 7.17. Prototype FRG stator assembly with permanent-magnets.

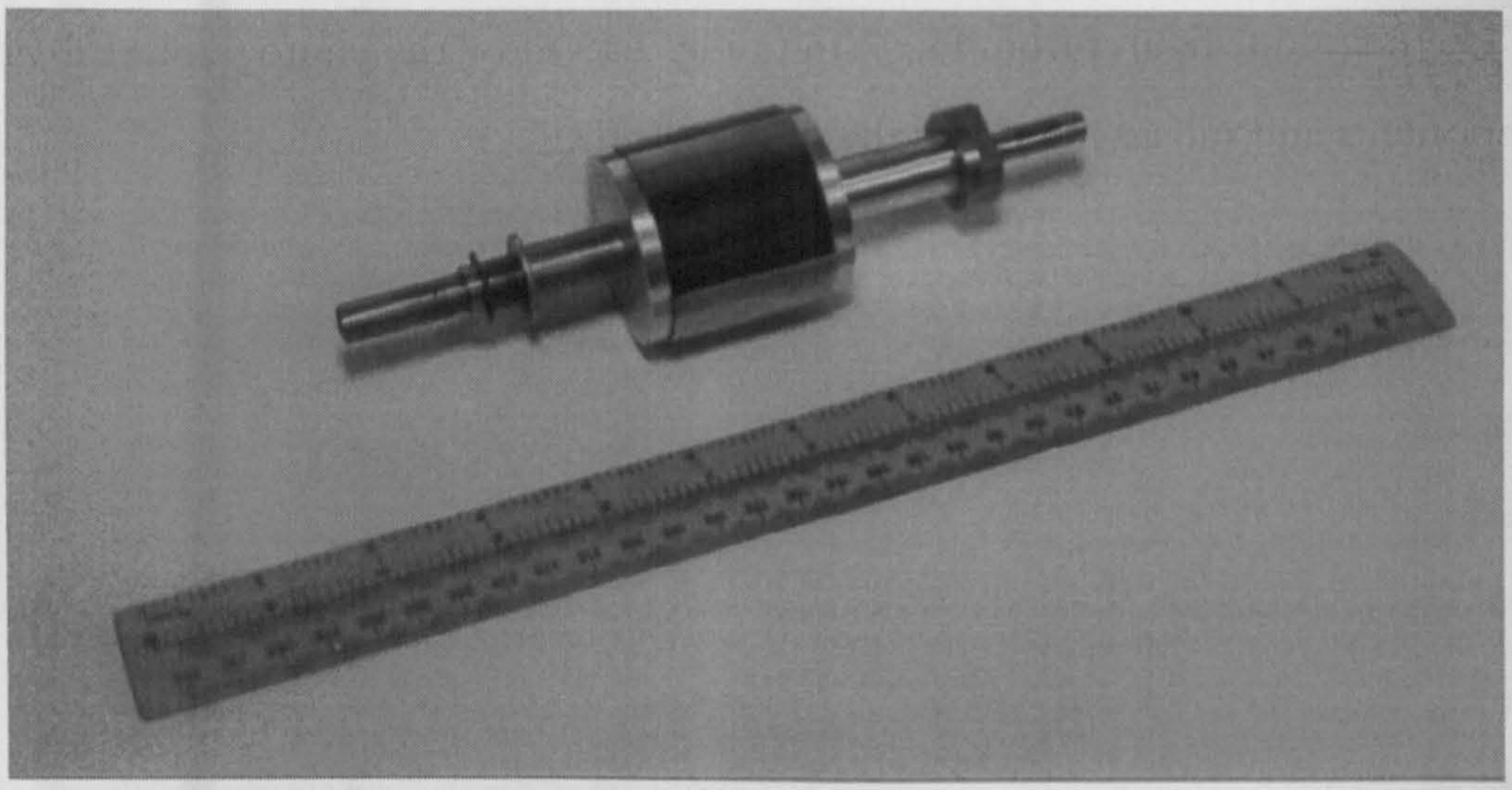

Figure 7.18. Prototype FRG variable reluctance rotor assembly.

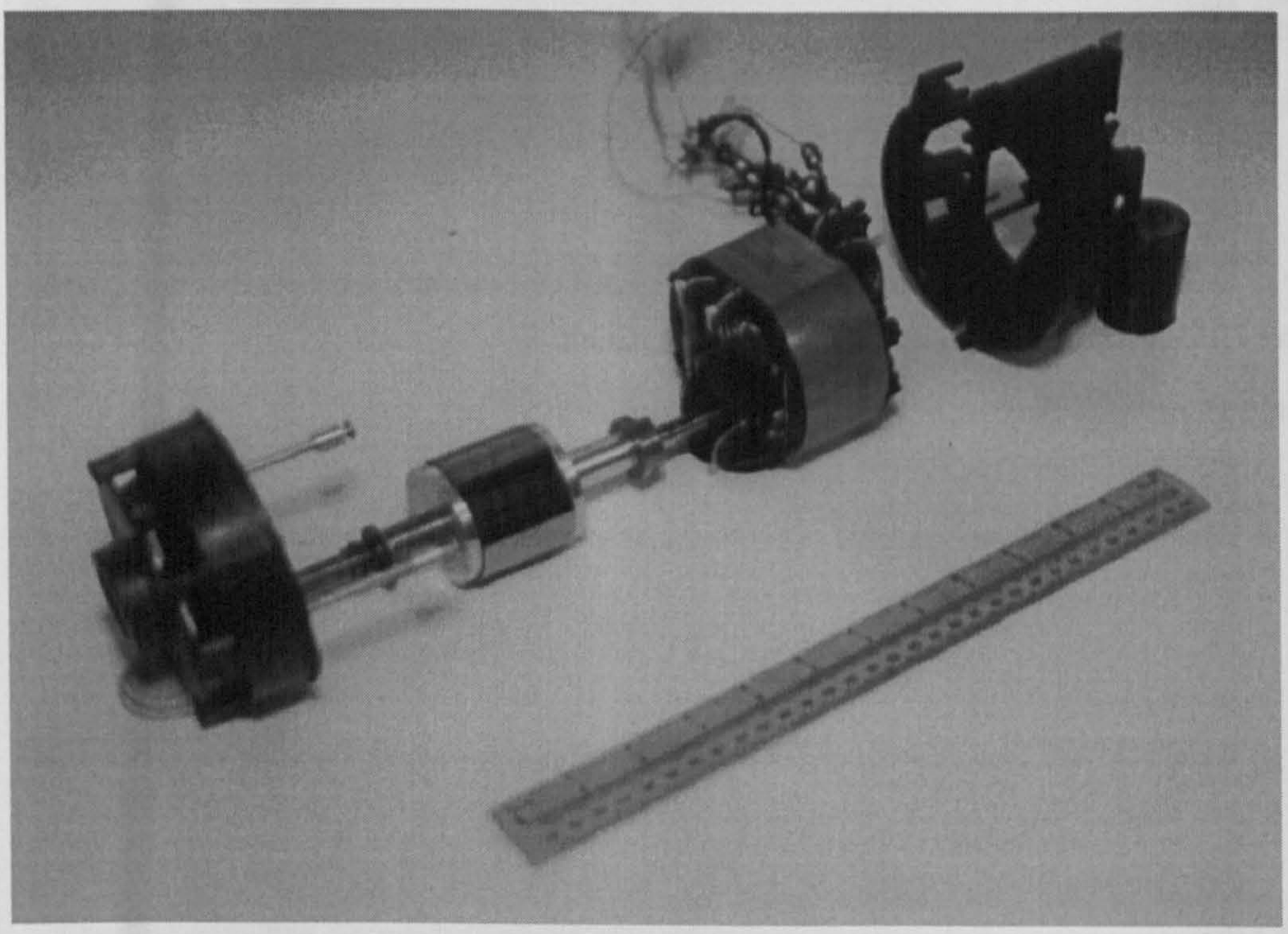

Figure 7.19. Prototype FRG complete assembly showing the stator, the rotor and the end-shields.

7.6.2 Electronic Controller

A simple electronic controller, shown in Fig. 7.20, was built to obtain a regulated DC voltage output from the generated AC voltage over a wide speed range.

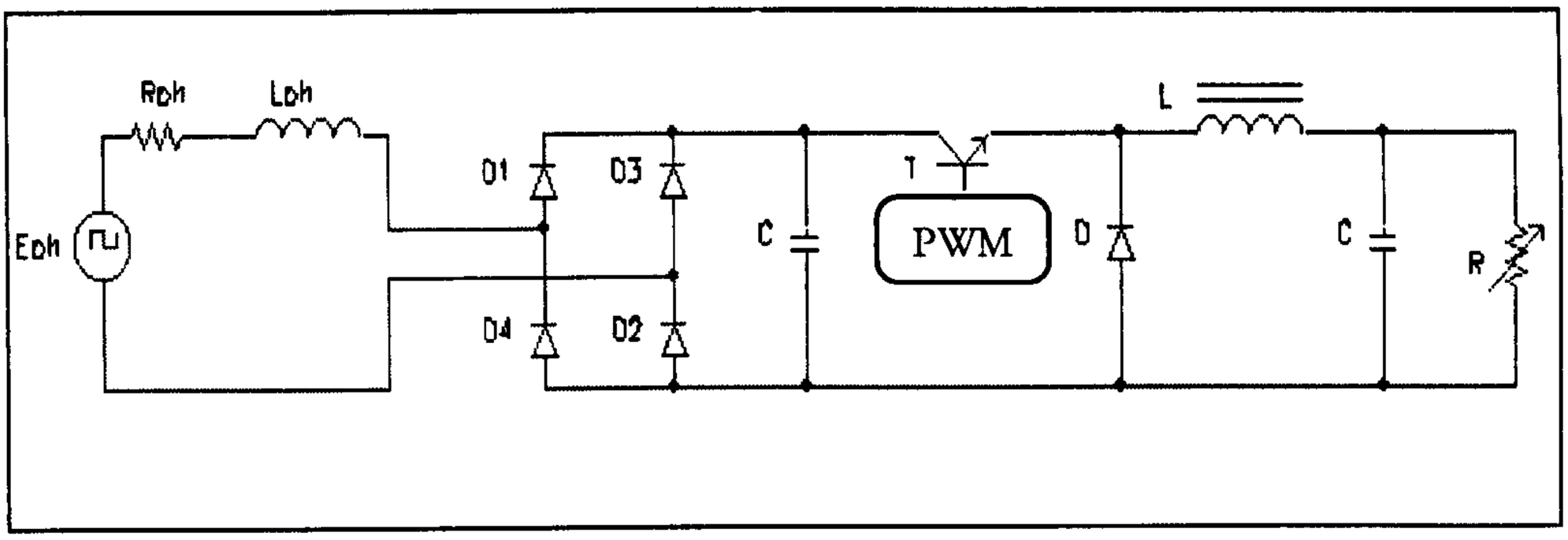

Figure 7.20. The electronic controller built to obtain regulated DC output (*Courtesy of W. K. Kom*).

The controller consisted of a single-phase bridge rectifier and a PWM controlled DC-to-DC converter. The details on the design, fabrication, and testing of the electronic controller and the validation of the PC-FRM calculations for a combined, generator-controller performance, are given in [98].

7.7 Experimental Results

7.7.1 Electromagnetic and Cogging Torque Ripple

The electromagnetic torque ripple at different currents and the cogging torque ripple at no-load, were measured using the static test set-up described in Chapter 2, Section 2.3.3. Figs. 7.21 and 7.22 compare the predicted and the measured electromagnetic and cogging torque ripple curves respectively.

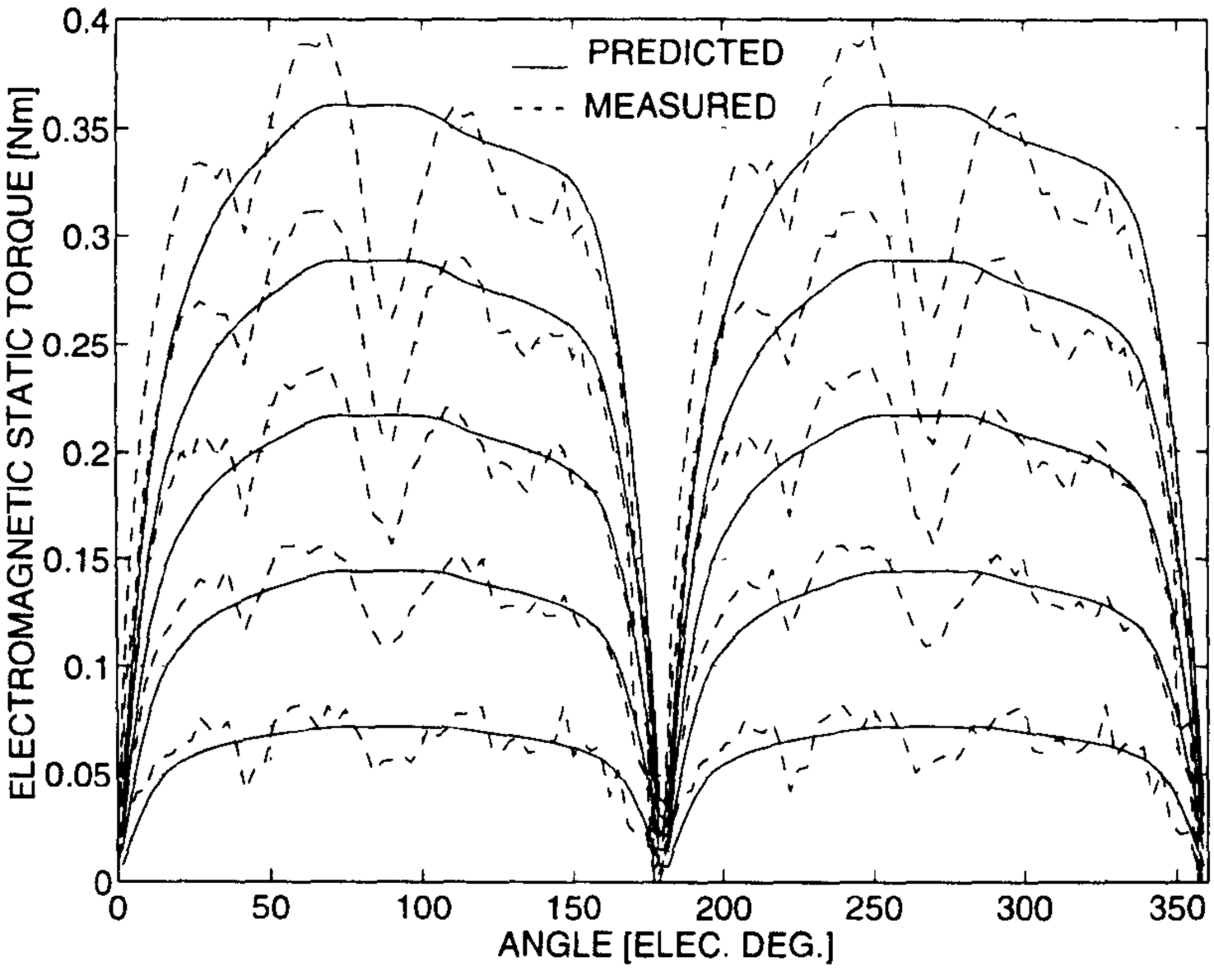

Figure 7.21. The predicted and the measured electromagnetic torque ripple at 0.2, 0.4, 0.6, 0.8 and 1.0 A peak currents.

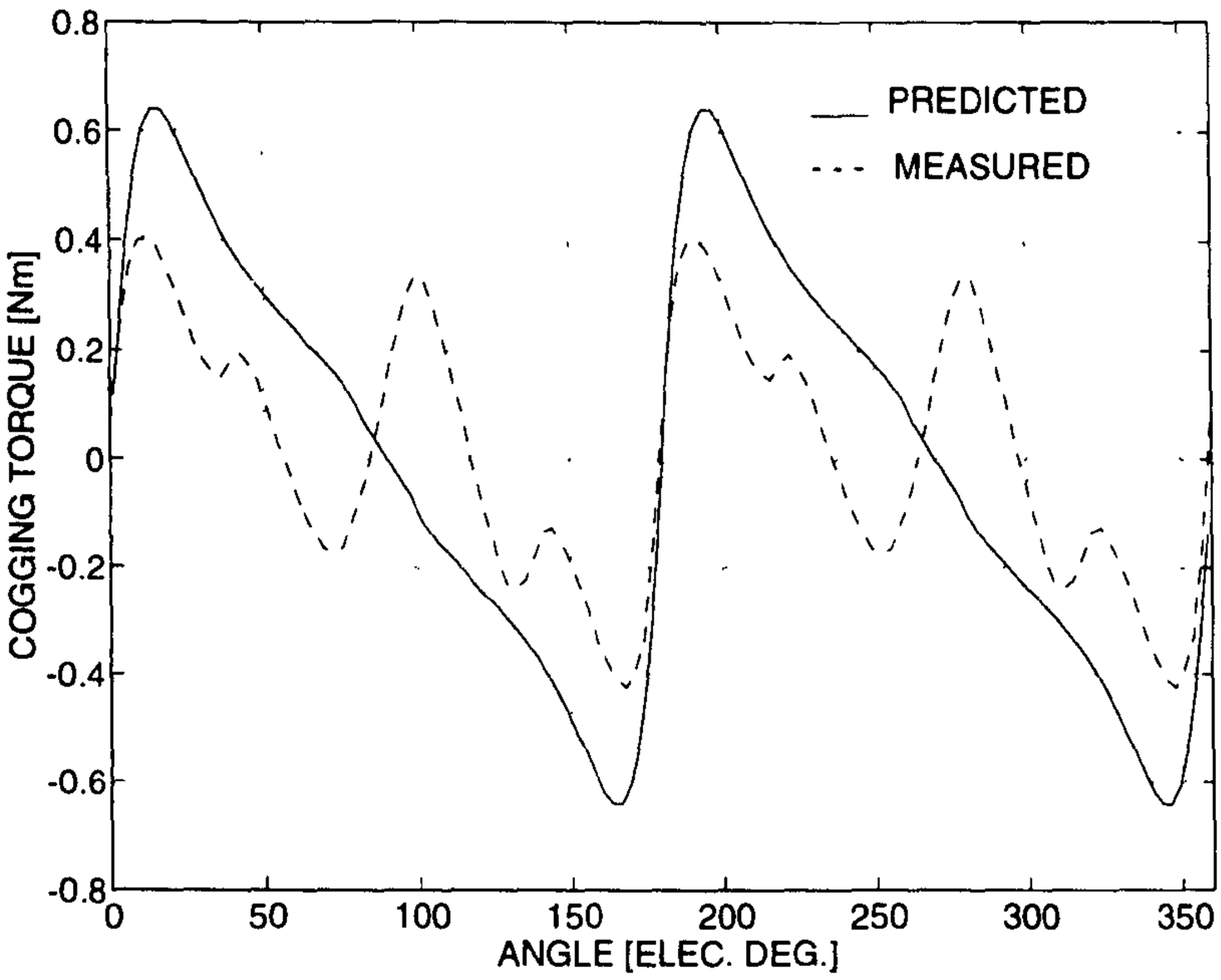

Figure 7.22. The predicted and the measured cogging torque ripple.

Briefly, the set-up consisted of a dividing head driving the machine under test through an in-line torque transducer. The rotor was stepped through 1° increments over half an electrical cycle (60° mechanical). The electromagnetic torque ripple curves were obtained by first measuring the total torque ripple curves at different currents and then subtracting the measured cogging torque ripple from it. The discrepancy between the predicted and measured curves resulted from the fact that certain manufacturing imperfections were developed during fabrication of the prototype. Especially the non-alignment of the adjacent magnet segments, resulted in the localised mismatch. The measured peak cogging torque is 0.41 Nm. This is a fairly large value for a machine of this size. However, among the various possible flux-reversal machine configurations, the 2/3 configuration has the largest amount of cogging torque. The cogging torque can be expected to be much lower for a 4/6 or a 6/8 configuration.

7.7.2 Phase Inductance

Fig. 7.24 compares the predicted and the measured phase inductance variation with position. The measurements were obtained using the static test set-up and Fig. 7.23 illustrates the method involved.

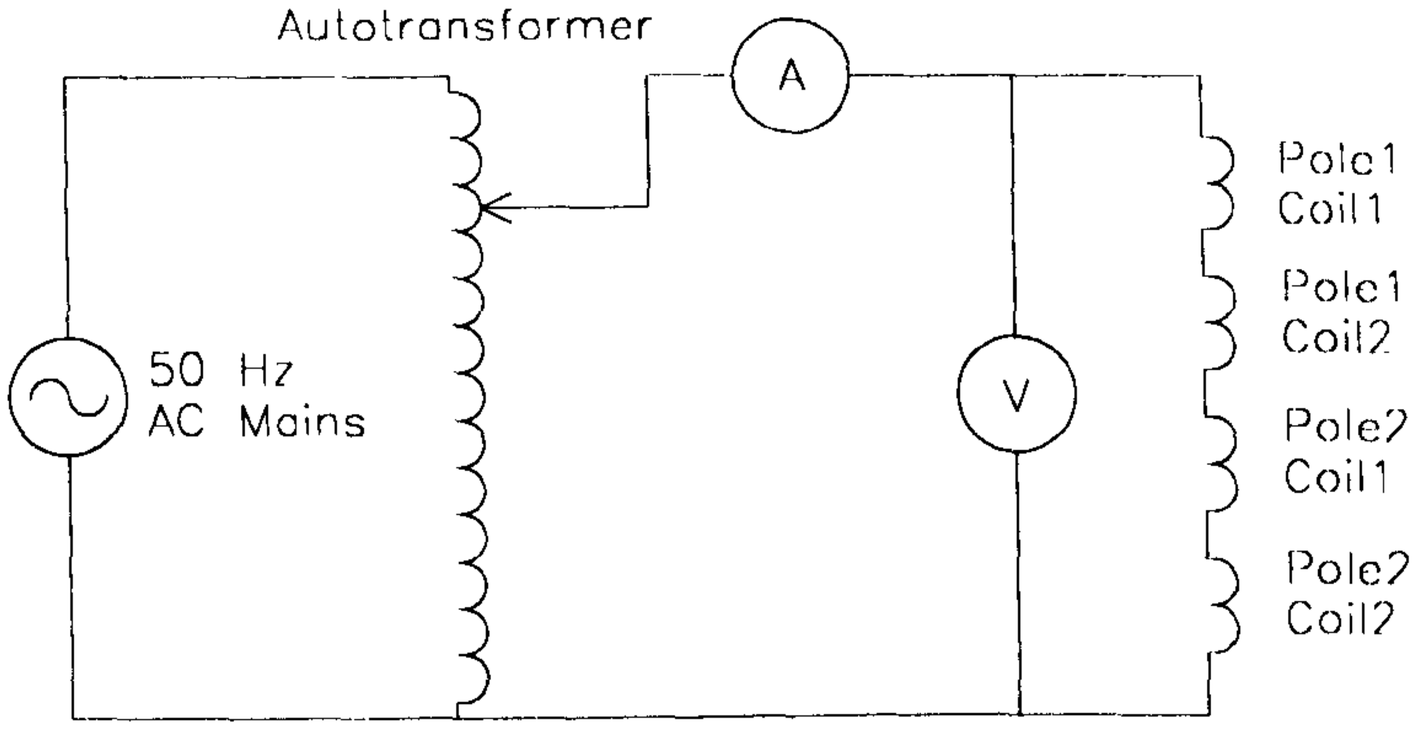

Figure 7.23. Test set-up used for phase inductance measurements.

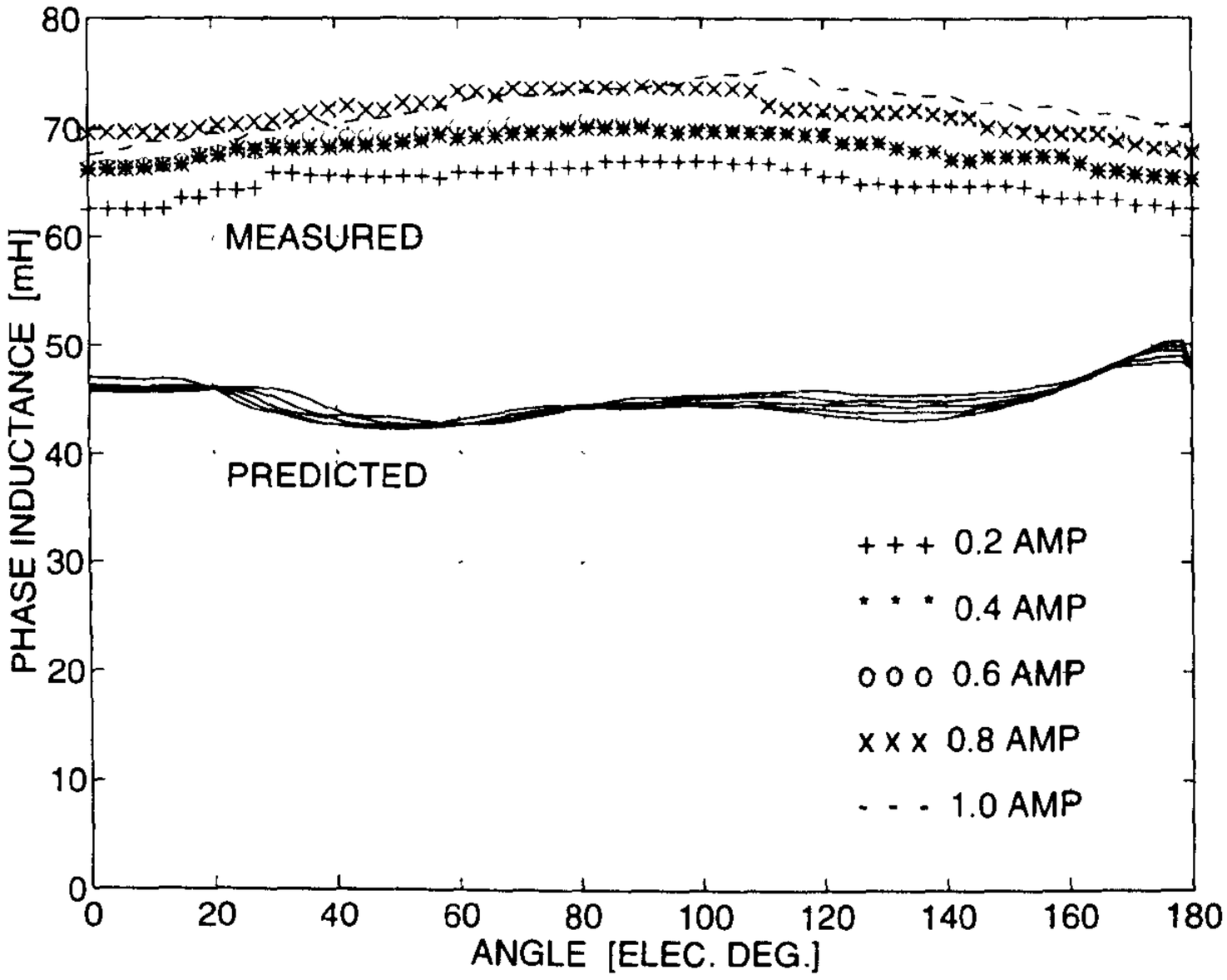

Figure 7.24. The predicted and the measured phase inductance variation with position.

The machine was excited with the 50 Hz AC mains supply, stepped down and varied through an auto-transformer. AC voltages and currents were measured at each rotor position and the phase inductance was calculated, knowing the phase resistance as shown in (7.4).

$$Z = \frac{V}{I} = \sqrt{R^2 + (\omega L)^2} \tag{7.4}$$

Fig. 7.24 shows that just as in the case of a brushless PM motor with surface permanent-magnets, the phase inductance of a flux-reversal machine is fairly independent of the rotor position as well as phase current. The predicted inductance variation curves, however, do not include the end winding and other leakage inductances, because they are obtained using a 2-D FE analysis. This accounts for the difference between the predicted and the measured phase inductance. The average measured phase inductance is 69.22 mH. With the phase resistance of 6.74 Ω, the electrical time constant of the generator is 10.27 ms.

7.7.3 Phase Flux and Generated EMF

Figs. 7.25 and 7.26 compare the predicted and the measured variation of phase flux and generated EMF respectively, with rotor position.

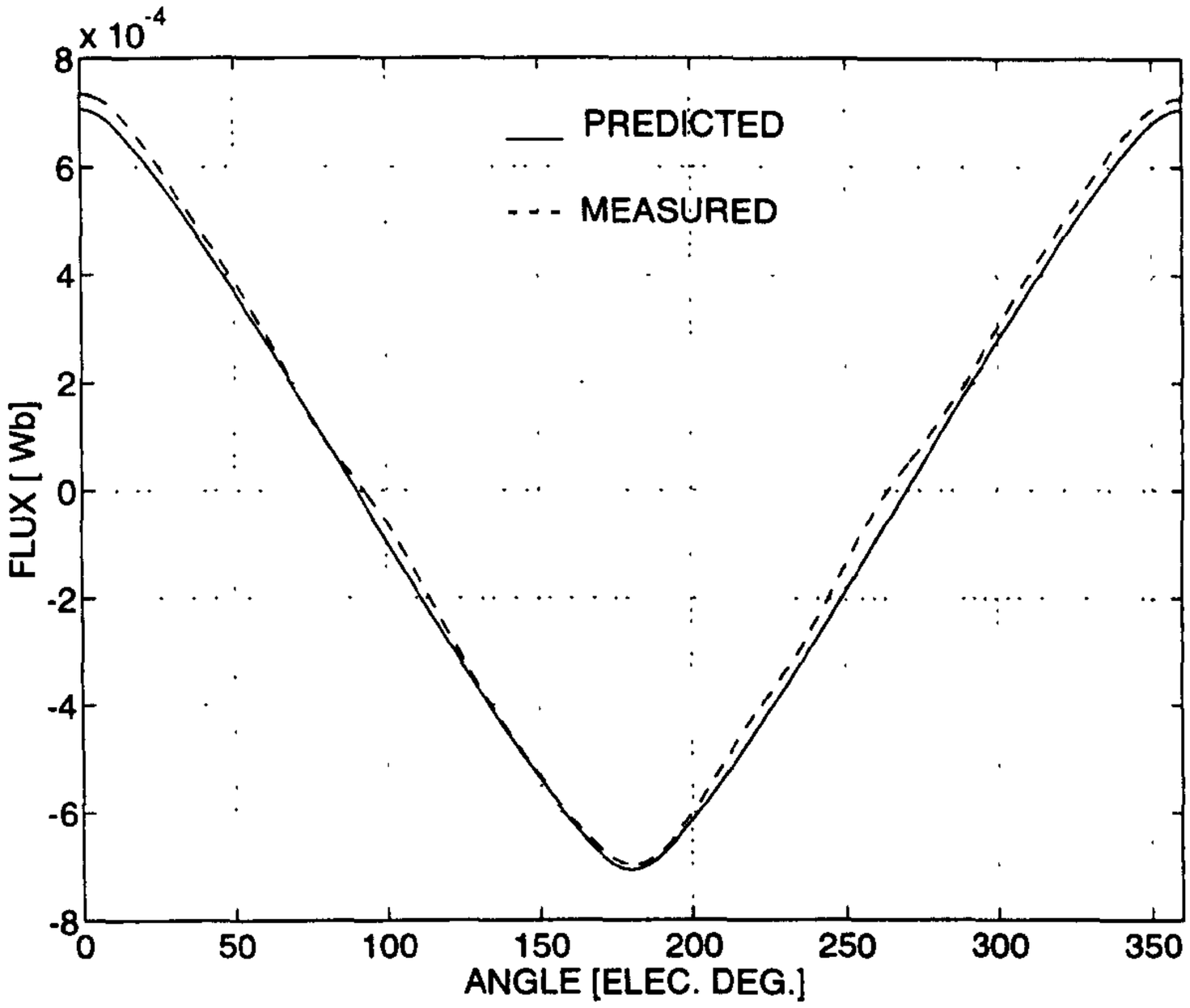

Figure 7.25. The predicted and the measured phase flux variation at 1000 rpm.

The measurements were carried out at no-load using the dynamic test set-up described in Chapter 4, Section 4.6.3. Briefly, the set-up consists of a PM brushless AC motor driving the machine under test through an in-line torque transducer at different speeds. The variation of phase flux with rotor position was measured by first capturing the search coil voltage waveforms on a digital storage oscilloscope (Model : Gould DSO 400), and then integrating the voltage variation to obtain the flux variation. The generated EMF waveforms were obtained in a similar manner by capturing the induced voltage waveforms in the main coil.

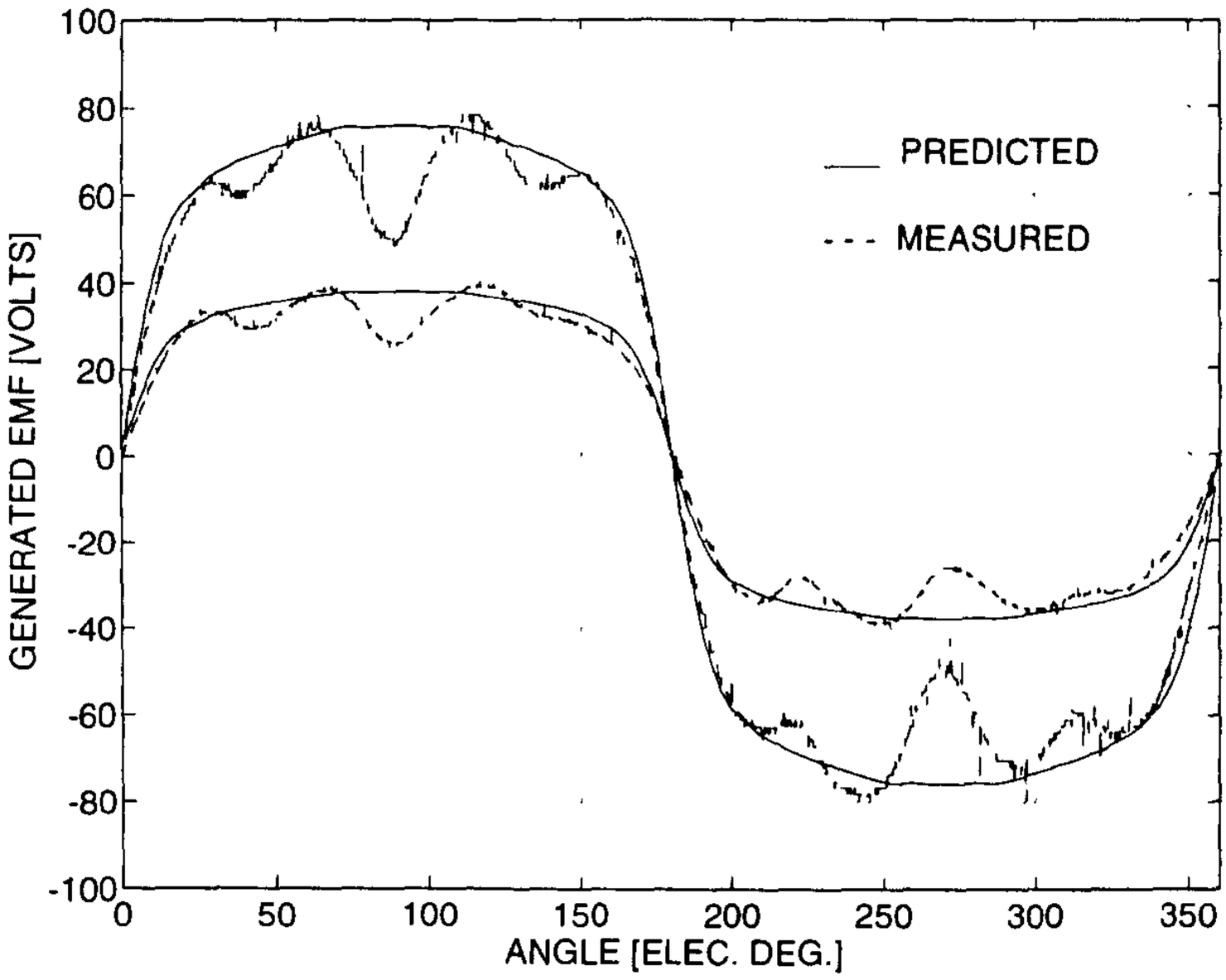

Figure 7.26. The predicted and the measured generated EMF at 1000 and 2000 rpm.

Again, Figs. 7.25 and 7.26 show a reasonable agreement between the predicted and the measured waveforms, except for some localised mismatch due to the manufacturing imperfections.

7.7.4 Generator Characteristics

Fig. 7.27 is a typical output of the dynamic test measurements captured on the digital storage oscilloscope. It shows the generator voltage and current on load, and the phase flux variation obtained from integrating the search coil voltage.

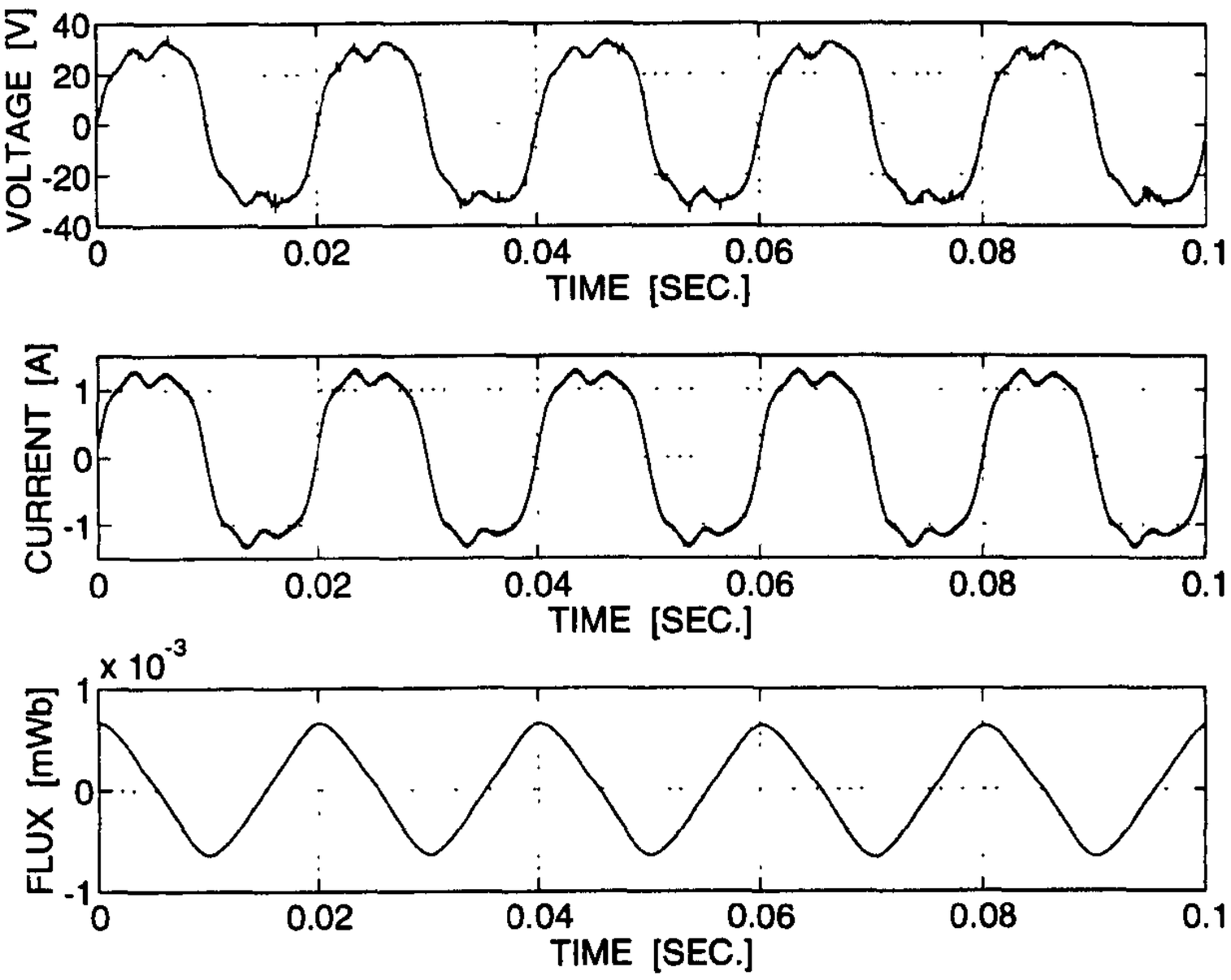

Figure 7.27. Typical output of the dynamic test measurements showing generated voltage, current and phase flux variation with a resistive load at 1000 rpm.

Such dynamic measurements were performed at different load currents over a wide speed range to obtain the generator characteristics. Figs. 7.28, 7.29 and 7.30 show the speed vs. power, speed vs. efficiency, and speed vs. torque characteristics respectively. The speed range was limited by the test set-up which had a maximum allowable speed of 4000 rpm. The input power was calculated from the input torque and speed. The output voltage, current and power were measured using a single phase power analyser (Model : Norma AC/DC Power Analyser D5235). A bank of variable resistances was used as a load to obtain measurements at different current values.

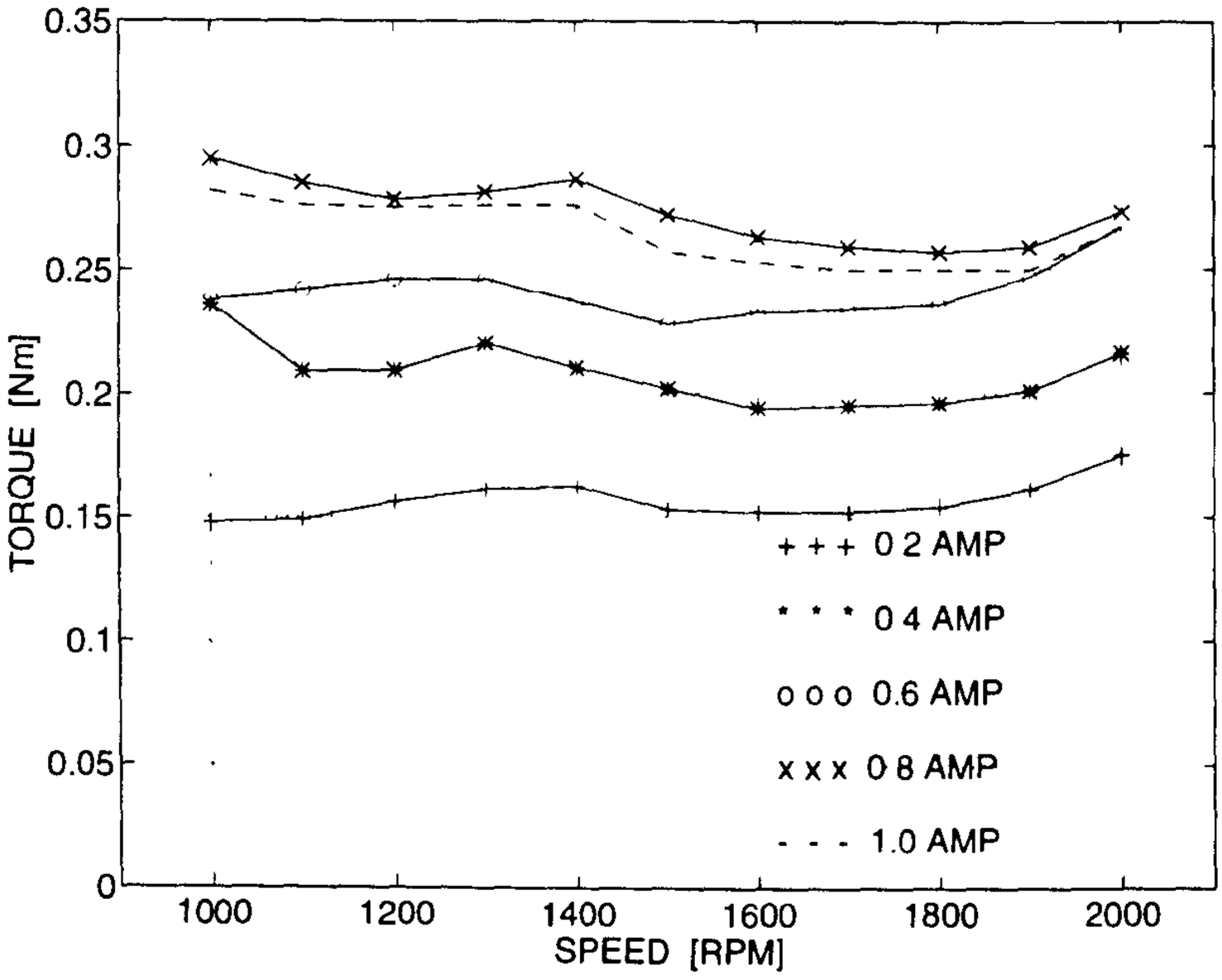

Figure 7.28. Generator speed vs. torque characteristics.

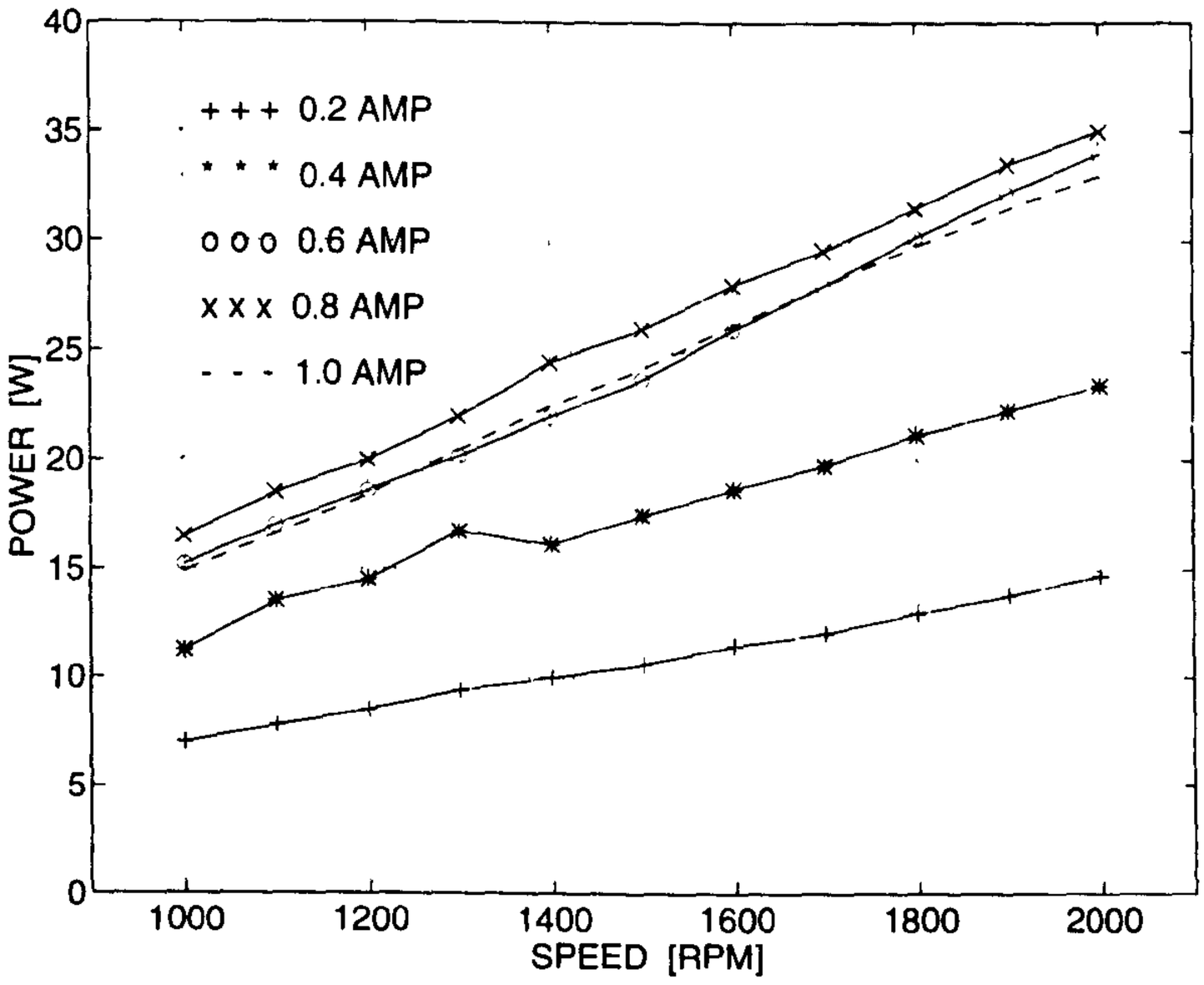

Figure 7.29. Generator speed vs. power characteristics.

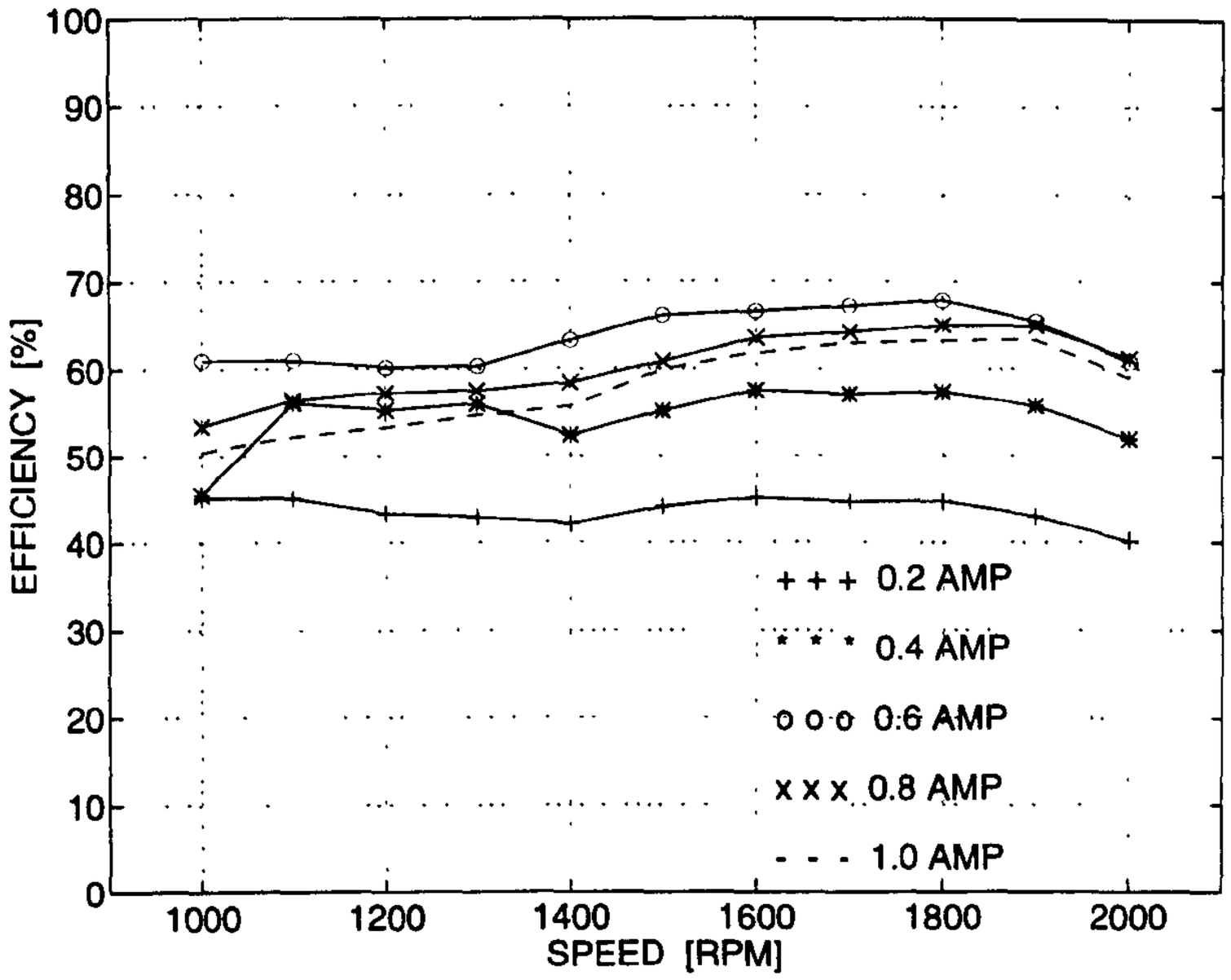

Figure 7.30. Generator speed vs. efficiency characteristics.

The generator shows a peak efficiency of 68 % at 1800 rpm. It also shows a maximum power output of 35 W at 2000 rpm and 0.8 A output current. This is roughly about half of the power output that can be obtained from a conventional brushless PM machine. Since an existing universal motor stator was used, its geometry was not optimised and this resulted in very high saturation in the stator pole tips. This can be observed in Fig. 7.10. However, with an overall design optimisation, it should be possible to improve the performance of this machine with regard to efficiency, output power, inductance, electrical time constant and cogging torque.

The temperature rise tests were performed by running the generator on a constant resistive load. The temperature measurements were made at the windings, the magnets and the stator back-iron. Fig. 7.31 shows a snap-shot of the temperature rise curves.

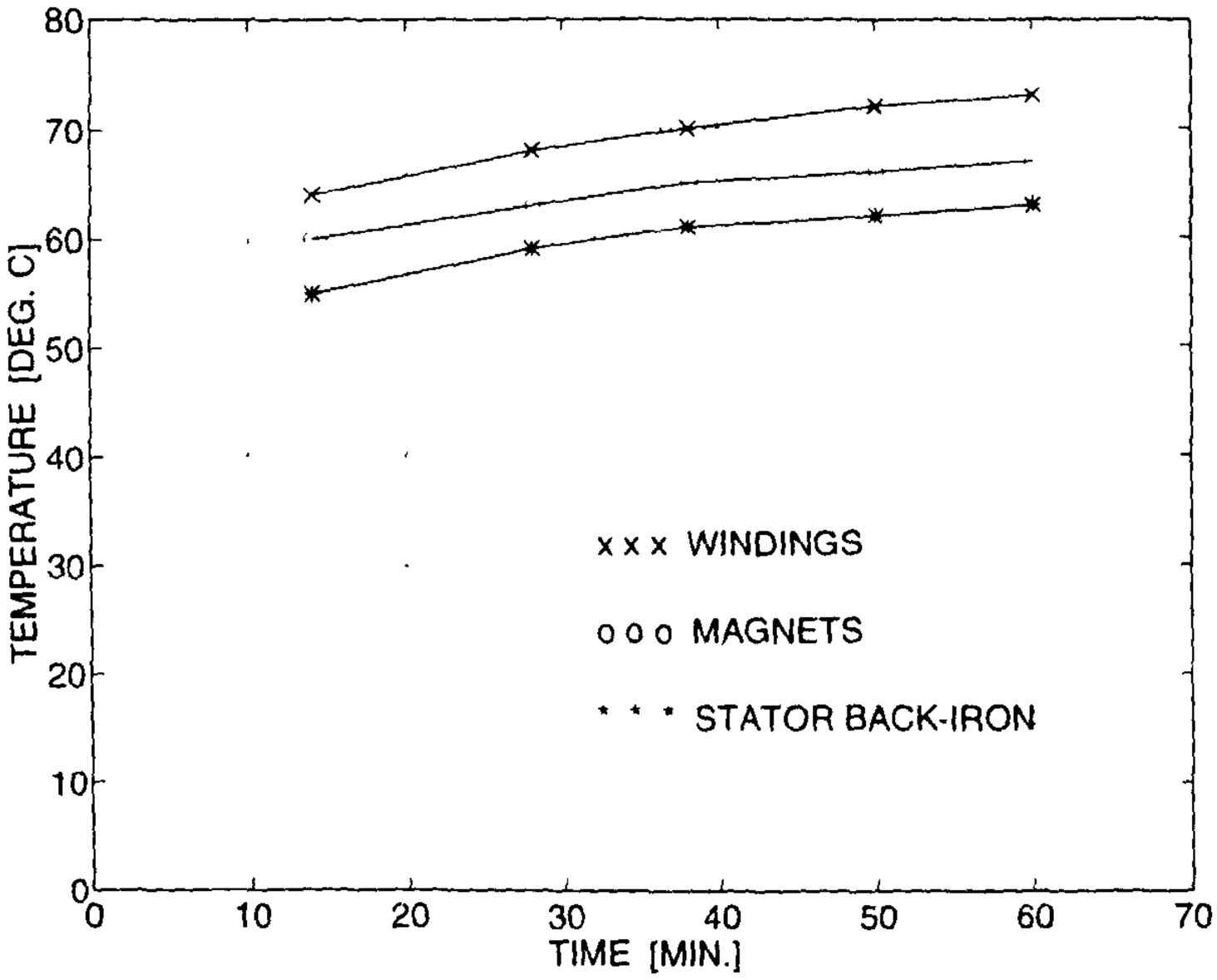

Figure 7.31. A snap-shot of the temperature rise measurements in different parts of the generator.

7.7.5 Voltage Regulation

The complete generator system consisting of the machine and the electronic controller was tested for the voltage regulation. The generator was run under two different resistive loads and the output voltages were measured after rectification, with and without the controller. The results, as shown in Fig. 7.32, indicate a good amount of voltage regulation over a wide speed range.

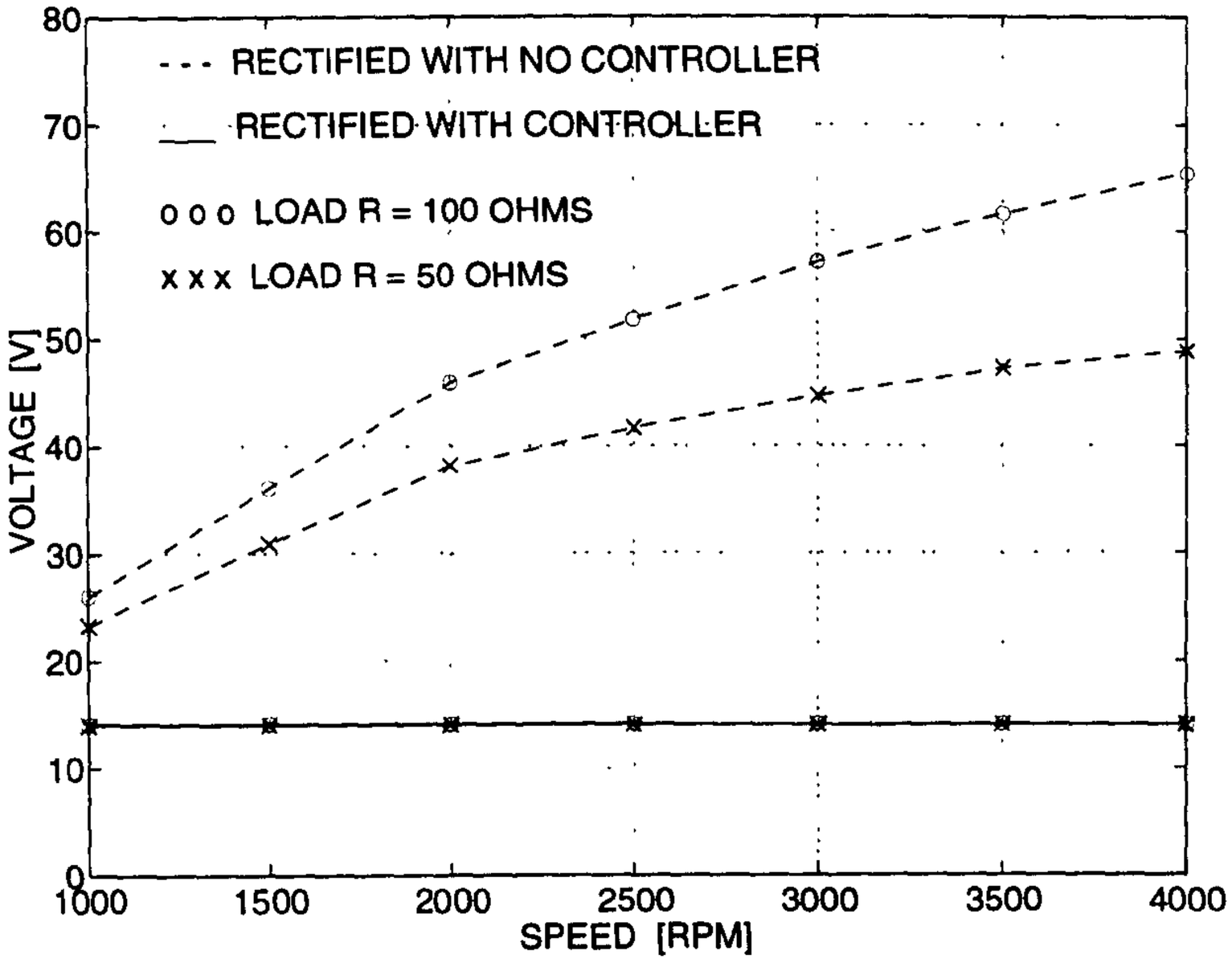

Figure 7.32. Controller voltage regulation over a wide speed range.

7.8 Chapter Summary

Chapter 7 has introduced a new brushless doubly-salient permanent-magnet machine, called the flux-reversal machine. The principle of operation of this machine has been explained and qualitative comparisons have been made with the other types brushless machines in its class.

A 'proof-of-principle' prototype single-phase flux-reversal generator, developed in the SPEED Laboratory, has been described. Its design, analysis based on the flux-MMF diagram technique, fabrication process, and detailed experimental results have been presented. Many of the perceived advantages of the flux-reversal machine, such as its simple and robust construction, low inductance variation with position and current, and low electrical time constant, have been demonstrated. Apart from the 2/3 single-phase prototype configuration, a few alternate configurations have also

been proposed, which would overcome some of the limitations of the 2/3 single-phase configuration.

8 Conclusions

8.1 The Flux-MMF Diagram Technique

The thesis has proposed and described a general theoretical means—the flux-MMF diagram—for calculating and comparing the average and the instantaneous torque in a range of electric machines of different types. The flux-MMF diagram is essentially a generalisation of the ψ-i diagram, used commonly in designing switched reluctance machines, which itself is based upon the principle of virtual work. The thesis has presented the flux-MMF diagram based analysis for the following machine types.

- Synchronous reluctance machine
- Induction machine
- PM brushless AC machine
- PM brushless DC machine
- Interior PM brushless machine
- DC commutator machine
- Flux-reversal machine

The following applications of the flux-MMF diagram technique have been demonstrated in the thesis, along with experimental validation where appropriate.

Prediction of electromagnetic torque ripple: This is the most important application of the FMDT and it has been presented in Chapter 2. The examples have included a PM brushless AC motor and a PM brushless DC motor, with and without saturation. Two different variations of the technique have been described each with its own set of advantages and disadvantages.

Prediction of Cogging torque ripple: Chapter 3 has presented the method of calculating cogging torque ripple using the flux-MMF diagram technique. It has been shown that the FMDT is a truly universal method of predicting cogging torque in permanent-magnet motors, and it offers a fundamental basis of design evaluation. Many of the commonly used cogging torque minimisation methods have been analysed in Chapter 3 using the FMDT.

Modelling of skew: A simple and elegant method of modelling the effect of skew on torque ripple, using the flux-MMF diagram, has been presented in Chapter 4. Although the treatment is confined to the PM brushless AC machines, it can be extended to the PM brushless DC machines as well provided the effect of skew on the flux-MMF trajectories at commutation instants is modelled correctly.

Modelling of the variation of torque constant: Chapter 5 has shown that the flux-MMF diagram provides a valuable means of modelling the saturation effects in electrical machines. One such important effect—the variation of torque constant with armature current—has been analysed for a PM brushless DC as well as a PM brushless AC motor.

Comparative evaluation of electrical machines: The usefulness of the FMDT in comparative evaluation of a wide variety of electrical machines has been demonstrated in Chapter 6. The chapter describes designs for seven different motor types based on common design constraints and provides qualitative as well as quantitative comparisons. Fig. 8.1, for example, shows a sketch which makes a qualitative comparison between eight different motor types including the flux-reversal machine, based on their respective flux-MMF trajectories at full-load.

It must be mentioned that the construction of a typical flux-MMF diagram involves extensive amount of finite-element analysis. With the present state-of-the-art computing resources, roughly speaking, the whole process takes about a day from start to finish.

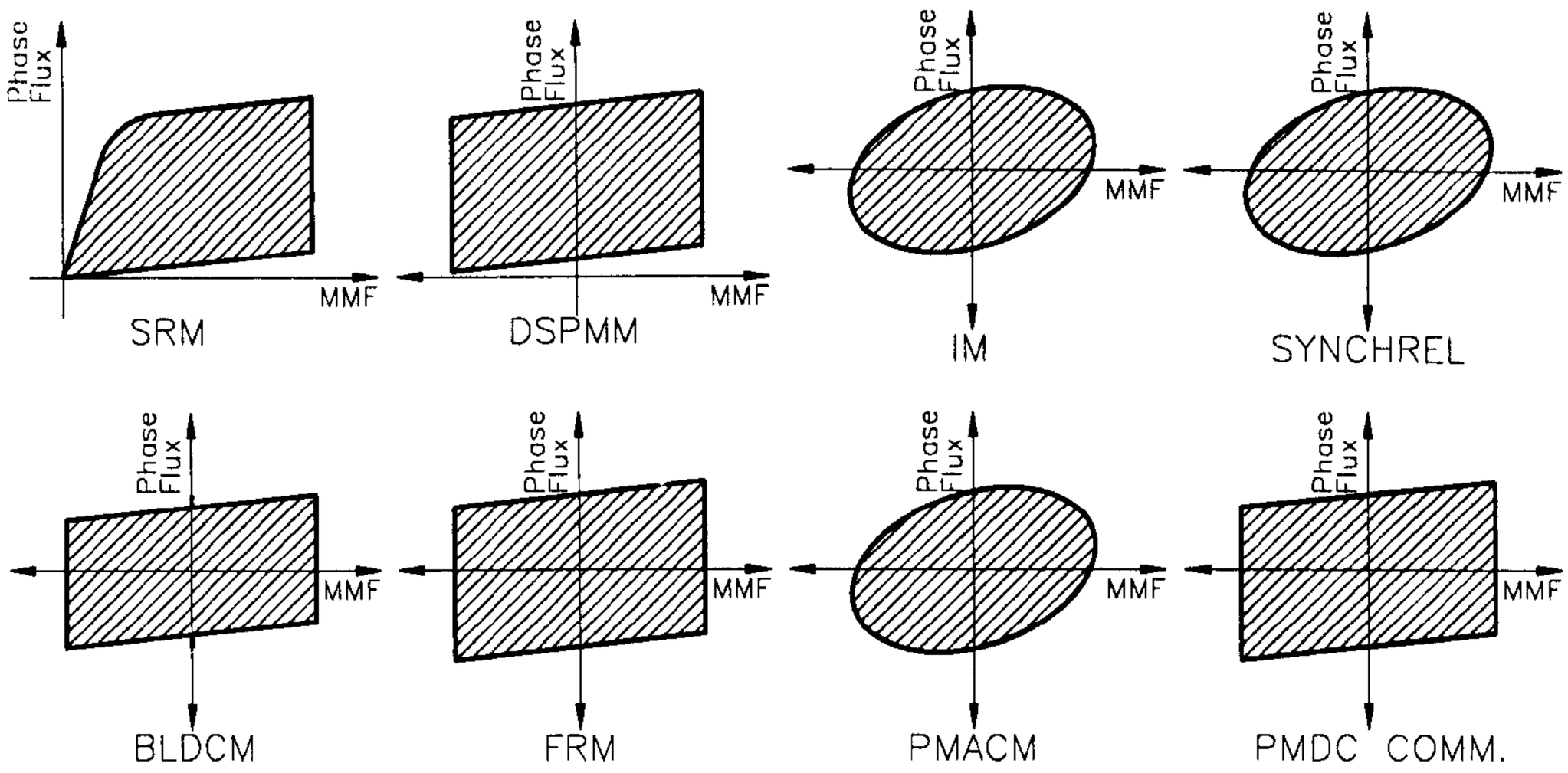

Figure 8.1. FMDT based qualitative comparison between eight different motor types.

In general, the flux-MMF diagram technique goes far beyond the capabilities of the so called 'unified' or 'generalised' machine theory. Some of its distinctive features are summarised below.

- It can deal with the conventional machine types such as commutator DC and PM synchronous machines, as well as the non-conventional machine types such as switched reluctance, doubly-salient brushless PM, squarewave brushless DC and flux-reversal machines, which cannot be analysed using traditional methods based on the dq-axis theory.
- It gives a clear physical insight and graphical interpretation of the torque producing mechanism in electrical machines.
- It can calculate cogging and electromagnetic torque ripple, as well as other performance characteristics such as generated EMF and in some cases, variation of phase inductance with position and current.
- It makes direct use of the finite-element calculations in a way that is not possible with the generalised-machine or 'lumped-parameter' theories, and presents many of its results via graphical images whose features are readily associated with particular

characteristics such as torque per unit volume, torque ripple, kVA requirement, and electric and magnetic loadings.

- Because it is based on the difference of coenergy calculations and non-linear magnetisation data, the technique is not restricted by any assumptions of linearity or sinusoidal excitation.

It would be unwise to proclaim the FMDT as a modern-day replacement for the generalised machine theory, which will surely always be the foundation theory for AC and DC machines as well as for field-oriented control and some aspects of power-systems analysis; but it should help in the analysis and comparative evaluation of a wide range of electrical machines including new arrivals that fit no classical model.

8.2 The Flux-Reversal Machine

Chapter 7 has presented the principle of operation, design, analysis, fabrication and experimental results for a new brushless doubly-salient permanent-magnet machine, called the flux-reversal machine. The first 'proof-of-principle' prototype has been built and tested as a simple 2/3 configuration single-phase high-speed generator.

The main advantages of the flux-reversal machine appear to be:

- Simple and robust rotor construction with low inertia.
- Fault-tolerance capability with its physical and electrical isolation between the phases in a multi-phase configuration.
- Small inductance variation with rotor position *and* current.
- High-speed capability due to non-rotating magnets.

With these advantages, the machine has a considerable potential in the following range of applications:

Automotive Generators: Presently, claw-pole alternators are used in automobiles and these have high rotor inertia, limited efficiency and limited ability to respond to sudden load changes. Although this is an established and mature technology, the flux-reversal machine promises to overcome some of these limitations. However, it must be mentioned that an extensive amount of research and development will be needed before the flux-reversal machine can compete with the existing technology.

Aerospace and Defence: With its robust mechanical construction and high fault-tolerance, the flux-reversal machine can be a good candidate for many applications in this field.

Industrial: Fig. 7.21 in Chapter 7 shows that the flux-reversal machine has a phase torque characteristic similar to the brushless DC motor and hence, in its multi-phase configuration, it can be a high-performance brushless PM motor suitable for certain industrial applications where size and weight of the machine are critical.

8.3 Future Work

Although the thesis has presented some important aspects relating to the two primary research contributions—the flux-MMF diagram technique and the flux-reversal machine—much remains to be explored. Some of the research ideas for future work on these two topics have been summarised in the following list.

- The capabilities of the FMDT, as a tool for analysis of electrical machines, have been amply demonstrated in this thesis. However, it has a potential to turn itself into a valid design tool in its own right. Indeed, it has been used as a design tool for building the first prototype flux-reversal machine. The reliance of the FMDT on FE analysis limits its speed and flexibility which are of paramount importance in any design tool. Hence, some alternatives other than the finite-elements need to be

considered, such as the Magnetic Equivalent Circuit (MEC) method. Although the MEC method could be faster than the FE method under certain conditions, it lacks the flexibility and wide-ranging applicability of the FE method and hence so far, it has not been used as widely as the FE method.

- The accuracy of the flux-MMF diagram technique, directly depends upon the accuracy of estimating the variation of flux with MMF and rotor position. The thesis has described finite-element based algorithms for obtaining this variation. However, these algorithms can be further improved to make them robust and insensitive to the mesh generation errors.

- At present, the FMDT based method of predicting cogging torque ripple assumes a linear demagnetisation characteristic and linear load-lines for a permanent-magnet. It also assumes that the cogging torque ripple is independent of the load current and hence can be superimposed on the electromagnetic torque ripple to obtain the total torque ripple. These assumptions are shown to be reasonably valid with the help of experimental measurements. However, the method can be extended to take account of the effect of saturation on load-lines, non-linearities in the demagnetisation characteristic and the effect of load current on cogging torque.

- Chapter 4 has dealt with the modelling of skew using FMDT in PM brushless AC motors. In order to implement the extension of this method to modelling of skew in PM brushless DC motors, the discontinuities in the MMF excitation at commutation points need to be modelled correctly in squarewave excited machines with skew.

- Chapter 5 has analysed the variation of torque constant with armature current in brushless PM motors. In the process, it has been pointed out that in PM brushless AC motors, the armature reaction is predominantly cross-magnetising in nature owing to the quadrature relationship maintained between the permanent-magnet field and the armature field. Whereas in PM brushless DC motors, the armature

reaction is always a combination of cross-magnetisation and de-magnetisation with both components varying in proportion between any two commutation instants. This in turn means that it is easier to predict the variation of torque constant for sinewave motors, where it remains stable throughout an electrical cycle, than for squarewave motors, where it changes dynamically within an electrical cycle. With the help of FMDT, it should be possible to analyse this dynamic variation of torque constant over an electrical cycle in a squarewave excited machine.

- Chapter 7 has described the 2/3 single-phase prototype flux-reversal machine configuration. A few other configurations have also been proposed, and these include the 4/6 two-phase, and the 6/8 three-phase configurations. These configurations appear to be especially promising as generators as well as high-performance brushless PM motors. They would also overcome some of the limitations of the 2/3 single-phase configuration such as the large amount of cogging torque and torque ripple, the unbalance in the magnetic circuit, and the noise and vibration arising out of it. It would certainly be worthwhile building some of these configurations and investigating their performance in order to validate their perceived advantages.

- The future work on the flux-reversal machine will also involve designing and building application-specific machines. This will facilitate direct and quantitative performance comparisons between the flux-reversal machine and the other competing brushless machines in its class.

A Publications

The following is a list of publications resulting from the research described in this thesis. It includes one book chapter, four IEEE-IAS Transaction papers, and six conference papers including two prize winning papers.

Book Chapter

1. TJE Miller, DA Staton, and **RP Deodhar** : "Sizing & Computer Aided Design", ***Design of Brushless Permanent-Magnet Motors***, Chapter 12, pp. 12-1–12-25, Monographs in Electrical and Electronic Engineering, Magna Physics Publications and Clarendon Press, Oxford Science Publications, 1994.

Refereed Journal Articles

2. DA Staton, **RP Deodhar**, WL Soong and TJE Miller : "Torque prediction using the flux-MMF diagram in AC, DC and reluctance motors", ***IEEE Transactions on Industry Applications***, Vol. 32, No. 1, pp. 180–188, January/February 1996.

3. **RP Deodhar**, DA Staton, TM Jahns and TJE Miller : "Prediction of cogging torque using the flux-MMF diagram technique", ***IEEE Transactions on Industry Applications***, Vol. 32, No. 3, pp. 569–576, May/June 1996.

4. **RP Deodhar**, DA Staton and TJE Miller : "Modelling of skew using the flux-MMF diagram", ***IEEE Transactions on Industry Applications***, Vol. 32, No. 6, November/December 1996 (in press).

5. **RP Deodhar**, S Andersson, I Boldea and TJE Miller : "Flux reversal machine : a new class of brushless doubly salient permanent-magnet machine", ***IEEE Transactions on Industry Applications***, (accepted).

Conference Papers

6. DA Staton, WL Soong, **RP Deodhar** and TJE Miller : "Unified theory of torque production in AC, DC and reluctance motors", *Conference Record of the 1994 IEEE-IAS Annual Meeting*, Denver, Colorado, Vol. 1, pp. 149–156, October 2-6, 1994.

7. **RP Deodhar**, DA Staton and TJE Miller : "Variation of torque constant with armature current in brushless PM motors", *Proceedings of the Seventh International Conference on Electric Machines and Drives, IEE-EMD'95*, Durham, England, pp. 405–409, September 11-13, 1995.

8. **RP Deodhar**, DA Staton, TM Jahns and TJE Miller : "Prediction of cogging torque using the flux-MMF diagram technique", *Conference Record of the 1995 IEEE-IAS Annual Meeting*, Orlando, Florida, Vol. 1, pp. 693–700, October 8-12, 1995.

9. **RP Deodhar**, DA Staton and TJE Miller : "Modelling of skew using the flux-MMF diagram", *Proceedings of the IEEE International Conference on Power Electronics, Drives and Energy Systems for Industrial Growth, IEEE-PEDES'96*, New Delhi, India, Vol. 1, pp. 546–551, January 8-11, 1996.

10. **RP Deodhar**, DA Staton and TJE Miller : "Flux-MMF diagram : a technique for analysis and comparative evaluation of electric machines", *Proceedings of the Fourth International Conference on Electrical Rotating Machines, ELROMA-96*, Bombay, India, pp. 57–62, January 19-20, 1996.

This paper received the ELROMA-96 Conference Committee Second Prize Paper Award).

11. **RP Deodhar**, S Andersson, I Boldea and TJE Miller : "Flux reversal machine : a new class of brushless doubly salient permanent-magnet machine", *Conference Record of the 1996 IEEE-IAS Annual Meeting*, San Diego, California, Vol. 1, pp. 786–793, October 6-10, 1996.

This paper received the IEEE-IAS Electric Machines Committee First Prize Paper Award).

The following is a list of co-authors, with their names and affiliations, who have collaborated with the author during the course of the research described in this thesis.

Co-author	Affiliation
Prof. T. J. E. Miller	SPEED Laboratory, University of Glasgow, UK.
Dr. D. A. Staton	Control Techniques R&D, UK.
Dr. W. L. Soong	General Electric Corporate R&D, USA.
Dr. T. M. Jahns	General Electric Corporate R&D, USA.
Prof. Ion Boldea	University Politehnica Timisoara, Romania.
Svante Andersson	Lund Institute of Technology, Sweden.

Finally, seven out of the total eleven listed publications, namely No. 1, 2, 3, 4, 7, 10 and 11, are included in this appendix.

Monographs in Electrical and Electronic Engineering

10. *The theory of linear induction machinery* (1980) Michel Poloujadoff
12. *Energy methods in electromagnetism* (1981) P. Hammond
15. *Superconducting rotating electrical machines* (1983) J. R. Bumby
16. *Stepping motors and their microprocessor controls* (1984) T. Kenjo
17. *Machinery noise measurement* (1985) S. J. Yang and A. J. Ellison
18. *Permanent-magnet and brushless d.c. motors* (1985) T. Kenjo and S. Nagamori
19. *Metal-semiconductor contracts: Second edition* (1988) E. H. Rhoderick and R. H. Williams
20. *Introduction to power electronics* (1988) Eiichi Ohno
21. *Brushless permanent-magnet and reluctance motor drives* (1989) TJE Miller
22. *Vector control of a.c. machines* (1990) Peter Vas
23. *Brushless servomotors: fundamentals and applications* (1990) Y. Dote and S. Kinoshita
24. *Semiconductor devices, circuits, and systems* (1991) Albrecht Möschwitzer
25. *Electrical machines and drives: a space-vector theory approach* (1992) Peter Vas
26. *Spiral vector theory of a.c. circuits and machines* (1992) Sakae Yamamura
27. *Parameter estimation, condition monitoring, and diagnosis of electrical machines* (1993) Peter Vas
28. *An introduction to ultrasonic motors* (1993) S. Sashida and T. Kenjo
29. *Ultrasonic motors: theory and applications* (1993) S. Ueha and Y. Tomikawa
30. *Linear induction drives* (1993) J. F. Gieras
31. *Switched reluctance motors and their control* (1993) TJE Miller
32. *Numerical modelling of eddy currents* (1993) Andrzej Krawczyk and John A. Tegopoulos
33. *Rectifiers, cycloconverters, and a.c. controllers* (1994) Thomas H. Barton
34. *Stepping motors and their microprocessor controls: Second edition* (1994) T. Kenjo and A. Sugawara
35. *Inverse problems and optimal design in electricity and magnetism* (1994) P.Neittaanmäki, M. Rudnicki, and A. Savini
36. *Applications of electric drive systems* (1994) Richard M. Crowder
37. *Design of Brushless Permanent-Magnet Motors* (1994) J. R. Hendershot Jr, and TJE Miller

Design of Brushless Permanent-Magnet Motors

J.R. Hendershot Jr.
General Manager
Magna Physics Tridelta
Hillsboro, OHIO 45133

TJE Miller
Lucas Professor in Power Electronics
Director, SPEED Consortium
University of Glasgow, UK

MAGNA PHYSICS PUBLISHING
AND
CLARENDON PRESS • OXFORD
1994

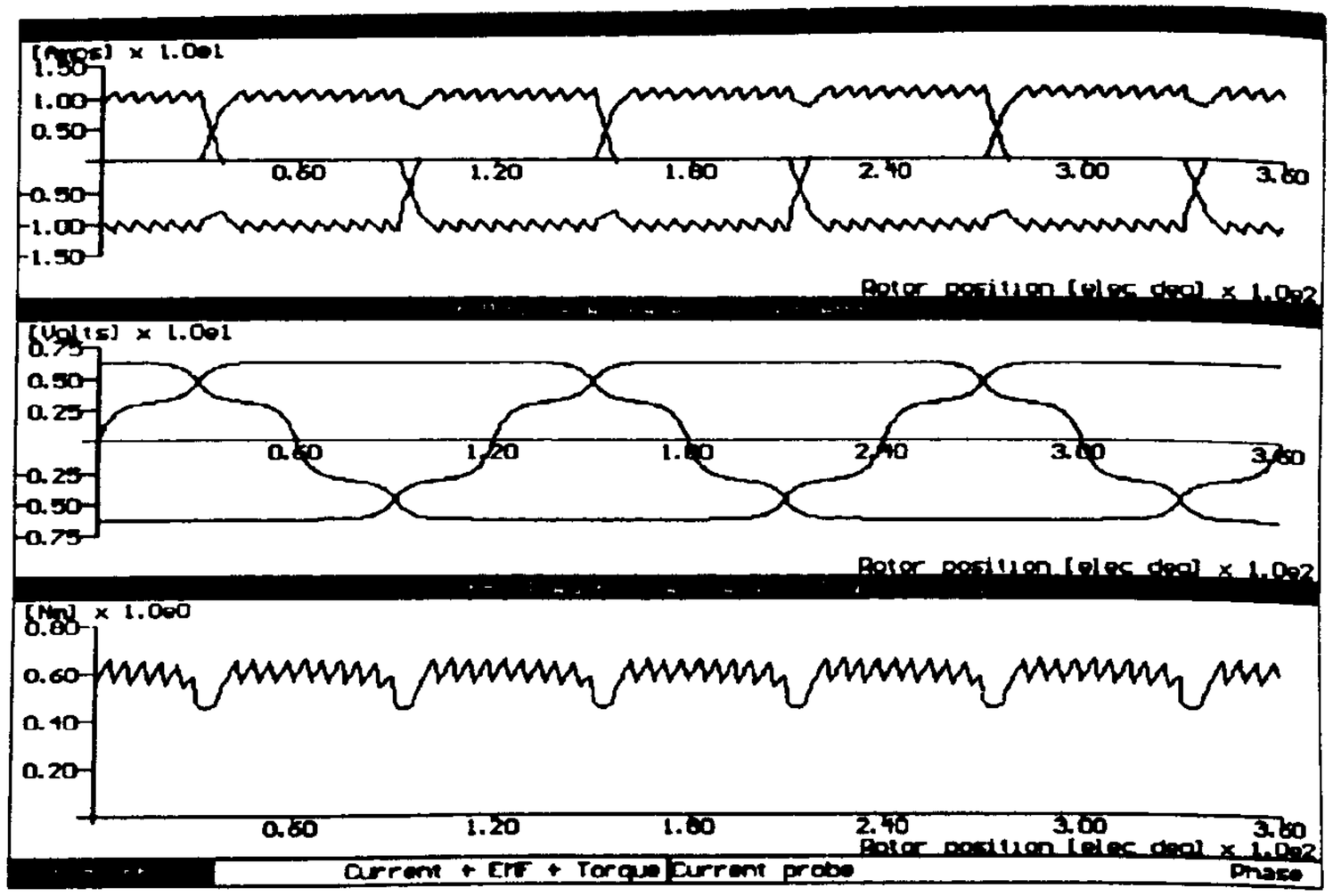

Fig. 12.7 Typical EMF, current, and torque waveforms in *PC-BDC*

```
PC-BDC 4.00: Design Sheet                                    74k 15
4 Winding Data:-------------------------------------------------------

WdgType        Lap          Connex    3-Ph Wye       Throw        5
TC              18          Coils/P      1.000       NSH          1
Tph          48.000         PPATHS          1        SPP      2.000
Layers        1.000         CSidesPh        8        Z      240.000
MLT         240.187 mm      LgthOEnd   94.735 mm     Ext      0.000 mm
EndFill       0.500         LaxPack    67.566 mm     TFRho    1.020
SFill         0.190         Wire          1.226      WireSpec BareDia
                            WireDia       1.226 mm   Liner    0.400 mm
SlotArea     62.127 mm^2    CondArea      1.100 mm^2 ASlotLL  49.185 mm^2
WdgTemp      25.000 DegC    Rph           0.141 Ohm/Ph Rterm   0.282 Ohms
Lph           0.272 mH/Ph   Mph          -0.057 mH/Ph Lterm    0.430 mH
Lg            0.142 mH/Ph   LSlot         0.099 mH/Ph Lendt    0.031 mH/Ph
Mg           -0.057 mH/Ph   MSlot         0.000 mH/Ph fz       1.149
PCSlot        1.955         XLph          1.000       XET      1.000
Ax1          52.500 mDeg

5 Magnetic Circuit Design:--------------------------------------------

BrT           0.401 T       BgOC          0.209 T     HcT    297.950 kA/m
Bg1OC         0.355 T       PhiM1         0.450 mWb   PhiG     0.407 mWb
BmOC          0.378 T       Bm/BrT        0.942       f_Lkg    0.050
Help: Average open circuit flux density in the magnet              F1 Help
```

Fig. 12.8 Typical output data from *PC-BDC*


```
PC-BDC 4.00: Design Sheet                                    74k 15
7 PM Dynamic design (time-stepping simulation):-----------------------

OpMode      Motoring
Torque        0.585 Nm      PowerSh    122.583 W     Eff      80.166 %
LossCu       20.150 W       LossFe_S     2.151 W     LossWF_S  0.000 W
LossTot      30.309 W       TempRise     3.031 DegC  Jrms      6.911 A/mm^2
IWpk         11.107 A       IWav         6.606 A     IWrms     8.154 A
ILpk         11.107 A       ILav         6.606 A     ILrms     8.154 A
IQchpk       11.107 A       IQchav       2.421 A     IQchrms   4.917 A
IQcmpk       11.107 A       IQcmav       3.311 A     IQcmrms   5.774 A
IDchpk       11.107 A       IDchav       0.092 A     IDchrms   2.001 A
IDcmpk        0.000 A       IDcmav       0.000 A     IDcmrms   0.000 A
IDClinkP      7.151 A       LossConv    10.003 W     EffDCSh  71.302 %

8 Miscellaneous:------------------------------------------------------

WtCu          0.299 kg      WtFe         1.690 kg    WtMag     0.191 kg
WtTot         2.101 kg      RotJ     1.547E-04 kg-m2 LosFe/Wt  1.272 W/kg
IDCLinkW      0.136 A       sigma        0.424 psi   XFe       1.000
Freq1        66.667 Hz      FreqChop     4.000 kHz
TempCalc     DegCW          DegCW        0.100 degC/W HTranAct 659.006 W/m2/C
Ambient      20.000 DegC    HTranEnd     0.000 W/m2/C
HysBand      12.500 %       IntStep      0.500 eDeg
Help: Width of hysteresis band as a percentage of ISP              F1 Help
```

Fig. 12.9 Typical performance data from *PC-BDC*

12.4 Finite Element Analysis

12.4.1 Introduction

The finite-element method is a numerical method for solving electromagnetic field problems which are too complex to be solved using analytical techniques, especially those involving non-linear material characteristics. The method basically involves the discretization of the motor cross-section (or volume in the case of 3-D analysis) into smaller areas/volumes called finite elements. The spatial variation of magnetic potential (vector or scalar) throughout the motor is described by a non-linear partial differential equation derived from Maxwell's equations. In its linear form this equation is Laplace's equation, Poisson's equation, or the Helmholtz equation, depending on the type of problem being solved.

Usually the partial differential equation is written in terms of the vector potential **A**, because of the economy with which important field quantities such as flux-density, flux, etc. can be subsequently determined. Accordingly the partial differential equation is solved, after discretization,

in terms of **A**, and the other "output" quantities are calculated from the nodal values of **A** in the "postprocessing" phase.

Within one element, the vector potential is assumed to vary according to a simple shape function, which may be a linear, quadratic, or higher-order function of the three sets of node coordinates for the vertices of the triangular element. Linear elements give the fastest solution but the least smoothness in the field variation.

Modern finite-element software is extremely robust and accurate, and has innumerable features to assist the user to set the problem up and extract the engineering parameters of interest. However, the point should be made that the finite-element method differs from rapid-design software like *PC-BDC* in two important ways:

1. The finite-element method is generally limited to one specific type of problem, such as electromagnetic or thermal analysis, whereas rapid- design software calculates a wide range of parameters ranging from weights and inertias through to performance and dynamic waveform calculations, temperature rise, and many non-electromagnetic parameters.

2. The finite-element method is intended for accurate analysis, and the emphasis on accuracy means that setup and execution time is much longer than with rapid-design software. A typical simple finite-element exercise might take days or weeks, but a complete motor can be designed in less than one day with a program like *PC-BDC*. Inevitably, *PC-BDC*'s electromagnetic calculations cannot be expected to be as accurate as those of the finite-element method, although the difference in accuracy is often too small to be of concern. On the other hand, many detailed problems such as the calculation of cogging torque, which are beyond the scope of rapid-design software, may require extremely lengthy finite-element calculations lasting several weeks.

Application of the finite element method to machine design involves three stages:

1. Pre-Processing
2. Field Solution
3. Post-Processing

12.4.2 Pre-Processing

In most cases this is the most user-intensive part of finite-element analysis. Three tasks must be performed:

1. Mesh Generation
2. Material Definition
3. Problem Definition

Mesh generation involves division of the motor cross-section into a set of triangular elements (2-D solutions) or division of the motor volume into 'bricks' (3-D solutions). Modern mesh generation is carried out using either interactive graphical techniques (using conventional CAD drafting software such as AUTOCAD®, or using the internal specialist drafting facilities of the finite-element software itself. Another alternative is the use of using specialist mesh generation code written in a high-level language or command file.

Interactive graphical mesh generation is the quickest way to form a finite-element mesh in the majority of cases. However, a drawback of using this technique is that when it is required to calculate a series of solutions for motors of the same general type, but with different dimensions, it will usually be necessary to generate the mesh individually from the beginning for each case. This problem can be overcome by writing specialist mesh-generation software, which may be in the command language of the finite-element program, or alternatively in C, PASCAL or FORTRAN. The interface to the finite-element program may use a standard data format such as .DXF or a format specific to the particular vendor. This method of mesh generation is especially useful when generating a range of meshes for motors of similar type but having either different dimensions or different rotor positions.

Specialist mesh generation software calculates the coordinates required to define the motor geometry. The cross-section is usually split up into *regions* representing different "materials" such as current-carrying conductors, air, steel, and magnets. Each region may define a different component used in the construction of the motor, for example, the shaft, rotor core, magnets, stator lamination, airgap, etc. In most cases it is beneficial to split the components further into smaller polygons along lines of symmetry.

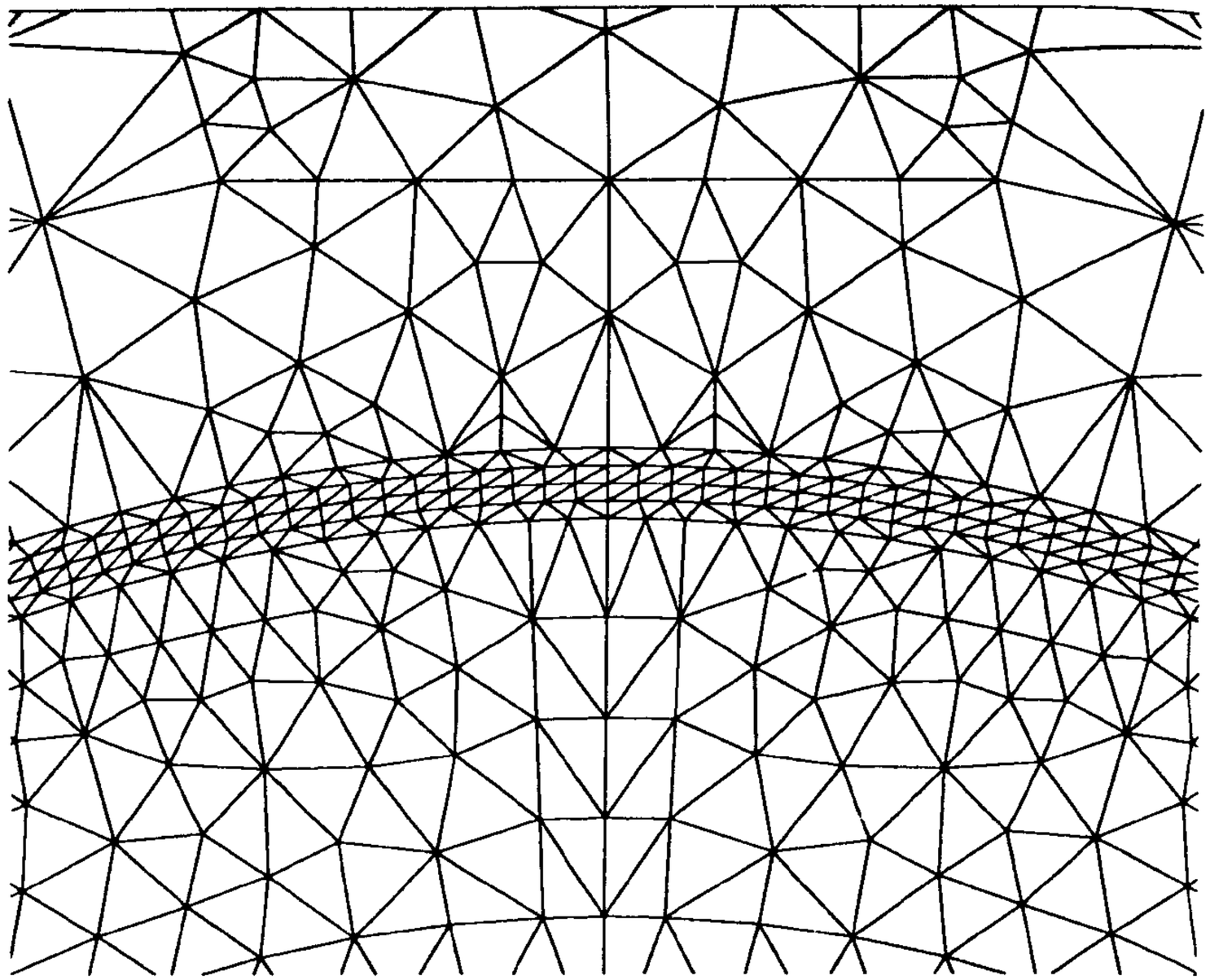

Fig. 12.10 Finite-element mesh showing details of airgap elements

For example, a stator lamination can be created by reflection followed by multiple rotational copies of half a slot pitch. This procedure reduces the amount of data needed to specify the geometry, and reduces the chance of errors.

The coordinates of vertices defining region boundaries must be calculated from dimensional parameters such as the outer frame diameter, slot depth, tooth width, etc. Usually this involves a "translation" calculation from the engineering parameters to the finite-element model. Mesh grading constants must also be specified. These determine the grading of the node-spacing along each edge of the polygonal regions.

When rotation of the motor rotor is to be modeled, it is essential to define the airgap using a sliding surface, splitting the airgap into at least two layers. One of these layers is fixed to the rotor and one to the stator.

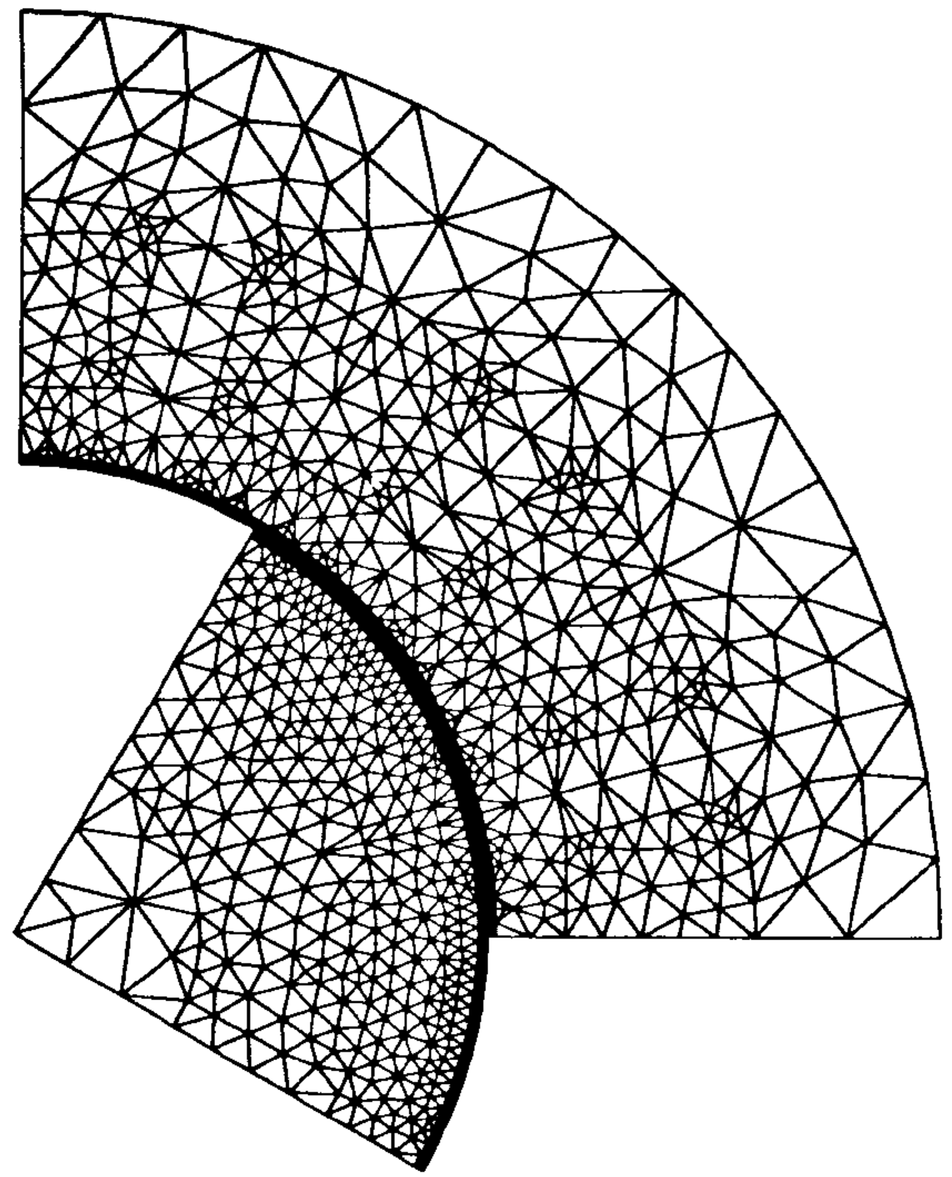

Fig. 12.11 Finite-element mesh for one pole-pitch of a brushless DC motor, showing the use of periodic boundary conditions

The node spacing on the central sliding surface is set to a constant such that it is possible to rotate the rotor by any multiple of this constant. Fig. 12.10 shows a mesh in which the airgap region is divided into four layers and the sliding surface is central to the airgap. Fig 12.11 shows the full mesh for one pole-pitch of the same motor.

An alternative approach involves developing algorithms in which the stator bore and rotor outer diameter nodal coordinates are calculated and the airgap elements are so defined as to give the best possible shape (as near as possible to equilateral triangles) [1].

Material definition involves curve fitting the non-linear B-H characteristics of the steel and magnet materials used in the construction of the motor. Many finite-element programs include databases of material data for the convenience of the user.

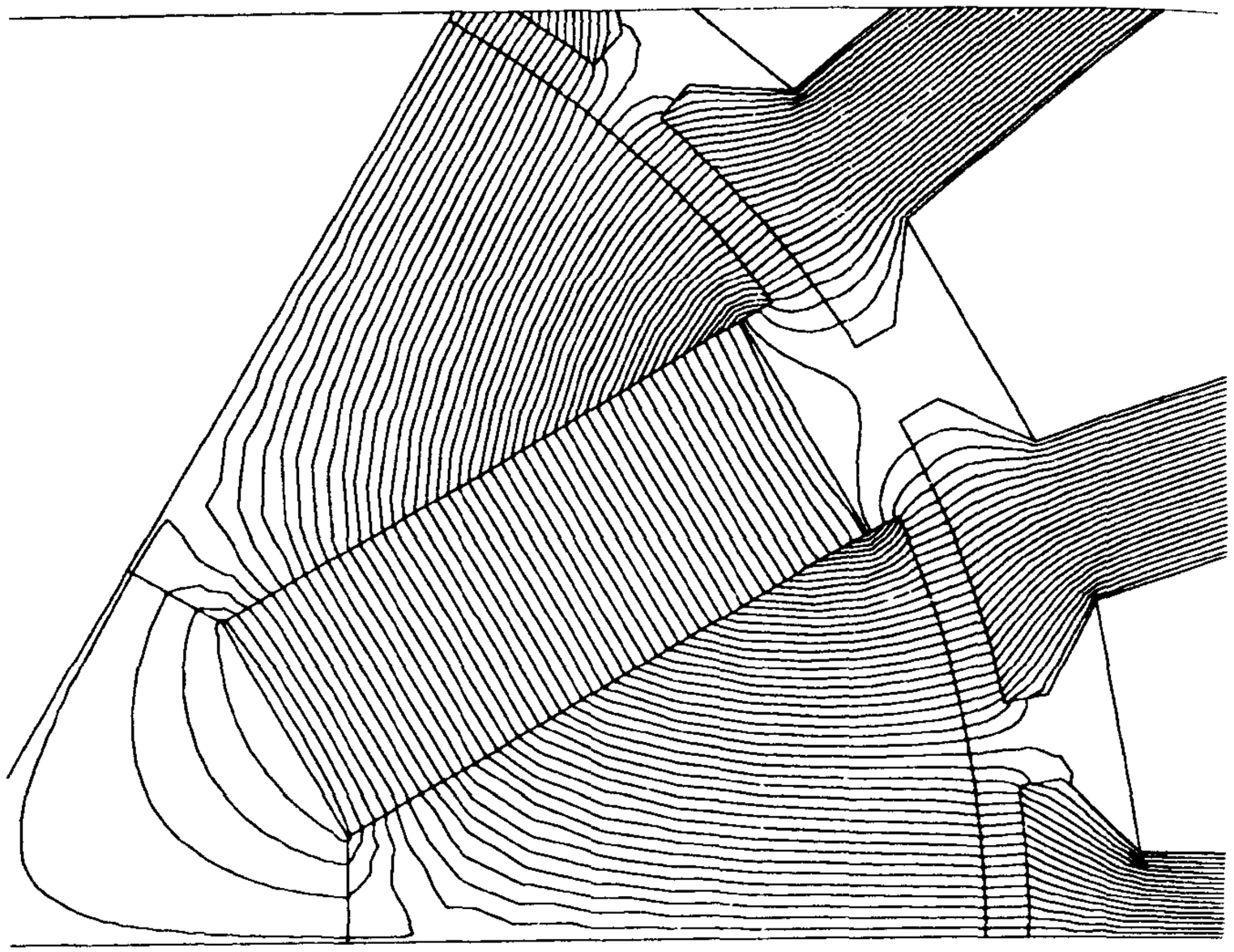

Fig. 12.12 Leakage flux paths in a "spoke" type brushless permanent-magnet motor

Problem definition involves the application of the correct boundary conditions, imposing the correct current densities in the appropriate winding elements, and definition of the direction of magnetization of magnets. Periodic boundary conditions should be used if possible, as they make it possible to model only a fraction of the cross-section (Fig. 12.11). For example, in the case of a 4-pole motor, if the number of slots/pole is an integer, it is only necessary to model the motor over one pole pitch.

12.4.3 Field Solution

The solution of the discretized partial differential equation uses specialized mathematical algorithms developed over many years [4]. The algorithm is often based on the minimisation of an energy functional, that is, a mathematical function that is related to the stored potential energy in the field.

The discretization transforms the partial differential equation into a large number of simultaneous nonlinear algebraic equations containing the unknown node potentials. Iteration is essential and the Newton-Raphson and congjugate-gradient procedures are widely used. With linear elements, the potential is assumed to vary linearly between nodes and the flux density is constant within each element. Current density is also assumed to be constant within each element associated with a winding.

12.4.4 Post-Processing

The field solution is in terms of magnetic vector or scalar potential, but the design engineer needs quantities such as flux densities, force and torque. The extraction of these quantities from the potential solution is called *post-processing*. A good interactive graphics facility is important for so that the essential information and parameters can be extracted from the large number of node potentials effectively and quickly. Finite-element analysis can be used to generate the following output:

1. ***Flux plots.*** These are especially useful for forming a picture of the flux. They can also be used for estimating leakage flux and calculating leakage permeances. Fig 12.12 shows a flux plot for a spoke type motor, in which the finite-element method is useful for calculating rotor leakage flux.

2. ***Flux calculations.*** The flux between two points of interest is calculated from the difference in vector potential at the two points, multiplied by the axial length. This calculation can be extended to obtain flux-*linkage*, and hence inductance of windings.

3. ***Flux density contours.*** Coloured filled zones can be used to indicate areas of high local saturation. Flux density values at any point can be readily obtained by using a cursor.

4. ***Graphs of flux density variation.*** The required component of flux density (radial, x-component, y-component etc.) can be plotted along a pre-determined path. For example, the variation in radial component of airgap flux density can be plotted around the rotor, and examples are shown in Figs. 12.8 and 12.19.

5. ***Flux density vector plot.*** A field of arrows is plotted over the cross-section, representing the local flux density vector.

6. ***Magnet working point distribution plot.*** The B/H working point within each magnet element can be superimposed on the major B/H curve of the magnet. This is useful for visualizing the effect of demagnetization.

7. ***Back-EMF and core-loss calculations.*** Finite-element analysis can be performed for incremental rotor positions from which variation of flux and flux-linkage against rotor position can be obtained. This can be used to calculate back-emf (by differentiation with respect to time) and core losses.

8. ***Force and torque.*** Force and torque are commonly calculated using the following three methods; Lorentz force, Maxwell stress and virtual work. All three are prone to errors [3], and the best method depends upon the type of problem and the user's preferences.

9. ***Inductance.*** Self and mutual inductances can be calculated from the stored energy or flux-linkage [4]. However, the calculation is made more complex due to the presence of magnet flux. One method sometimes used to overcome this problem is to carry out a field solution analysis at a particular value of load current. The permeability values from this solution are stored and used in a second solution which has the magnets removed.

While there are many finite-element programs on the market, the general form of the pre-processor, solver and post-processor does not vary greatly from one program to another. In this discussion all results were obtained using the package OPERA-2d [5]. To illustrate the use of finite-element analysis in machine design it might be useful to include an example. Section 12.5 describes the analysis of armature reaction in brushless DC motors using finite-element analysis.

12.5 Example: armature reaction in brushless DC motor

Permanent-magnet motors produce torque by interaction between the magnet flux and the current flowing through the armature windings. The armature current sets up its own magnetic field which distorts the airgap flux distribution. The effect is similar to that in DC and synchronous machines and is known as 'armature reaction' [6].

While the magnet flux remains substantially constant, the field set up by the armature windings is proportional to the current. Motors are usually designed such that the armature reaction does not affect the torque per ampere, k_T. Under heavy load conditions armature reaction is liable to decrease k_T.

Even under normal load conditions, the distortion in the airgap flux-density distribution tends to increase the core losses. It is not unusual for the core losses at rated load to be double the no-load value, even though k_T may not vary significantly between no-load and full load. This is because k_T depends on the magnet flux alone, whereas the core losses depend on the total airgap flux and its distribution.

The effects of armature reaction can be classified into *q*-axis effects and *d*-axis effects:

1. *q*-axis : cross-magnetization or distortion

2. *d*-axis : demagnetization or reduction of airgap flux density.

These effects are illustrated with the help of flux plots and flux density graphs generated using finite-element analysis. A small squarewave brushless DC motor with four poles and twelve slots is used as an example.

The examples can be understood by looking first at the flux distribution set up by the magnets alone, then at the flux distribution set up by the armature current alone, and finally at the superposition of both, keeping in mind the fact that the superposition is non-linear due to magnetic saturation effects.

12.5.1 Open-circuit flux distribution

Fig. 12.13 shows the flux distribution created by the rotor magnets alone. This is also referred to as the 'open-circuit' flux distribution since the armature or stator windings are not excited in this case.

Many important features are immediately apparent in Fig. 12.13, for example, the radial magnetization of the magnets, the concentration of flux in the teeth, and the variation of flux-density in the stator and rotor yokes.

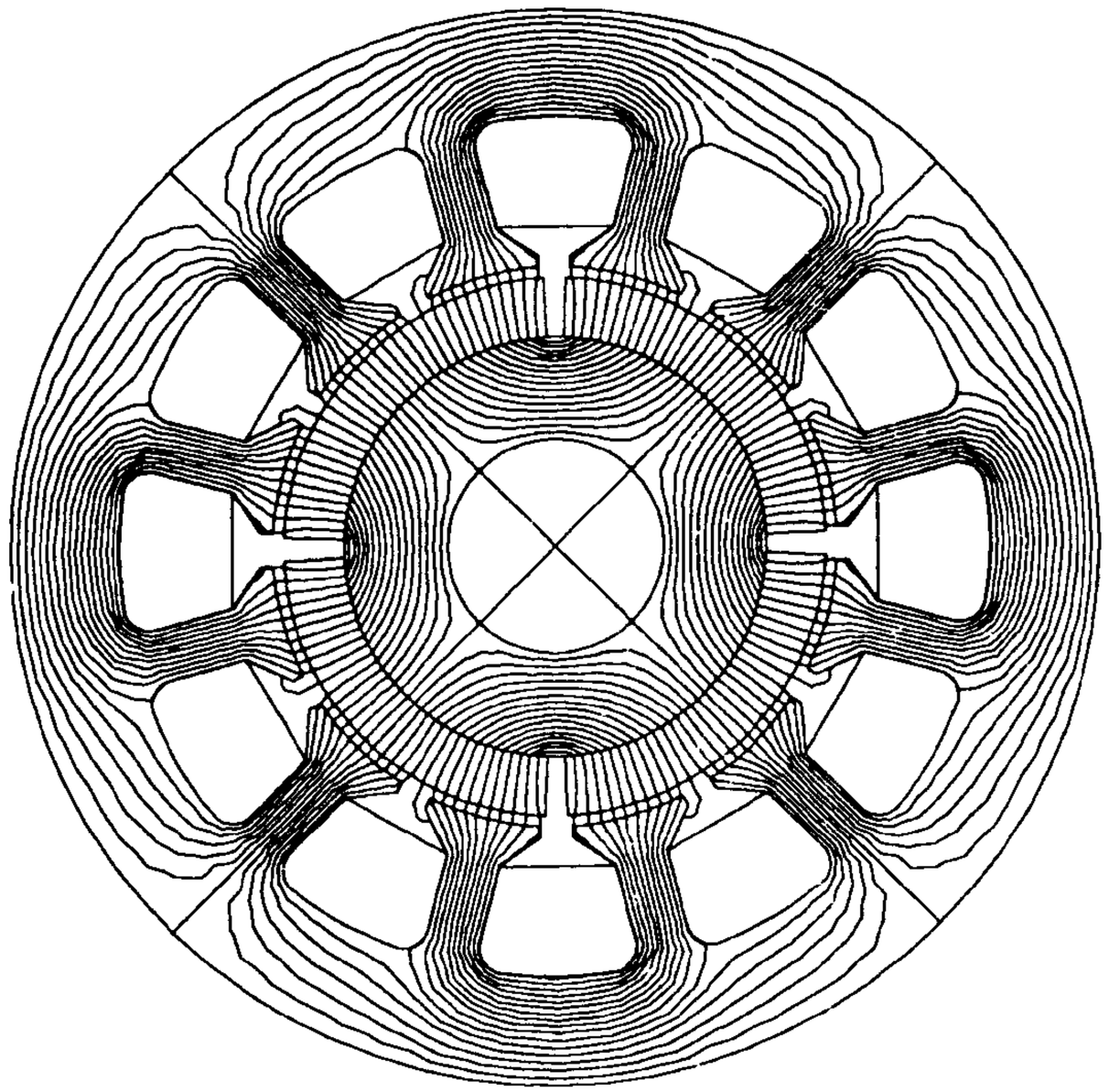

Fig. 12.13 Flux distribution due to magnets acting alone (open-circuit condition)

Closer examination shows more subtle effects such as the fringing around the slot openings, discussed at length in Chapter 8. The high coercivity and low recoil permeability of the magnets is the reason for the extreme regularity of the field lines in the magnets. "Hard" magnets such as ferrite or rare-earth magnets act as "rigid" sources of flux, and there is very little distortion of the field inside the magnets due to slotting.

12.5.2 Armature reaction field alone

Fig. 12.14 shows the flux distribution set up by the armature currents acting alone, assuming two-phase-on operation with a severe overload. The airgap as seen by the armature includes the magnet thickness and hence appears as a high-reluctance path for the armature field. The magnets are considered to be removed or unmagnetized, and have no effect on this distribution. Note that the flux encircles the ampere-conductors in the manner of Ampere's Law, and appears in four loops.

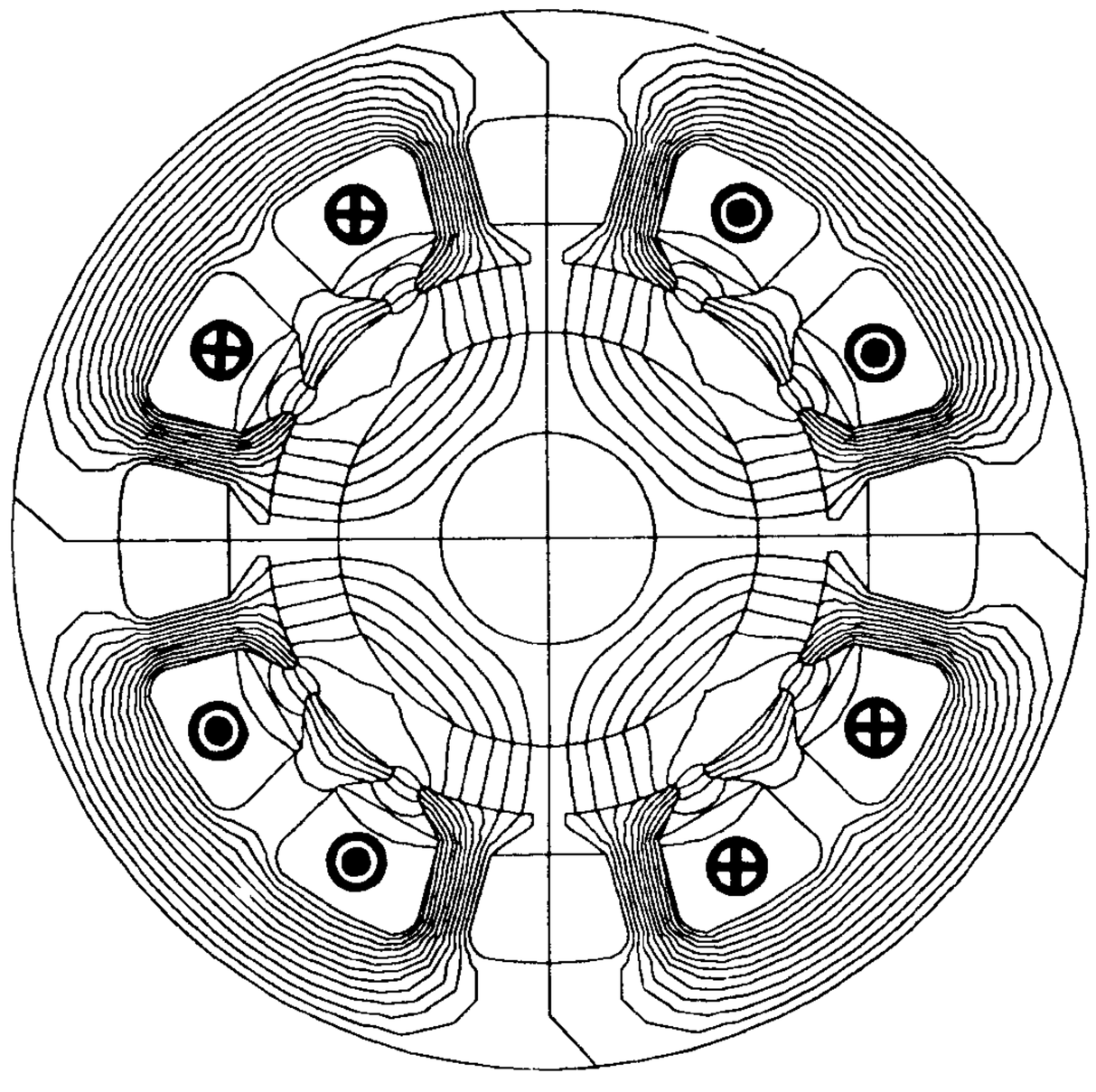

Fig. 12.14 Flux distribution due to armature current acting alone (two phases on). The dots and crosses show the polarities and locations of the armature currents. There are approximately 1600 Ampere-conductors per slot, with a high value of current density (17.3 A/mm^2)

A proportion of the flux in each loop crosses the long airgap into the rotor yoke twice. Most of the remainder crosses the tooth-tops, while a small fraction travels circumferentially around the space left by the magnets. These separate components of flux are estimated by simple formulas in Chapters 5 and 6, in the calculation of the self-inductance of the winding and the mutual inductance between windings. The somewhat complex shape of the flux paths shows that this type of calculation can only ever be an approximation, although surprisingly accurate results are often achieved. With finite-element analysis, the inductance can in principle be calculated more accurately.

Note that all the flux-plots shown here are two-dimensional, and three-dimensional effects (end-effects) are neglected.

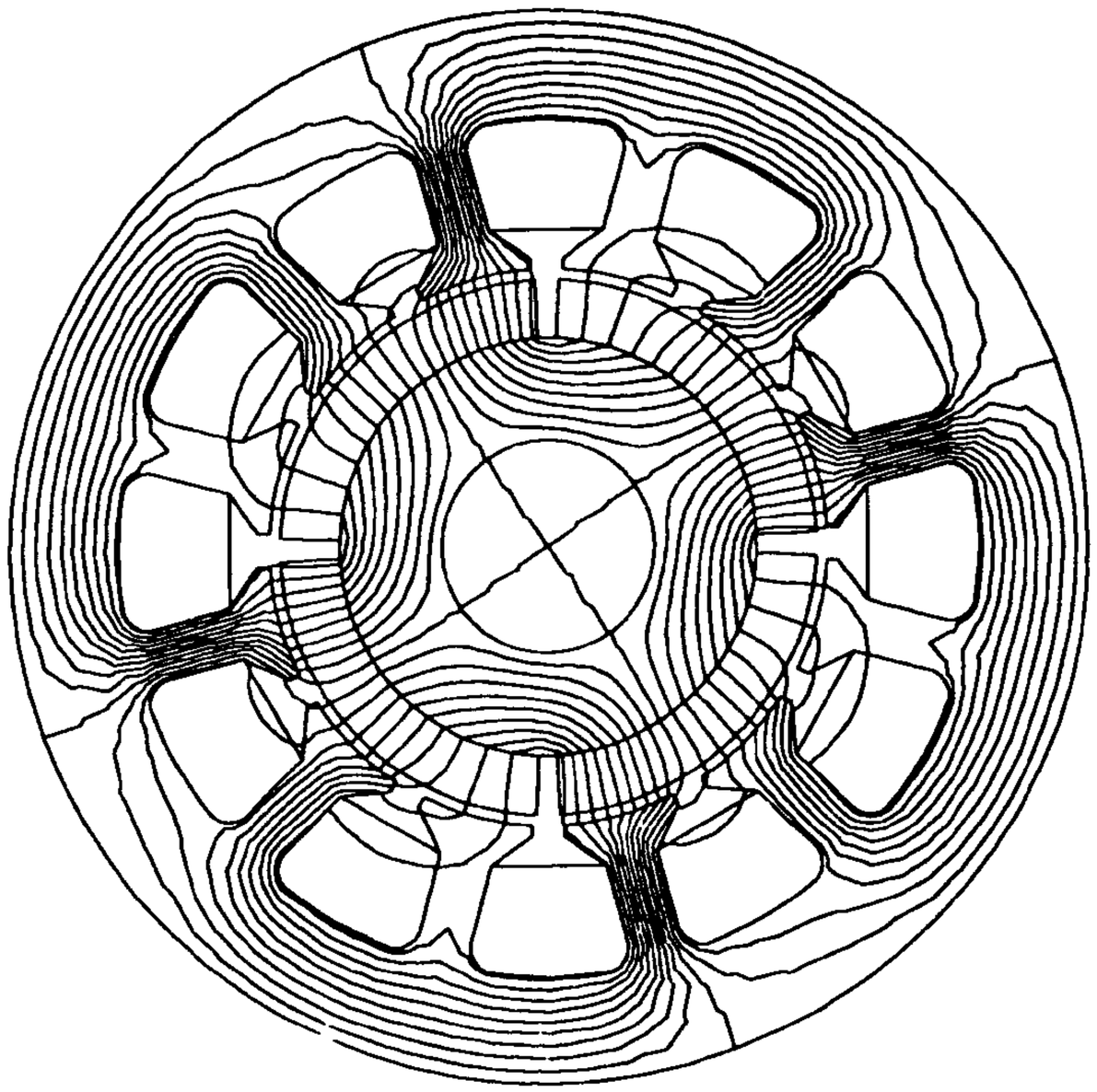

Fig. 12.15 Resultant flux-distribution with magnets and cross-magnetizing armature reaction. The currents are as defined in Fig. 12.14.

The inductance associated with the flux pattern in Fig. 12.14 is a static inductance, which is directly useable in time-stepping simulation of squarewave or sinewave brushless motors, but is quite distinct from the synchronous reactance X_s discussed in Chapter 6.

The synchronous reactance cannot be directly calculated from a static finite-element flux-plot, except in the special case when the windings and the flux are perfectly sine-distributed. In the general case, the synchronous reactance calculation requires the stepping of the rotor through at least one electrical revolution, followed by a differentiation of the flux-linkages of the phase windings and a harmonic analysis to extract the fundamental component. This is because the synchronous reactance is defined for a fundamental space-harmonic field so that it can appear correctly in the phasor diagram.

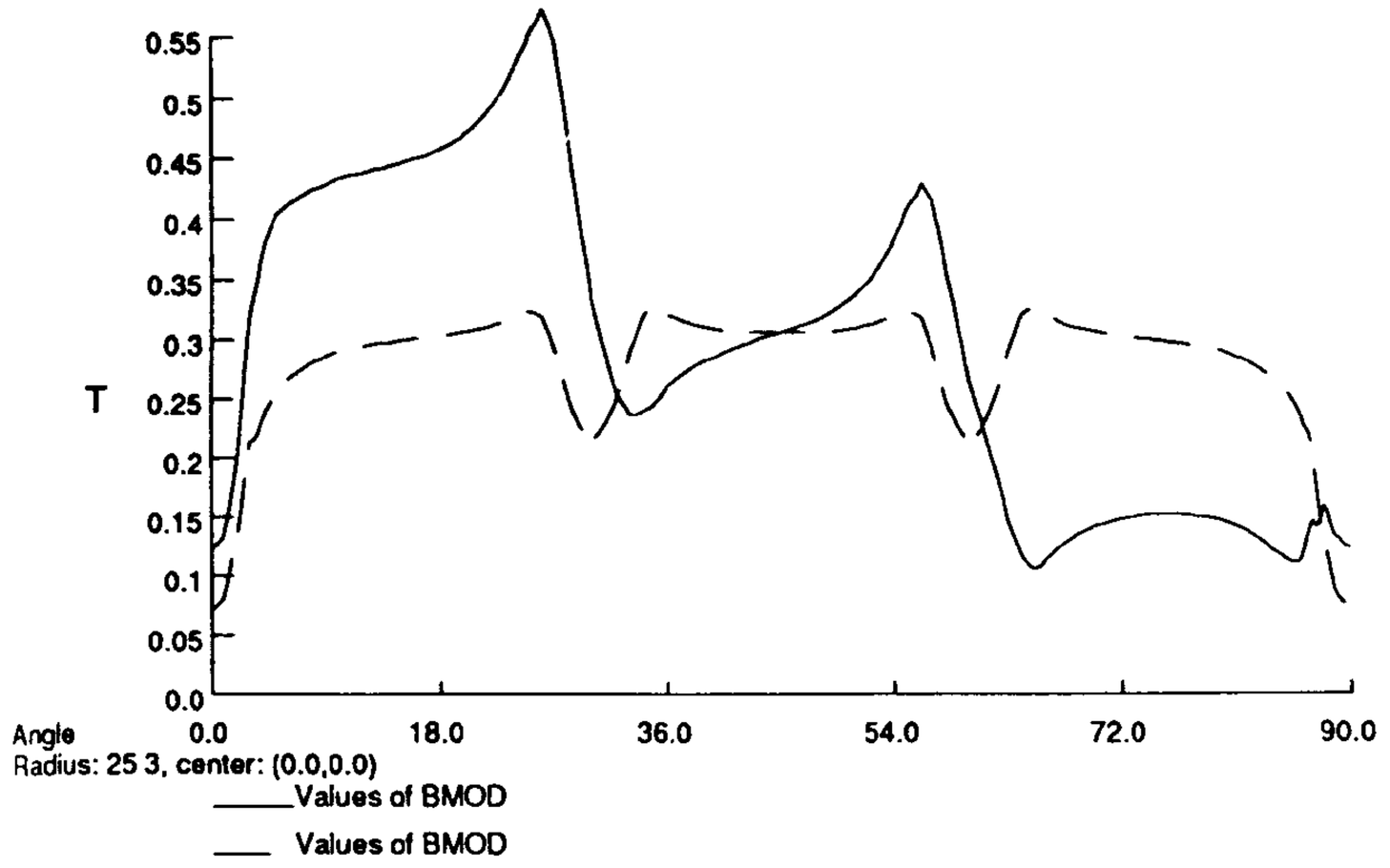

Fig 12.16 Variation of airgap flux-density under one pole. Dotted line : magnets alone. Solid line : resultant with cross-magnetizing armature reaction.

12.5.3 Cross-magnetization

The cross-magnetization effect is greatest when the rotor magnet field is in quadrature with the armature field, as in Fig. 12.15. Many significant features of the effect of armature reaction can be observed from Fig. 12.15, most important of which is the increase in flux-density at the leading tip of the magnet pole and the decrease in flux-density at the trailing tip. This effect is illustrated in Fig. 12.16, which shows the variation of airgap flux density under one magnet pole around the airgap. The dotted line corresponds to Fig. 12.13 showing the variation in flux density due to magnets alone. The solid line corresponds to Fig. 12.15 showing the resultant distorted flux distribution when both magnets and armature current are present.

12.5.4 Demagnetization

The demagnetizing effect is greatest when the axis of symmetry of the magnet (the *d*-axis) is aligned with the axis of symmetry of the armature

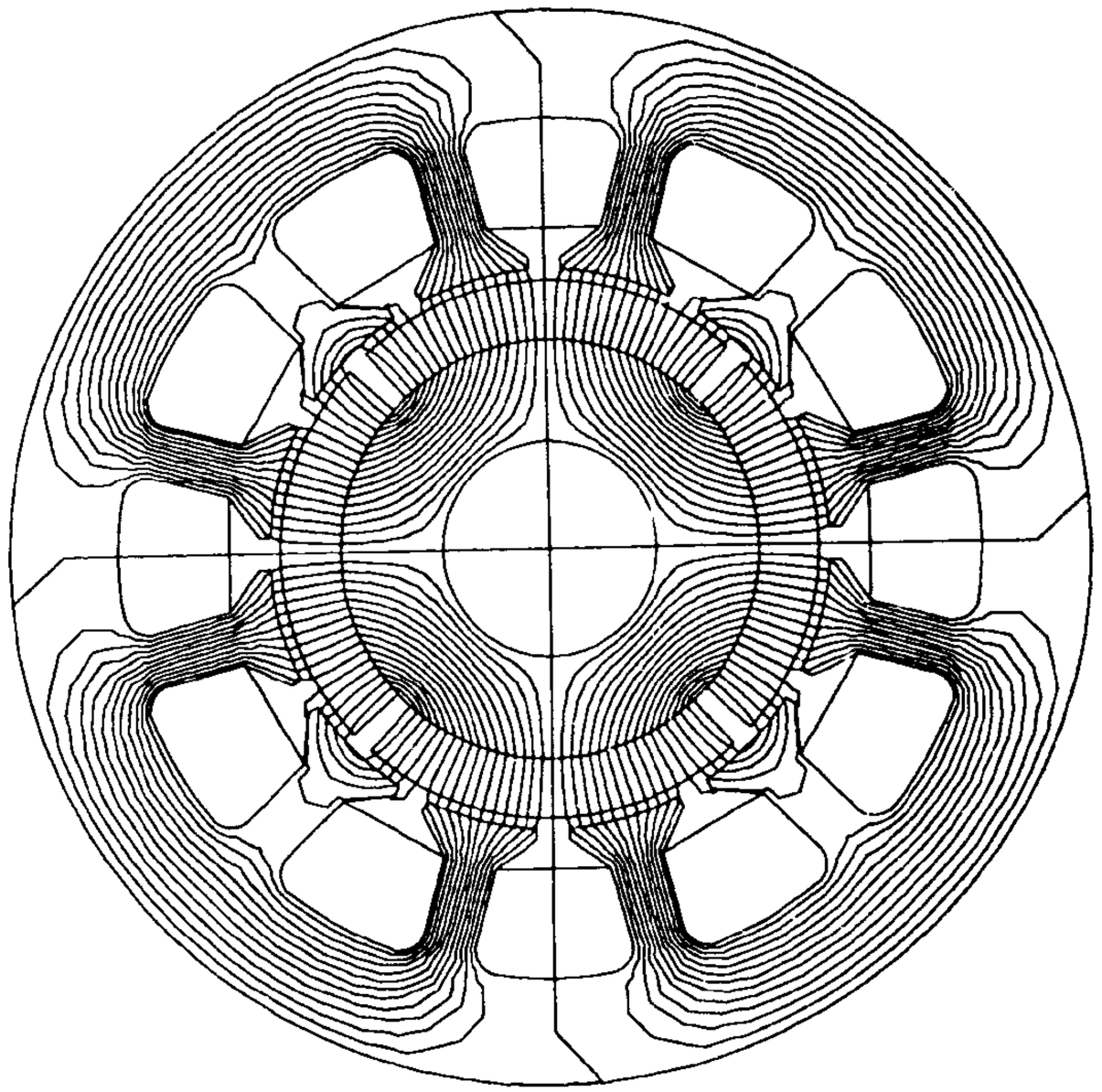

Fig. 12.17 Flux distribution due to magnets acting alone The rotor is turned 45° clockwise relative to its position in Fig. 12.13

ampere-conductor distribution. Fig. 12.17 is again the 'open-circuit' flux distribution due to magnets alone, but the rotor is rotated 45 degrees (90 electrical degrees) to align the two axes as required.

The armature ampere-conductor distribution remains unchanged from that of Fig. 12.14, and the resultant flux distribution is shown in Fig. 12.18. The airgap flux density at the centre of the magnet is much less than the open-circuit value in Fig. 12.17. The MMF's of the magnet and the armature current combine in the region of the quadrature axis, where the flux is forced to return from one magnet pole to the next across the tooth-tops, rather than following its normal course through the teeth and round the stator yoke. The stator yoke flux is greatly reduced.

The armature reaction in all these examples is for very high current, corresponding to locked-rotor condition.

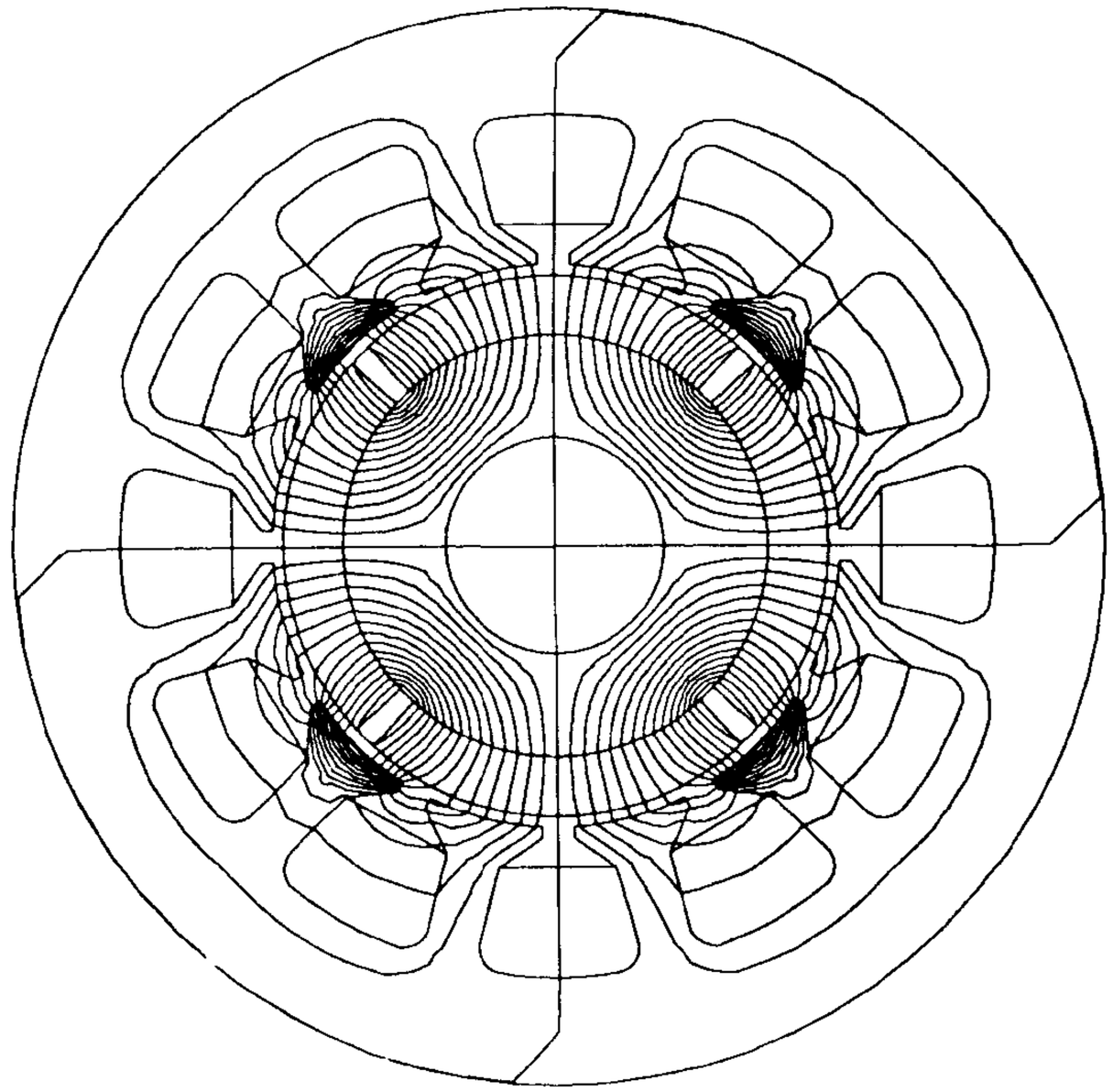

Fig 12 18 Resultant flux distribution with magnets and demagnetizing armature reaction The magnet *d*-axis is aligned with the axis of symmetry of the armature ampere-conductor distribution, such that their MMF's are in opposition

In Fig. 12.19 the dotted line shows the variation of flux density around the airgap with the magnets acting alone. The solid line shows the flux density variation when both magnets and armature current are present.

Note that both the cross-magnetizing and demagnetizing components of armature-reaction MMF distort the airgap flux waveform and introduce additional time-harmonics into the variation of the flux-density in the teeth and yokes. This is the main cause of increased eddy-current loss in the core. The peak flux-density is also increased, and this contributes to an increase in the hysteresis loss. It is difficult to estimate the magnitude of these effects by simple formulations, but the finite element method quickly brings the effects to light and provides an accurate means for estimating them with a high degree of confidence.

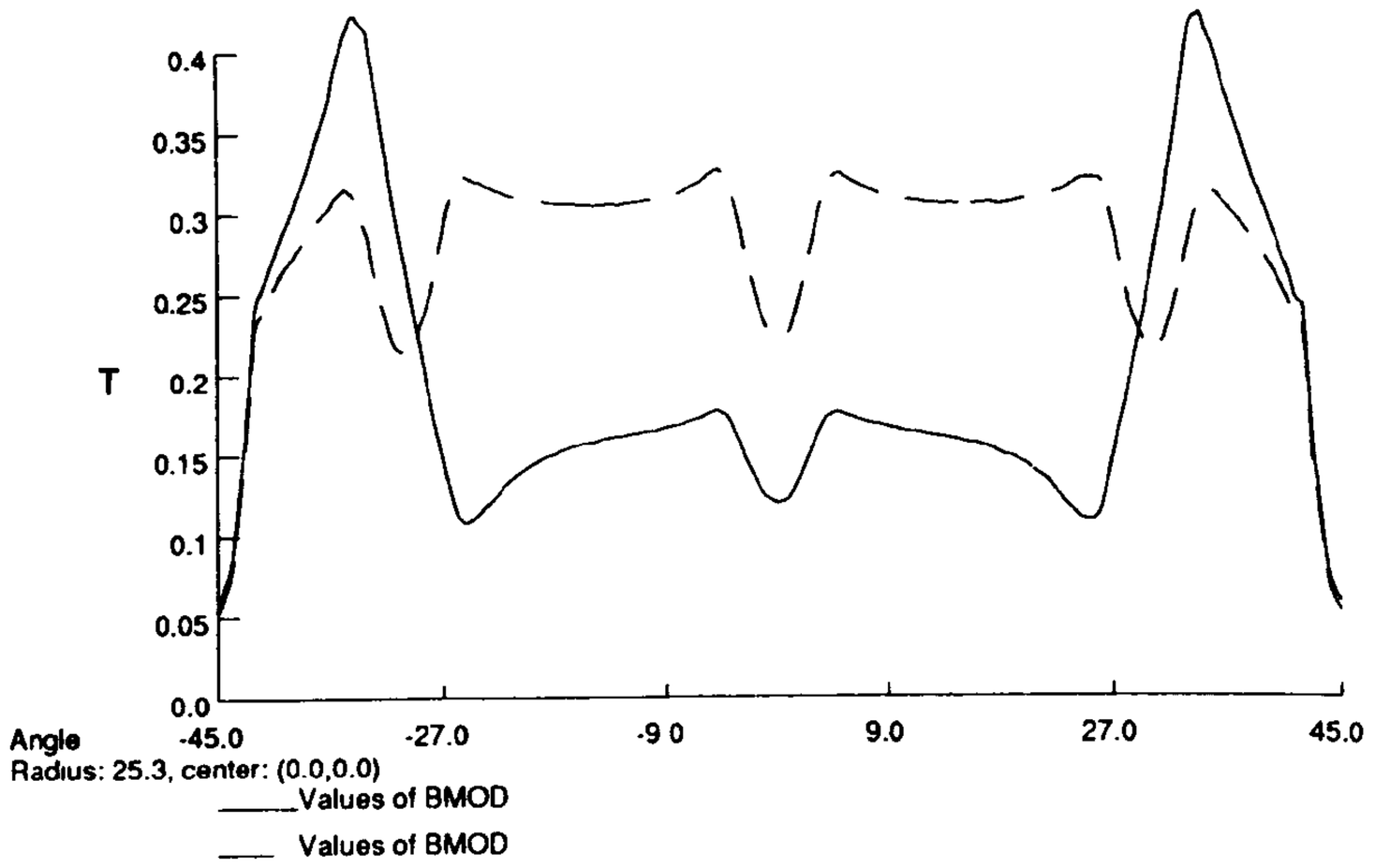

Fig. 12.19 Airgap flux-density variation under one pole with strong demagnetizing armature reaction. Dotted line : magnets alone. Solid line : resultant.

References

1. Fouad FA, Nehl TW and Demerdash NA [1981] *Magnetic field modelling of permanent magnet type electronically operated synchronous machines using finite elements*, IEEE Transactions, Vol. PAS-100, No.9, pp. 4125-4135

2. Reece ABJ : *Electrical machines and electromagnetics - computer aids to design*, GEC Review, Vol.5, No.1, 1989, 34-41.

3. Hamdi ES, Licariao-Nogueira AF and Silvester PP [1993] *Torque computation by mean and difference potentials*, IEE Proceedings-A, Vol.140, No.2, 151-154.

4. Lowther DA and Silvester PP [1986] *Computer-aided design in magnetics*, Springer-Verlag.

5. Opera-2d *Reference and User Guide*, Vector Fields Ltd., Oxford

6. Fitzgerald AE, Kingsley C and Umans SD [1990] *Electric Machinery*, fifth edition, McGraw-Hill

13. EXAMPLES CALCULATED BY HAND

13.1 Introduction

The use and proliferation of brushless permanent-magnet motors over the past ten years or so has been largely application-specific without any standardization. For example, the motors used in computer hard disc storage drives have been designed to keep pace with developments in the disc drive. In a short period the data storage capacity of Winchester disc drives increased 100-fold: the access time decreased by a factor of 10, and the drive envelope decreased by a factor or 3 or 4. Needless to say, the brushless drive motors used in these drives have evolved at a comparable rate.

Another example of an application-specific brushless motor family is the high performance servo motor used to drive specific loads without the use of gearing or clutches and brakes in order to achieve elegant programmable motion. The configuration of these designs is driven by high torque to inertia and ease of cooling the stator. Based on a casual inspection of most vendor offerings it would appear that there are some similarities, but their differences are more significant. It would seem that among the various designs of similar motors each designer is able to achieve acceptable performance for a particular physical size using different magnet grades, number of poles and stator coils. There is also a wide variety of feedback sensors in use. The author assumes that these differences in design details from one vendor to another are attributed principally to economic issues relative to each manufacturing operation. The other possible reason would be that each designer achieves acceptable results using design parameters which are within his or her scope of understanding and experience.

Other motor products such as AC induction motors seem to all be alike. If you disassemble them it is difficult to discern one from the other. DC brush type motors are somewhat the same in their configuration. Most companies which have developed brushless servo motors have been known for their DC motors not AC motors. The large US induction motor manufacturers were the last ones to enter the brushless AC or DC servo business with new products so their design approaches are somewhat different from those of the DC motor companies.

Most recently there have been several significant developments of

Torque Prediction Using the Flux-MMF Diagram in AC, DC, and Reluctance Motors

David A. Staton, Rajesh P. Deodhar, *Student Member, IEEE,* Wen L. Soong, *Member, IEEE,* and Timothy J. E. Miller, *Senior Member, IEEE*

***Abstract*—This paper uses the flux-MMF diagram to compare and contrast the torque production mechanism in seven common types of electric motor. The flux-mmf diagram is a generalized version of the flux-linkage versus current (ψ-i) diagram for switched-reluctance motors. It is illustrated for switched-reluctance, synchronous-reluctance, induction, brushless ac, brushless dc, interior PM and dc commutator motors. The calculated flux-MMF diagrams for motors with the same electromagnetic volume, airgap, slotfill, and total copper loss are shown and are used to compare the low-speed torque and torque ripple performance. The motor designs used were reasonably optimized using a combination of commercially available motor CAD packages and finite-element analysis.**

I. Introduction

THE FLUX-LINKAGE versus current (ψ-i) diagram has traditionally been used to analyze the switched-reluctance motor (SRM) performance characteristics [1]–[6]. Recently this concept has been extended to synchronous-reluctance (SYNCHREL) motors [5] and doubly salient permanent magnet (DSPM) motors [6] in order to facilitate a direct comparison with the SRM. The concept of electromagnetic torque being derived from the (ψ-i) characteristics is however fundamental to all electric motors [7]–[9]. This paper shows how the flux-MMF diagram can be derived from the (ψ-i) diagram and applied to several motor types, providing a unified method of analysis and evaluation.

Section II describes the salient features of the flux-MMF diagram and gives the relevant definitions of flux and MMF. Section III explains the constraints applied in designing the seven motor types used in the comparison. Section IV describes the flux-MMF diagram of each motor. Finally Section V compares and contrasts the seven motor types.

II. The Flux-MMF Diagram

The ψ-i diagram is based on plotting the variation of instantaneous phase flux-linkage against the instantaneous phase current. The *instantaneous torque* per phase is given by [1]–[3]

$$T = \left.\frac{\partial W'(i,\theta)}{\partial \theta}\right|_{i=constant} \tag{1}$$

where W' is the *co-energy*, i is the instantaneous phase current and θ is the rotor position. The partial differentiation is performed by dividing the area enclosed between two successive magnetization curves by the rotor displacement. The *average electromagnetic torque* per phase is proportional to the area enclosed by the ψ-i locus over one electrical cycle. Thus

$$T_{AV} = \frac{mp}{2\pi} \times W' \tag{2}$$

where W' is the energy converted as shown in Fig. 1, m is the number of phases and p is the number of pole-pairs.

To eliminate the arbitrariness of the number of turns from the analysis, the phase flux-linkage and current are respectively divided and multiplied by N_{ph}, the series turns/phase, to give the "effective" phase flux and phase MMF. These are similar to per-unit quantities. The quantity ψ/N_{ph} is not the actual flux in the machine but the *effective flux* which links the winding and thus produces torque. The converted energy can be calculated from either the flux-MMF or ψ-i locus, since both enclose the same area as shown in Fig. 1. The flux-MMF diagram is independent of the particular voltage level for which the motor happens to be wound. The important features of the flux-MMF diagram are the following:

- Area enclosed indicates torque capability.
- Shape indicates nature of excitation (ideally ellipsoidal for sinewave and rectangular for squarewave).
- Deviation from ideal shape and uneven spacing of magnetization curves indicates torque ripple and saturation.
- Whereas d-q axis theory can only predict average torque, this method can predict torque ripple as well.
- Orientation of the major axis with respect to the MMF-axis indicates the kVA utilization (power factor in sinewave motors).
- Electric and magnetic loadings and their utilization are indicated graphically.

The flux-MMF diagram for a particular motor is shown with *magnetization curves* superimposed (e.g., Figs. 5 and 12). These are generated using a series of static finite-element analyses at incremental rotor positions (θ) and increasing loads.

The method of predicting torque ripple using the ψ-i diagram has been validated for synchronous reluctance motors

Paper IPCSD 95–53, approved by the Electric Machines Committee of the IEEE Industry Applications Society for presentation at the 1994 Industry Applications Society Annual Meeting, Denver, CO, October 2–7 Manuscript released for publication July 11, 1995.

D. A. Staton is with Control Techniques plc, Newtown, Wales SY16 3AJ, U.K.

R. P. Deodhar and T. J. E Miller are with the SPEED Laboratory, University of Glasgow, U K.

W. L. Soong is with the GE Corporate Research and Development, Schenectady, NY 12301 USA.

Publisher Item Identifier S 0093-9994(96)00322-2.

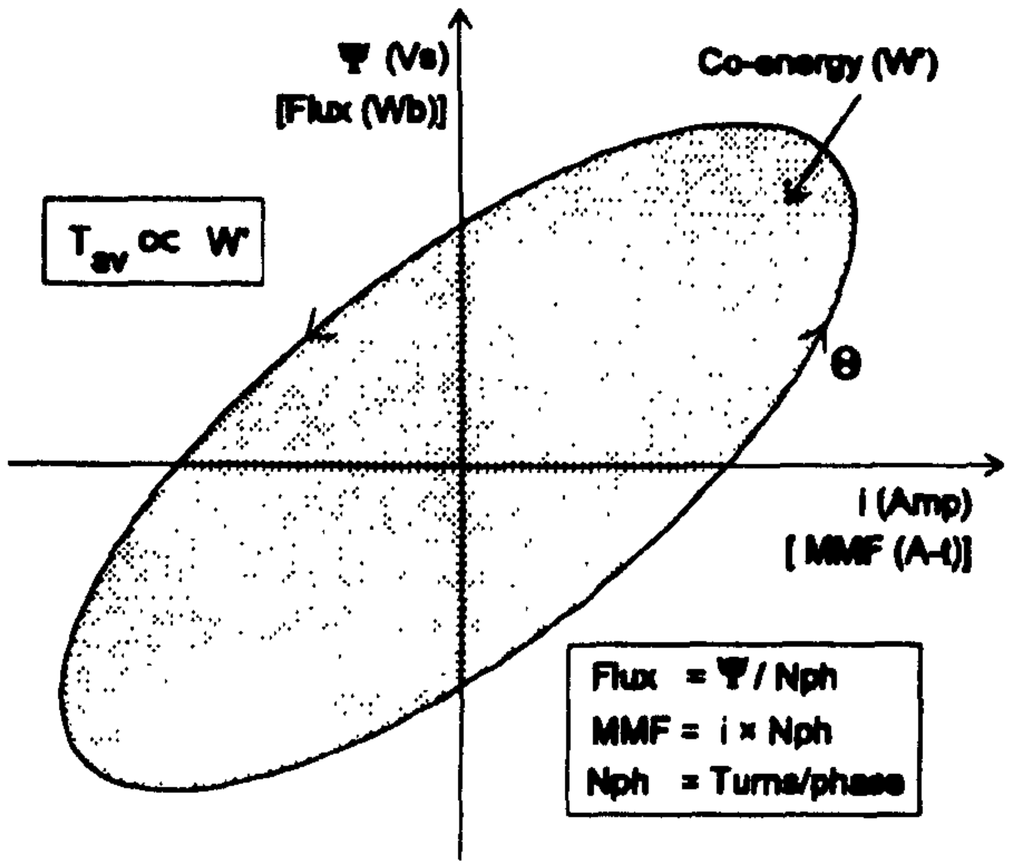

Fig. 1. The equivalence between the Ψ-i and flux-MMF diagrams.

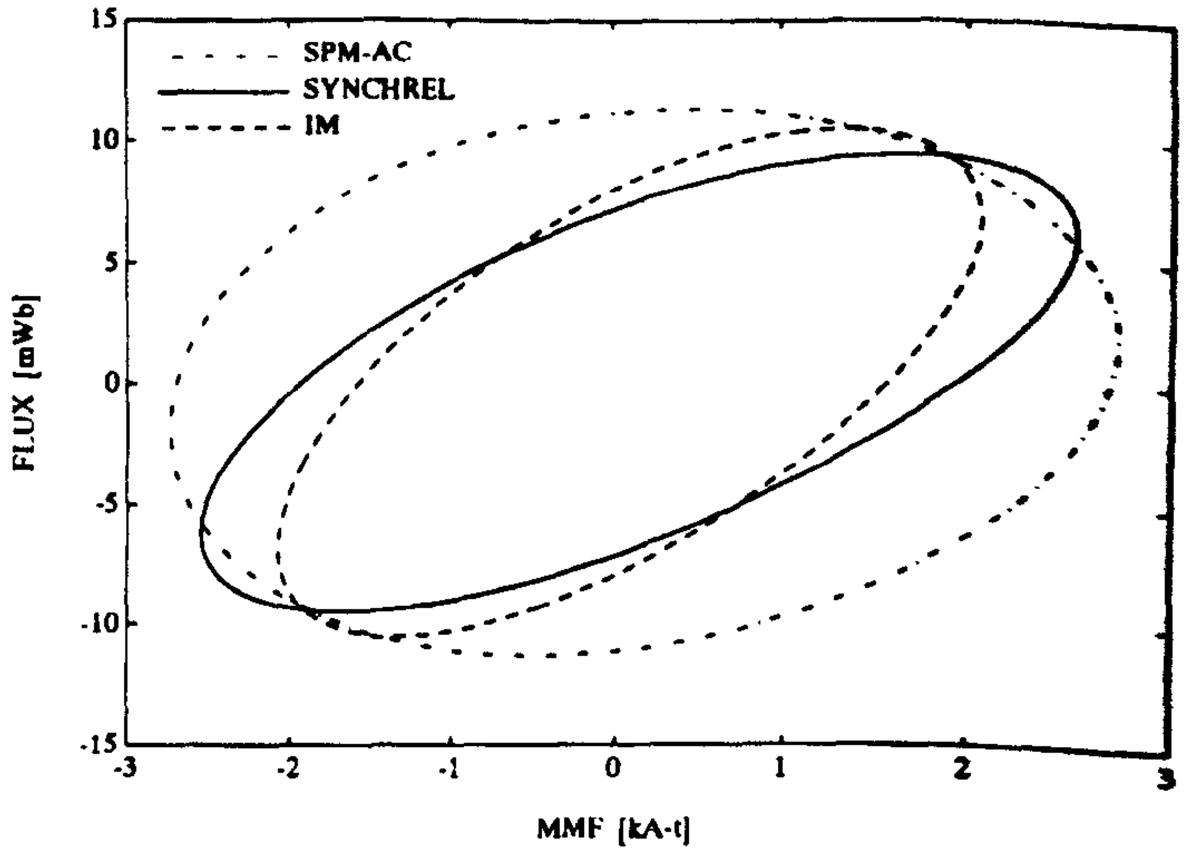

Fig 2. flux-MMF diagram for the IM, SYNCHREL and SPM-AC motors (full-load)

TABLE I
DESIGN CONSTRAINTS

Parameter	Constraint
Stator outer diameter	8 inches (203.2mm)
Active length	8 inches (203.2mm)
Airgap	0.5mm
Slot fill	40%
Copper loss	634W

with measurements as shown in Figs. 5 and 6 [5]. In the interest of simplicity this paper presents only the electromagnetic torque and neglects *cogging*, which contributes no useful average torque. However, it is possible to calculate the cogging torque using the flux-MMF diagram technique [10]. Briefly, this is done by calculating the variation in magnet working point with rotation. The flux-MMF diagram is then constructed using the demagnetization characteristic.

III. Design Constraints

A standard D132 frame induction motor (Section IV-A) has been used as the basis for designing all the motors used in this comparison. Each has the same electromagnetic volume, airgap, slot-fill, and total copper loss (at 115°C and 7.5 kW rating) as the induction motor (Table I). Friction, windage, and iron losses are not quoted here, so that the conclusions made from the comparison are strictly valid at low speed.

IV. Motors Used in the Comparison

A. Induction Motor (IM)

This is a standard D132 induction motor, capable of 11 kW when operated from a 50-Hz sinusoidal supply. It must be derated to 7.5 kW for operation from a variable speed supply

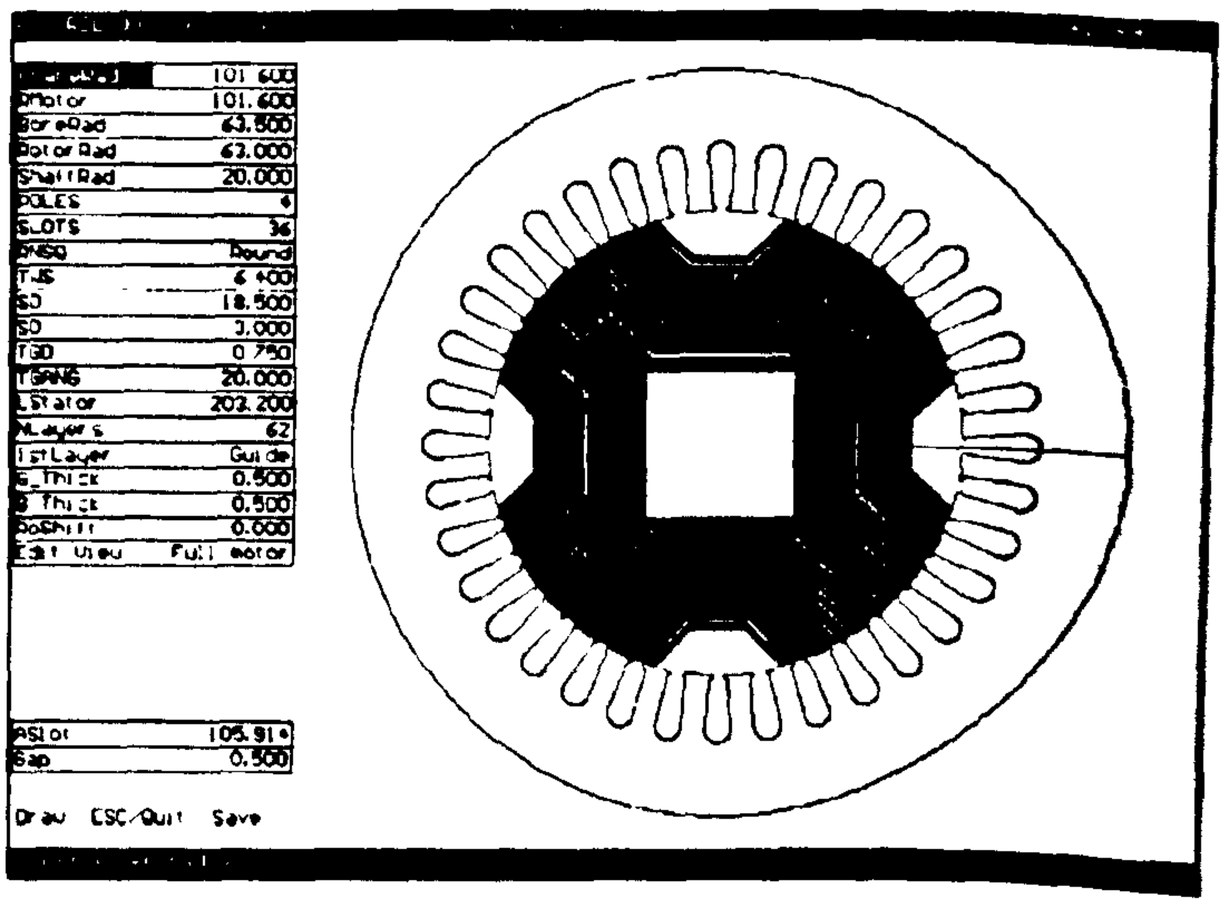

Fig 3 SYNCHREL motor design.

(10 : 1 speed ratio) with constant torque (50 Nm). The total copper loss at the 7.5 kW rating is equal to 634 W (stator copper loss = 426 W; rotor copper loss = 208 W); this is the main design constraint used in the comparison.

The flux-MMF diagram for the IM is derived from the phasor diagram. The instantaneous voltage and current is given by

$$i = \hat{I}\cos(\omega t - \varphi); \qquad v = \hat{V}\cos(\omega t).$$

The flux-linkage is calculated using

$$\lambda = \int v\,dt = \hat{V}/\omega \sin(\omega t).$$

The flux-MMF diagram for the IM at full-load is shown together with that of the SYNCHREL (Section IV-B) and SPM-AC (Section IV-D) motors in Fig. 2.

B. Synchronous Reluctance Motor (SYNCHREL)

An axially laminated rotor is used in the comparison since it has been shown that this construction gives the maximum

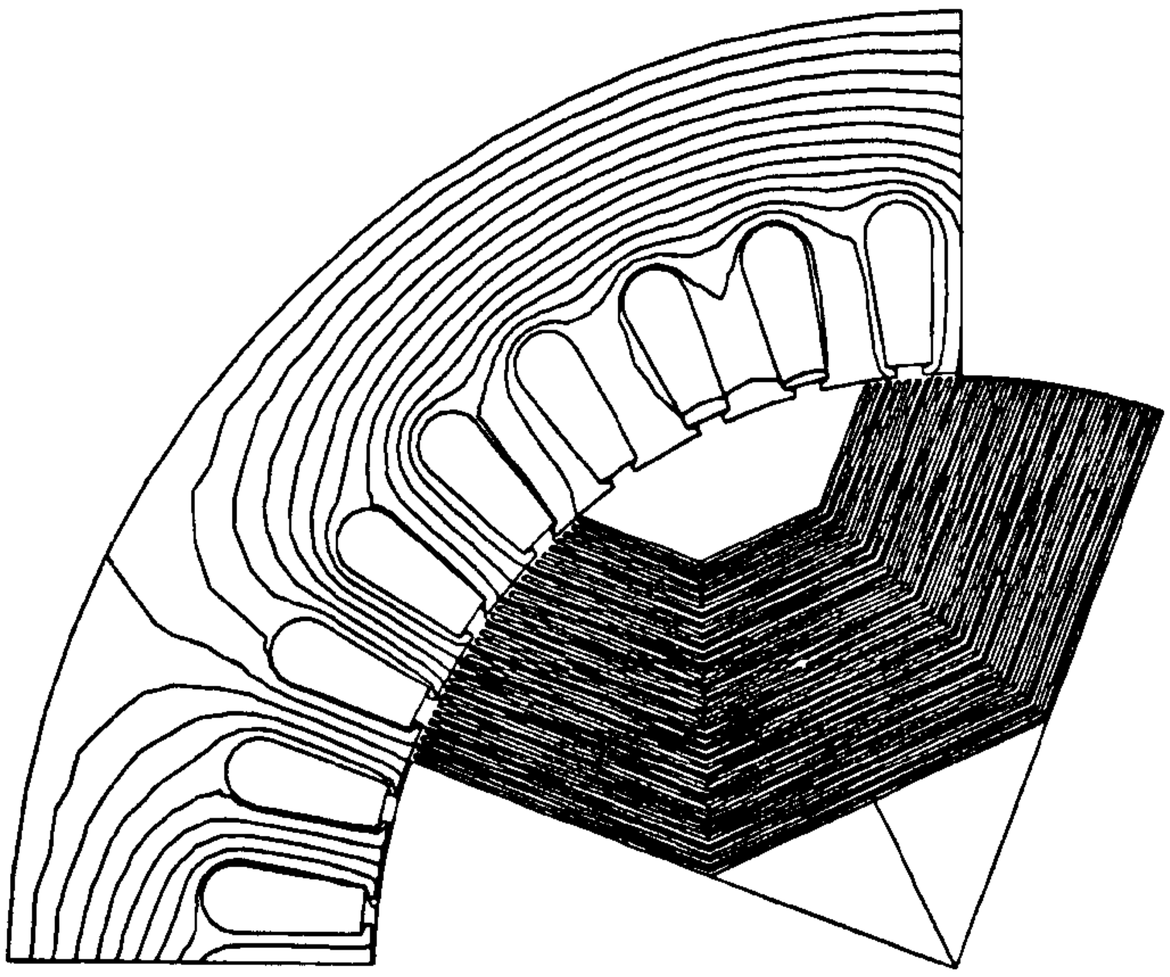

Fig. 4. SYNCHREL flux-plot (full-load, $\theta = 20°$, $\gamma = 60°$).

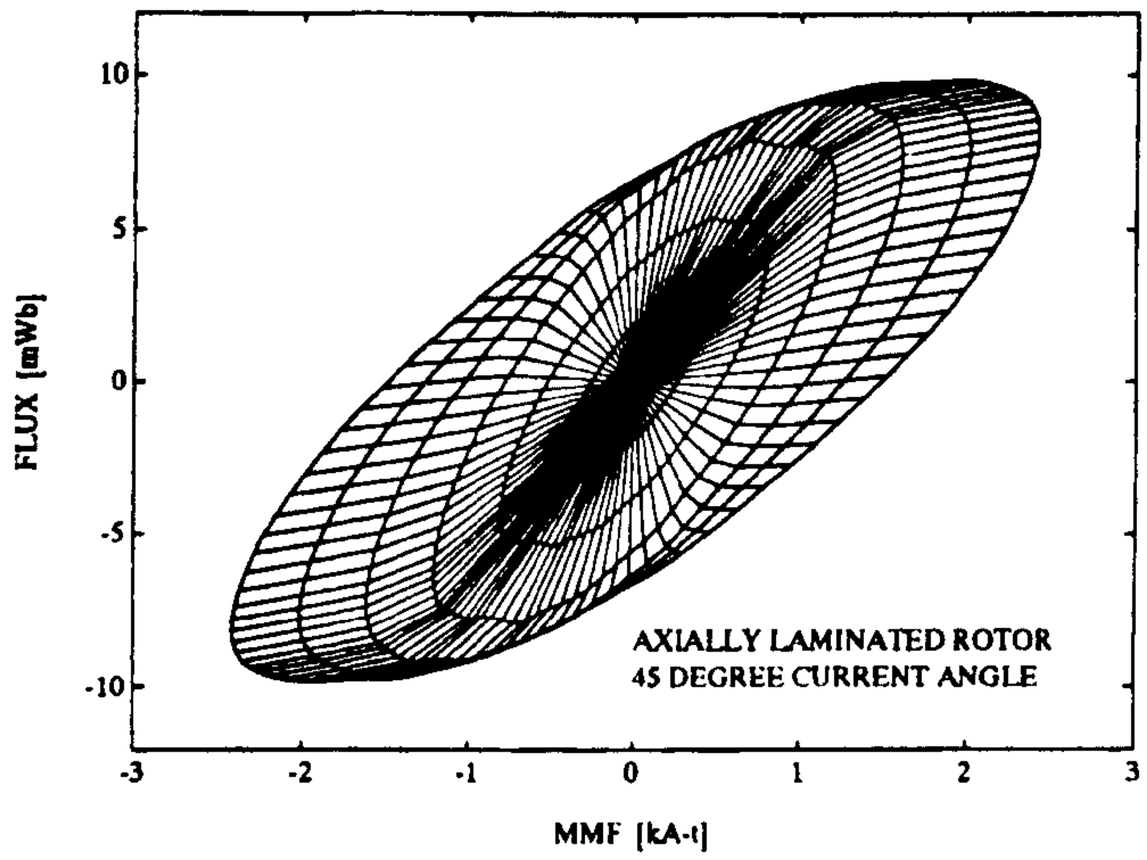

Fig. 5. Flux-MMF diagram and magnetization curves for the SYNCHREL motor (6 phase current values with the maximum at full-load)

saliency ratio [11]–[20]. The stator and winding type are the same as used in the induction motor. The motor cross section is shown in Fig. 3. This is a screen-capture taken from a synchronous reluctance motor design program *(PC-SREL)*. An on-load flux plot taken from the finite-element analysis is shown in Fig. 4. The predicted flux-MMF diagram is shown in Fig. 5 and the torque waveform in Fig. 6. The angle γ between the stator MMF axis and the rotor q-axis (high-inductance axis) is set at 60° to give maximum torque/ampere under saturated conditions [12].

C. Switched Reluctance Motor (SRM)

The calculation of SRM torque from the ψ-i locus is well documented [1]-[3]. The 6:4 SRM used in this analysis was designed using the *PC-SRD* program [1], [3], [22] and is shown in Fig. 7. It has the same number of phases and energy conversion strokes per revolution as the other brushless motors used in the comparison. The 6:4 motor has high torque ripple

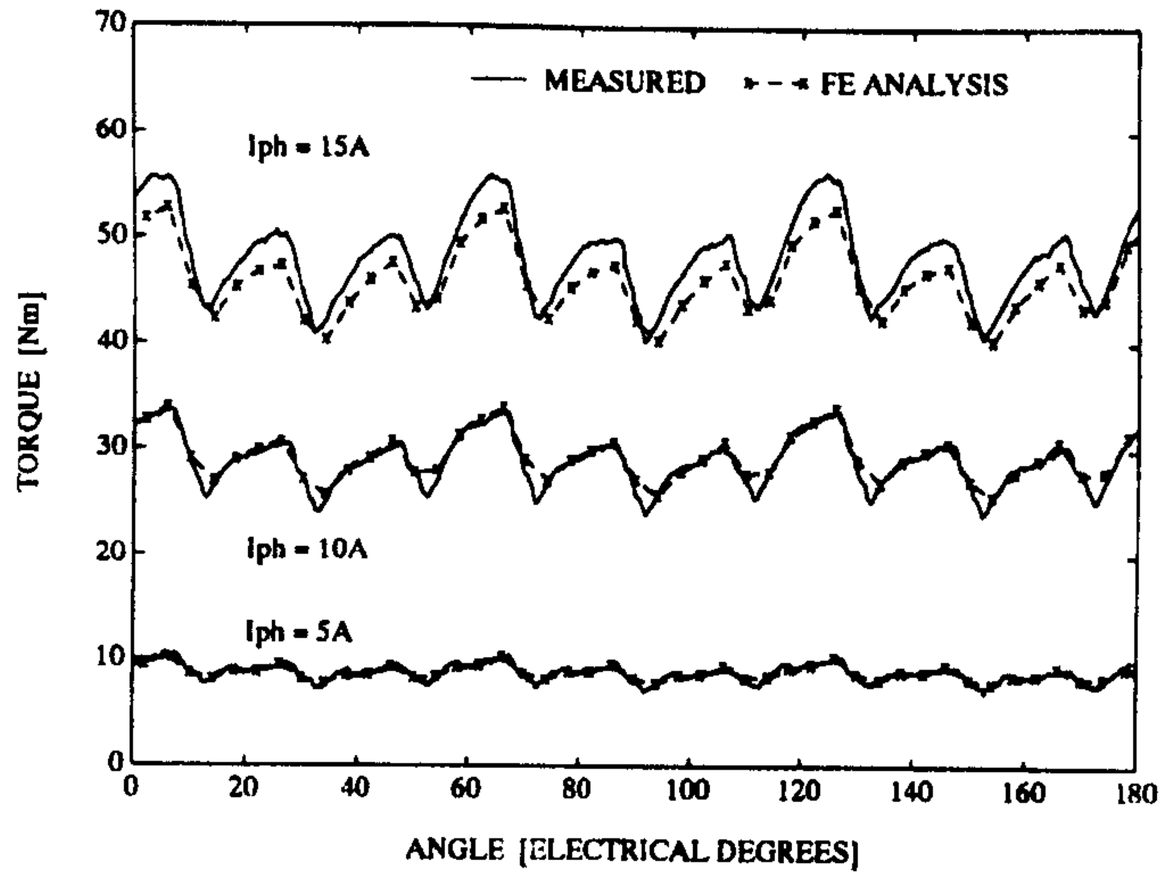

Fig. 6. SYNCHREL measured and calculated (FE analysis) torque-ripple.

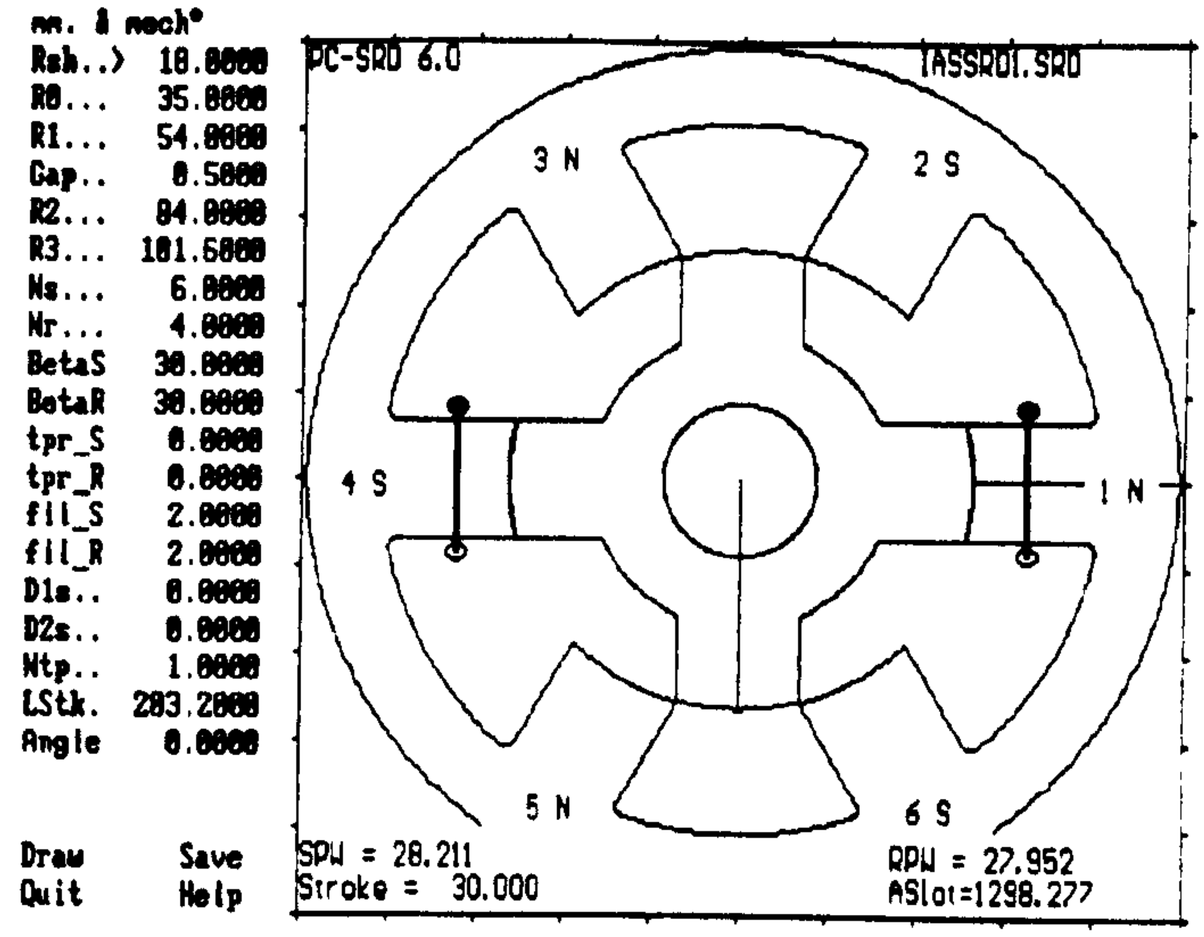

Fig. 7. SRM design.

as shown in Fig. 8. Fig. 9 compares the flux-MMF diagram at full-load with that of the SYNCHREL motor (Section V-B).

D. Surface Permanent Magnet Brushless AC (SPM-AC)

The surface permanent magnet brushless ac (SPM-AC) motor used in the analysis is shown in Fig. 10. It was designed using the *PC-BDC* program [21], [22]. It has rare-earth magnets with a remanence of 1.1 T to give flux-density levels comparable to those in the IM. The magnet arc and distributed winding configuration were selected to give a sinusoidal back-emf.

Fig. 12 plots the flux-MMF diagram (with magnetization curves) at 6 currents ranging from no-load to full-load. The dynamic locus of the operating point (whose coordinates are MMF and effective flux) is nearly elliptical. The magnetization curves are virtually straight because the flux-linkage is set by the magnets and is virtually independent of the current. Slight irregularities in the otherwise regular spacing of the magnetization curves indicate a small amount of torque ripple

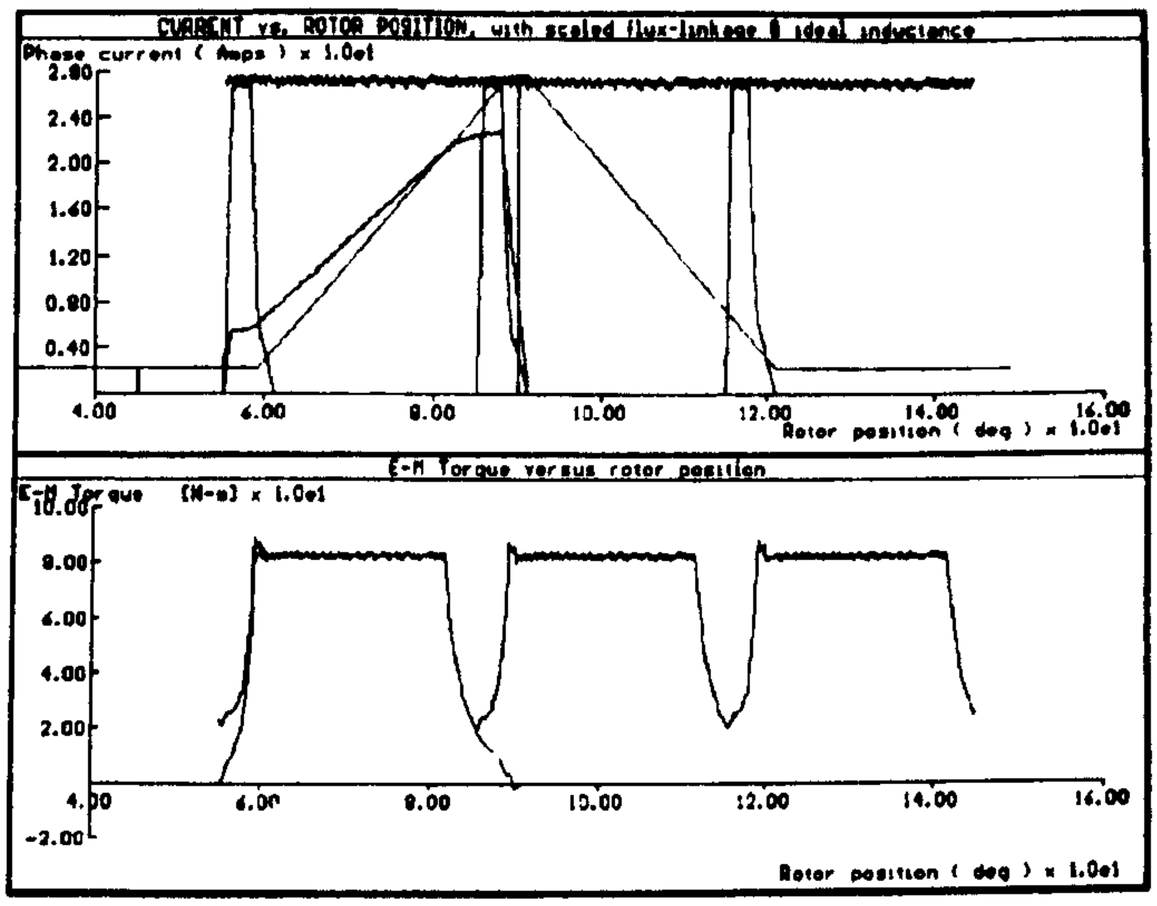

Fig. 8. SRM phase current and torque waveforms (150 r/min)

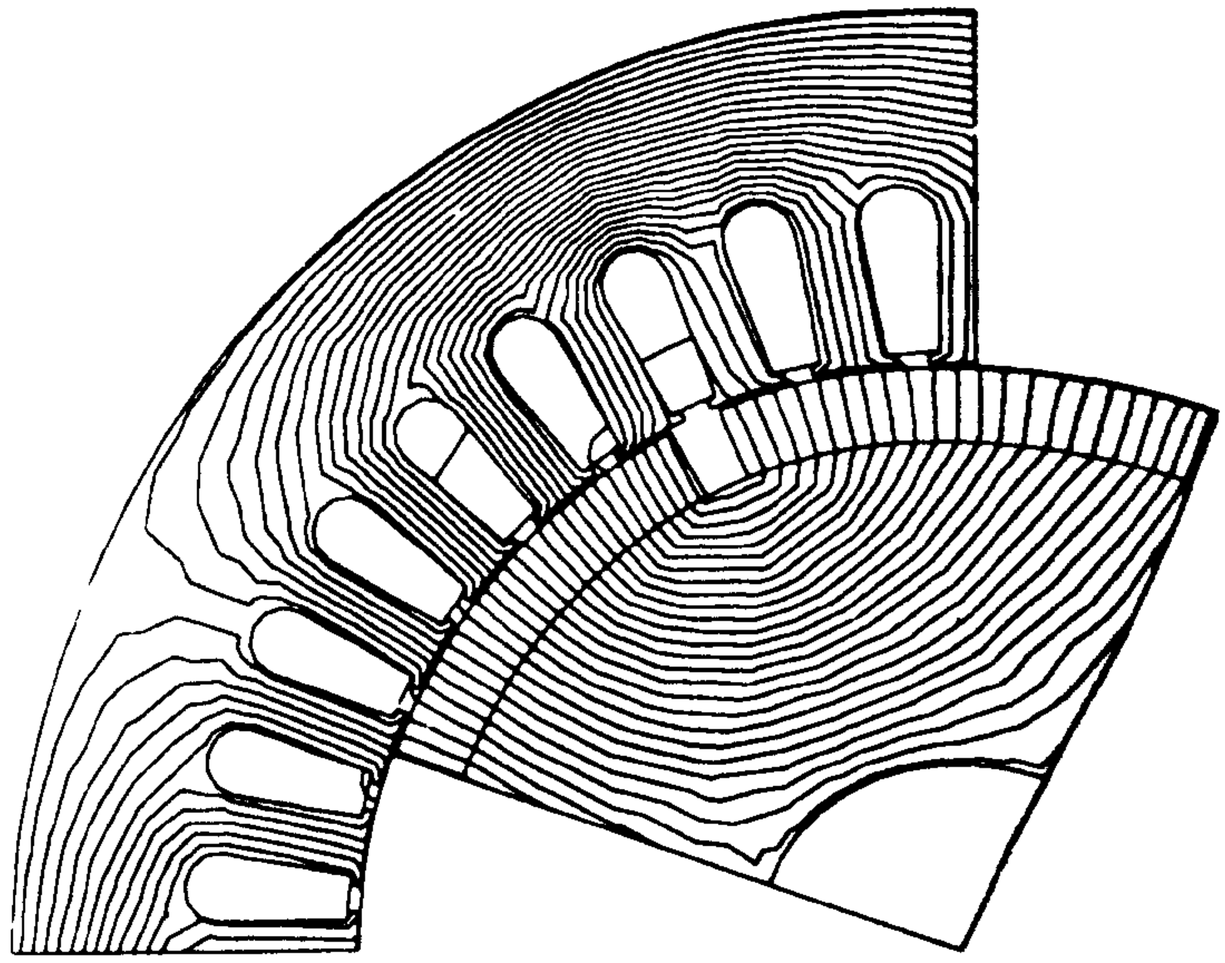

Fig. 11 SPM-AC flux plot (full-load, $\theta = 20°$).

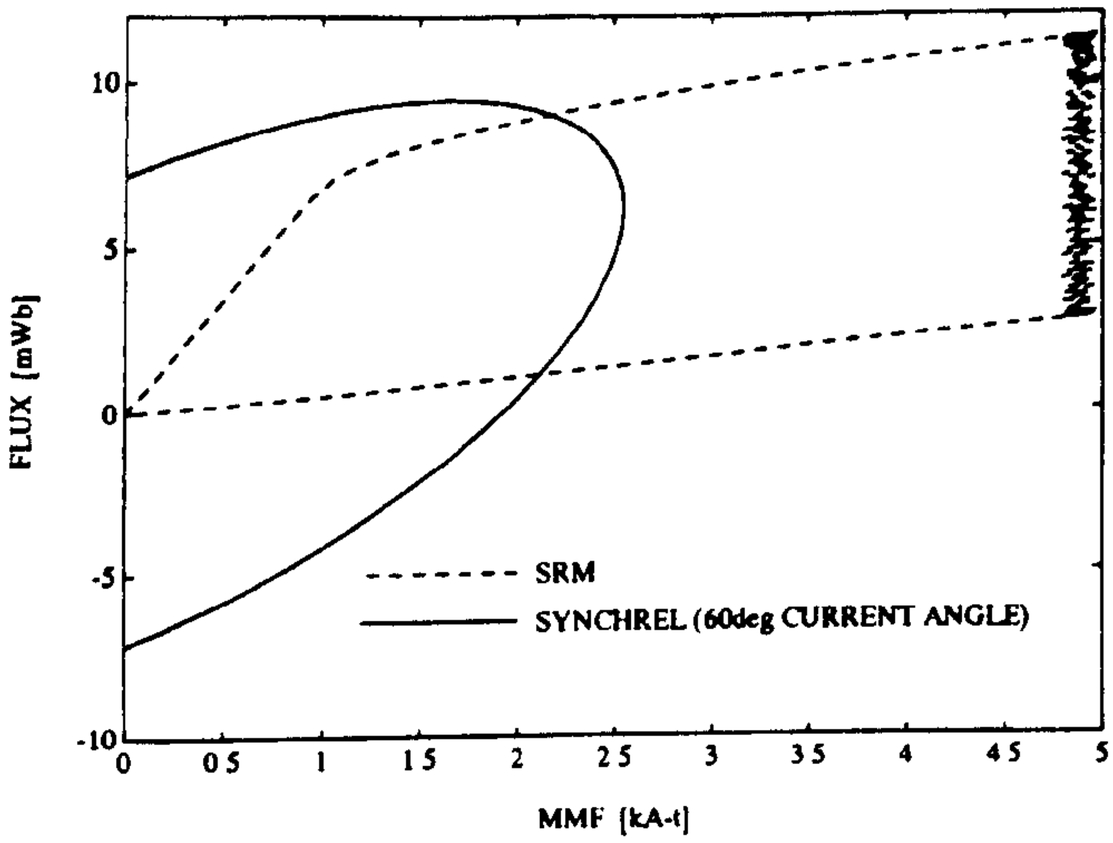

Fig. 9. Flux-MMF diagram for the SYNCHREL and SRM

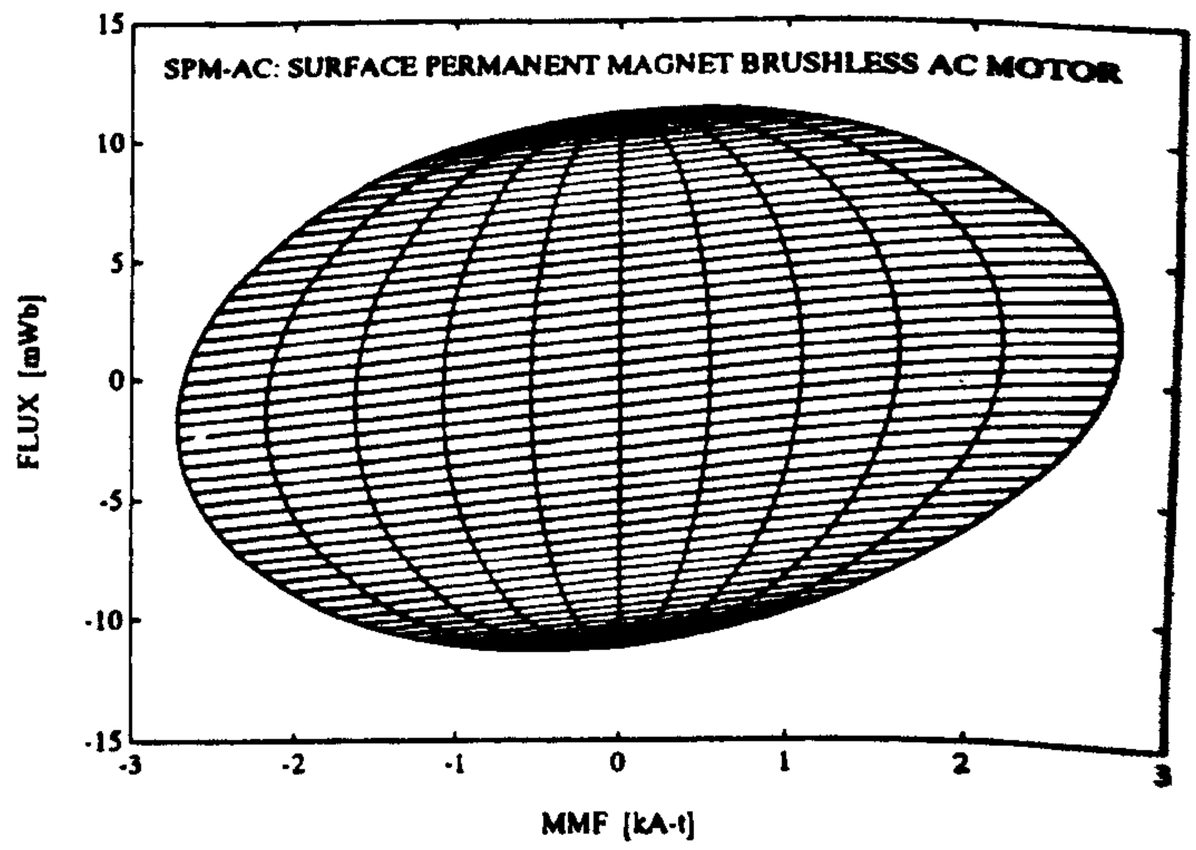

Fig. 12 flux-MMF diagram and magnetization curves for the SPM-AC motor (6 phase current values with the maximum at full-load).

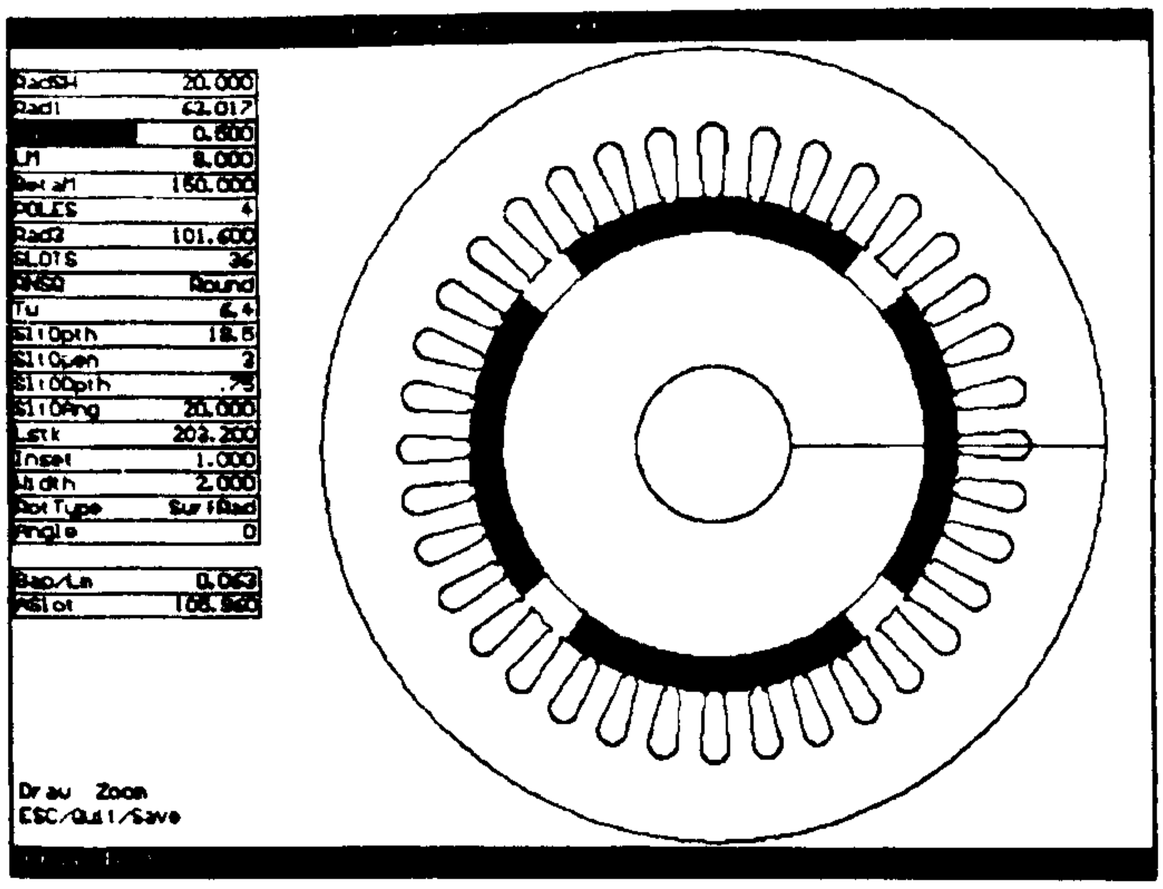

Fig 10 SPM-AC and SPM-DC1 motor designs

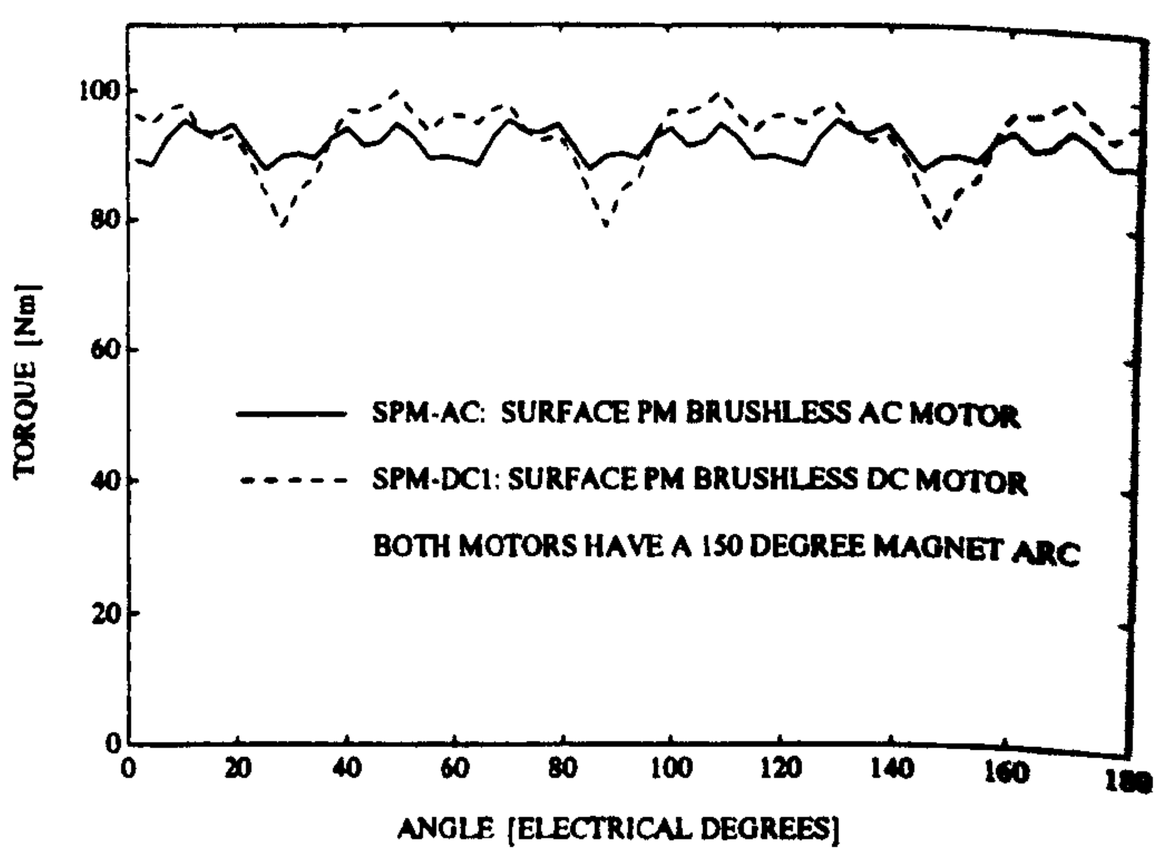

Fig. 13. SPM-AC and SPM-DC1 torque ripple (FE predication at full-load).

due to slotting (Fig. 13). A typical full-load flux plot taken from the finite-element analysis is shown in Fig. 11.

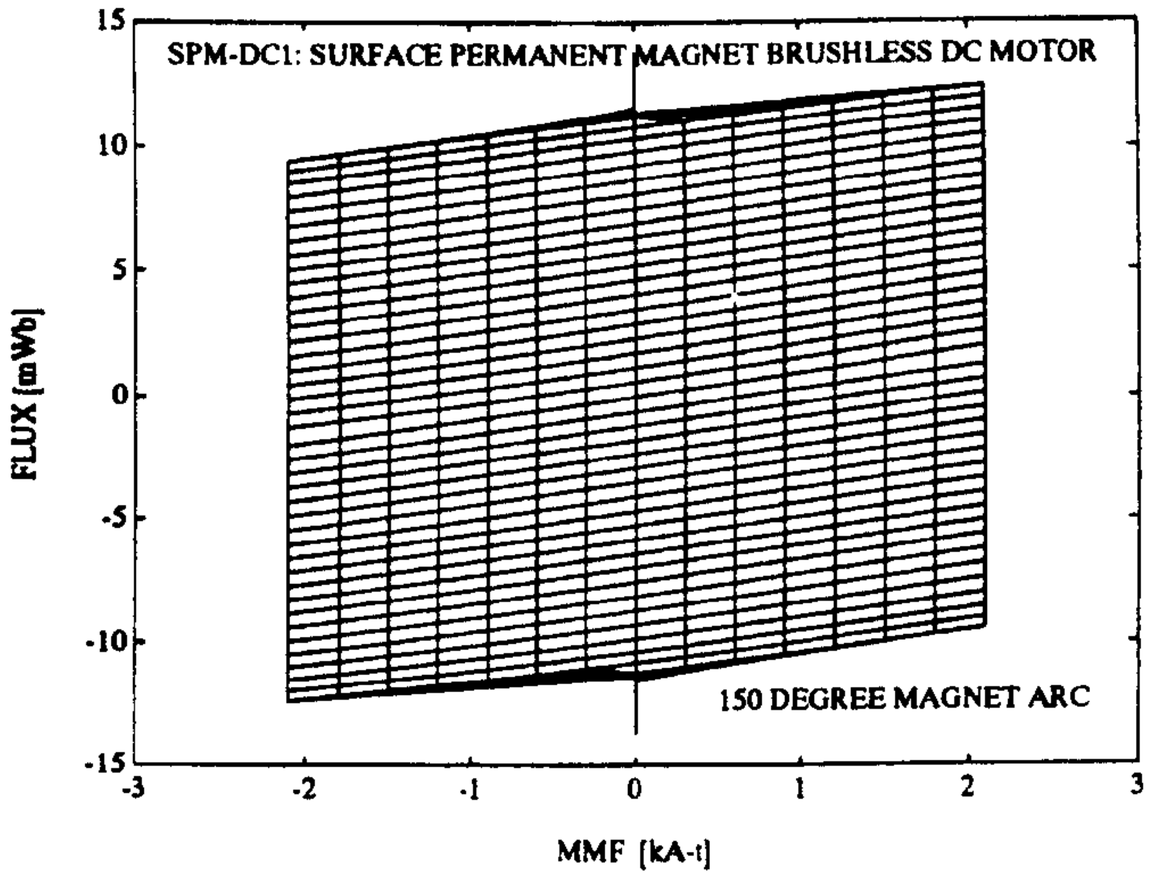

Fig. 14. Flux-MMF diagram and magnetization curves for the SPM-DC1 motor (8 phase current values with the maximum at full-load).

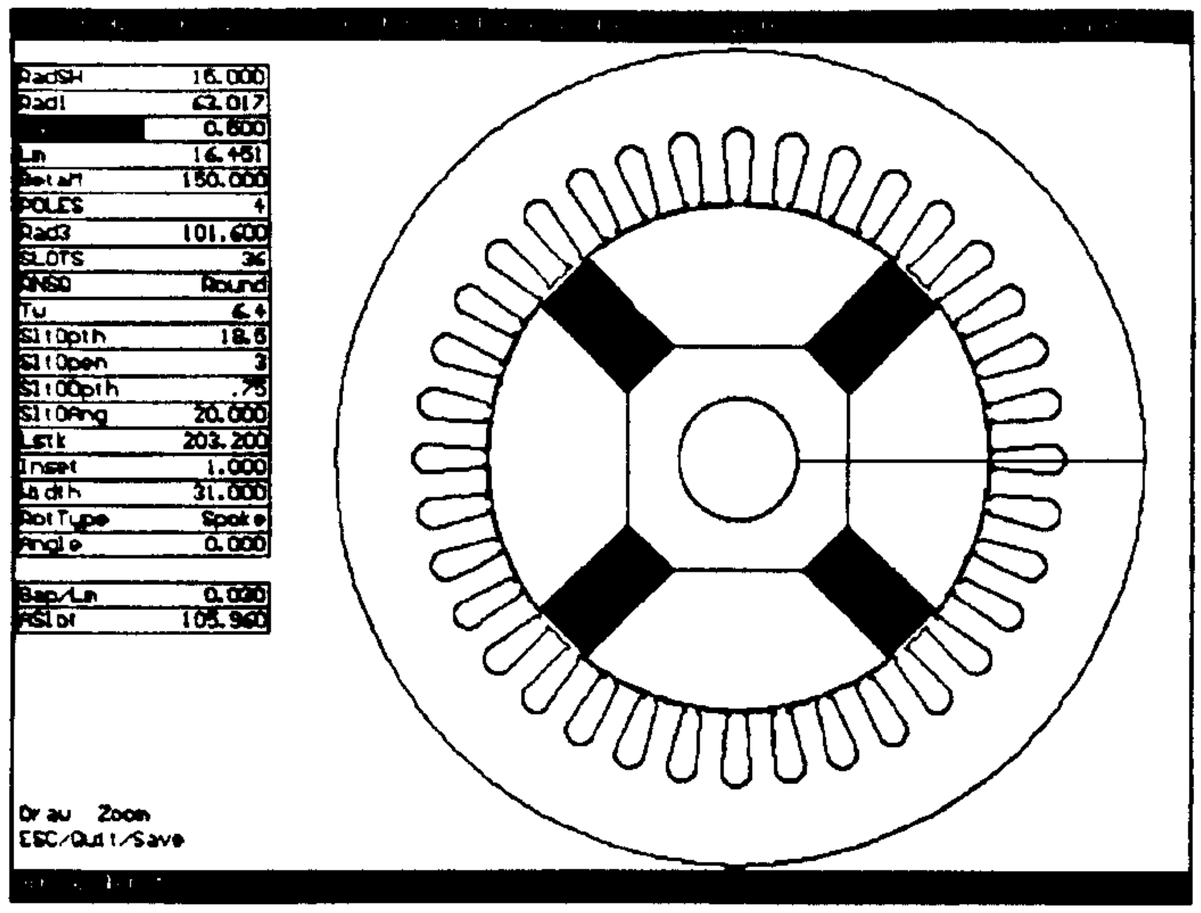

Fig. 16. IPM motor design.

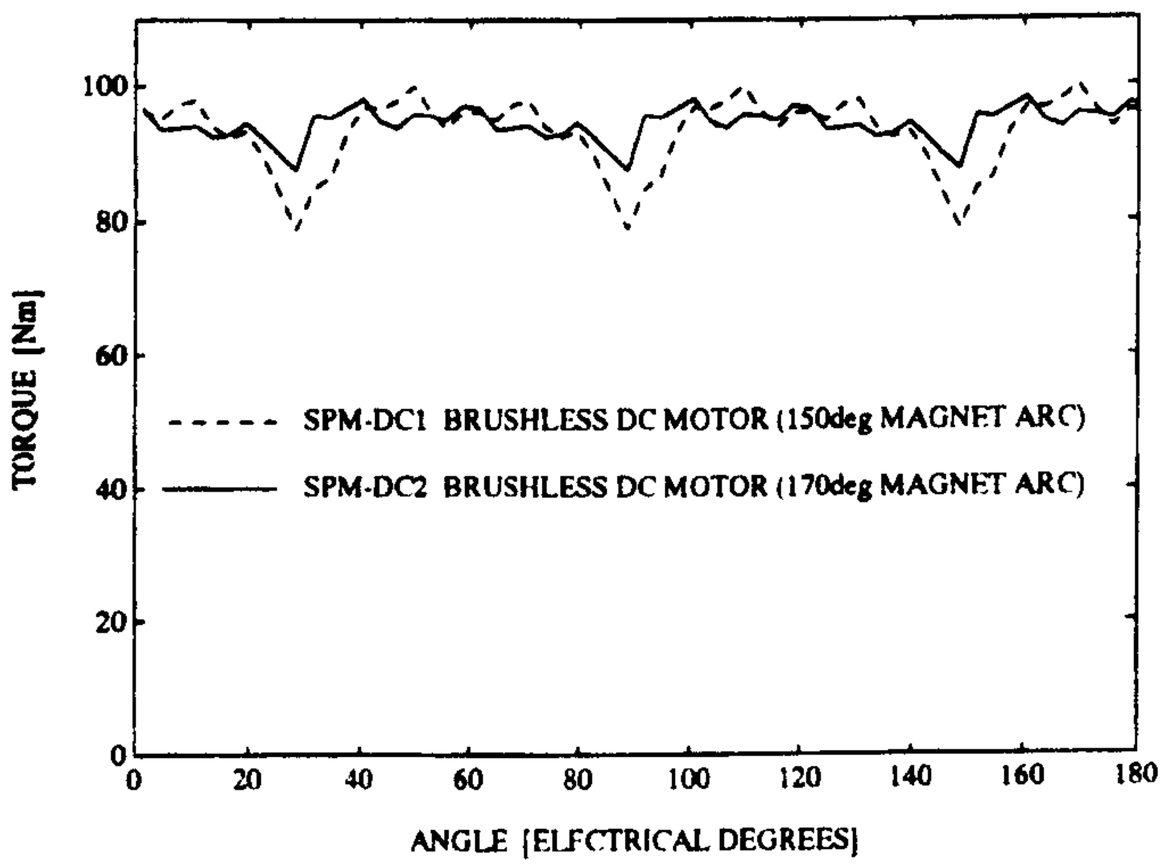

Fig. 15 SPM-DC1 and SPM-DC2 torque ripple (FE prediction at full-load).

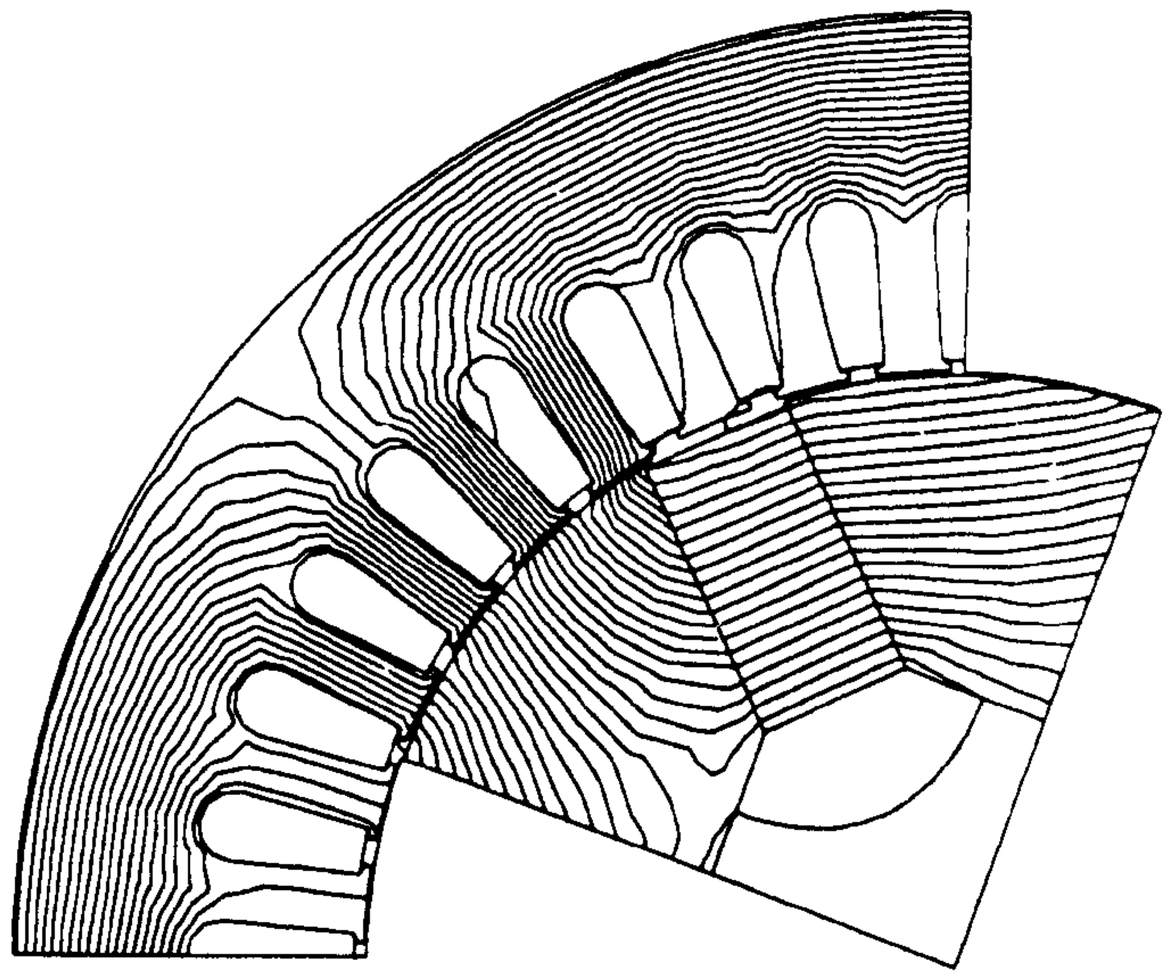

Fig. 17. IPM flux plot (full-load, $\theta = 20°$).

E. Surface Permanent Magnet Brushless DC (SPM-DC)

Two surface permanent magnet brushless dc (SPM-DC) motors were designed to operate with 120° squarewave line currents:

1) SPM-DC1 with a 150° magnet arc: this uses the same geometry and magnets as the SPM-AC motor, with a concentrated winding to give a flat-top back-emf waveform.
2) SPM-DC2 with a 170° magnet arc: this motor is exactly the same as SPM-DC1 except that it uses a larger magnet arc to reduce the torque ripple.

Fig. 14 is the flux-MMF diagram for the SPM-DC1 motor. The diagram has a nearly ideal rectangular shape and regular spacing of the magnetization curves, with a small amount of torque ripple that is reduced in the SPM-DC2 design (Fig. 15).

F. Interior Permanent Magnet Motor (IPM)

The interior permanent magnet (IPM) motor was also designed using *PC-BDC*, Fig. 16. It was designed to operate from a sinusoidal supply and uses the same stator and winding as the SPM-AC motor. Fig. 18 is the flux-MMF diagram (with $\gamma = 30°$ selected for maximum torque/ampere). The contrast between flux-MMF diagrams for the SPM-AC and IPM motors is evident from Figs. 12 and 18, respectively. Although both motors have the same average torque, the deviation from the near ideal elliptical shape and uneven spacing of the magnetization curves indicate larger torque ripple in the IPM (Fig. 19). A typical full-load flux plot taken from the finite-element analysis is shown in Fig. 17.

G. Permanent Magnet DC Commutator Motor (PMDC)

The permanent magnet dc commutator motor (PMDC) used in the analysis is shown in Fig. 20. It was designed using the *PC-DCM* program [23]. It has the same numbers of slots and poles as the SPM-DC motor, resulting in a "9 phase" motor. The magnet has a remanence of 0.75 T. This is less than the 1.1 T used in the SPM-DC motor but is required to increase the copper space, noting the flux-concentration in PMDC motors. The flux-MMF diagram is shown in Fig. 22 and the predicted

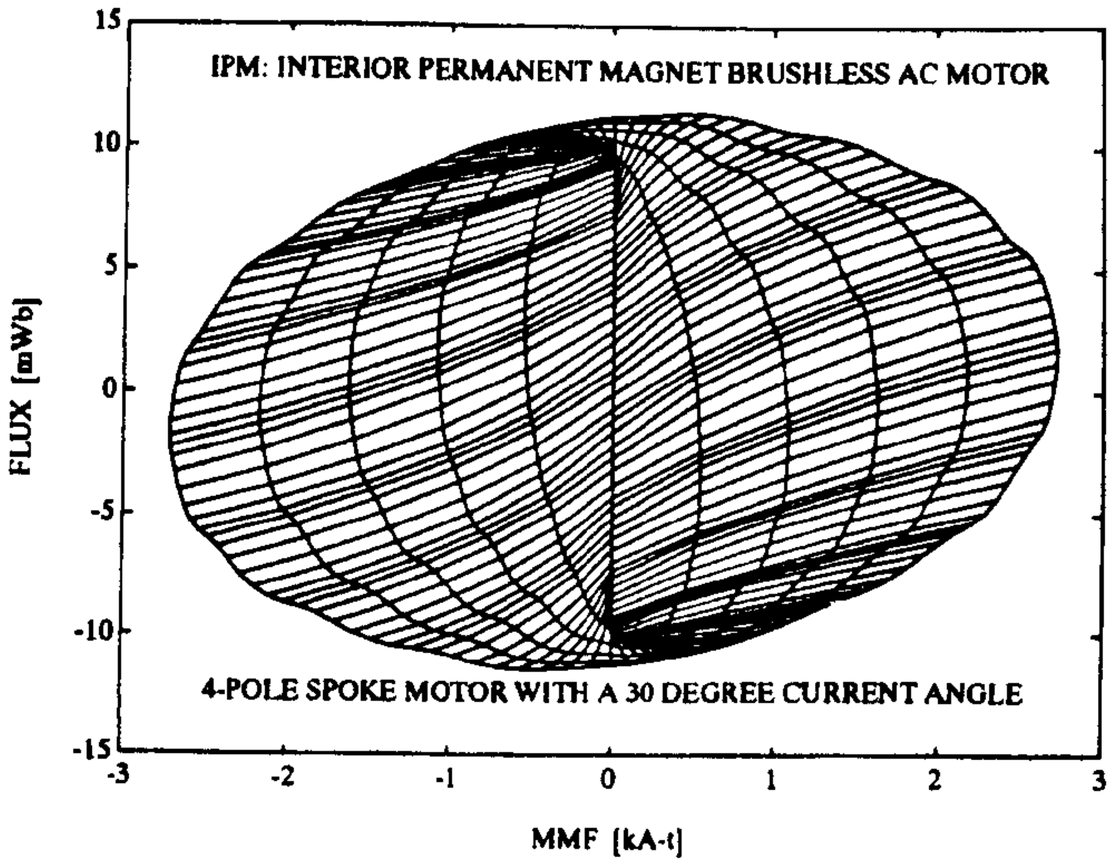

Fig. 18. Flux-MMF diagram and magnetization curves for the IPM motor (6 phase current values with the maximum at full-load).

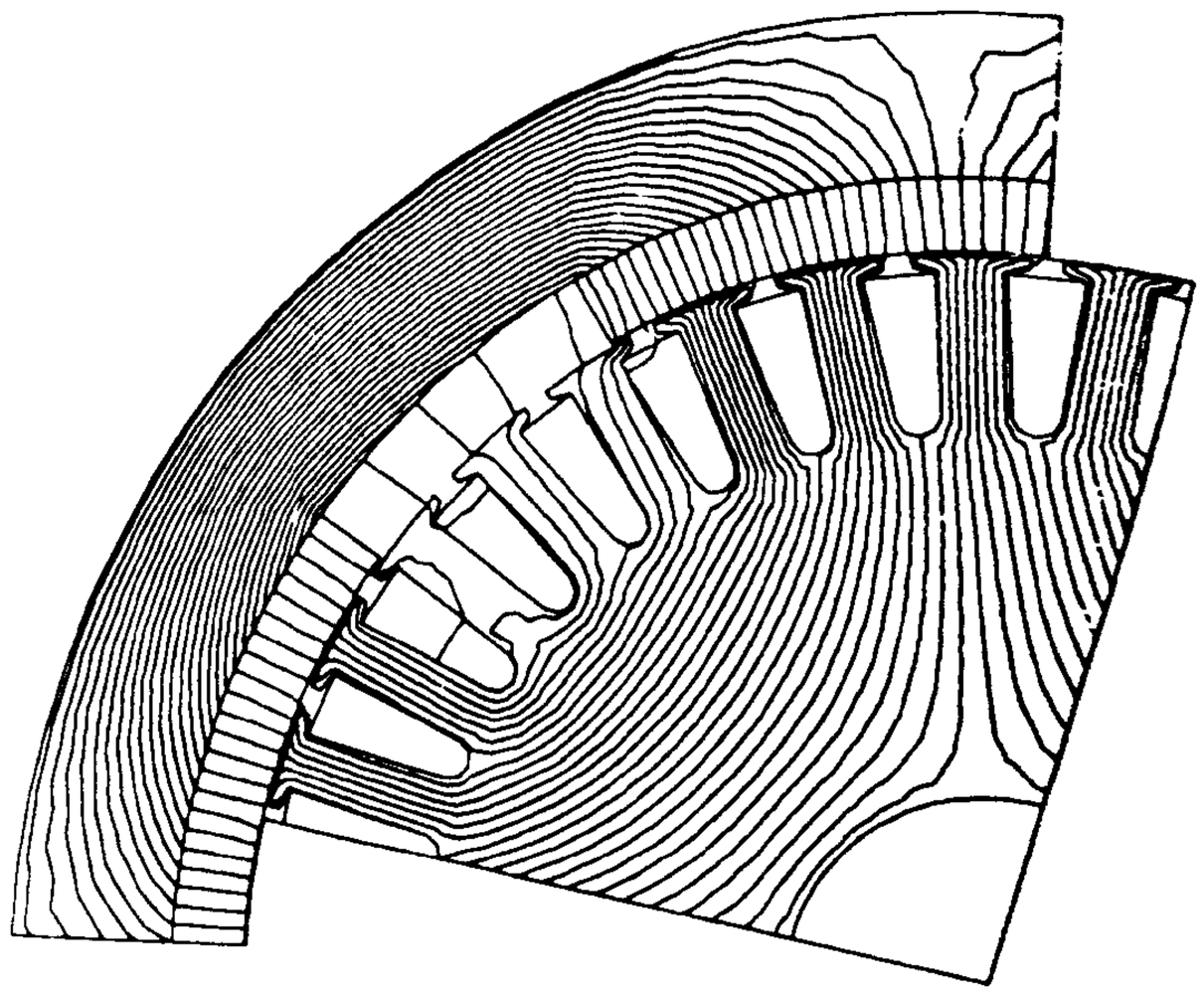

Fig 21 PMDC flux plot (full-load, $\theta = 10°$)

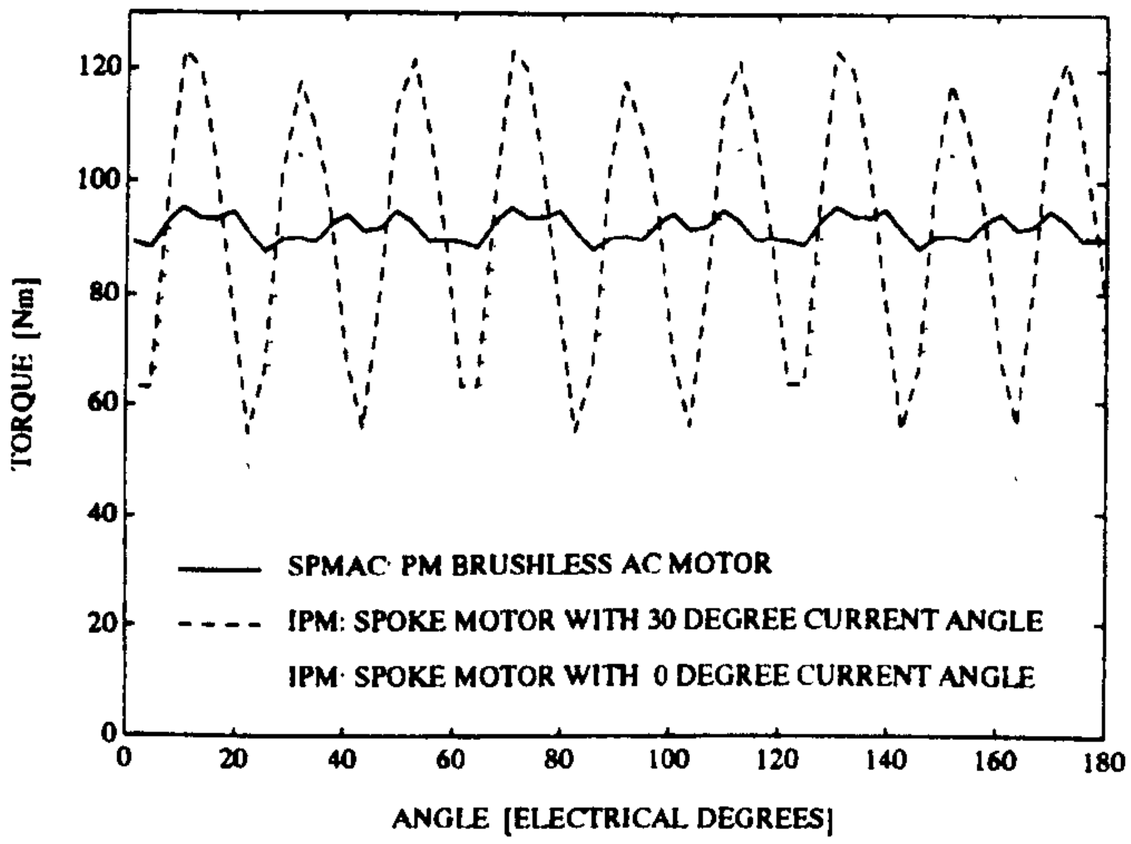

Fig. 19. SPM-AC and IPM torque ripple (FE prediction at full-load).

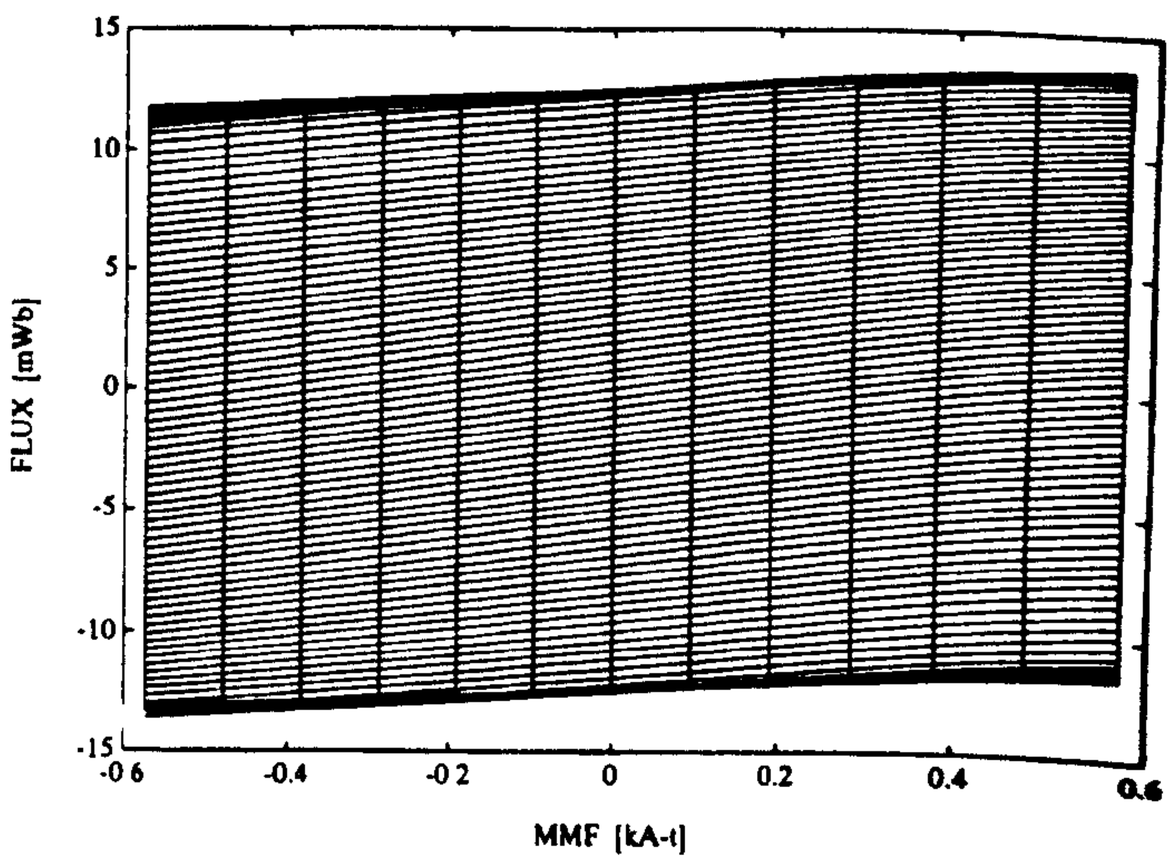

Fig 22. Flux-MMF diagram and magnetization curves for the PMDC motor (6 values of current with the maximum at full-load).

Fig 20 PMDC motor design.

torque ripple in Fig. 23. A typical full-load flux plot taken from the finite-element analysis is shown in Fig. 21.

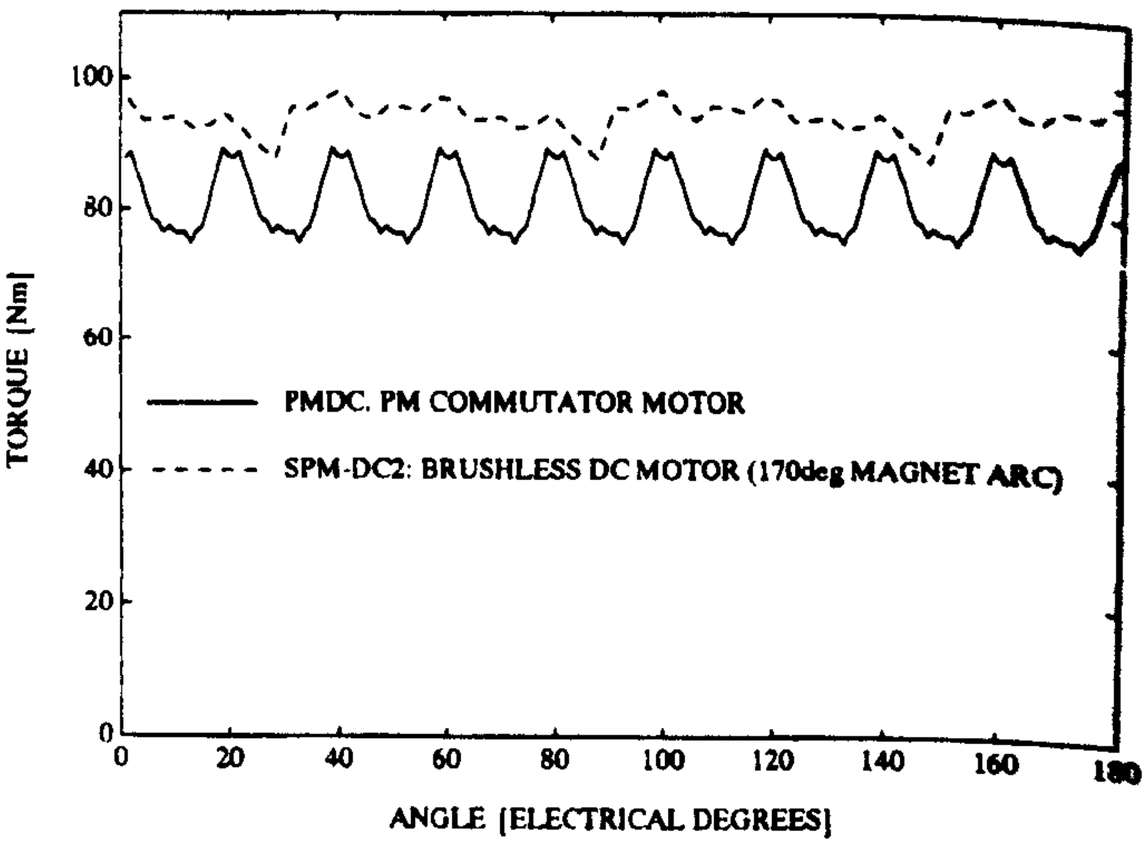

Fig 23. Torque ripple in the PMDC and SPM-DC2 motors (full-load).

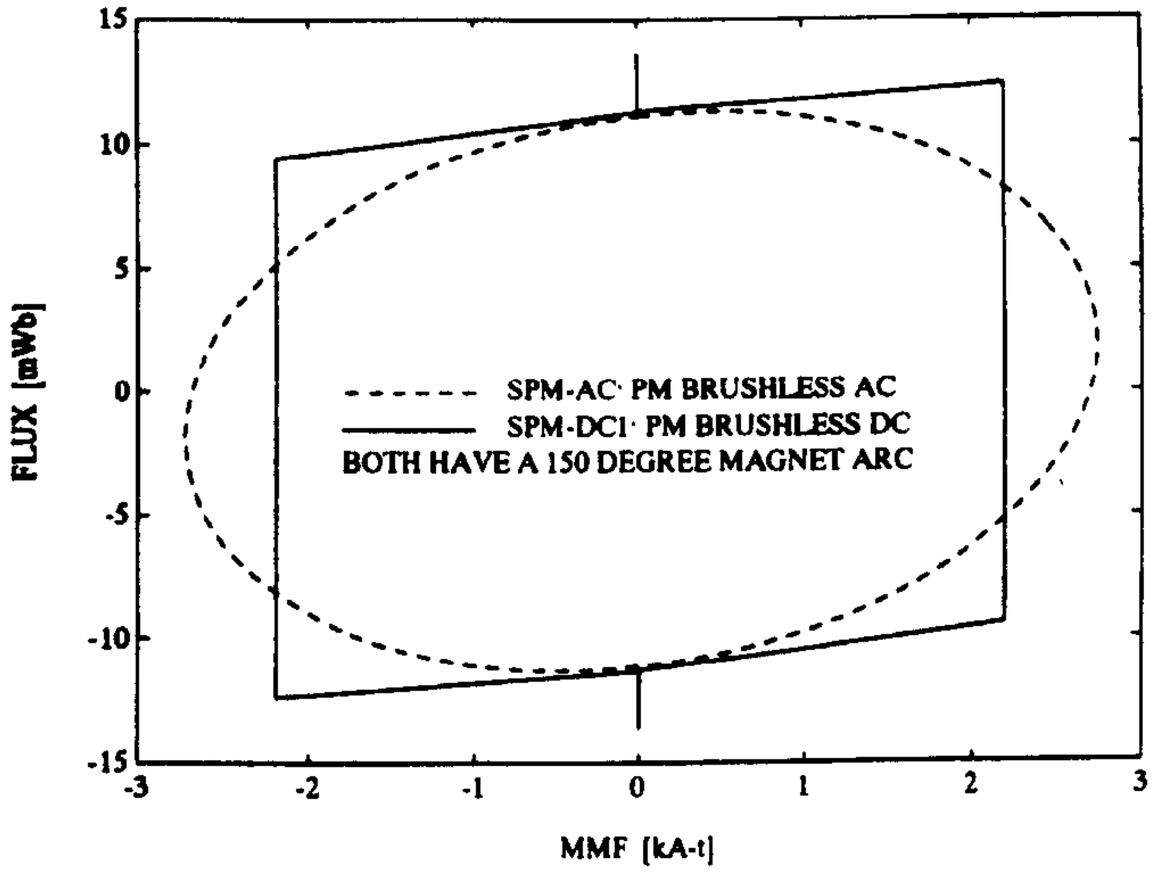

Fig. 24. Flux-MMF diagram for the SPM-AC and SPM-DC1 motors (full-load).

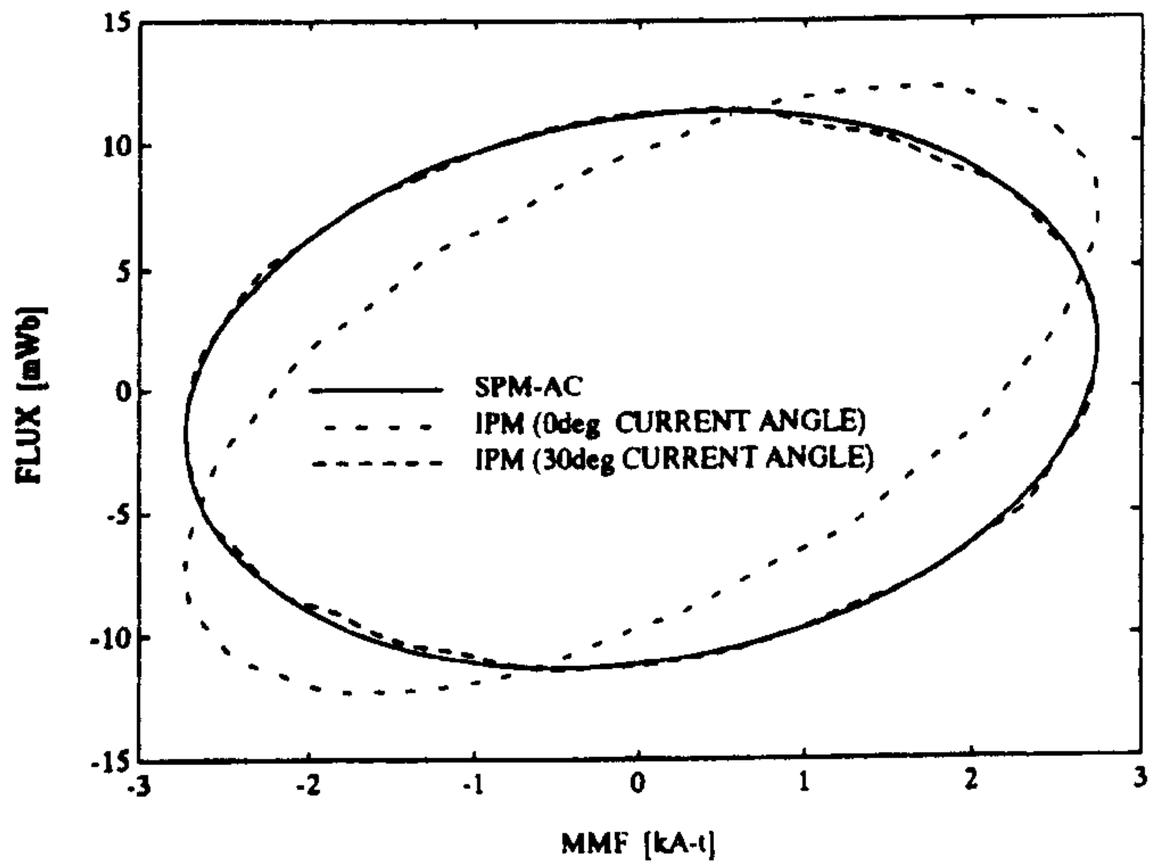

Fig. 25. Flux-MMF diagram for the SPM-AC and IPM motors (full-load).

V. Comparisons Based on the Flux-MMF Diagram

Table II and Figs. 26–29 compare average torque, torque ripple (expressed as the ratio of peak-peak to mean), peak phase MMF and peak effective phase flux for each motor type.

A. IM, SYNCHREL, and SPM-AC

Fig. 2 compares the IM, SYNCHREL, and SPM-AC motors. The maximum electric and magnetic loadings for the three motors are roughly comparable. However the SPM-AC motor can generate substantially more torque. The difference is due to the power-factor. The SPM-AC motor has close to unity power-factor while the other two motors have a lower value. The poor power factor is compounded in the case of the IM as it has been derated from 11 kW to 7.5 kW (Section IV-A). Thus the IM and SYNCHREL motors are being limited by their magnetizing current requirements. The SPM-AC motor requires no magnetizing current and so it can operate at a near unity power-factor, as is reflected by the near alignment

TABLE II
Comparison Between Motor Types

Motor	T_{AV} (Nm)	T_{RIPPLE} (%)	Peak MMF (kA-t)	Peak Flux (mWb)
IM	49.7	-	2.07	10.53
SYNCHREL	54.8	25	2.55	9.50
SRM	63.4	75	4.98	11.33
SPM-AC	91.7	8	2.74	11.32
SPM-DC1	93.0	23	2.19	13.6
SPM-DC2	94.2	11	2.19	13.98
IPM (γ=0°)	80.9	85	2.74	12.58
IPM (γ=30°)	91.3	75	2.74	11.62
PMDC	81.1	18	1.74*	13.62

*The peak phase MMF for the PMDC motor has been multipled by 3 as it is a "9-phase" motor (all the other motors have 3 phases)

between the major axis of the ellipse and the MMF axis (Fig. 12).

B. SYNCHREL and SRM

Fig. 9 compares the SYNCHREL with the SRM. The SRM shows a similar flux level and much higher MMF. Torque is not dramatically better as the SRM is limited to the first quadrant while the SYNCHREL (and other ac motors) can benefit from mutual flux-linkage and so extend into the fourth quadrant. The SRM has high torque ripple, although no attempt has been made to reduce it in this design.

C. SPM-AC and SPM-DC

Fig. 24 compares the flux-MMF diagrams of the SPM-AC and SPM-DC1 motors. Both have almost the same area and average torque. However, the torque ripple is less in the SPM-AC motor. It is to be noted that the peak current rating of the inverter is higher with the sinusoidal drive. The peak flux in the SPM-DC motor is larger than in the SPM-AC motor (even when they have the same geometry and magnets), because the winding is concentrated rather than distributed.

SPM-DC2 has a 170° magnet arc to reduce the torque ripple to levels comparable with the SPM-AC motor. (This does not take account of imperfect commutation at higher speeds.)

D. SPM-AC and IPM

The IPM has almost the same torque as the SPM-AC motor, as reflected by equivalent ellipsoidal areas in Fig. 25. However, the torque ripple is much larger (Fig. 19). This is due to the uneven spacing of the magnetization curves shown in Fig. 18. The torque ripple is due to harmonics in the airgap permeance caused by slotting. The torque ripple can be minimized by skewing [24], which also reduces the cogging torque [10]. The IPM with $\gamma = 30°$ has a better power factor than with $\gamma = 0°$, as indicated by the orientation of the ellipses in Fig. 25.

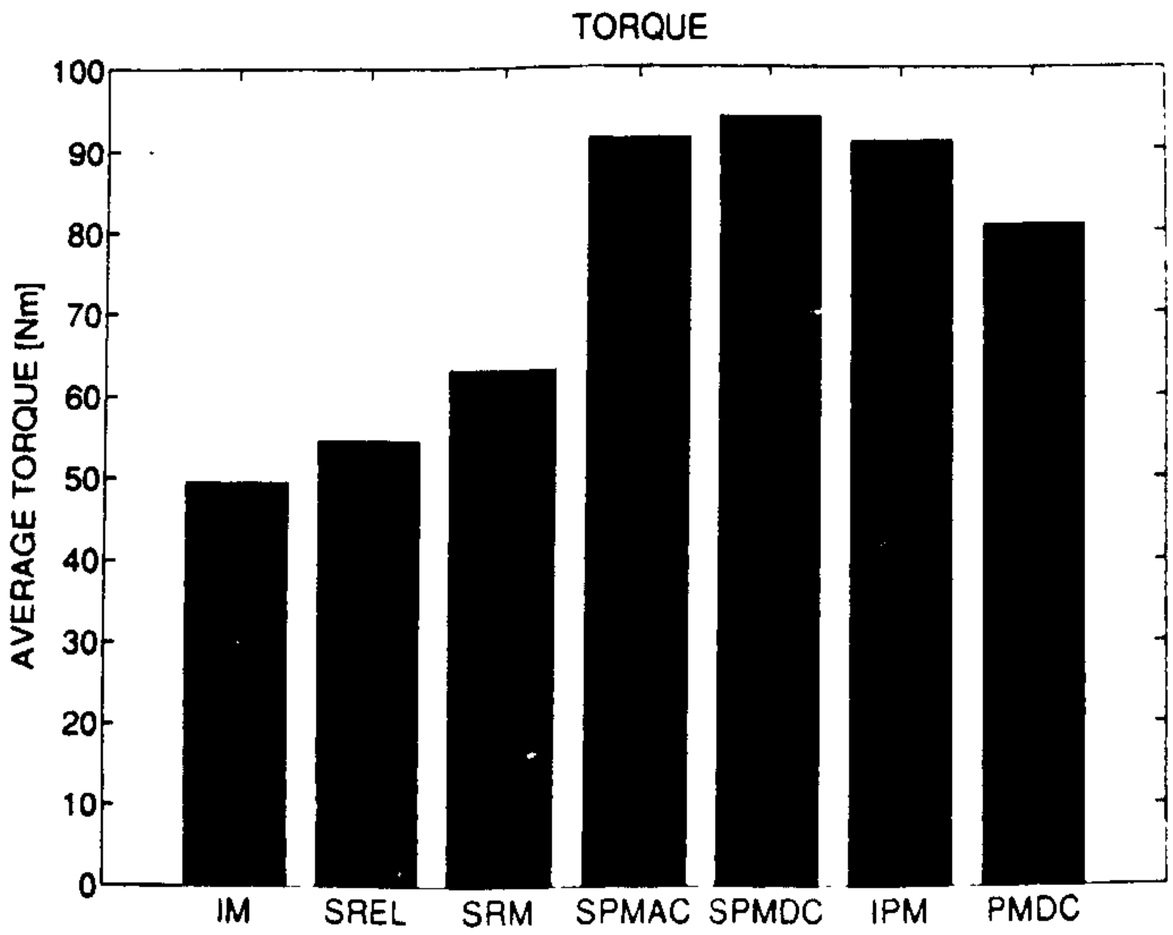

Fig. 26. Average rated torque in the 7 motors used in the comparison

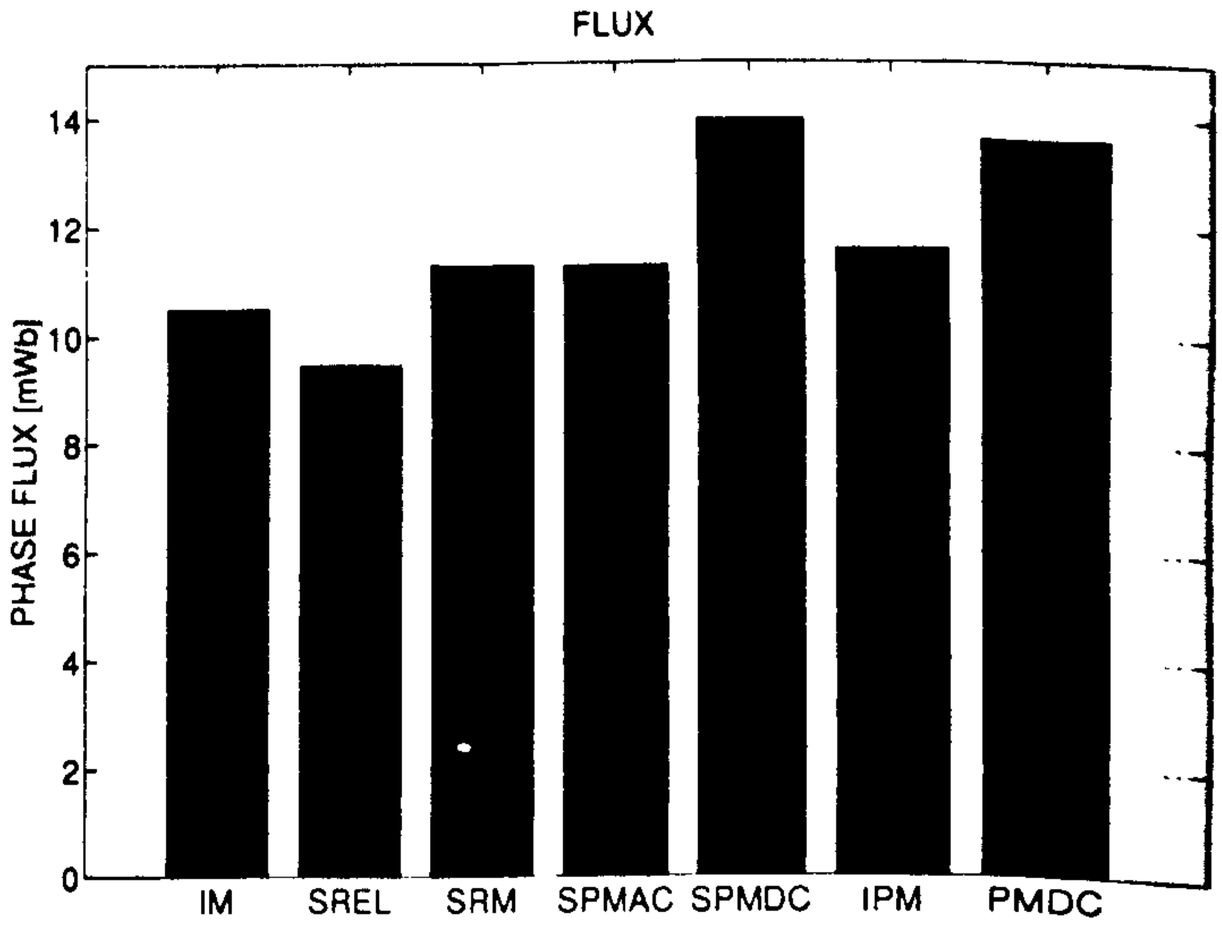

Fig 28 Effective flux in the 7 motors used in the comparison.

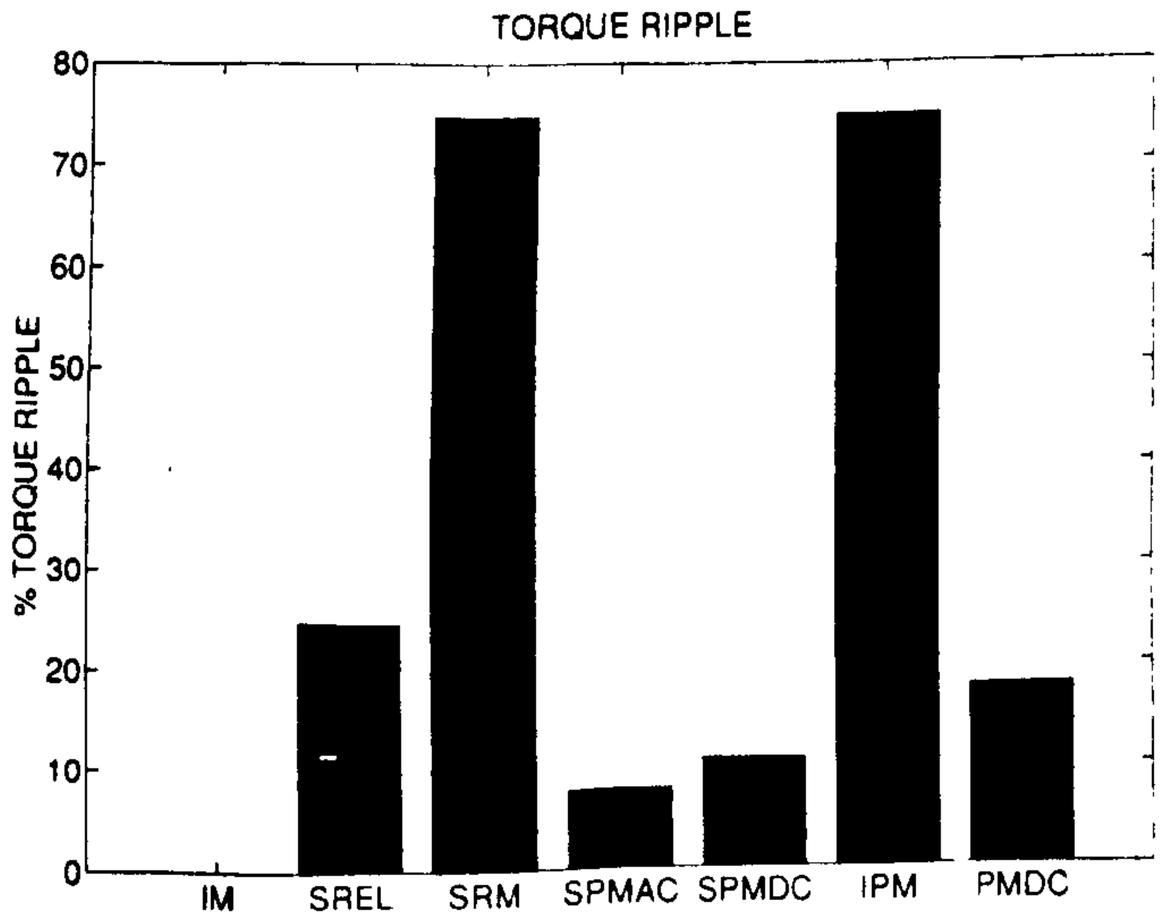

Fig. 27. Torque ripple in the 7 motors used in the comparison

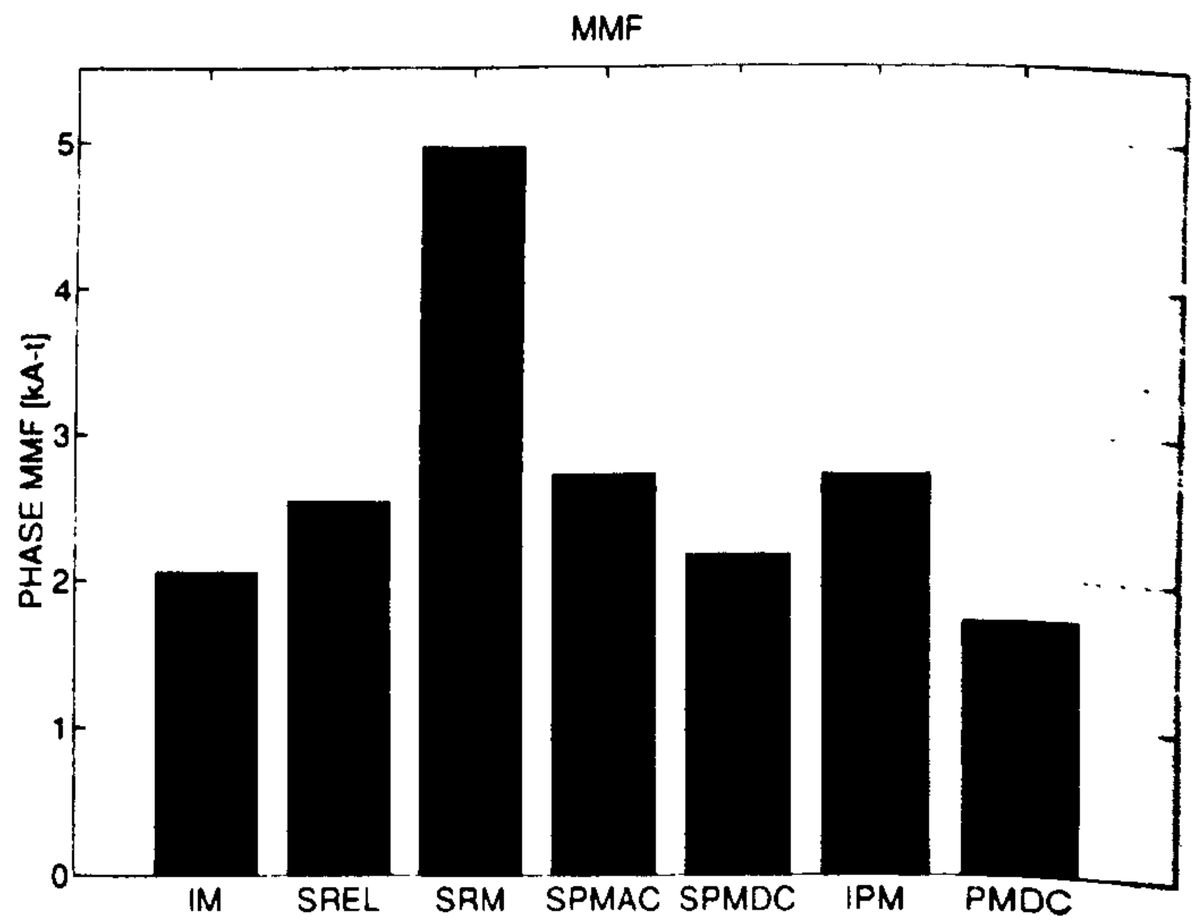

Fig. 29 MMF in the 7 motors used in the comparison

E. SPM-DC and PMDC

The comparison between the SPM-DC and PMDC motors is complicated by the fact that they have different number of phases. This results in a low peak phase MMF in the PMDC motor. Even if the phase ratio (9/3) is used to scale MMF's, the PMDC motor has a smaller MMF. This is mainly due to the fact that the SPM-DC motor has its slots on the outside of the motor and has a greater winding area. Even though a lower grade magnet is used in the PMDC motor, the effective flux is the same as in the SPM-DC motor. This is mainly due to the larger rotor diameter in the PMDC motor.

The PMDC motor may need to be derated with respect to the other motors because most of the losses are generated in the armature which is not as easily cooled as when it is on the outside of the motor.

VI. Conclusions

The flux-MMF diagram is a general theoretical means for calculating and comparing the average and instantaneous torque of a range of electric motors of different types. The method goes far beyond the capability of "unified" or "generalized" machine theory:

- It can deal with motors that cannot be analyzed using traditional methods for example, the doubly-salient SRM and the squarewave brushless dc motor.
- It can calculate instantaneous as well as average torque.
- It can calculate cogging and electromagnetic torque [10].
- It makes direct use of finite-element calculations in a way that is not possible with generalized-machine or "lumped-parameter" theories, and presents many of its results via graphical images whose features are readily associated with particular characteristics such as torque per unit volume, kVA requirement, torque ripple, etc.
- Because it is based on co-energy calculations and nonlinear magnetization data, the method is not restricted by assumptions of linearity or sinusoidal MMF distributions.

It would be unwise to proclaim the method as a modern-day replacement for generalized machine theory, which will

surely always be the foundation theory for ac and dc machines as well as for field-oriented control and some aspects of power-systems analysis; but it should help in the analysis and comparative evaluation of a wide range of electrical machines including new arrivals that fit no classical model.

REFERENCES

[1] T. J .E. Miller, *Switched Reluctance Motors and Their Control.* Oxford. Magna Physics Publishing and Oxford University Press, 1993.

[2] ———. *Brushless Permanent-Magnet and Reluctance Motor Drives.* Oxford. Oxford University Press, 1989.

[3] T. J. E. Miller and M. I. McGilp, "Nonlinear theory of the switched reluctance motor for rapid computer-aided design," in *IEE Proc.-B*, vol 137, no. 6, Nov. 1990.

[4] F. Liang, Y. Liao, and T. A. Lipo, "A new variable reluctance motor utilizing an auxiliary commutation winding," *IEEE Trans Ind. Applicat.*, vol. 30, no. 2, March/April 1994.

[5] D. A Staton, W L. Soong, and T. J E. Miller, "Unified theory of torque production in switched reluctance and synchronous reluctance motors," *IEEE Trans Ind. Applicat.*, vol 31, no. 2, March/April 1995

[6] Y. Liao, F. Liang, and T. A. Lipo, "A novel permanent magnet motor with doubly salient structure," in *Conf Rec. IEEE-IAS Annu. Meeting*, Houston, Oct. 1992

[7] H. H. Woodson and E Melchen, *Electromechanical Dynamics.* New York. Wiley, 1968.

[8] D C White and H. H. Woodson, *Electromechanical Energy Conversion* New York: Wiley, 1959.

[9] A. E Fitzgerald and J R. Kingsley, *Electrical Machinery*, 2nd Ed New York: McGraw-Hill, 1961.

[10] R. P. Deodhar, D A. Staton, T M. Jahns, and T. J. E. Miller, "Prediction of cogging torque using the flux-MMF diagram technique," in *Conf Rec IEEE-IAS Annu. Meeting*, Orlando, FL. Oct 1995

[11] D. A. Staton, T. J E Miller, and S E Wood, "Maximising the saliency ratio of the synchronous reluctance motor," in *IEE Proc. B*, vol.140, no 4, July 1993, pp 249–259.

[12] L. Xu, X. Xu, T A Lipo, and D. W. Novotny, "Control of a synchronous reluctance motor including saturation and iron loss," *IEEE Trans Ind Applicat.*, vol 27, no 5, pp. 977–985, Sept/Oct 1991.

[13] I. Boldea, Z. X. Fu, and S. A Nasar, "Performance evaluation of axially laminated anisotropic (ALA) rotor reluctance synchronous motors," *IEEE Trans. Ind. Applicat.*, vol 30, no 4, July/August 1994

[14] A. J O Cruickshank, A. F Anderson, and R W. Menzies, "Theory and performances of reluctance motors with axially laminated anisotropic rotors," in *Proc. IEE*, vol 118, no 7, 1971.

[15] D Platt, "Reluctance motor with strong anisotropy," in *Conf Rec IEEE-IAS Annu Meeting*, Seattle, WA, Oct. 1990, pp. 225–229

[16] A. Fratta and A Vagati, "Axially laminated reluctance motor: An analytical approach to the magnetic behaviour," in *Int Conf. Elec Mach.*, Pisa, Italy, vol. III, Sept 1988, pp 1–6

[17] T A Lipo, A Vagati, L Malesani and T Fukao, "Synchronous reluctance motors and drives—A new alternative," in *IEEE-IAS Annu. Meeting*, Houston, Oct 1992

[18] A. Vagati and T A. Lipo, "Synchronous reluctance motors and drives—A new alternative," in *IEEE-IAS Annu Meeting*, Denver, Oct 1994

[19] R. E. Betz and T J E Miller, "Aspects of the control of synchronous reluctance machines," in *European Power Electron Conf., EPE91*, Florence, Sept 1991.

[20] W L Soong, D A Staton, and T J E Miller, "Design of a new axially-laminated interior permanent magnet motor," *IEEE Trans Ind Applicat* vol 31, no 2, March/April 1995

[21] J. R Hendershot and T. J E Miller, *Design of brushless permanent-magnet motors.* Oxford: Magna Physics Publishing and Oxford University Press, 1994

[22] D. A. Staton, M I. McGilp, T. J E Miller, and G. Gray, "High-speed PC-based CAD for motor drives," in *5th EPE Conf*, Brighton, Sept 1993

[23] D A Staton, T. J E Miller, and M I McGilp "Interactive computer aided design of permanent magnet DC motors," in *Conf Rec IEEE-IAS Annu Meeting*, Toronto, Canada, Oct. 1993

[24] R P Deodhar, D. A. Staton, and T J E. Miller, "Modelling of skew using the flux-MMF diagram," *IEEE-PEDES Conf* New Delhi, India, Jan 1996, in press

David A. Staton was born in Chesterfield, England, on July 29, 1961. He received the B Sc (Hons.) degree in electrical and electronic engineering from Trent Polytechnic, Nottingham, England, in 1983 and the Ph.D degree from the University of Sheffield, England, in 1988.

From 1977 to 1984, he was employed by British Coal, who sponsored him while he was undertaking the B.Sc. degree. While at the University of Sheffield, he developed CAD software for permanent-magnet dc motors in collaboration with GEC Electromotors Ltd From 1988 to 1989, he was with Thorn EMI Central Research Laboratories and was engaged in the design of motors for the Kenwood range of food processors. From 1989 to 1995, he was employed as a research assistant in the SPEED Laboratory at the University of Glasgow. Presently he is with Control Techniques plc, Newtown, Wales. His research interests are in the computer aided design of permanent-magnet and reluctance motors.

Rajesh P. Deodhar (S'88–M'90–S'94) was born in Bombay, India, on February 22, 1968. He received the Bachelor of Engineering (B.Eng.) degree in electronics engineering from the University of Bombay in 1989 and the Master of Technology (M.Tech.) degree in electronic product design from the Center for Electronic Design and Technology (CEDT) at the Indian Institute of Science, Bangalore, in 1991 Since the beginning of 1994, he has been working towards the Ph.D. degree in the SPEED Laboratory, University of Glasgow, Scotland, in the generalized area of design and analysis of electric machines and drives

From 1991 to 1993, he worked as a Design Engineer with Crompton Greaves Ltd., Bombay, on the design of induction and brushless PM motors and drives In 1993 he spent six months in Japan, working with Hitachi Ltd., on the applications of electric machines and drives in home appliances.

Mr Deodhar was awarded the CEDT Design Gold Medal by the Indian Institute of Science in 1991 He also received the Hitachi-AOTS scholarship in 1993 which enabled him to work with Hitachi Ltd. in Japan for six months. He is an Associate Member of the IEE, U K

Wen L. Soong (S'89–M'90–S'90–M'93) was born in Kuala Lampur, Malayasia, and received the B.Eng. degree from Adelaide University, Australia, in 1989, and the Ph.D. degree from Glasgow University, Scotland, in 1993

He is an electrical engineer in the Power Controls Programs at General Electric Corporate Research and Development, Schenectady, NY. His research interests include permanent magnet and reluctance motor design and modeling, field-weakening control, and sensorless control.

Timothy J. E. Miller (M'74–SM'82) is a native of Wigan, U.K. He was educated at Atlantic College, the University of Glasgow, Scotland, and the University of Leeds.

From 1979 to 1986 he was an electrical engineer and program manager at General Electric Corporate Research and Development, Schenectady, NY. His industrial experience includes periods with GEC (U.K.), British Gas, International Research and Development, and a student-apprenticeship with Tube Investments Ltd. He is Lucas Professor in Power Electronics, and founder and Director of the SPEED Consortium at the University of Glasgow, Scotland He is the author of 105 publications in the fields of motors drives, power systems, and power electronics.

Prof Miller is a Fellow of the Royal Society of Edinburgh and a Fellow of the IEE

Prediction of Cogging Torque Using the Flux-MMF Diagram Technique

Rajesh P. Deodhar, *Student Member, IEEE*, David A. Staton, Thomas M. Jahns, *Fellow, IEEE*, and Timothy J. E. Miller, *Fellow, IEEE*

***Abstract*—An improved approach to predicting cogging torque in permanent magnet motors using the flux-MMF diagram technique is presented and validated. A brief review of cogging torque calculation and minimization techniques is included. It is shown that the flux-MMF diagram can be constructed for any one pole of a permanent magnet machine using the demagnetization characteristic of the permanent magnet; then by applying the principle of virtual work, cogging torque can be predicted. It is also shown that the flux-MMF diagram technique is a truly universal technique of cogging torque prediction and gives greater insight into many of the methods used for cogging torque minimization.**

NOMENCLATURE

T_e	Electromagnetic torque.	(N·m)
W'	Co-energy.	(J)
i	Instantaneous current.	(A)
θ	Rotor position.	(° or rad)
φ	Magnetic flux.	(Wb)
ψ	Magnetic flux-linkage.	(V-s)
MMF	Magnetomotive force.	(A-t)
l_m	Length of magnet.	(m)
A_m	Area of magnet.	(m^2)
B_r	Remanent flux density.	(T)
μ_0	Permeability of air.	(H/m)
μ_r	Recoil permeability of magnet.	

I. INTRODUCTION

COGGING torque in permanent magnet (PM) motors is gaining increasing importance along with the demand for high-performance brushless PM motors. It is a vital design consideration in power steering, robotics, machine spindle, high-precision position control, and, indeed, any application where minimizing torque ripple, vibration, and noise is an essential requirement. In order to be able to develop alternate and improved techniques of reducing cogging torque, it is important to be able to predict it accurately for any given motor geometry and configuration. Most of the recent literature on cogging makes use of some form of analytical method, the Maxwell stress method or the stored energy method, often enhanced by finite element analysis (FEA) [1]–[30]. The calculations involved in these methods can be cumbersome and often obscure the physical picture. Also, many cogging torque calculations are specific to a particular method of reducing cogging and it is difficult to generalize them. The flux-MMF diagram technique on the other hand, offers a fundamental basis of design evaluation and a clear physical insight based on graphical interpretation of diagrams such as Figs. 1 and 3 [31]–[35].

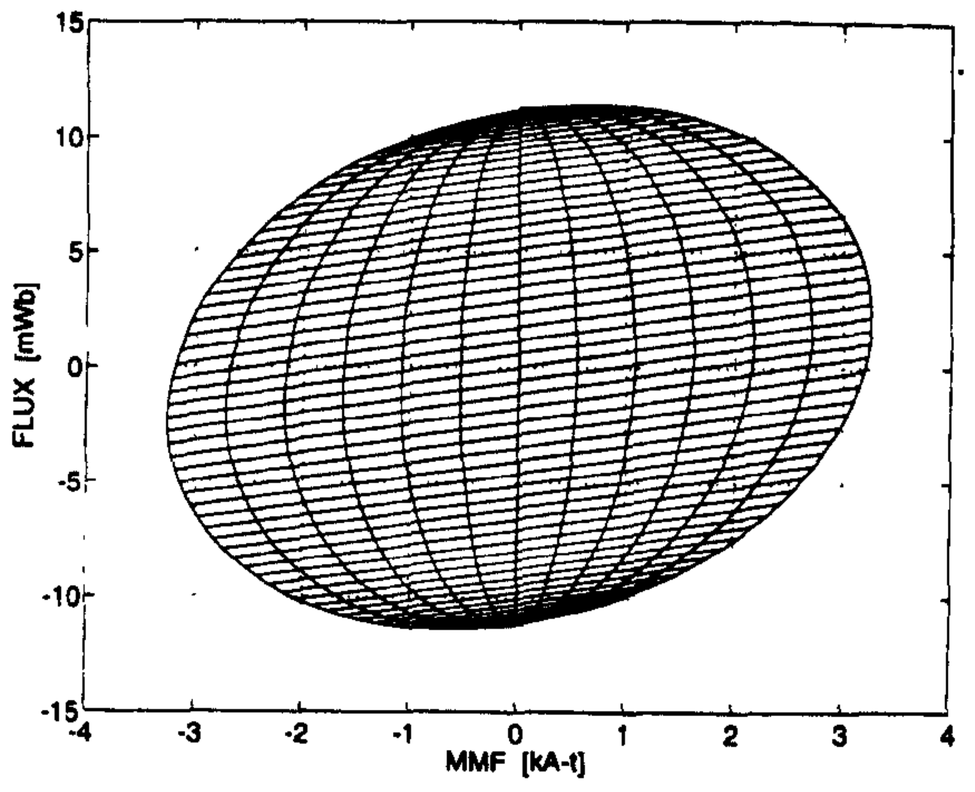

Fig. 1. Flux-MMF diagram for any one phase of a typical 4-pole, rare-earth magnet, sinewave brushless ac motor at RMS currents of 0, 4, 8, 12, 16, 20, and 24 A. Area enclosed by an ellipse indicates *average* torque. Incremental areas enclosed by the magnetization curves at successive rotor positions indicate *instantaneous* torque.

The technique is well adapted for use with the FEA. It also satisfies the need for a universal technique of cogging torque prediction, which can be used with all the commonly employed methods of cogging torque minimization.

Section II reviews the state of the art on cogging torque calculation and minimization techniques. Section III discusses the conventional flux-MMF diagram and brings out the crucial difference between the electromagnetic torque ripple and the cogging torque ripple in permanent magnet motors. Section IV

Paper IPCSD 95–74, approved by the Electric Machine Committee of the IEEE Industry Applications Society for presentation at the 1995 IEEE Industry Applications Society Annual Meeting, Lake Buena Vista, FL, October 8–12. This work was supported in part by the University of Glasgow and the Committee of Vice-Chancellors and Principals (CVCP), U.K. Manuscript released for publication November 6, 1995.

R. P. Deodhar and T. J. E. Miller are with the SPEED Laboratory, Department of Electronics and Electrical Engineering, University of Glasgow, Glasgow G12 8LT, Scotland, U.K.

D. A. Staton was with the SPEED Laboratory, Department of Electronics and Electrical Engineering, University of Glasgow, Glasgow G12 8LT, Scotland, U.K. He is now with Control Techniques plc, Powys, SY16 3AJ, Wales, U.K.

T. M. Jahns is with GE Corporate Research and Development, Schenectady, NY 12301 USA.

Publisher Item Identifier S 0093-9994(96)02094-4

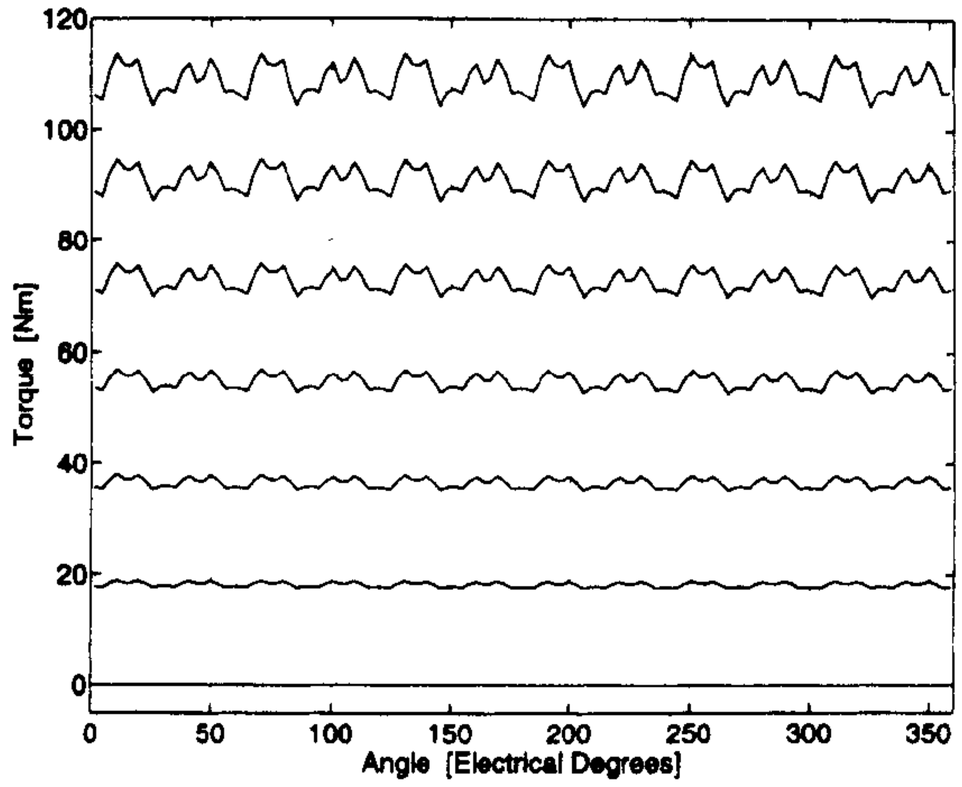

Fig. 2. Electromagnetic torque ripple curves at the RMS currents of 0, 4, 8, 12, 16, 20, and 24 A, obtained from the flux-MMF diagram shown in Fig. 1.

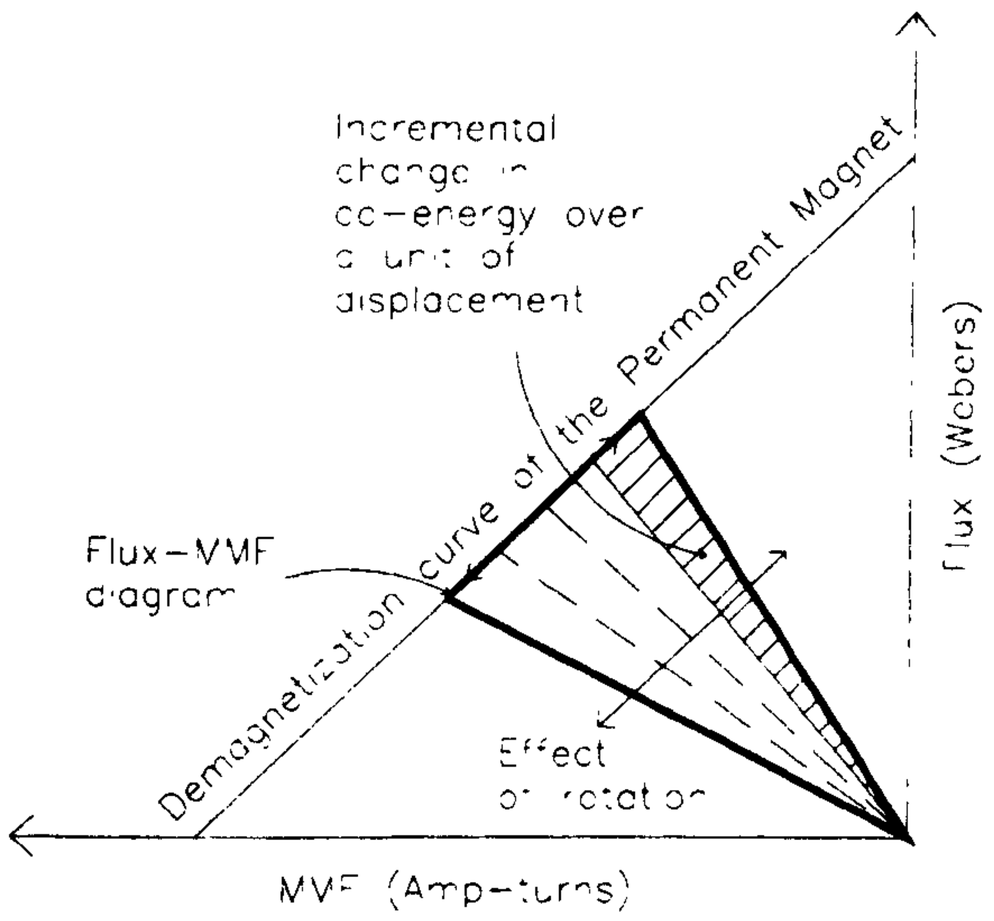

Fig. 3. The flux-MMF diagram for a permanent magnet.

explains the methodology of plotting the flux-MMF diagram for a permanent magnet, and predicting cogging torque from it by applying the principle of virtual work. Section V analyzes many of the methods employed for cogging torque minimization using the flux-MMF diagram technique. Finally, Section VI summarizes the main advantages of the flux-MMF diagram technique and discusses the improvements which could be implemented to make the technique faster and more comprehensive.

II. Review of Cogging Torque Calculation and Minimization Techniques

A. Calculation Techniques

Documented techniques for calculating cogging torque fall into two primary categories—analytical and numerical. Analytical approaches typically begin with calculation of the magnetic flux density distribution along the machine's airgap [3]–[5], [8], [9], [14], [15], [26]. These calculations invariably require a series of simplifying approximations in order to make the problem more tractable, such as assumptions of infinite iron permeability and/or zero flux density under the stator slots [3], [5]. Cogging torque is then derived from the flux density distribution either by taking the derivative of the associated coenergy [3], [4] or by summing the lateral magnetic force along the sides of the stator teeth [5].

Finite element analysis is by far the most popular approach for numerically calculating the cogging torque [12], [16]–[25]. However, closer examination indicates that there are many variations in how FEA is used. Although the majority of reported studies have used well-established 2-dimensional (2-D) FEA techniques, more recent work has applied 3-dimensional (3-D) formulations in efforts to model the influence of machine end effects and structure skewing more accurately [2], [21]. Torque is typically extracted from the FEA results using one of two approaches: 1) the energy method by which the torque is calculated from differences in the magnetic vector potential at incremental angular positions [12], [18], [23], and 2) more direct torque calculation by integrating the resulting Maxwell stress tensor over the machine's airgap surface [19], [22]–[24].

Reported results suggest that no one of these cogging torque calculation methods can be judged superior to the others under all conditions. Although the FEA-based techniques offer opportunities for more precise field calculations than the analytical approaches based on simplifying assumptions, the FEA results are also subject to errors introduced by mesh generation problems or inadequate models of the iron and magnet characteristics [4]. Given the complicated machine geometries and associated nonlinearities in material properties, there is a general trade-off between calculation complexity and required torque prediction accuracy which must be judged on a case-by-case basis.

B. Cogging Torque Minimization Techniques

An extensive variety of techniques for minimizing cogging torque is documented in the literature for both sinusoidal and trapezoidal permanent magnet machines. The majority of this work has been carried out during the past decade coincident with the growing interest in brushless PM machines for high-performance applications. However, many of these techniques trace their origins to the same fundamental methods developed years earlier for minimizing ripple torque in conventional ac and dc machines.

One of the most effective of these familiar techniques for cogging torque minimization is stator slot skewing. Several studies have demonstrated that skewing the stator slots by one stator tooth pitch can reduce the cogging torque to very low levels [3], [8], [9], [23], [28]. If stator skewing poses unacceptable manufacturability problems, the alternative approach of skewing the rotor magnetic field distribution via either skewed rotor magnets (or magnetization) [20], [28] or skewed mounting of discrete magnet segments on the rotor [9] has been demonstrated to yield similar cogging torque reductions.

Since the airgap magnetic permeance variations caused by stator slots are such an important factor in cogging torque generation, a variety of additional techniques have been sug-

gested for minimizing these variations or at least favorably modifying their harmonic spectra. One of the more obvious of these approaches is minimization of the stator slot openings [4], [5], [8], [17], [23] which has the undesirable effect of complicating the stator construction. Taking this approach a step further, slotless stator configurations have been adopted in some special applications where total elimination of cogging torque is required [25], [26].

Other techniques seek to reduce cogging torque production by pushing the harmonic components in the spatial airgap permeance distribution to higher frequencies by either adding dummy slots [29] or dummy teeth [30] to the stator laminations. Alternatively, this frequency spectrum can be beneficially modified to reduce cogging torque either by shifting the angular positions of individual stator slots [5] or by adopting a fractional number of slots per pole design [8], [24], [28]. However, the impact of such techniques on both the average and ripple torque production when the windings are excited must be carefully considered.

The tight interrelationship between cogging torque production (without current excitation) and ripple torque production (during excitation) is particularly apparent in trapezoidal PM machines where conflicts often arise during attempts to reduce both components simultaneously. Since trapezoidal machines favor concentrated stator windings in order to minimize ripple torque, skewing of the stator slots to reduce the cogging torque has the undesired effect of increasing the ripple torque [3].

As a result of this trade-off, alternative approaches for reducing the cogging torque in trapezoidal machines have been investigated with unskewed stators. For example, optimal ratios of magnet arc width to pole pitch have been identified for minimizing cogging torque, combined with a strategy of shifting alternate magnet arcs by one-half stator slot pitch in multi-pole-pair designs [9], [12], [22]. However, the effectiveness of these techniques is dependent on maintaining accurate mechanical tolerances on the physical dimensions and magnetization of the rotor magnets. Other rotor-based techniques which have been proposed for reducing cogging torque include shaping of the rotor magnet segments [23] and addition of a thin magnetic retaining ring [16].

All of the cogging torque minimization techniques reviewed in this section involve modifications of the machine design. If circumstances make it impractical to reduce cogging and/or ripple torque sufficiently in the basic machine design, a separate set of control-based techniques have been developed to compensate these parasitic torque components by modifying the current excitation waveforms [6].

III. The Flux-MMF Diagram

The flux-MMF diagram and its application to various motor types have been described in detail in [31]–[35]. It is a generalized version of the flux-linkage versus current ($\psi - i$) diagram used commonly for analyzing switched reluctance motors, relays, etc. [36]–[41]. It plots the variation of instantaneous effective flux linking a particular phase against the instantaneous MMF in that phase. Both the quantities are functions of rotor position and the flux-MMF diagram is a closed trajectory over one electrical cycle. The shape of this trajectory is an ellipse for a sinusoidally excited machine and a parallelogram for a squarewave excited machine [33]. Fig. 1 shows the flux-MMF diagram for any one phase of a typical 4-pole, rare-earth magnet sinewave brushless ac motor, at different load currents. Instantaneous as well as average torque at any given current can be calculated from the flux-MMF diagram by applying the principle of virtual work

$$T_e = \left.\frac{\partial W'(i,\theta)}{\partial \theta}\right|_{i=\text{constant}}. \tag{1}$$

The total area enclosed by a flux-MMF diagram is fixed by its particular shape, and this area indicates the *average* torque produced over one electrical cycle for any one phase. The total area consists of a number of incremental areas bound by the magnetization curves at successive rotor positions and each of these areas indicates the *instantaneous* torque at a particular rotor position for any one phase. This makes it possible to calculate torque ripple at any given current.

Fig. 2 shows the *electromagnetic* torque ripple curves obtained from the flux-MMF diagram shown in Fig. 1. Note that these curves are valid only at low speed where friction, windage, and iron losses can be neglected. At zero current, the predicted torque ripple is zero. The reason is straightforward: at any nonzero current, the flux-MMF diagram is an ellipse enclosing an area which is proportional to current; but, at zero current, the diagram is just a vertical line which does not enclose any area and hence does not predict any torque. This confirms the fact that cogging torque ripple, by itself, is independent of any current excitation.

As seen from Figs. 1 and 2, with the conventional way of plotting the flux-MMF diagram for any one phase, it is not possible to predict cogging torque in a permanent magnet motor, as the phenomenon of cogging depends only on the interaction of permanent magnets with stator slotting, and it is independent of the nature of any current excitation and distribution of conductors in any one phase. In order to circumvent this problem, it is proposed that rather than plotting the flux-MMF diagram for any one *phase*, the flux-MMF diagram could be plotted for a *permanent magnet* corresponding to any one pole so that the cogging torque can be predicted by applying the principle of virtual work. The next section describes the methodology in detail.

IV. Flux-MMF Diagram for a Permanent Magnet

Fig. 3 shows a typical flux-MMF diagram for permanent magnet which is constructed using a combination of flux-MMF data obtained from the finite element analysis and the demagnetization characteristic. Just as in the case of conventional flux-MMF diagram, finite element solutions are generated at incremental rotor positions over one cogging torque cycle. Using these solutions, values of total flux emanating from the permanent magnet for any one pole are obtained at each rotor position. The corresponding MMF values are obtained using the demagnetization curve as in

$$\text{MMF} = \frac{l_m}{\mu_0 \mu_r}\left(\frac{\varphi}{A_m} - B_r\right). \tag{2}$$

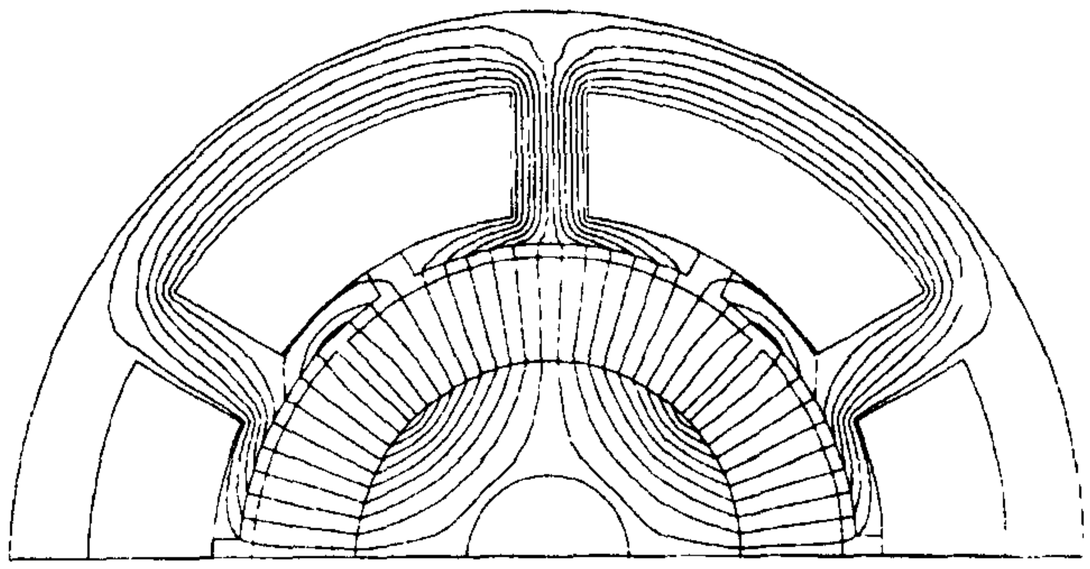

Fig. 4. Flux plot for a 6-slot, 4-pole ferrite magnet brushless dc motor.

Variation of flux is then plotted against the variation of MMF over one cogging torque cycle. This represents the flux-MMF diagram for a permanent magnet corresponding to any one pole—a triangle in dark solid lines in Fig. 3. The so-called "load lines" at each incremental rotor position, shown by dotted lines in Fig. 3, are assumed to be linear. This is adequate in most cases except when there is high saturation in stator tooth tips or when the magnet working point is pushed beyond the "knee point" due to extremely high load currents, in which case, the load lines may be nonlinear [42].

Note that the flux-MMF diagram for a permanent magnet is similar to the flux-linkage versus current $(\psi - i)$ diagram for a switched reluctance motor or a relay. While the PM diagram is plotted in the second quadrant, the SR diagram is usually plotted in the first quadrant and both can take account of linear as well as nonlinear magnetization curves. Once the flux-MMF diagram for any one pole is obtained, predicting cogging torque becomes an easy matter of calculating *instantaneous* torque for every incremental rotor position using the rate of change of co-energy with displacement as in (1). Even when no current is flowing, (1) can still be applied by replacing "i" with "MMF" of the permanent magnet. Finally, total cogging torque is obtained by simply adding together the cogging torques for the individual poles.

The technique is validated by performing finite element analysis as well as experimental measurements on a small 6/4 (6-slot, 4-pole) ferrite magnet brushless dc motor. Fig. 4 is a flux plot showing the cross section over two poles. Fig. 5 compares the predicted cogging torque curve against measured points and it shows a close match between the two. The measured points were obtained using an experimental setup in which the motor under test was driven by a dividing head through a sensitive torque transducer. The rotor was taken through each incremental position over a cogging torque cycle in both directions and the results were averaged to eliminate the effect of friction.

It is interesting to note that in Fig. 5 total predicted cogging torque is made up of two slightly different cogging torque curves corresponding to the set of north and south poles which are mirror images of each other. The reason can be seen clearly from Fig. 4. While one set of poles with same polarity is facing teeth, the other set is facing slots, which means that the two sets are subjected to different magnetic circuits. When the flux-MMF diagrams are plotted for each set, they are slightly different from each other, giving rise to cogging torque ripple

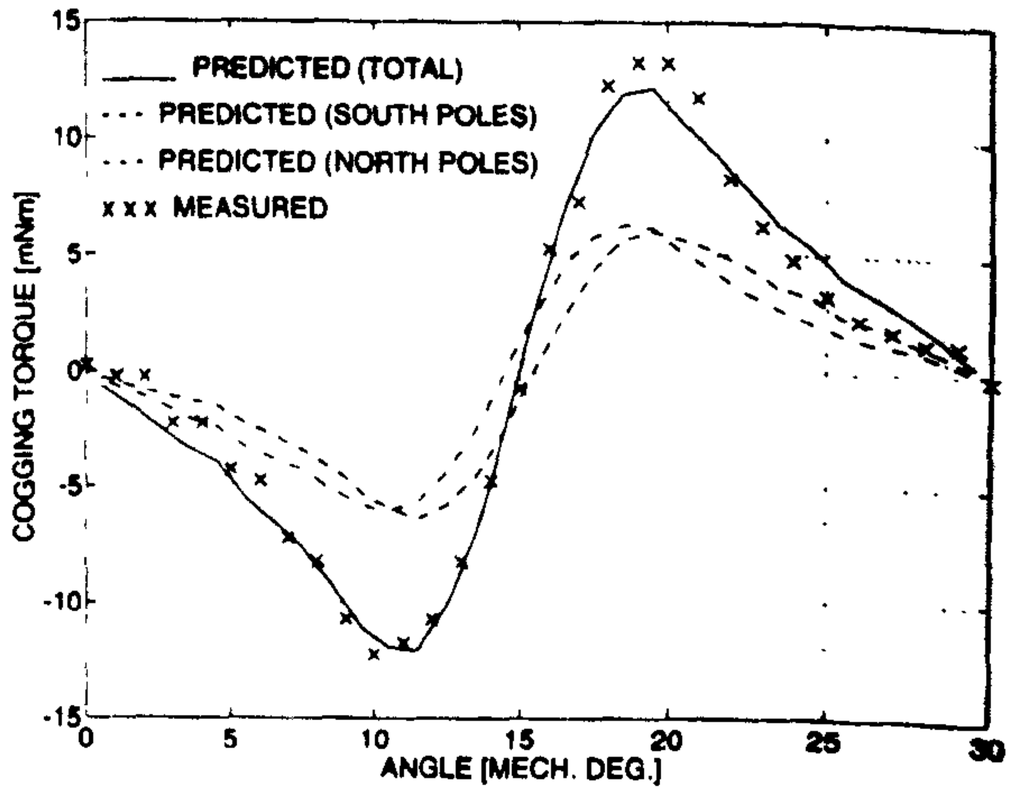

Fig. 5. Comparison between the predicted and the measured cogging torque for the motor shown in Fig. 4.

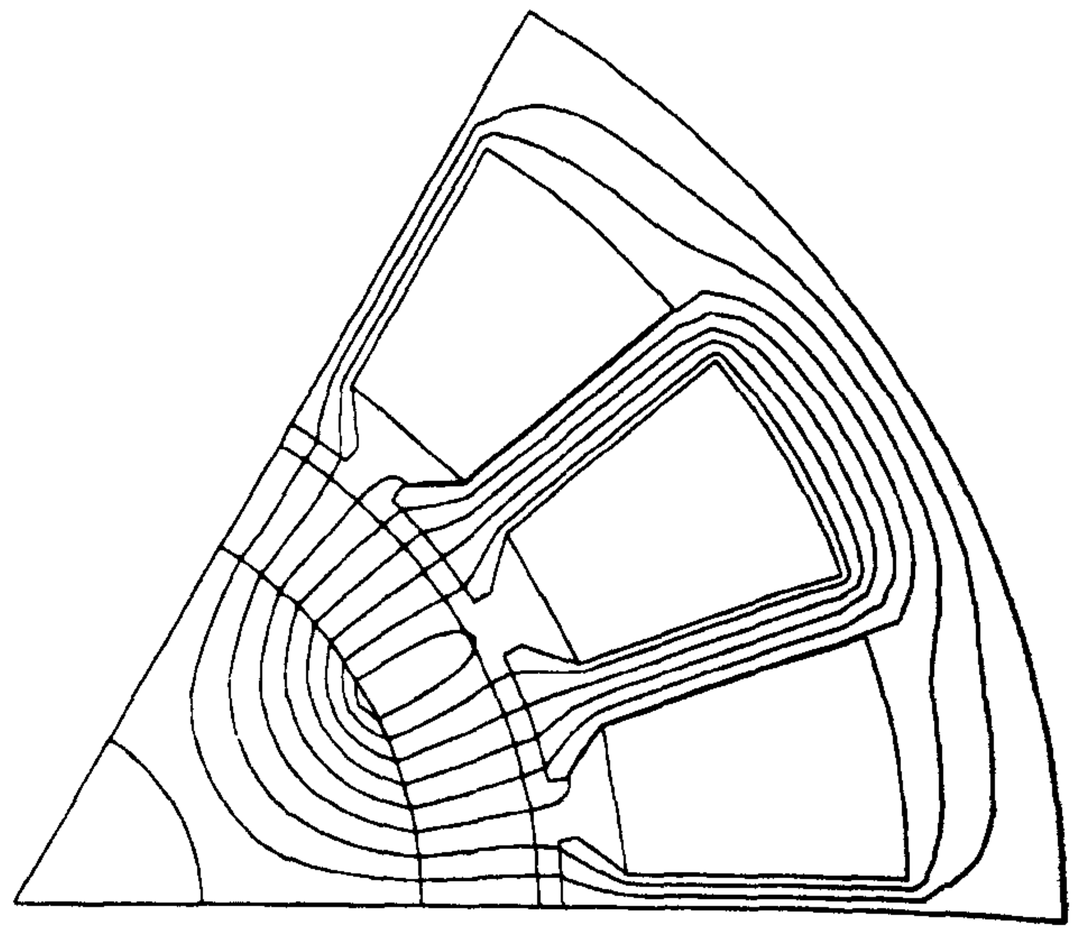

Fig. 6. Flux plot for an 18-slot, 6-pole ferrite magnet brushless dc motor.

curves which are consequently different from each other. This phenomenon is peculiar to motors with fractional number of slots per pole. In motors with integral number of slots per pole (an 18-slot, 6-pole motor shown in Fig. 6, for example), each pole is subjected to an identical magnetic circuit and the flux-MMF diagram is exactly the same for all poles.

V. Analysis of Various Methods of Cogging Torque Minimization Using the Flux-MMF Diagram Technique

A. Skewing

This is the most common method applied for reducing cogging torque in permanent magnet motors. Either the stator or the magnets can be skewed but both have essentially the same electromagnetic effect on motor operation and cogging torque. The choice is generally dictated by the manufacturability of a particular design. The flux-MMF diagram technique is adept at taking account of fractional as well as integral slot pitch skew [34].

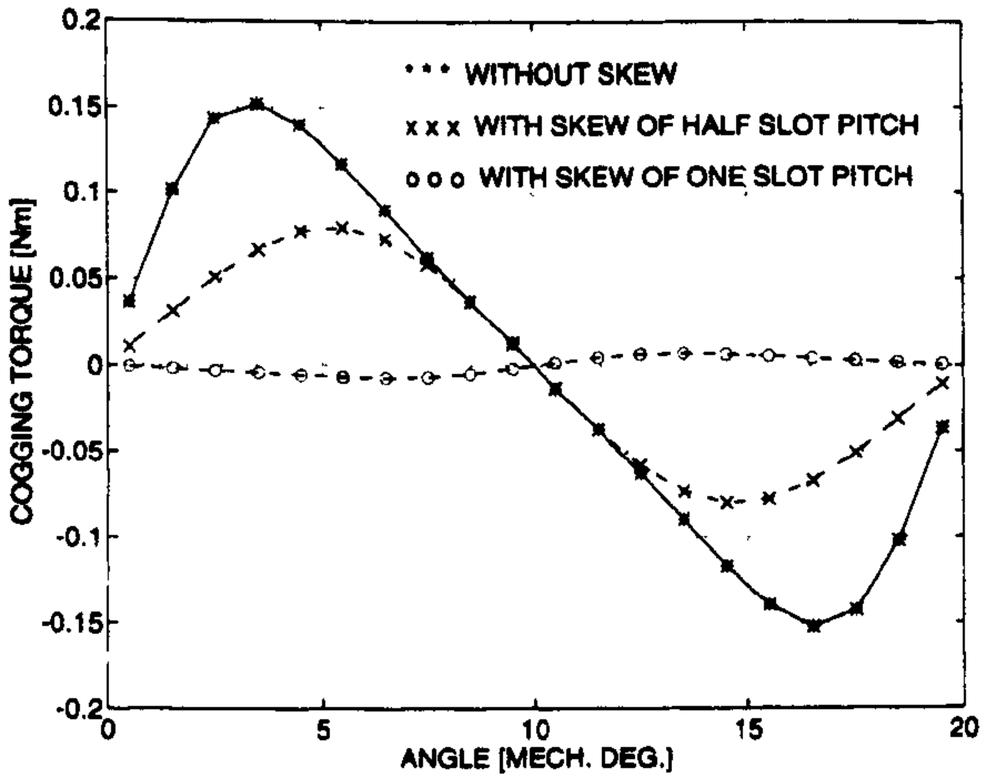

Fig. 7. Cogging torque curves at different stator skew factors for the motor shown in Fig. 6.

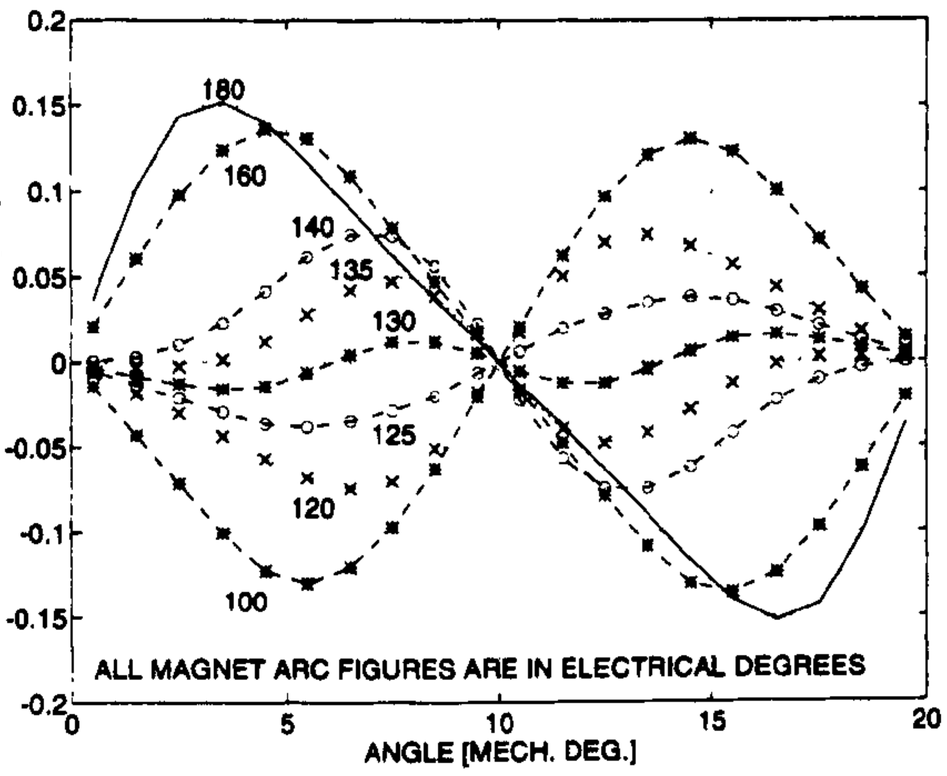

Fig. 8. Cogging torque curves at different magnet arcs for the motor shown in Fig. 6.

Fig. 6 is a flux plot for an 18-slot, 6-pole ferrite magnet brushless dc motor showing motor cross section over one pole. Fig. 7 compares cogging torque curves, for the motor shown in Fig. 6, obtained at different stator skew factors. It shows that the peak cogging torque with a skew of half slot pitch is roughly 50% of the peak cogging torque without skew. With a skew of one slot pitch, the cogging torque is almost zero, as expected.

B. Varying the Magnet Arc

Varying the magnet arc has a significant effect on the magnitude and the shape of cogging torque curve. The motor shown in Fig. 6 has full (180° electrical) magnet arc. If the magnet arc is reduced, the peak cogging torque is also reduced, only up to a certain value of magnet arc (130°) beyond which it starts to increase again (125°, 120° and 100°) as shown in Fig. 8.

It is noted that changing the magnet arc will affect both cogging and electromagnetic torque ripple in completely different ways. While cogging torque depends only on the interaction between the magnets and the stator slots, electromagnetic torque ripple depends, among many other factors, on the shape

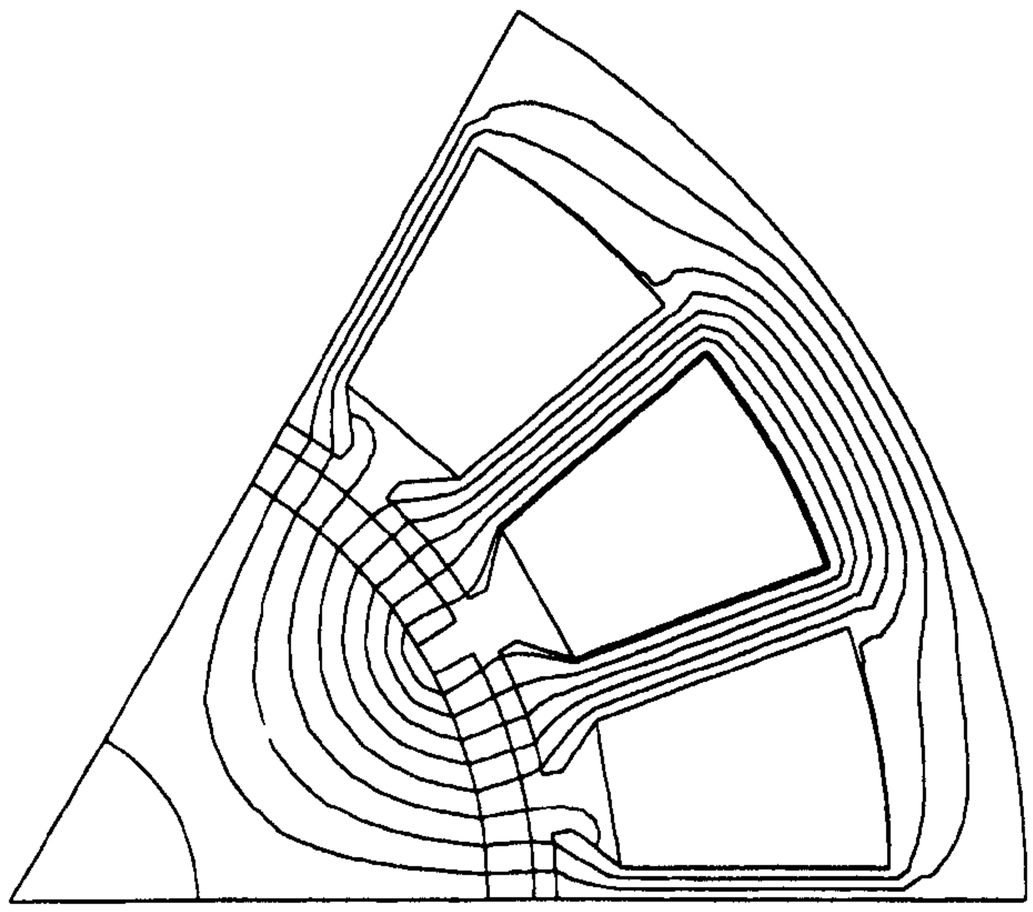

Fig. 9. Flux plot for an 18-slot, 6-pole rare-earth magnet brushless dc motor with normal teeth.

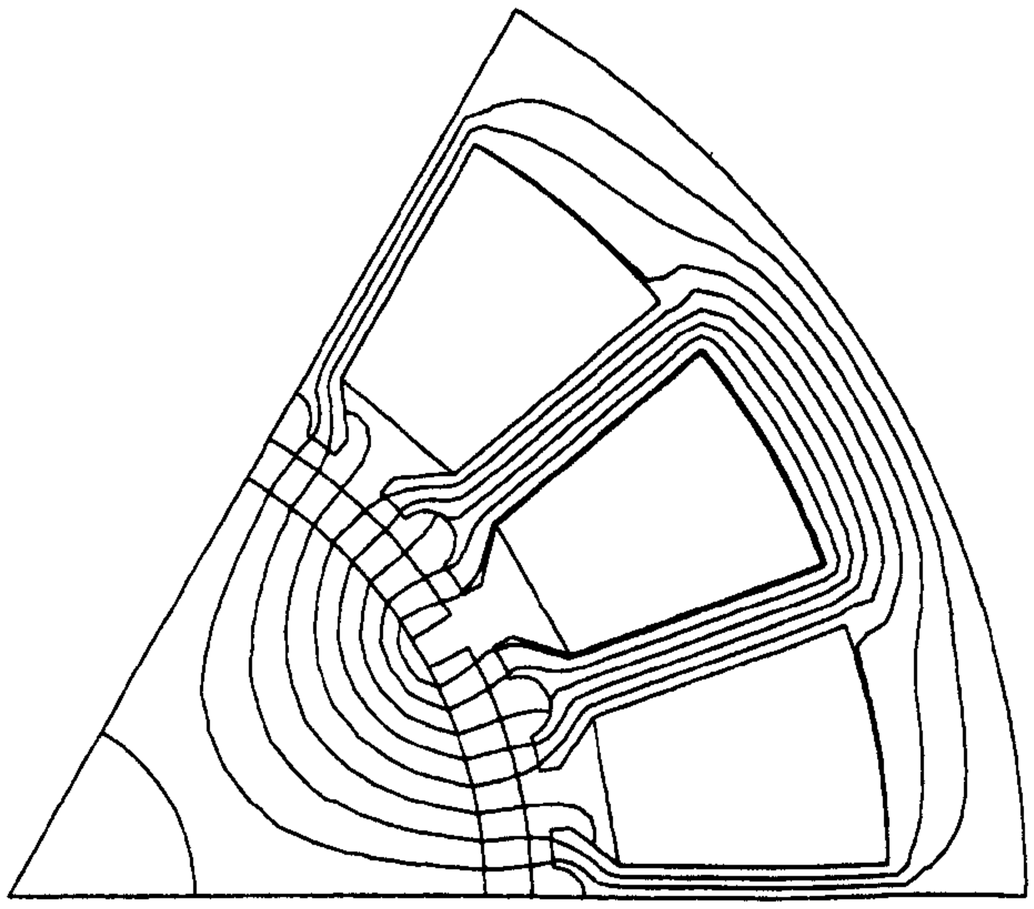

Fig. 10. Flux plot for the same motor as in Fig. 9, but with bifurcated teeth.

of the generated (back) electromotive force (EMF) which in turn depends upon the magnet arc. It is unlikely that a particular value of magnet arc will minimize both kinds of torque variation at the same time. In most cases, a compromise has to be made in order to minimize the total torque ripple.

C. Bifurcated Teeth

In this method, dummy slots, which do not carry any winding, are added at the tooth tip such that every tooth is bifurcated and the number of slots "seen" by the magnets is effectively doubled. This halves the period (doubles the frequency) and reduces the cogging torque. Fig. 9 is a flux plot for an 18-slot, 6-pole rare-earth magnet brushless dc motor showing motor cross section over one pole. This motor has normal teeth.

Fig. 10 is a flux plot for a motor which is identical to the one shown in Fig. 9, except that it has bifurcated teeth. Fig. 11 compares the cogging torque curves for the two motors

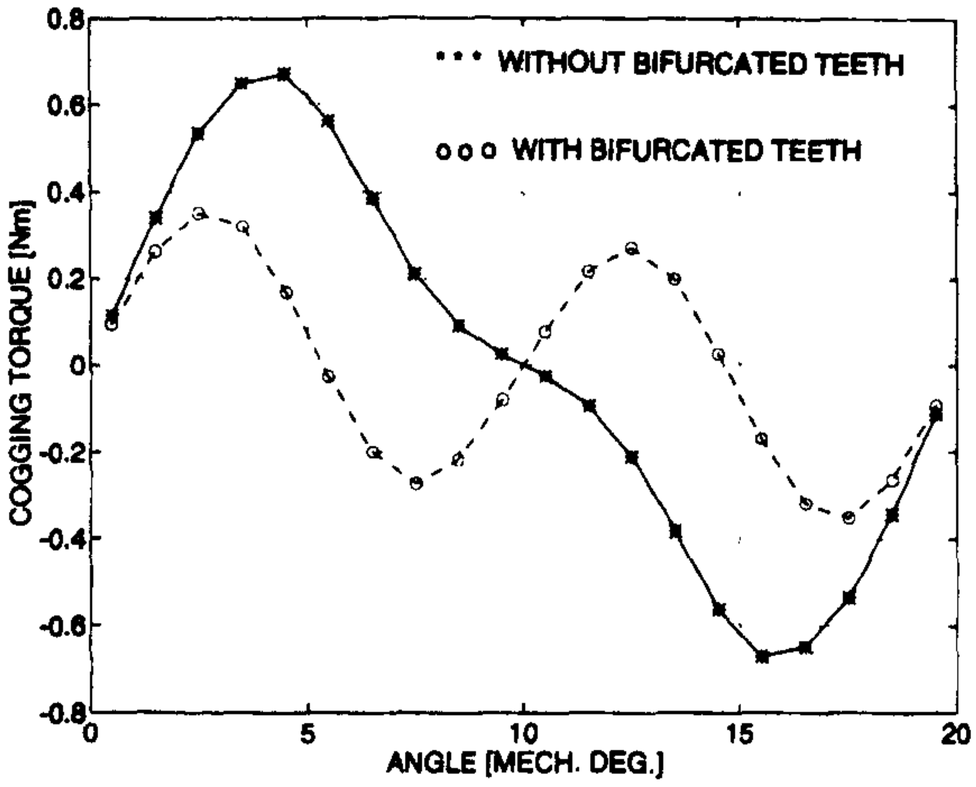

Fig. 11. Cogging torque curves with and without bifurcated teeth for the motors shown in Figs. 9 and 10, respectively.

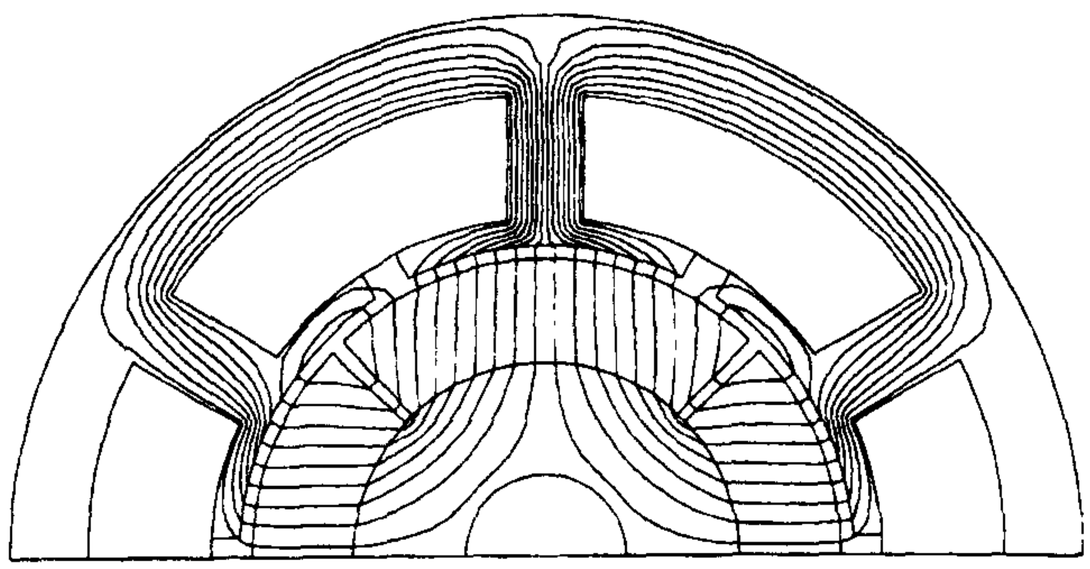

Fig. 12. Flux plot for the same motor as in Fig. 4 but with parallel magnetization of magnets.

shown in Figs. 9 and 10. It can be observed that bifurcated teeth double the frequency and simultaneously reduce the peak cogging torque by about 50%.

D. Varying the Magnetization of Magnets

Just like varying the magnet *arc*, varying the *magnetization* (radial or parallel) of magnets has an effect on the shape and the magnitude of cogging torque. This can be illustrated with an example.

The motor shown in Fig. 4 has radial magnetization of magnets. Fig. 12 shows flux plot for the same motor except that it has parallel magnetization of magnets.

Fig. 13 compares the cogging torque curves for the two motors shown in Figs. 4 and 12. It can be seen that parallel magnetization of magnets leads to about 20% less peak cogging torque as compared to the radial magnetization.

E. Other Methods

The method of shifting alternate magnet poles by one-half stator slot pitch in multipole-pair designs and the method of varying the radial air-gap length around the full circumference of a machine can both be analyzed using the flux-MMF diagram technique. In such cases, the full machine, rather than just the pole or the pole pair, needs to be modeled using the FEA. Flux-MMF diagram needs to be obtained for all the poles as each pole is subjected to different magnetic circuit.

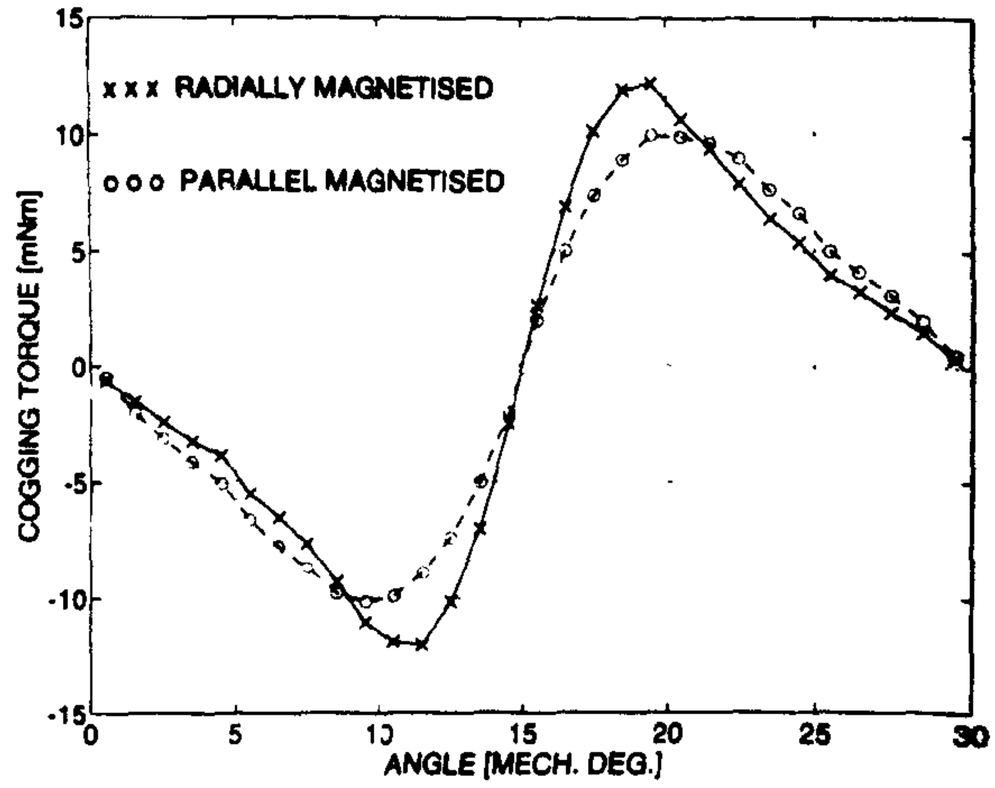

Fig. 13. Cogging torque curves with radial and parallel magnetization of magnets for the motors shown in Figs. 4 and 12, respectively.

VI. Discussion and Conclusion

The flux-MMF diagram technique is a generalized method of predicting cogging torque in permanent magnet motors. Its main advantages are as follows.

- It can deal with all types of permanent magnet motors such as surface PM, interior PM (IPM), and spoke type.
- Since the method is based on a combination of the principle of virtual work and the demagnetization characteristic of a permanent magnet, it serves as a truly universal method of cogging torque prediction and offers a fundamental basis for design evaluation.
- It gives a clear physical insight and graphical interpretation of the phenomenon of cogging torque.
- It can analyze and take account of many of the methods commonly used for minimizing cogging torque such as skewing, bifurcated teeth, varying magnet arc, and varying the magnetization of magnets.
- Unlike most analytical methods, it can be used with any degree of magnetic saturation.

The accuracy of the flux-MMF diagram technique, directly depends upon the accuracy of estimating the variation of magnet flux at incremental rotor positions over a cogging torque cycle. At present, the technique relies upon FEA for this purpose and hence it is sensitive to certain aspects of FEA such as mesh generation. However, the technique is well placed to take advantage of expected improvements in FEA.

Research is also being carried out on alternate methods, such as magnetic lumped circuits, among others, to adapt the technique for rapid calculation. Further work is being done on the technique to take account of the effects of saturation, nonliearities in the demagnetization characteristic and the effect of load current on cogging torque.

Acknowledgment

Thanks are due to SPEED Consortium and in particular to Oriental Motor Company and SEM Ltd. for providing prototypes for testing. The authors would also like thank Jimmy Kelly and Peter Miller for help with the experimental setups.

REFERENCES

[1] D. Howe and Z. Q. Zhu, "The influence of finite element discretisation on the prediction of cogging torque in permanent magnet excited motors," *IEEE Trans. Magn.*, vol. 28, no. 2, pp 1080–1083, Mar. 1992.

[2] Y. Kawase, T. Yamaguchi , and Y. Hayashi, "Analysis of cogging torque of permanent magnet motor by 3-D finite element method," *IEEE Trans. Magn.*, vol. 31, no. 3, pp. 2044–2047, May 1995.

[3] J. De La Ree and N. Boules, "Torque production in permanent magnet synchronous motors," *IEEE Trans. Ind. Applicat.*, vol. 25, no. 1, pp. 107–112, Jan./Feb. 1989.

[4] B. Ackermann, J. H. H. Janssen, R. Sottek, and R. I. Van Steen, "New technique for reducing cogging torque in a class of brushless DC motors," *IEE Proc.*, July 1992, vol. 139, pt. B, no. 4, pp. 315–320.

[5] Z. Q. Zhu and D. Howe, "Analytical prediction of the cogging torque in radial-field permanent magnet brushless motors," *IEEE Trans. Magn.*, vol. 28, no. 2, pp. 1371–1374, Mar. 1992.

[6] E. Favre, L. Cardoletti and M. Jufer, "Permanent magnet synchronous motors: A comprehensive approach to cogging torque suppression," *IEEE Trans. Ind. Applicat.*, vol. 29, no. 6, pp. 1141–1149, Nov./Dec. 1993.

[7] T. Sebastian, G. R. Slemon, and M. A. Rahaman, "Design considerations for variable speed permanent magnet motors," in *Proc. Int. Conf. Elec. Machines*, Munchen, Germany, vol. 3, pp. 1099-1102, Sept. 1986.

[8] J. De La Ree and J. Latorre, "Permanent magnet machines torque considerations," in *Rec. IEEE Ind. Applicat. Soc. Annu. Meeting*, 1988, pp. 32–37.

[9] R. Carlson, A. A. Tavares, J. P. Bastos, and M. Lajoie-Mazenc, "Torque ripple attenuation in permanent magnet synchronous motors," in *Rec. IEEE Ind. Applicat. Soc. Annu. Meeting*, 1989, pp. 57–62.

[10] K. H. Kim, D. J Sim, and J. S. Won, "Analysis of skew effects on cogging torque and BEMF for BLDCM," in *Rec. IEEE Ind. Applicat. Soc. Annu. Meeting*, 1991, pp. 191–197.

[11] J. Y. Hung and Z. Ding, "Design of currents to reduce torque ripple in brushless permanent magnet motors," *IEE Proc.*, July 1993, vol. 140, pt. B, no. 4, pp. 260–266.

[12] T. Li and G. Slemon, "Reduction of cogging torque in permanent magnet motors," *IEEE Trans. Magn.*, vol. 24, no. 6, pp. 2901–2903, Nov. 1988.

[13] C. Hanselman, *Brushless Permanent-Magnet Motor Design*. New York: McGraw Hill, 1994.

[14] B. Nogarede and M. Lajoie-Mazenc, "Torque ripple minimization methods in sinusoidal fed synchronous permanent magnet machines," in *Proc. IEE Electric Machines & Drives Conf.*, 1991, pp. 41–45.

[15] H. Bolton and N. Mallinson, "Investigation into a class of brushless DC motor with quasisquare voltages and currents," *IEE Proc* , vol. 133, pt. B, no. 2, pp. 103–111, Mar 1986.

[16] A. Miraoui, L. De Fang, and J. Kauffman, "Performance analysis of permanent magnet brushless DC motor," in *Proc. IEE Int. Conf. Elec. Machines & Drives*, Oxford, 1993, pp. 371–375.

[17] T. Sebastian and V Gangla, "Analysis of induced EMF and torque waveforms in a brushless permanent magnet machine," in *Rec. IEEE Ind. Applicat. Soc Annu. Meeting*, Denver, CO, 1994, pp 240–246

[18] E. Hamdi, A. Licariao-Nogueira, and P. Silvester, "Torque computation by mean and difference potentials," *IEE Proc.*, vol 140, pt. A, no. 2, pp. 151–154, Mar. 1993.

[19] G. Jang and D. Lieu, "Vibration reduction in electric machine by magnet interlacing," *IEEE Trans. Magn.*, vol 28, no. 5, pp. 3024–3026, Sept. 1992

[20] K. Binns, F Chaaban, and A. Hameed, "Major design parameters of a solid canned permanent magnet motor with skewed magnets," *IEE Proc.*, vol. 140, pt. B, no. 3, pp. 161–165, May 1993.

[21] M. Alhamadi and N. Demerdash, "Three dimensional magnetic field computation by a coupled vector-scalar potential method in brushless DC motors with skewed permanent magnet mounts-The no-load and load results," *IEEE Trans. Energy Conversion*, vol. 9, no 1, pp. 15–22, Mar. 1994.

[22] T Ishikawa and G Slemon, "A method of reducing ripple torque in permanent magnet motors without skewing," *IEEE Trans. Magn.*, vol. 29, no. 2, pp. 2028–2031, Mar. 1993.

[23] M. Jug, B. Hribernik, A. Hamler, M. Trlep, and B. Kreca, "Investigation of reluctance torque of brushless DC motor," in *Proc. Int. Conf. Elec Machines*, Boston, 1990, pp. 132–137.

[24] C. Chan, J. Jiang, G. Chen, X. Wang, and K Chau, "A novel polyphase multipole square-wave permanent magnet motor drive for electric vehicles," *IEEE Trans. Ind Applicat* , vol. 30, no. 5, pp. 1258–1266, Sept./Oct. 1994

[25] A. Kaddouri and H Le-Huy, "Analysis and design of a slotless NdFeB permanent-magnet synchronous motor for direct drive," in *Rec IEEE Ind. Applicat. Soc. Annu. Meeting*, 1992, pp. 271–278.

[26] R. Hanitsch, R. Belmans, L. Walkoff, and W. Geysen, "Brushless DC motor with airgap windings—Influence of back iron material on motor efficiency," in *Proc. IEE Elec. Machines and Drives Conf.*, 1991, pp. 126–130.

[27] A. Murray, "Torque and EMF ripple reduction in brushless machines," in *Proc. IEE Colloqium on PM Machines and Drives*, 1993, pp. 8/1–8/4.

[28] M. Lajoie-Mazenc, B. Nogarede, and J. C. Fagundes, "Analysis of torque ripple in electronically commutated permanent magnet machines and minimization methods," in *Proc. IEE Elec. Machines and Drives Conf.*, London, U.K., 1989, pp. 85–89.

[29] M. Goto and K. Kobayashi, "An analysis of the cogging torque of a DC motor and a new technique of reducing the cogging torque," *Elec. Eng. in Jpn.*, vol. 103, no. 5, pp. 113–120, 1983.

[30] K. Kobayashi and M. Goto, "A brushless DC motor of a new structure with reduced torque fluctuations," *Elec. Eng. in Jpn.*, vol. 105, no. 3, pp. 104–112, 1985.

[31] D. A. Staton, W. L. Soong, and T. J. E. Miller, "Unified theory of torque production in switched reluctance and synchronous reluctance motors," *IEEE Trans. Ind. Applicat.*, vol. 31, no. 2, pp. 329–337, Mar./Apr. 1995.

[32] D. A. Staton, R. P. Deodhar, W. L. Soong, and T. J. E. Miller, "Flux-MMF based torque calculations in AC, DC, and reluctance motors," *IEEE Trans. Ind. Applicat.*, (in press).

[33] R. P. Deodhar, D. A. Staton, and T. J. E. Miller, "Variation of torque constant in brushless PM motors," in *Proc. IEE Elec. Machines and Drives Conf.*, Durham, U.K., Sept. 1995, pp. 405–409.

[34] ———, "Modeling of skew using the flux-MMF diagram," in *Proc. Int. Conf. Power Electronics, Drives and Energy Sys. for Ind. Growth*, Jan. 1996 (in press).

[35] Y. Liao, F. Liang, and T. A. Lipo, "A novel permanent magnet motor with doubly salient structure," in *Rec. IEEE Ind. Applicat. Soc. Annu. Meeting*, Houston, TX, 1992, pp. 308–314.

[36] A. E. Fitzgerald and C. Kingsley Jr., *Electric Machinery*, 2nd ed. New York: McGraw-Hill, 1961.

[37] J. R. Hendershot and T. J. E. Miller, *Design of Brushless Permanent Magnet Motors*, 1st Edition, Oxford/Magna Physics, 1994.

[38] T. J. E. Miller, *Switched Reluctance Motors and Their Control*,. Oxford: Oxford, 1993.

[39] ———, *Brushless Permanent Magnet and Reluctance Motor Drives*. Oxford: Oxford, 1989.

[40] H. H. Woodson and J. R. Melcher, *Electromechanical Dynamics Part I: Discrete Systems*. New York: Wiley, 1968.

[41] D. C. White and H. H. Woodson, *Dynamics of the Electromechanical Energy Conversion*. New York: Wiley, 1963.

[42] D. A. Staton, "C.A.D. of permanent magnet D.C. motors for industrial drives," Ph. D. dissertation, University of Sheffield, U.K., 1988.

Rajesh P. Deodhar (S'88–M'90–S'94) was born in Bombay, India, on February 22, 1968. He received the B.Eng. degree in electronics engineering from the University of Bombay in 1989 and the M.Tech. degree in electronic product design from the Center for Electronic Design and Technology (CEDT) at the Indian Institute of Science, Bangalore, in 1991. Since the beginning of 1994, he has been working toward the Ph.D. degree in the SPEED Laboratory, University of Glasgow, Scotland, in the generalized area of design and analysis of electric machines and drives.

From 1991 to 1993, he worked as a Design Engineer with Crompton Greaves Ltd., Bombay, India, on the design of induction and brushless PM motors and drives. In 1993 he spent six months in Japan, working with Hitachi Ltd., on the applications of electric machines and drives in home appliances.

Mr Deodhar was awarded the CEDT Design Gold Medal by the Indian Institute of Science in 1991. He also received the Hitachi-AOTS scholarship in 1993 which enabled him to work with Hitachi Ltd. in Japan for six months. He is a Member of the IEEE Industry Applications Society and also an Associate Member of the Institute of Electrical Engineers, U.K.

David A. Staton was born in Chesterfield, England, on July 29, 1961. He received the B.Sc. (Hons.) degree in electrical and electronic engineering from Trent Polytechnic, Nottingham, England, in 1983, and the Ph.D. degree from the University of Sheffield, England, in 1988.

From 1977 to 1984, he was employed by British Coal, who sponsored him while he was undertaking the B.Sc. degree. While at the University of Sheffield, he developed CAD software for permanent-magnet dc motors in collaboration with GEC Electromotors Ltd. From 1988 to 1989, he was with Thorn EMI Central Research Laboratories and was engaged in the design of motors for the Kenwood range of food processors. From 1989 to 1995, he was employed as a research assistant in the SPEED Laboratory at the University of Glasgow. Presently, he is with Control Techniques plc, Newtown, Wales. His research interests are in the computer aided design of permanent-magnet and reluctance motors.

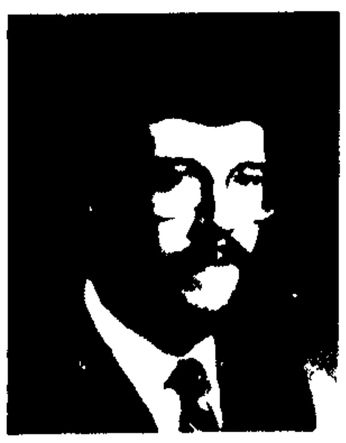

Thomas M. Jahns (M'78–SM'91–F'93) received the B.S. and M.S. degrees in 1974 and the Ph.D. degree in 1978 from the Massachusetts Institute of Technology, Cambridge, MA, all in electrical engineering.

He joined GE Corporate Research and Development, Schenectady, NY, in 1983, where he has pursued new adjustable-speed motor drive technology in the Control Systems & Electronic Technologies Laboratory (CSETL). His technical efforts have included development of high-performance permanent magnet motor servo drives and high-power resonant converters for machine tools and aerospace applications. In 1986, he was appointed Manager of the Power Controls Program, leading efforts to develop advanced permanent magnet and switched reluctance motor drives for a variety of industrial, commercial, and aerospace applications In his present position as Project Manager, he is leading research activities which have included high-performance aerospace generating equipment and low-cost adjustable-speed motor drives for commercial/residential applications.

Dr. Jahns has been an active member of IEEE-IAS Industrial Drives Committee since 1978, including two years of service as Committee Chair during 1988–89. He has served as Chair of the IAS Industrial Power Conversion Systems Department during 1992–93 and is presently serving as an At-Large Member of the IAS Executive Board

Timothy J. E. Miller (M'74–SM'82–F'96) is a native of Wigan, U.K. He received the B.Sc. degree from the University of Glasgow, Scotland, and the Ph.D. degree from the University of Leeds, U.K.

From 1979 to 1986 he was an electrical engineer and program manager at General Electric Corporate Research and Development, Schenectady, NY. His industrial experience also includes periods with GEC (U.K.), British Gas, International Research and Development, and a student-apprenticeship with Tube Investments Ltd. He is Lucas Professor in Power Electronics and founder and Director of the SPEED Consortium at the University of Glasgow, where he is responsible for teaching and research in power electronics and electrical power engineering. The SPEED Laboratory serves some 30 industrial companies in the U.K., the U.S., Europe, and the Far East with design software for electric motor design, electronic controls and development equipment for motor drive systems. He has authored or coauthored more than 100 publications in the field of motors, drives, power systems and power electronics, including five books.

Prof Miller is a Fellow of the Royal Society of Edinburgh and a Fellow of the Institute of Electrical Engineers.

Modeling of Skew Using the Flux–MMF Diagram

Rajesh P. Deodhar, *Student Member, IEEE*, David A. Staton, and Timothy J. E. Miller, *Fellow, IEEE*

***Abstract*—The flux-MMF diagram has recently been used to predict torque ripple in different machine types. This paper describes a simple and elegant method, based on this technique, for predicting the effect of skew on torque ripple in permanent magnet machines. Although it is well known that skewing minimizes torque ripple, the paper quantifies the difference in the extent of minimization between the electromagnetic torque ripple and the cogging torque.**

***Index Terms*—Skew, cogging, torque ripple.**

NOMENCLATURE

Symbol	Meaning	Units
ψ	Instantaneous flux-linkage	[V · s]
T_e	Electromagnetic torque	[N · m]
W'	Co-energy	[J]
θ	Rotor position	[deg or rad]
MMF	Magnetomotive force	[A · t]
θ_i	Incremental angle between each magnet segment	[deg or rad]
k_s	Skew factor	[deg or rad]
n	Number of magnet segments	
φ_i	Instantaneous flux at a rotor position corresponding to the ith magnet segment	[Wb]
φ_{av}	averaged flux over n magnet segments	[Wb]

I. INTRODUCTION

IN PERMANENT magnet machines, skewing of either the stator or the rotor is usually incorporated in order to reduce the torque ripple as well as noise and vibration. While both may have roughly the same electromagnetic effect on the machine operation, the choice is generally dictated by manufacturability. Analytical as well as finite element based methods have been developed to investigate the effect of skew on machine performance [1]–[4]. Analytical methods usually involve formulation of expressions for airgap permeances, MMF and flux density distribution. Quantities such as back-emf and cogging torque are then derived from these expressions such that the effect of skew can be taken into account [1], [2]. Finite element based methods make use of either the 2-D or the 3-D analysis. In the case of 2-D analysis, multiple finite element meshes are required at different positions along the axis [4], while in the case of 3-D analysis, a single finite element mesh is sufficient [3] to incorporate the effect of skew at a particular rotor position.

The flux–MMF diagram technique, which has recently been introduced for analysis and comparative evaluation of a wide variety of electric machines [5]–[9], provides a simple and elegant method of analysing the effect of skew on torque ripple. An advantage with this technique is its ability to represent many performance characteristics of a machine graphically, including torque capability and torque smoothness. It uses 2-D finite element analysis to construct the flux–MMF diagram [5], [6]. Once the diagram is constructed, the effect of skew on torque ripple can be analyzed quickly with minimal amount of computation. Although one slot pitch is a fairly common value for the skew factor in permanent magnet machines, different values can be tried, by constructing a flux–MMF diagram and calculating torque ripple in each case, before finalizing on a particular value of skew factor.

In the following discussion, three different terms have been used to refer to different types of torque ripple. These terms are defined as follows.

- *Electromagnetic torque ripple*: The variation of instantaneous electromagnetic torque with rotor position and includes both the average and the ripple components.
- *Cogging torque ripple*: The variation of instantaneous cogging torque with rotor position and it includes only the ripple component, as the average component is always zero.
- *Total torque ripple*: The variation of instantaneous total torque (summation of instantaneous electromagnetic and cogging torque) with rotor position and it includes both the average and the ripple component.

Fig. 1 shows the important features of a typical flux-MMF diagram for any one phase of a multi-phase sinewave brushless ac machine. It is essentially a "scaled" representation of a conventional ψ-i locus used commonly for analyzing switched reluctance machines [6], [10]–[15]. For a given geometry and phase current excitation, a series of 2-D finite element analyzes are performed at incremental rotor positions and increasing current values over a certain portion of an electrical cycle such that using symmetry, flux–MMF diagram can be constructed over the entire electrical cycle. For calculating electromagnetic torque ripple, the flux–MMF diagram is always plotted for any one phase and hereafter it is simply referred to as the

Paper IPCSD 96-23, approved by the Electric Machines Committee of the IEEE Industry Applications Society for presentation at the 1996 PEDES International Conference on Power Electronics, Drives, and Energy Systems for Industrial Grwoth, New Delhi, India, January 8–11, 1996. This work was supported by the University of Glasgow and the CVCP (Committee of Vice-Chancellors and Principals), U.K. Manuscript released for publication April 15, 1996.

R. P. Deodhar and T. J. E. Miller are with SPEED Laboratory, Department of Electronics and Electrical Engineering, University of Glasgow, Glasgow G12 8LT, Scotland, U.K.

D. A. Staton is with Control Techniques, St. Giles, Newtown, Powys SY16 3AJ, Wales, U.K.

Publisher Item Identifier S 0093-9994(96)06636-4.

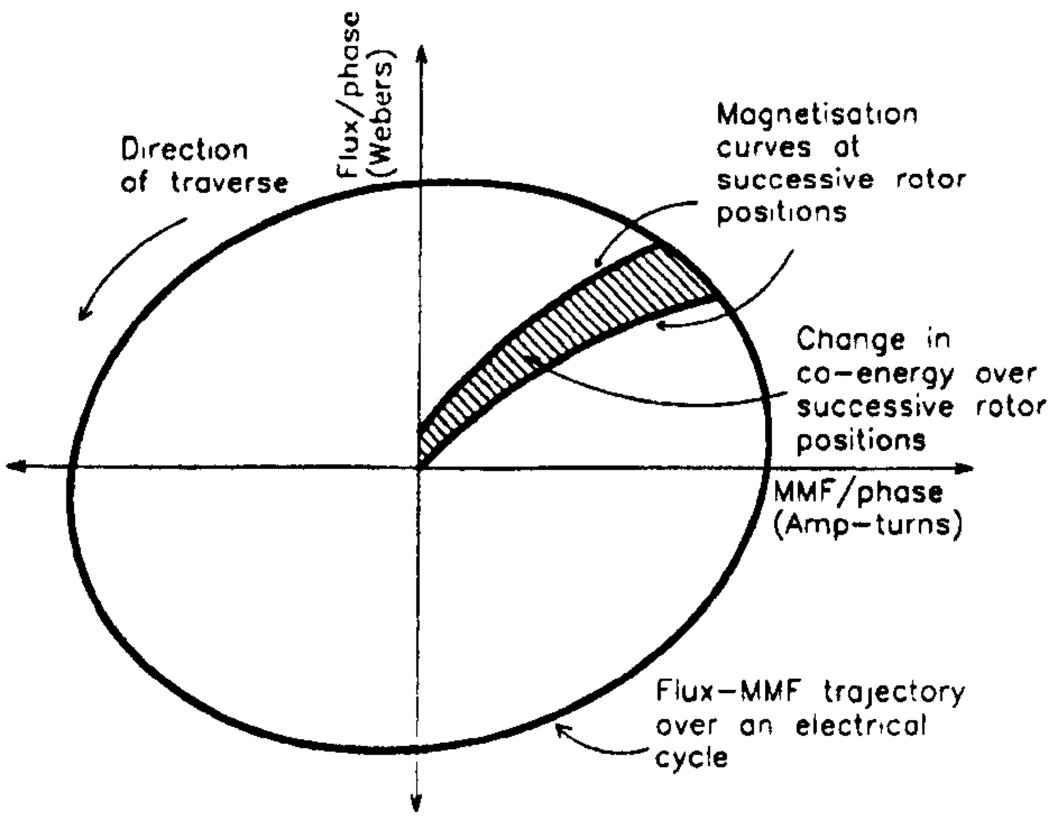

Fig. 1. Flux-MMF diagram for any one phase of a multi-phase sinewave brushless ac machine.

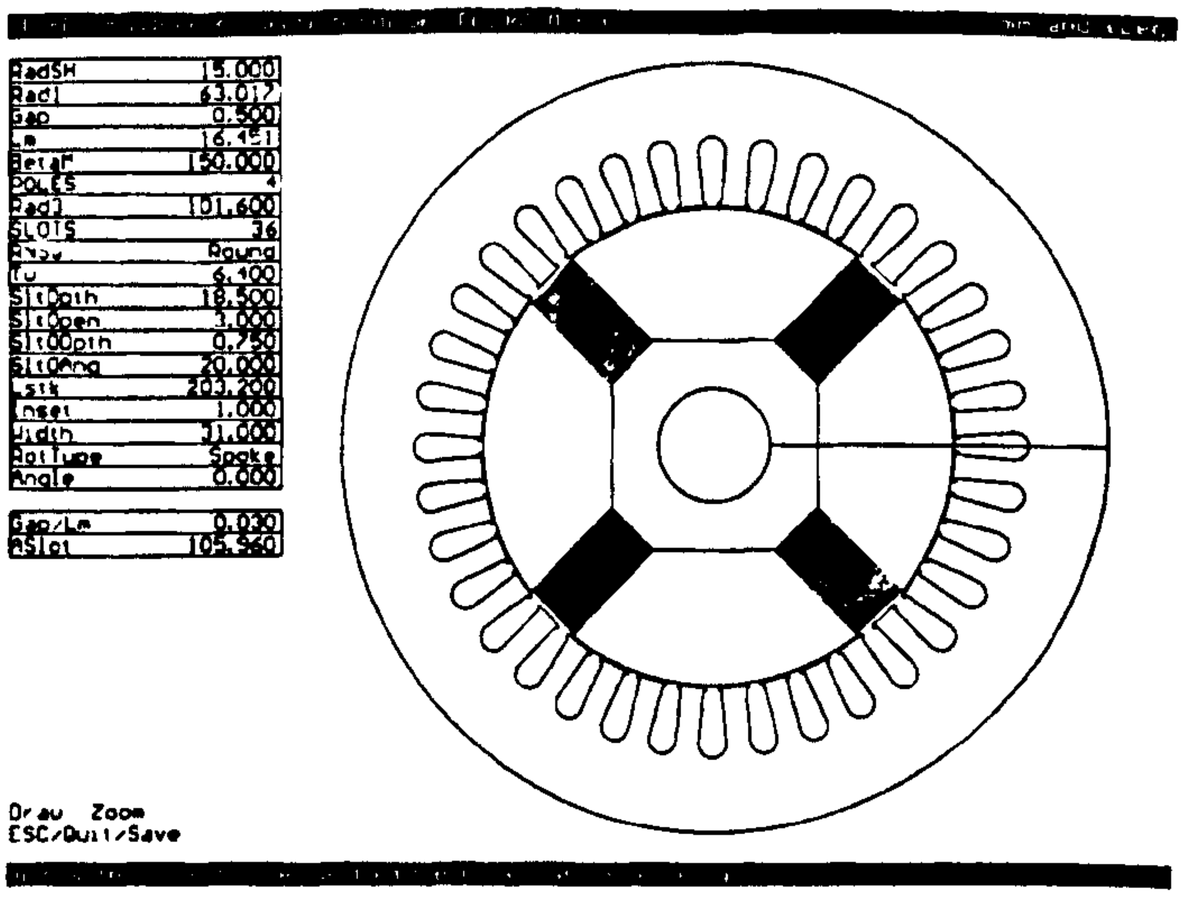

Fig. 3. Cross section of a 3-phase, 4-pole, 36-slot, rare-earth interior permanent magnet, spoke type brushless ac motor.

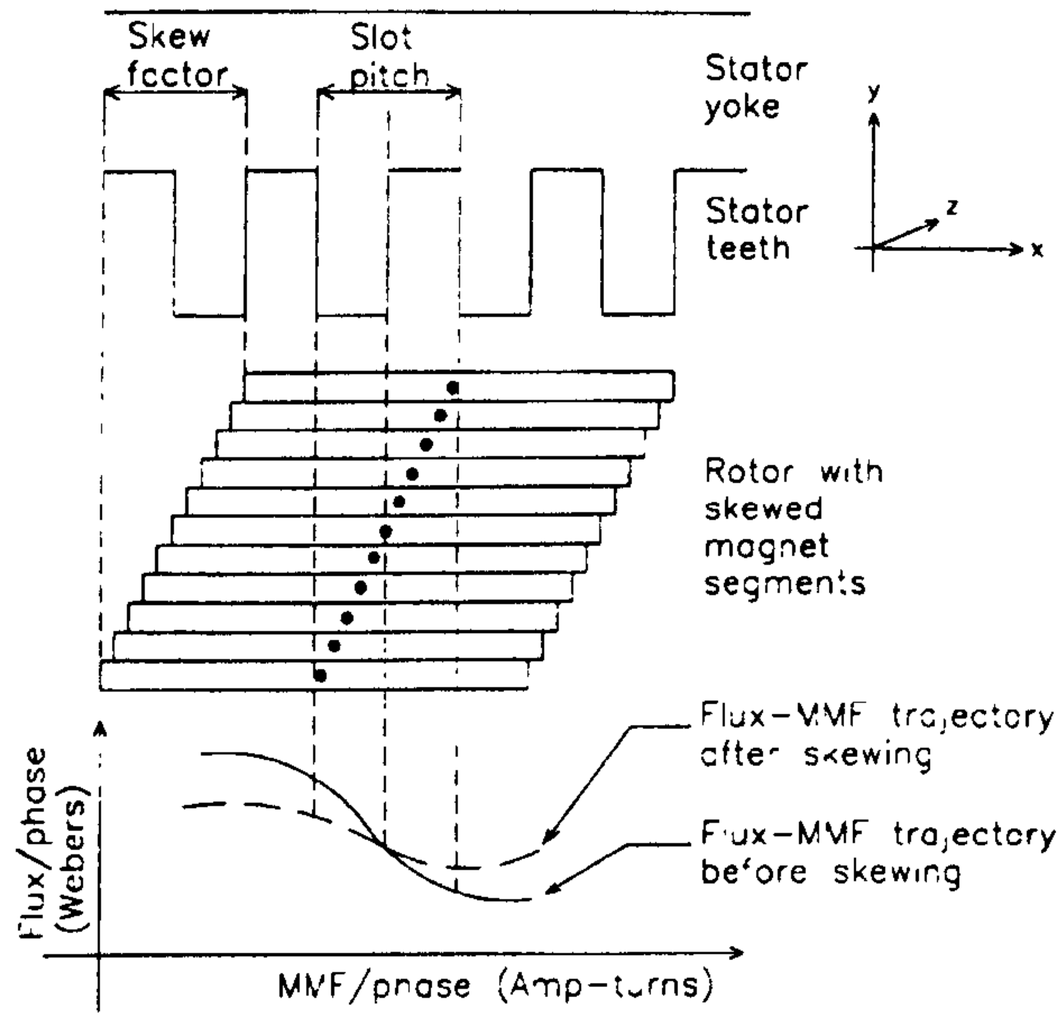

Fig. 2. A developed view of the skewed magnet segments showing the effect of skew on the flux-MMF trajectory.

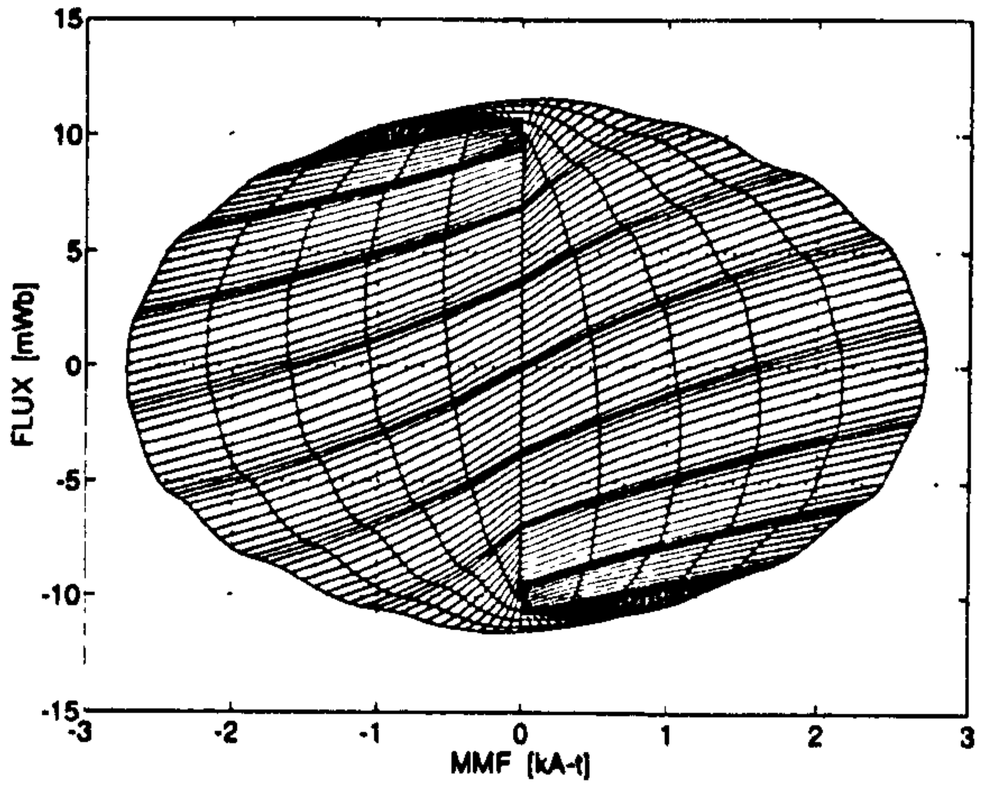

Fig. 4. Calculated flux-MMF diagram for the spoke type motor without skew at rms currents of 0, 4, 8, 12, 16, and 20 A.

"flux-MMF diagram."

For example, the flux-MMF diagram shown in Fig. 4 has flux-MMF trajectories plotted for 6 values of rms current with each trajectory having 180 data points corresponding to the rotor displacement of one electrical cycle. Thus there are 1080 data points in total. However, by exploiting the symmetry that exists in a balanced 3-phase sinewave distribution, only one-sixth of an electrical cycle needs to be modeled in order to plot the flux-MMF diagram over an entire electrical cycle. In this case only 30 finite element meshes were required at 1° increments, with six solutions carried out at each rotor position, i.e., 180 solutions in total.

The instantaneous effective flux linking a particular phase is plotted against the instantaneous MMF in that phase to obtain a closed trajectory, which is an ellipse in the case of a sinusoidally excited machine. The area enclosed by such a closed trajectory indicates *average* energy conversion over one electrical cycle associated with any one phase. In addition, nonlinear magnetization curves—taking saturation into account—are obtained for each successive rotor position. Incremental areas enclosed by such magnetization curves at successive rotor positions indicate *instantaneous* energy conversion over small displacements associated with any one phase. The average, as well as the instantaneous electromagnetic, torque values for any one phase are calculated by applying the principle of virtual work (1):

$$T_e = \left.\frac{\partial W'(\mathrm{MMF},\theta)}{\partial\theta}\right|_{\mathrm{MMF=constant.}} \tag{1}$$

The total electromagnetic torque ripple for a multiphase machine is then obtained by simply adding phase shifted torque contributions from each of the machine phases, assuming a symmetrical machine. In the case of a nonsymmetrical machine, flux-MMF diagram needs to be constructed and electromagnetic torque ripple calculated for each of the phases separately. Individual torque contributions can then be added with an appropriate amount of phase shift to obtain total

electromagnetic torque ripple, as before. The procedure of adding up torque contributions from individual phases holds good even when the machine is saturated; since saturation is already taken into account in calculating the instantaneous effective flux linking a particular phase, which includes both the self and the mutual components.

Section II explains how skew is represented in a flux–MMF diagram. Sections III and IV discuss the effect of skew on the electromagnetic torque ripple and the cogging torque ripple, respectively. Section V describes experimental validation. Finally Section VI summarizes and discusses the difference in the extent of minimization, due to skewing, in the case of the electromagnetic and cogging torque ripples.

II. Skew: As Seen Through the Flux-MMF Diagram

To understand how skew is represented in a flux–MMF diagram, consider any point on this diagram which corresponds to an instantaneous value of flux for a particular rotor position of a machine with skew. Fig. 2 shows a developed view of skewed rotor magnet segments against the stator slots. Note that a radial flux machine geometry is assumed. In practice, the magnets need not be segmented. Even if the rotor (or the stator) is skewed continuously, sections of varying magnet discretization can be considered to develop the theory. It can easily be deduced from Fig. 2 that flux at a particular rotor position for the machine with skew is an *average* of flux values at successive rotor positions over the skew angle for the machine without skew. Mathematically, this averaging can be represented as in (2):

$$\varphi_{av} = \frac{\sum_{i=1}^{n} \varphi_i}{n} \tag{2}$$

where

- n is known for a segmented rotor, or chosen, if a continuously skewed magnet is discretized,
- φ_i instantaneous flux values at successive rotor positions with an incremental angle of $\theta_i = k_s/n$.

Torque ripple curves can now be obtained from the flux–MMF diagram [6], and thus torque ripple magnitude can be calculated as a function of skew.

III. Effect of Skew on the Electromagnetic Torque Ripple

Fig. 3 shows a cross section of a 3-phase rare-earth interior permanent magnet brushless ac motor, also known as a "spoke-type" motor. Fig. 4 is the calculated flux–MMF diagram for the spoke-type motor without skew. The deviation from the ideal elliptical shape and highly irregular spacing of the magnetization curves indicate a large amount of electromagnetic torque ripple as shown in Fig. 6. Since this is a salient pole machine, the torque ripple is a combination of mutual and reluctance torque components and both are taken into account in Fig. 6. Fig. 5 is the calculated flux-MMF diagram for the same motor with a skew of one slot pitch. Graphical comparison between Figs. 4 and 5 shows that the effect of skew on the flux-MMF diagram is of two kinds. First, the spacing of magnetization curves in Fig. 5 is more regular than in Fig. 4. Secondly,

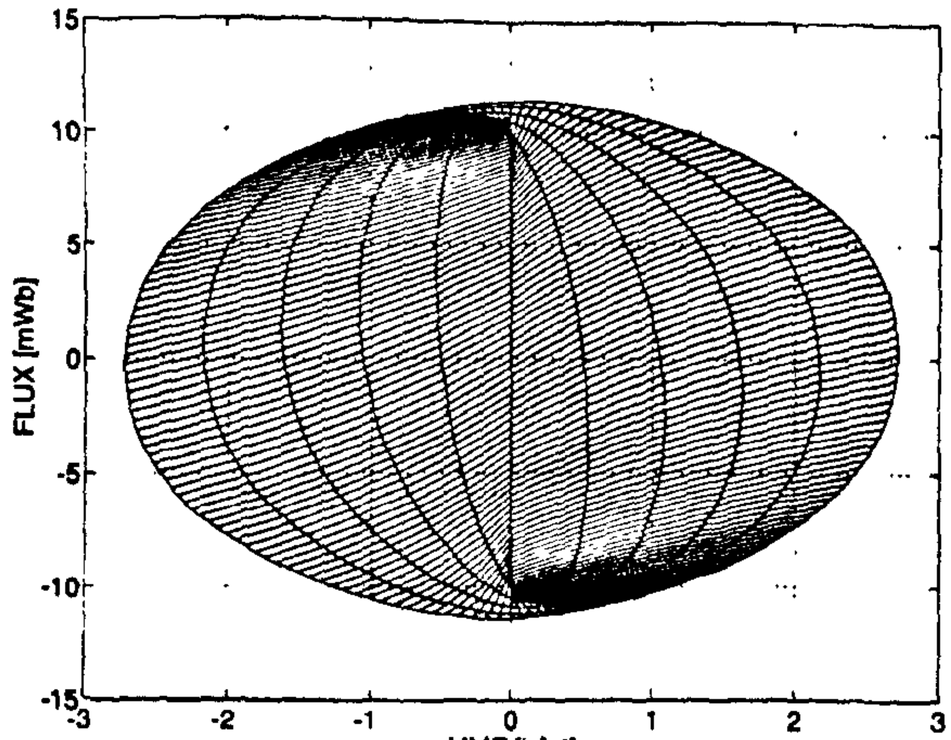

Fig. 5. Calculated flux–MMF diagram for the spoke type motor with a skew of one slot pitch at rms currents of 0, 4, 8, 12, 16, and 20 A.

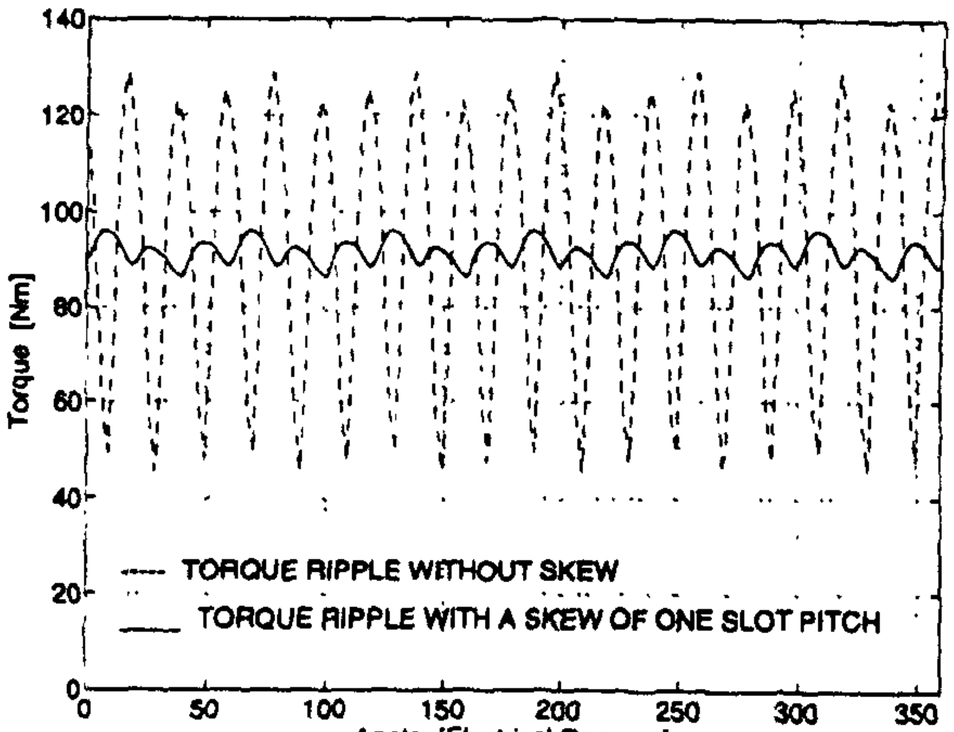

Fig. 6. Comparison of calculated electromagnetic torque ripple for the spoke-type motor without skew and with a skew of one slot pitch at the rms current of 20 A.

the shape of flux–MMF trajectories is closer to ideal elliptical shape in Fig. 5 than in Fig. 4. Both these effects lead to a reduction in electromagnetic torque ripple as shown in Fig. 6.

IV. Effect of Skew on the Cogging Torque Ripple

It has been shown in [8] that the flux–MMF diagram for any one phase of a machine can only predict electromagnetic torque ripple at a certain nonzero load current. Since the flux–MMF diagram is merely a vertical line at zero current, it does not enclose an area and hence does not predict any torque. In order to be able to predict cogging torque ripple which is present even at zero current, the flux–MMF diagram is plotted for a permanent magnet corresponding to *any one pole* rather than for *any one phase*. Fig. 7 is the calculated flux-MMF diagram for a permanent magnet corresponding to one pole of a 3-phase ferrite magnet brushless ac motor shown in Fig. 8 (Note that in the finite element analysis, each rotor pole was modeled with uniform radial magnetization over the entire pole arc of 60°). The method of predicting cogging

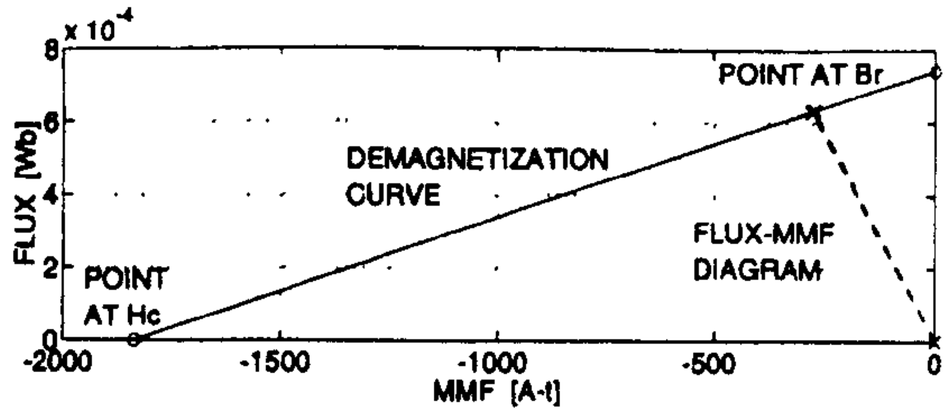

(a)

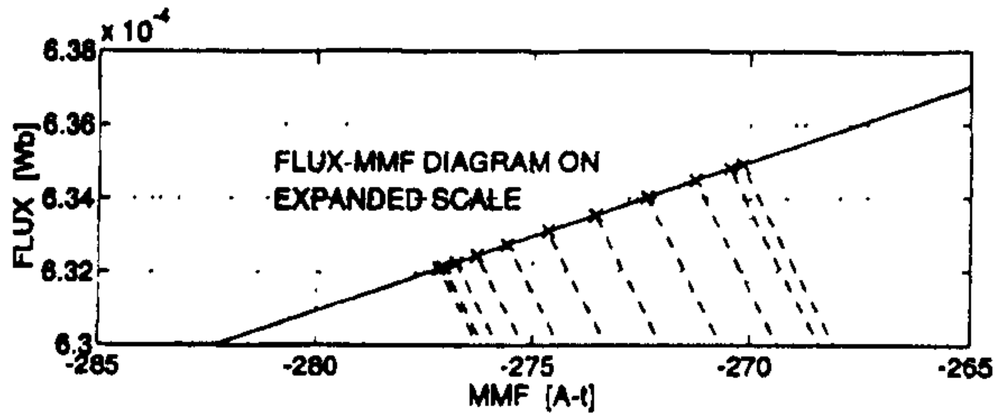

(b)

Fig. 7. Calculated flux–MMF diagram for a permanent magnet corresponding to one pole of the motor shown in Fig. 8. (a) Very small areas enclosed by dotted load lines at successive rotor positions. (b) The same as (a) on an expanded scale.

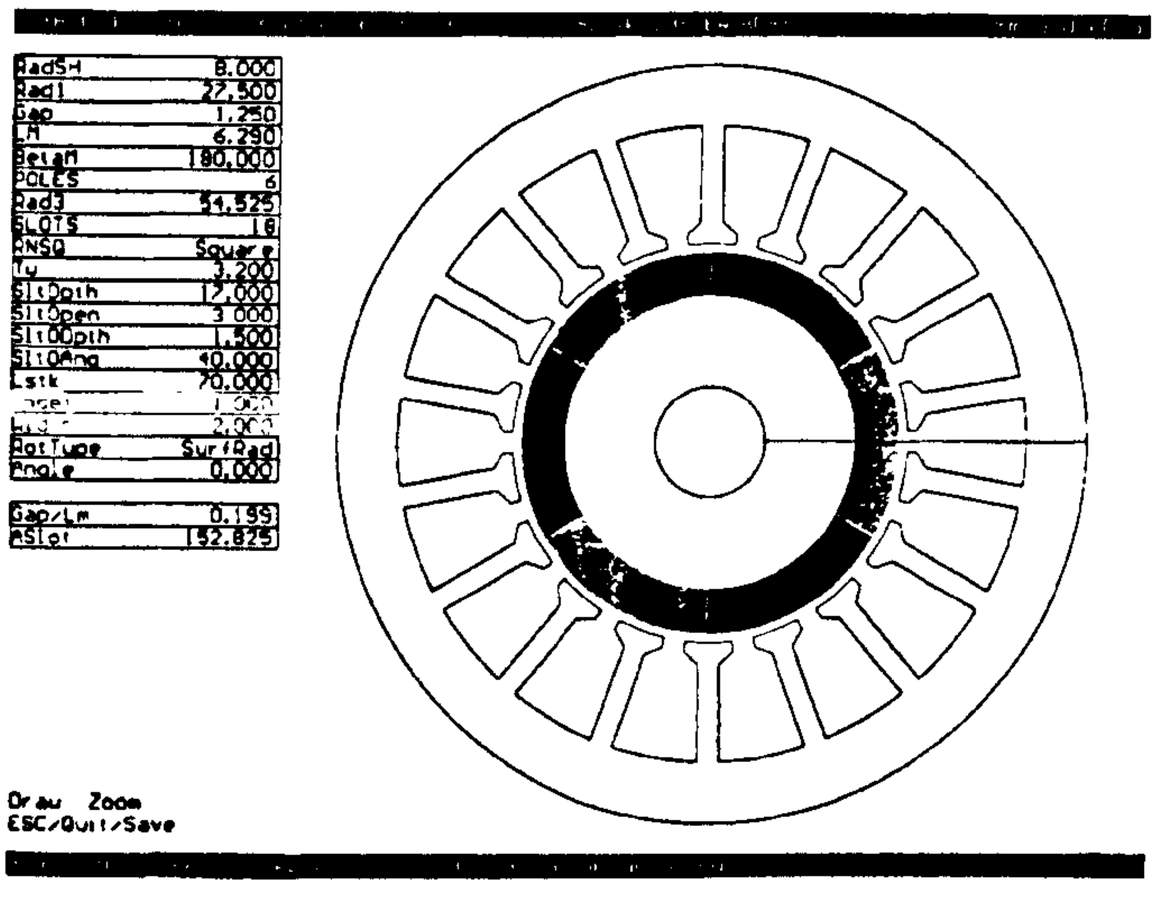

Fig. 8. Cross-section of a 3-phase, 6-pole, 18-slot, ferrite magnet brushless ac motor.

torque ripple using the flux–MMF diagram for a permanent magnet is described in detail in [8].

Fig. 9 shows that the calculated variation of flux and MMF in the permanent magnet over a cogging torque cycle is very small. This is also reflected in the flux–MMF diagram shown in Fig. 7(a). Fig. 7(b) shows the same flux–MMF diagram on an expanded scale to indicate the areas enclosed by the "average load lines" at successive rotor positions. These areas indicate incremental change in co-energy over a unit of rotor displacement and the cogging torque is then calculated by applying (1). The effect of skew on the flux–MMF diagram of Fig. 7 is demonstrated in Fig. 10 where the same method, as described in Section II, was used to construct the flux–MMF diagram with skew (from the one without skew). It shows that

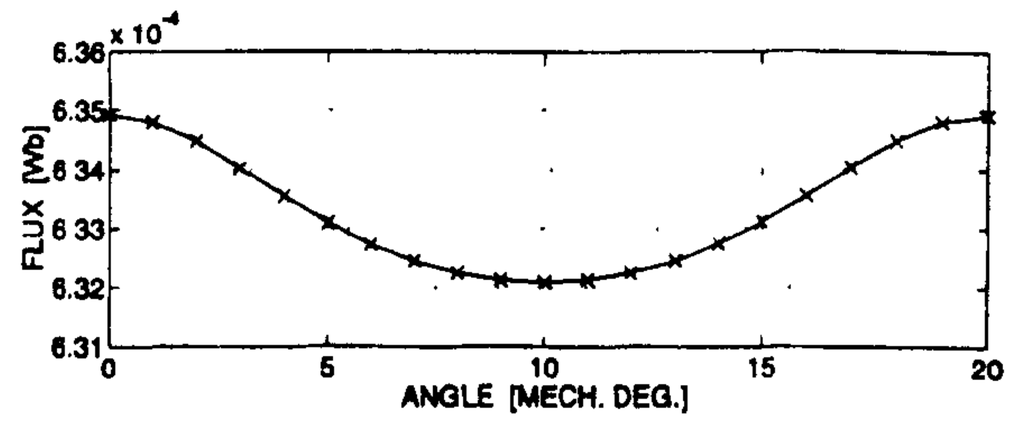

(a)

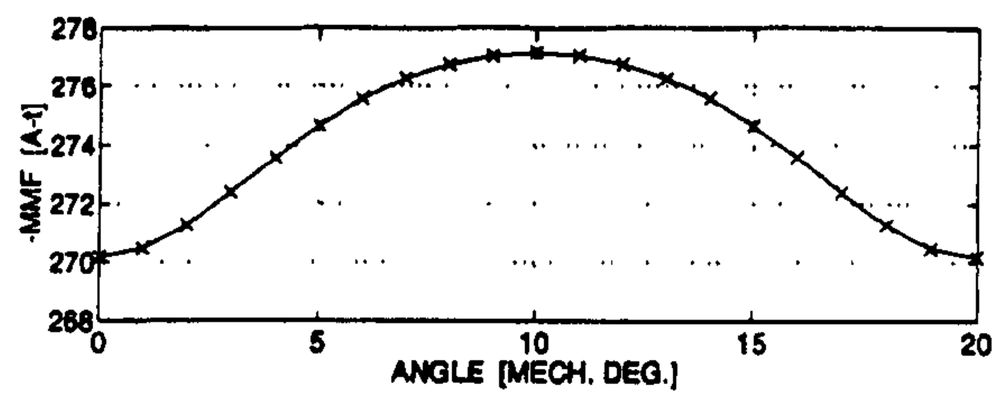

(b)

Fig. 9. Calculated flux and MMF variation in the permanent magnet over a cogging torque cycle, used to construct the flux–MMF diagram shown in Fig. 7.

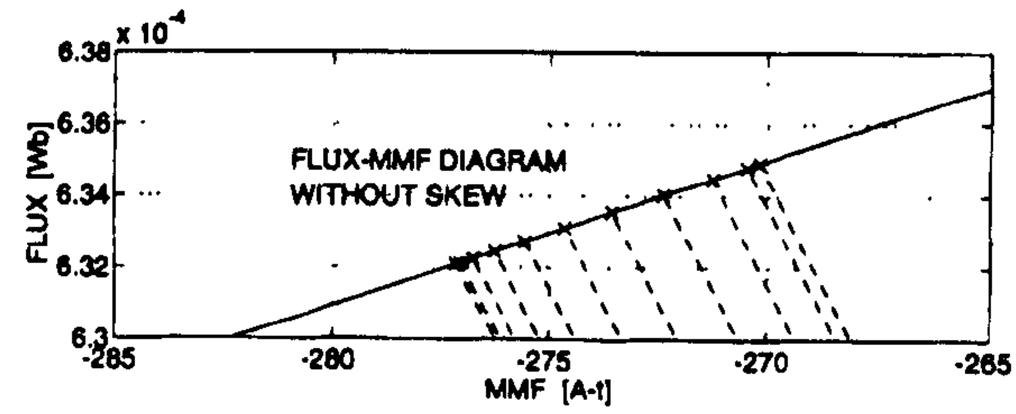

(a)

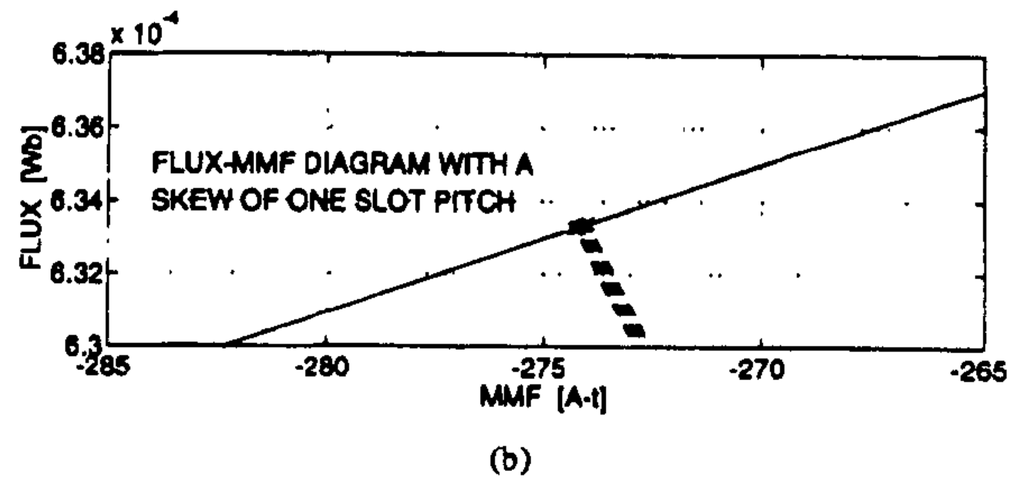

(b)

Fig. 10. Graphical representation of the effect of skew on the flux–MMF diagram of Fig. 7.

a skew of one slot pitch leads to a substantial reduction in the areas enclosed between any two load lines at successive rotor positions with a proportional decrease in the cogging torque. Fig. 11 shows the comparison of calculated cogging torque ripple at different skew factors. It is important to note that for the same amount of skewing of one slot pitch, the effect of skew is different in the case of electromagnetic torque ripple (Fig. 6) and cogging torque ripple (Fig. 11).

V. Experimental Validation

This section discusses experimental validation provided by comparing finite element analysis predictions of torque ripple with measurements made on a 3-phase, 6-pole, 18-slot, rare-earth magnet brushless ac motor (shown in Fig. 12). Fig. 13 is

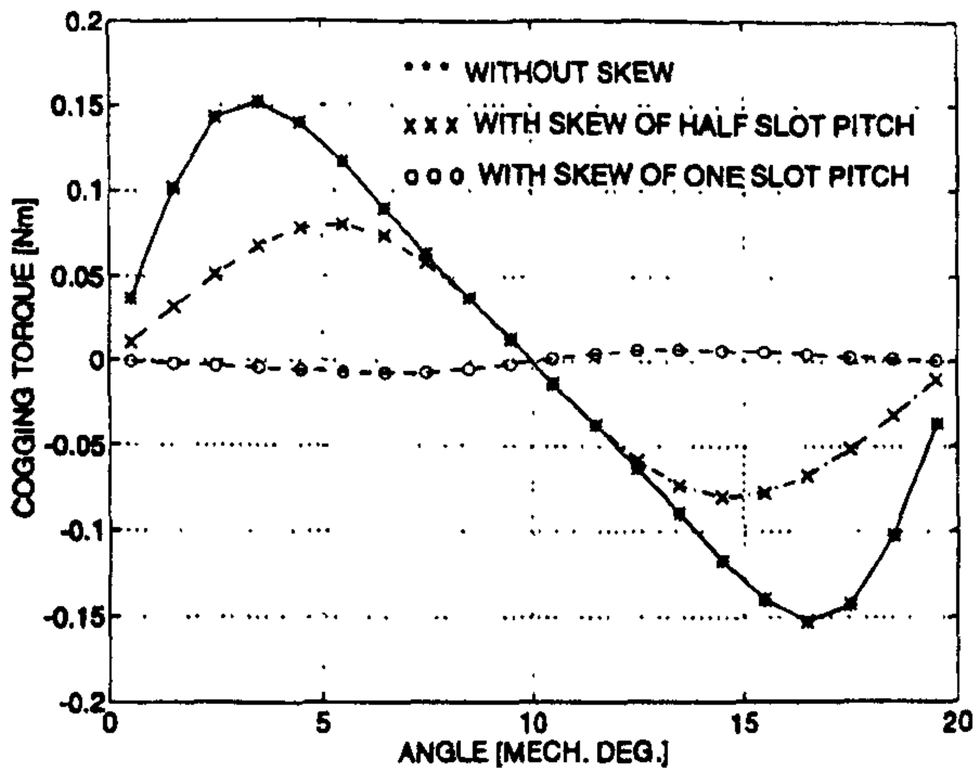

Fig. 11. Comparison of calculated cogging torque ripple at different skew factors for the motor shown in Fig. 8.

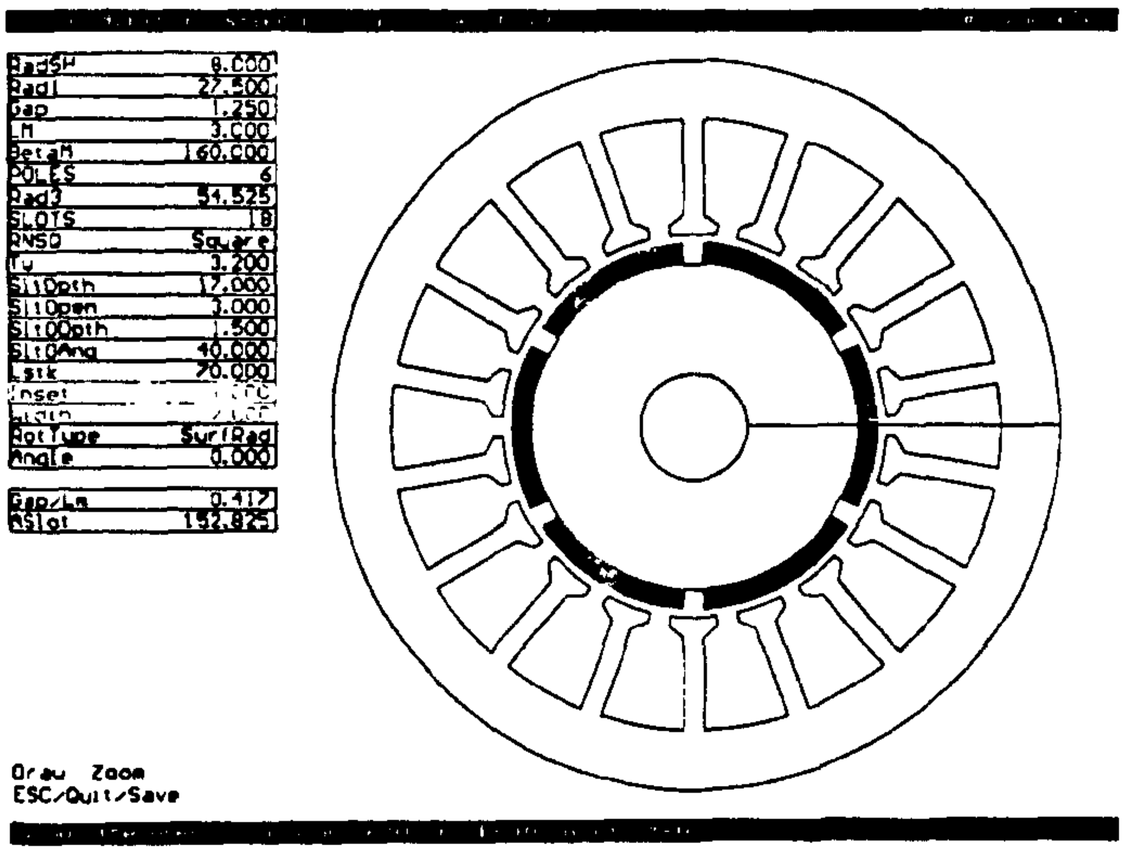

Fig. 12. Cross section of a 3-phase, 6-pole, 18-slot, rare-earth magnet brushless ac motor.

a typical flux plot at no load obtained from the finite element analysis showing the bifurcated stator teeth used in this motor to reduce cogging torque ripple. The effect of bifurcated teeth on cogging torque ripple has been analyzed in detail in [8].

A. Electromagnetic Torque Ripple Calculation

The calculated flux-MMF diagram of the motor without skew is shown in Fig. 14. The equivalent diagram for the motor with skew is shown in Fig. 15. Fig. 16 makes a direct comparison of the two cases. It shows that on one hand skewing reduces torque ripple, as indicated by the shape of the diagram being closer to the ideal elliptical shape for the motor with skew. On the other hand, there is a price to be paid for this gain in terms of a slight reduction in average torque, again as indicated by the smaller area enclosed by the diagram for the motor with skew. Table I illustrates this point with the help of quantitative analysis carried out on the total torque ripple.

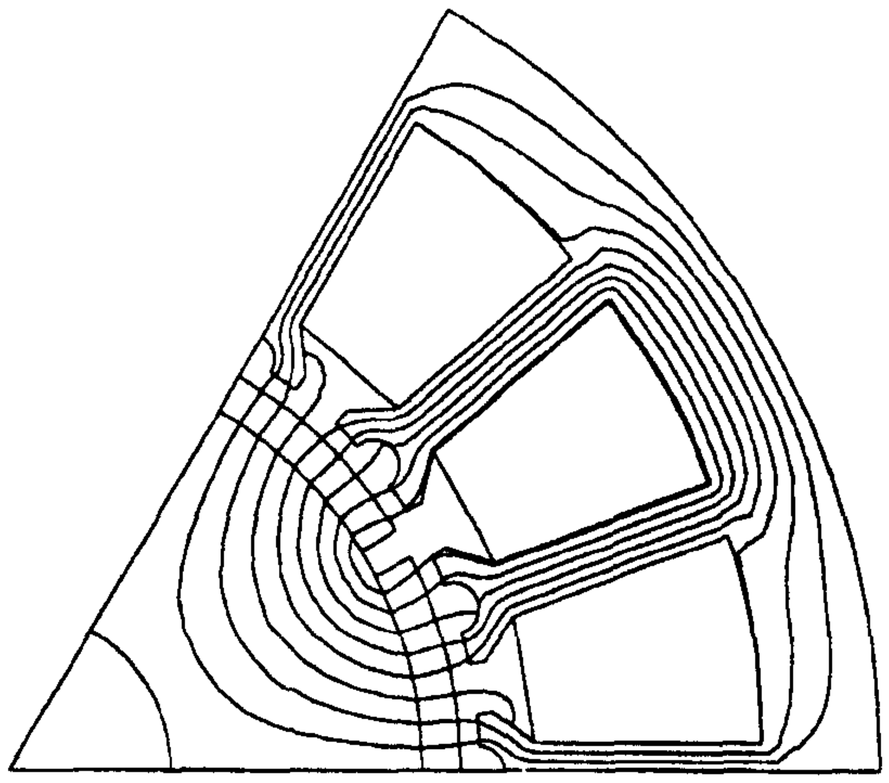

Fig. 13. Flux plot at no load displaying bifurcated stator teeth for the motor shown in Fig. 12.

TABLE I
QUANTITATIVE ANALYSIS OF THE EFFECT OF SKEW WITH RESPECT TO FIG. 24

Phase current (rms)	T_{RIPPLE}[a] without skew	T_{RIPPLE}[a] with skew	T_{AV} without skew	T_{AV} with skew	% drop in T_{AV} due to skew
1 A	82.6%	8.1%	0.86 N·m	0.82 N·m	5%
2 A	46.3%	6.7%	1.72 N·m	1.63 N·m	5%
3 A	34.5%	6.2%	2.57 N·m	2.44 N·m	5%
4 A	29.1%	6.0%	3.41 N·m	3.24 N·m	5%

[a] T_{RIPPLE} is expressed as ratio % of peak-to-peak to average torque

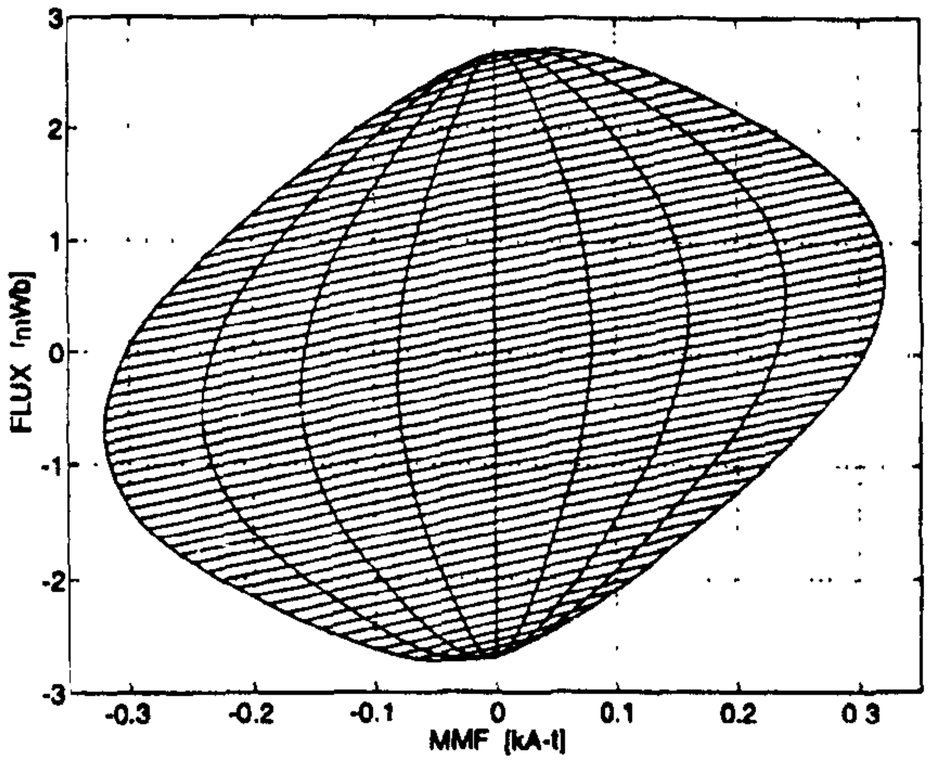

Fig. 14. Calculated flux-MMF diagram for the motor shown in Fig. 12 without skew at the RMS currents of 0–4 A.

Fig. 17 shows the effect of skew on the calculated electromagnetic torque ripple for any one phase. It shows that even with a regular spacing of magnetization curves shown in Fig. 14, there is some amount of torque ripple present due to deviation from the ideal elliptical shape of the flux-MMF trajectories. Fig. 18 compares the calculated total electromagnetic torque ripple in the two cases, with and without skew, which are derived from Fig. 17 by adding phase shifted torque contributions from each of the motor phases. A comparison between Figs. 6 and 18 brings out the difference in

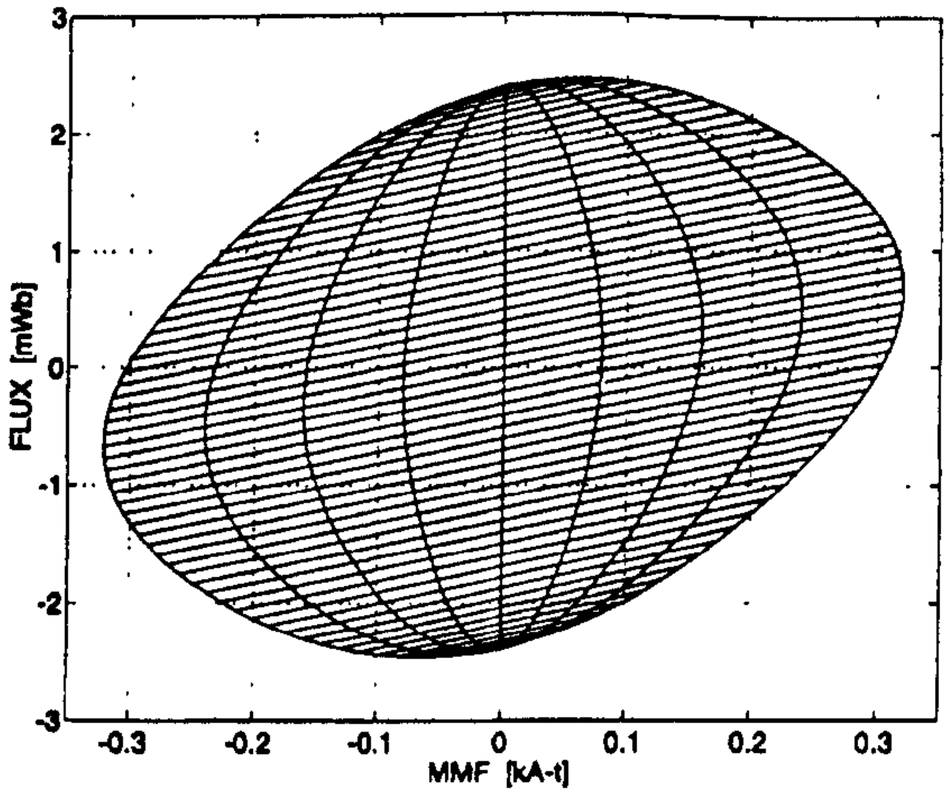

Fig. 15. Calculated flux-MMF diagram for the motor shown in Fig. 12 with a skew of one slot pitch at the rms currents of 0–4 A.

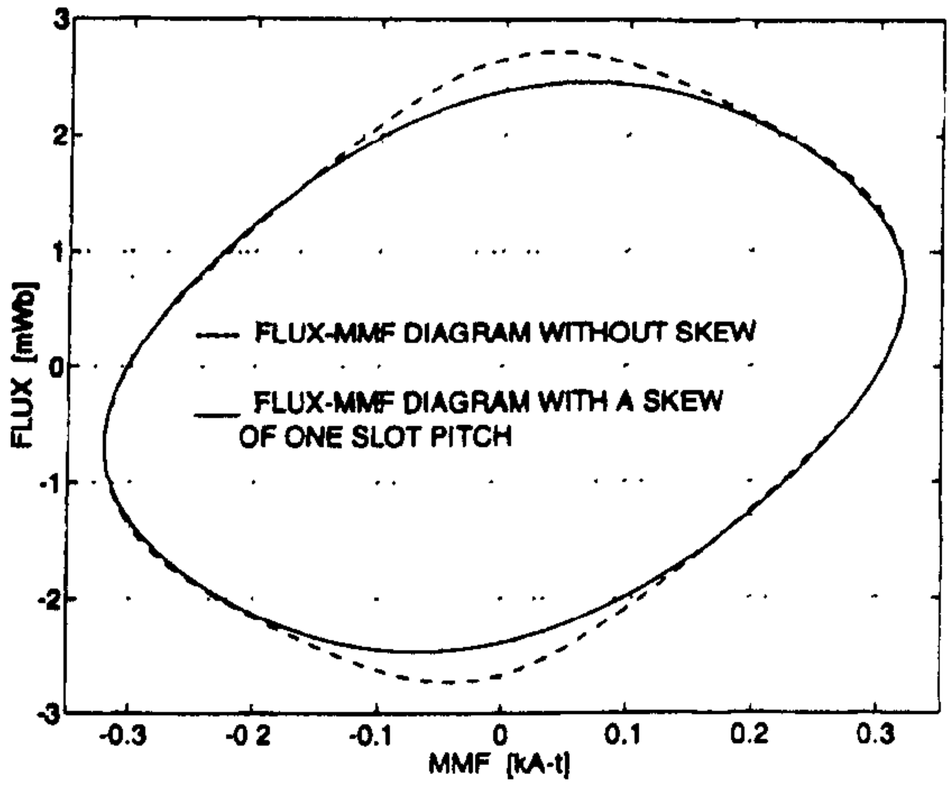

Fig. 16. Comparison of calculated flux-MMF trajectory for the motor shown in Fig. 12 without skew and with a skew of one slot pitch at the rms current of 4 A.

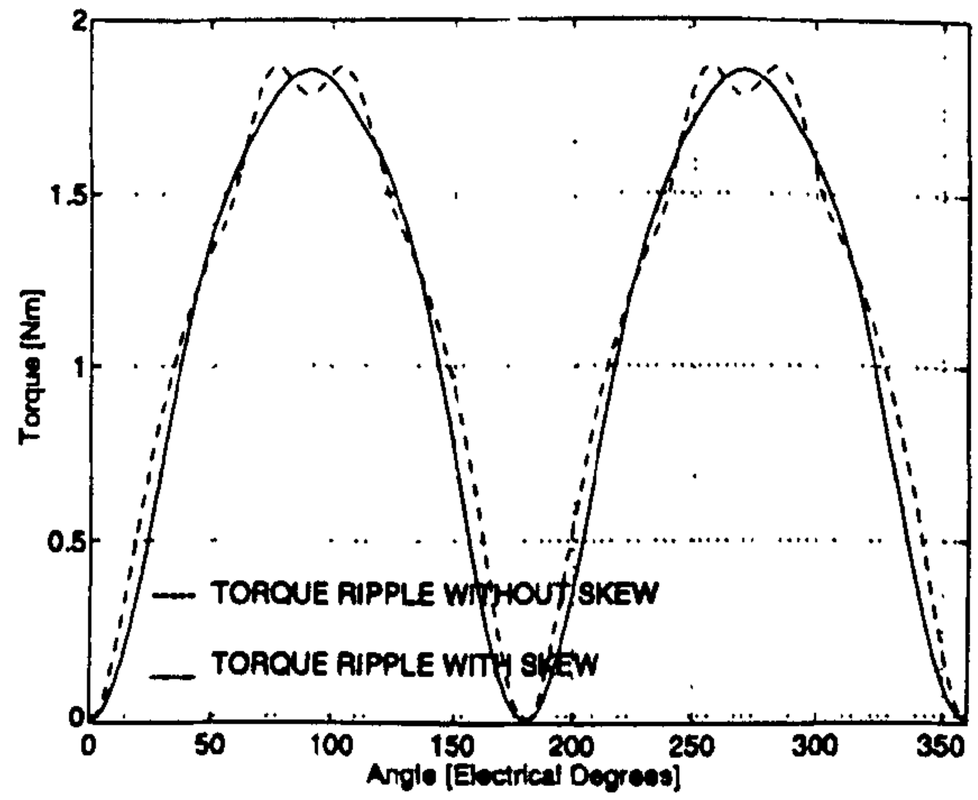

Fig. 17. Comparison of calculated electromagnetic torque ripple for any one phase of the motor shown in Fig. 12 without skew and with a skew of one slot pitch at the rms current of 4 A.

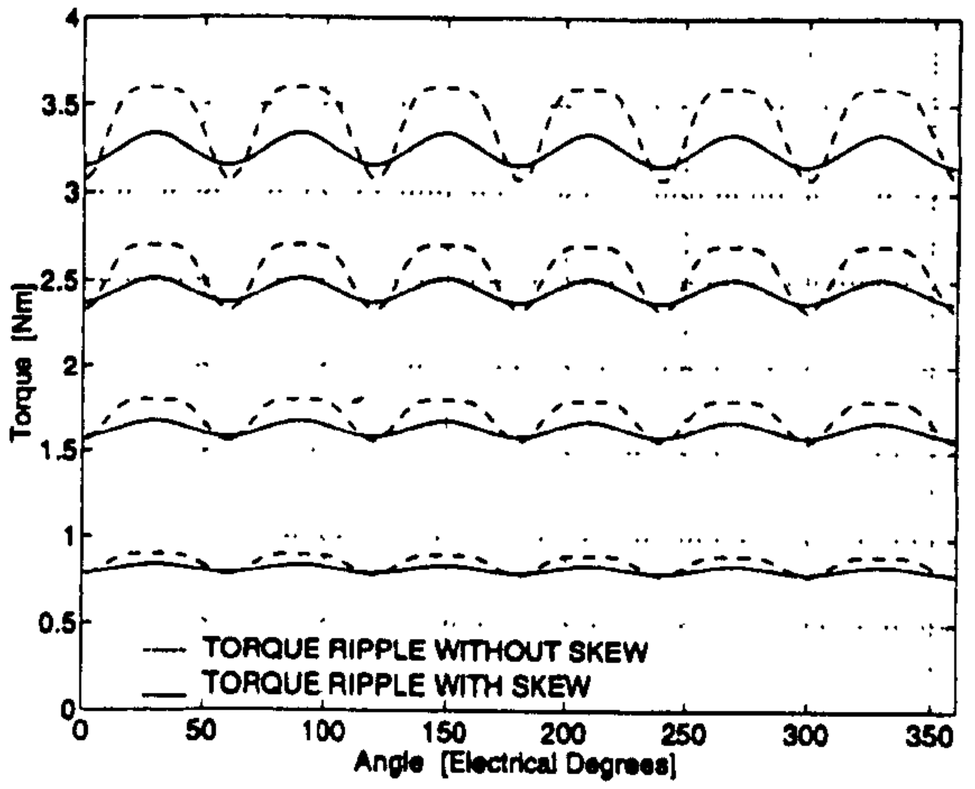

Fig. 18. Comparison of calculated total electromagnetic torque ripple for the motor shown in Fig. 12 without skew and with a skew of one slot pitch at the rms currents of 1–4 A.

electromagnetic torque ripple between a salient pole machine (Fig. 3) and a nonsalient pole machine (Fig. 12). Both Figs. 6 and 18 have six ripple cycles per electrical cycle, but in the case of Fig. 6 an additional high-frequency ripple of eighteen ripple cycles per electric cycle is superimposed owing to the salient pole nature of the machine.

B. Cogging Torque Ripple Calculation

Using the method described in Section IV, the flux-MMF diagram for a permanent magnet is plotted and the resulting cogging torque ripple is calculated for the machine shown in Fig. 12. Fig. 19 shows the flux and MMF variation in the permanent magnet over a cogging torque cycle. In comparison to Fig. 9, it can be seen that bifurcated teeth cause an additional ripple of double the frequency (12 cycles per electrical cycle) to be superimposed on the original slot ripple (six cycles per electrical cycle). At the same time, bifurcated teeth also cause a reduction in the net variation of flux and MMF in the permanent magnet which leads to a net reduction in cogging torque ripple [8]. Fig. 20 is the calculated flux-MMF diagram for a permanent magnet corresponding to one pole for the machine shown in Fig. 12. Figs. 7 and 20 make an interesting comparison. While Fig. 7 is for a ferrite magnet ($B_r = 0.39$ T), Fig. 20 is for a rare-earth magnet ($B_r = 0.85$ T). Since the length of magnet is different in the two cases (Figs. 8 and 12) for the same stator lamination geometry, the operating points for the rare-earth magnet motor are further down the demagnetization curve as compared to the ferrite magnet motor. Also, the bottom halves of Figs. 7 and 20 show that the rare-earth magnets operate at a higher level of flux and MMF as compared to the ferrite magnets, as expected. Fig. 21 shows the effect of skew on the flux-MMF diagram of Fig. 20 while Fig. 22 shows the effect of skew on the calculated cogging torque ripple.

C. Total Torque Ripple Calculation and Measurements

Fig. 23 shows the effect of skew on the calculated total torque ripple and Table I gives a quantitative analysis of the same. It shows that while the extent of minimization of torque

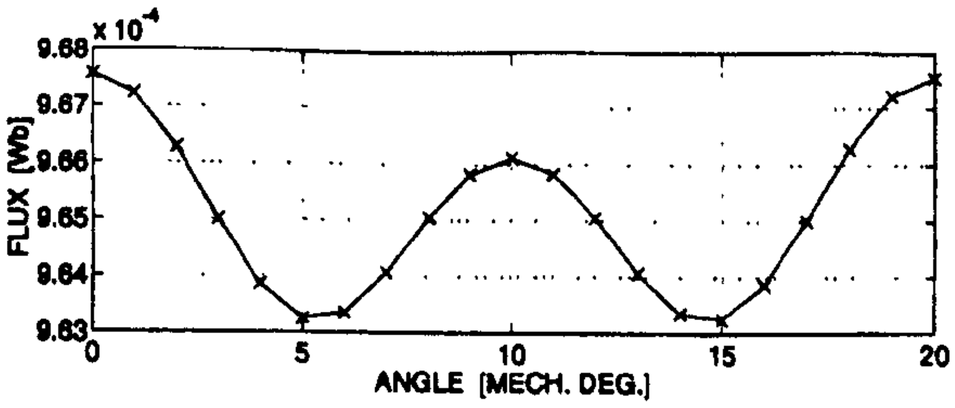

(a)

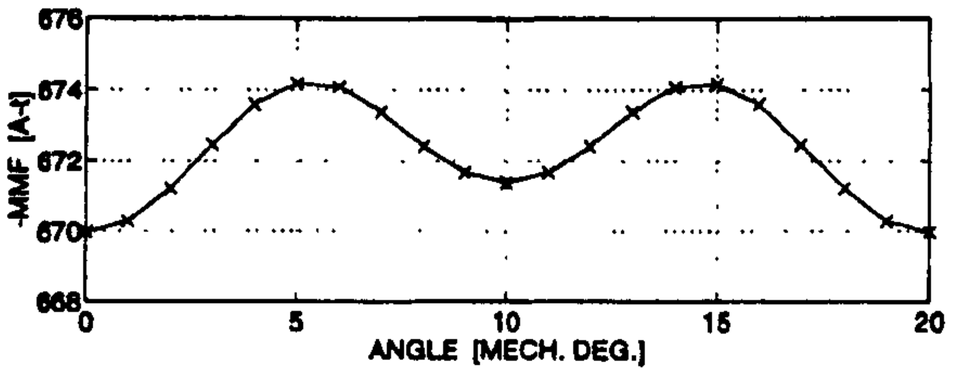

(b)

Fig. 19. Calculated flux and MMF variation in the permanent magnet over a cogging torque cycle, used to construct the flux-MMF diagram shown in Fig. 20.

(a)

(b)

Fig. 20. Calculated flux–MMF diagram for a permanent magnet corresponding to one pole of the motor shown in Fig. 12. (a) Very small areas enclosed by dotted load lines at successive rotor positions. (b) The same as (a) on an expanded scale.

ripple decreases with increasing load current, the percentage drop in average torque remains the same for all values of load current. Measurements were carried out on the motor shown in Fig. 12 with a skew of one slot pitch. The experimental setup was built using a precision dynamometer and developed in the SPEED Laboratory [16], where the machine-under-test was driven by a load machine and drive—capable of a four-quadrant operation—through a torque transducer in series.

Fig. 24 compares the predicted and the measured total torque ripple. PWM chopping of sinewave currents in the actual drive introduces an additional high frequency ripple in the measured torque waveforms superimposed on the low frequency ripple of interest. To avoid the unnecessary complexity of modeling

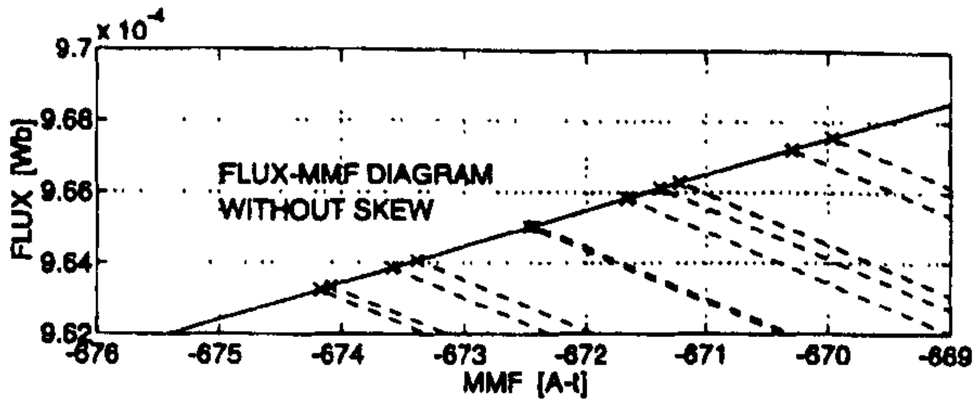

(a)

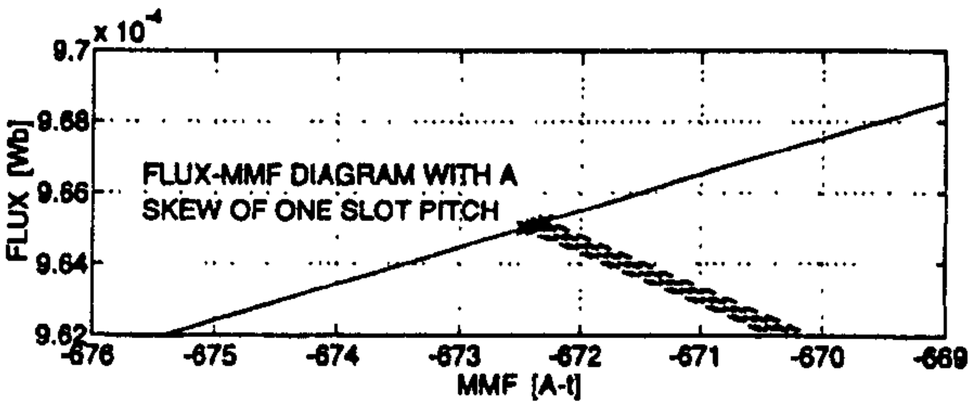

(b)

Fig. 21. Graphical representation of the effect of skew on the flux-MMF diagram of Fig. 20.

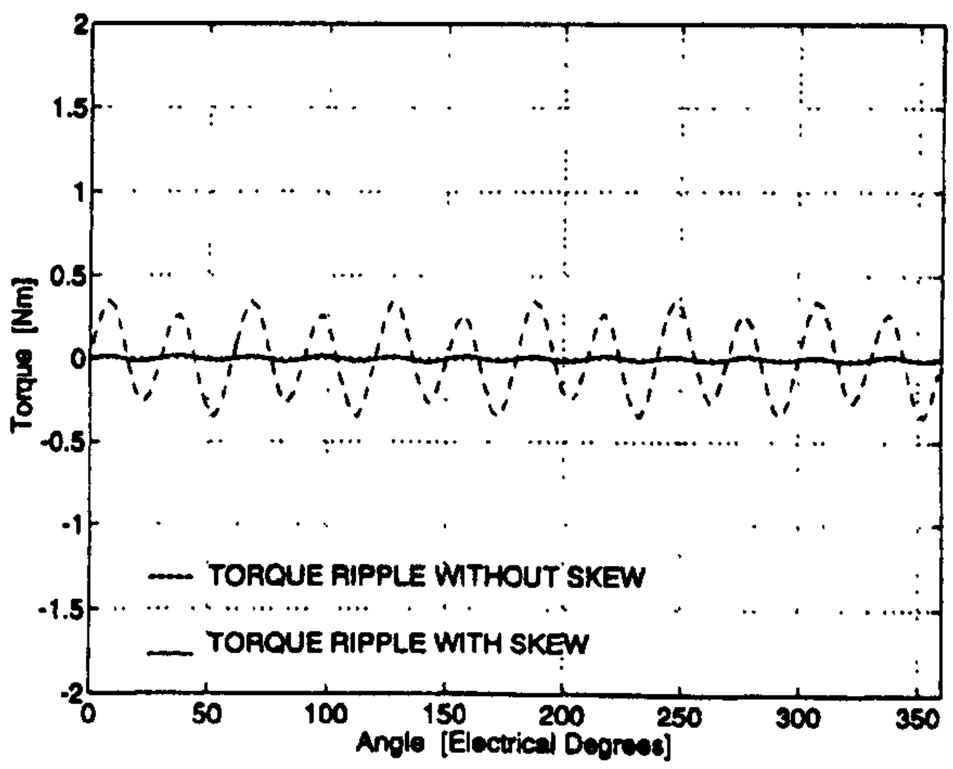

Fig. 22. Comparison of calculated cogging torque ripple for the motor shown in Fig. 12 without skew and with a skew of one slot pitch.

PWM chopped currents in the finite element analysis, ideal sinewave currents were assumed resulting in a relatively smooth calculated torque waveforms. Since the assumption of ideal sinewave currents is strictly valid at low speeds, the measurements were also performed at low speeds (200 r/m). Fig. 24 shows a good agreement between the calculated and the measured total torque ripple.

VI. Discussion

In this paper, it has been shown that the flux–MMF diagram technique is able to model the effect of skew on both the electromagnetic and the cogging torque ripple in permanent magnet machines. Although at present the technique is suitable only for the purpose of analysis; with enhanced finite element capabilities it can be a viable design tool. The technique offers a number of advantages which are summarized below.

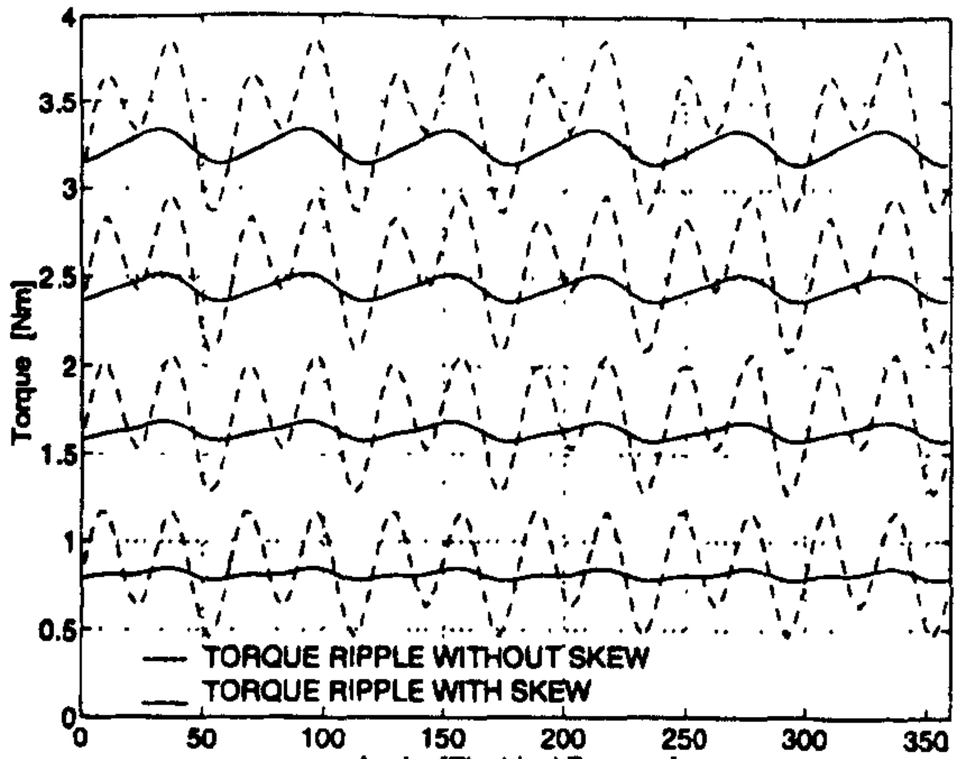

Fig. 23. Comparison of calculated total torque ripple for the motor shown in Fig. 12 without skew and with a skew of one slot pitch at the rms currents of 1–4 A.

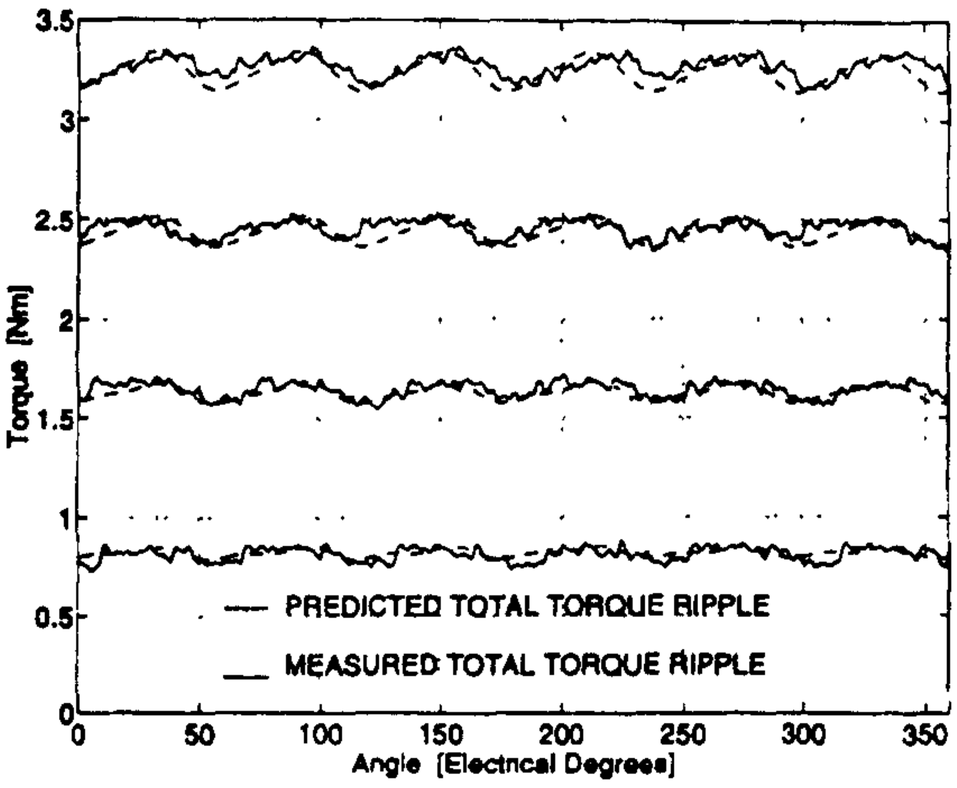

Fig. 24. Comparison of calculated and measured total torque ripple for the motor shown in Fig. 12 with a skew of one slot pitch at the rms currents of 1–4 A.

- It gives a physical insight and graphical interpretation of the torque producing mechanism in electric machines.
- Unlike some analytical methods, it can be used with any degree of magnetic saturation since the nonlinear magnetization curves used in constructing flux-MMF diagram readily take account of saturation. However, in the case of flux-MMF diagram for a permanent magnet, further work is being carried out to model nonlinear load lines.
- For any particular value of skew factor, it quantifies the difference in the extent of minimization between the electromagnetic torque ripple and the cogging torque ripple.
- It gives a graphical as well as quantitative indication of the reduction in average torque due to skewing which is the price paid for obtaining reduction in torque ripple (Fig. 16 and Table I, respectively).

This paper deals only with sinusoidally excited machines but the approach could be extended to deal with squarewave excited machines as well for which the flux-MMF diagram has already been used [7]. However, in the case of squarewave excited machines with skew, discontinuities in the MMF excitation at commutation points need to be modeled correctly, which is the subject of further investigation and research.

ACKNOWLEDGMENT

The authors thank SPEED Consortium and, in particular, SEM Ltd. for providing prototype for testing. The finite element analysis was performed using Vector Fields' OPERA-2d.

REFERENCES

[1] K. Binns, F. Chaaban, and A. Hameed, "Major design parameters of a solid canned permanent magnet motor with skewed magnets," *Proc. Inst. Elect. Eng.*, vol. 140, pt. B, no. 3, pp. 161–165, May 1993.

[2] K. H. Kim, D. J. Sim, and J. S. Won, "Analysis of skew effects on cogging torque and BEMF for BLDCM," in *Conf. Rec. IEEE Ind. Appl. Soc. Ann. Meeting*., Dearborn, MI, Oct. 1991, pp. 191–197.

[3] M. Alhamadi and N. Demerdash, "Modeling and experimental verification of the performance of a skewed mounted permanent magnet brushless DC motor drive with parameters computed from 3D-FE magnetic field solutions," *IEEE Trans. Energy Conv.*, vol. 9, no. 1, pp. 26–35, Mar. 1994.

[4] M. Alhamadi and N. Demerdash, "Modeling of effects of skewing of rotor mounted permanent magnets on the performance of brushless DC motors," *IEEE Trans. Energy Conv.*, vol. 6, no. 4, pp. 721–729, Dec. 1991.

[5] D. A. Staton, W. L. Soong, and T. J. E. Miller, "Unified theory of torque production in switched reluctance and synchronous reluctance motors," *IEEE Trans. Ind. Appl.*, vol. 31, no. 2, pp. 329–337, Mar./Apr. 1995.

[6] D. A. Staton, R. P. Deodhar, W. L. Soong, and T. J. E. Miller, "Torque prediction using the Flux-MMF diagram in AC, DC, and reluctance motors," *IEEE Trans. Ind. Appl.*, vol. 32, no. 1, pp. 180–188, Jan./Feb. 1996.

[7] R. P. Deodhar, D. A. Staton, and T. J. E. Miller, "Variation of torque constant in brushless PM motors," in *Proc. IEE Elec. Machines and Drives Conf.*, Durham, U.K., Sept. 1995, pp. 405–409.

[8] R. P. Deodhar, D. A. Staton, T M. Jahns, and T. J. E. Miller, "Prediction of cogging torque using the flux-MMF diagram technique," *IEEE Trans. on Ind. Appl.*, vol. 32, no. 3, May/June 1996, in press.

[9] Y. Liao, F. Liang, and T. A. Lipo, "A novel permanent magnet motor with doubly salient structure," *IEEE Trans. Ind. Appl.*, pp. 1069–1078, Vol. 31, no. 5, Sept./Oct. 1995.

[10] A. E. Fitzgerald and C. Kingsley Jr., *Electric Machinery*, 2nd Edition, McGraw Hill, 1961.

[11] J. R. Hendershot and T. J. E. Miller, *Design of Brushless Permanent Magnet Motors*. Oxford, U.K.: Clarendon, 1994.

[12] T. J. E. Miller, *Switched Reluctance Motors and Their Control*. Oxford, U.K.: Clarendon, 1993.

[13] T. J. E. Miller, *Brushless Permanent Magnet and Reluctance Motor Drives*. Oxford, U.K.: Clarendon, 1989.

[14] H. H. Woodson and J. R. Melcher, *Electromechanical Dynamics Part I: Discrete Systems*. New York: Wiley, 1968.

[15] D. C. White and H. H. Woodson, *Dynamics of Electromechanical Energy Conversion*. New York: Wiley, 1963.

[16] D. A. Staton and T. J. E. Miller, "Validation of PC-CAD using a precision dynamometer," in *Proc. Int. Conf. on Elec. Machines*, Manchester, U.K, Sept. 1992, vol. 3, pp. 1221–1225.

Rajesh P. Deodhar (S'88-M'90-S'94) was born in Bombay, India, on February 22, 1968. He received the Bachelor's degree in electronics engineering from the University of Bombay in 1989 and the Master's degree in electronic product design from the Center for Electronic Design and Technology (CEDT), Indian Institute of Science in 1991. Since 1994, he has been working toward his Ph.D. in the SPEED Laboratory, University of Glasgow, Scotland, in the generalized area of design and analysis of electric machines.

From 1991 to 1993, he worked as a Design Engineer with Crompton Greaves Ltd., Bombay, India, designing induction and brushless PM drives. In 1993, he received the Hitachi Industrial Scholarship and spent six months in Japan working on the applications of electric machines and drives in home appliances.

Mr. Deodhar was awarded gold medal by the Indian Institute of Science in 1991 and has received numerous other awards and scholarships. He is a member of the IEEE Industry Applications Society and an associate member of the Institution of Electrical Engineers, U.K.

David A Staton was born in Chesterfield, England, on July 29, 1961. He received the B.Sc. (Hons.) degree in electrical and electronic engineering from Trent Polytechnic, Nottingham, England, in 1983 and the Ph.D. degree from the University of Sheffield, England, in 1988.

From 1977 to 1984, he was employed by British Coal, who sponsored him while he was working toward the B.Sc. degree. While at the University of Sheffield, he developed CAD software for permanent-magnet dc motors in collaboration with GEC Electromotors Ltd. From 1988 to 1989, he was with Thorn EMI Central Research Laboratories and was engaged in the design of motors for the Kenwood range of food processors. From 1989 to 1995, he was employed as a research assistant in the SPEED Laboratory at the University of Glasgow. Presently, he is with Control Techniques plc, Newtown, Wales. His research interests are in the computer-aided design of permanent-magnet and reluctance motors.

Timothy J. E. Miller (M'74-SM'82-F'96) was born in Wigan, U.K. He received the B.Sc. degree from the University of Glasgow, Scotland, and the Ph.D. degree from the University of Leeds.

From 1979 to 1986 he was an Electrical Engineer and program manager at General Electric Corporate Research and Development, Schenectady, NY. His industrial experience also includes periods with GEC (UK), British Gas, International Research and Development, and a student–apprenticeship with Tube Investments Ltd. He is Lucas Professor in Power Electronics and founder and Director of the SPEED Consortium at the University of Glasgow, where he is responsible for teaching and research in power electronics and electrical power engineering. The SPEED Laboratory serves some 30 industrial companies in the U.K., the U.S., Europe, and the Far East with design software for electric motor design, electronic controls and development equipment for motor drive systems. He has authored or co-authored more than 100 publications in the field of motors, drives, power systems and power electronics, including five books.

Prof. Miller is a Fellow of the Royal Society of Edinburgh and of the Institution of Electrical Engineers, U.K.

International Conference on Electric Machines and Drives, IEE-EMD'95, Durham, UK, September 11–13, 1995

VARIATION OF TORQUE CONSTANT WITH ARMATURE CURRENT IN BRUSHLESS PM MOTORS

R P DEODHAR, D A STATON and T J E MILLER

SPEED Laboratory, University of Glasgow, UK

ABSTRACT

This paper examines the phenomenon of armature reaction and its effect on the torque per ampere characteristic or torque constant - k_T - in squarewave brushless DC and sinewave brushless AC permanent magnet motors.

Armature reaction is a well known phenomenon in commutator DC motors and it refers to the effect of magnetic field set up by the armature current on the net airgap flux density distribution. The effect is of two types : cross-magnetisation and de-magnetisation. Because of saturation, both effects cause the torque constant to vary with armature current. The armature reaction becomes more significant when the machine is saturated.

These effects are also present in brushless DC and AC motors. In this paper, they are analysed by presenting both the predicted as well as the experimental results. In order to take account of saturation, finite element analysis is used together with the flux-MMF diagram. The technique of the flux-MMF diagram makes accurate prediction of instantaneous as well as average torque in both linear (Fig. 1 and Fig. 2) and saturated (Fig. 3 and Fig. 4) electric machines.

It is shown that the new graphical method permits the analysis of armature reaction effects accurately and with clear physical interpretation. This problem is not easy to deal with using classical methods of magnetic circuit analysis. Although such methods have been developed for DC commutator motors, the brushless PM motor is not amenable to them because of the nature of the supply current waveforms, the small number of phases and the time-variation of the total magnetic flux distribution.

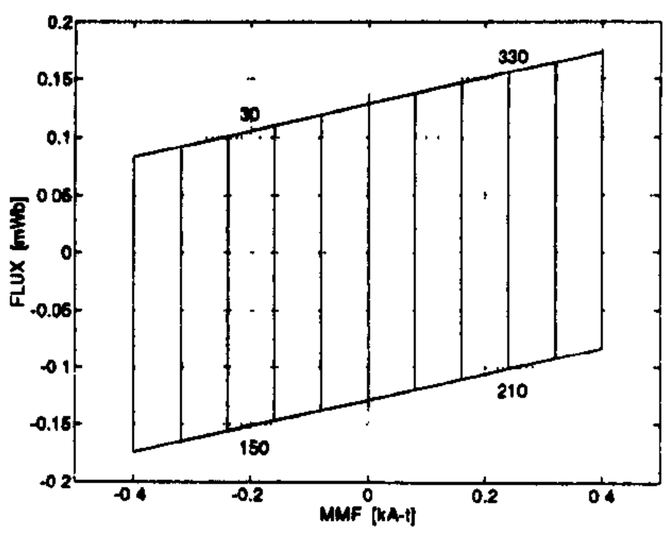

Figure 1 : *Flux-MMF diagram for the unsaturated squarewave brushless DC motor*

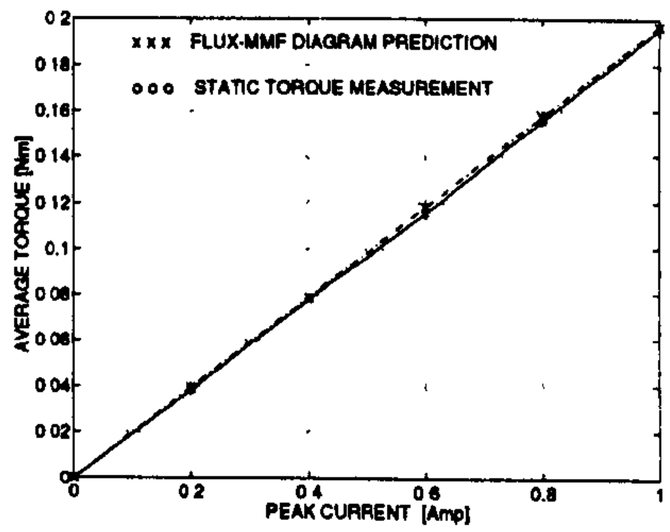

Figure 2 : *Torque per ampere characteristic for the unsaturated squarewave brushless DC motor*

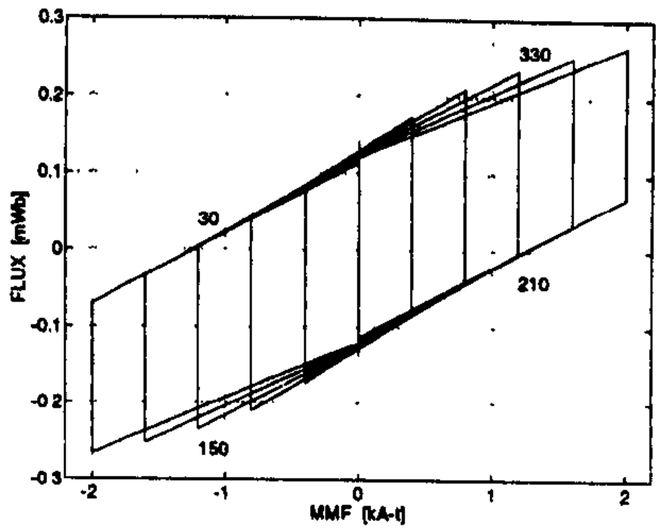

Figure 3 : *Flux-MMF diagram for the saturated squarewave brushless DC motor*

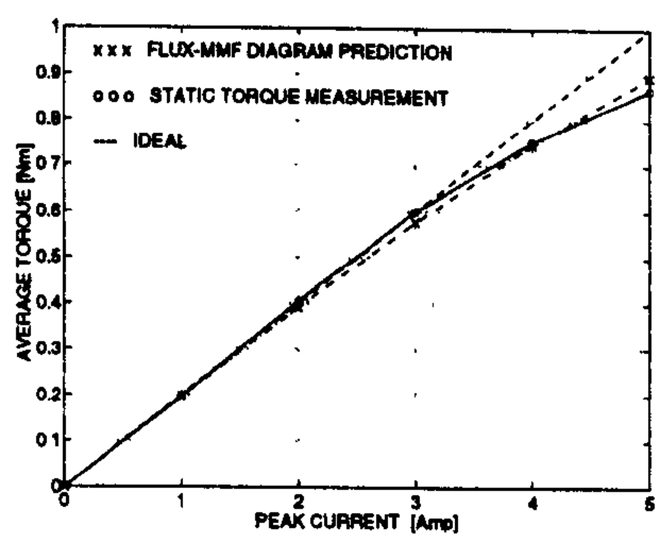

Figure 4 : *Torque per ampere characteristic for the saturated squarewave brushless DC motor*

VARIATION OF TORQUE CONSTANT WITH ARMATURE CURRENT IN BRUSHLESS PM MOTORS

R P DEODHAR, D A STATON and T J E MILLER

SPEED Laboratory, University of Glasgow, UK

ABSTRACT

This paper examines the phenomenon of armature reaction and its effect on the torque per ampere characteristic or torque constant - k_T - in brushless PM motors. In order to take account of saturation, finite element analysis is used together with the flux-MMF diagram. The technique of the flux-MMF diagram makes accurate prediction of instantaneous as well as average torque in both linear and saturated electric machines. The predicted results are presented along with the experimental data for a squarewave brushless DC and a sinewave brushless AC motor.

1. INTRODUCTION

Armature reaction is a well known phenomenon in commutator DC motors and it refers to the effect of magnetic field set up by the armature current on the net airgap flux density distribution. The effect is of two types : cross-magnetisation and de-magnetisation [1]. Usually, the brushes are positioned in such a way that the armature field is in quadrature with the field set up by the permanent magnets and in this case only a cross-magnetising effect is present. But if the brushes are shifted from this position, a de-magnetising effect is also present. Because of saturation, both effects cause the torque constant to vary with armature current. The armature reaction becomes more significant when the machine is saturated.

These effects are also present in brushless DC motors [2] (as well as PM synchronous motors which are termed sinewave brushless AC motors here). In this paper, they are analysed using the flux-MMF diagram technique [3, 4]. The methodology is straightforward. The flux-MMF diagram is constructed for any one phase of the machine using a series of finite element solutions at incremental rotor positions and different armature currents. The shape of the diagram is an ellipse for a sinewave machine and a parallelogram for a squarewave machine. The area enclosed by this diagram consists of a number of incremental areas bounded by the magnetisation curves at each rotor position. Each incremental area represents an incremental change in co-energy which when partially differentiated with respect to the rotor position, gives the instantaneous torque for one phase at a given rotor position. In a similar manner, average torque produced over one electrical cycle for one phase is calculated from the total area enclosed by the flux-MMF diagram. Thus, for any given armature current, average torque can be calculated and the torque per ampere can be obtained at different values of armature current. Note that all the flux-MMF diagrams illustrated in the following sections are for one phase only.

2. ARMATURE REACTION REVISITED

The fact that armature reaction becomes increasingly significant as the machine becomes more saturated can be demonstrated with the help of finite element method. Fig. 1 shows the flux plot for a brushless DC motor under the open-circuit or no-load condition.

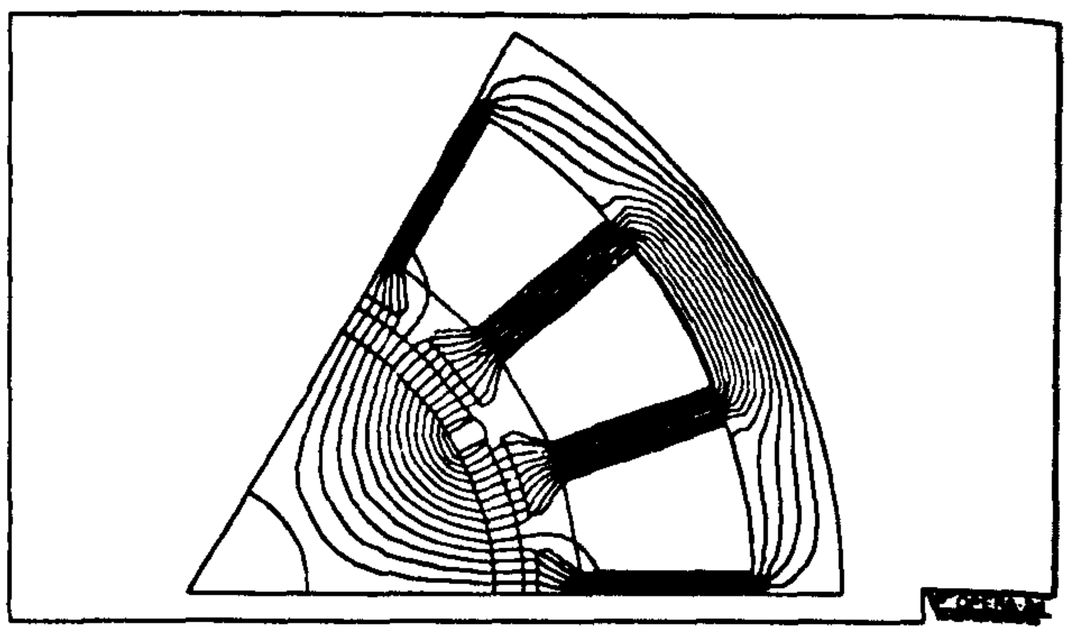

Figure 1 : *Flux plot for a brushless PM motor*

If an armature current is applied such that its field is in quadrature with that set up by the permanent magnets, the resulting effect on the net airgap flux density distribution can be seen in Fig. 2. It shows the airgap flux density distribution graphs for increasing values of armature current from no load to a maximum. Due to the cross-magnetising effect of armature reaction, flux density increases at one end of a pole and decreases at the other end. It is important to note that the increase is not to the same extent as the decrease in airgap flux density, owing to the non-linear effect of saturation. This results in a net reduction in total or average airgap

flux as compared to its open-circuit value, as the armature current increases.

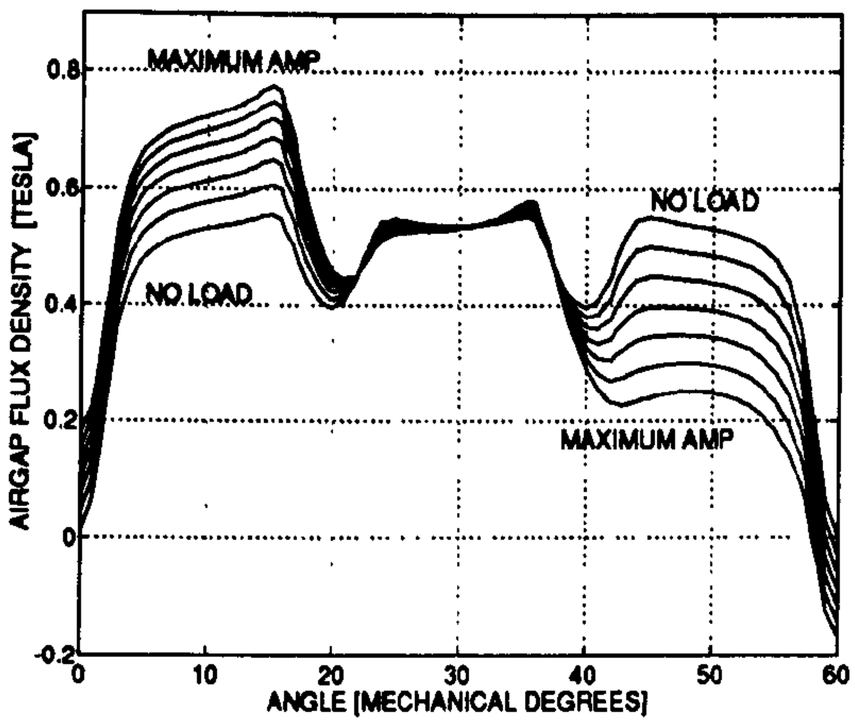

Figure 2 : *Airgap flux density distribution graphs showing variation in cross-magnetising armature reaction with saturation*

On the other hand, if an armature current is applied such that its field is in alignment with that set up by the permanent magnets, the result can be seen in Fig. 3.

Figure 3 : *Airgap flux density distribution graphs showing variation in de-magnetising armature reaction with saturation*

This is the de-magnetising effect of armature reaction and it also reduces the net airgap flux as the armature current increases. Both these effects, the cross-magnetisation and the de-magnetisation, combined with saturation, cause variation of torque constant in brushless DC motors.

It is also interesting to note that for sinewave brushless AC motors, the armature reaction is predominantly cross-magnetising in nature owing to the quadrature relationship maintained between the permanent magnet field and the armature field. Whereas for squarewave brushless DC motors, the armature reaction is always a combination of cross-magnetisation and de-magnetisation with both components varying in proportion between two commutation instants. This in turn means that it is easier to predict the variation in k_T for sinewave motors, where it remains stable throughout an electrical cycle, than for squarewave motors, where it changes dynamically within an electrical cycle.

3. VARIATION OF k_T IN A SQUAREWAVE BRUSHLESS DC MOTOR

Fig. 4 shows the cross section of a typical 3-phase, ferrite magnet squarewave brushless DC motor.

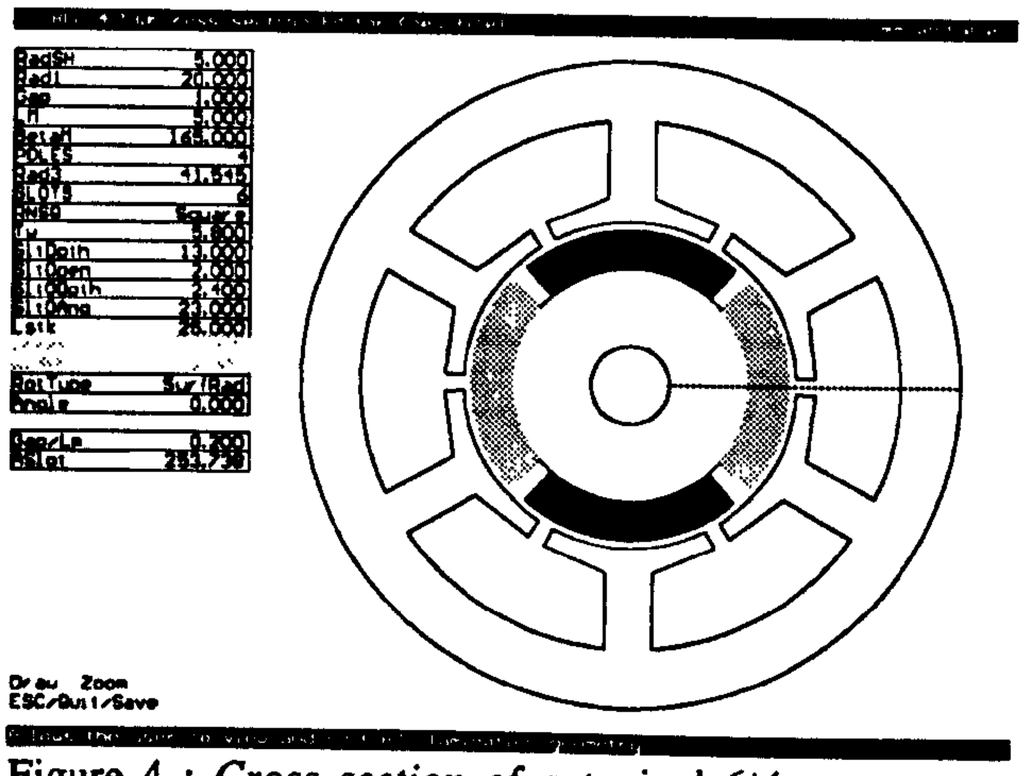

Figure 4 : *Cross section of a typical 6/4 squarewave brushless DC motor*

The flux-MMF diagram for the unsaturated machine is shown in Fig. 5. The shape of every flux-MMF loop is a straight sided parallelogram since the current excitation, as indicated in Fig. 6, is squarewave in shape.

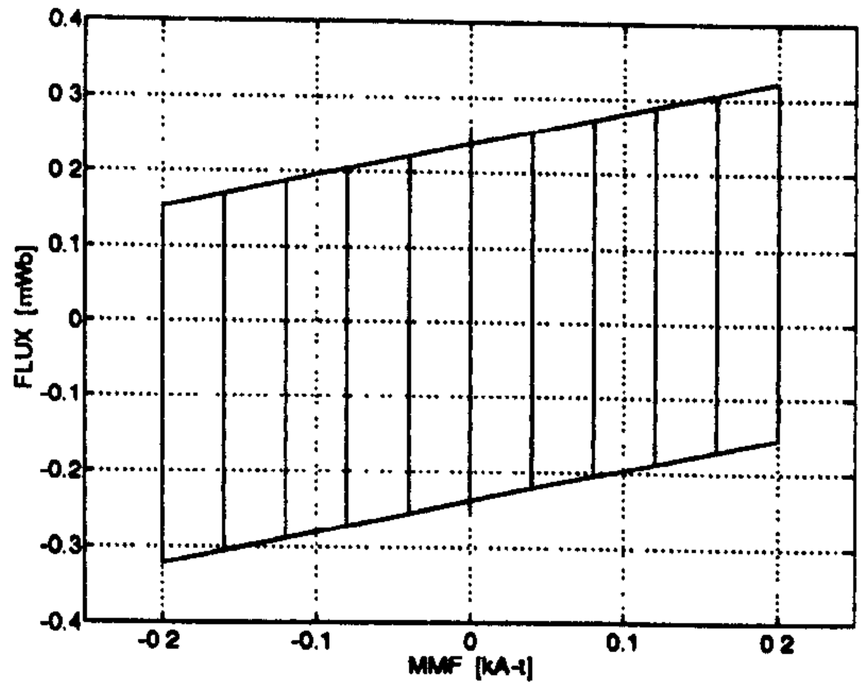

Figure 5 : *Flux-MMF diagram for the unsaturated machine (at peak currents of 0, 0.2, 0.4, 0.6, 0.8 and 1.0 Amps)*

Fig. 6 and Fig. 7 show the MMF and flux variation respectively, against rotor position at different values of current.

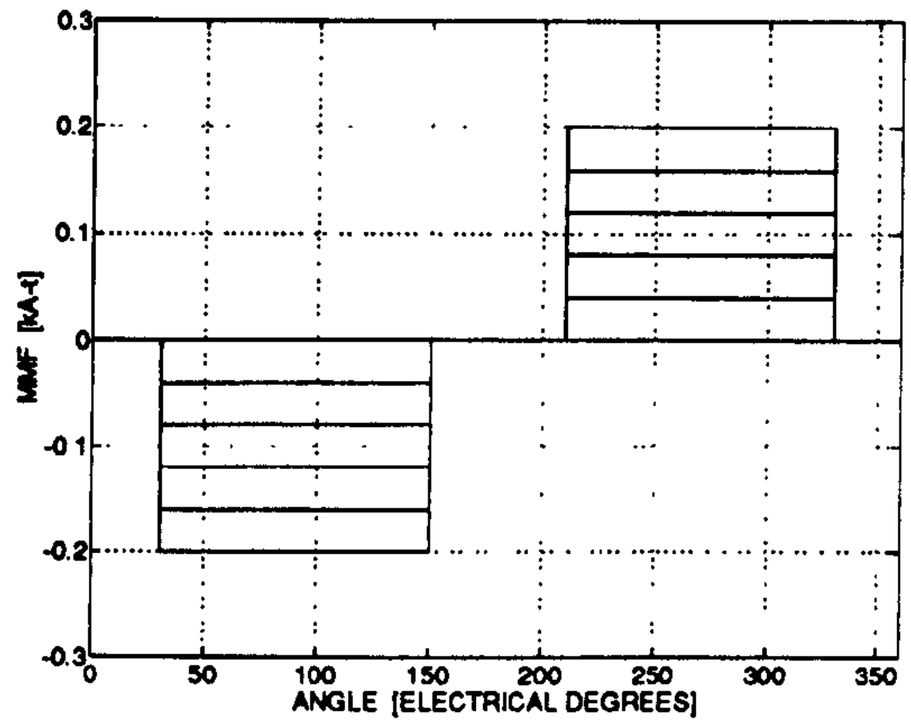

Figure 6 : *MMF variation with rotor position as in Fig. 5 (at peak currents of 0, 0.2, 0.4, 0.6, 0.8 and 1.0 Amps)*

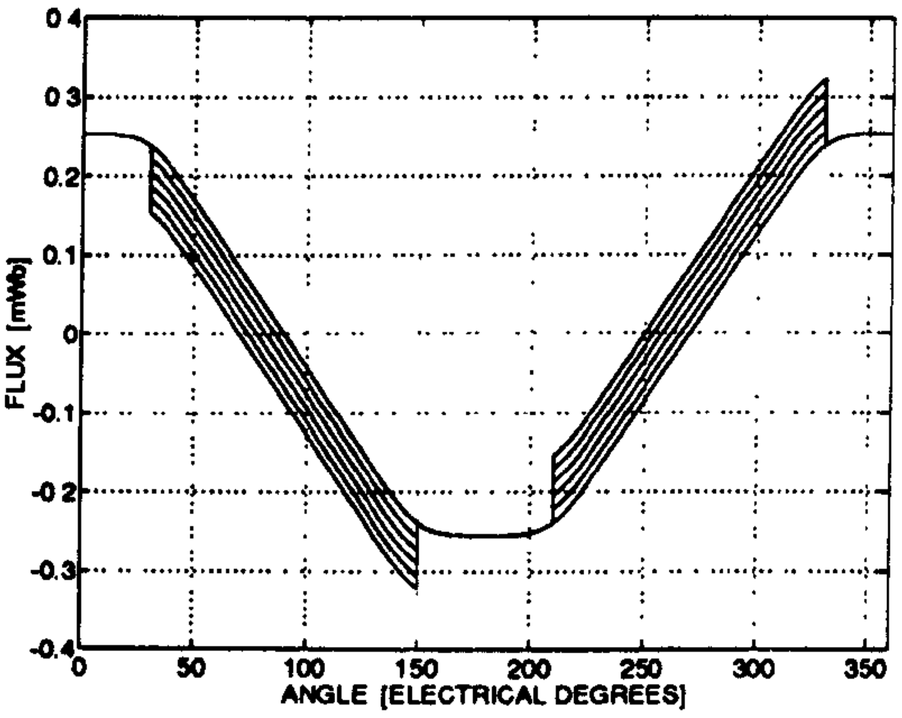

Figure 7 : *Flux variation with rotor position as in Fig. 5 (at peak currents of 0, 0.2, 0.4, 0.6, 0.8 and 1.0 Amps)*

The torque per ampere characteristic predicted using the flux-MMF diagram is compared against static torque measurements in Fig. 8.

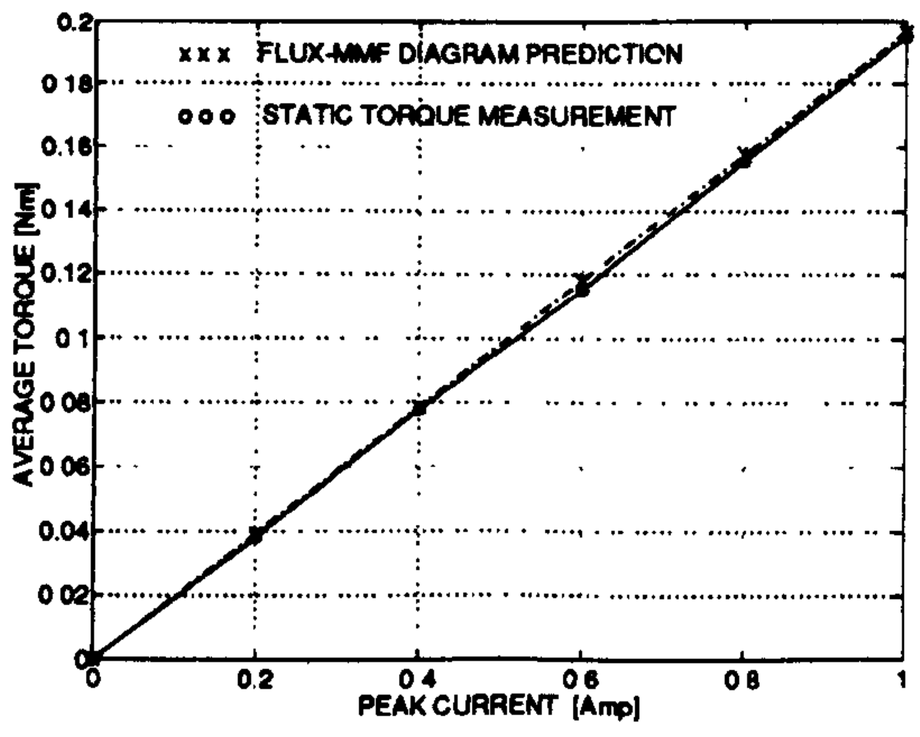

Figure 8 : *Torque per ampere characteristic for the unsaturated machine*

As expected, the characteristic is linear which means that there is no variation in torque constant for an unsaturated machine.

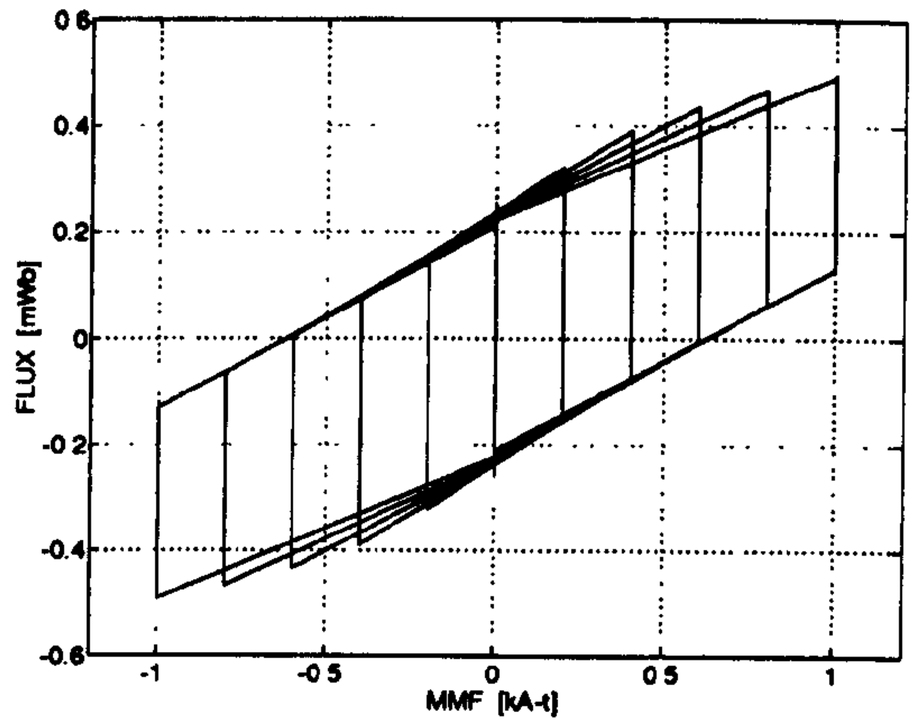

Figure 9 : *Flux-MMF diagram for the saturated machine (at peak currents of 0, 1, 2, 3, 4 and 5 Amps)*

Fig. 9 is the flux-MMF diagram for the saturated machine. Graphical representation by way of the change in the shape of flux-MMF diagrams clearly brings out the effect of saturation.

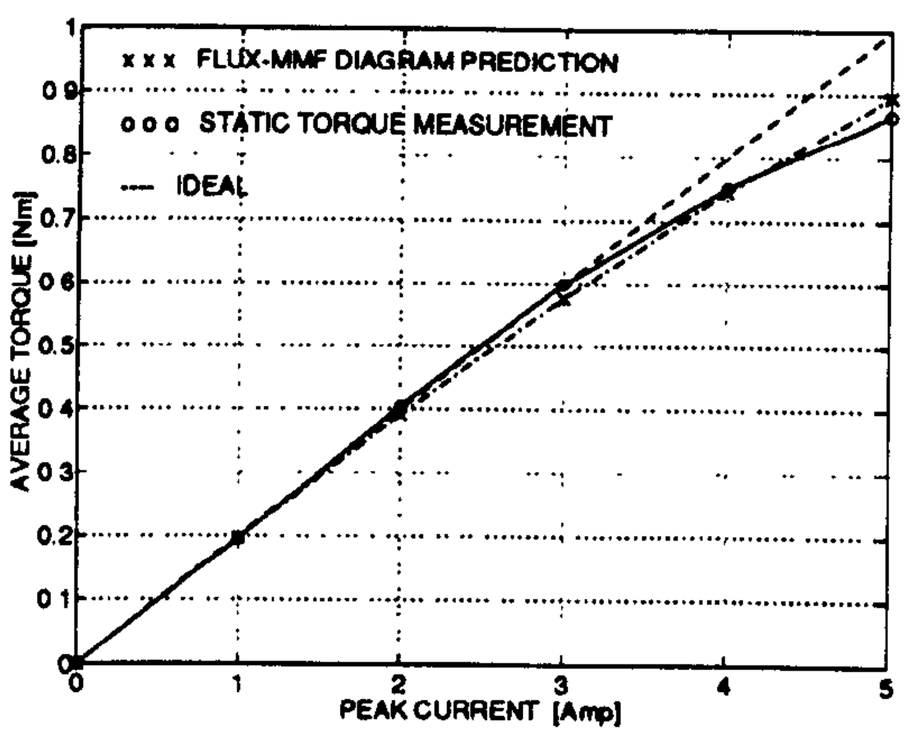

Figure 10 : *Torque per ampere characteristic for the saturated machine*

Fig. 10 compares the predicted torque per ampere characteristic with static torque measurements. The characteristic is non-linear, which indicates that the value of torque constant varies with armature current when the machine is saturated.

4. VARIATION OF k_T IN A SINEWAVE BRUSHLESS AC MOTOR

Figure 11 shows the cross section of a typical 3-phase, rare-earth magnet sinewave brushless AC motor.

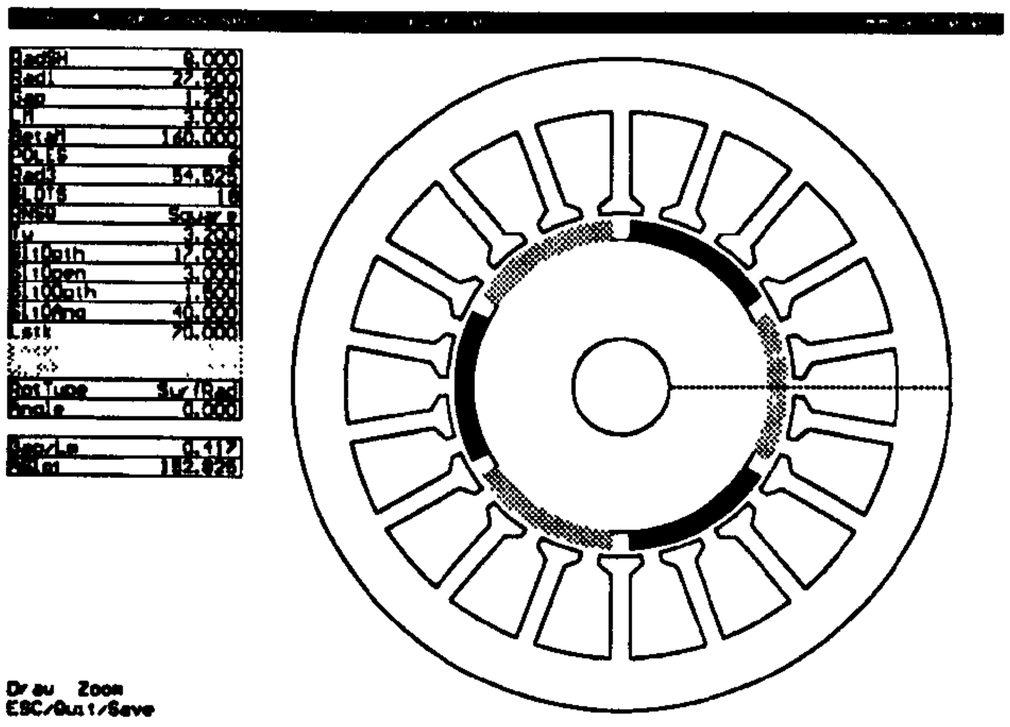

Figure 11 : *Cross section of a typical sinewave brushless AC motor*

Just as in the case of the squarewave brushless DC motor, analysis is presented for the unsaturated as well as the saturated machine. Fig. 12 is the flux-MMF diagram for the unsaturated machine.

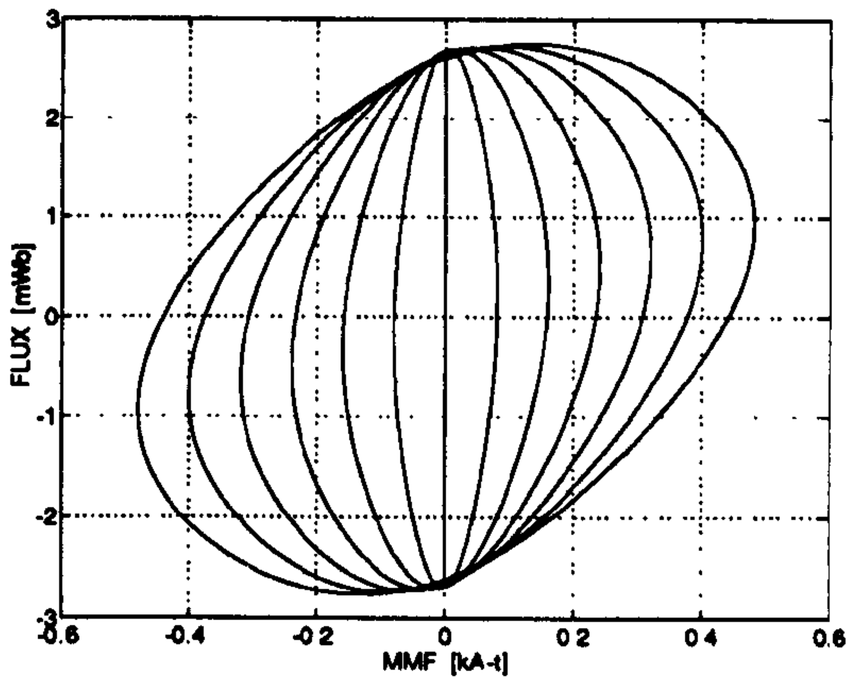

Figure 12 : *Flux-MMF diagram for the unsaturated machine (at RMS currents of 0, 1, 2, 3, 4, 5 and 6 Amps)*

The shape of every flux-MMF diagram is elliptical since the current excitation is, as indicated in Fig. 13, sinusoidal.

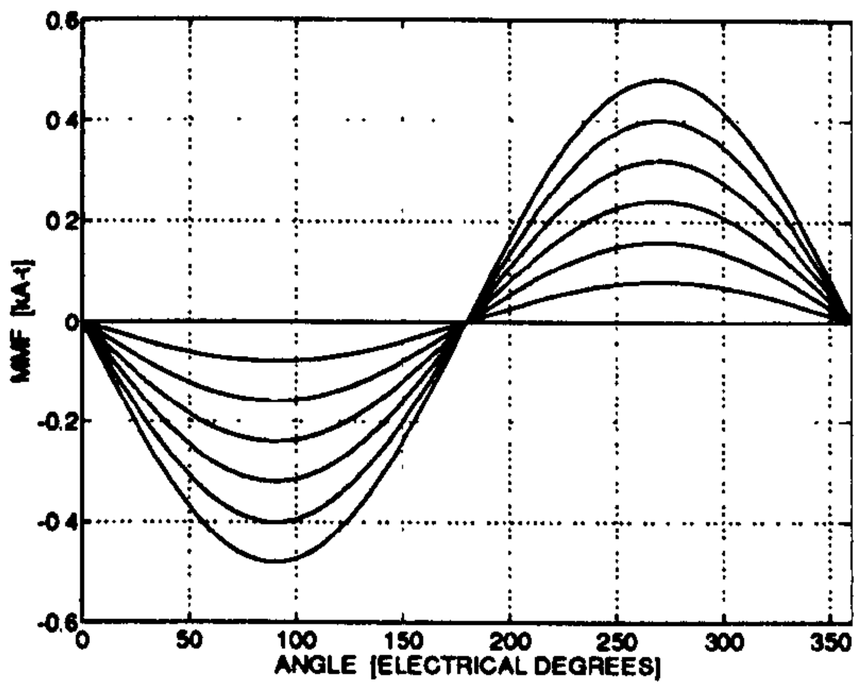

Figure 13 : *MMF variation with rotor position as in Fig. 12 (at RMS currents of 0, 1, 2, 3, 4, 5 and 6 Amps)*

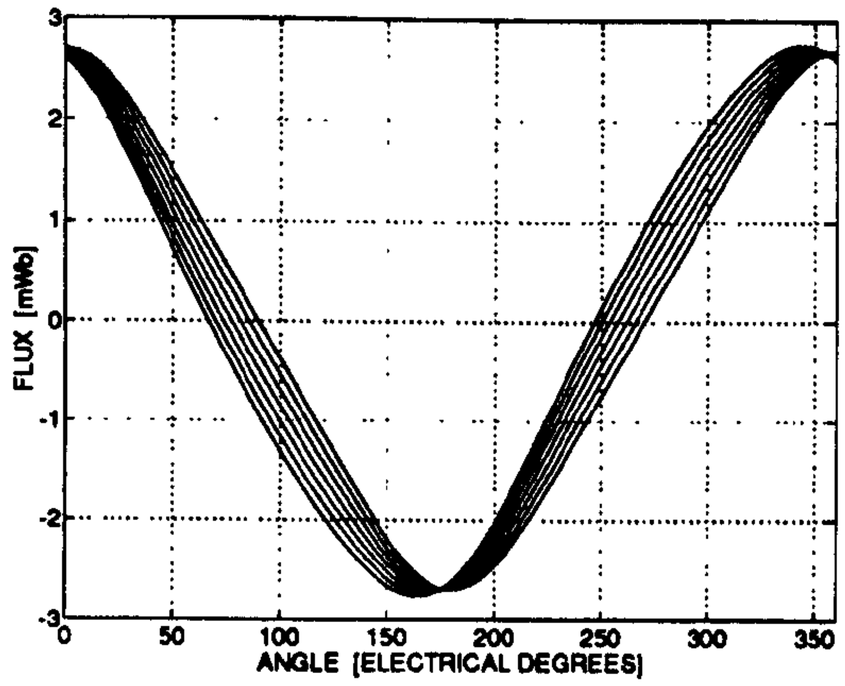

Figure 14 : *Flux variation with rotor position as in Fig. 12 (at RMS currents of 0, 1, 2, 3, 4, 5 and 6 Amps)*

Fig. 13 and Fig. 14 show MMF and flux variation respectively against rotor position at different values of current.

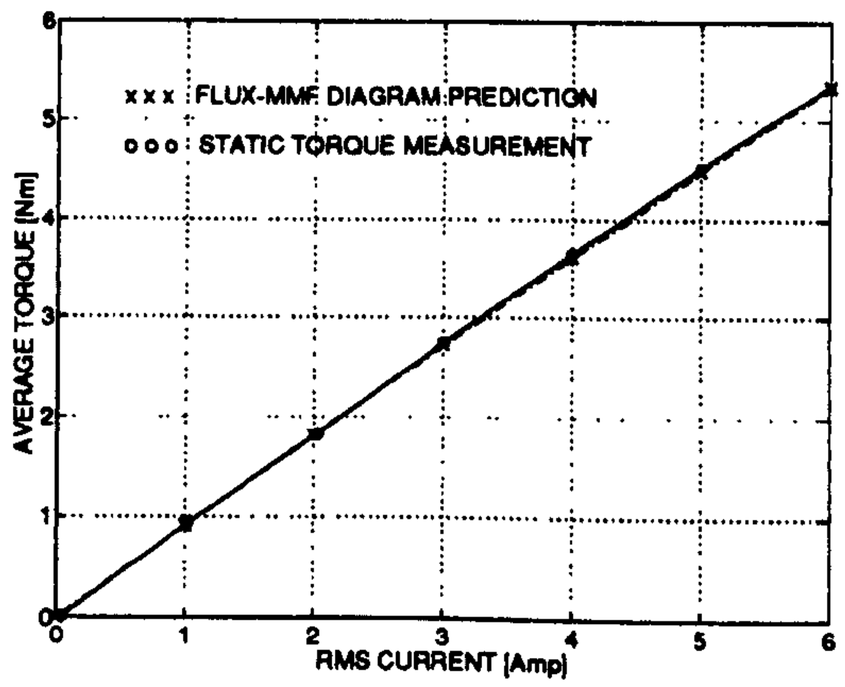

Figure 15 : *Torque per ampere characteristic for the unsaturated machine*

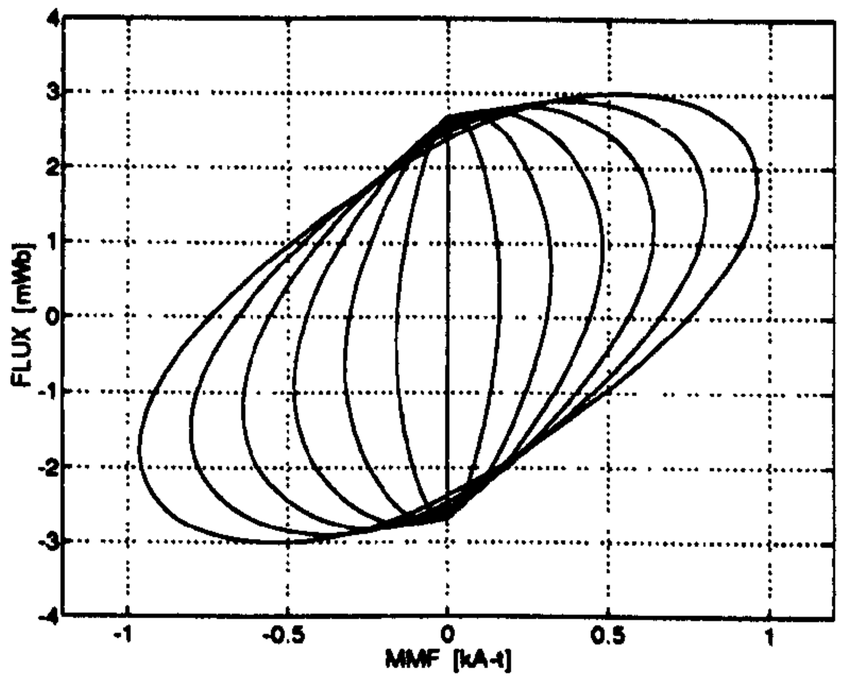

Figure 16 : *Flux-MMF diagram for the saturated machine (at RMS currents of 0, 2, 4, 6, 8, 10 and 12 Amps)*

Fig. 15 compares the predicted torque per ampere characteristic with the static torque measurements. The

characteristic is linear, indicating no change in torque constant in the case of the unsaturated machine. Fig. 16 is the flux-MMF diagram for the saturated case. The extent of deviation from the elliptical shape indicates the extent of saturation. Fig. 17 compares the predicted torque per ampere characteristic with static torque measurements.

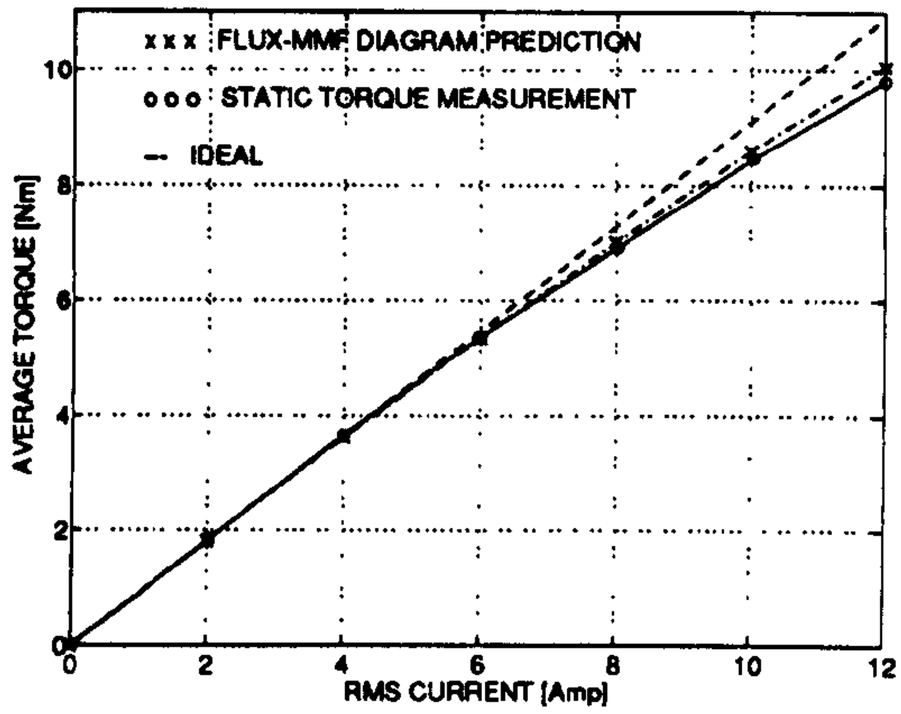

Figure 17 : *Torque per ampere characteristic for the saturated machine*

5. DISCUSSION

The flux-MMF diagram can be used effectively to model saturation effects in brushless PM motors. One such important effect - the variation of torque constant with armature current - has been analysed and presented here.

It is shown that the new graphical method permits the analysis of armature reaction effects accurately and with clear physical interpretation. This problem is not easy to deal with using classical methods of magnetic circuit analysis. Although such methods have been developed for DC commutator motors [5], the brushless PM motor is not amenable to them because of the nature of the supply current waveforms, the small number of phases and the time-variation of the total magnetic flux distribution.

ACKNOWLEDGEMENTS

Financial support by the University of Glasgow and the CVCP (Committee of Vice-Chancellors and Principals), UK, is hereby acknowledged. The support of the SPEED Consortium, by way of providing research facilities, is also acknowledged. Thanks to Jimmy Kelly and Peter Miller for help with the experimental set-ups.

REFERENCES

[1] Fitzgerald AE and Kingsley C. Jr., 1961, "Electric Machinery", McGraw Hill, New York, USA, 2nd Edition, 384-387

[2] Hendershot JR and Miller TJE, 1994, "Design of Brushless Permanent Magnet Motors", Oxford Science Publications/Magna Physics Publishing, Oxford, England, 1st Edition, ISBN 0-19-859389-9, 12.20-12.28

[3] Staton DA, Soong WL and Miller TJE, 1993, "Unified Theory of Torque Production in Switched and Synchronous Reluctance Motors", Proceedings of the fifth IEE International Conference on Electrical Machines and Drives, Oxford, England, 67-72

[4] Staton DA, Soong WL, Deodhar RP and Miller TJE, 1994, "Unified Theory of Torque Production in AC, DC and Reluctance Motors", Conference Proceedings of the 1994 IEEE-IAS Annual Meeting, Denver, Colorado, USA, 149-156

[5] Liwschitz-Garik M and Whipple CC, 1956, "Direct Current Machines", Princeton, New Jersey USA, 2nd Edition, 67-77

International Conference on Electrical Rotating Machines, ELROMA-96, Bombay, India, January 19–20, 1996
(Recipient of the ELROMA-96 Conference Committee Second Prize Paper Award)

FLUX-MMF DIAGRAM : A TECHNIQUE FOR ANALYSIS AND COMPARATIVE EVALUATION OF ELECTRIC MACHINES

R. P. Deodhar, D. A. Staton and T. J. E. Miller

SPEED Laboratory, University of Glasgow, Scotland, UK

1.0 INTRODUCTION

Electric machines could be classified in many ways depending on various factors such as nature of electric supply (AC or DC), mode of operation (synchronous or asynchronous), geometry (salient pole or non-salient pole), nature of rotation (smooth or stepped) and mode of excitation (single or double excitation). Different machines belong to different classes and there is a clear distinction between the methods of design and analysis for each of these. With the rapid advances of technology in the fields of power electronics, microcontrollers and permanent magnet materials, performance of the relatively new machine types such as switched reluctance and brushless DC is improving dramatically. At the same time, performance of the traditional or established machine types such as induction and synchronous is also being enhanced. Claims of superior performance for a particular motor type are constantly being made based on certain parameters such as torque per ampere, power to weight ratio and efficiency. Such comparisons, although adequate for certain purposes, are not comprehensive in nature since they are not made at the design stage and they do not take account of radical differences which exist between operation of different machine types.

In these circumstances, clearly, there is a need for a generalised method of analysis and comparative evaluation which would encompass all types of electric machines and enable real performance comparisons to be made at the design stage itself. So called 'generalised theory of electric machines' which has long been established and which is based on the dq-axis transformation, works on certain basic assumptions regarding the geometry and the nature of excitation for an electric machine. This theory does not and cannot deal with machines having double saliency and/or non-sinusoidal mode of excitation.

This paper describes the technique of flux-MMF diagram–based on the principle of virtual work–for analysis and comparative evaluation of a wide variety of electric machines. Although the principle of virtual work is established for a long time and its utilization through finite element method analyzed to some extent, there remains immense scope and challenge to explore it further in alternate directions. While the theory and certain applications of the flux-MMF diagram technique have been documented through some recent publications [1–6], the main objective of this paper is to bring out the comprehensive analysis and comparative evaluation capabilities of the technique by addressing such crucial issues as prediction of electromagnetic and cogging torque ripple, the effect of skew on torque ripple and the effect of saturation on the torque per ampere characteristic. The technique offers many distinct advantages including a unique capability of comparison between different types of electrical machines–such as squarewave brushless DC and synchronous PM–through graphical representation and an ability to take account of the effects of saturation due to the use of the modern computer aided design tool of finite element analysis. Moreover, since the flux-MMF diagram technique is based on the principle of energy conversion which is universal to all motor types, it is not constrained by any assumptions regarding the geometry or the nature of excitation.

2.0 WHAT EXACTLY IS A FLUX-MMF DIAGRAM?

The flux-MMF diagram is a generalised version of the flux-linkage vs. current (ψ-i) diagram used commonly for analysis and design of switched reluctance motors [1-2, 5]. Fig. 1 is a typical flux-MMF diagram over one electrical cycle for any one phase of a sinusoidally excited brushless PM machine. It not only shows many of its important features, but also shows the equivalence between the ψ-i and the flux-MMF diagram. It plots the variation of instantaneous effective flux linking a particular phase against the instantaneous MMF in that phase. Both the quantities are functions of rotor position and the flux-MMF

diagram is a closed trajectory over one electrical cycle.

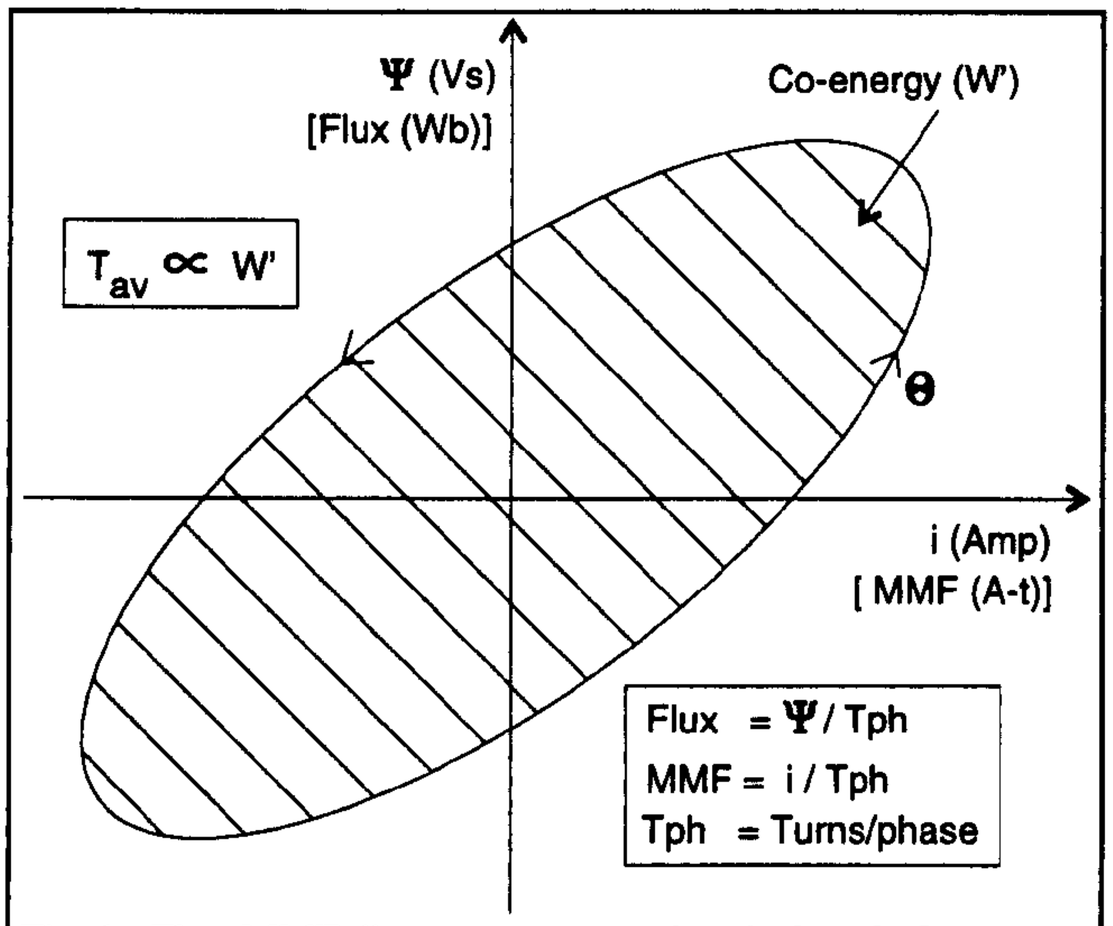

Fig. 1: Flux-MMF diagram over one electrical cycle for any one phase of a sinusoidally excited brushless PM machine

The shape of this trajectory is an ellipse for a sinusoidally excited machine and a parallelogram for a squarewave excited machine. The *average* as well as the *instantaneous* electromagnetic torque at any given current can be obtained from such a diagram using the principle of virtual work, as given in Eqn. (1) [7-12].

$$T_e = \left. \frac{\partial W'(i,\theta)}{\partial \theta} \right|_{i = constant} \qquad (1)$$

Where;

T_e = Electromagnetic torque
W' = Co-energy
i = Instantaneous current
θ = Rotor position

The total area enclosed by a flux-MMF diagram is fixed by its particular shape, and this area indicates the *average* torque produced over one electrical cycle for any one phase. The total area consists of a number of incremental areas bound by the magnetization curves at successive rotor positions and each of these areas indicates the *instantaneous* torque at a particular rotor position for any one phase. This makes it possible to calculate torque ripple at any given current. The next few sections deal with various applications of the flux-MMF diagram technique and clearly bring out its capabilities with respect to analysis and comparative evaluation of electric machines.

3.0 PREDICTION OF ELECTROMAGNETIC TORQUE RIPPLE

Fig. 2 shows the cross-section of a 3-phase rare-earth magnet sinewave brushless AC motor.

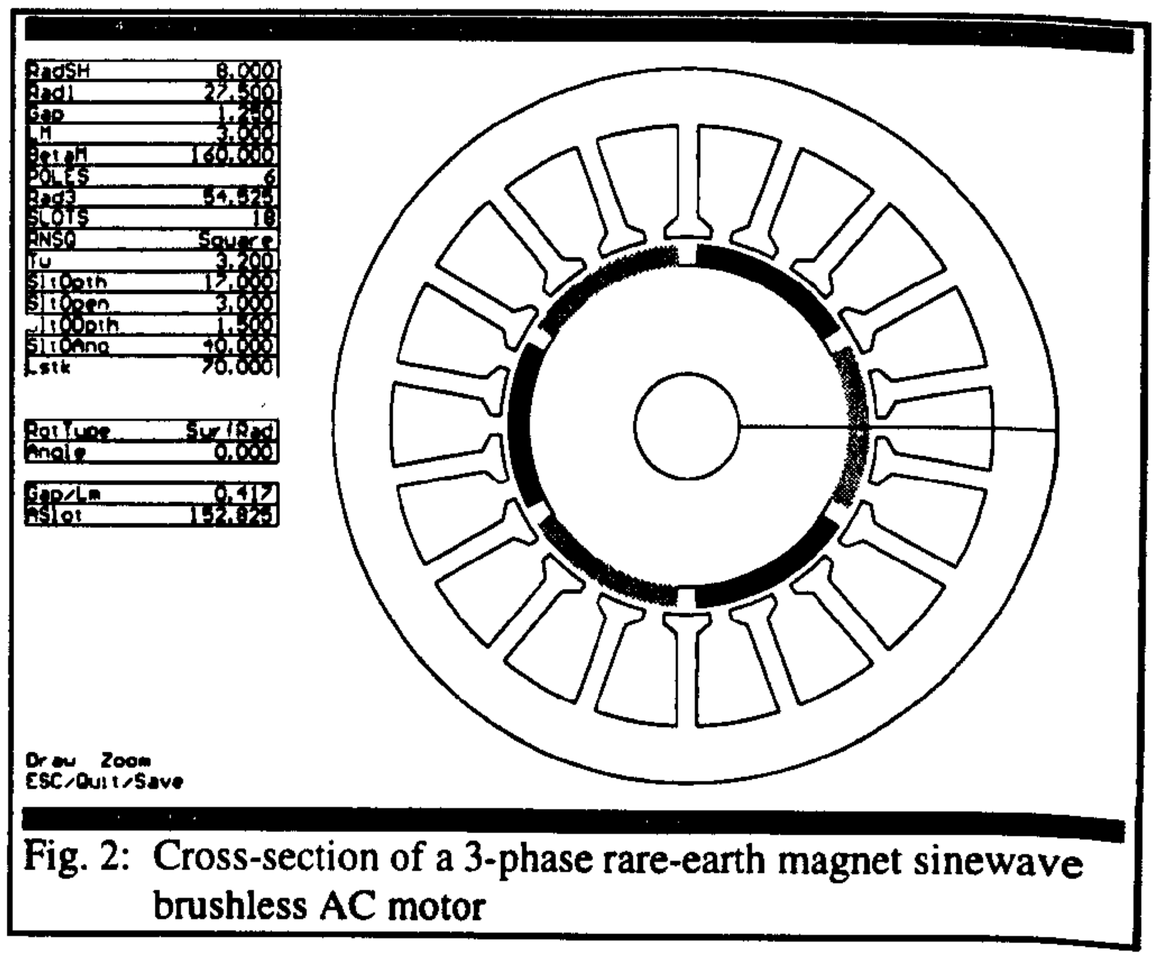

Fig. 2: Cross-section of a 3-phase rare-earth magnet sinewave brushless AC motor

Fig. 3 is the flux-MMF diagram for this motor for any one phase, obtained through a series of finite element analyses performed at incremental rotor positions and at five different phase current values.

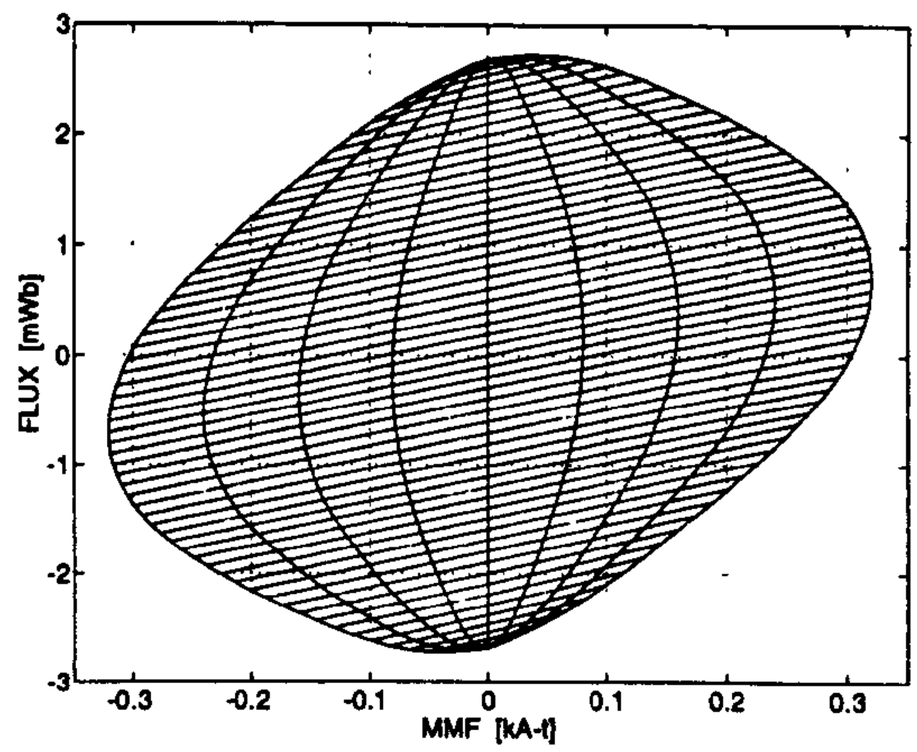

Fig. 3: Flux-MMF diagram for the motor of Fig. 2 at the RMS currents of 0, 1, 2, 3 and 4 A

Fig. 4 shows the electromagnetic torque ripple predicted using the flux-MMF diagram of Fig. 3. In actual practice, it is not possible to validate such purely electromagnetic torque ripple curves by experimental measurements, as the cogging torque ripple inherent in the PM motors, is always superimposed on it. Later on in section 5.0, validation is provided for the total torque ripple of the same motor but with a skew of one slot pitch on the stator.

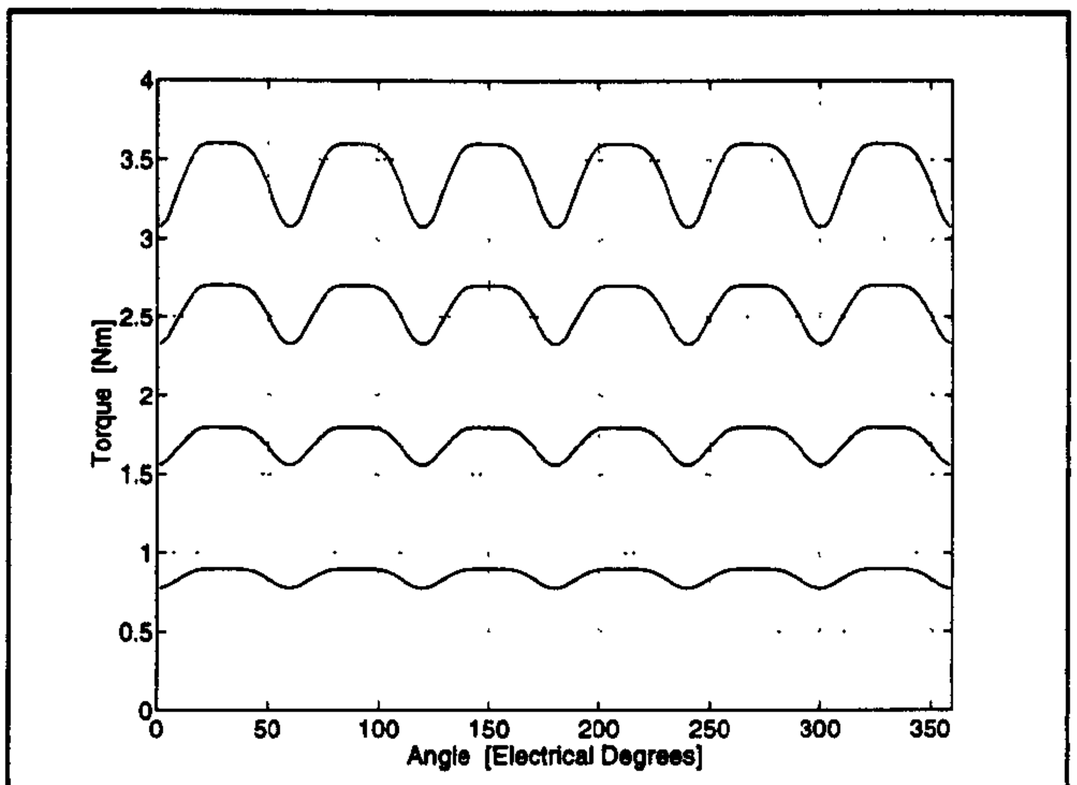

Fig. 4: Electromagnetic torque ripple for the motor of Fig. 2 at RMS currents of 0, 1, 2, 3 and 4 A

4.0 PREDICTION OF COGGING TORQUE RIPPLE

As seen from Figs. 3 and 4, with the conventional way of plotting the flux-MMF diagram for any one phase, it is not possible to predict cogging torque in a permanent magnet motor, as the phenomenon of cogging depends only on the interaction of permanent magnets with stator slotting, and it is independent of the nature of any current excitation and distribution of conductors in any one phase. In order to circumvent this problem, it is proposed that rather than plotting the flux-MMF diagram for any one *phase*, the flux-MMF diagram could be plotted for a *permanent magnet* corresponding to any one pole so that the cogging torque can be predicted by applying the principle of virtual work. Fig. 5 is a sketch illustrating the important features of the flux-MMF diagram for a permanent magnet.

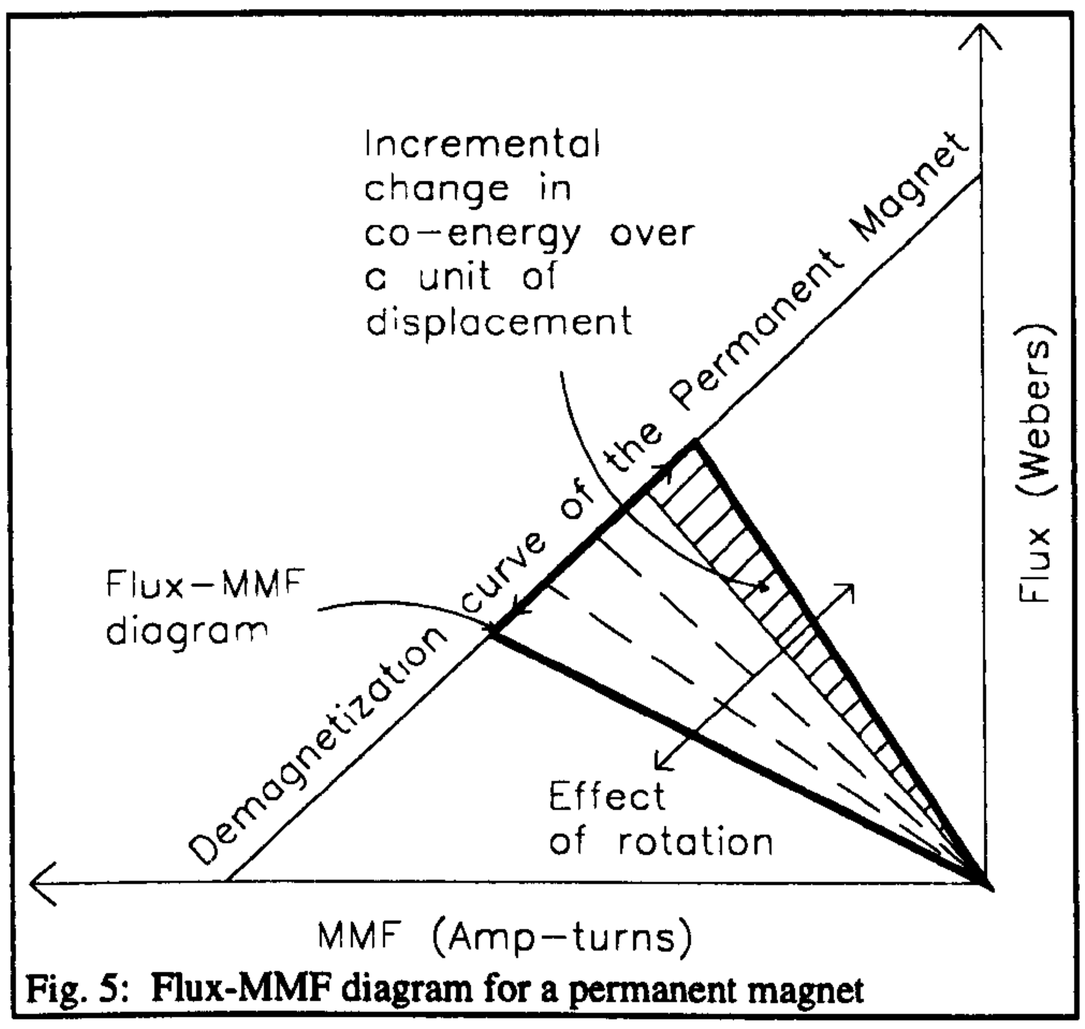

Fig. 5: Flux-MMF diagram for a permanent magnet

Cogging torque ripple can be obtained from such a diagram using the principle of virtual work (Eqn. 1), where *'i'* can be replaced with *'MMF'* of the permanent magnet [6].

Fig. 6 shows the cross-section of a 3-phase ferrite magnet squarewave brushless DC motor.

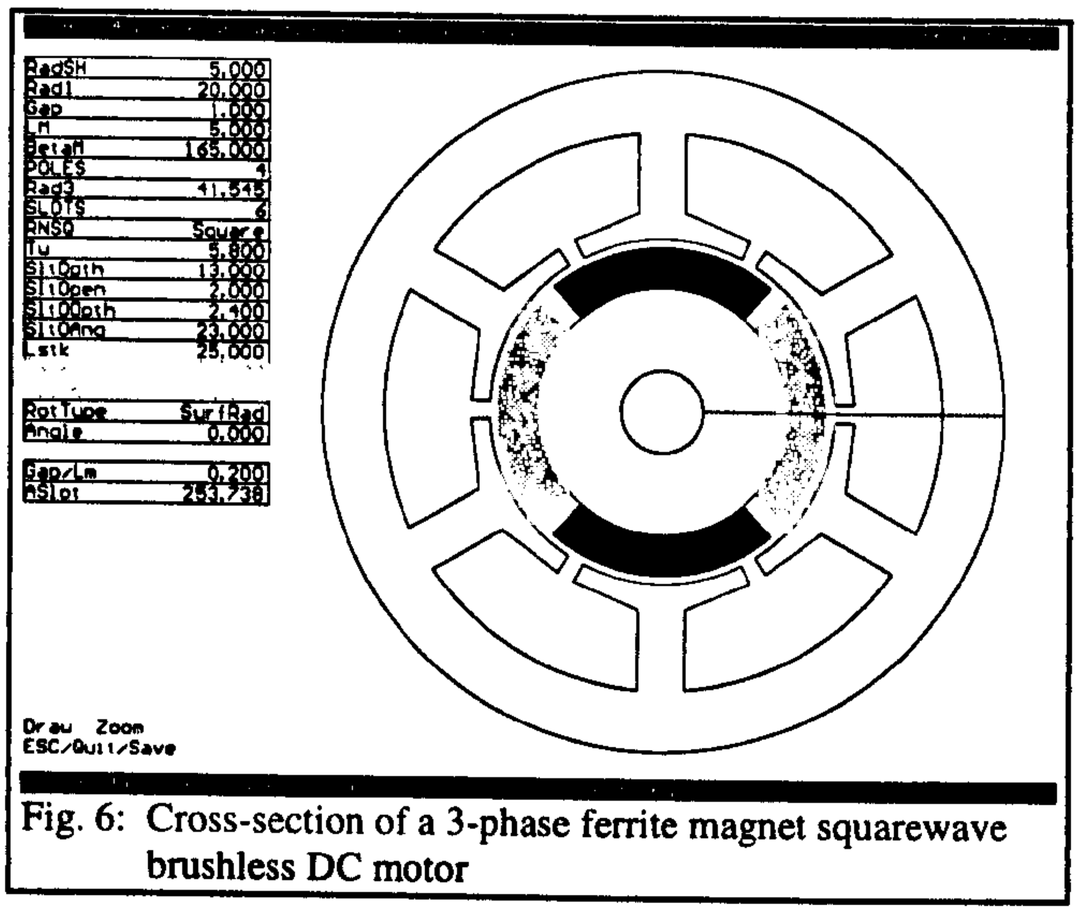

Fig. 6: Cross-section of a 3-phase ferrite magnet squarewave brushless DC motor

Fig. 7 compares the predicted and the measured cogging torque ripple for this motor and it shows a good agreement between the two. Since the motor has fractional number of slots per pole, the cogging is slightly different for the two pairs of poles as seen in Fig. 7.

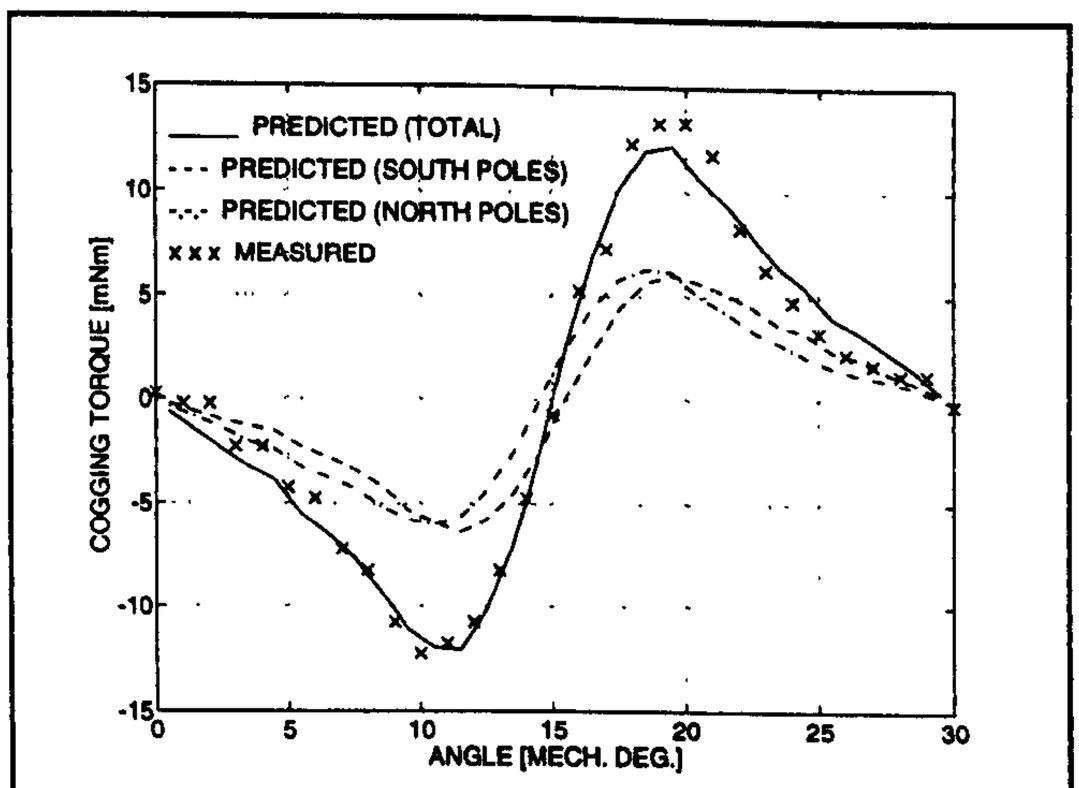

Fig. 7: Comparison between the predicted and the measured cogging torque ripple for the motor of Fig. 6

5.0 EFFECT OF SKEW ON TORQUE RIPPLE

The effect of skew on torque ripple in an electric machine can be analyzed in a simple and comprehensive manner using the flux-MMF diagram. The flux-MMF diagram for a skewed motor can be

obtained easily from the one for an unskewed motor by averaging the instantaneous flux values at a particular current over a number of rotor positions corresponding to the skew pitch [4]. Torque ripple curves obtained from such a 'skewed' flux-MMF diagram then reflect the attenuation in torque ripple achieved due to skewing. Fig. 8 makes a direct comparison between the flux-MMF diagrams for the unskewed and the skewed motor of Fig. 2 at a phase current of 4 A.

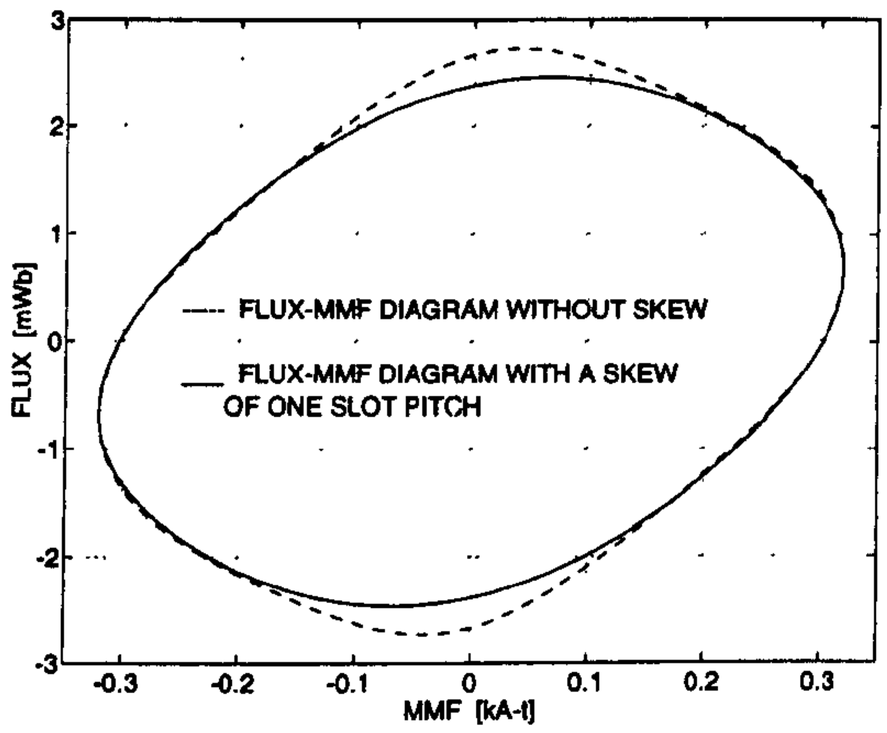

Fig. 8: Flux-MMF diagrams for the unskewed and the skewed motor of Fig. 2 at the RMS current of 4 A

It shows that on one hand skewing reduces torque ripple, as indicated by the shape of the diagram being closer to the ideal elliptical shape for the skewed motor. On the other hand, there is a price to be paid for this gain in terms of a slight reduction in average torque, again as indicated by the smaller area enclosed by the diagram for the skewed motor. Fig. 9 illustrates this point clearly by comparing the total torque ripple in both the cases.

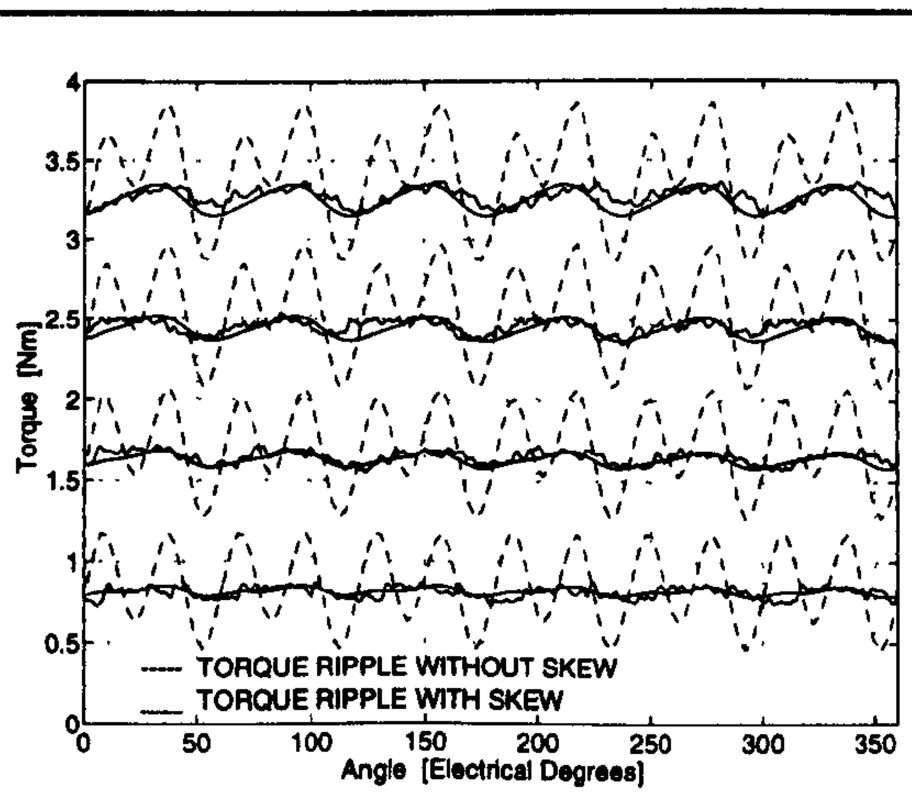

Fig. 9: Total torque ripple curves for the unskewed and the skewed motor of Fig. 2 at the RMS currents of 1, 2, 3 and 4 A, validation in the case of skewed motor is provided by the experimentally measured torque ripple

6.0 EFFECT OF SATURATION ON THE TORQUE PER AMPERE CHARACTERISTIC.

Fig. 10 is the flux-MMF diagram for the unsaturated squarewave brushless DC motor of Fig. 6. The shape of every flux-MMF loop is a straight sided parallelogram due to squarewave current excitation. The torque per ampere characteristic predicted using Fig. 10 is compared against static torque measurements in Fig. 11. As expected the characteristic is linear indicating no variation in torque constant for the unsaturated machine.

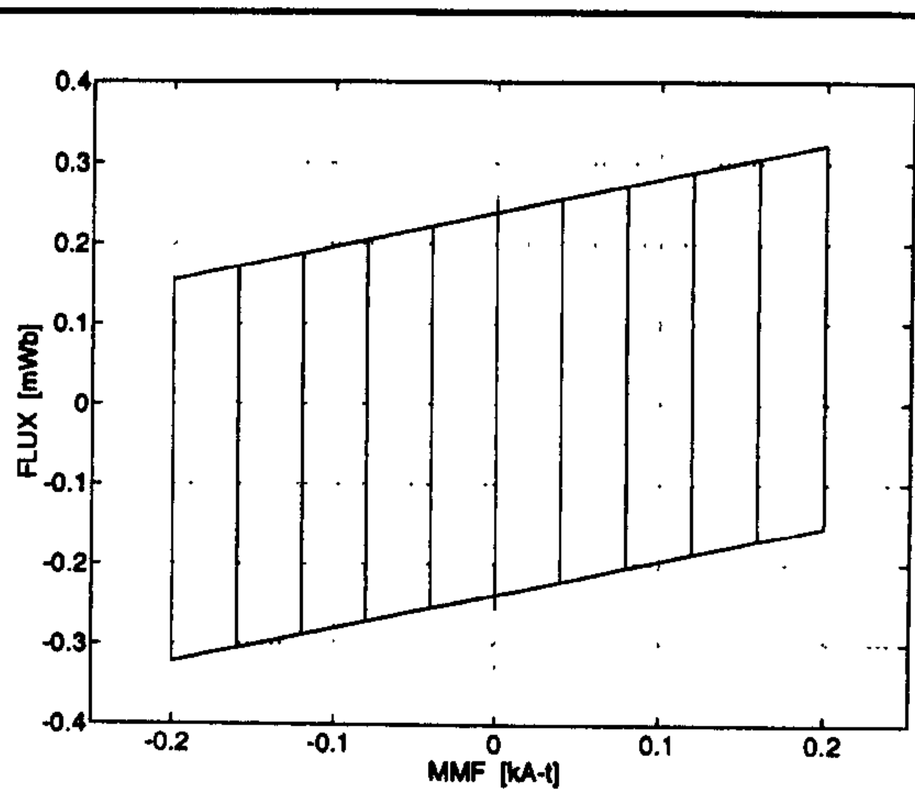

Fig. 10: Flux-MMF diagram for the unsaturated machine of Fig. 6 at peak currents of 0, 0.2, 0.4, 0.6, 0.8 and 1.0 A

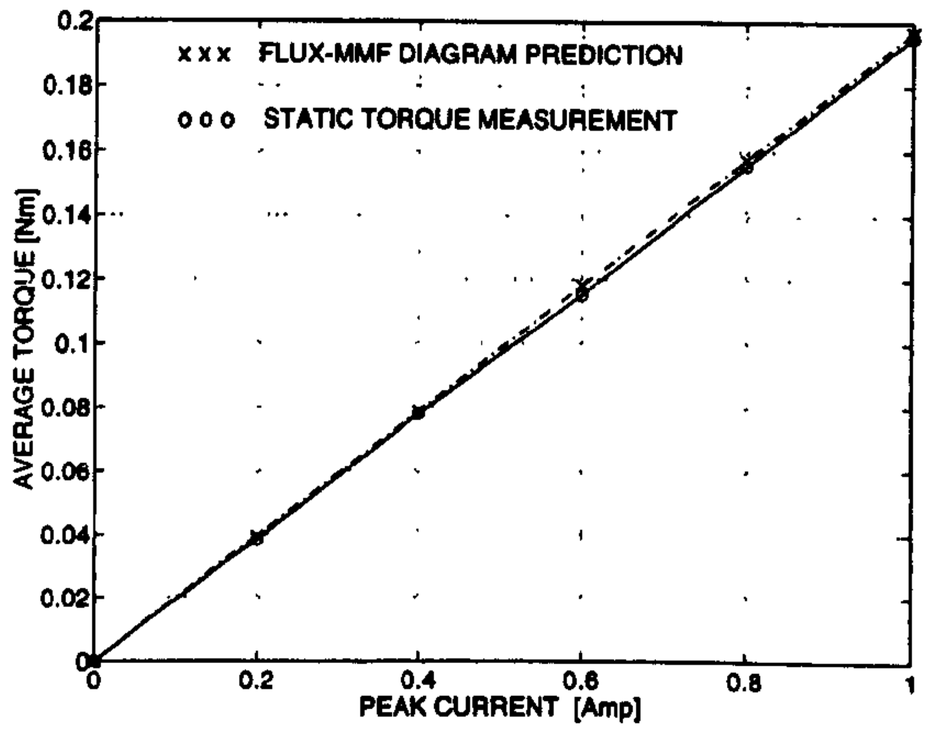

Fig. 11: Torque per ampere characteristic for the unsaturated machine of Fig. 6

Fig. 12 is the flux-MMF diagram for the saturated machine of Fig. 6. Graphical representation by way of change in the shape of these diagrams clearly brings out the effect of saturation. Fig. 13 compares the predicted torque per ampere characteristic with static torque measurements. The characteristic is non-linear indicating variation in torque constant for the saturated machine. A good agreement between the measured and the predicted curves in Figs. 11 and 13

shows that the flux-MMF diagram is able to take account of the effect of saturation accurately [3].

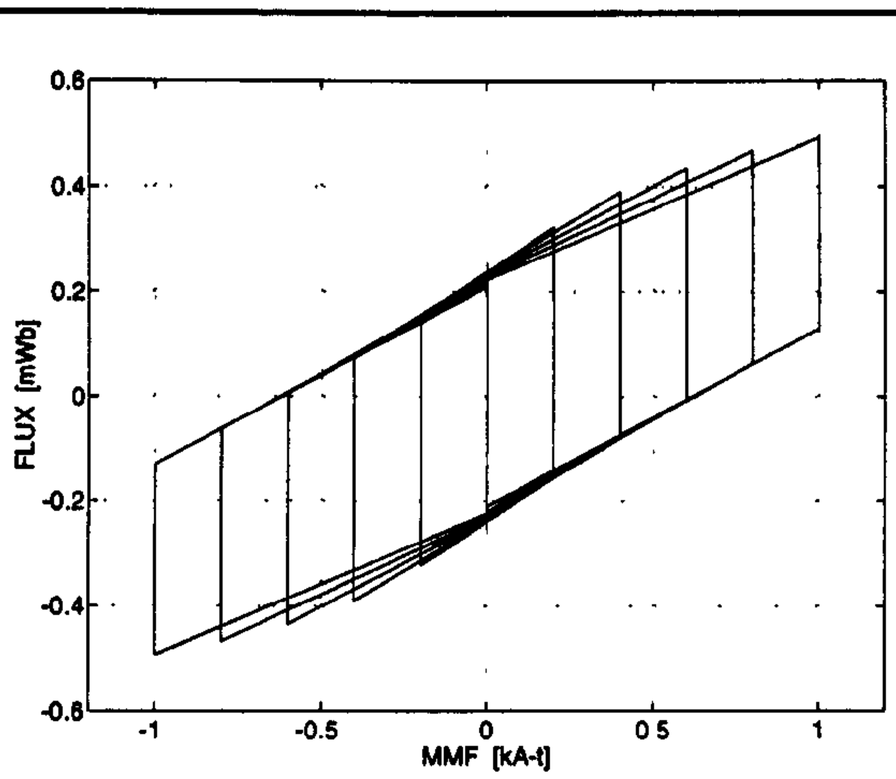

Fig. 12: Flux-MMF diagram for the saturated machine of Fig. 6 at peak currents of 0, 1, 2, 3, 4, 5 and 6 A

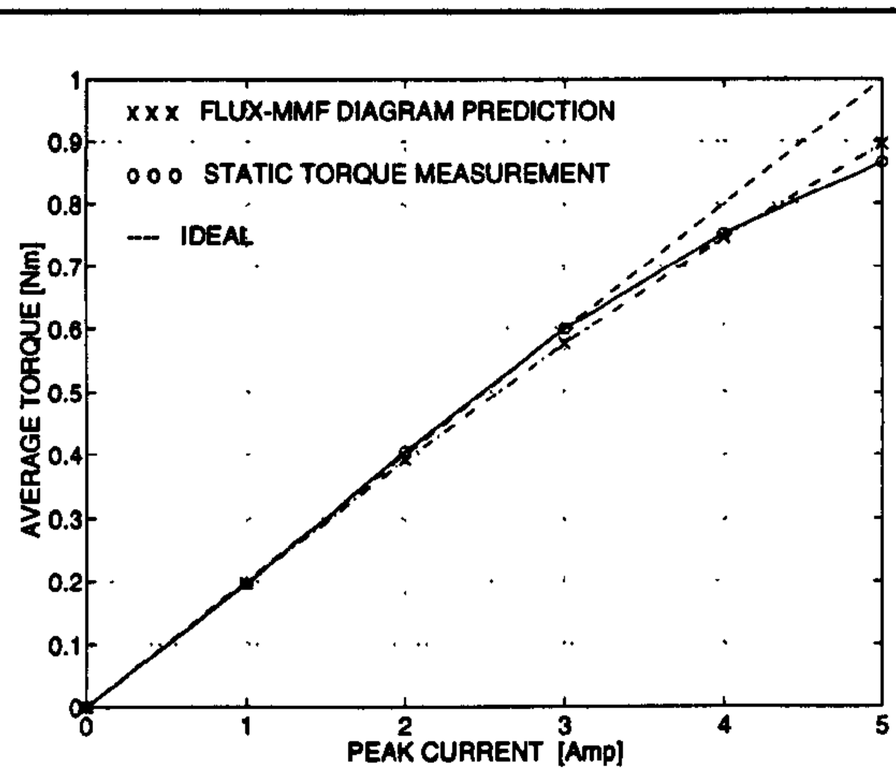

Fig. 13: Torque per ampere characteristic for the saturated machine of Fig. 6

7.0 COMPARATIVE EVALUATION OF ELECTRIC MACHINES

It is possible to construct a flux-MMF diagram for essentially any type of electric machine, including the squarewave brushless DC and the switched reluctance motor which cannot be analysed using the classical dq-axis theory. With the help of flux-MMF diagrams, it is possible to compare average torque, torque ripple, electric and magnetic loadings, kVA utilization and many other performance characteristics of any two electric machines, *even if they are of different types*. A few examples of such comparisons follow.

Fig. 14 compares three types of machines; induction motor (IM), synchronous reluctance motor (SYNCHREL) and the surface permanent magnet brushless AC motor (SPM-AC), all operating at the full load point. Although the maximum electric and magnetic loadings for the three motors are roughly comparable, the SPM-AC can generate substantially more torque as indicated by the largest area of its ellipse among the three. The main reason being the difference in their power factors. The SPM-AC ellipse major axis is almost aligned with the horizontal MMF axis indicating a power factor which is close to unity. But the IM and the SYNCHREL ellipse major axes are at an angle indicating a lagging power factor. This is due to the fact that the IM and the SYNCHREL provide magnetization through load current while it is provided by the permanent magnets for the SPM-AC.

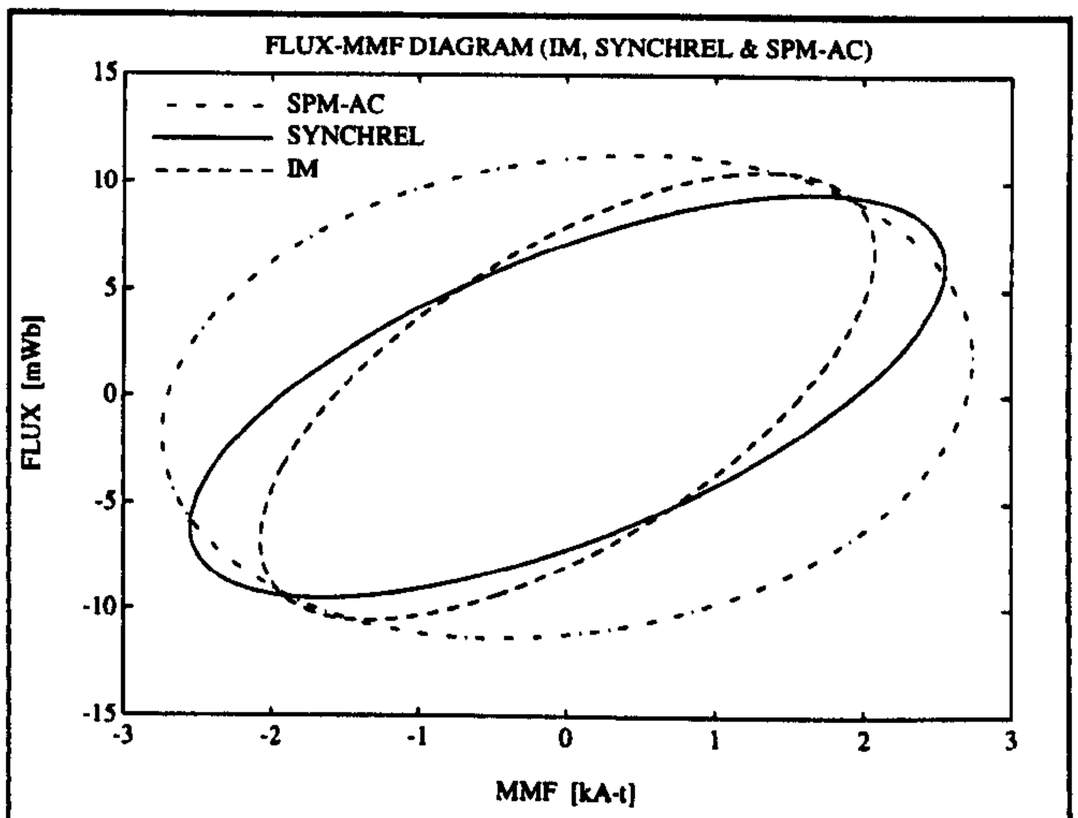

Fig. 14: Comparison between the IM, the SYNCHREL and the SPM-AC

Fig. 15 compares the SYNCHREL with the SRM. The magnetic loading is similar in both the cases but the SRM has much higher electric loading. The torque levels are not very different between the two as the SRM covers a large area only in the first quadrant while the SYNCHREL covers an equivalent area in both the quadrants.

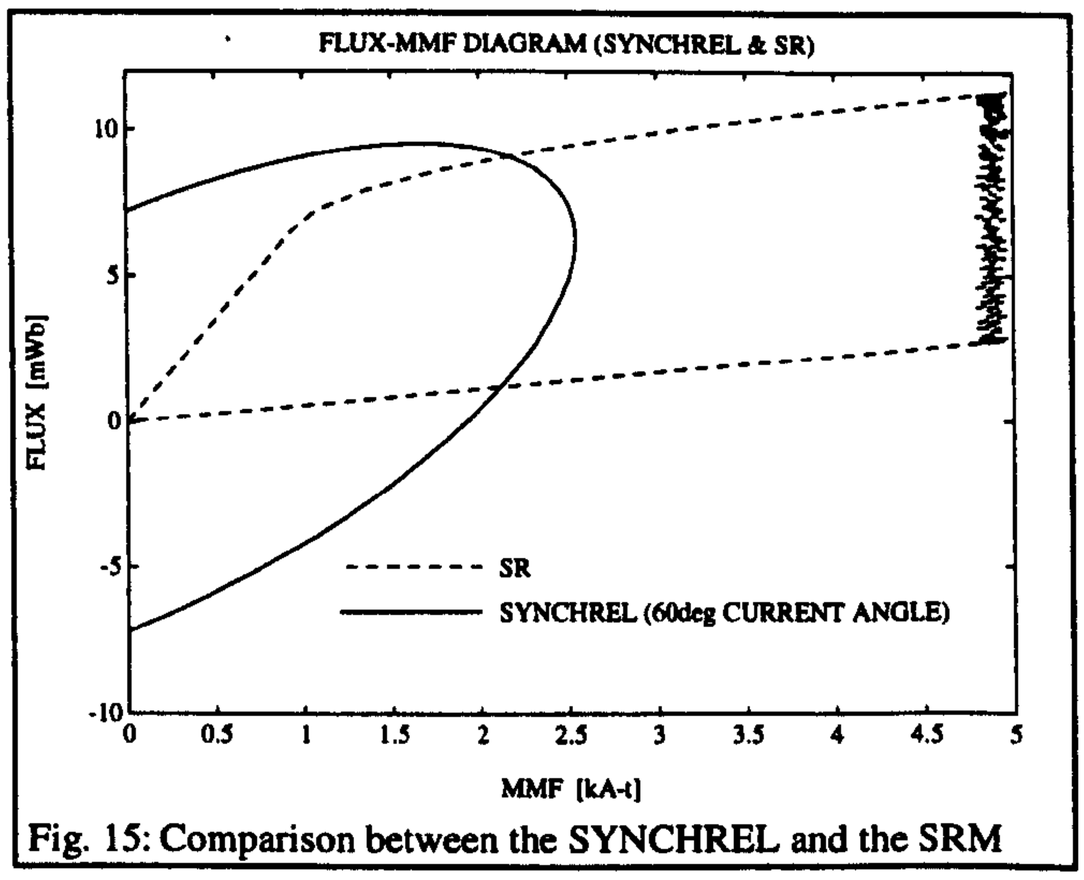

Fig. 15: Comparison between the SYNCHREL and the SRM

Fig. 16 compares the SPM-AC with the surface permanent magnet squarewave brushless DC motor (SPM-DC1) at the full load operating point. Both have almost the same area and hence the same level of average torque. However, the peak flux is higher in the case of SPM-DC1 while the peak MMF is higher in the case of SPM-AC.

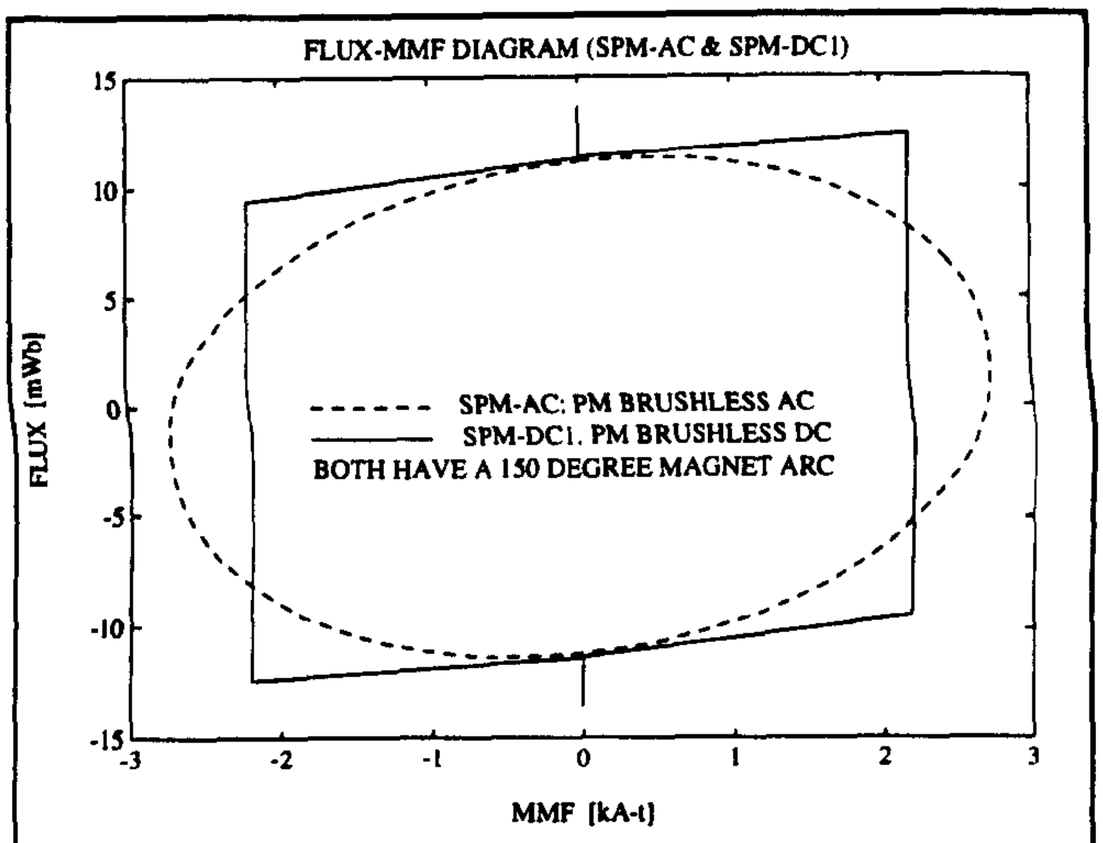

Fig. 16: Comparison between the SPM-AC and the SPM-DC1

8.0 DISCUSSION

The flux-MMF diagram technique is a general theoretical means for analysis and comparative evaluation of different types of electric machines. The main features of this technique are:

- It is based on the principle of virtual work and hence forms a universal basis for analysis and comparative evaluation.
- It can deal with classical as well as non-classical machine types having double saliency and/or non-sinusoidal excitation.
- It gives a clear physical insight of the torque producing mechanism and gives a graphical interpretation for many of the common machine characteristics.
- It makes an elegant use of the simple static finite element solutions and is able to take account of saturation effects.

REFERENCES

[1] D. A. Staton, W. L. Soong, and T. J. E. Miller, "Unified theory of torque production in switched reluctance and synchronous reluctance motors," *IEEE Trans. on Ind. Appl.*, Vol. 31, No. 2, March/April 1995, pp. 329-337.

[2] D. A. Staton, R. P. Deodhar, W. L. Soong, and T. J. E. Miller, "Flux-MMF based torque calculations in AC, DC and reluctance motors," *IEEE Trans. on Ind. Appl.*, (in press).

[3] R. P. Deodhar, D. A. Staton, and T. J. E. Miller, "Variation of torque constant in brushless PM motors," *Proc. of IEE Elec. Machines and Drives Conf.* , Durham, United Kingdom, September 1995 (in press).

[4] R. P. Deodhar, D. A. Staton, and T. J. E. Miller, "Modelling of skew using the flux-MMF diagram," *Proc. of the Intnl. Conf. on Power Electronics, Drives and Energy Sys. for Ind. Growth*, January 1996 (in press).

[5] Y. Liao, F. Liang, and T. A. Lipo, "A novel permanent magnet motor with doubly salient structure," *Rec. of IEEE Ind. Appl. Soc. Ann. Mtg.*, Houston, TX, 1992, pp. 308-314.

[6] R. P. Deodhar, D. A. Staton, and T. J. E. Miller, "Prediction of cogging torque using the flux-MMF diagram technique," *Rec. of IEEE Ind. Appl. Soc. Ann. Mtg.*, 1995 (in press).

[7] A. E. Fitzgerald and C. Kingsley Jr., *Electric Machinery*, 2nd Edition, McGraw Hill, 1961.

[8] J. R. Hendershot and T. J. E. Miller, *Design of brushless permanent magnet motors*, 1st Edition, Oxford/Magna Physics, 1994.

[9] T. J. E. Miller, *Switched reluctance motors and their control*, Oxford, 1993.

[10] T. J. E. Miller, *Brushless permanent magnet and reluctance motor drives*, Oxford, 1989.

[11] H. H. Woodson and J. R. Melcher, *Electromechanical Dynamics Part I: Discrete Systems*, John Wiley, 1968.

[12] D. C. White and H. H. Woodson, *Dynamics of the electromechanical energy conversion*, Wiley, 1963.

1996 IEEE-IAS Annual Meeting, San Diego, California, October 6–10, 1996
(Recipient of the IEEE-IAS Electric Machines Committee First Prize Paper Award)

The Flux-Reversal Machine : A New Brushless Doubly-Salient Permanent-Magnet Machine

Rajesh P. Deodhar†, *Student Member, IEEE*, Svante Andersson‡,
Ion Boldea§, *Fellow, IEEE*, and TJE Miller†, *Fellow, IEEE*

†SPEED Laboratory, University of Glasgow, Scotland, UK
‡Industrial Electrical Engineering and Automation, Lund Institute of Technology, Sweden
§University Politehnica 1900 Timisoara, Romania

***Abstract*—A new brushless doubly-salient permanent-magnet machine called the flux-reversal machine is described. Design, analysis, construction and experimental results for a prototype machine built as a single-phase, high-speed generator are presented. Qualitative comparisons are made with the other types of brushless machines in its class, using the flux-MMF diagram technique. An elementary CAD program developed for designing flux-reversal machines and the associated drive electronics is also described.**

NOMENCLATURE

Symbol	Meaning	Units
B_r	Remanent flux density	[T]
l_m	Length of magnet	[mm]
K_f	Fringing coefficient	
Φ_{ph}	Phase flux	[Wb]
Φ_m	Magnet flux	[Wb]
A_m	Area of magnet	[mm^2]
B_m	Magnet flux density	[T]
g	Length of air-gap	[mm]
μ_{rec}	Recoil permeability	
E	Generated EMF	[Volts]
ω	Speed	[rad/sec]
N_{ph}	Turns per phase	
θ	Rotor position	[° or Rad]

I. INTRODUCTION

Research interest in the switched reluctance machine (SRM) has grown significantly in recent years because of their apparent advantages such as simple construction, fault tolerance and mechanical robustness [1]. On the other hand, some of their limitations (such as excitation penalty, control complexity, noise and vibration) have prompted research into the incorporation of permanent magnets into the basic SRM structure . One of the new topologies proposed recently is the doubly-salient permanent magnet machine (DSPMM) [2] which essentially has the same construction as a SRM but with high energy magnets placed in the stator back iron. The flux-reversal machine (FRM) is a new brushless doubly-salient permanent-magnet machine proposed with the same aim of combining the advantages of the SRM and the PMM into one machine.

While the FRM is not the first DSPMM to have stationary magnets combined with a simple unexcited variable reluctance rotor, it appears to be the first to have bipolar flux *and* MMF variation with rotor position. It also appears that the FRM has a naturally low inductance and therefore a low electrical time constant. This feature, combined with its simple construction and low rotor inertia appear to make the FRM attractive as a low-cost, high-speed generator. This is interesting in the context of current attempts in the automotive industry to deal with certain limitations of the standard claw-pole alternator, such as limited efficiency and limited ability to respond quickly to sudden load changes. These problems become more severe as vehicle electric loads continue to increase [3]–[4].

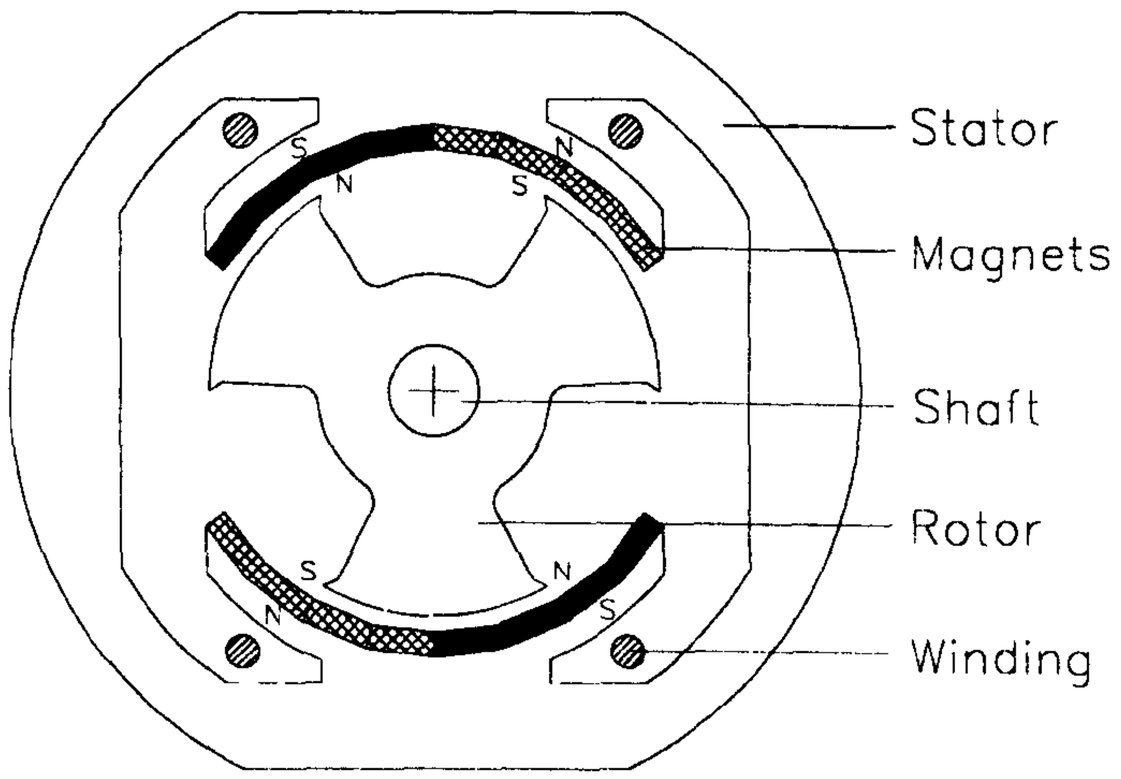

Fig. 1. The single-phase, 2/3 configuration flux-reversal generator prototype.

Fig. 1 shows the cross-section of a single-phase FRM with a two-pole stator and a three-pole variable-reluctance rotor. Two magnets of opposite polarity are placed on each stator pole face. Fig. 2 shows the variation of field and current, while Fig. 3 shows the variation of phase flux and MMF with rotor position. Note that all flux-linkages in this paper are plotted on a "per turn" basis. Thus "phase flux" means phase flux-linkage per turn, while "phase MMF" simply refers to the product of the phase current and the number of turns per phase [5]. The phase flux variation is bipolar (ideally a triangular wave), leading to a flat-topped or trapezoidal generated EMF waveform. The current is alternating current

(ideally squarewave). The flux reversing nature of the machine can clearly be seen from Figs. 2 and 3. The phase flux reverses sign for every electrical cycle of rotor displacement (i.e., one rotor pole-pitch). Although Fig. 1 is a single-phase 2/3 configuration, many other variations are possible with regard to the number of phases, and the numbers of stator and rotor poles.

Section II describes the principle of operation of the FRM. Section III makes a qualitative comparison between the FRM and the other types of brushless machines in its class. Section IV describes the design, analysis and construction of a prototype FRM built as a single-phase, high-speed generator. Section V describes a CAD program developed for designing FRMs and the associated drive electronics. Detailed experimental results on the prototype are presented in section VI. Finally, section VII summarizes important features and advantages of the flux-reversal machine and discusses its possible applications.

II. Principle of Operation

The principle of operation of the flux-reversal machine can be explained with the help of Figs. 2 and 3. In Fig 2, (a) is an equilibrium position, where the flux set up by the magnets circulates entirely within each stator pole and there is no flux in the stator back-iron. No flux links the coils at this position (point (a) in Fig. 3). In (b), the rotor is displaced by 30° counter-clockwise, so that the rotor poles overlap one or other of the magnets. The flux now passes through the coils and the back-iron and the phase flux is maximum at this position (point (b) in Fig. 3). In (c), the rotor is at a second equilibrium position, displaced from the first one by 60°, where again there is no flux in the stator back-iron and no flux linking the coils (point (c) in Fig. 3). A further displacement of 30° in the counter-clockwise direction leads to the position shown in (d), where phase flux is maximum in the direction opposite to the one shown in (b) (point (d) in Fig. 3).

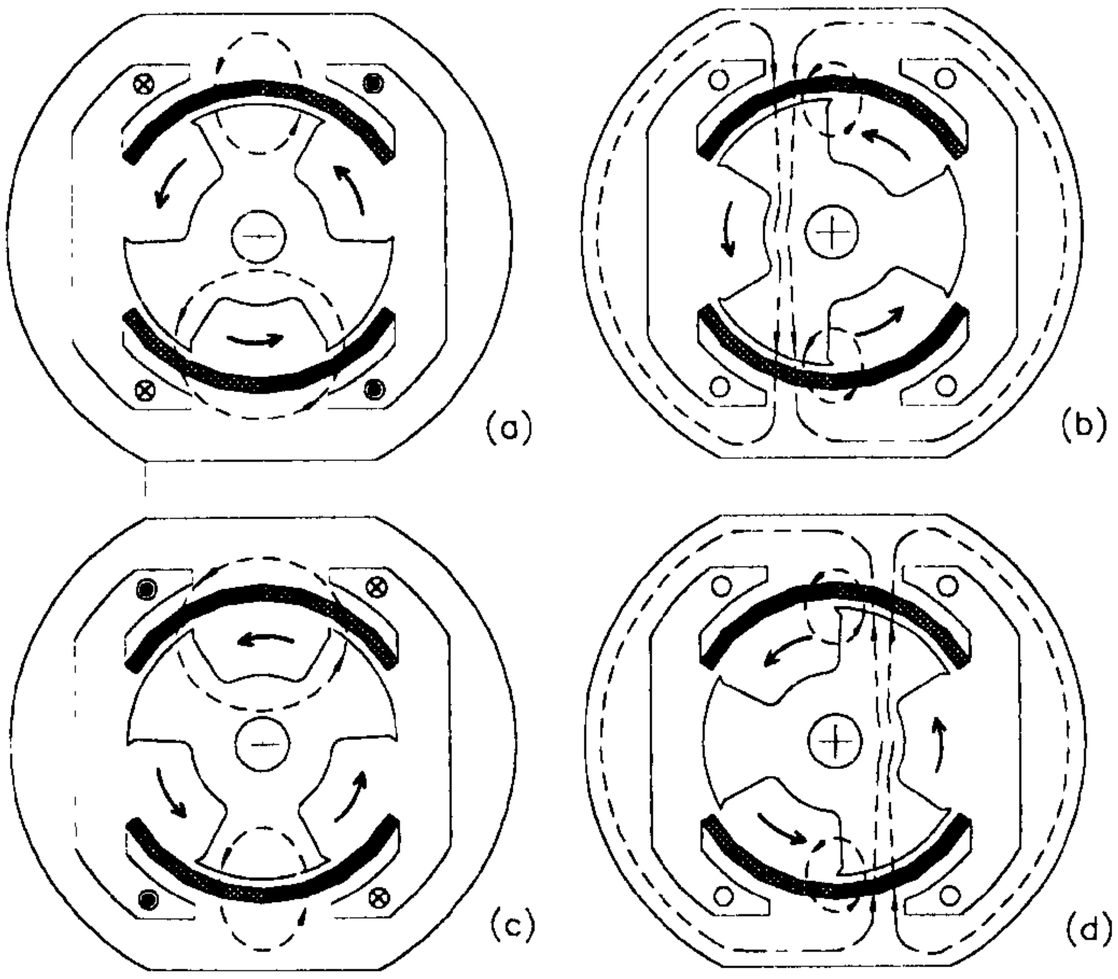

Fig. 2. The principle of operation of the flux-reversal machine.

The linear bipolar variation of phase flux leads to a squarewave EMF. Applying Faraday's law, it can be seen from Fig. 2 that the EMF is maximum at (a), negative maximum at (c) and zero at (b) and (d). Based on the foregoing discussion, the following observations can be made regarding the operation of an FRM:

- Like the PMM, the FRM works on the principle of variable flux-linkage inducing an EMF that interacts with an alternating armature current.
- Although the field excitation is provided by the permanent magnets, the flux-linkage of the armature windings is modulated by the variation of the magnetic circuit reluctance as the rotor rotates, in such a way that a bipolar EMF is induced without rotating magnets.

III. Comparison with Other Machine Types

In order to be able to evaluate the capabilities of the FRM, it is important to compare its torque producing mechanism and operational characteristics with other types of brushless machines in its class. In this section, such a comparison is made between the SRM, the DSPMM, the brushless DC machine (BLDCM) and the FRM, using the flux-MMF diagram technique (FMDT). The FMDT is a generalization of the *principle of virtual work* in which the cyclic variation of flux and MMF over an electrical cycle for any one phase of an electric machine is used to calculate the converted energy and the average and the instantaneous torque [5]–[6]. Fig. 3 shows the ideal variation of phase flux and MMF with rotor position for four types of brushless machines used in the comparison.

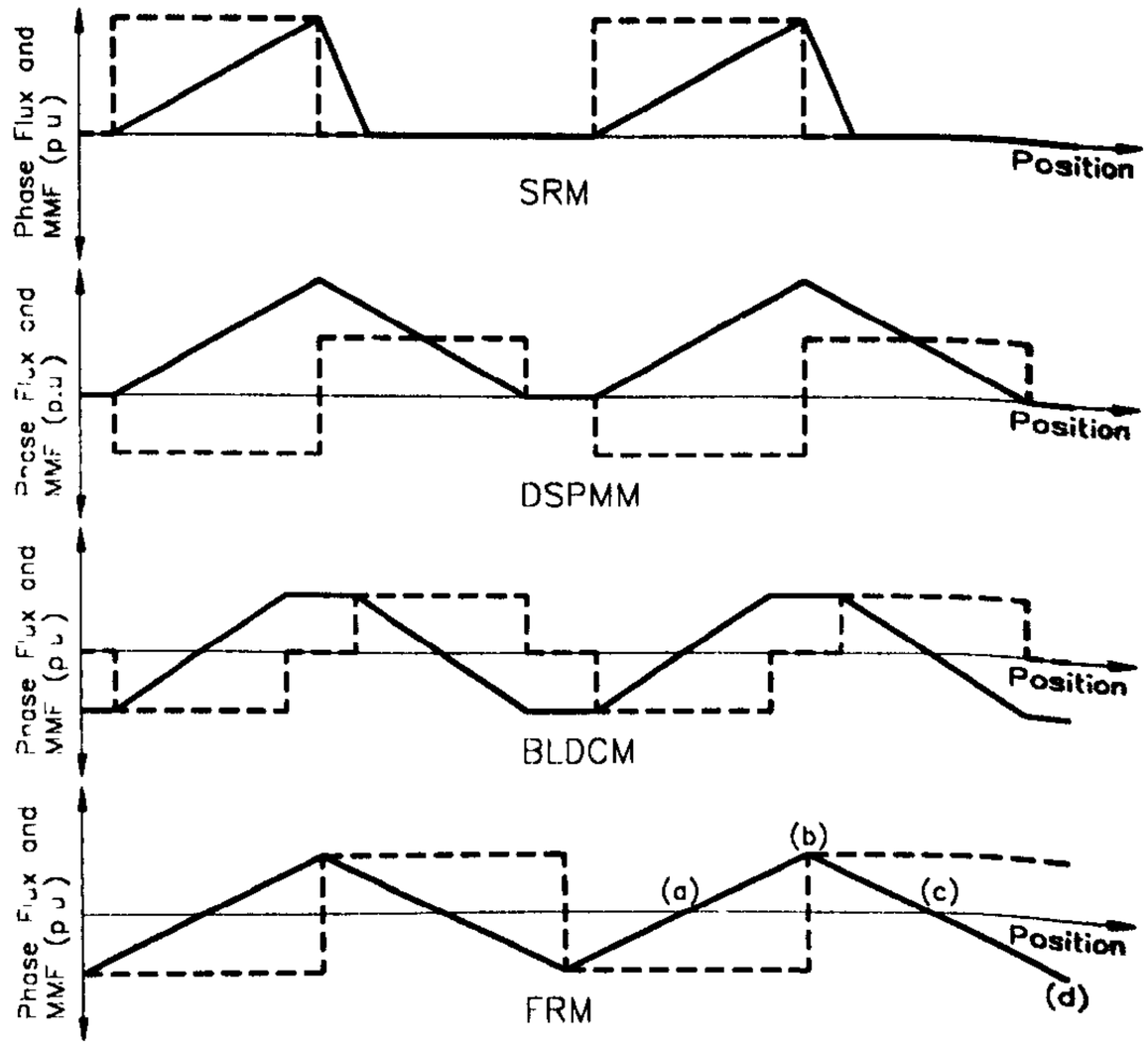

Fig. 3. The ideal variation of phase flux (solid line) and MMF (dotted line) with position for different types of brushless machines.

Fig. 4 shows the flux-MMF diagram for each machine type plotted using the variation of phase flux and MMF shown in Fig. 3. The area enclosed by the flux-MMF loop, shown in dark solid line, is the energy converted over a 'stroke' or an

electrical cycle and it indicates the *average* electromagnetic torque produced over the corresponding displacement [5]. Note that the same amount of net phase flux and MMF variation over a 'stroke' or an electrical cycle is assumed in each case.

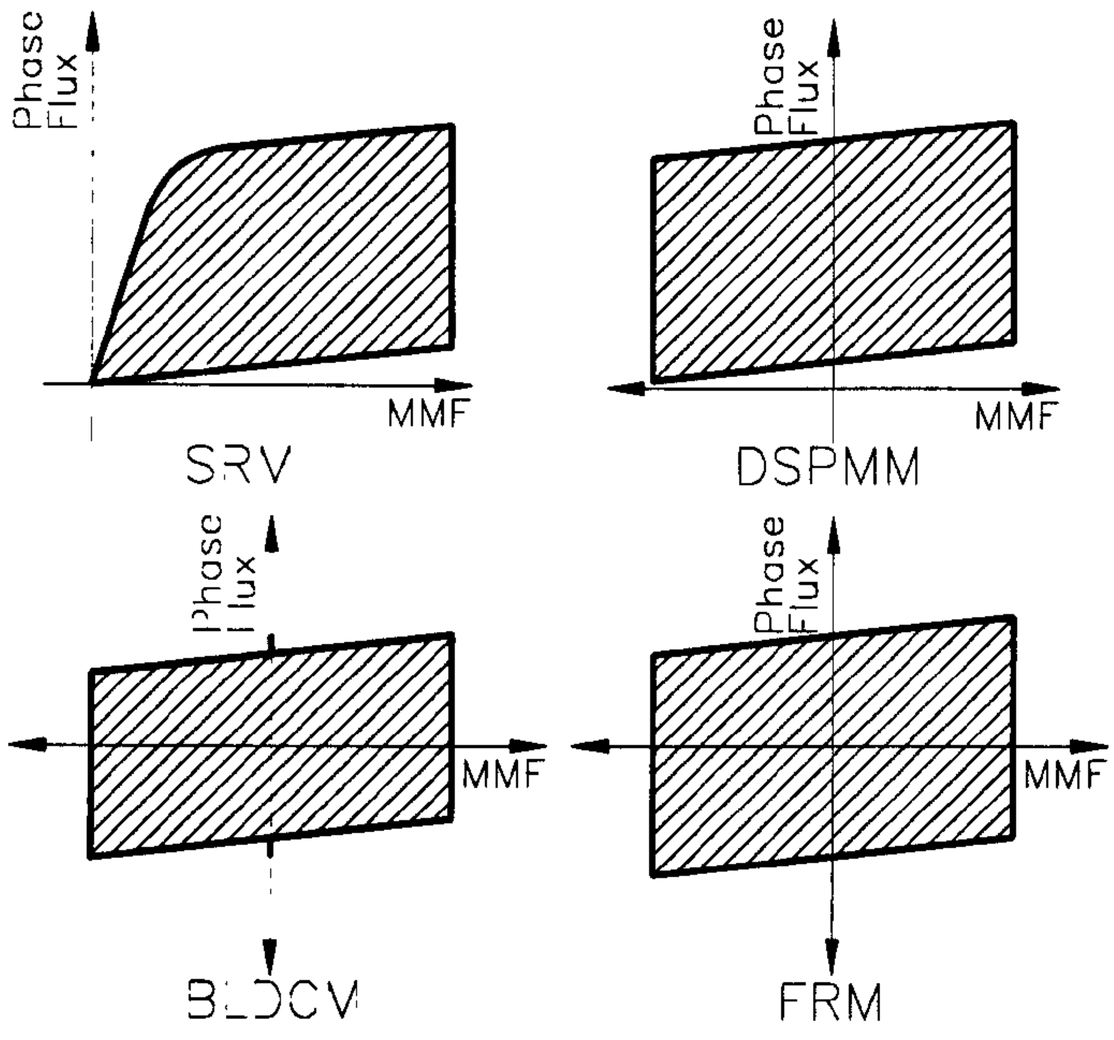

Fig. 4. Comparison between the SRM, the DSPMM, the BLDCM and the FRM, using the flux-MMF diagram.

The following points can be noted on the comparative evaluation of each of the four machine types:

- The SRM has unipolar phase flux *and* MMF variation while the DSPMM has unipolar phase flux variation and bipolar MMF variation. The BLDCM and the FRM, both have bipolar phase flux *and* MMF variation.
- In the case of SRM, the energy conversion loop is limited to the first quadrant, while in the case of DSPMM, it is limited to the first two quadrants. In the case of BLDCM and FRM, it covers all four quadrants in the flux-MMF plane.

IV. Prototype Design, Analysis and Construction

A. Prototype Design

The principal objective was to design and construct a 'proof-of-principle' prototype flux-reversal machine to see if any of its apparent advantages were of practical value. It was decided to build a 2/3 configuration, low-cost, high-speed, single-phase generator, called the flux-reversal generator (FRG), with a simple electronic voltage controller. An existing two-pole universal motor stator was modified and used while a new three-pole variable reluctance rotor was built. Sm-Co block magnets were used with four blocks making up a single pole arc of 60° (see Fig. 1). The air-gap was designed to be 0.5 mm to obtain a reasonable permeance coefficient value of 4.9. The stator and the rotor pole arcs were designed to be 120° and 60° respectively. The rotor geometry was optimized with the help of finite-element analysis (FEA). Fig. 1 shows the details of the stator and the rotor lamination geometry. An important parameter in designing flux-reversal machines is the fringing coefficient, K_f, which is the ratio of maximum flux linking a stator phase to magnet flux (1). An accurate estimate of K_f was needed in designing the prototype and hence FEA was used to obtain a value of $K_f = 0.45$.

$$K_f = \frac{\Phi_{ph}}{\Phi_m} = \frac{\Phi_{ph}}{A_m B_m} = \frac{\Phi_{ph}}{A_m B_r / 1+(g\mu_{rec}/l_m)} \tag{1}$$

The number of turns per phase, N_{ph}, was obtained using (2), which is derived specifically for the 2/3 configuration from the Faraday's law assuming a linear variation of phase flux with rotor position.

$$E = -\omega N_{ph} \frac{d\Phi_{ph}}{d\theta} = -\omega N_{ph} \frac{2K_f \Phi_m}{\pi / 3} \tag{2}$$

End-shields from the existing universal motor were used and a new shaft was designed to suit the FRG rotor and the end-shields. Table I, given at the end of this section, summarizes the important FRG design specifications. Certain specifications, such as the generator speed and voltage range, were based on the existing automotive generators.

B. Prototype FRG Analysis Using the FMDT

The FMDT, together with the FEA, was used to analyze the prototype FRG and predict such important performance characteristics as electromagnetic torque ripple, cogging torque ripple, and the variation of phase inductance, phase flux and generated EMF with position. Fig. 5 shows a typical flux-plot at no-load obtained using the FEA.

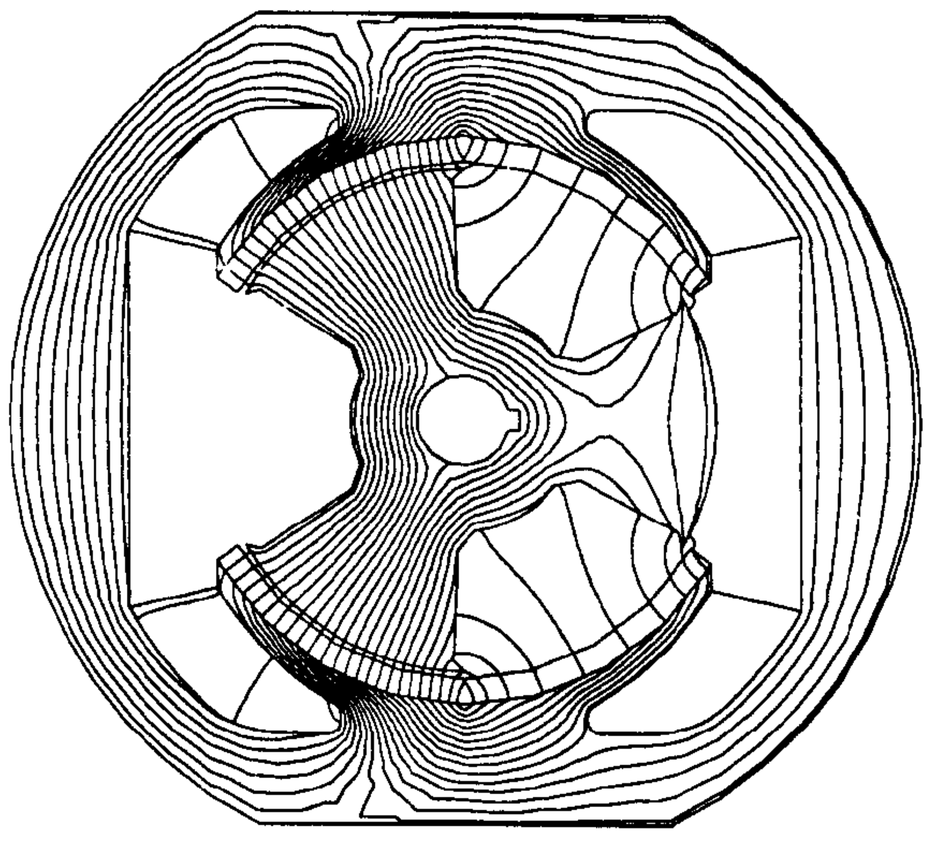

Fig. 5. The flux-plot at no-load obtained from the finite-element analysis.

Fig. 6 shows the phase flux-MMF diagram for the prototype FRG and Fig. 15 shows the predicted electromagnetic torque ripple obtained from it [5].

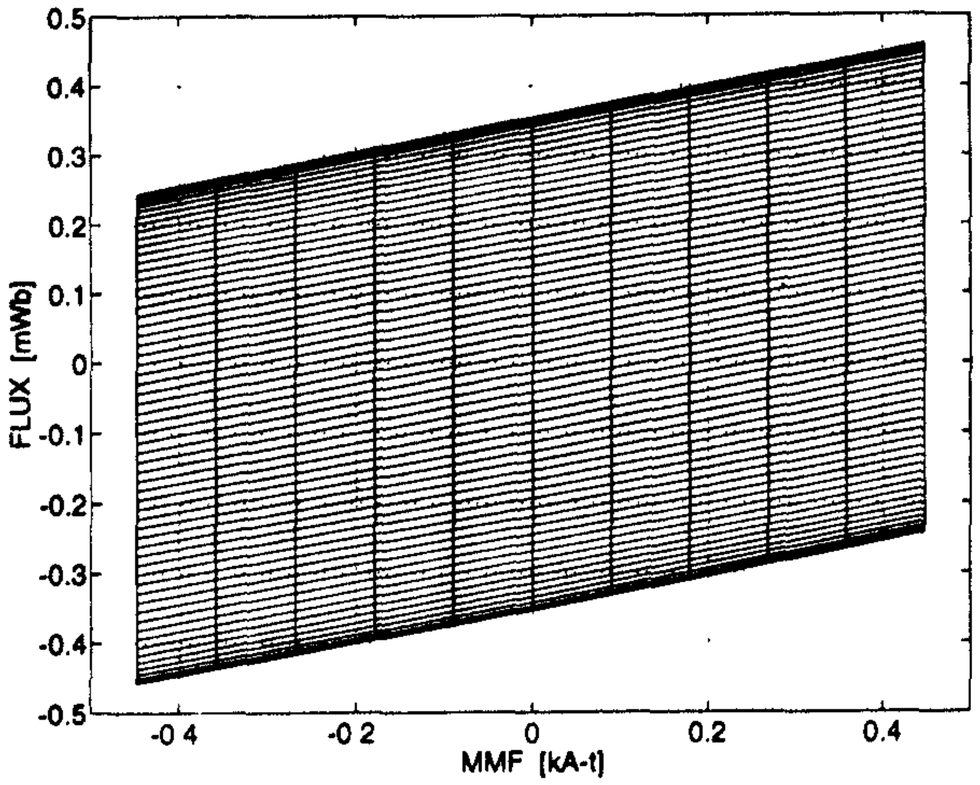

Fig. 6. The phase flux-MMF diagram for the prototype FRG at peak currents of 0, 0.2, 0.4, 0.6, 0.8 and 1.0 Amps.

The cogging torque ripple was predicted by obtaining the flux and MMF variation for each of the four magnet poles over a cogging torque period as shown in Fig. 7. Fig. 8 shows the flux-MMF diagram plotted for one pole (pole1)using the demagnetization characteristics of the magnet [6].

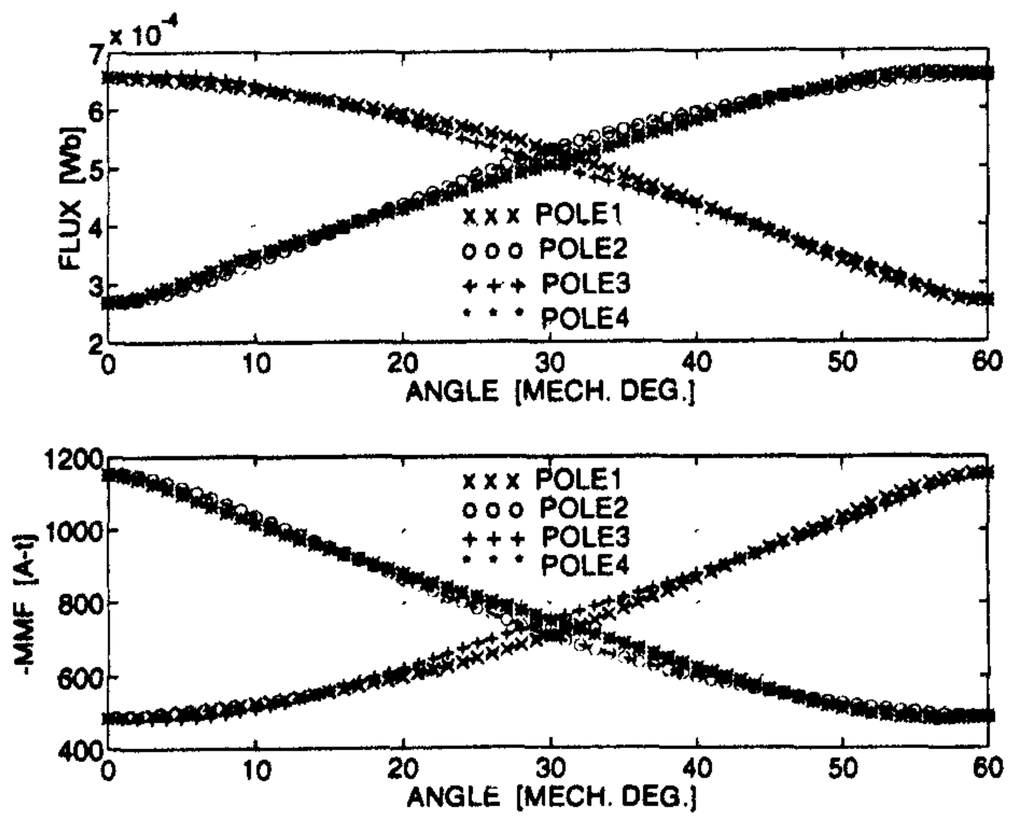

Fig. 7. The flux and MMF variation for each magnet pole. The poles are numbered clockwise from the top left-hand corner in Fig 1.

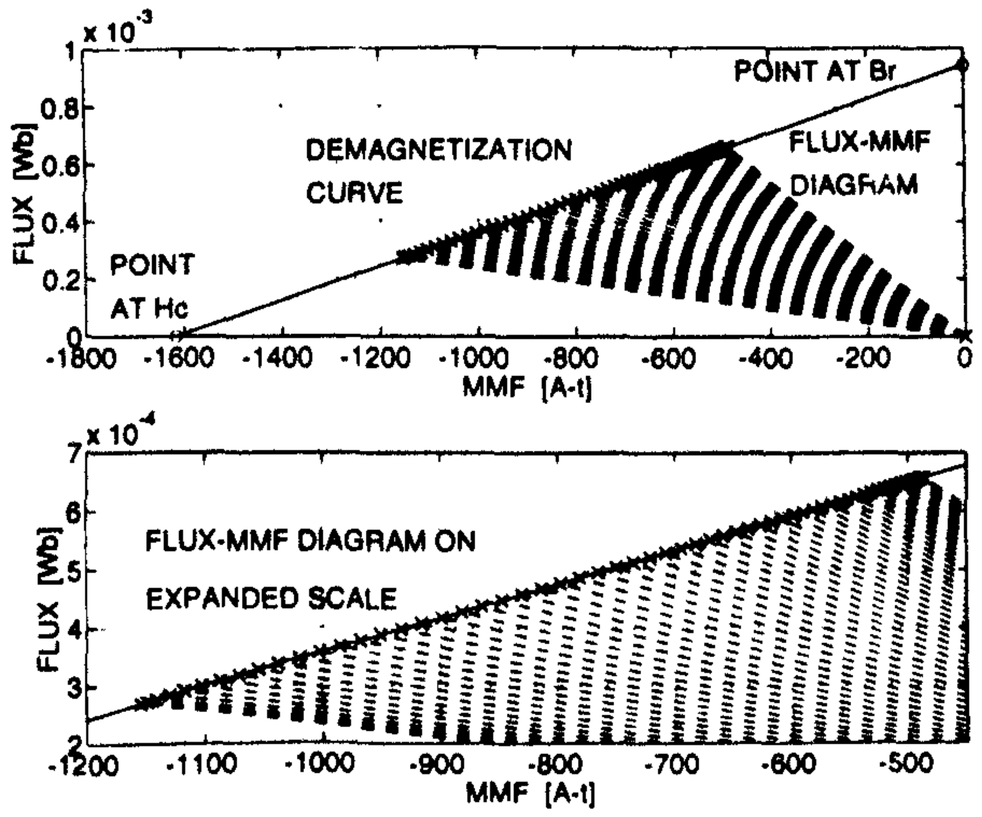

Fig. 8. The top half shows the flux-MMF diagram for pole1 of the prototype FRG. The bottom half shows the same on an expanded scale.

Fig. 9 shows the cogging torque ripple contribution due to pole1, obtained from Fig. 8. The procedure was repeated for each of the four poles and the corresponding individual cogging torque ripple contributions are shown in Fig. 9. The resultant predicted cogging torque ripple for the entire machine, shown in Figs. 9 and 16, is simply the superposition of all the individual contributions. Note that the superposition is valid even under saturated conditions, since the effect of saturation is already taken into account in deriving individual cogging torque ripple waveforms. It is interesting to note that while the cogging torque period for each pole contribution is 120°, the resultant cogging torque period is only 60°.

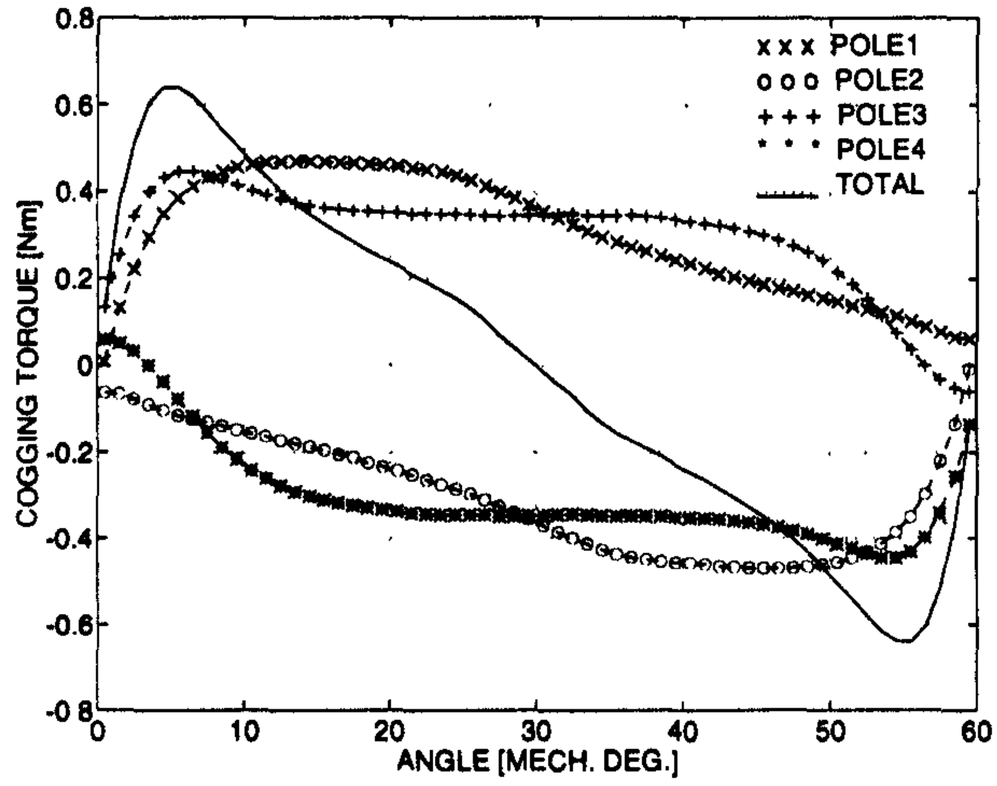

Fig. 9. The predicted cogging torque ripple–for each pole and for the entire machine.

Fig. 17 shows the predicted variation of phase inductance with position at different currents. It was obtained from Fig. 6, by simply calculating the incremental slopes of the magnetisation curves at each rotor position. The predicted variation of phase flux and generated EMF with position is shown in Figs. 18 and 19 respectively.

C. Prototype FRG Construction

The existing universal motor stator was modified to accommodate the block magnets. The wire EDM process was used to give fine cuts on the pole faces and edges to obtain a flat surface and an accurate pole arc of 120°. Magnets were glued onto these flat surfaces using Locktite 326 anaerobic superglue. Rotor laminations were cut from a stack of lamination material. Again, the wire EDM process was used to obtain superior surface finish and to maintain accurate tolerances. The main stator coils and the additional 10-turn search coils, used for sensing flux, were wound on each stator pole. Fine-wire thermocouples were used on the winding, magnet and stator back-iron surfaces to measure temperature rise in different parts of the machine.

D. Electronic Controller

A simple electronic controller was built, as shown in Fig. 10, to obtain a regulated DC voltage output from the generated AC voltage over a wide speed range. It consists of a bridge rectifier and a PWM controlled dc-to-dc converter.

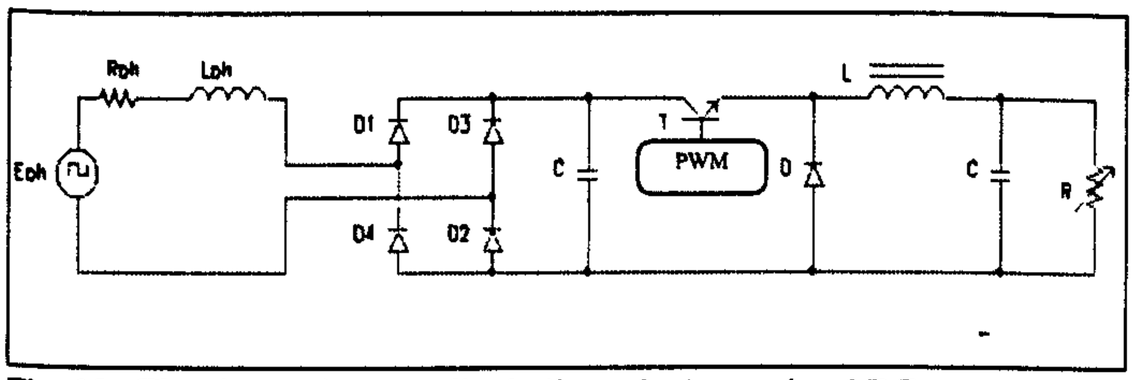

Fig. 10. The electronic controller built to obtain regulated DC output.

Table I gives design specifications for the complete generator system consisting of the generator and the electronic controller.

TABLE I
PROTOTYPE FRG SYSTEM DESIGN SPECIFICATIONS

Stator lamination material	Newcor800, 0.65 mm thick
Rotor lamination material	Lossil 400/50, 0.5 mm thick
Magnet material	$SmCo_5$
Length of magnet	2.45 mm
Magnet B_r	0.85 T
Stator outer diameter	89.10 mm
Stator lamination inner diameter	55.30 mm
Stator bore diameter	50.40 mm
Length of air-gap	00.50 mm
Stack Length	40.00 mm
Rotor outer diameter	49.40 mm
Rotor pole length	13.75 mm
Number of turns per pole	112
Copper wire gauge	AWG 23
Generator speed range	900 to 9000 rpm
Generated peak AC voltage range	30 to 300 Volts
Output DC voltage of the controller	14 Volts

V. PC-FRM–A Preliminary CAD Program for Designing Flux-reversal Machines

A preliminary CAD program for designing FRMs and the associated drive electronics was developed. Fig. 11 shows the cross-section editor of the program, where machine geometry can be viewed and modified. It shows a single-phase, 2/3 configuration similar to the one shown in Fig. 1. The program has a 'dynamic analysis' option which carries out design calculations and generates an 'output design sheet' containing a detailed list of design parameters. It also generates output waveforms as shown in Fig. 12.

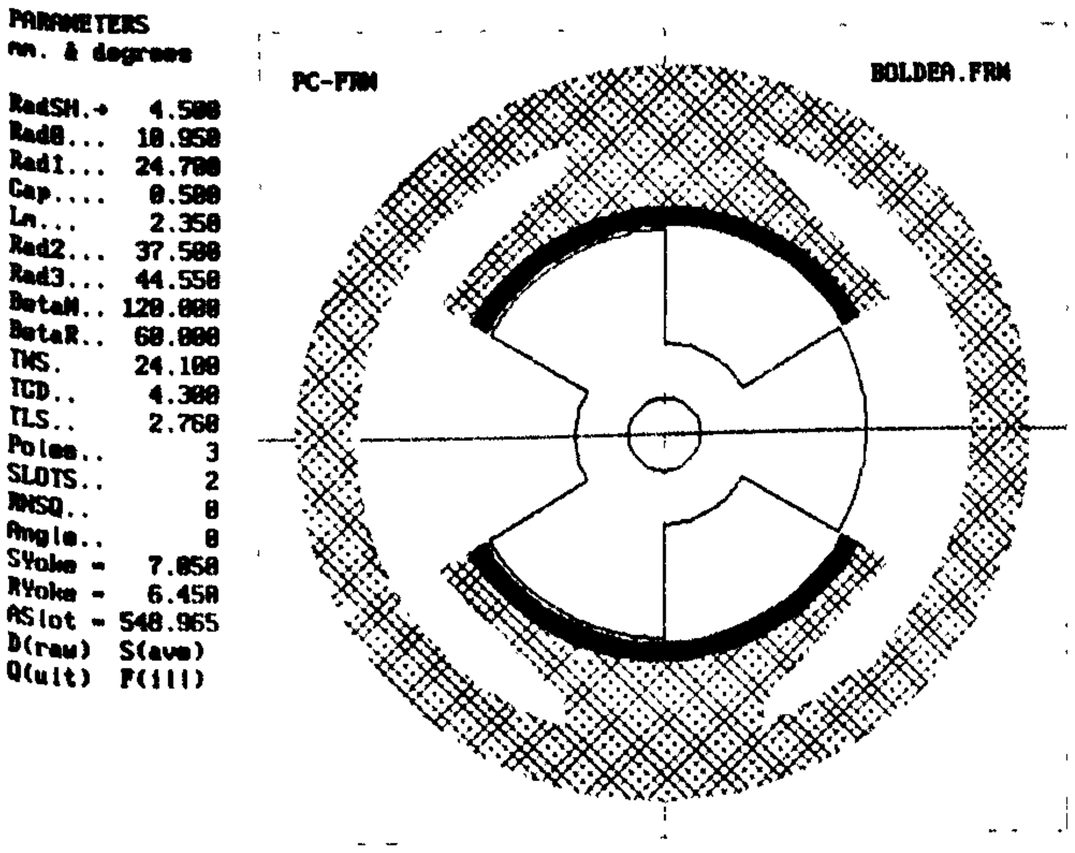

Fig. 11. The cross-section editor showing a single-phase 2/3 configuration.

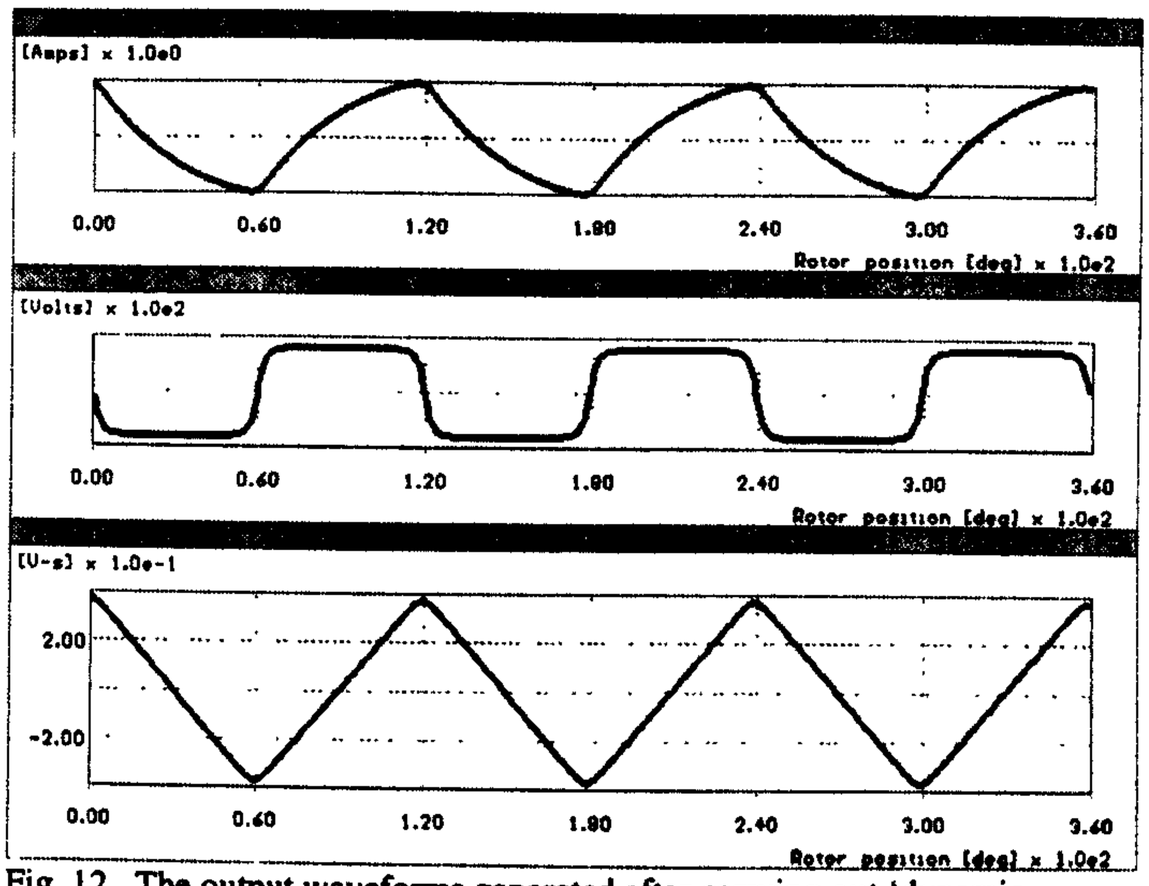

Fig. 12. The output waveforms generated after carrying out 'dynamic analysis' on the design shown in Fig. 11.

Some other possible configurations for the flux-reversal machine, such as a 4/6 or a 6/8, are shown in Figs. 13 and 14.

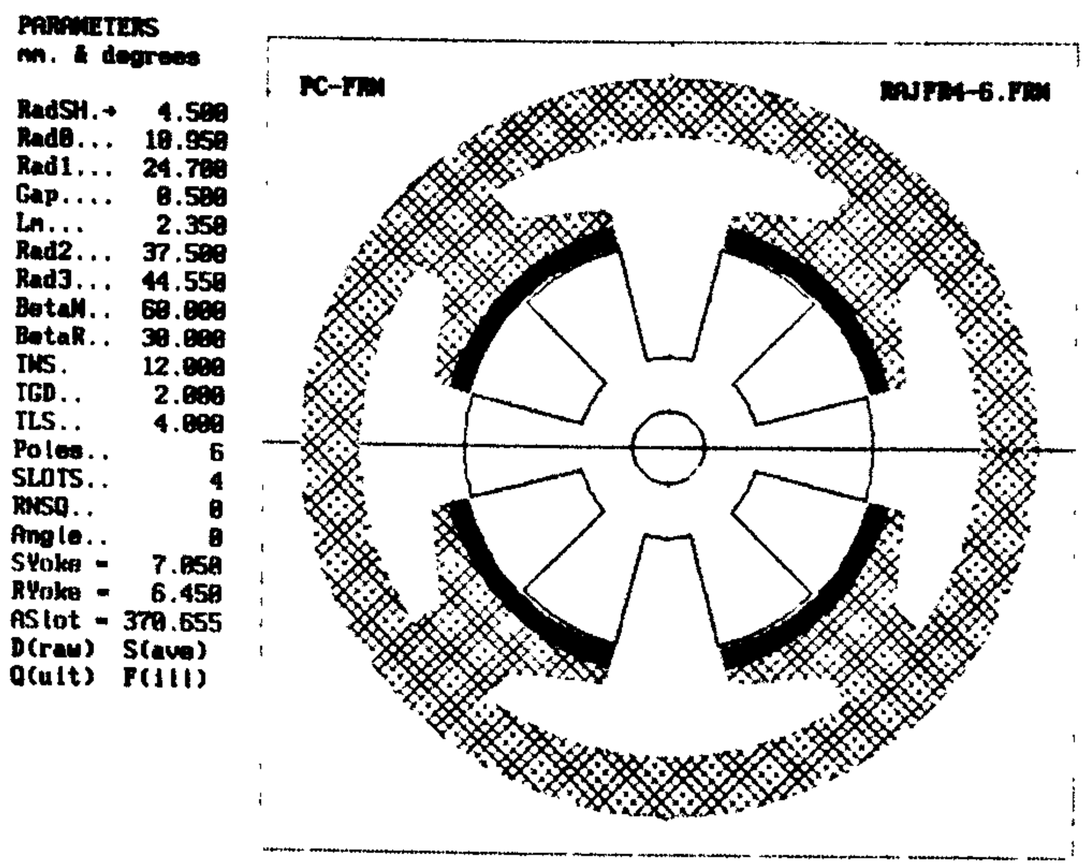

Fig. 13. A 4/6 flux-reversal machine configuration.

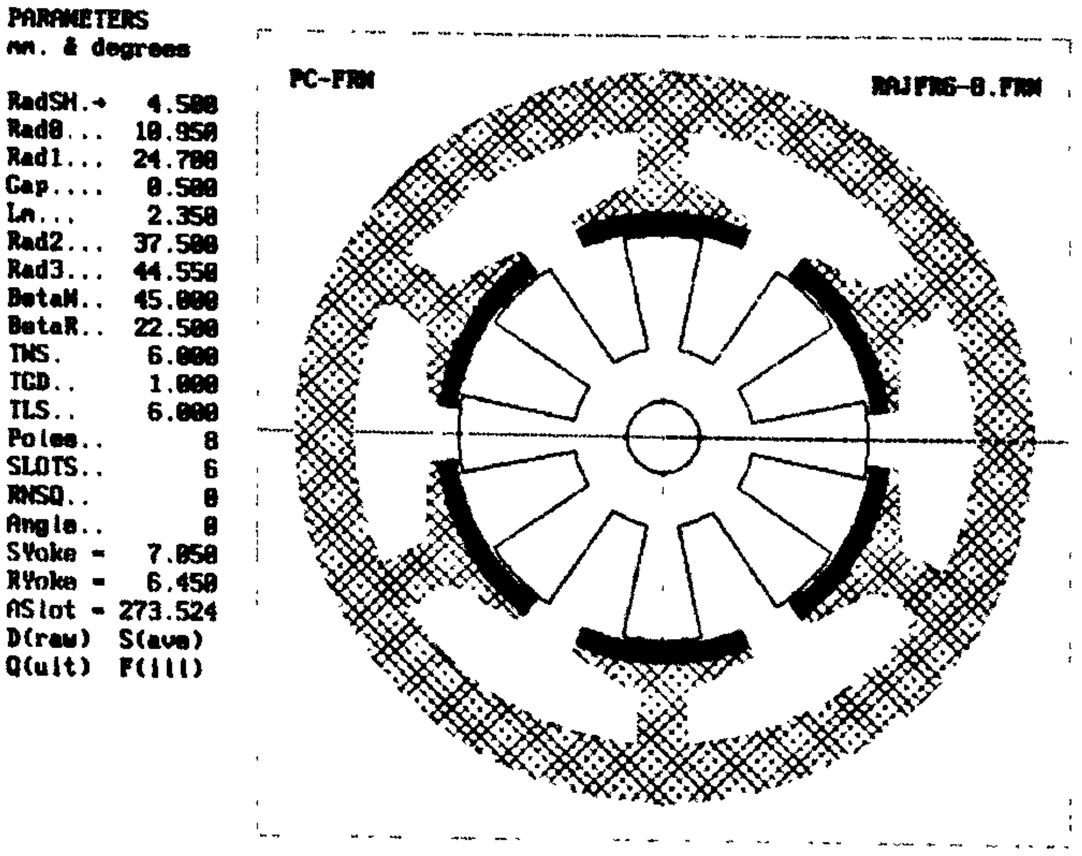

Fig. 14. A 6/8 flux-reversal machine configuration.

The program essentially serves as a quick and simple 'sizing' software and complements the other more accurate

but slower analytical techniques such as the FEA and the FMDT. It offers high speed of design calculations together with the flexibility to evaluate a wide range of design options and parameter variations.

VI. Experimental Results

A. Electromagnetic and Cogging Torque Ripple

Figs. 15 and 16 compare the predicted and the measured electromagnetic and cogging torque ripple respectively. The static test set-up was made up of a dividing head driving the machine through an in-line torque transducer. The rotor was stepped through 1° increments over half an electrical cycle. The electromagnetic torque ripple was obtained by first measuring the total torque ripple at different currents and then subtracting the measured cogging torque ripple from it.

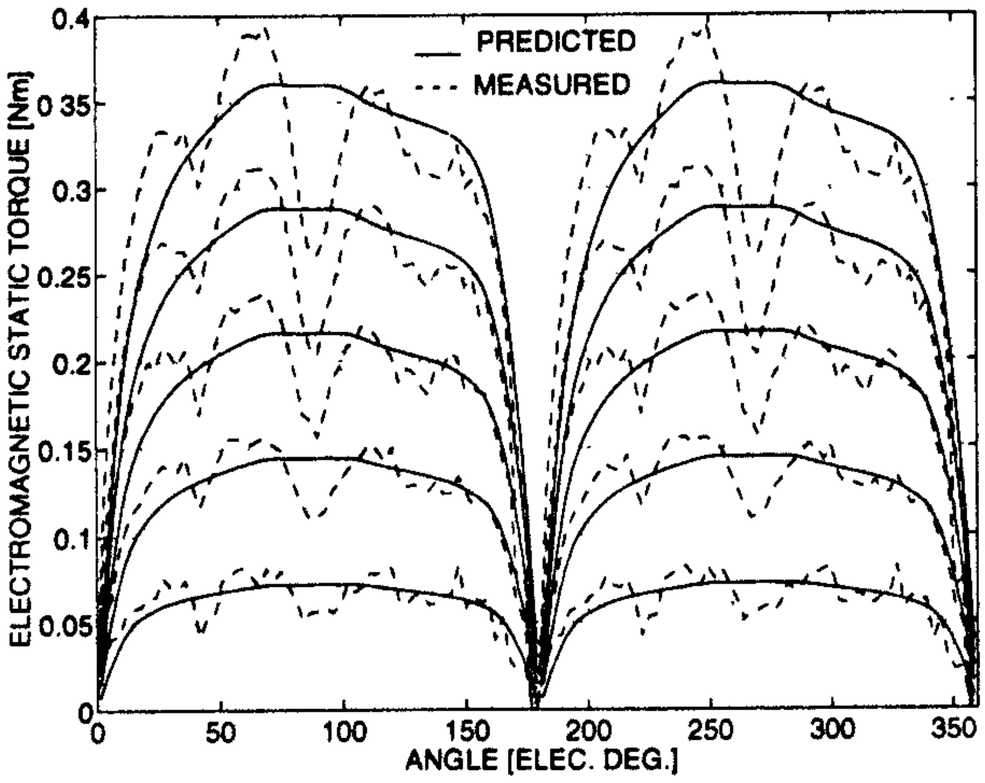

Fig. 15. The predicted and the measured electromagnetic torque ripple at peak currents of 0.2, 0.4, 0.6, 0.8 and 1.0 A.

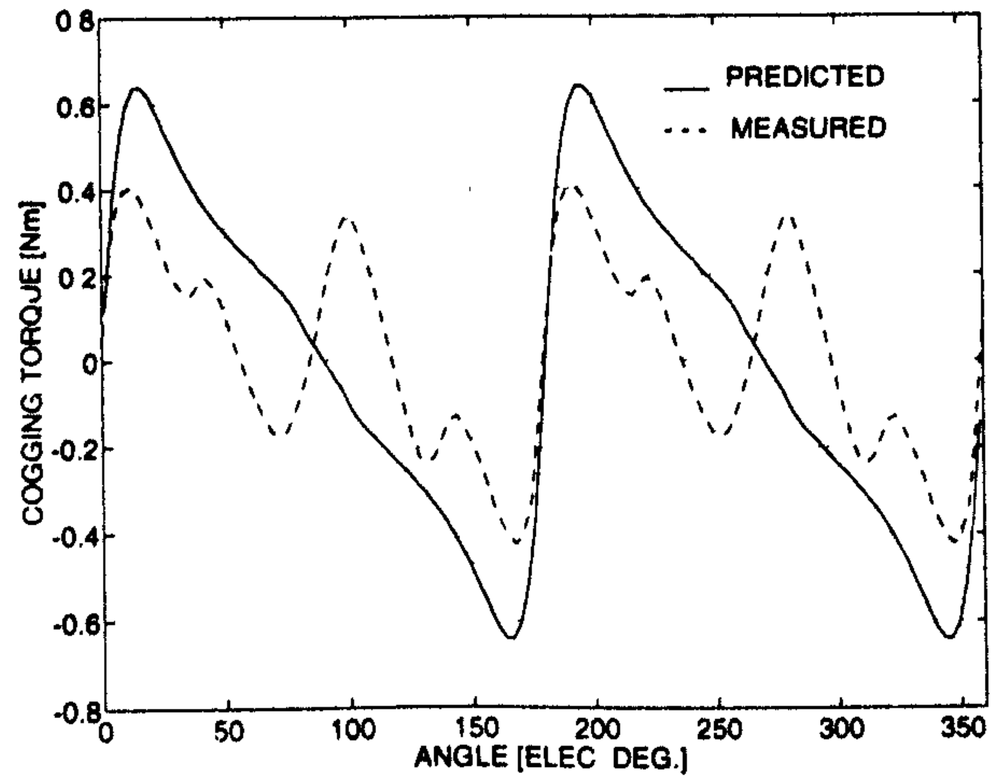

Fig. 16. The predicted and the measured cogging torque ripple.

B. Phase Inductance

Fig. 17 compares the predicted and the measured phase inductance variation with position. The measurements were obtained by using the static test set-up. The machine was excited with the 50 Hz AC mains supply, stepped down and varied through an auto-transformer. AC voltages and currents were measured at each rotor position and the phase inductance was calculated, knowing the phase resistance.

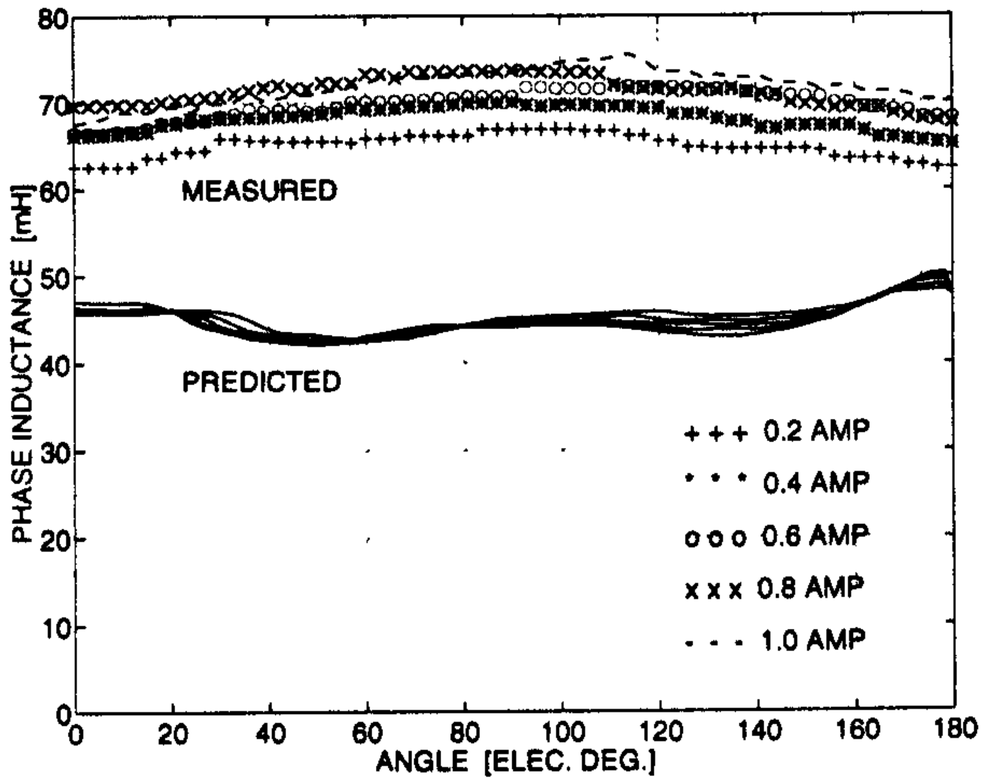

Fig. 17. The predicted and the measured phase inductance variation with position.

C. Phase Flux and Generated EMF

Figs. 18 and 19 compare the predicted and the measured variation of phase flux and generated EMF respectively.

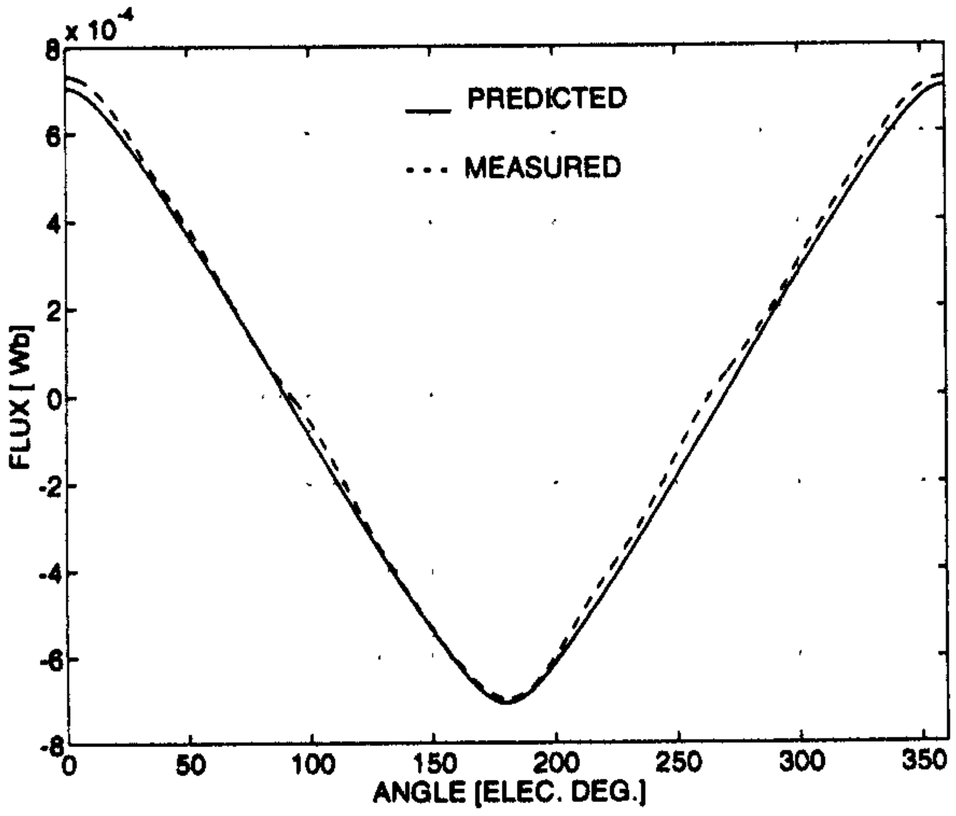

Fig. 18. The predicted and the measured phase flux variation at 1000 rpm.

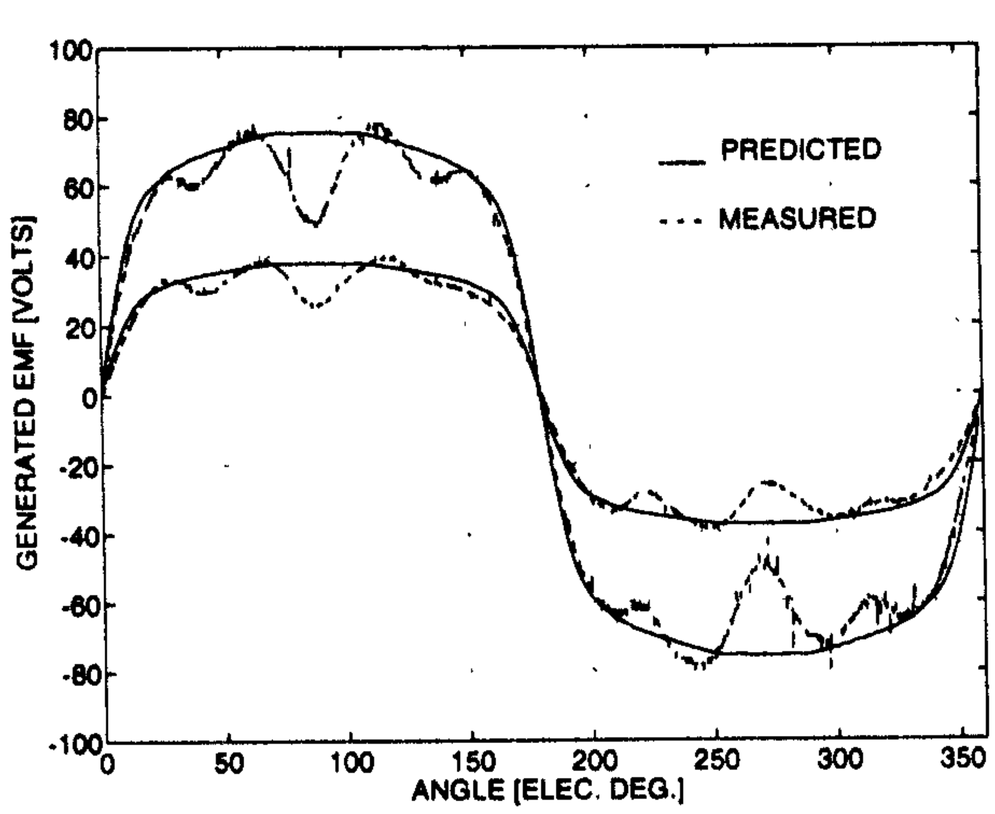

Fig. 19. The predicted and the measured generated EMF at 1000 and 2000 rpm.

The measurements were carried out at no-load by driving the machine from a brushless PM motor at different speeds. The main winding and search coil voltages were captured on a digital storage oscilloscope. The phase flux variation was obtained by integrating the search coil voltages.

D. Generator Characteristics

Fig. 20 shows a typical output of the dynamic test measurements captured on a digital storage oscilloscope. Using the dynamic tests, speed vs. torque (Fig. 21), speed vs. power (Fig. 22) and speed vs. efficiency (Fig. 23) characteristics were obtained.

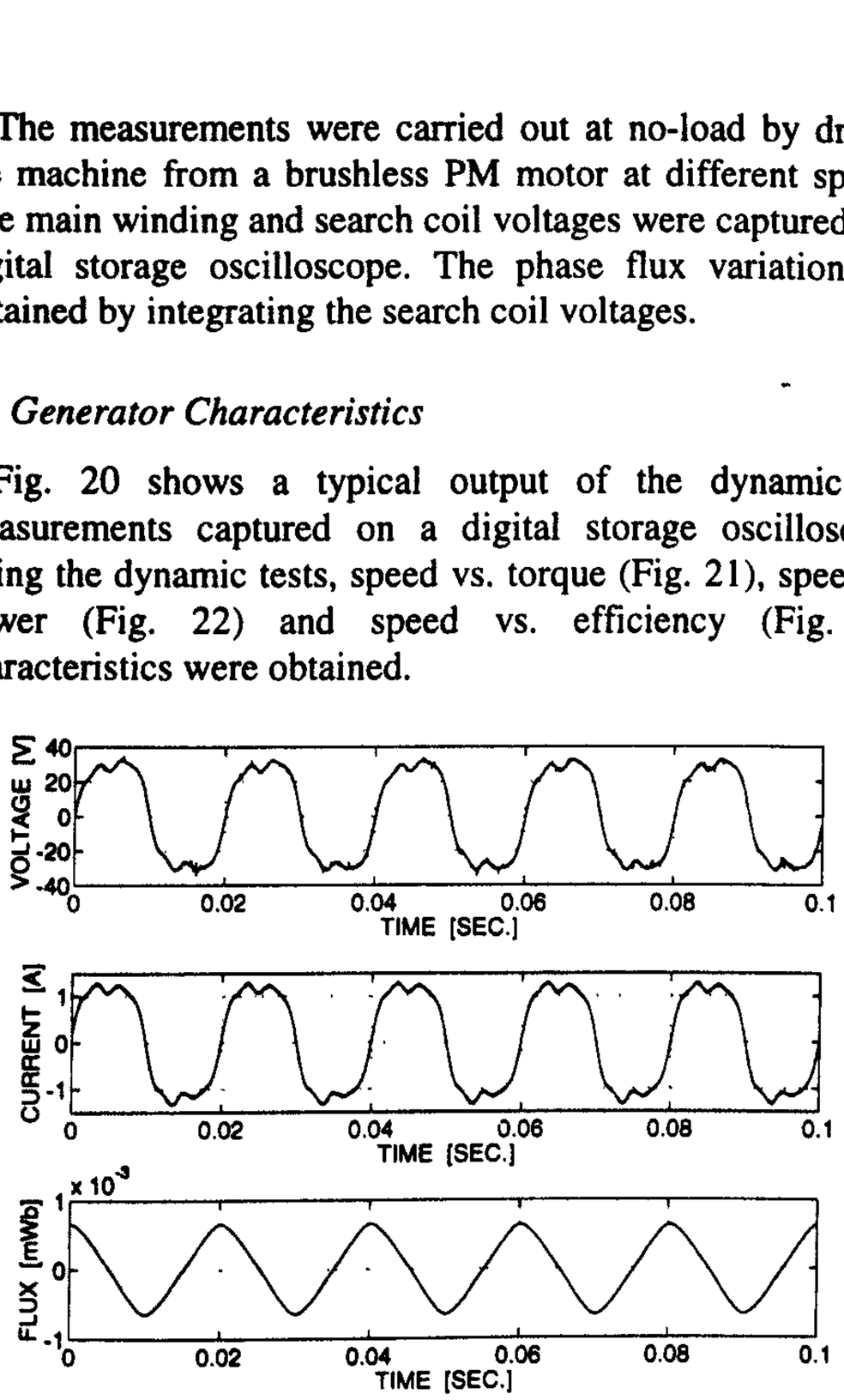

Fig. 20. Typical output of the dynamic test measurements showing generated voltage, current and phase flux variation with a resistive load at 1000 rpm.

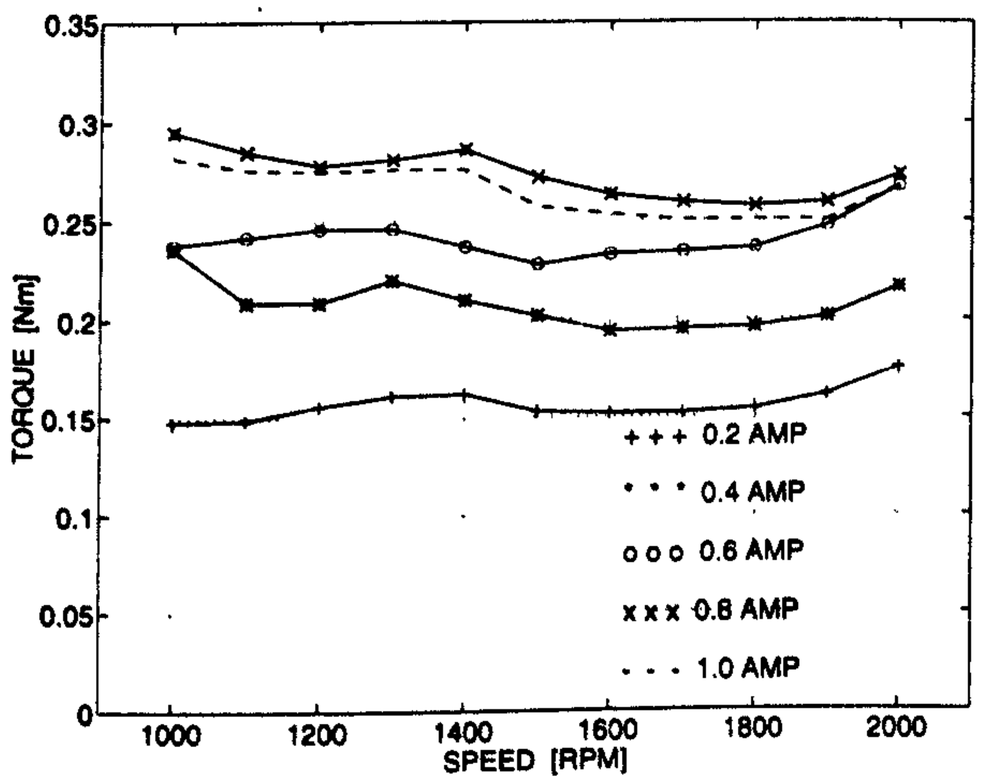

Fig. 21. Generator speed vs. torque characteristics.

The dynamic test set-up was made up of a brushless PM motor driving the generator at different speeds through an in-line torque transducer used for measuring input torque and input power. Output voltage, current and power were measured using a power analyzer. A variable resistive load was used to obtain measurements at different current values.

Fig. 24 shows a snap-shot of the temperature rise curves. The tests were performed by running the generator on constant resistive load for a reasonable length of time.

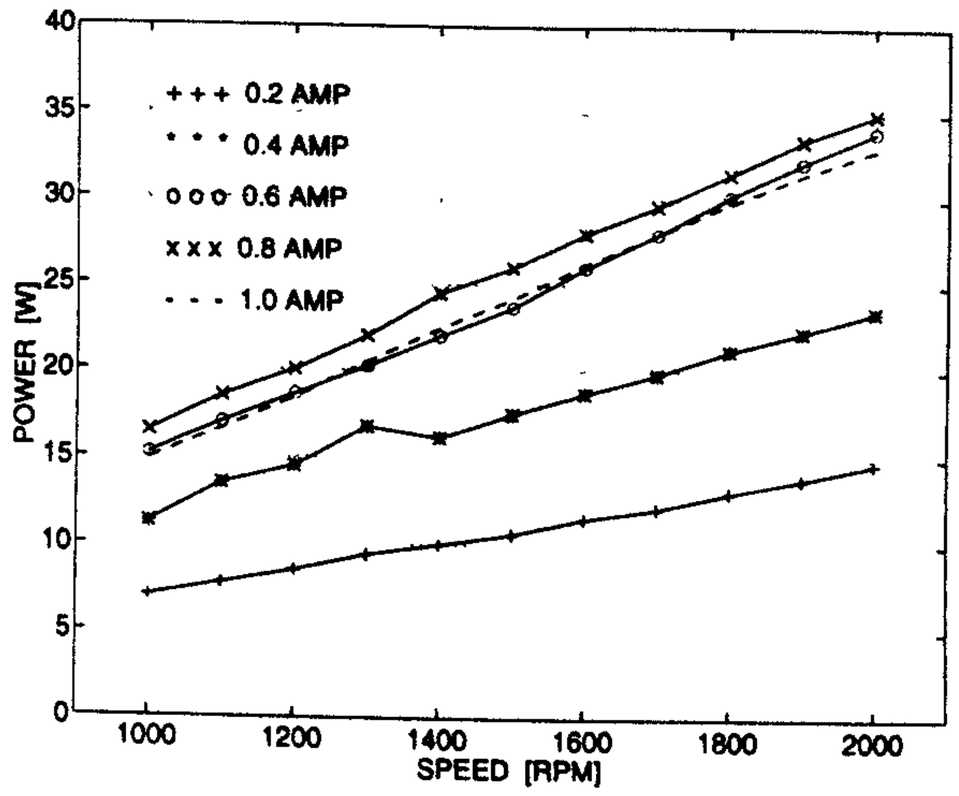

Fig. 22. Generator speed vs. power characteristics.

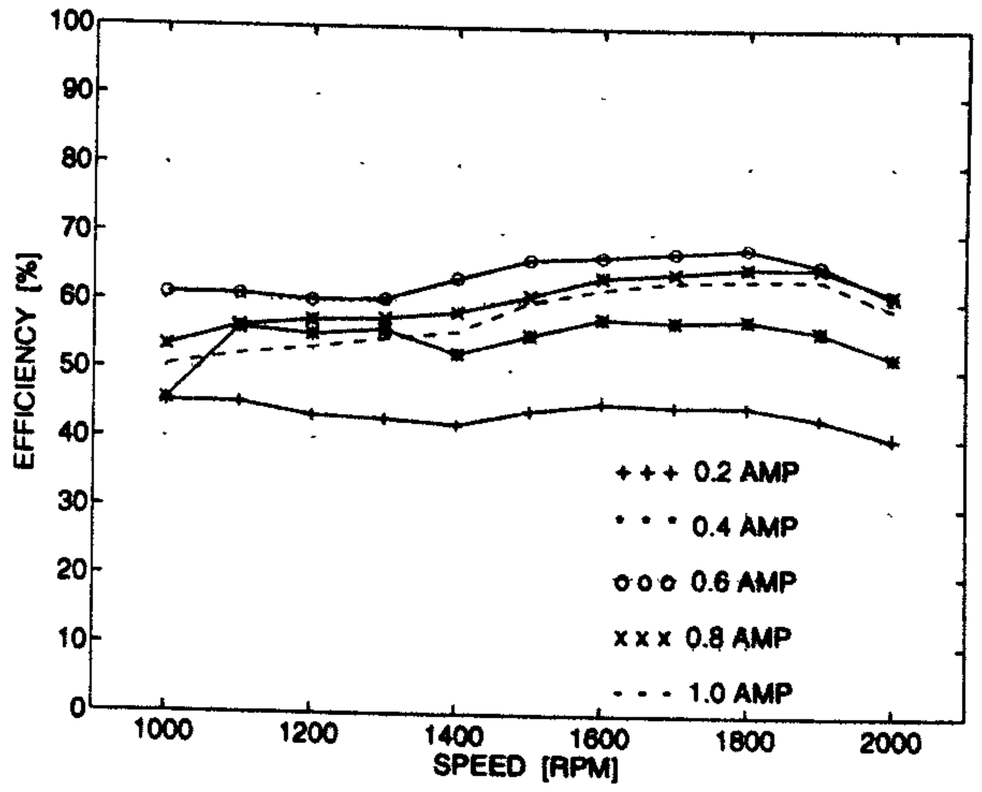

Fig. 23. Generator speed vs. efficiency characteristics.

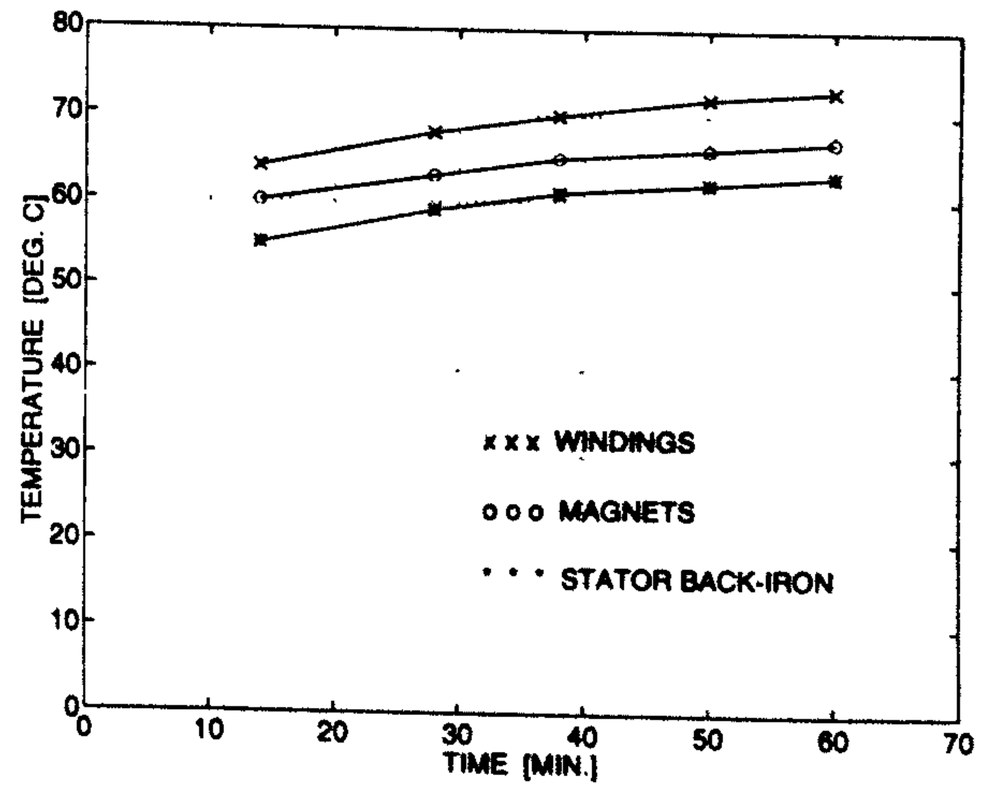

Fig. 24. A snap-shot of the temperature rise measurements in different parts of the generator.

E. Electronic Controller

The complete generator system consisting of the machine and the electronic controller was tested. For this purpose, the generator was loaded, with and without the controller, using fixed resistive loads. The results, as shown in Fig. 25, indicate a good amount of voltage regulation over a wide speed range.

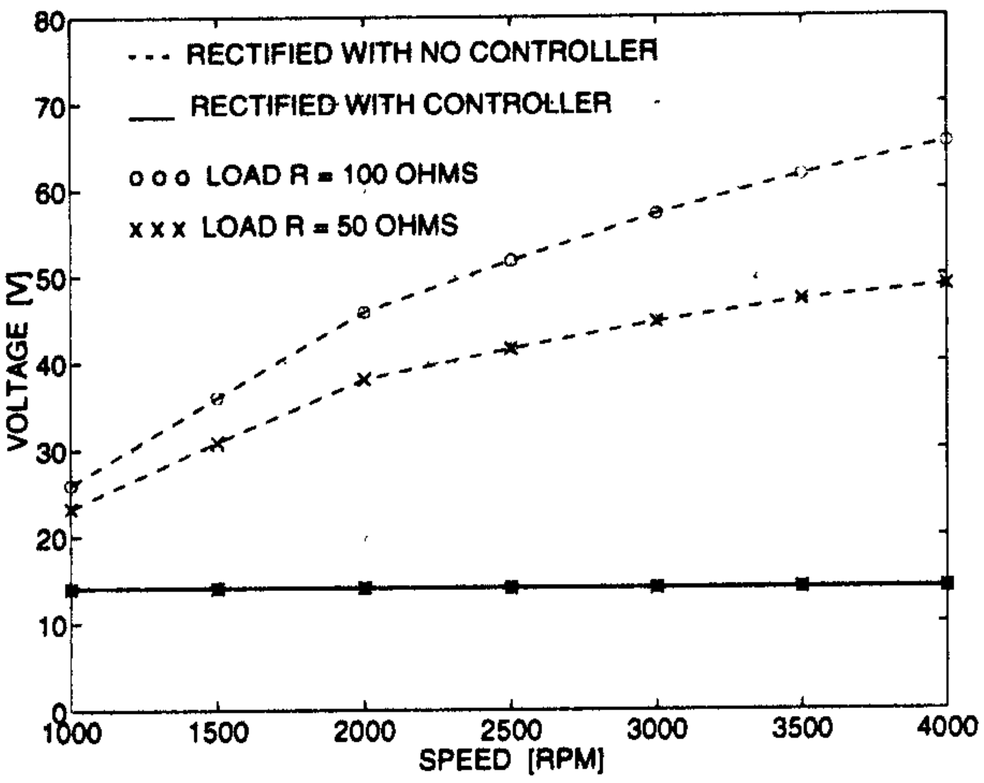

Fig. 25. Controller voltage regulation over a wide speed range.

H. Comments on the Experimental Results

Because of the speed limitations of the dynamic test set-up, the generator was tested only over a limited speed range. The overall agreement between the measured and the predicted results is reasonable. However, imperfections in fabricating the prototype resulted in some amount of localized mismatch in Figs. 15, 16, 18 and 19. Fig. 17 shows that the phase inductance is fairly independent of the rotor position *and* current. The FEA inductance calculations, however, do not include end winding and other leakage inductances. This accounts for the difference between the predicted and the measured results. With the average phase inductance of 69.22 mH and resistance of 6.74 Ω, the electrical time constant of the generator is 10.27 mS. The measured peak cogging torque is 0.41 Nm. Fig. 23 shows a peak generator efficiency of 67.89 %. Since an existing universal motor stator was used, its geometry was not optimized and this resulted in high saturation in stator pole tips as shown in Fig. 5. However, with an overall design optimization, it is possible to lower the inductance, electrical time constant and cogging torque and improve the efficiency.

VII. Discussion

The paper has presented the principle, design, analysis, construction and experimental results for a prototype flux-reversal machine. The main advantages of this machine appear to be;

- Simple and robust rotor construction with low inertia.
- Fault-tolerance capability with its natural isolation between the phases in a multi-phase configuration.
- Small inductance variation with rotor position *and* current.
- High-speed capability due to non-rotating magnets.

With these advantages, the machine can have a considerable potential in the following applications:

- Automotive Generators. Presently, claw-pole alternators are used which have high rotor inertia, limited efficiency and limited ability to respond to sudden load changes.
- Aerospace and Defence. With its robust mechanical construction and high fault-tolerance, the FRM can be a good candidate for many applications in this field.
- Industrial. Fig. 15 shows that the FRM has a phase torque characteristic similar to the BLDCM and hence, in its multi-phase configuration, the FRM can be a high-performance brushless PM motor.

Table II gives a summary of the qualitative comparison between the FRM and the other types of brushless machines in its class.

TABLE II
Comparison of FRM with Other Machine Types

Design Issue	SRM	DSPMM	BLDCM	FRM
Phase flux variation	Unipolar	Unipolar	Bipolar	Bipolar
MMF variation	Unipolar	Bipolar	Bipolar	Bipolar
Energy conversion loop	First quadrant only	First and second quadrant	All four quadrants	All four quadrants
PMs	No PMs	PMs in stator back iron	PMs on the rotor	PMs on the stator tooth faces
High speed capability	Limited by time constant	Limited by time constant	Limited by PM mountings	Limited by time constant
Rotor inertia	Low	Low	High or medium	Low

The future work on the FRM will involve designing and building application-specific machines. This will facilitate direct and quantitative performance comparisons between the FRM and the other competing brushless machines in its class.

Acknowledgements

Financial support from the University of Glasgow, the Committee of Vice-Chancellors and Principles (CVCP), UK, and the SPEED Consortium is gratefully acknowledged. The authors would like to thank J. Kelly for constructing the rotor, W. K. Kom for building the electronics and helping with the measurements and the CAD program, and P. Miller for helping with the prototype construction and the test set-ups.

References

[1] T. J. E. Miller, *Switched reluctance motors and their control*, Magna Physics Publishing/Oxford Science Publications, 1993.

[2] Y. Liao, F. Liang, and T. A. Lipo, "A novel permanent magnet motor with doubly salient structure," *IEEE Trans. on Ind. Appl.*, Vol. 31, No. 5, Sept./Oct. 1995, pp. 1069–1078.

[3] M. Naidu, N. Boules, and R. Henry, "A high-efficiency, high-power generation system for automobiles," *Conf. Rec. of the IEEE Ind. Appl. Soc. Ann. Mtg.*, Vol. 1, Orlando, Florida, Oct. 1995, pp. 709–716.

[4] R. Block and G. Henneberger, "Numerical calculation and simulation of a claw-pole alternator," *Proc. of the Intl. Conf. on Elec. Machines*, Vol. 1, Manchester, UK, Sept. 1992, pp. 127–131.

[5] D. A. Staton, R. P. Deodhar, W. L. Soong, and T. J. E. Miller, "Torque prediction using the flux-MMF diagram in AC, DC and reluctance motors," *IEEE Trans. on Ind. Appl.*, Vol. 32, No. 1, Jan./Feb. 1996, pp. 180–188.

[6] R. P. Deodhar, D. A. Staton, T. M. Jahns and T. J. E. Miller, "Prediction of cogging torque using the flux-MMF diagram technique," *IEEE Trans. on Ind. Appl.*, Vol. 32, No. 3, May/Jun. 1996, in press.

B OPERA-2d Program Listings

This appendix contains listings of programs written in OPERA-2d high-level programming language. These programs form a part of the *PC-BDC–OPERA-2d link program* described in Chapter 1. The following programs are included.

Meshgen.comi

This is pre-processing routine which creates the required fraction of motor cross-section from the PC-BDC input parameters and generates the mesh.

Postfl1.comi

This is a post-processing routine used for obtaining the variation of flux-linkage with rotor position and current for all the motor phases.

Postfl2.comi

This program is called from Postfl1.comi and it calculates the flux-linkage for all the motor phases for a given rotor position and current.

Postcog1.comi

This is a post-processing routine used for obtaining the variation of magnet flux over a cogging torque cycle for all the motor poles.

Postcog2.comi

This program is called from Postcog1.comi and it calculates the magnet flux for all the motor poles at a given rotor position.

Meshgen.comi

```
/+*************************************************************************
/+********** ROUTINE TO GENERATE AN FE MESH FOR BDC MOTOR ****************
/+*************************************************************************
/+************************** R. P. DEODHAR ********************************
/+************* SPEED LABORATORY, UNIVERSITY OF GLASGOW *******************
/+*************************** 14th MAY 1994 *******************************
/+*************************************************************************

$comi mode=cont
unit leng=mm dens=amm2

/+*** INPUT BH DATA
/+*** ============
/+*** VF BHDATA COMMAND SHOULD BE USED TO CREATE THE
/+*** STEEL AND MAGNET DATA FILES

/+*** IN THIS CASE, THE FOLLOWING MATREIAL DATA IS USED:
/+*** (1) STATOR STEEL    - M1929 (M19H.BH)
/+*** (2) ROTOR STEEL     - M1929 (M19H.BH)
/+*** (3) MAGNET          - SINTERED IAS1: RARE-EARTH MATERIAL

/+*** STATOR STEEL
bhdata 4
   load M19H
q
/+*** ROTOR STEEL
bhdata 5
   load M19H
q
/+*** MAGNET MATERIAL
bhdata 6
   load IAS1
q

/+**** SET UP USEFUL CONVERSION FACTORS
$cons #D2R pi/180
$cons #R2D 180/pi

/$$$$$$$$$$$$$$$$$$$$$$$$$$$$$$$$$$$$$$$$$$$$$$$$$$$$$$$$$$$$$$$$$$$$$$$$$$
/$$$$$$$$$$$$$$$$$$$$$$$$ IMPORTANT SETTINGS $$$$$$$$$$$$$$$$$$$$$$$$$$$$$
/$$$$$$$$$$$$$$$$$$$$$$$$$$$$$$$$$$$$$$$$$$$$$$$$$$$$$$$$$$$$$$$$$$$$$$$$$$

/+**** Rotp Minimum Angle By Which Rotor can be Rotated
/+****      ie. Airgap Element Spacing in degrees

/+**** material types are : 0=air, 4=stator stee,l 5=rotor steel, 6=magnet
/+**** Msh  - material type number for shaft
/+**** Mden  measure of the density of nodes (higher number = higher density)
/+**** ++++++++++++++++++++++++++++++++++++++++++++++++++++++++++++++++++++
/+**** +   (1)   (1/2 SLOT PITCH ANGLE) / Rotp  SHOULD BE INTEGER   +
/+**** +   (2)   (1/2 POLE PITCH ANGLE) / Rotp  SHOULD BE INTEGER   +
/+**** +   (3)   Rang / Rotp SHOULD BE INTEGER                      +
/+**** ++++++++++++++++++++++++++++++++++++++++++++++++++++++++++++++++++++

$cons #Rotp 0.5
$cons #Mden 1.0
$cons #Msh  0

/$$$$$$$$$$$$$$$$$$$$$$$$$$$$$$$$$$$$$$$$$$$$$$$$$$$$$$$$$$$$$$$$$$$$$$$$$$
/$$$$$$$$$$$$$$$$$$$$$$$$ MOTOR DIMENSIONAL DATA $$$$$$$$$$$$$$$$$$$$$$$$$$
/$$$$$$$$$$$$$$$$$$$$$$$$$$$$$$$$$$$$$$$$$$$$$$$$$$$$$$$$$$$$$$$$$$$$$$$$$$
/+**** N.B. As close as possible this is the same as that given in PC-BDC
/+**** RadS - Shaft Radius
/+**** Lm   - Magnet radial thickness
```

```
/+**** Rad1 - Rotor surface radius
/+**** Rad3 - Stator outside radius
/+**** Lstk - Stack length
/+**** Gap  - Airgap length
/+**** BetE - Magnet arc (Electrical Degrees)
/+**** SO   - Slot opening
/+**** SD   - Slot Depth
/+**** TWS  - Tooth widt h
/+**** TGD  - Tang Depth
/+**** Tang - Slot opening angle (mech degrees)
/+**** Pole - Number of poles
/+**** Slot - Number of Slots
/+**** RNSQ - 0 = Square; 1 = Round slot bottom
/+**** MTY  - 1 = arc magnet; 3 = breadloaf magnet; 2 = spoke magnet

/+**** NPM  - Number of Poles to be modeled
/+**** NSM  - Number of Slots to be modeled
/+**** BetM - Magnet arc (Mechanical Degrees)

$cons #RadS  20.000
$cons #Lm     8.000
$cons #Rad1  63.017
$cons #Rad3 101.600
$cons #Lstk 203.200
$cons #Gap    0.500
$cons #BetE 150.000
$cons #SO     2.920
$cons #SD    18.542
$cons #TWS    6.350
$cons #TGD    0.762
$cons #Tang  20.000*#D2R
$cons #Pole   4
$cons #Slot  36
$cons #RNSQ   1
$cons #MTY    1
$cons #NSM    9
$cons #NPM    1

$cons #BetM   #BetE/(#Pole/2)

/+************************ SET ROTATION ANGLE *********************************
/+**** Rang - Rotation Angle (Degrees)

cons #Rang 30

/+************************ TEST THAT DATA IS O.K. *****************************
/+**** +++++++++++++++++++++++++++++++++++++++++++++++++++++++++++++++++++++++
/+**** +   (1)   (1/2 SLOT PITCH ANGLE) / Rotp  SHOULD BE INTEGER   +
/+**** +   (2)   (1/2 POLE PITCH ANGLE) / Rotp  SHOULD BE INTEGER   +
/+**** +   (3)   Rang / Rotp SHOULD BE INTEGER                      +
/+**** +   (4)   (No. 1/2 slots modeled) must be INTEGER            +
/+**** ++++++++++++++++++++++++++++++++++++++++++++++++++++++++++++++++++++++++
/+**** Rotp - Spacing of nodes in central region of airgap (Degrees)
/+****       (SET IN DATA FILE)
/+**** Sp2d - Half slot pitch (Degrees)
/+**** Pp2d - Half pole pitch (Degrees)

$cons #Sp2d   pi/#SLOT*#R2D
$cons #Pp2d   180/#Pole
$cons #OK     1

$cons #TST1   mod(#Sp2d;#Rotp)
$cons #TST2   mod(#Pp2d;#Rotp)
$cons #TST3   mod(#Rang;#Rotp)
$cons #TST4   mod(2*#Slot;#Pole)

$IF #TST1 NE 0
   $cons #OK  0
   /+******* ERROR: (1/2 SLOT PITCH ANGLE) / Rotp  NOT INTEGER **********
```

```
$END IF

$IF #TST2 NE 0
   $cons #OK  0
   /+****** ERROR: (1/2 POLE PITCH ANGLE) / Rotp  NOT INTEGER **********
$END IF

$IF #TST3 NE 0
   $cons #OK  0
   /+****** ERROR: (ROTATION ANGLE) / Rotp  NOT INTEGER **********
$END IF

$IF #TST4 NE 0
   $cons #OK  0
   /+****** ERROR: NUMBER OF 1/2 SLOTS MODELED IS NOT INTEGER **********
$END IF

/+**** end program if OK = 0

$IF #OK NE 1
   end
   y
$END IF

/+**** SET ELEMENT TYPE (LINEAR/QUADRATIC)
set elem=line

/+*************************************************************************
/+******************* SET UP SCALING FOR OUTLINE PLOT **********************
/+*************************************************************************

$cons #xmin 0
$cons #xmax #Rad3
$cons #ymin 0
$cons #ymax #xmax

/   $IF #NSM GT #Slot/4
/      $cons #xmin -#xmax
/      $cons #ymin -#ymax
/   $ENDIF

reco xmin=#xmin ymin=#ymin xmax=#xmax ymax=#ymax label=no
reco

/+*************************************************************************
/+************************** AIRGAP DATA **********************************
/+*************************************************************************
/+**** There are 4 layers in the gap.
/+**** Sgr and Sgt define the polar coordinates of the 3 nodes on the
/+**** stator surface over the 1st half slot slot pitch
/+**** Rad1 - Rotor Outer Radius
/+**** Rgm  - Centre of Airgap Radius
/+**** Rgs  - Airgap Layer Closer to Stator
/+**** Rgr  - Airgap Layer Closer to Rotor

$cons #Rgm  #Rad1+0.50*#Gap
$cons #Rgs  #Rad1+0.75*#Gap
$cons #Rgr  #Rad1+0.25*#Gap

/+*************************************************************************
/+************************** CREATE STATOR ********************************
/+*************************************************************************
/+**** THE STATOR IS CREATED BY REFLECTION AND ROTATION OF THE BASIC
/+**** BUILDING BLOCK (HALF A SLOT PITCH).
/+**** SEE FIG. 18 FOR DIAGRAM OF THE BASIC STATOR BUILDING BLOCKS

/+**** STATOR CONSTANTS:
/+**** Rad2 - Radius to slot bottom (Rad2 = Rad1 + Gap + TGD + SD)
/+**** Nmod - Number of HALF slots modelled (MUST BE INTEGER)
```

```
/+**** NSM  - Number of Slots modeled (SET IN DATA.CMI)
/+**** Bore - Stator Inner Radius
/+**** Sp2  - Half slot pitch (Radians)
/+**** Sp2d - Half slot pitch (Degrees)
/+**** RSB  - Radius of Slot Bottom (curve section radius)
/+**** Std  - Slot Tang Depth (Fslot+Eslot)
/+**** Sreg - Number of regions in half a slot (4)
/+****        (This normally includes the outer airgap layer)
/+****        In this particular program outer airgap layer is created
/+****        separately at the end of this program hence Sreg DOES NOT
/+****        include outer airgap layer.

$cons #Nmod   #NSM*2
$cons #Bore   #Rad1+#Gap
$cons #Rad2   #Bore+#TGD+#SD
$cons #Sp2    pi/#SLOT
$cons #Sp2d   pi/#SLOT*#R2D

/+****        refer to the hand drawn sketch for definition of x0

$cons #x0     #TWS/2/sin(#Sp2)
$IF #RNSQ EQ 1
   $cons #RSB    sin(#Sp2)*(#Rad2-#x0)/(1+sin(#Sp2))
$ELSE
   $cons #RSB    0
$END IF

$cons #Std    ((#Bore+#TGD)*tan(#Sp2)-#TWS/2-#So/2)*tan(#Tang)+#TGD

/+****        Sreg is set to 3 because outer airgap layer is not included
/+****        in the basic stator building block.

$cons #Sreg   4

/+***** POLAR/CARTESIAN COORDINATES OF STATOR HALF SLOT
/+***** Sr? ; St? : POLAR COORDINATES OF STATOR NODES (SEE FIG. 1)
/+***** Sx? ; Sy? : CARTESIAN COORDINATES OF STATOR NODES (SEE FIG. 1)
/+***** Sn??      : SPECIFIES THE NUMBER OF ELEMENTS ON THE FACE BETWEEM
/+*****            THE TWO SPECIFIED NODES (E.G. Sn46 = 5*#Mden,
/+*****            THERE ARE 5*Mden ELEMENTS ON THE FACE BETWEEN NODES
/+*****            4 AND 6)
/+***** SEE FIG. 18 FOR LOCATION OF STATOR NODES

$cons #Sr1    #Bore
$cons #Sr2    #Bore
$cons #Sr3    #Bore
$cons #Sr4    #Bore+#Std
$cons #Sx5    #Sr4
$cons #Sr6    #Bore+#Sd+#TGD
$cons #Sr7    #Rad3
$cons #Sr8    #Rad3
$IF #RNSQ EQ 1
   $cons #Sx9    #Sr6-#RSB-#RSB*sin(#Sp2)
$ELSE
   $cons #Sx9    (#Sr6-#x0)*cos(#Sp2)+#x0
$END IF
$cons #Sxa    #Bore+#TGD
$cons #Srb    #Rgs
$cons #Src    #Rgs

$cons #St1    #Sp2d
$cons #St2    asin(#So/(2*#Bore))*#R2D
$cons #St3    0
$cons #St4    0
$cons #Sy5    #Sx5*tan(#Sp2)-(#TWS/2)/cos(#Sp2)
$cons #St6    0
$cons #St7    0
$cons #St8    #Sp2d
$IF #RNSQ EQ 1
```

```
   $cons #Sy9     #Sx9*tan(#Sp2)-(#TWS/2)/cos(#Sp2)
$ELSE
   $cons #Sy9     (#Sr6-#x0)*sin(#Sp2)
$END IF
$cons #Sya     #So/2              -
$cons #Stb     #Sp2d
$cons #Stc     0

/+***** STATOR MESH GRADING CONSTANTS

$cons #Sn12    (#St1-#St2)/#Rotp*0.6*#Mden
$cons #Sn23    #St2/#Rotp*0.6*#Mden
$cons #Sn34    2*#Mden
$cons #Sn46    5*#Mden
$cons #Sn67    2*#Mden
$cons #Sn78    3*#Mden
$cons #Sn18    8*#Mden
$cons #Sn5a    3*#Mden
$cons #Sn45    4*#Mden
$cons #Sn59    6*#Mden
$cons #Sn69    3*#Mden
$cons #Sn2a    2*#Mden
$cons #Snbc    %int(#Sp2d/#Rotp)

/+***** CONSTRUCT BASIC STATOR BLOCKS (4 IN ALL)

/+***** region (1) (STATOR STEEL)

$IF #RNSQ EQ 1
draw poly mate=4
     pola #Sr6    #St6
     pola #Sr7    #St7     n=#Sn67   c=0.0       b=0.5    f=NO
     pola #Sr8    #St8     n=#Sn78   c=-1/#Sr8   b=0.5    f=V
     pola #Sr1    #St1     n=#Sn18   c=0.0       b=0.7    f=NO
     pola #Sr2    #St2     n=#Sn12   c=1/#Sr1    b=0.5    f=NO
     cart #Sxa    #Sya     n=#Sn2a   c=0.0       b=0.5    f=NO
     cart #Sx5    #Sy5     n=#Sn5a   c=0.0       b=0.5    f=NO
     cart #Sx9    #Sy9     n=#Sn59   c=0.0       b=0.3    f=NO
     fini                  n=#Sn69   c=1/#RSB    b=0.5    f=NO
q

$ELSE
draw poly mate=4
     pola #Sr6    #St6
     pola #Sr7    #St7     n=#Sn67   c=0.0       b=0.5    f=NO
     pola #Sr8    #St8     n=#Sn78   c=-1/#Sr8   b=0.5    f=V
     pola #Sr1    #St1     n=#Sn18   c=0.0       b=0.7    f=NO
     pola #Sr2    #St2     n=#Sn12   c=1/#Sr1    b=0.5    f=NO
     cart #Sxa    #Sya     n=#Sn2a   c=0.0       b=0.5    f=NO
     cart #Sx5    #Sy5     n=#Sn5a   c=0.0       b=0.5    f=NO
     cart #Sx9    #Sy9     n=#Sn59   c=0.0       b=0.3    f=NO
     fini                  n=#Sn69   c=1/#Sx9    b=0.5    f=NO
q
$END IF

/+***** region (2) (STATOR AIR-SPACE - SLOT WEDGE AREA)
draw poly mate=0
     pola #Sr3    #St3
     pola #Sr4    #St4     n=#Sn34   c=0.0       b=0.5    f=NO
     cart #Sx5    #Sy5     n=#Sn45   c=0.0       b=0.5    f=NO
     cart #Sxa    #Sya     n=#Sn5a   c=0.0       b=0.5    f=NO
     pola #Sr2    #St2     n=#Sn2a   c=0.0       b=0.5    f=NO
     fini                  n=#Sn23   c=1/#Sr2    b=0.5    f=NO
q

/+***** region (3) (CONDUCTOR)

$IF #RNSQ EQ 1
draw poly mate=1
```

```
      pola #Sr4    #St4
      pola #Sr6    #St6    n=#Sn46   c=0.0       b=0.5    f=NO
      cart #Sx9    #Sy9    n=#Sn69   c=-1/#RSB   b=0.5    f=NO
      cart #Sx5    #Sy5    n=#Sn59   c=0.0       b=0.7    f=NO
      fini                 n=#Sn45   c=0..0      b=0.5    f=NO
q

$ELSE
draw poly mate=1
      pola #Sr4    #St4
      pola #Sr6    #St6    n=#Sn46   c=0.0       b=0.5    f=NO
      cart #Sx9    #Sy9    n=#Sn69   c=-1/#Sx9   b=0.5    f=NO
      cart #Sx5    #Sy5    n=#Sn59   c=0.0       b=0.7    f=NO
      fini                 n=#Sn45   c=0.0       b=0.5    f=NO
q
$END IF

/+***** region (4) (OUTER AIRGAP LAYER)

draw poly mate=0
      pola #Sr1    #St1
      pola #Srb    #Stb    n=1       c=0.0       b=0.5    f=NO
      pola #Src    #Stc    n=#Snbc   c=1/#Src    b=0.5    f=NO
      pola #Sr3    #St3    n=1       c=0.0       b=0.5    f=NO
      pola #Sr2    #St2    n=#Sn23   c=-1/#Sr2   b=0.5    f=NO
      fini                 n=#Sn12   c=-1/#Sr2   b=0.5    f=NO
q

/+***** MIRROR HALF SLOT TO CREATE FULL SLOT PITCH

copy reg1=1 reg2=%int(#Sreg) t=#Sp2d

/+***** CREATE REQUIRED SECTION OF MOTOR BY MULTIPLE ROTATIONS

$do #i 1 #Nmod/2-1 1
   copy reg1=1 reg2=%int(2*#Sreg) t=#i*#Sp2d*2 MIRR=no
$end do

/+***** SET UP THE PERIODIC BOUNDARY CONDITIONS ON THE STATOR
/+***** THE REGIONS ON THE x=0 AND y=0 SURFACES MUST BE RE-CREATED
/+***** IF THE NUMBER OF SLOTS TO BE MODELLED IS EQUAL TO THE TOTAL
/+*****    NUMBER OF SLOTS THEN PERIDICITY IS NOT REQUIRED

$IF #NSM NE #Slot
   erase reg1=%int((#Nmod-1)*#Sreg+1) reg2=%int(#Nmod*#Sreg)
   erase reg1=1 reg2=%int(#Sreg)

/+***** region (1) (STATOR STEEL)

   $IF #RNSQ EQ 1
   draw poly mate=4
        pola #Sr6    #St6
        pola #Sr7    #St7    n=#Sn67   c=0.0       b=0.5    f=SYMM
        pola #Sr8    #St8    n=#Sn78   c=-1/#Sr8   b=0.5    f=V
        pola #Sr1    #St1    n=#Sn18   c=0.0       b=0.7    f=NO
        pola #Sr2    #St2    n=#Sn12   c=1/#Sr1    b=0.5    f=NO
        cart #Sxa    #Sya    n=#Sn2a   c=0.0       b=0.5    f=NO
        cart #Sx5    #Sy5    n=#Sn5a   c=0.0       b=0.5    f=NO
        cart #Sx9    #Sy9    n=#Sn59   c=0.0       b=0.3    f=NO
        fini                 n=#Sn69   c=1/#RSB    b=0.5    f=NO
q
$ELSE
draw poly mate=4
        pola #Sr6    #St6
        pola #Sr7    #St7    n=#Sn67   c=0.0       b=0.5    f=SYMM
        pola #Sr8    #St8    n=#Sn78   c=-1/#Sr8   b=0.5    f=V
        pola #Sr1    #St1    n=#Sn18   c=0.0       b=0.7    f=NO
        pola #Sr2    #St2    n=#Sn12   c=1/#Sr1    b=0.5    f=NO
        cart #Sxa    #Sya    n=#Sn2a   c=0.0       b=0.5    f=NO
```

```
      cart #Sx5   #Sy5    n=#Sn5a  c=0.0      b=0.5   f=NO
      cart #Sx9   #Sy9    n=#Sn59  c=0.0      b=0.3   f=NO
      fini                n=#Sn69  c=1/#Sx9   b=0.5   f=NO
   q
   $END IF

/+***** region (2) (STATOR AIR-SPACE - SLOT WEDGE AREA)
   draw poly mate=0
      pola #Sr3   #St3
      pola #Sr4   #St4     n=#Sn34  c=0.0      b=0.5   f=SYMM
      cart #Sx5   #Sy5     n=#Sn45  c=0.0      b=0.5   f=NO
      cart #Sxa   #Sya     n=#Sn5a  c=0.0      b=0.5   f=NO
      pola #Sr2   #St2     n=#Sn2a  c=0.0      b=0.5   f=NO
      fini                 n=#Sn23  c=1/#Sr2   b=0.5   f=NO
   q

/+***** region (3) (CONDUCTOR)

   $IF #RNSQ EQ 1
   draw poly mate=1
      pola #Sr4   #St4
      pola #Sr6   #St6    n=#Sn46  c=0.0      b=0.5   f=SYMM
      cart #Sx9   #Sy9    n=#Sn69  c=-1/#RSB  b=0.5   f=NO
      cart #Sx5   #Sy5    n=#Sn59  c=0.0      b=0.7   f=NO
      fini                n=#Sn45  c=0.0      b=0.5   f=NO
   q
   $ELSE
   draw poly mate=1
      pola #Sr4   #St4
      pola #Sr6   #St6    n=#Sn46  c=0.0      b=0.5   f=SYMM
      cart #Sx9   #Sy9    n=#Sn69  c=-1/#Sx9  b=0.5   f=NO
      cart #Sx5   #Sy5    n=#Sn59  c=0.0      b=0.7   f=NO
      fini                n=#Sn45  c=0.0      b=0.5   f=NO
   q
   $END IF

/+***** region (4) (OUTER AIRGAP LAYER)
   draw poly mate=0
      pola #Sr1   #St1
      pola #Srb   #Stb    n=1      c=0.0      b=0.5   f=NO
      pola #Src   #Stc    n=#Snbc  c=1/#Src   b=0.5   f=NO
      pola #Sr3   #St3    n=1      c=0.0      b=0.5   f=SYMM
      pola #Sr2   #St2    n=#Sn23  c=-1/#Sr2  b=0.5   f=NO
      fini                n=#Sn12  c=-1/#Sr2  b=0.5   f=NO
   q

   $cons #R1 ((#Nmod-2)*#Sreg+1)
   $cons #R2 ((#Nmod-2)*#Sreg+#Sreg)
   copy  reg1=%int(#R1) reg2=%int(#R2) t=45 MIRR=yes

$END IF

/=============================================================================
/+++++ SET UP THE RELEVANT CURRENT DENSITY LEVELS IN THE SLOTS

/+++++ Rang = angle by which rotor is rotated in mechanical degrees
/+++++ Cang = angle by which current phasor leads rotor q-axis in
/+++++              electrical degrees
/+++++ Aoff = angle by which rotor q-axis is offset from stator +ve
/+++++              x-axis in electrical degrees
/+++++ curr = rms phase current in amperes
/+++++ turn = number of conductors per coil
/+++++ Pol2 = poles divided by 2

$cons #Cang 0

$cons #curr 1.0
$cons #Turn 8
$cons #Pol2 2
```

```
$cons #Aoff 90

$cons #cosA  cos(#Pol2*#Rang*#D2R+#Cang*#D2R+#Aoff*#D2R-0*#D2R)
$cons #cosB  cos(#Pol2*#Rang*#D2R+#Cang*#D2R+#Aoff*#D2R-240*#D2R)
$cons #cosC  cos(#Pol2*#Rang*#D2R+#Cang*#D2R+#Aoff*#D2R-120*#D2R)

$cons #AmpA sqrt(2)*#curr*#cosA
$cons #AmpB sqrt(2)*#curr*#cosB
$cons #AmpC sqrt(2)*#curr*#cosC

/+****** Lap winding

/+calculate total area of half slot, note that must use some operation
/+using "area" in order to set its value

modi reg1=67  reg2=67  dens=area

$cons #atot  area

modi reg1=67  reg2=67  dens=-#Turn/2*#AmpB/#atot+#Turn/2*#AmpC/#atot

modi reg1=3   reg2=3   dens=-#Turn/2*#AmpB/#atot+#Turn/2*#AmpC/#atot
modi reg1=7   reg2=7   dens=-#Turn/2*#AmpB/#atot+#Turn/2*#AmpC/#atot

modi reg1=11  reg2=11  dens=-#Turn/2*#AmpB/#atot+#Turn/2*#AmpA/#atot
modi reg1=15  reg2=15  dens=-#Turn/2*#AmpB/#atot+#Turn/2*#AmpA/#atot

modi reg1=19  reg2=19  dens=-#Turn/2*#AmpB/#atot+#Turn/2*#AmpA/#atot
modi reg1=23  reg2=23  dens=-#Turn/2*#AmpB/#atot+#Turn/2*#AmpA/#atot

modi reg1=27  reg2=27  dens=-#Turn/2*#AmpB/#atot+#Turn/2*#AmpA/#atot
modi reg1=31  reg2=31  dens=-#Turn/2*#AmpB/#atot+#Turn/2*#AmpA/#atot

modi reg1=35  reg2=35  dens=-#Turn/2*#AmpC/#atot+#Turn/2*#AmpA/#atot
modi reg1=39  reg2=39  dens=-#Turn/2*#Ampc/#atot+#Turn/2*#AmpA/#atot

modi reg1=43  reg2=43  dens=-#Turn/2*#AmpC/#atot+#Turn/2*#AmpA/#atot
modi reg1=47  reg2=47  dens=-#Turn/2*#Ampc/#atot+#Turn/2*#AmpA/#atot

modi reg1=51  reg2=51  dens=-#Turn/2*#AmpC/#atot+#Turn/2*#AmpA/#atot
modi reg1=55  reg2=55  dens=-#Turn/2*#Ampc/#atot+#Turn/2*#AmpA/#atot

modi reg1=59  reg2=59  dens=-#Turn/2*#AmpC/#atot+#Turn/2*#AmpB/#atot
modi reg1=63  reg2=63  dens=-#Turn/2*#Ampc/#atot+#Turn/2*#AmpB/#atot

modi reg1=71  reg2=71  dens=-#Turn/2*#AmpC/#atot+#Turn/2*#AmpB/#atot

/=============================================================================

/+**** N.B.: THE TOTAL NUMBER OF REGIONS IN THE STATOR IS EQUAL TO:
/+****       Nmod*Sreg

/+*************************************************************************
/+************************** CREATE ROTOR *********************************
/+*************************************************************************
/+**** THE ROTOR IS CREATED BY REFLECTION OF THE BASIC
/+**** BUILDING BLOCK (HALF A POLE PITCH).
/+**** SEE FIG. 19 FOR DIAGRAM OF THE BASIC ROTOR BUILDING BLOCKS

/+**** ROTOR CONSTANTS:
/+**** Rreg - Number of regions in 1/2 pole pitch of rotor
/+****       (This includes the inner airgap layer)
/+****       (there are 5 in this case)

/+***** POLAR COORDINATES OF ROTOR HALF POLE
/+***** Rr? ; Rt? : POLAR COORDINATES OF ROTOR NODES (SEE FIG. 2)
/+***** Rn??      : SPECIFIES THE NUMBER OF ELEMENTS ON THE FACE BETWEEM
/+*****            THE TWO SPECIFIED NODES (E.G. Rn16 = 4*#Mden,
/+*****            THERE ARE 4*Mden ELEMENTS ON THE FACE BETWEEN NODES
```

```
/+*****                1 AND 6)
/+***** SEE FIG. 19 FOR LOCATION OF ROTOR NODES
/+***** pp2  - half pole pitch (radians)
/+***** pp2d - half pole pitch (degrees)

$cons #pp2  pi/#Pole
$cons #pp2d 180/#Pole

$cons #Rreg 5
$cons #Rr1  0.0
$cons #Rr2  #RadS
$cons #Rr3  #Rad1-#Lm
$cons #Rr4  #Rad1
$cons #Rr5  #Rgr
$cons #Rr6  #RadS
$cons #Rr7  #Rad1
$cons #Rr8  #Rgr
$IF #MTY EQ 1
   $cons #Rr9  #Rad1-#Lm
$END IF
$IF #MTY EQ 3
   $cons #Rx9  #Rr3
$END IF
$cons #Rra  #Rad1
$IF #MTY EQ 1
   $cons #Rrb  #Rad1-#Lm
$END IF
$IF #MTY EQ 3
   $cons #Rrb  #Rad1*sin(#BetM/2*#D2R)/sin(#pp2)
$END IF

$cons #Rt1  0.0
$cons #Rt2  0.0
$cons #Rt3  0.0
$cons #Rt4  0.0
$cons #Rt5  0.0
$cons #Rt6  180/#POLE
$cons #Rt7  180/#POLE
$cons #Rt8  180/#POLE
$IF #MTY EQ 1
   $cons #Rt9  #BetM/2
$END IF
$IF #MTY EQ 3
   $cons #Ry9  #Rad1*sin(#BetM/2*#D2R)
$END IF
$cons #Rta  #BetM/2
$cons #Rtb  #pp2*#R2D

/+***** ROTOR MESH GRADING CONSTANTS

$cons #Rn12 3*#Mden
$cons #Rn16 3*#Mden
$cons #Rn26 5*#Mden
$cons #Rn23 4*#Mden
$cons #Rn6b 4*#Mden
$cons #Rn34 4*#Mden
$cons #Rn9a 4*#Mden
$cons #Rn7b 4*#Mden
$cons #Rn45 1
$cons #Rn78 1
$cons #Rn4a #BetM/2/#Rotp*0.6*#Mden
$cons #Rn39 #BetM/2/#Rotp*0.25*#Mden
$cons #Rn7a ((180/#POLE)-#BetM/2)/#Rotp*0.6*#Mden
$cons #Rn9b ((180/#POLE)-#BetM/2)/#Rotp*0.25*#Mden
$cons #Rn58 (180/#POLE)/#Rotp

/+***** CONSTRUCT BASIC ROTOR BLOCKS (5 IN ALL)

$IF #NSM NE #Slot
```

```
/+***** (1) SHAFT
   draw poly mate=#Msh xcen=0 ycen=0 angle=-#Rang
        pola #Rr1    #Rt1
        pola #Rr2    #Rt2    n=#Rn12  c=0        b=0.5   f=SYMM
        pola #Rr6    #Rt6    n=#Rn26  c=-1/#Rr2  b=0.5   f=NO
        fini                 n=#Rn16  c=0        b=0.5   f=NO
   q

/+***** (2) CORE
   $IF #MTY EQ 1
      draw poly mate=5 xcen=0 ycen=0 angle=-#Rang
           pola #Rr2    #Rt2
           pola #Rr3    #Rt3    n=#Rn23  c=0        b=0.5   f=SYMM
           pola #Rr9    #Rt9    n=#Rn39  c=-1/#Rr9  b=0.5   f=NO
           pola #Rrb    #Rtb    n=#Rn9b  c=-1/#Rr9  b=0.5   f=NO
           pola #Rr6    #Rt6    n=#Rn6b  c=0        b=0.5   f=NO
           fini                 n=#Rn26  c=1/#Rr2   b=0.5   f=NO
      q
   $END IF
   $IF #MTY EQ 3
      draw poly mate=5 xcen=0 ycen=0 angle=-#Rang
           pola #Rr2    #Rt2
           pola #Rr3    #Rt3    n=#Rn23  c=0        b=0.5   f=SYMM
           cart #Rx9    #Ry9    n=#Rn39  c=0        b=0.5   f=NO
           pola #Rrb    #Rtb    n=#Rn9b  c=0        b=0.5   f=NO
           pola #Rr6    #Rt6    n=#Rn6b  c=0        b=0.5   f=NO
           fini                 n=#Rn26  c=1/#Rr2   b=0.5   f=NO
      q
   $END IF

/+***** (3) REGION BETWEEN MAGNET ARCS

   $IF #MTY EQ 1
      draw poly mate=0 xcen=0 ycen=0 angle=-#Rang
           pola #Rr9    #Rt9
           pola #Rra    #Rta    n=#Rn9a  c=0        b=0.5   f=NO
           pola #Rr7    #Rt7    n=#Rn7a  c=-1/#Rr7  b=0.5   f=NO
           pola #Rrb    #Rtb    n=#Rn7b  c=0        b=0.5   f=NO
           fini                 n=#Rn9b  c=1/#Rr9   b=0.5   f=NO
      q
   $END IF
   $IF #MTY EQ 3
      draw poly mate=0 xcen=0 ycen=0 angle=-#Rang
           cart #Rx9    #Ry9
           pola #Rra    #Rta    n=#Rn9a  c=0        b=0.5   f=NO
           pola #Rr7    #Rt7    n=#Rn7a  c=-1/#Rr7  b=0.5   f=NO
           pola #Rrb    #Rtb    n=#Rn7b  c=0        b=0.5   f=NO
           fini                 n=#Rn9b  c=0        b=0.5   f=NO
      q
   $END IF

/+***** (4) MAGNET

      $IF #MTY EQ 1
         draw poly mate=6 xcen=0 ycen=0 angle=-#Rang phase=0-#Rang
              pola #Rr3    #Rt3
              pola #Rr4    #Rt4    n=#Rn34  c=0        b=0.5   f=SYMM
              pola #Rra    #Rta    n=#Rn4a  c=-1/#Rra  b=0.5   f=NO
              pola #Rr9    #Rt9    n=#Rn9a  c=0        b=0.5   f=NO
              fini                 n=#Rn39  c=1/#Rr9   b=0.5   f=NO
         q
      $END IF
      $IF #MTY EQ 3
         draw poly mate=6 xcen=0 ycen=0 angle=-#Rang phase=0-#Rang
              pola #Rr3    #Rt3
              pola #Rr4    #Rt4    n=#Rn34  c=0        b=0.5   f=SYMM
              pola #Rra    #Rta    n=#Rn4a  c=-1/#Rra  b=0.5   f=NO
              cart #Rx9    #Ry9    n=#Rn9a  c=0        b=0.5   f=NO
```

```
         fini                    n=#Rn39   c=0        b=0.5    f=NO
      q
   $END IF


/+**** (5) INNER AIRGAP LAYER

   draw poly mate=0 xcen=0 ycen=0 angle=-#Rang
        pola #Rr4    #Rt4
        pola #Rr5    #Rt5    n=#Rn45  c=0        b=0.5    f=SYMM
        pola #Rr8    #Rt8    n=#Rn58  c=-1/#Rr8  b=0.5    f=NO
        pola #Rr7    #Rt7    n=#Rn78  c=0        b=0.5    f=NO
        pola #Rra    #Rta    n=#Rn7a  c=1/#Rra   b=0.5    f=NO
        fini                 n=#Rn4a  c=1/#Rra   b=0.5    f=NO
      q

   $ELSE

   /+**** (1) SHAFT
      draw poly mate=#Msh xcen=0 ycen=0 angle=-#Rang
           pola #Rr1    #Rt1
           pola #Rr2    #Rt2    n=#Rn12  c=0        b=0.5    f=NO
           pola #Rr6    #Rt6    n=#Rn26  c=-1/#Rr2  b=0.5    f=NO
           fini                 n=#Rn16  c=0        b=0.5    f=NO
      q

   /+**** (2) CORE
      $IF #MTY EQ 1
         draw poly mate=5 xcen=0 ycen=0 angle=-#Rang
              pola #Rr2    #Rt2
              pola #Rr3    #Rt3    n=#Rn23  c=0        b=0.5    f=NO
              pola #Rr9    #Rt9    n=#Rn39  c=-1/#Rr9  b=0.5    f=NO
              pola #Rrb    #Rtb    n=#Rn9b  c=-1/#Rr9  b=0.5    f=NO
              pola #Rr6    #Rt6    n=#Rn6b  c=0        b=0.5    f=NO
              fini                 n=#Rn26  c=1/#Rr2   b=0.5    f=NO
         q
      $END IF
      $IF #MTY EQ 3
         draw poly mate=5 xcen=0 ycen=0 angle=-#Rang
              pola #Rr2    #Rt2
              pola #Rr3    #Rt3    n=#Rn23  c=0        b=0.5    f=NO
              cart #Rx9    #Ry9    n=#Rn39  c=0        b=0.5    f=NO
              pola #Rrb    #Rtb    n=#Rn9b  c=0        b=0.5    f=NO
              pola #Rr6    #Rt6    n=#Rn6b  c=0        b=0.5    f=NO
              fini                 n=#Rn26  c=1/#Rr2   b=0.5    f=NO
         q
      $END IF

   /+**** (3) REGION BETWEEN MAGNET ARCS

      $IF #MTY EQ 1
         draw poly mate=0 xcen=0 ycen=0 angle=-#Rang
              pola #Rr9    #Rt9
              pola #Rra    #Rta    n=#Rn9a  c=0        b=0.5    f=NO
              pola #Rr7    #Rt7    n=#Rn7a  c=-1/#Rr7  b=0.5    f=NO
              pola #Rrb    #Rtb    n=#Rn7b  c=0        b=0.5    f=NO
              fini                 n=#Rn9b  c=1/#Rr9   b=0.5    f=NO
         q
      $END IF
      $IF #MTY EQ 3
         draw poly mate=0 xcen=0 ycen=0 angle=-#Rang
              cart #Rx9    #Ry9
              pola #Rra    #Rta    n=#Rn9a  c=0        b=0.5    f=NO
              pola #Rr7    #Rt7    n=#Rn7a  c=-1/#Rr7  b=0.5    f=NO
              pola #Rrb    #Rtb    n=#Rn7b  c=0        b=0.5    f=NO
              fini                 n=#Rn9b  c=0        b=0.5    f=NO
         q
      $END IF
```

```
/+***** (4) MAGNET

   $IF #MTY EQ 1
      draw poly mate=6 xcen=0 ycen=0 angle=-#Rang phase=0-#Rang
           pola #Rr3    #Rt3
           pola #Rr4    #Rt4    n=#Rn34  c=0        b=0.5   f=NO
           pola #Rra    #Rta    n=#Rn4a  c=-1/#Rra  b=0.5   f=NO
           pola #Rr9    #Rt9    n=#Rn9a  c=0        b=0.5   f=NO
           fini                 n=#Rn39  c=1/#Rr9   b=0.5   f=NO
      q
   $END IF
   $IF #MTY EQ 3
      draw poly mate=6 xcen=0 ycen=0 angle=-#Rang phase=0-#Rang
           pola #Rr3    #Rt3
           pola #Rr4    #Rt4    n=#Rn34  c=0        b=0.5   f=NO
           pola #Rra    #Rta    n=#Rn4a  c=-1/#Rra  b=0.5   f=NO
           cart #Rx9    #Ry9    n=#Rn9a  c=0        b=0.5   f=NO
           fini                 n=#Rn39  c=0        b=0.5   f=NO
      q
   $END IF


/+***** (5) INNER AIRGAP LAYER

   draw poly mate=0 xcen=0 ycen=0 angle=-#Rang
        pola #Rr4    #Rt4
        pola #Rr5    #Rt5    n=#Rn45  c=0        b=0.5   f=NO
        pola #Rr8    #Rt8    n=#Rn58  c=-1/#Rr8  b=0.5   f=NO
        pola #Rr7    #Rt7    n=#Rn78  c=0        b=0.5   f=NO
        pola #Rra    #Rta    n=#Rn7a  c=1/#Rra   b=0.5   f=NO
        fini                 n=#Rn4a  c=1/#Rra   b=0.5   f=NO
   q
$END IF

/+***** CREATE FULL POLE-PITCH ROTOR SECTION

$cons #R1 #Nmod*#Sreg+1
$cons #R2 #Nmod*#Sreg+#Rreg
copy reg1=%int(#R1) reg2=%int(#R2) t=180/#POLE MIRR=yes

/+***** CREATE REQUIRED NUMBER OF ROTOR POLES

/$cons #R1 #Nmod*#Sreg+1
/$cons #R2 #Nmod*#Sreg+#Rreg*2
/$do #i 1 (#NPM-1) 1
/   copy reg1=%int(#R1) reg2=%int(#R2) t=#i*#pp2*2*#R2D MIRR=no
/$end do

reco

/+*************************************************************************
/+********************* CREATE AIRGAP REGIONS *****************************
/+*************************************************************************
/+***** THESE ARE THE REGIONS IN THE INNER TWO LAYERS OF THE AIRGAP
/+***** THE SPACING OF NODES IS SET BY THE VARIABLE Rotp
/+***** THIS IS THE SPACING IN MECHANICAL DEGREES
/+***** THE ROTOR CAN BE ROTATED (Rang) BY ANY MULTIPLE OF Rotp
/+***** FOUR REGIONS ARE REQUIRED SO THAT THE SYMM BOUNDARY CONDITION
/+***** CAN BE SET ON THE APPROPRIATE FACES OF THE AIGAP REGIONS
/+***** IF Rang = 0 IS A SPECIAL CASE WHICH ONLY REQUIRED TWO AIRGAP REGIONS
/+***** SEE FIG. 17 FOR DIAGRAM OF THE BASIC AIRGAP BUILDING BLOCKS

/+***** POLAR COORDINATES OF AIRGAP REGIONS
/+***** Gr? ; Gt? : POLAR COORDINATES OF AIRGAP NODES (SEE FIG. 3)
/+***** Gn1 ; Gn2 : SPECIFIES THE NUMBER OF ELEMENTS ON THE CENTRAL
/+*****             FACES OF THE INNER TWO AIRGAP LAYERS
/+***** SEE FIG. 17 FOR LOCATION OF AIRGAP NODES
/+***** ppd  - pole pitch (mechanical degrees)
/+***** ppmd - pole pitch x Number of poles modeled (mechanical degrees)
```

```
$cons #Gr1  #Rgm
$cons #Gr2  #Rgr
$cons #Gr3  #Rgr
$cons #Gr4  #Rgm
$cons #Gr5  #Rgs
$cons #Gr6  #Rgs
$cons #Gr7  #Rgm
$cons #Gr8  #Rgr
$cons #Gr9  #Rgm
$cons #Gr10 #Rgs

$cons #ppd   #pp2*2*#R2D
$cons #ppmd  #ppd*#NPM
$cons #Gt1  -#Rang
$cons #Gt2  -#Rang
$cons #Gt3  0
$cons #Gt4  0
$cons #Gt5  0
$cons #Gt6  #ppd-#Rang
$cons #Gt7  #ppd-#Rang
$cons #Gt8  #ppd-#Rang
$cons #Gt9  #ppd
$cons #Gt10 #ppd

/+***** AIRGAP MESH GRADING CONSTANTS

$cons #Gn1  #Rang/#Rotp
$cons #Gn2  (#ppd-#Rang)/#Rotp

/+***** CONSTRUCT INNER AIRGAP LAYER REGIONS (4 IN ALL)

$IF #NSM NE #Slot

   $IF #Rang NE 0

/+****** airgap region (1)
   draw poly   mate=0 xcen=0 ycen=0 angle=0
        pola #Gr1   #Gt1
        pola #Gr2   #Gt2   n=1      c=0.0      b=0.5   f=SYMM
        pola #Gr3   #Gt3   n=#Gn1   c=-1/#Gr3  b=0.5   f=NO
        pola #Gr4   #Gt4   n=1      c=0.0      b=0.5
        fini               n=#Gn1   c=1/#Gr4   b=0.5   f=SYMM
   y
   q

/+****** airgap region (2)
   draw poly    mate=0 xcen=0 ycen=0 angle=0
        pola #Gr4   #Gt4
        pola #Gr3   #Gt3   n=1      c=0.0      b=0.5   f=NO
        pola #Gr8   #Gt8   n=#Gn2   c=-1/#Gr3  b=0.5
        pola #Gr7   #Gt7   n=1      c=0.0      b=0.5   f=SYMM
        fini               n=#Gn2   c=1/#Gr4   b=0.5   f=NO
   y
   q

/+****** airgap region (3)
   draw poly    mate=0 xcen=0 ycen=0 angle=0
        pola #Gr5   #Gt5
        pola #Gr4   #Gt4   n=1      c=0.0      b=0.5   f=SYMM
        pola #Gr7   #Gt7   n=#Gn2   c=-1/#Gr7  b=0.5   f=NO
        pola #Gr6   #Gt6   n=1      c=0.0      b=0.5
        fini               n=#Gn2   c=1/#Gr6   b=0.5
   y
   q

/+****** airgap region (4)
   draw poly    mate=0 xcen=0 ycen=0 angle=0
        pola #Gr6   #Gt6
```

```
      pola #Gr7   #Gt7   n=1      c=0.0      b=0.5   f=NO
      pola #Gr9   #Gt9   n=#Gn1   c=-1/#Gr7  b=0.5   f=SYMM
      pola #Gr10  #Gt10  n=1      c=0.0      b=0.5   f=SYMM
      fini               n=#Gn1   c=1/#Gr6   b=0.5   f=NO
   y
   q

   $ELSE

/+***** airgap region (2)
   draw poly    mate=0 xcen=0 ycen=0 angle=0
      pola #Gr4   #Gt4
      pola #Gr3   #Gt3   n=1      c=0.0      b=0.5   f=SYMM
      pola #Gr8   #Gt8   n=#Gn2   c=-1/#Gr3  b=0.5   f=NO
      pola #Gr7   #Gt7   n=1      c=0.0      b=0.5   f=SYMM
      fini               n=#Gn2   c=1/#Gr4   b=0.5   f=NO
   y
   q

/+***** airgap region (3)
   draw poly    mate=0 xcen=0 ycen=0 angle=0
      pola #Gr5   #Gt5
      pola #Gr4   #Gt4   n=1      c=0.0      b=0.5   f=SYMM
      pola #Gr7   #Gt7   n=#Gn2   c=-1/#Gr7  b=0.5   f=NO
      pola #Gr6   #Gt6   n=1      c=0.0      b=0.5   f=SYMM
      fini               n=#Gn2   c=1/#Gr6   b=0.5   f=NO
   y
   q

   $END IF

$ELSE
   $IF #Rang NE 0

/+***** airgap region (1)
   draw poly    mate=0 xcen=0 ycen=0 angle=0
      pola #Gr1   #Gt1
      pola #Gr2   #Gt2   n=1      c=0.0      b=0.5   f=NO
      pola #Gr3   #Gt3   n=#Gn1   c=-1/#Gr3  b=0.5   f=NO
      pola #Gr4   #Gt4   n=1      c=0.0      b=0.5
      fini               n=#Gn1   c=1/#Gr4   b=0.5   f=NO
   y
   q

/+***** airgap region (2)
   draw poly    mate=0 xcen=0 ycen=0 angle=0
      pola #Gr4   #Gt4
      pola #Gr3   #Gt3   n=1      c=0.0      b=0.5   f=NO
      pola #Gr8   #Gt8   n=#Gn2   c=-1/#Gr3  b=0.5
      pola #Gr7   #Gt7   n=1      c=0.0      b=0.5   f=NO
      fini               n=#Gn2   c=1/#Gr4   b=0.5   f=NO
   y
   q

/+***** airgap region (3)
   draw poly    mate=0 xcen=0 ycen=0 angle=0
      pola #Gr5   #Gt5
      pola #Gr4   #Gt4   n=1      c=0.0      b=0.5   f=NO
      pola #Gr7   #Gt7   n=#Gn2   c=-1/#Gr7  b=0.5   f=NO
      pola #Gr6   #Gt6   n=1      c=0.0      b=0.5
      fini               n=#Gn2   c=1/#Gr6   b=0.5
   y
   q

/+***** airgap region (4)
   draw poly    mate=0 xcen=0 ycen=0 angle=0
      pola #Gr6   #Gt6
      pola #Gr7   #Gt7   n=1      c=0.0      b=0.5   f=NO
```

```
      pola #Gr9   #Gt9   n=#Gn1  c=-1/#Gr7 b=0.5   f=NO
      pola #Gr10  #Gt10  n=1     c=0.0     b=0.5   f=NO
      fini                n=#Gn1  c=1/#Gr6  b=0.5   f=NO
   y
   q

   $ELSE

/****** airgap region (2)
   draw poly    mate=0 xcen=0 ycen=0 angle=0
      pola #Gr4   #Gt4
      pola #Gr3   #Gt3   n=1     c=0.0     b=0.5   f=NO
      pola #Gr8   #Gt8   n=#Gn2  c=-1/#Gr3 b=0.5   f=NO
      pola #Gr7   #Gt7   n=1     c=0.0     b=0.5   f=NO
      fini               n=#Gn2  c=1/#Gr4  b=0.5   f=NO
   y
   q

/****** airgap region (3)
   draw poly    mate=0 xcen=0 ycen=0 angle=0
      pola #Gr5   #Gt5
      pola #Gr4   #Gt4   n=1     c=0.0     b=0.5   f=NO
      pola #Gr7   #Gt7   n=#Gn2  c=-1/#Gr7 b=0.5   f=NO
      pola #Gr6   #Gt6   n=1     c=0.0     b=0.5   f=NO
      fini               n=#Gn2  c=1/#Gr6  b=0.5   f=NO
   y
   q

   $END IF

$END IF

/******  CONVERT AIRGAP TO QUADRILATERALS
/******  (THIS REDUCES THE CHANCES OF MESHING ERRORS)

$cons #R1 #Nmod*#Sreg+(2*#Rreg)*#NPM+1

$IF #Rang NE 0
  $cons #R2 #Nmod*#Sreg+(2*#Rreg)*#NPM+4
$ELSE
  $cons #R2 #Nmod*#Sreg+(2*#Rreg)*#NPM+2
$END IF

conv reg1=%int(#R1) reg2=%int(#R2) shap=q

/***** CREATE REQUIRED NUMBER OF AIRGAP SECTIONS

$IF #NPM GT 1

    $do #i 1 (#NPM-1) 1
       copy reg1=%int(#R1) reg2=%int(#R2) t=#i*#pp2*2*#R2D MIRR=no
    $end do

$END IF

reco

/+*************************************************************************
/+********************** SET THE F=SYMM BOUNDARY CONDITIONS ***************
/+*************************************************************************

symm angl=90 conn=nega dx=0 dy=0

/+*************************************************************************
/+****************************** CREATE THE MESH **************************
/+*************************************************************************

mesh
n
```

```
/+**********************************************************************
/+********************** SET MAGNETISATION DIRECTION ***********************
/+**********************************************************************

/+**** MODIFY MAGNET REGIONS TO SET CORRECT MAGNETISATION DIRECTION

extra

/Magnetisation for Rang=0

regi %int(#Nmod*#Sreg+4)          cond=phase func=180/pi*atan(y/x)+180
regi %int(#Nmod*#Sreg+4+#Rreg)    cond=phase func=180/pi*atan(y/x)
/regi %int(#Nmod*#Sreg+4+2*#Rreg) cond=phase func=180/pi*atan(y/x)
/regi %int(#Nmod*#Sreg+4+3*#Rreg) cond=phase func=180/pi*atan(y/x)+180
/regi %int(#Nmod*#Sreg+4+4*#Rreg) cond=phase func=180/pi*atan(y/x)+180
/regi %int(#Nmod*#Sreg+4+5*#Rreg) cond=phase func=180/pi*atan(y/x)
/regi %int(#Nmod*#Sreg+4+6*#Rreg) cond=phase func=180/pi*atan(y/x)+180
/regi %int(#Nmod*#Sreg+4+7*#Rreg) cond=phase func=180/pi*atan(y/x)

/Magnetization for Rang=45

/regi %int(#Nmod*#Sreg+4)          cond=phase func=180/pi*atan(y/x)
/regi %int(#Nmod*#Sreg+4+#Rreg)    cond=phase func=180/pi*atan(y/x)+180
/regi %int(#Nmod*#Sreg+4+2*#Rreg) cond=phase func=180/pi*atan(y/x)+180
/regi %int(#Nmod*#Sreg+4+3*#Rreg) cond=phase func=180/pi*atan(y/x)+180
/regi %int(#Nmod*#Sreg+4+4*#Rreg) cond=phase func=180/pi*atan(y/x)+180
/regi %int(#Nmod*#Sreg+4+5*#Rreg) cond=phase func=180/pi*atan(y/x)
/regi %int(#Nmod*#Sreg+4+6*#Rreg) cond=phase func=180/pi*atan(y/x)
/regi %int(#Nmod*#Sreg+4+7*#Rreg) cond=phase func=180/pi*atan(y/x)

q
```

Postfl1.comi

```
/+*********************************************************************
/+******************** ROUTINE FOR POST-PROCESSING ***********************
/+*********************************************************************
/+***************************** R. P. DEODHAR ***************************
/+************* SPEED LABORATORY, UNIVERSITY OF GLASGOW *****************
/+************************** 17th JUNE 1994 *****************************
/+*********************************************************************

/+**** POST PROCESSOR FOR IASSPM1 MOTOR
/+**** reads a *.ST file and postprocesses it.
/+**** Uses postfl2.comi
/+**** Solutions:

/  0  -  0.0 degrees
/  1  -  1.5 degrees
/  2  -  3.0 degrees
/  3  -  4.5 degrees
/  4  -  6.0 degrees
/  5  -  7.5 degrees
/  6  -  9.0 degrees
/  7  - 10.5 degrees
/  8  - 12.0 degrees
/  9  - 13.5 degrees
/  10 - 15.0 degrees
/  11 - 16.5 degrees
/  12 - 18.0 degrees
/  13 - 19.5 degrees
/  14 - 21.0 degrees
/  15 - 22.5 degrees
/  16 - 24.0 degrees
/  17 - 25.5 degrees
/  18 - 27.0 degrees
/  19 - 28.5 degrees
/  20 - 30.0 degrees

/+**** Solutions:

/  a -  0   Amp
/  b -  4   Amp

/Coding of Variables : For example, #fbdh means following
/f = flux linkage
/b = pahse b
/d = Rang = 19.5 degrees
/b = Solution for case 2 (Current = 4 Amp)

$comi mode=cont

$cons #Cang 0

$cons #Rang 0
read deg0a.st case=1
$comi postfl2
$cons #fa0a #va
$cons #fb0a #vb
$cons #fc0a #vc

read deg0a.st case=2
$comi postfl2
$cons #fa0b #va
$cons #fb0b #vb
$cons #fc0b #vc

$cons #Rang 1.5
read deg1a.st case=1
```

```
$comi postfl2
$cons #fa1a #va
$cons #fb1a #vb
$cons #fc1a #vc

read deg1a.st case=2
$comi postfl2
$cons #fa1b #va
$cons #fb1b #vb
$cons #fc1b #vc

$cons #Rang 3
read deg2a.st case=1
$comi postfl2
$cons #fa2a #va
$cons #fb2a #vb
$cons #fc2a #vc

read deg2a.st case=2
$comi postfl2
$cons #fa2b #va
$cons #fb2b #vb
$cons #fc2b #vc

cons #Rang 4.5
read deg3a.st case=1
$comi postfl2
$cons #fa3a #va
$cons #fb3a #vb
$cons #fc3a #vc

read deg3a.st case=2
$comi postfl2
$cons #fa3b #va
$cons #fb3b #vb
$cons #fc3b #vc

$cons #Rang 6
read deg4a.st case=1
$comi postfl2
$cons #fa4a #va
$cons #fb4a #vb
$cons #fc4a #vc

read deg4a.st case=2
$comi postfl2
$cons #fa4b #va
$cons #fb4b #vb
$cons #fc4b #vc

$cons #Rang 7.5
read deg5a.st case=1
$comi postfl2
$cons #fa5a #va
$cons #fb5a #vb
$cons #fc5a #vc

read deg5a.st case=2
$comi postfl2
$cons #fa5b #va
$cons #fb5b #vb
$cons #fc5b #vc

$cons #Rang 9
read deg6a.st case=1
$comi postfl2
$cons #fa6a #va
$cons #fb6a #vb
$cons #fc6a #vc
```

```
read deg6a.st case=2
$comi postfl2
$cons #fa6b #va
$cons #fb6b #vb
$cons #fc6b #vc

$cons #Rang 10.5
read deg7a.st case=1
$comi postfl2
$cons #fa7a #va
$cons #fb7a #vb
$cons #fc7a #vc

read deg7a.st case=2
$comi postfl2
$cons #fa7b #va
$cons #fb7b #vb
$cons #fc7b #vc

$cons #Rang 12
read deg8a.st case=1
$comi postfl2
$cons #fa8a #va
$cons #fb8a #vb
$cons #fc8a #vc

read deg8a.st case=2
$comi postfl2
$cons #fa8b #va
$cons #fb8b #vb
$cons #fc8b #vc

$cons #Rang 13.5
read deg9a.st case=1
$comi postfl2
$cons #fa9a #va
$cons #fb9a #vb
$cons #fc9a #vc

read deg9a.st case=2
$comi postfl2
$cons #fa9b #va
$cons #fb9b #vb
$cons #fc9b #vc

$cons #Rang 15
read deg10a.st case=1
$comi postfl2
$cons #faaa #va
$cons #fbaa #vb
$cons #fcaa #vc

read deg10a.st case=2
$comi postfl2
$cons #faab #va
$cons #fbab #vb
$cons #fcab #vc

$cons #Rang 16.5
read deg11a.st case=1
$comi postfl2
$cons #faba #va
$cons #fbba #vb
$cons #fcba #vc

read deg11a.st case=2
$comi postfl2
$cons #fabb #va
```

```
$cons #fbbb #vb
$cons #fcbb #vc

$cons #Rang 18
read degl2a.st case=1
$comi postfl2
$cons #faca #va
$cons #fbca #vb
$cons #fcca #vc

read degl2a.st case=2
$comi postfl2
$cons #facb #va
$cons #fbcb #vb
$cons #fccb #vc

$cons #Rang 19.5
read degl3a.st case=1
$comi postfl2
$cons #fada #va
$cons #fbda #vb
$cons #fcda #vc

read degl3a.st case=2
$comi postfl2
$cons #fadb #va
$cons #fbdb #vb
$cons #fcdb #vc

$cons #Rang 21
read degl4a.st case=1
$comi postfl2
$cons #faea #va
$cons #fbea #vb
$cons #fcea #vc

read degl4a.st case=2
$comi postfl2
$cons #faeb #va
$cons #fbeb #vb
$cons #fceb #vc

$cons #Rang 22.5
read degl5a.st case=1
$comi postfl2
$cons #fafa #va
$cons #fbfa #vb
$cons #fcfa #vc

read degl5a.st case=2
$comi postfl2
$cons #fafb #va
$cons #fbfb #vb
$cons #fcfb #vc

$cons #Rang 24
read degl6a.st case=1
$comi postfl2
$cons #faga #va
$cons #fbga #vb
$cons #fcga #vc

read degl6a.st case=2
$comi postfl2
$cons #fagb #va
$cons #fbgb #vb
$cons #fcgb #vc

$cons #Rang 25.5
```

```
read deg17a.st case=1
$comi postfl2
$cons #faha #va
$cons #fbha #vb
$cons #fcha #vc

read deg17a.st case=2
$comi postfl2
$cons #fahb #va
$cons #fbhb #vb
$cons #fchb #vc

$cons #Rang 27
read deg18a.st case=1
$comi postfl2
$cons #faia #va
$cons #fbia #vb
$cons #fcia #vc

read deg18a.st case=2
$comi postfl2
$cons #faib #va
$cons #fbib #vb
$cons #fcib #vc

$cons #Rang 28.5
read deg19a.st case=1
$comi postfl2
$cons #faja #va
$cons #fbja #vb
$cons #fcja #vc

read deg19a.st case=2
$comi postfl2
$cons #fajb #va
$cons #fbjb #vb
$cons #fcjb #vc

$cons #Rang 30
read deg20a.st case=1
$comi postfl2
$cons #faka #va
$cons #fbka #vb
$cons #fcka #vc

read deg20a.st case=2
$comi postfl2
$cons #fakb #va
$cons #fbkb #vb
$cons #fckb #vc

$cons n=!
```

Postfl2.comi

```
/+*************************************************************************
/+********************* ROUTINE FOR POST-PROCESSING ************************
/+*************************************************************************
/+***************************** R. P. DEODHAR ******************************
/+************* SPEED LABORATORY, UNIVERSITY OF GLASGOW ********************
/+*************************** 17th JUNE 1994 ******************************
/+*************************************************************************
/Called from Postfl1.comi

/   CALCULATES THE FLUX LINKAGE IN THE MOTOR USING
/   AVERAGE VECTOR POTENTAL OVER A CONDUCTOR REGION (FLUX-LINKAGE)
/   (a) INTEGRATE VECTOR POTENTIAL OVER EACH CONDUCTOR IN TURN
/   (b) USING SYMMETRY THE OPPOSITE CONDUCTOR WILL HAVE EQUAL AND
/       OPPOSITE POTENTIAL (A2 = -A1)
/   (c) THE FLUX-LINKING THE COIL IS GIVEN BY TWO TIMES A1 x TURNS

$comi mode=cont

/STACK LENGTH (La)  8 inches = 203.2 mm

$cons #La 203.2

/CONDUCTORS PER COIL (BUT REMEMBER THAT WE ARE ONLY LOOKING AT 1/2 A SLOT AT A TIME

/                     THUS WE NEED Zc/2 IN CALCULATIONS)

$cons #Zc 8

/#P = number of poles

$cons #P 4

/+*** #vc?  - Average vector potential in a portion of a slot (Phase A)
/+***         multipled by the conductors in that portion (1/2 slot)
/+***         This is equal to flux-linkage with the 1/2 slot
/+*** The sum of the #va??'s is the total flux-linkage with phase A


/PHASE-A SLOTS :

inta reg1=11 reg2=11 comp=pot
$cons #va1 (flux*#La/(area))*#Zc/2
inta reg1=15 reg2=15 comp=pot
$cons #va2 (flux*#La/(area))*#Zc/2

inta reg1=19 reg2=19 comp=pot
$cons #va3 (flux*#La/(area))*#Zc/2
inta reg1=23 reg2=23 comp=pot
$cons #va4 (flux*#La/(area))*#Zc/2

inta reg1=27 reg2=27 comp=pot
$cons #va5 (flux*#La/(area))*#Zc/2
inta reg1=31 reg2=31 comp=pot
$cons #va6 (flux*#La/(area))*#Zc/2

inta reg1=35 reg2=35 comp=pot
$cons #va7 (flux*#La/(area))*#Zc/2
inta reg1=39 reg2=39 comp=pot
$cons #va8 (flux*#La/(area))*#Zc/2

inta reg1=43 reg2=43 comp=pot
$cons #va9 (flux*#La/(area))*#Zc/2
inta reg1=47 reg2=47 comp=pot
$cons #va10 (flux*#La/(area))*#Zc/2
```

```
inta reg1=51 reg2=51 comp=pot
$cons #va11 (flux*#La/(area))*#Zc/2
inta reg1=55 reg2=55 comp=pot
$cons #va12 (flux*#La/(area))*#Zc/2

$cons #va #P*(#va1+#va2+#va3+#va4+#va5+#va6+#va7+#va8+#va9+#va10+#va11+#va12)


/PHASE-B SLOTS :

inta reg1=67 reg2=67 comp=pot
$cons #vb1 (flux*#La/(area))*#Zc/2

inta reg1=3 reg2=3 comp=pot
$cons #vb2 (flux*#La/(area))*#Zc/2
inta reg1=7 reg2=7 comp=pot
$cons #vb3 (flux*#La/(area))*#Zc/2

inta reg1=11 reg2=11 comp=pot
$cons #vb4 (flux*#La/(area))*#Zc/2
inta reg1=15 reg2=15 comp=pot
$cons #vb5 (flux*#La/(area))*#Zc/2

inta reg1=19 reg2=19 comp=pot
$cons #vb6 (flux*#La/(area))*#Zc/2
inta reg1=23 reg2=23 comp=pot
$cons #vb7 (flux*#La/(area))*#Zc/2

inta reg1=27 reg2=27 comp=pot
$cons #vb8 (flux*#La/(area))*#Zc/2
inta reg1=31 reg2=31 comp=pot
$cons #vb9 (flux*#La/(area))*#Zc/2

inta reg1=59 reg2=59 comp=pot
$cons #vb10 (flux*#La/(area))*#Zc/2
inta reg1=63 reg2=63 comp=pot
$cons #vb11 (flux*#La/(area))*#Zc/2

inta reg1=71 reg2=71 comp=pot
$cons #vb12 (flux*#La/(area))*#Zc/2

$cons #vb #P*(-#vb1-#vb2-#vb3-#vb4-#vb5-#vb6-#vb7-#vb8-#vb9+#vb10+#vb11+#vb12)


/PHASE-C SLOTS

inta reg1=67 reg2=67 comp=pot
$cons #vc1 (flux*#La/(area))*#Zc/2

inta reg1=3 reg2=3 comp=pot
$cons #vc2 (flux*#La/(area))*#Zc/2
inta reg1=7 reg2=7 comp=pot
$cons #vc3 (flux*#La/(area))*#Zc/2

inta reg1=35 reg2=35 comp=pot
$cons #vc4 (flux*#La/(area))*#Zc/2
inta reg1=39 reg2=39 comp=pot
$cons #vc5 (flux*#La/(area))*#Zc/2

inta reg1=43 reg2=43 comp=pot
$cons #vc6 (flux*#La/(area))*#Zc/2
inta reg1=47 reg2=47 comp=pot
$cons #vc7 (flux*#La/(area))*#Zc/2

inta reg1=51 reg2=51 comp=pot
$cons #vc8 (flux*#La/(area))*#Zc/2
inta reg1=55 reg2=55 comp=pot
$cons #vc9 (flux*#La/(area))*#Zc/2
```

```
inta reg1=59 reg2=59 comp=pot
$cons #vc10 (flux*#La/(area))*#Zc/2
inta reg1=63 reg2=63 comp=pot
$cons #vc11 (flux*#La/(area))*#Zc/2

inta reg1=71 reg2=71 comp=pot
$cons #vc12 (flux*#La/(area))*#Zc/2

$cons #vc #P*(#vc1+#vc2+#vc3-#vc4-#vc5-#vc6-#vc7-#vc8-#vc9-#vc10-#vc11-#vc12)
```

Postcog1.comi

```
/+*************************************************************************
/+********************* ROUTINE FOR POST-PROCESSING ************************
/+*************************************************************************
/+*************************** R. P. DEODHAR ********************************
/+************* SPEED LABORATORY, UNIVERSITY OF GLASGOW ********************
/+************************ 25th NOVEMBER 1994 ******************************
/+*************************************************************************

/ PROGRAM FOR POST-PROCESSING OF ORIENTAL MOTOR SOLUTIONS TO OBTAIN COGGING
/ TORQUE

/ Uses postcog2.comi

/#lstk must be in meters because unit of magnetic vector potential is WBM

$comi mode=cont

$cons #rad   22.9-7.9/2
$cons #betm  90*pi/180
$cons #lstk  0.02

$cons #radm  #rad*.001
$cons #arem  #radm*#betm*#lstk


$do #j 1 6 1

/ New loop for each of the files
  $do #loop 0 30
    $cons #rang %real(#loop)
    read ../omsatmoh/deg%int(#loop)a.st case=%int(#j)
    $comi ompostcog2
    $if #loop le 9
      $cons #fn0%int(#loop)  #vn
      $cons #fs0%int(#loop)  #vs
    $else
      $cons #fn%int(#loop)  #vn
      $cons #fs%int(#loop)  #vs
    $end if

  $end do
  $cons n=!
$end do
```

Postcog2.comi

```
/+*************************************************************************
/+********************* ROUTINE FOR POST-PROCESSING ************************
/+*************************************************************************
/+***************************** R. P. DEODHAR ******************************
/+************* SPEED LABORATORY, UNIVERSITY OF GLASGOW ********************
/+************************** 25th NOVEMBER 1994 ****************************
/+*************************************************************************
/ PROGRAM FOR POST-PROCESSING OF ORIENTAL MOTOR SOLUTIONS TO OBTAIN COGGING
/ TORQUE

/Called from postcog1.comi

/ FOLLOWING CODE IS TO OBTAIN FLUX OVER ONE FULL POLE IN THE CENTER

point comp=pot, method=pola, xp=#rad, yp=46.5-#rang
$cons #v1  pot
point comp=pot, method=pola, xp=#rad, yp=133.5-#rang
$cons #v2  pot
$cons #vn  (#v1-#v2)*#lstk

/ FOLLOWING CODE IS TO OBTAIN FLUX OVER TWO HALF POLES AT LEFT AND RIGHT

point comp=pot, method=pola, xp=#rad, yp=43.5-#rang
$cons #v1  pot
point comp=pot, method=pola, xp=#rad, yp=-#rang
$cons #v2  pot

point comp=pot, method=pola, xp=#rad, yp=136.5-#rang
$cons #v3  pot
point comp=pot, method=pola, xp=#rad, yp=180-#rang
$cons #v4  pot

$cons #vs  ((#v1-#v2)+(#v4-#v3))*#lstk
```

C MATLAB Program Listings

This appendix contains listings of programs written in MATLAB programming language. These programs form a part of the *PC-BDC–OPERA-2d link program* described in Chapter 1. The following programs are included.

Conv3ph.m

This program reads in the flux-linkage data for all the motor phases generated by OPERA-2d and converts it into a 2-dimensional matrix 'flmat' containing variation of flux-linkage with respect to rotor position at increasing current values.

Convskew.m

This program reads in the 'flmat' matrix for a motor without skew and converts it into 'flmatskew' matrix for the motor with skew for a given skew angle.

Ellipse.m

This program reads in the 'flmat' matrix and plots the flux-MMF diagram consisting of elliptical flux-MMF trajectories and non-linear magnetisation curves at successive rotor positions.

Torque.m

This program reads in the 'flmat' matrix and calculates the incremental areas enclosed by the magnetisation curves at successive rotor positions. Using these incremental areas, it then calculates the average electromagnetic torque and torque ripple.

Tcog.m

This program reads in the magnet flux variation data for all the motor poles generated by OPERA-2d, calculates the corresponding magnet MMF variation data using the demagnetisation characteristics, and then calculates the cogging torque ripple.

Conv3ph.m

```
% ************************************************************
% ******* PROGRAM FOR CONVERTING OPERA-2d DATA TO A MATRIX **********
% ************************************************************
% ************************* R.P.DEODHAR ****************************
% ************************************************************
% ************************ 20th JUNE 1994 ***************************

% FOLLOWING PARAMETERS NEED TO BE REDIFINED FOR EVERY MOTOR
% ************************************************************

ph =  3;                        % no. of phases (if other than 3, the
                                % program will need major changes)
poles = 6;                      % no. of poles
iang =   0;                     % current angle
amp =    [0:4:24]./3;           % vector containing all rms current values
soln =   21;                    % no. of solutions in FEA
inc = 1;                        % increment in mech. degrees
filename1 = 'iasspm1.dat'; % name of OPERA-2d file containing fldata

% name of *.mat file containing 'flmat' matrix needs to be set at the
% end of this program in 'save' command

% ************************************************************

[m,n]=size(amp);     % extract no. of currents value = n
ampval = n;       % no. of currents

%function flmat = convert3ph(filename1, poles, ampval, soln, inc)

% This function reads OPERA-2d flux linkage data
% and returns a matrix called 'flmat'
% 'flmat' has the following format

% 1st col.        2nd col.       3rd col. ...       'n+ampval'th col.
% (ang)           (1st ampval)   (2nd ampval)       ('ampval'th ampval)

% 0               fldata...      fldata...    ...   fldata...
% 0+inc*poles/2   fldata...      fldata...    ...   fldata...
% ...             ...            ...          ...   ...
% ...             ...            ...          ...   ...
% 180             fldata...      fldata...    ...   fldata...

ph = 3;                         % no. of phases is 3
ang = 0:inc*poles/2:360;        % 'ang' is a vector with angles in elec. deg.
ang = ang';                     % transpose a from row to coulmn vector
[m n] = size(ang);              % extract size of a
flmat = zeros(m,n+ampval); % pre-alocate a matrix with all zeros which
                                % will contain final data
flmat(:,1) = ang;               % first coulmn is angs coulmn
fid = fopen(filename1);         % open OPERA-2d data file
[temp,c]=fscanf(fid,'%*5s %lg %lg',[2 inf]);    % skip #fa0a ... etc. And
                                                % read the next two values
                                                % on every line and store
                                                % in a temporary matrix 'temp'

fclose(fid);                    % close file
temp=temp';                     % convert from row vector to coulmn vector
temp=temp(:,1);                 % extract first coulmn only as both columns are
                                % identical, all the data to be extracted from this vector


for l=2:ampval+1                % for all ampval values (2,3,...ampval+1) do the following

   j=1;                         % j - row counter in flmat matrix this is reset for every
                                % 'ampval' column iteration
```

```
for h=0:5   % h - variable which decides the sequence of picking up each phase
            % fldata in the order of A -C B -A C -B (for 3 pahse)
   if h==0
      k=0;
   end
   if h==1
      k=2;
   end
   if h==2
      k=1;
   end
   if h==3
      k=0;
   end
   if h==4
      k=2;
   end
   if h==5
      k=1;
   end
   for i=3*(l-2)+1:ph*ampval:ph*ampval*(soln-2)+1+3*(l-2)+1   % ph*ampval is the
                                                              % 'jump' value. Start
                                                              % and end values are
                                                              % governed by 'l'
% when                          l = 2, 3, 4, 5, ...
% Start of i (counter for 'temp' matrix elements) will be i = 1, 4, 7, 11, ...
% this choice of start of i is governed by the nature of OPERA-2d input data

      flmat(j,l) = temp(i+k);          % assign 'right' value from 't' vector to the
                                       % 'right' column of 'flmat' matrix
   j = j+1;                            % increment j for next row
   end
      temp=-temp;                      % 'complement' whole of 'temp' such that A -C B
                                       % -A C -B sequence for 3
                                       % phase is maintained

   end
   flmat(m,l) = flmat(1,l);            % last element of each column of 'flmat' is same
                                       % as first one
end

save iasspml flmat
```

Convskew.m

```
% ************************************************************************
% ********************** PROGRAM FOR OBTAINING SKEW ******************
% ************************ ON THE 'flmat' MATRIX *********************
% ************************************************************************
% ***************************** R.P.DEODHAR ******************************
% ************************************************************************
% ***************************** 28 JUNE 1994 *****************************

% FOLLOWING PARAMETERS NEED TO BE REDIFINED FOR EVERY MOTOR
% ************************************************************************

ph =  3;                                % no. of phases (if other than 3, the
                                        % program will need major changes)
poles = 4;                              % no. of poles
iang  =  0;                             % current angle
amp   = 0:4:24;                         % vector containing all rms current values
soln  =  31;                            % no. of solutions in FEA
inc   =  1;                             % increment in mech. degrees
skew  = 10;                             % skew in mech. deg
skewf = skew/inc;                       % skew factor in terms of no. of 'inc'
shiftf = skewf/2;                       % shift factor which decides starting point(element)
                                        % in skewing calculations

load iasspm1;                           % name of file containing flmat matrix

% name of file containing final 'skewed' 'flmat' matrix needs to be set
% in 'save' command at the end of this program

% ************************************************************************

% ******************************** SKEW **********************************

[m,n] = size(flmat);                    % extract no. of rows = m
fltemp1 = zeros(2*m-1,n);               % create a temporary matrix with twice the
                                        % no. of rows as 'flmat' matrix
fltemp1(1:m-1,:) = flmat(1:m-1,:);      % fill-up fltemp with 'two flmat's
fltemp1(m:2*m-1,:) = flmat;
fltemp2 = zeros(2*m-1,n);               % create another temporary matrix identical
                                        % to 'fltemp1'
                                        % final 'flmat' will be extracted from this matrix

% THE FOLLOWING NESTED DOUBLE LOOP DOES 'AVERAGING' OF EVERY 'skewf' NO. OF ELEMENTS OF
% 'flmat'

for i = 1+shiftf:m+shiftf               % for each of first 'm' rows, do
   add = zeros(1,n-1);                  % define a temporary register for adding
   for j = i-shiftf:i+shiftf            % for a set of 'i+sekwf-1' rows from 'i'th row, do
      add = add+fltemp1(j,2:n);         % add all rows in progress (ignore first column, as it
                                        % is only an 'angle' column and add the rest)
   end
   fltemp2(i-shiftf,2:n) = add/(skewf+1);% take average and assign new 'averaged'
                                        % elements in a row back to 'fltemp2` matrix
end

fltemp2(m:2*m-1,2:n) = fltemp2(1:m,2:n);              % double-up fltemp2 matrix
flmat(1:m,2:n) = fltemp2(m-shiftf:2*m-1-shiftf,2:n); % extract 'flmat' matrix
flmatskew = flmat;
save iasspm1skew10 flmatskew
```

Ellipse.m

```
% ************************************************************************
% ************** PROGRAM FOR PLOTTING ELLIPSE DIAGRAM ********************
% ************************************************************************
% ************************** R.P.DEODHAR *********************************
% ************************************************************************
% ************************** 28 JUNE 1994 ********************************

% FOLLOWING PARAMETERS NEED TO BE REDIFINED FOR EVERY MOTOR
% ************************************************************************

ph =  3;                                % no. of phases (if other than 3, the
                                        % program will need major changes)
poles = 4;                              % no. of poles
iang =   0;                             % current angle
amp =    [0:4:24];                      % vector containing all rms current values
soln =   21;                            % no. of solutions in FEA
inc = 1.5;                              % increment in mech. degrees
nph = 96;                               % number of series turns per phase

load iasspm1;                           % name of file containing flmat matrix

% ************************************************************************

[m,n]=size(amp);                        % extract no. of currents value = n
ampval = n;                             % no. of currents
theta   = flmat(:,1);                   % 'theta' is the angle vector
thetar = theta*pi/180;                  % theta in electrical radians
ia = zeros(size(flmat));                % pre-alocate matrix of the same size as 'flmat'
ia(:,1) = flmat(:,1);                   % first column should be same as 'flmat'
ipk = sqrt(2.0)*amp;                    % vector containing peak current values
ipk = ipk.*(nph/1000);                  % convert current values to MMF values if req.
r90 = 90*pi/180;
iangr = iang*pi/180;

% Generate a current matrix for phase 'a'

for i=1:ampval
   ia(:,i+1) = ipk(i).*cos(thetar+iangr+r90);
end

% Plot variation in total flux-linkage with its associated phase current

[p,q] = size(flmat);
flmat(:,2:q) = flmat(:,2:q)./nph;       % convert flux-linkage values to flux

plot(ia(:,ampval),flmat(:,ampval),':')% plot the largest ellipse first
axis([-3 3 -15 15])
hold on
grid on

for i=2:ampval
   plot(ia(:,i),flmat(:,i),':')         % plot rest of the ellipses
end

% Plot magnetization curves at all angles

[m,n] = size(flmat);

for i=1:m
   curr = ia(i,2:ampval);               % extract ith row from ia
   flin = flmat(i,2:ampval);            % extract ith row from flmat
   plot(curr,flin,':')                  % plot magnetization curve
end
```

```
%title('FLUX-MMF DIAGRAM FOR IASSPM1 SINEWAVE MOTOR');
xlabel('MMF  [kA-t]');
ylabel('FLUX  [mWb]');

% PLOT MMF AND FLUX VARIATION WITH ANGLE

plot(ia(:,1),ia(:,2:ampval))
hold on
grid on
plot(ia(:,1),ia(:,2:ampval),'x')
axis([0 360 -3 3])
xlabel('ANGLE  [ELEC. DEG.]')
ylabel('MMF  [kA-t]')
text(120,.2,' 0 AMP')
text(120,-2.6,'20 AMP')
pause
hold off

plot(flmat(:,1),flmat(:,2:ampval))
hold on
grid on
plot(flmat(:,1),flmat(:,2:ampval),'x')
axis([0 360 -15 15])
xlabel('ANGLE  [ELEC. DEG.]')
ylabel('FLUX  [mWb]')
text(45,-2.5,'20 AMP')
text(110,-2.5,'0 AMP')
pause
hold off
```

Torque.m

```
% ************************************************************************
% ********* PLOT TORQUE RIPPLE CURVE USING ELLIPSE DIAGRAM **********
% ************************************************************************
% ***************************** R.P.DEODHAR ******************************
% ************************************************************************
% ***************************** 20 JULY 1994 *****************************
% ************************************************************************

% FOLLOWING PARAMETERS NEED TO BE REDIFINED FOR EVERY MOTOR

% ************************************************************************

ph =  3;                          % no. of phases (if other than 3, the
                                  % program will need major changes)
phsh = 20;                        % this parameter decides the phase shift
                                  % in terms of row counter in 'torque' matrix
poles = 4;                        % no. of poles
iang =   0;                       % current angle
amp =    [0:4:24];                % vector containing all rms current values
soln =   21;                      % no. of solutions in FEA
inc  =   1.5;                     % increment in mech. degrees

load iasspm1;                     % name of OPERA-2d file containing 'flmat' matrix

% ************************************************************************

[m,n]=size(amp);                  % extract no. of currents value = n
ampval = n;                       % no. of currents
theta   = flmat(:,1);             % 'theta' is the angle vector
thetar = theta*pi/18;             % theta in electrical radians
ia = zeros(size(flmat));          % pre-alocate current matrix of the same size as 'flmat'
ia(:,1) = flmat(:,1);             % first column should be same as 'flmat'
ipk = sqrt(2.0)*amp;              % vector containing peak current values
r90 = 90*pi/180;
iangr = iang*pi/180;

% Generate a current matrix for phase 'a'

for i=1:ampval
   ia(:,i+1) = ipk(i).*cos(thetar+iangr+r90);
end

% Plots static torque characteristic calculated from the
% incremental co-energy area's

% ************************************************************************

% CALCULATE CO-ENERGY AREA'S

[m,n] = size(ia);
area = zeros(m-1,(ampval-1)*2);  % pre-allocate 'area' matrix
 for curve = 1:m-1               % calculate incremental areas
  for k = 2:ampval               % and accumulate total in 'area' matrix
    x1 = ia(curve,k);
    x2 = ia(curve,k+1);
    x3 = ia(curve+1,k+1);
    y1 = flmat(curve,k);
    y2 = flmat(curve,k+1);
    y3 = flmat(curve+1,k+1);
    area(curve,(k-1)*2-1) = 0.5 .* (x3 .* (y1-y2) + x2 .* (y3-y1) + x1 .* (y2-y3));
    x1 = ia(curve,k);
    x2 = ia(curve+1,k+1);
    x3 = ia(curve+1,k);
    y1 = flmat(curve,k);
    y2 = flmat(curve+1,k+1);
```

```
    y3 = flmat(curve+1,k);
    area(curve,(k-1)*2) = 0.5 .* (x3 .* (y1-y2) + x2 .* (y3-y1) + x1 .* (y2-y3));
  end
end

angle = inc:inc*poles/2:360-inc;
incr = inc*pi/180;                          %mech deg increment in radians
convf = 0.001;                              % conversion factor from Nmm to Nm
torque = zeros(2*(m-1),ampval);             % pre-allocate 'torque' matrix

for j = 1:ampval-1
   torque(1:m-1,j+1) = (area(:,2*j-1)+area(:,2*j))/incr*convf+torque(1:m-1,j);
% add two adjecent columns of 'area' matrix and add the total to previous
% column of 'torque' matrix to create present column of it
end

torque(m:2*(m-1),:) = torque(1:m-1,:);% repeat first half of 'torque' matrix

ta = zeros(m-1,ampval-1);                   % pre-allocate ta,tb,tc and tt matrices
tb = zeros(m-1,ampval-1);
tc = zeros(m-1,ampval-1);
tt = zeros(m-1,ampval-1);
ta = torque(1:m-1,:);                       % fill-up ta,tb,tc and tt with proper sections
tb = torque(1+phsh:m-1+phsh,:);             % of 'torque' matrix
tc = torque(1+2*phsh:m-1+2*phsh,:);
tt = ta +tb +tc;

plot(angle,ta(:,1:ampval-1),'-');
axis([0 360 -5 65])
hold on
grid on
title('PHASE A TORQUE RIPPLE : IASSPM1 MOTOR (IANG = 0 DEG)');
xlabel('ANGLE  [ELEC. DEG.]');
ylabel('TORQUE  [Nm]');
pause
hold off

plot(angle,tb(:,ampval-1),'--');
axis([0 360 -5 65])
hold on
grid on
title('PHASE B TORQUE RIPPLE : IASSPM1 MOTOR (IANG = 0 DEG)');
xlabel('ANGLE  [ELEC. DEG.]');
ylabel('TORQUE  [Nm]');
pause
hold off

plot(angle,tc(:,ampval-1),'-.');
axis([0 360 -5 65])
hold on
grid on
title('PHASE C TORQUE RIPPLE : IASSPM1 MOTOR (IANG = 0 DEG)');
xlabel('ANGLE  [ELEC. DEG.]');
ylabel('TORQUE  [Nm]');
pause
hold off

plot(angle,tt(:,1:ampval-1));
axis([0 360 -5 105])
hold on
grid on
%plot(angle(60),tt(60,ampval-1),'x')
%title('TORQUE RIPPLE (SPM4 MOTOR - UNSKEWED, IANG = 0 DEG)');
xlabel('ANGLE  [ELEC. DEG.]');
ylabel('TORQUE  [Nm]');
pause
hold off
```

Tcog.m

```
% ************************************************************************
% ***** PROGRAM FOR PREDICTING COGGING TORQUE IN ORIENTAL MOTOR *****
% ************************************************************************
% ************************** R.P.DEODHAR **************************
% ************************************************************************
% ************************** 20 JULY 1995 **************************
% ************************************************************************
% FOLLOWING PARAMETERS NEED TO BE REDIFINED FOR EVERY MOTOR

% ************************************************************************

tcogp = 30;                                     % Cogging torque period in mech. deg.
soln =   31;                                    % no. of solutions in FEA
inc = 1;                                        % increment in mech. degrees
pole = 4;                                       % Number of poles
filename1 = 'omcogatmid.dat';                   % name of OPERA-2d data file

% ************************************************************************

angle = [inc/2:inc:tcogp-inc/2];

fid = fopen(filename1);                         % open OPERA-2d data file
[temp,c]=fscanf(fid,'%*5s %lg %lg',[2 inf]);    % skip #fa0a ... etc. and read the next
                                                % two values on every line and store in a
                                                % temporary matrix 'temp'
fclose(fid);      % close file

incr = inc*pi/180;                              % increment in radians
lstk = 20e-3;                                   % Stack length
rad1 = (22.9-7.9/2)*1e-3;                       % Radius at magnet arc
lm = 7.9e-3;                                    % length of magnet
betam = 87*pi/180;                              % magnet arc in radians
murec = 1.27;                                   % recoil permeability
mu0 = 4e-7*pi;                                  % permeability of air
aream = lstk*rad1*betam;                        % area of a magnet pole at rad1
br = 0.4425;                                    % remanent flux density (adjusted to
                                                % take account of the magnet overhang)

%******** COGGING TORQUE CALCULATION FOR ALL THE 'NORTH' POLES ***********

fluxn = temp(1,1:2:61);                         % vector containing instantaneous flux per
                                                % pole values for each rotor position
                                                % (north pole)
bmn = fluxn./aream;                             % instantaneous flux density variation
mmfn = ((bmn-br)./(murec*mu0)).*lm;             % instantaneous mmf variation

for i=1:30,
   x1 = 0;
   x2 = mmfn(i);
   x3 = mmfn(i+1);

   y1 = 0;
   y2 = fluxn(i);
   y3 = fluxn(i+1);
   area = 0.5*(x3*(y1-y2)+x2*(y3-y1)+x1*(y2-y3));

% 'tcog' is multiplied by the number of poles since the total torque will
% be derived from the incremental co-energy areas associated with each pole

   tcogn(i) = 1000*(pole/2)*area/incr; % multiply by 1000 to convert from Nm to mNm
end
```

```
%******** COGGING TORQUE CALCULATION FOR ALL THE 'SOUTH' POLES ***********

fluxs = temp(1,2:2:62);                    % vector containing instantaneous flux per pole
                                           % values for each rotor position (south pole)
bms = fluxs./aream;                        % instantaneous flux density variation
mmfs = ((bms-br)./(murec*mu0)).*lm;        % instantaneous mmf variation

for i=1:30,
   x1 = 0;
   x2 = mmfs(i);
   x3 = mmfs(i+1);

   y1 = 0;
   y2 = fluxs(i);
   y3 = fluxs(i+1);
   area = 0.5*(x3*(y1-y2)+x2*(y3-y1)+x1*(y2-y3));

% 'tcog' is multiplied by the number of poles since the total torque will
% be derived from the incremental co-energy areas associated with each pole

   tcogs(i) = 1000*(pole/2)*area/incr; % multiply by 1000 to convert from Nm to mNm

end

%*********** TOTAL COGGING TORQUE ****************************************

tcog = tcogn+tcogs;

plot(angle,tcog,'-')
hold on
grid on
plot(angle,tcog,'o')
axis([0 30 -15 15])

% texpcogom plots the measured points

texpcogom                                  % read measured data

xlabel('ANGLE [MECH. DEG.]')
ylabel('COGGING TORQUE [mNm]')
text(1,11,'_____  FEA')
text(.5,13,'_____  PREDICTED (TOTAL)')
text(.5,11,'- - -  PREDICTED (SOUTH POLES)')
text(.5,9,'-.-.-  PREDICTED (NORTH POLES)')
text(.5,13,'_____  PREDICTED')
text(1,9,'x x x  MEASURED')
```

D Flux-Reversal Generator Drawings

This appendix contains the mechanical drawings for components and sub-assemblies of the prototype single-phase 2/3 configuration flux-reversal generator described in Chapter 7.

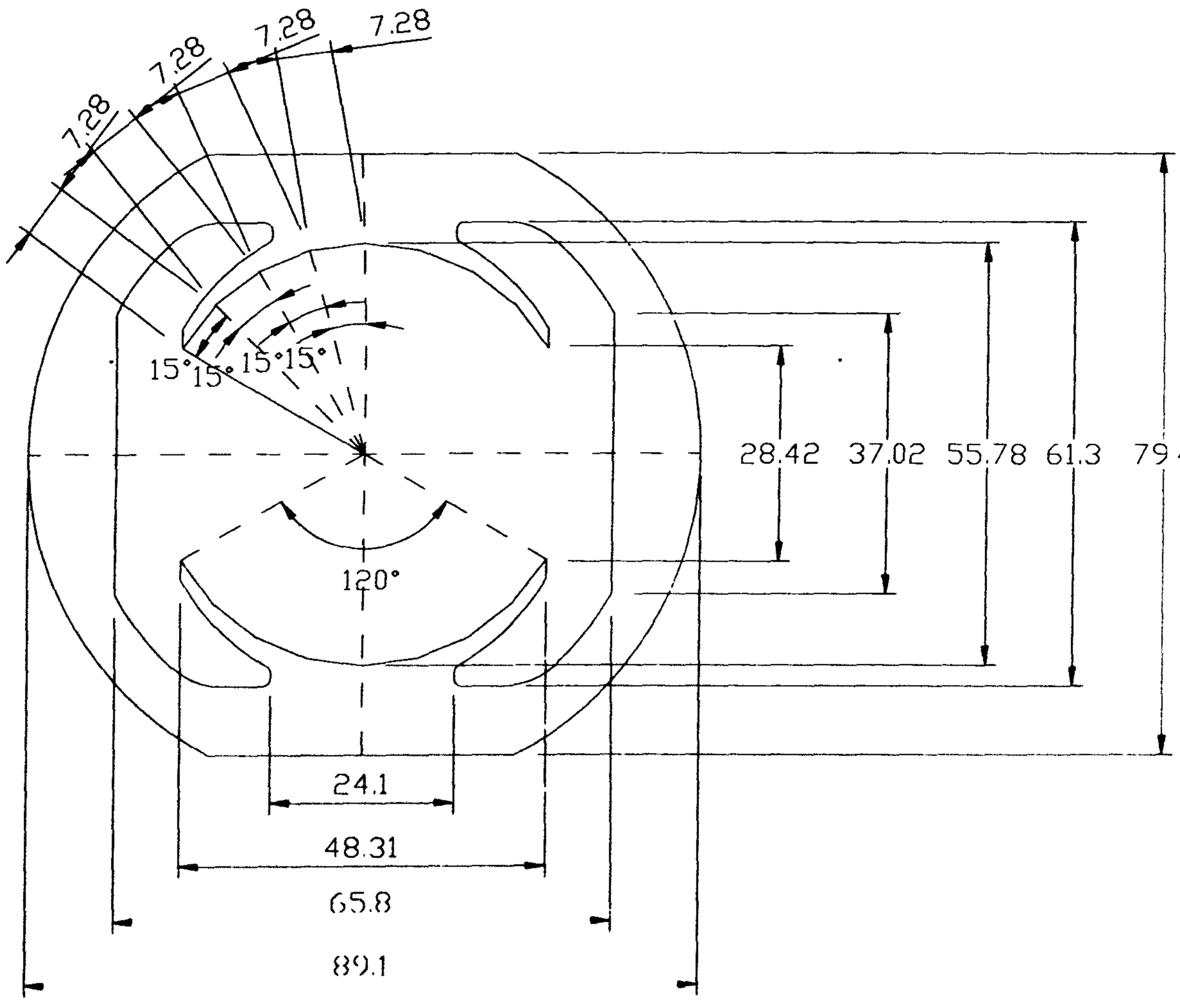

FRM – Stator
Material: Vacuumschmelze Vacodur Vacoflux Newcor800

All tolerances: +0.1 −0.1
All dimensions are in mm

Stack length on the lamination clamps=50mm
Stack length on the actual motor =40mm

Drawing not to scale

Svante Andersson
Rajesh P. Deodhar

SPEED Laboratory
University of Glasgow

Phone: 0141-330-5235
Fax: 0141 330 4907

1 Nov 95

6mc22sw3

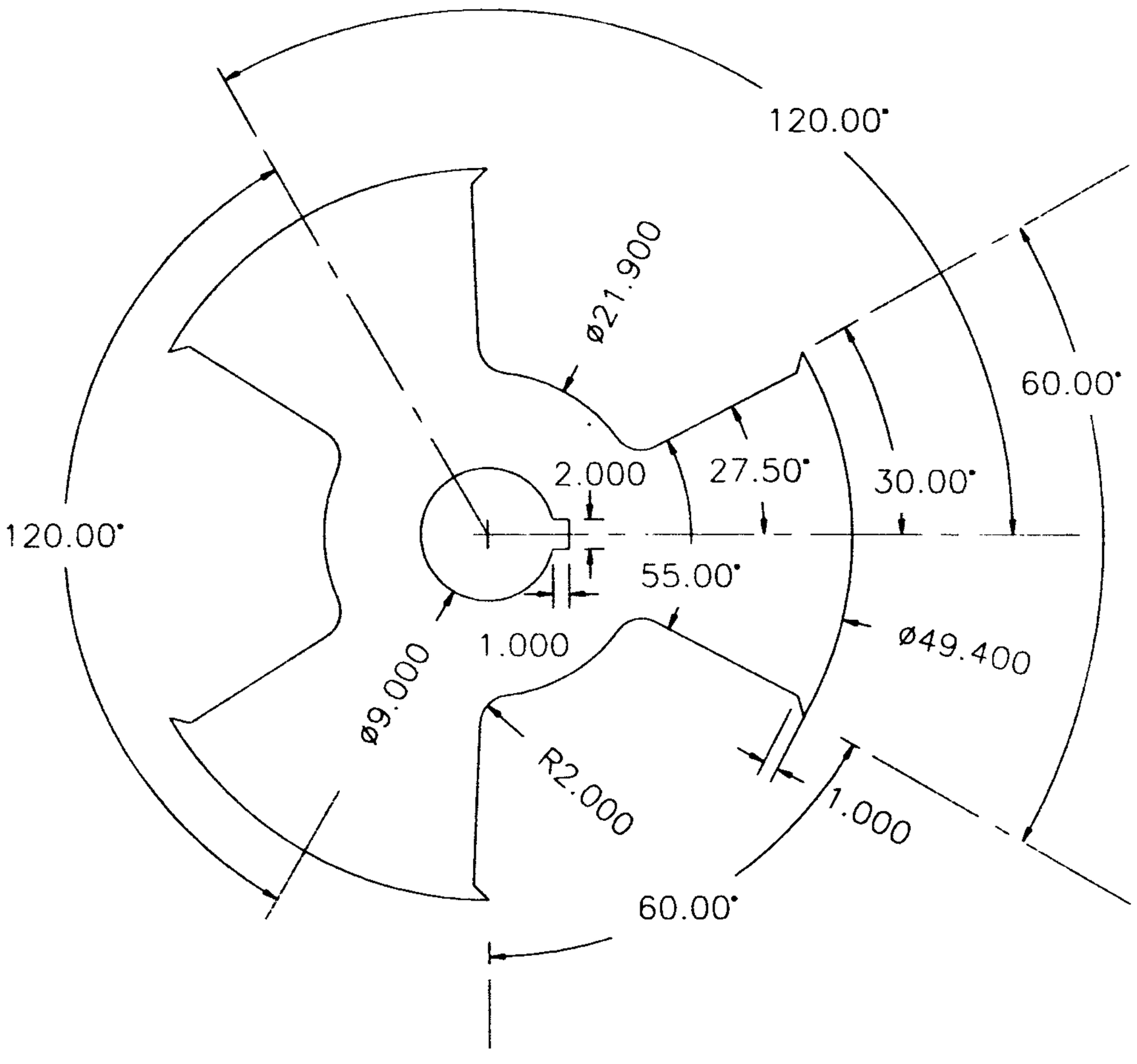

FRM – Rotor
Vaterial: _osi 400/50

A tolerances: ±0.1 ±0.1
All dimensions are in mm

Stack length on the lamination clamps=70mm
Stack length on the actual motor =40mm

Drawing not to scale

Svante Andersson
Rajesh P. Deodhar

SPEED Laboratory
University of Glasgow

Phone: 0141 330 5235
Fax: 0141 330 4907

1-Nov 95

FRM – rotor shaft
Material: Drill steel
Total length: 190.000 mm
Maximum diameter: 14.000 mm

Svante Andersson
Rojesh P. Deodhar

SPEED laboratory
University of Glasgow

Phone: 0141 – 330 5235
Fax: 0141 – 330 4907

9–Nov–95

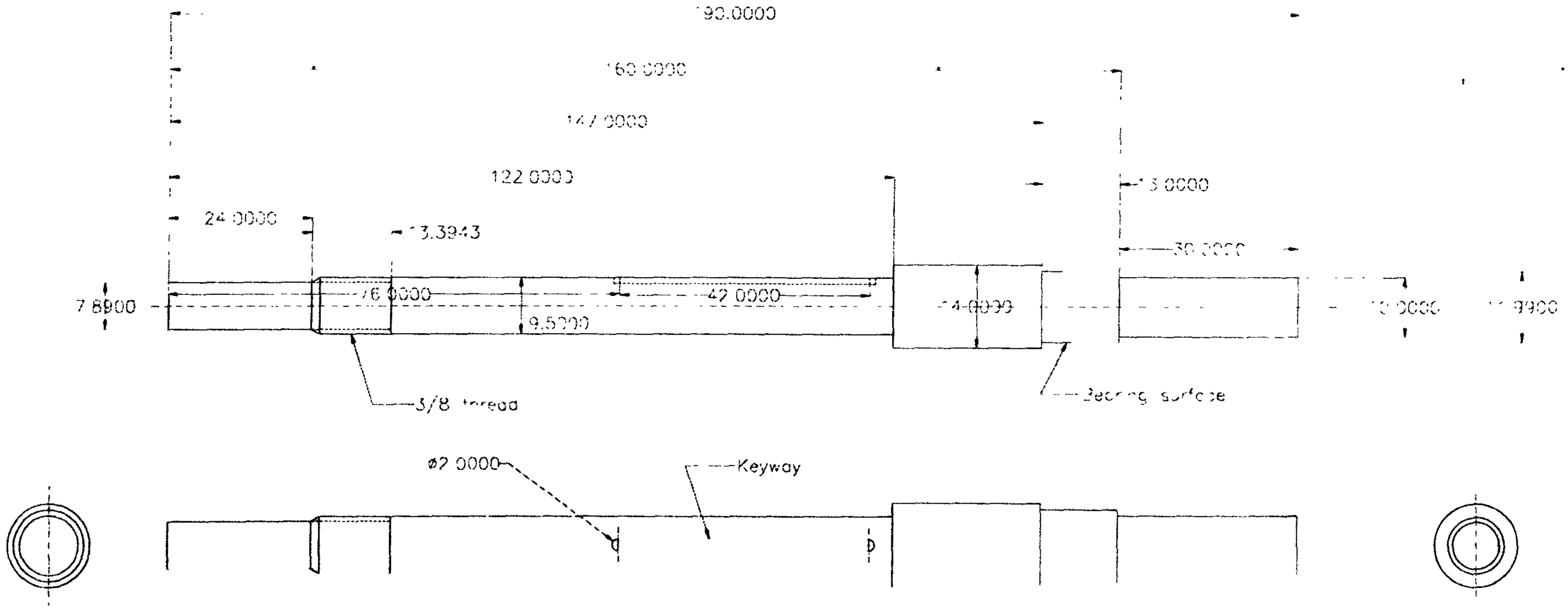

FRM – Spacer for rotor
Material: Aluminium
Length: 34.6 mm
Diameter: 15.5 mm

Svante Andersson
Rajesh P Deohdar

SPEED Laboratory
University of Glasgow

Phone: 0141 – 330 5235
Fax: 0141 – 330 4907

9-Nov-95

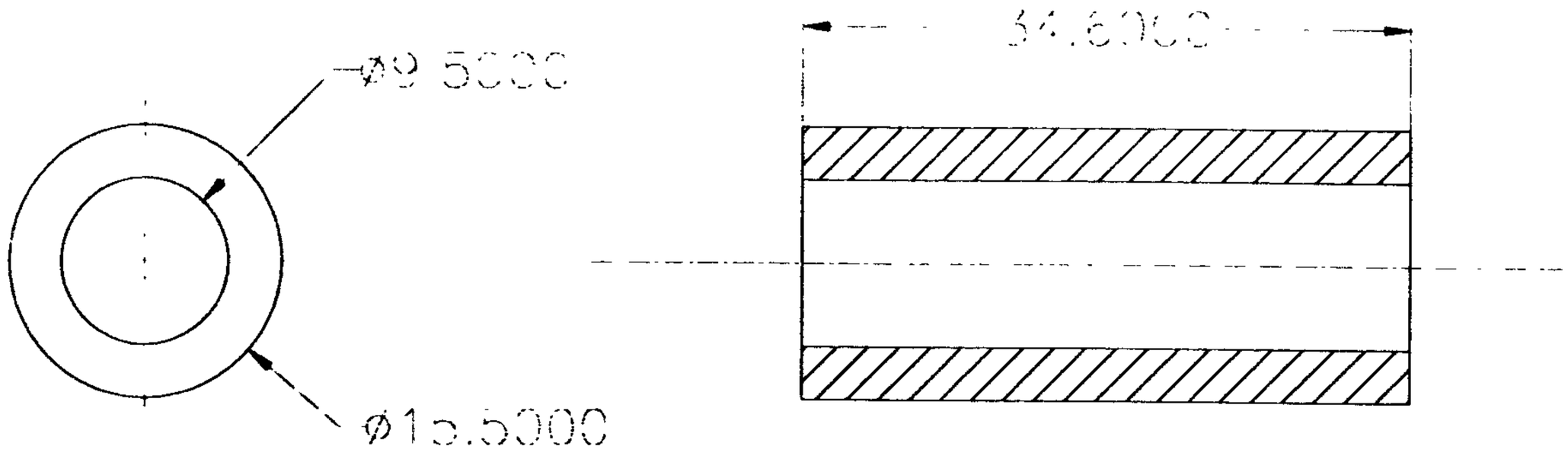

FRM – Washers for rotor
Material : Aluminium

Outer diameter: 47.400 mm
Length: 5.000 mm

Svante Andersson
Rajesh P. Deohdar

SPEED Laboratory
University of Glasgow

Phone: 0141 – 330 5235
Fax: 0141 – 330 4907

9–Nov–95

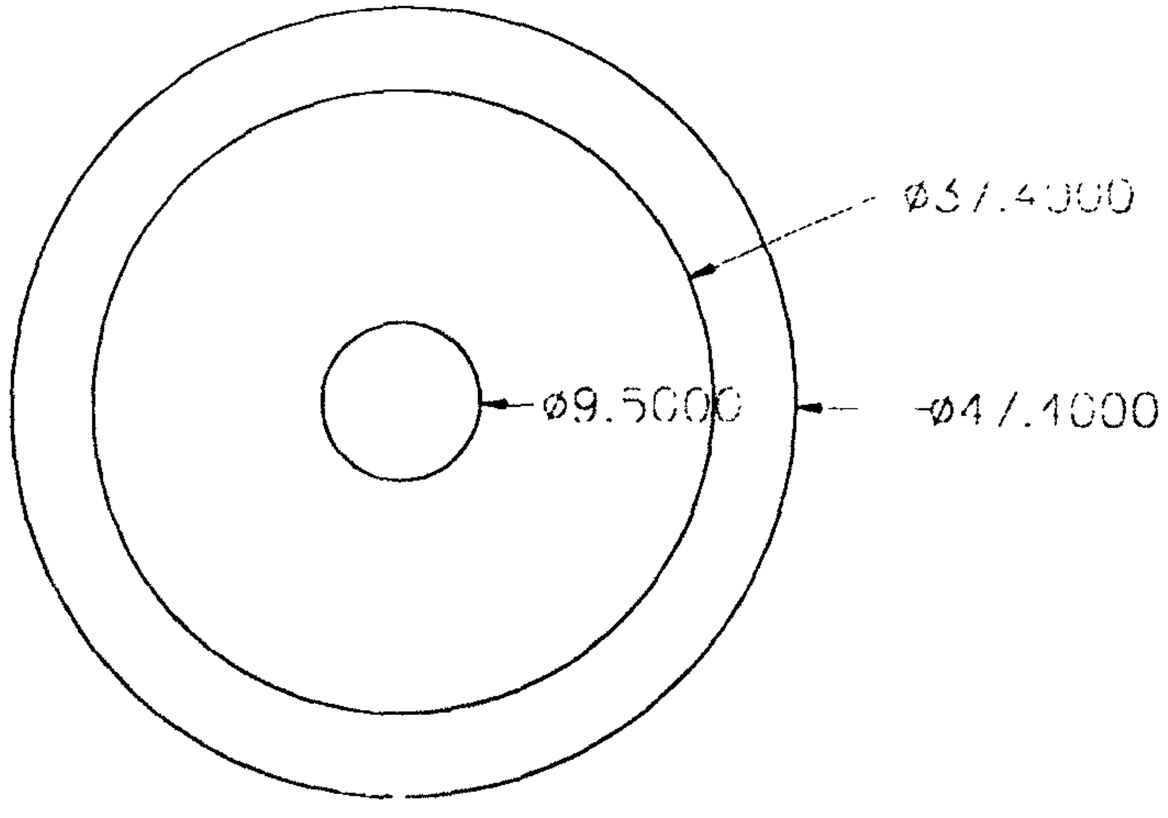

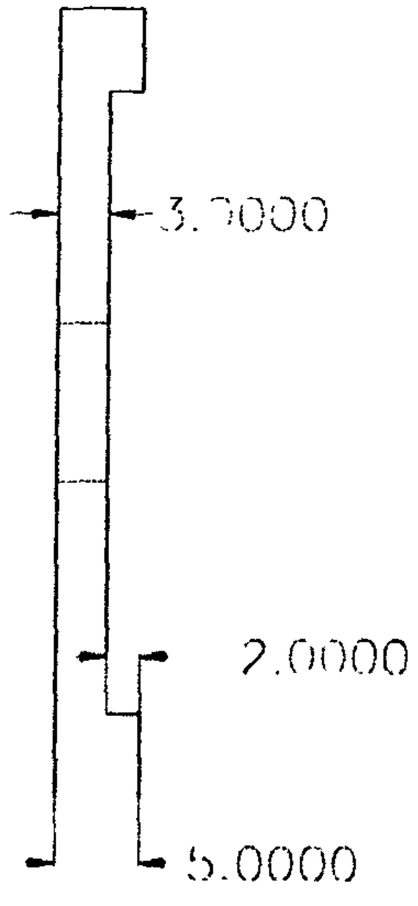

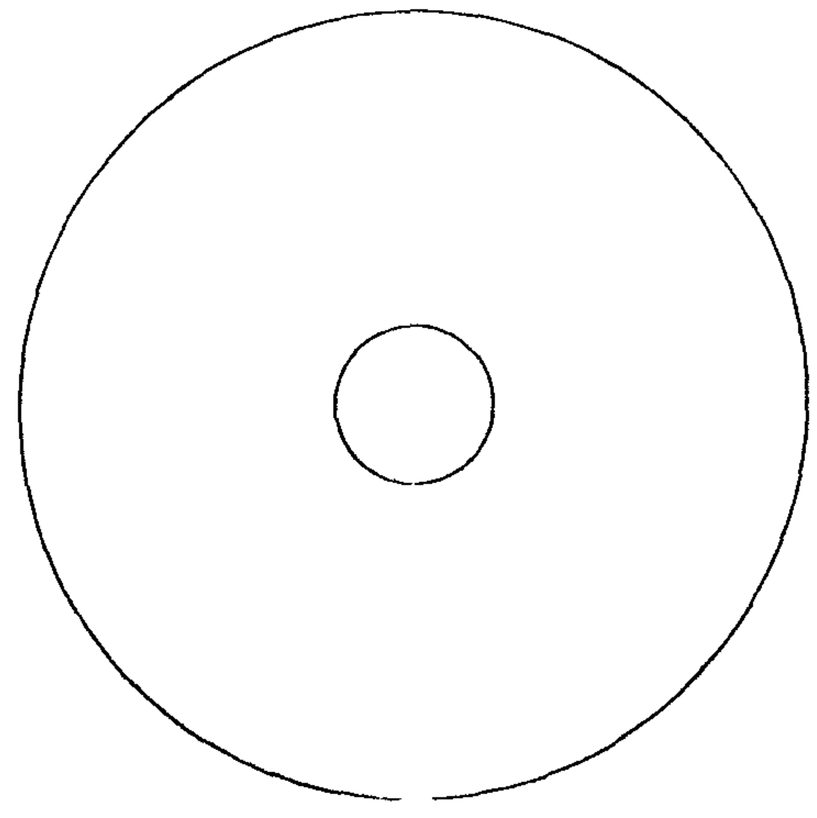

E PC-BDC and PC-SRD Manual Sections

This appendix contains reference sections from the PC-BDC 4.7 and PC-SRD 6.2 manuals which explain the motor geometry terms, symbols, and definitions used in the PC-BDC and PC-SRD software.

5. REFERENCE SECTION

5.1 Input parameters first seen in cross-section editor

Please refer to Figs. 29-32 for further information about dimensional parameters.

RadSH	Shaft radius. For interior-rotor motors, this is the innermost radius of the rotor. For exterior-rotor motors ([Alt+5],[Alt+6) it is the outermost radius of the motor.
Rad1	Rotor surface radius.
Gap	Airgap length.
LM	Length of magnet in direction of magnetisation. If **RotType = Spoke**, this is not an input parameter but is determined by **BetaM** and **Rad1**. In this case it is a "spreadsheet" parameter, i.e., it is updated every time the geometry is edited.
BetaM	Magnet pole arc. For spoke-type and IPM rotors, **BetaM** is the pole-arc of the pole-piece. **BetaM** is normally in elec° but can be specified in mech° (see *Ted*/3).
POLES	Number of poles (2-480)
Rad3	For interior-rotor motors, **Rad3** is the outermost radius of the motor. For exterior-rotor motors ([Alt+5],[Alt+6), **Rad3** is the innermost radius of the stator body..
SLOTS	Number of stator slots (2-480). For standard winding types (**Conc/Equal, Conc/Sine** and **Lap**), **Slots/Poles**/Phases must be an integer. For fractional-slot windings, **Slots**/Phases must be an integer. Note that the number of phases is not directly an input parameter; it is selected via **Connex** (*Ted*/3).
RNSQ	Stator slot bottom shape. (Use **[Spacebar]** to toggle, or **[F2]** popup menu to select from list). Options available are: **Round** Round slot bottom **Square** Square slot bottom
Tw	Stator tooth width. PC-BDC assumes parallel-sided teeth.
SltDpth	Slot depth, measured from stator bore. (**SltDpth** is TGD+SD in PC-BDC 2.7/3.7).
SltOpen	Slot opening.
SltODpth	Radial depth of stator tooth tip. (**SltODpth** is TGD in PC-BDC 2.7/3.7.
SltOAng	Undercut angle of stator tooth tip (slot opening angle). This parameter is the same as TGANG in PC-BDC 2.7/3.7. See Fig. 30a.
Lstk	Stack length. The rotor and stator stack lengths are equal (but see **MOH**).
Inset	Amount by which edge of magnet is inset from the rotor surface in spoke-type rotors. (Used only when **RotType = Spoke**).
MagWid	Radial width of the magnet slot in spoke-type rotors. It is measured inwards from the from the radius **Rad1**-**Inset**. (Used only when**RotType = Spoke**).
IPMagWid	Magnet width in IPM rotor
Bridge	Bridge connecting the (laminated) pole-piece on either side to the web which runs along each q-axis in the IPM rotor. This bridge is generally saturated on open-circuit. It must be thick enough to carry the centrifugal force on the pole-piece and the magnet. (Used only when **RotType = IPM**).
Web	Web running along the q-axis in the IPM rotor. (Used only when **RotType = IPM**).

RotType	**Rotor type (Use [Spacebar] to toggle or [F2] popup menu to select from a list):** **SurfRad** Radially magnetized surface magnets **SurfPll** Parallel magnetized surface magnets **Breadloaf** Breadloaf type magnets **Spoke** Spoke type magnets **ExtRad** External radially magnetized surface magnets **ExtPll** External parallel magnetized surface magnets **IPM** Interior permanent magnets **Inset/CP** Inset magnets/consequent-pole type **Inset/Rel** Inset magnets/hybrid reluctance type
RotorAng	**Rotor offset angle. Used to draw the rotor at different angles.**

Spreadsheet Parameters

LM/Gap	**Ratio of magnet length to airgap length. This gives a rough guide to the permeance coefficient and therefore to the likely operating point of the magnet on open-circuit, before any magnetic calculations have been performed.**
Aslot	**Stator slot area (the same as SlotArea in the *Speed sheet*). It is useful to monitor this parameter when changing the lamination geometry, because it helps to keep control of the available winding area which is important for the efficiency.**
Axis1	**The position of the axis of phase 1 [in mech°]. (Same as Ax1 in the *Speed sheet*).**

Note : there is no Section 5.2. The sub-section numbers correspond to OPTIONS in the MAIN MENU.

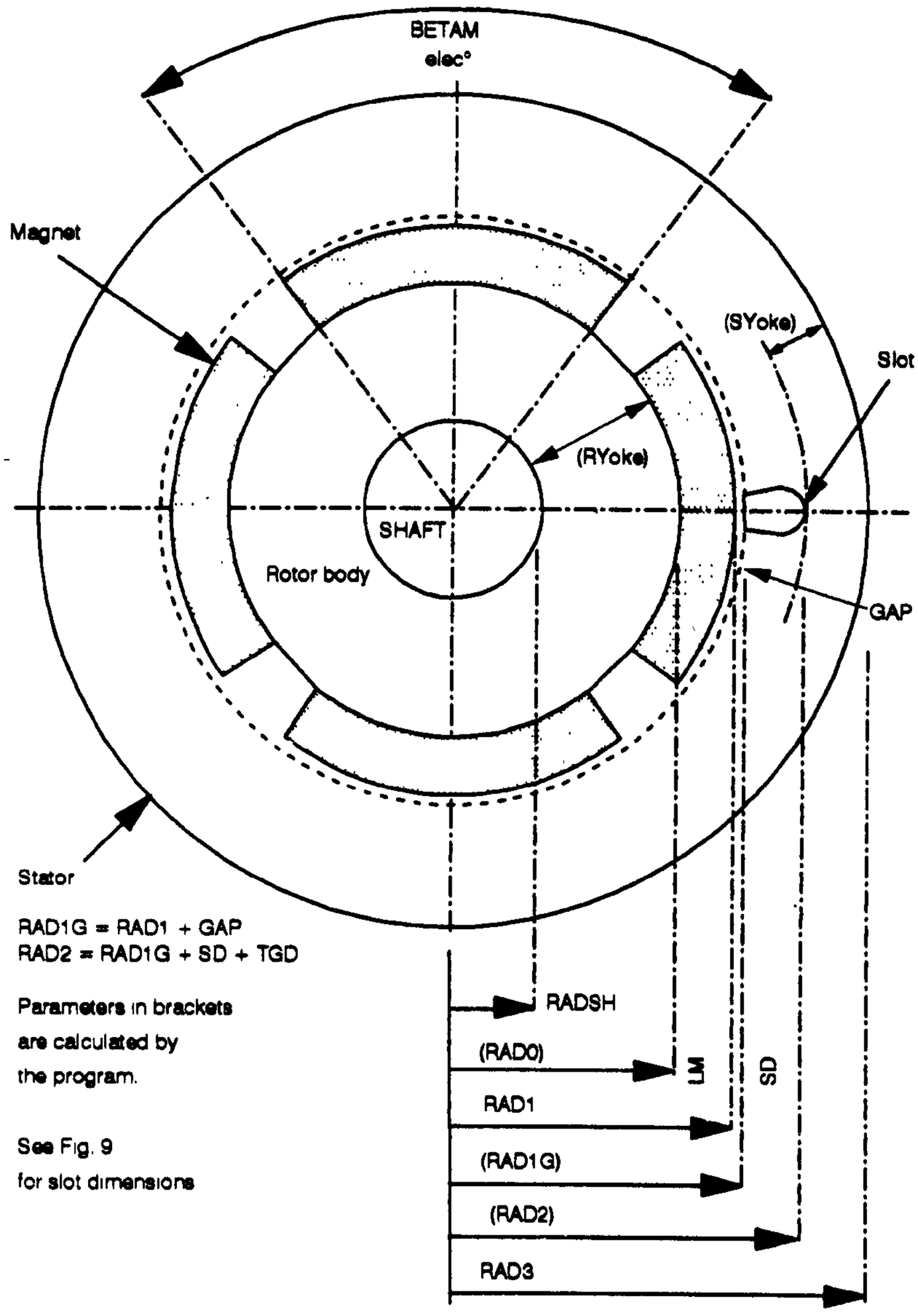

Fig. 29 Definition of motor dimensions

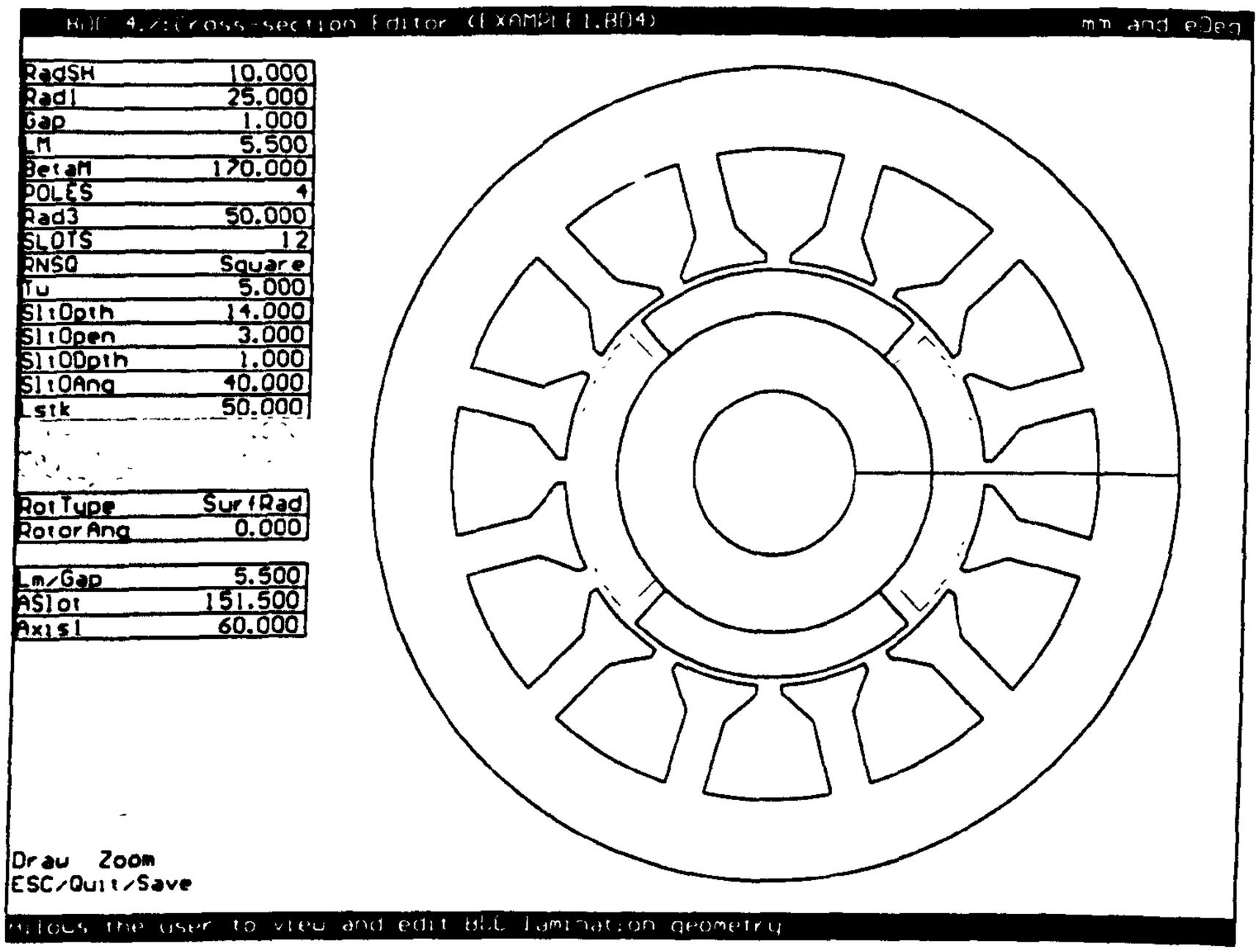

Fig. 29a : 1 PC-BDC 4.7 Surface Radial cross-section

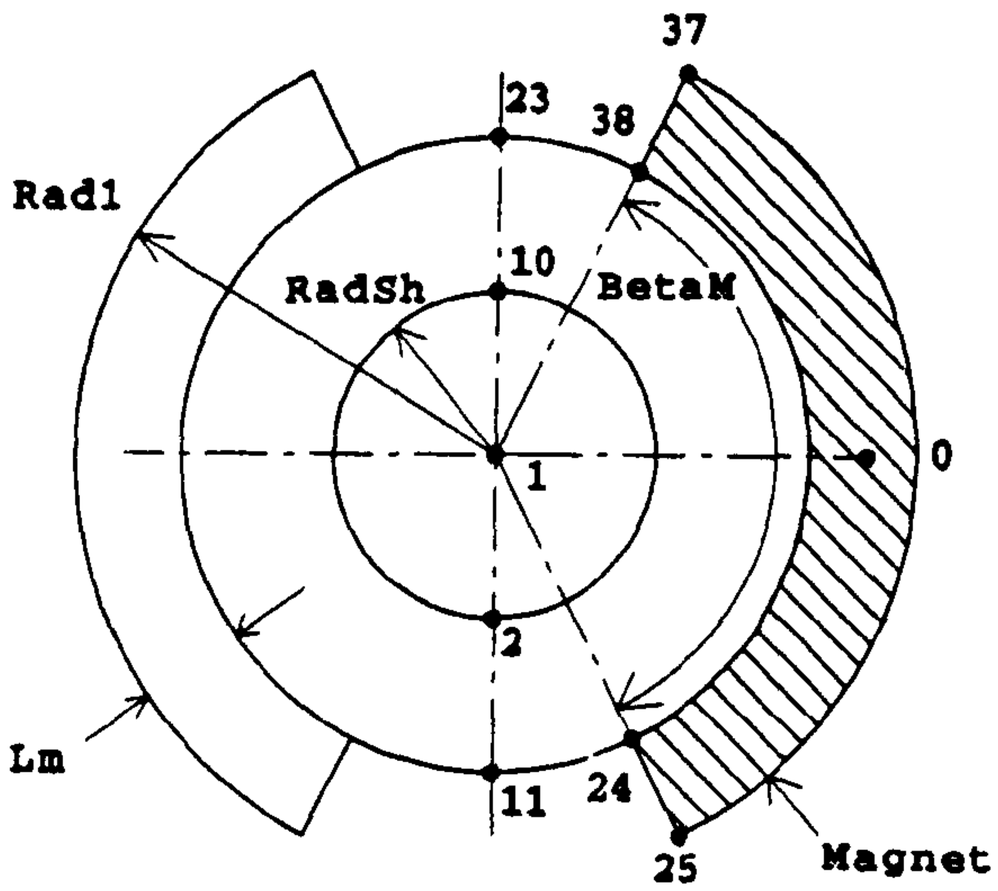

Fig. 29b : 1 Surface radial

PAGE
MISSING
IN
ORIGINAL

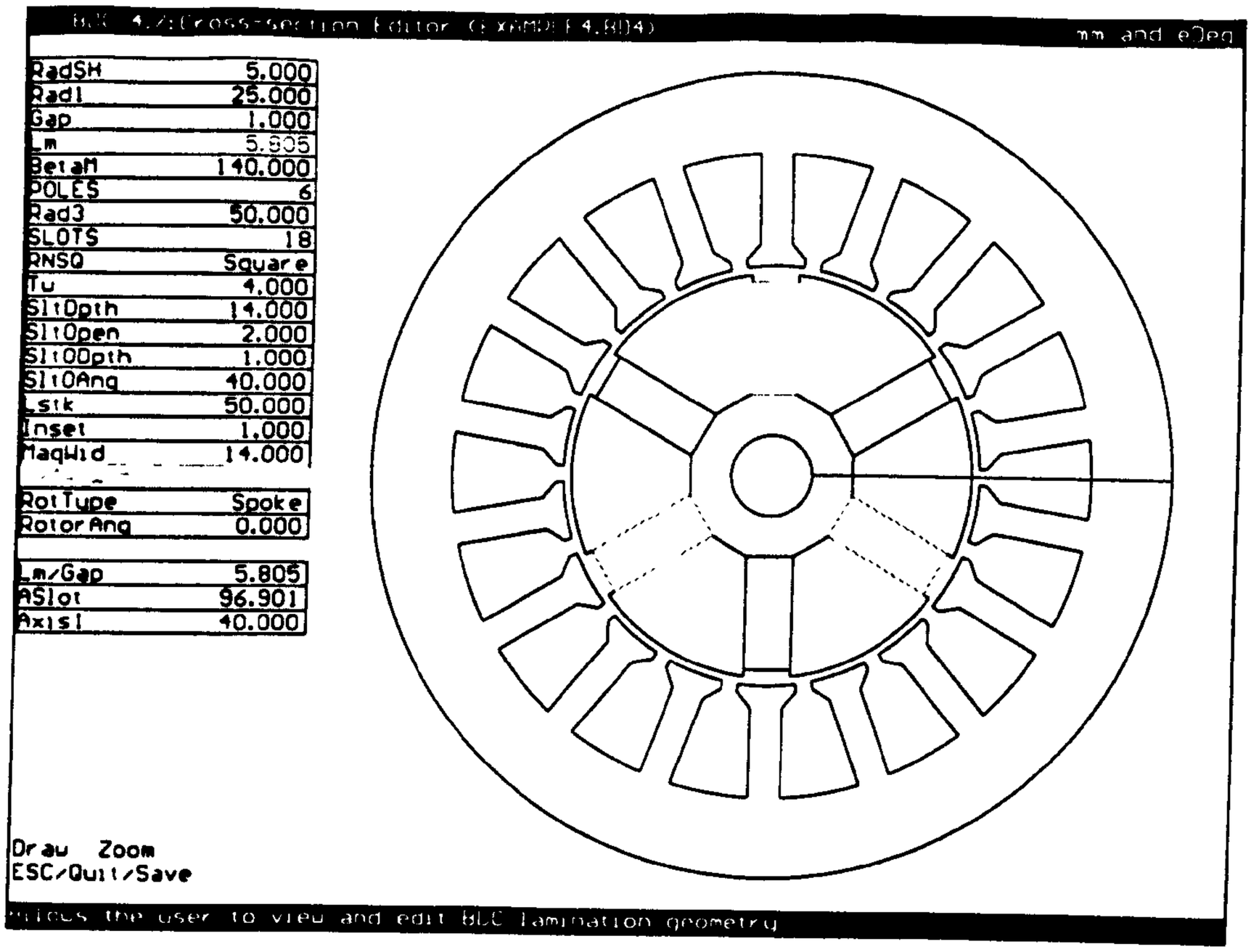

Fig. 29a : 4 PC-BDC 4.7 Spoke cross-section

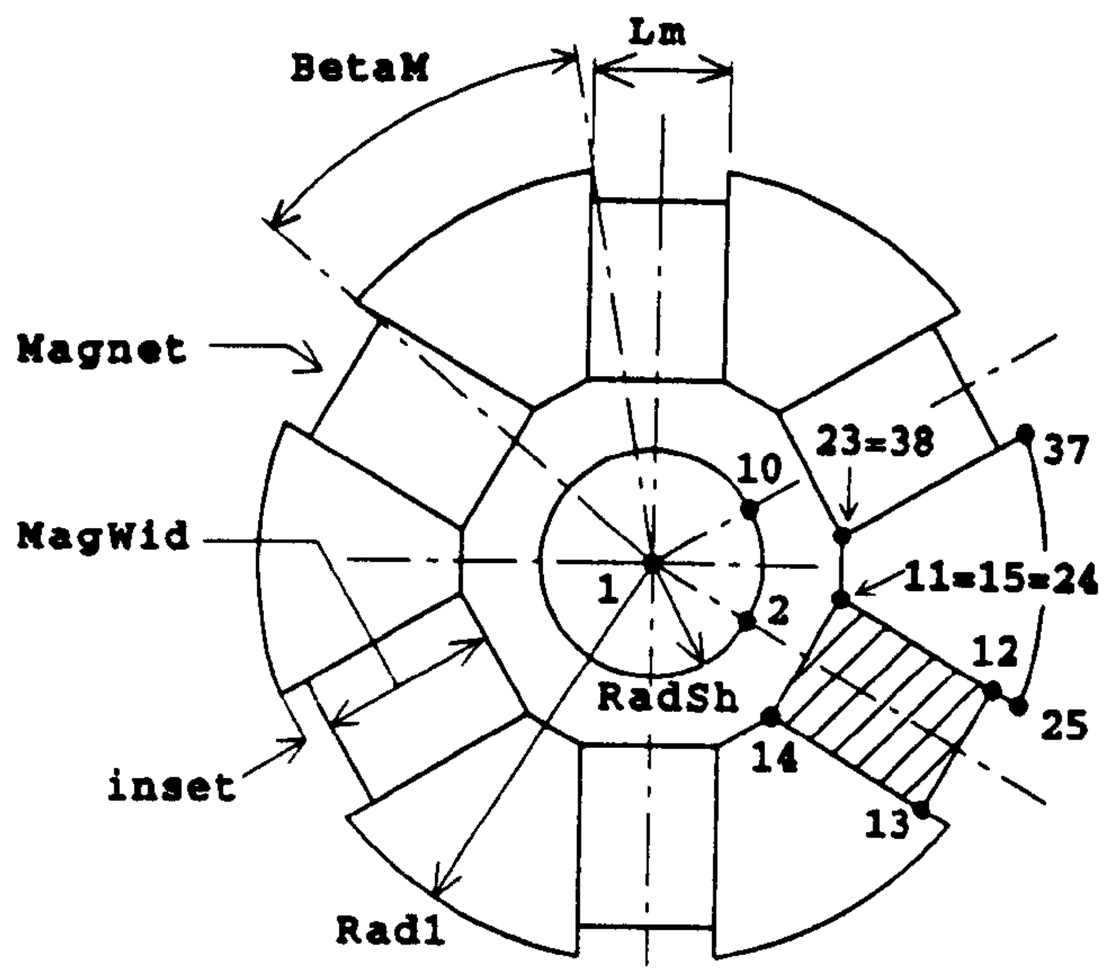

Fig. 29b : 4 Spoke

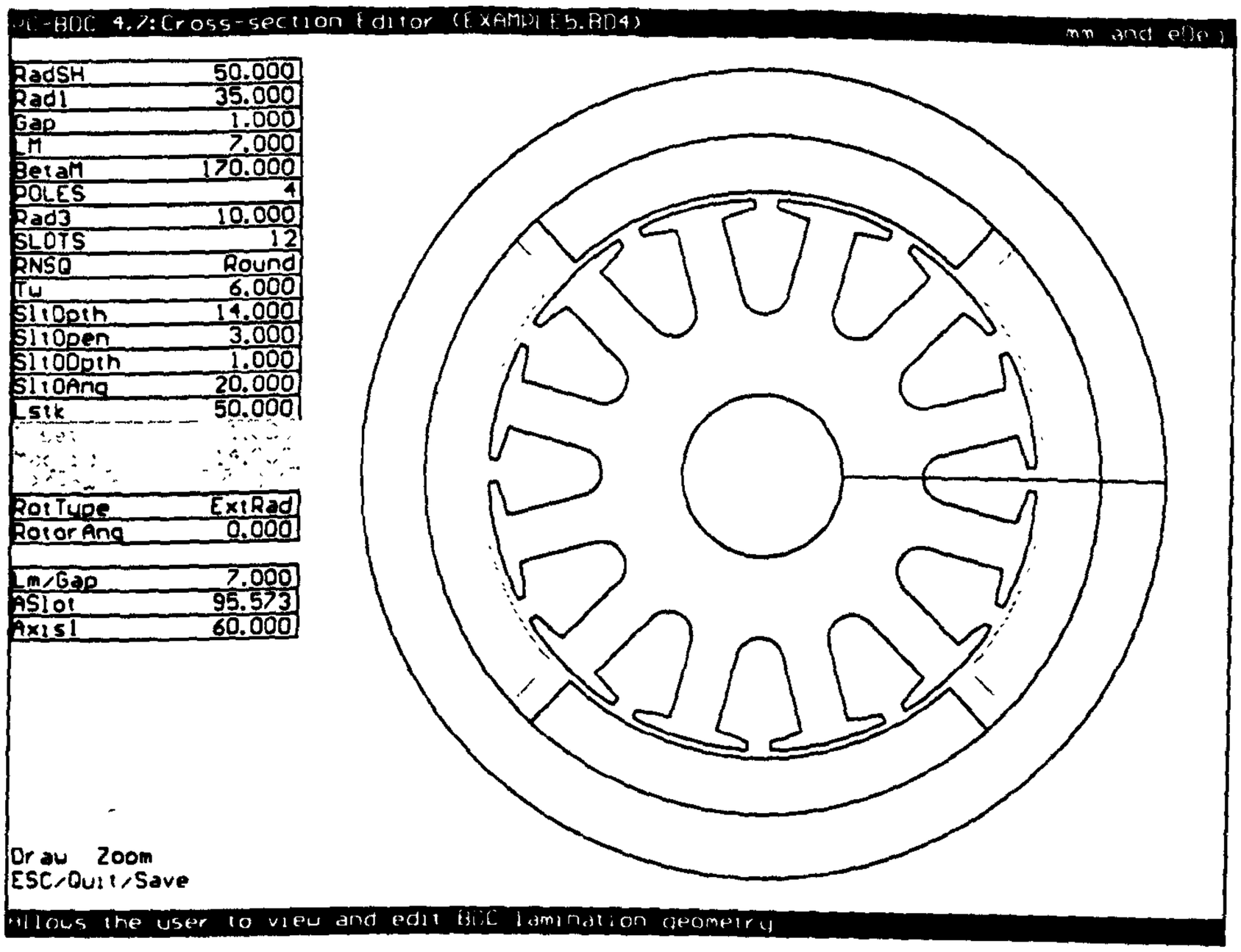

Fig. 29a : 5 PC-BDC 4.7 Exterior Surface Radial cross-section

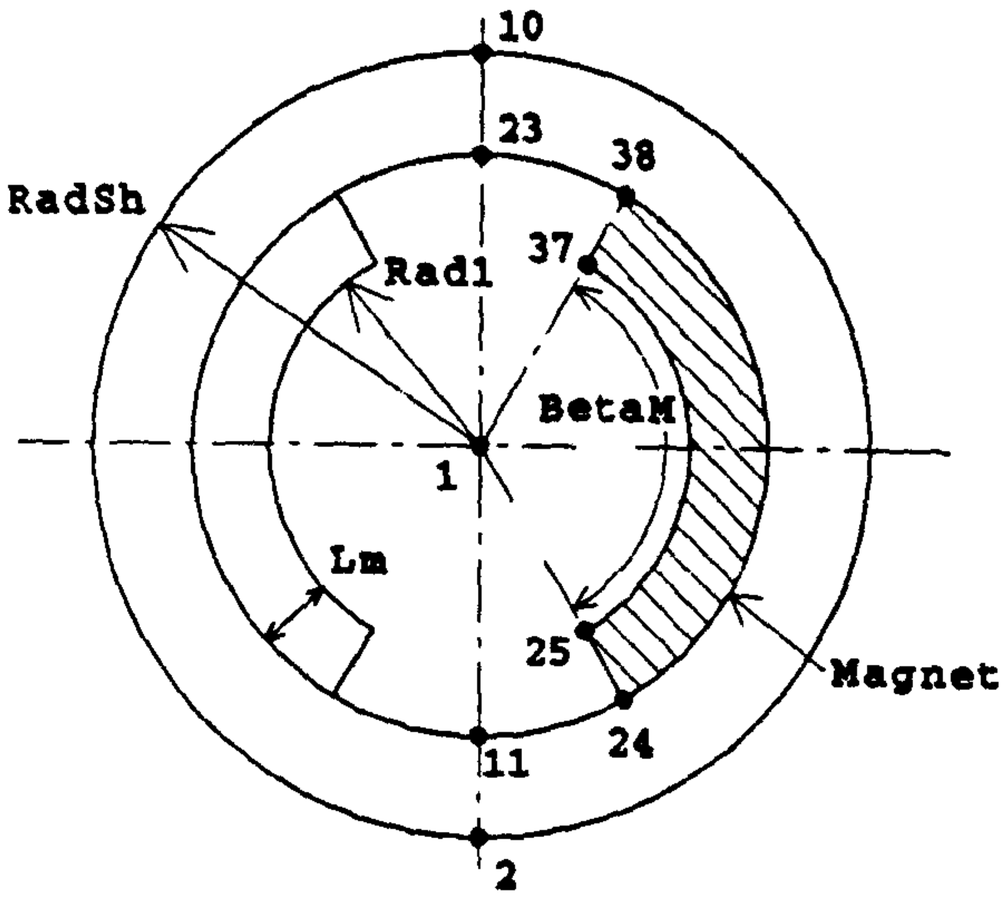

Fig. 29b : 5 Ext. surface radial

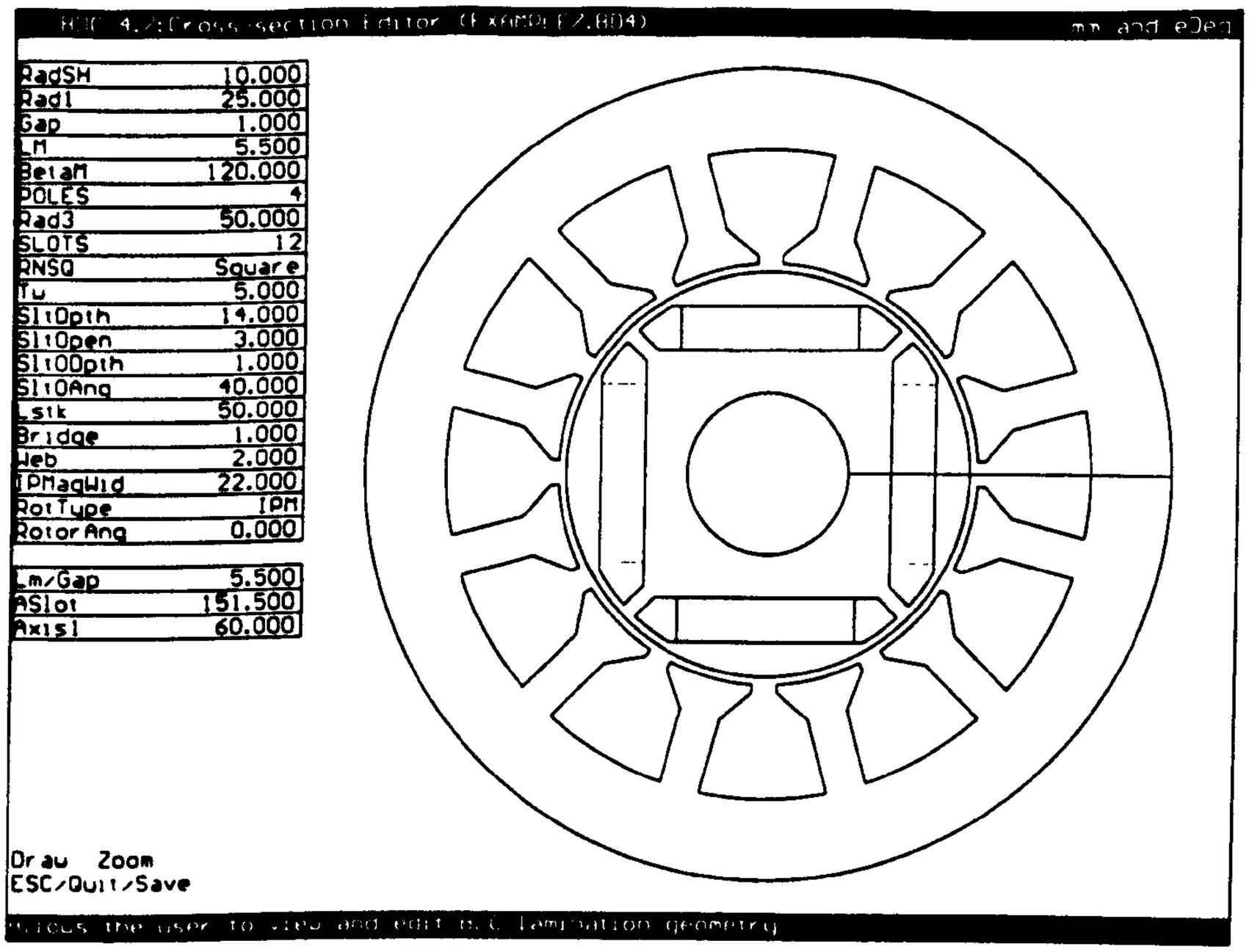

Fig. 29a : 7 PC-BDC 4.7 IPM cross-section

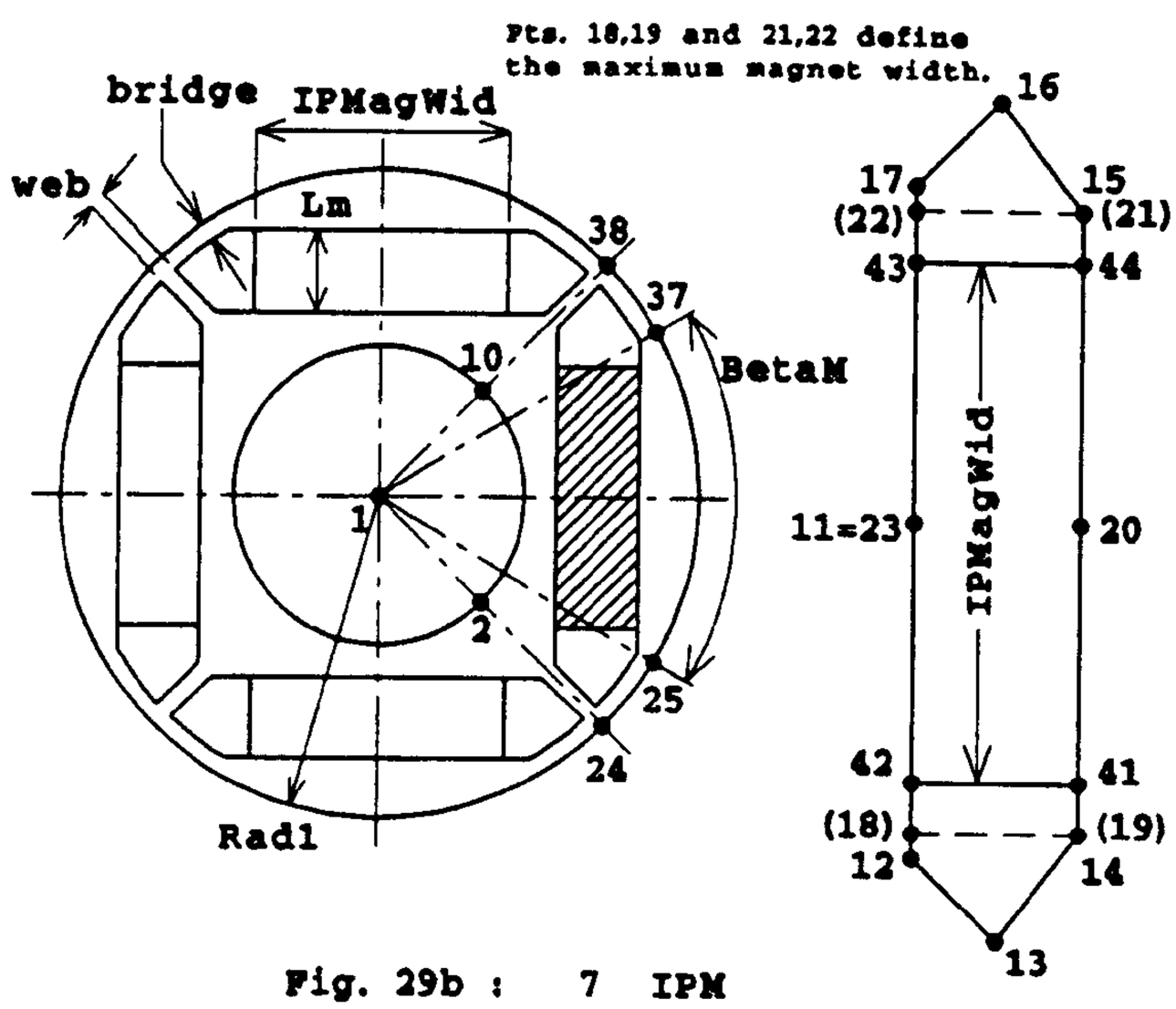

Fig. 29b : 7 IPM

PAGE NUMBERING AS ORIGINAL

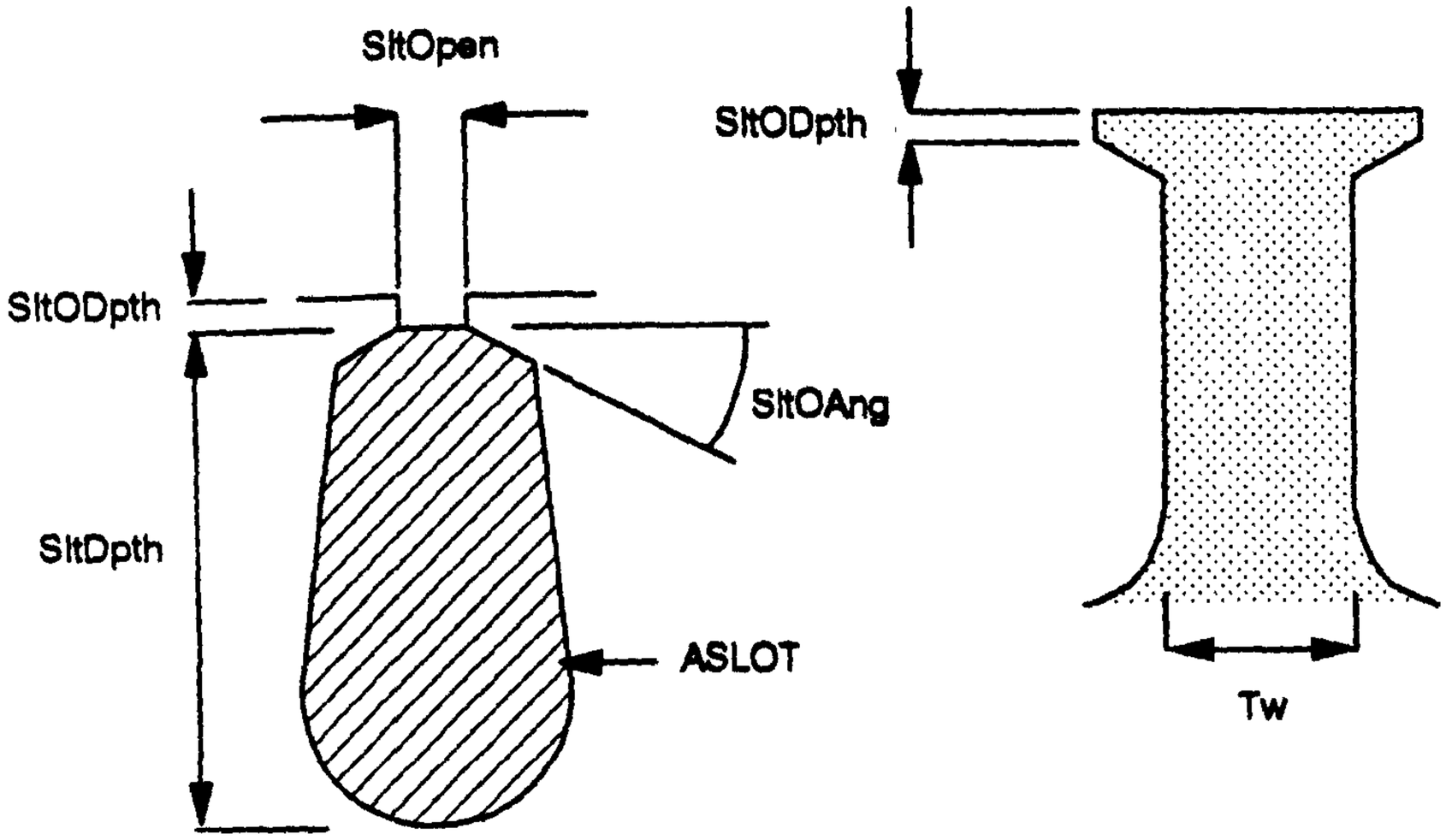

Fig. 30a Slot dimensions

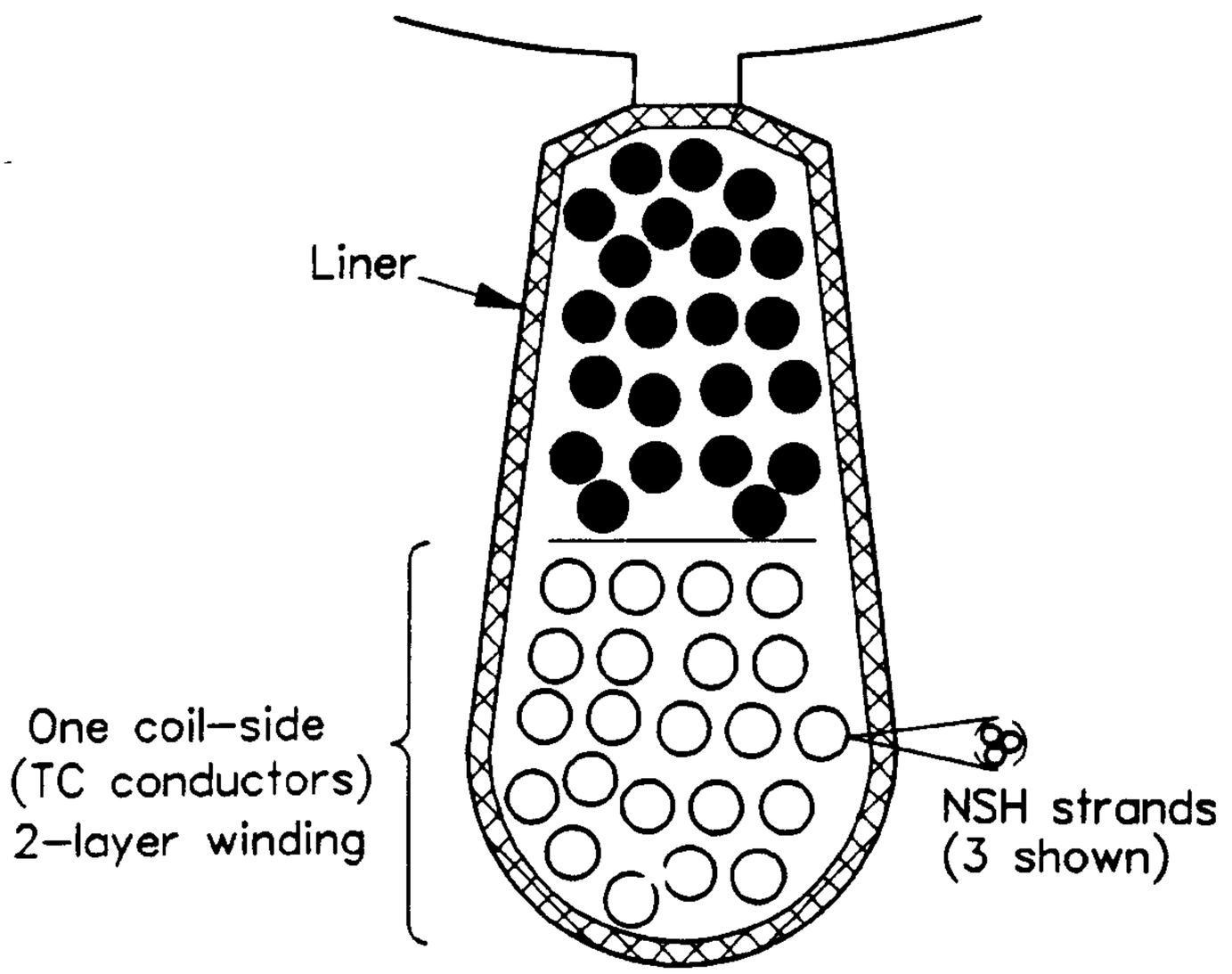

Fig. 31 Definition of TC, NSH, Layers, and Coilside

6 DEFINITION OF PARAMETERS

The parameter definitions are grouped as follows:

Section 6.1	Parameters first seen in Cross-section editor ①
Section 6.2	Parameters first seen in Dynamic Design ②
Section 6.3	Parameters first seen in Template Editor ③
Section 6.4	Parameters first seen in Output ④

STEEL DATA - Important Note

The importance of the steel data cannot be over-emphasized. (See §4.6 and Table 3). The B/H data needs to extend smoothly up to at least the value of **Bm** (§6.3, below). Smoothness in this data is especially important when using cobalt-iron.

Bs should be set just below the knee of the B/H curve : typically around 1.3T for normal electrical steels and around 1.8T for cobalt-iron. Use the template editor ③) to adjust **Bs**.

The core-loss coefficients **CfCh**, **Cfa**, **Cfb**, and **CfCe** can be extracted from graphs or tables of core-losses as described in Appendix 1, or by use of the auxiliary program ILCE.EXE (Appendix 1).

The sample steels included in STEEL10.SDB are examples only, and users should provide their own steel data once PC-SRD is running.

The units for B/H curves are always T and A/m. The units for core-loss coefficients **CfCh**, **Cfa**, **Cfb**, and **CfCe** are always derived from W/lb values.

6.1 Cross-section editor input parameters [1]

Rsh	mm or in	shaft radius (Fig. 7)
R0	mm or in	radius of rotor slot-bottom (Fig. 7)
R1	mm or in	rotor radius (Fig. 7)
Gap	mm or in	airgap length
R2	mm or in	radius of stator slot-bottom (Fig. 6a)
R3	mm or in	stator outside radius (Fig. 6a)
Ns		No. of stator poles (see Table 1, §4.1)
Nr		No. of rotor poles (see Table 1, §4.1)
BetaS	mech°	stator pole arc (Fig. 6a)
BetaR	mech°	rotor pole arc (Fig. 7)
tpr_S	mech°	stator pole taper (Fig. 6c)
tpr_R	mech°	rotor pole taper (Fig. 6c)
fil_S	mm or in	stator pole fillet radius (Fig. 6c)
fil_R	mm or in	rotor pole fillet radius (Fig. 6c)
D1s	mm or in	stator tooth tang (Figs. 6a and 6c)
D2s	mm or in	stator pole shank (Figs. 6a and 6c)
Ntp		No. of teeth per stator pole (default = 1)
LStk	mm or in	stack length (Fig. 6b)
Angle	mech° or elec°	rotor position in drawing
SigmR	mech°	wide rotor pole-arc (STEPPED-GAP rotors only) (Fig. 7)
SG	mm or in	Step in rotor surface (STEPPED-GAP rotors only) (Fig. 7)

These parameters are illustrated in Figs. 2, 6 and 7. All except **Angle** are included in the main datafile. They also appear in the template editor [3]. **Angle** is included for convenience in viewing the rotor at different positions.

tpr_S and **tpr_R** can both be positive or negative, Fig. 6c. If **tpr_S** is negative, the stator pole is "undercut" and then **D1s** and **D2s** are used to define the geometry, Fig. 6c. If **tpr_S** is positive, **D1s** and **D2s** are not used unless **Ntp** > 1 (Fig. 6a).

Multiple teeth per stator pole

Most SRM designs have one tooth per stator pole (Fig. 2a, Fig. 6a), but PC-SRD can model motors with up to 4 teeth per stator pole. Fig. 2b shows an example with **Ntp** = 2. Another example is obtained using [Alt-4]. It has three phases (**Nph** = 3), six stator poles (**Ns** = 6), 12 stator teeth (**Ns** * **Ntp**) and 10 rotor teeth (**Nr** = 10). The rotor tooth number **Nr** must be made equal to (**Ns** * **Ntp**) - 2. The alternative choice of **Nr** = (**Ns** * **Ntp**) + 2 is not supported. Generally the smaller value of **Nr** is preferable because it permits a lower UNALIGNED inductance and lower switching frequency. Conventional single-tooth/pole designs run with **Ntp** = 1 and **D1s** = **D2s** = 0. When **Ntp** > 1, the stator tooth arc is made equal to **BetaR**.

PC-SRD's internal calculation of mag. curves is less accurate with multiple-teeth/pole, because of the fine tooth structure. It is recommended to supplement PC-SRD with EXTERNAL MAG CURVES obtained from finite-element calculations or measurements (§8).

STEPPED-GAP *rotors*

The two parameters associated with STEPPED-GAP rotors, **SigmR** and **SG**, appear only in the cross-section editor [1], and not in the template editor [3]. NON-SYMMETRIC rotor geometry has the same parameters as for symmetric STEPPED-GAP rotor geometry, but is selected with [Alt-Y].

PC-SRD's internal calculation of mag. curves is less accurate with STEPPED-GAP geometry. It is recommended to supplement PC-SRD with EXTERNAL MAG CURVES obtained from finite-element calculations or measurements.

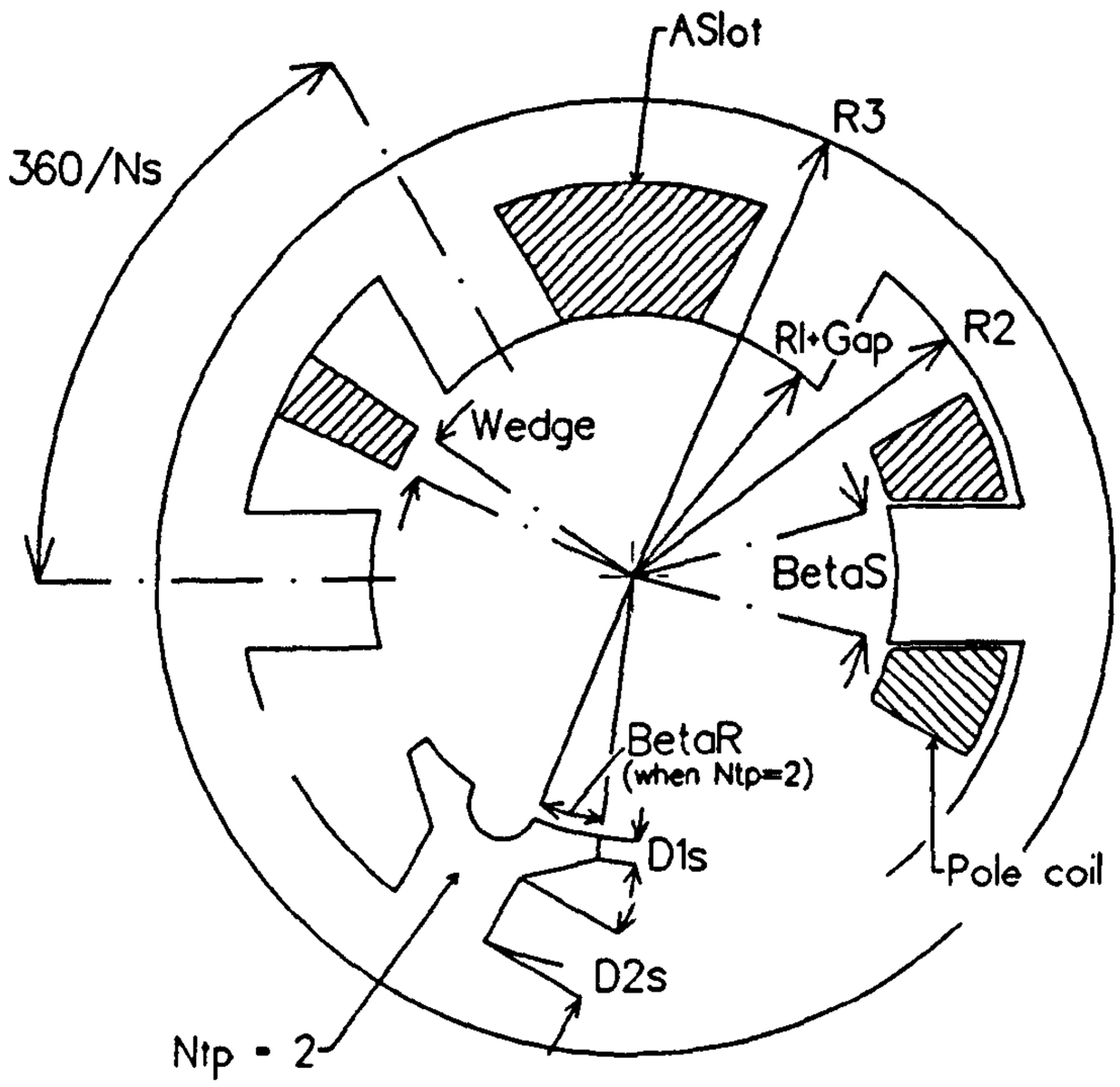

Fig. 6a. Definition of stator cross-section parameters. The reference stator pole is the one shown with the pole coil. Geometry is shown for both **Ntp** = 1 and **Ntp** = 2.

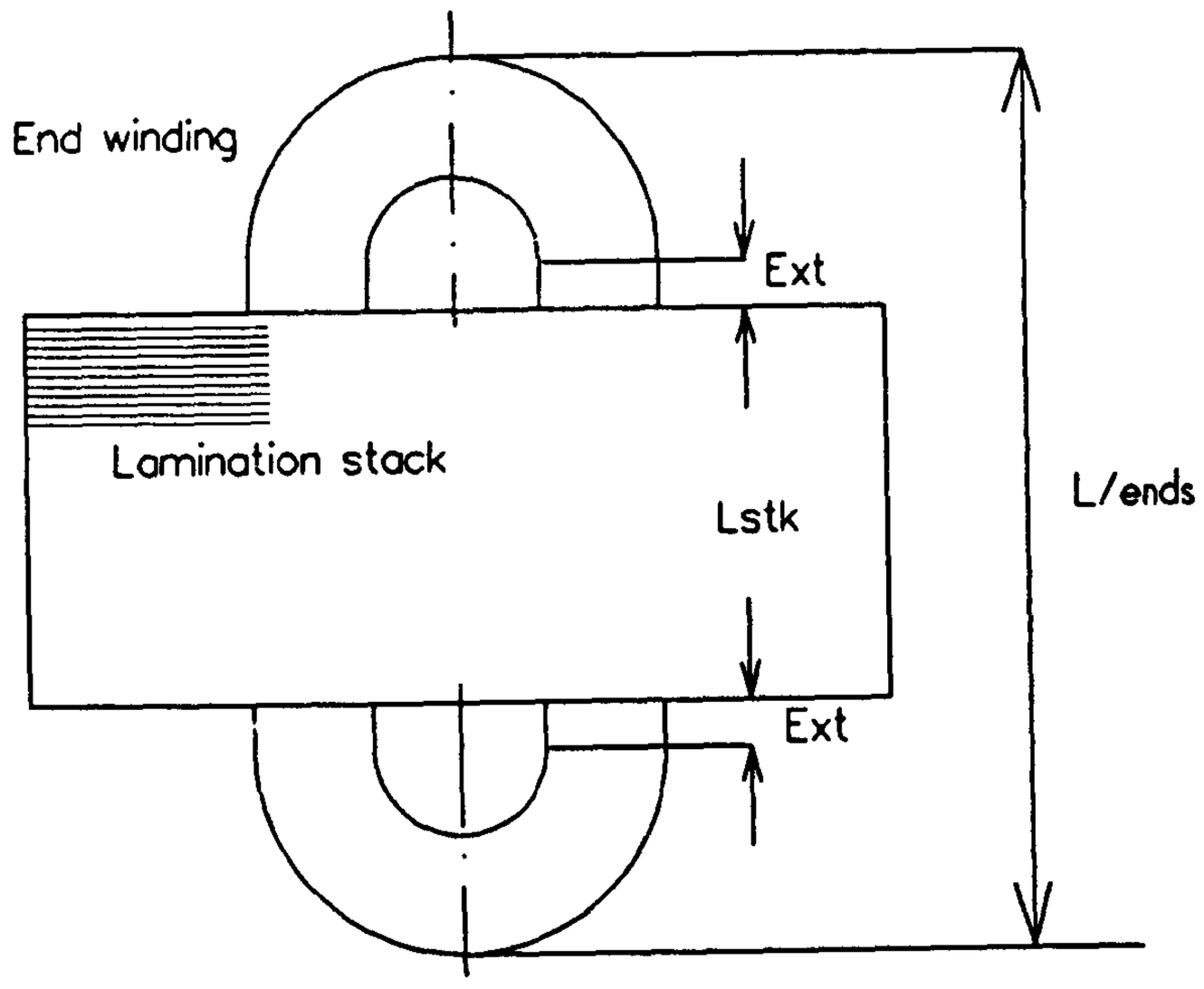

Fig. 6b. Definition of axial parameters.

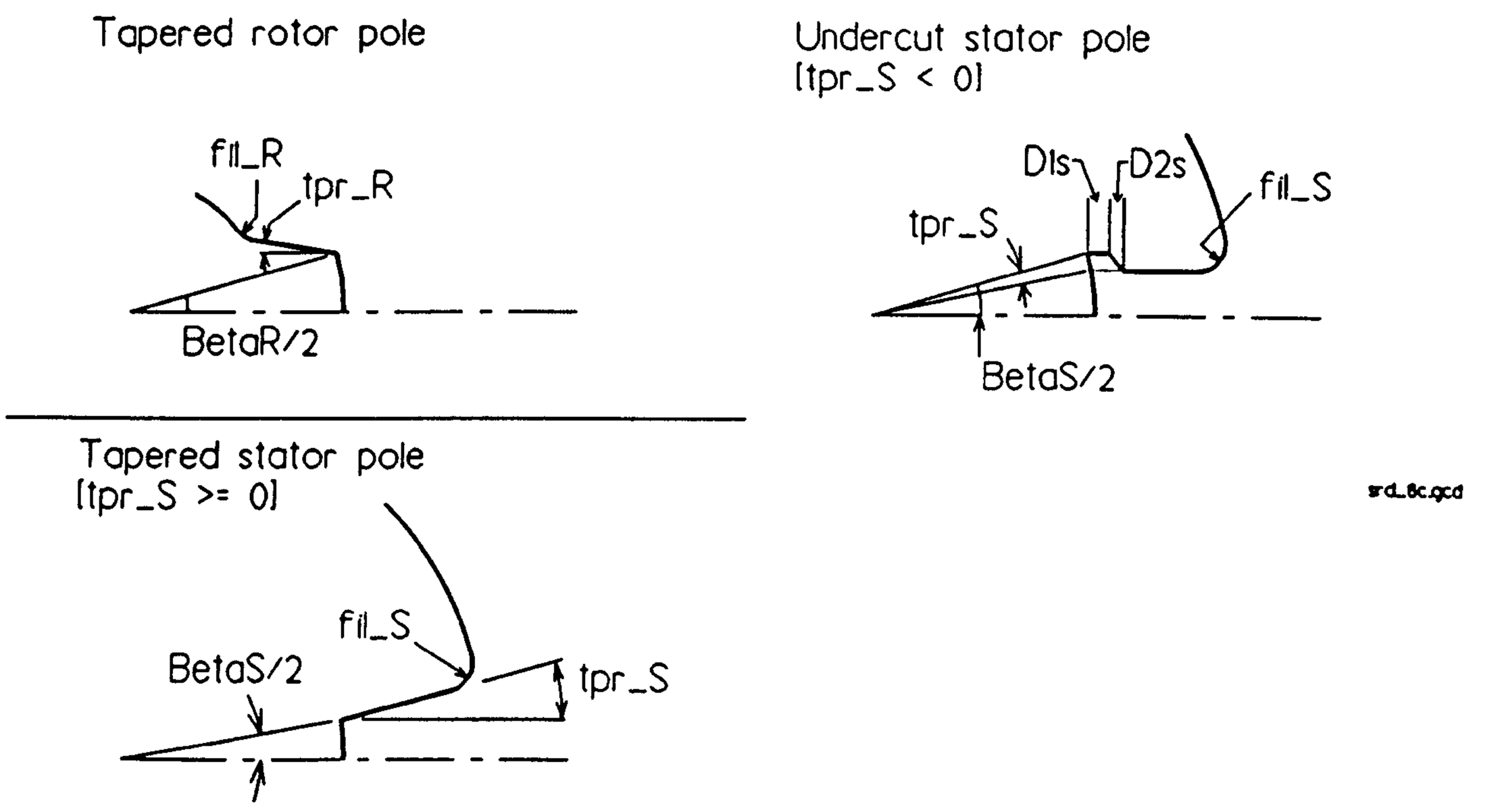

Fig. 6c. Definition of taper and fillet parameters.

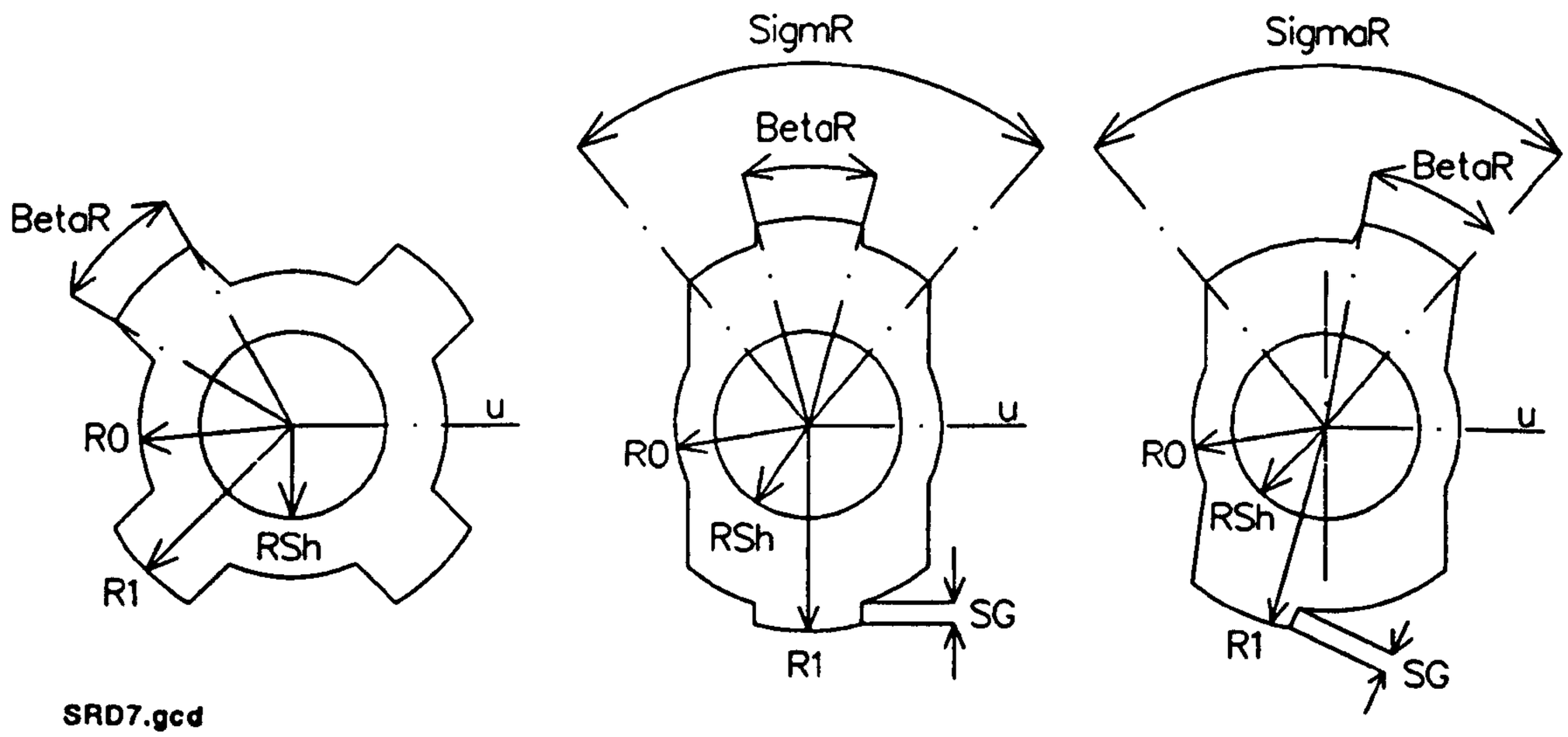

Fig. 7. Definition of rotor cross-section parameters. From left to right: NORMAL rotor; STEPPED-GAP rotor; NON-SYMMETRIC STEPPED-GAP rotor.

Each rotor is shown with its *reference interpolar axis u* aligned with the reference stator pole in Fig. 6a, corresponding to the UNALIGNED position. In the NON-SYMMETRIC rotor the interpolar axis is defined with reference to the *wide* pole-arc **SigmR**, not the narrow pole-arc **BetaR**.

References

[1] M. Faraday, *A reproduction of some portions of Faraday's diary : presented by the managers of the Royal Institution of Great Britain*. Cambridge University Press, W. Lewis, Massachusetts, 1931.

[2] J. C. Maxwell, *A Treatise on Electricity and Magnetism*, Third Edition, Clarendon Press, Oxford, 1892.

[3] P. J. Lawrenson, J. M. Stephenson, P. T. Blenkinsop, J. Corda, and N. N. Fulton, "Variable-speed switched reluctance motors," *IEE Proceedings*, Vol. 127, Pt. B, No. 4, July 1980, pp. 253–265.

[4] M. R. Harris and T. J. E. Miller, "Comparison of design and performance parameters in switched reluctance and induction motors," *Proceedings of International Conference on Electric Machines and Drives*, London, United Kingdom, September 1989, pp. 303–307.

[5] M. K. Jenkins, T. S. Birch, and D. Howe, "Static torque production in hybrid stepper motors : the influence of saturation and magnet MMF," *Proceedings of International Conference on Electric Machines and Drives*, London, United Kingdom, November 1987, pp. 270–274.

[6] M. R. Harris, P. J. Lawrenson, J. M. Stephenson, *Per Unit Systems*, Cambridge University Press, 1970.

[7] J. D. Kraus, *Electromagnetics*, McGraw-Hill, Third Edition, 1989.

[8] C. J. Carpenter, "Surface-integral methods of calculating forces on magnetized iron parts," *Proceedings IEE*, Vol. 107C, 1960, pp. 19–28.

[9] J. Penman and M. D. Grieve, "Efficient calculation of force in electromagnetic devices," *IEE Proceedings*, Vol. 133, Pt. B No. 4, July 1986, pp. 212–216.

[10] L. Chang, A. R. Eastham, and G. E. Dawson, "Permanent magnet synchronous motor: finite element torque calculations," *Conference Record of the IEEE Industry Application Society Annual Meeting*, San Diego, California, October 1989, pp. 69–73.

[11] T. Tärnhuvud and K. Reichert, "Accuracy problems of force and torque calculation in FE-systems," *IEEE Transactions on Magnetics*, Vol. 24, No. 1, January 1988, pp. 443–446.

[12] S. McFee and D. A. Lowther, "Towards accurate and consistent force calculation in finite element based computational magnetostatics," *IEEE Transactions on Magnetics*, Vol. 23, No. 5, September 1987, pp. 3771–3773.

[13] J. L. Coulomb, "A methodology for the determination of global electromechanical quantities from a finite element analysis and its application to the evaluation of magnetic forces, torques and stiffness," *IEEE Transactions on Magnetics*, Vol. 19, No. 6, November 1983, pp. 2514–2519.

[14] J. L. Coulomb and G. Meunier, "Finite element implementation of virtual work principle for magnetic or electric force and torque computation," *IEEE Transactions on Magnetics*, Vol. 20, No. 5, September 1984, pp. 1894–1896.

[15] E. M. Freeman and R. A. Ashen, "Force calculation in magnetic field problems using virtual work with only one solution," Proceedings of the International Conference on Electric Machines and Drives, Oxford, United Kingdom, September 1993, pp. 318–322.

[16] E. A. Aronson and J. R. Brauer, "Magnetic torque and force calculation by direct differentiation of finite element coenergy," *IEEE Transactions on Magnetics*, Vol. 25, No. 5, September 1989, pp. 3578–3580.

[17] M. J. DeBortoli and S. J. Salon, "Computation of forces and torque in electromagnetic devices using the finite element method," *Proceedings of the International conference on Electrical Machines*, Boston, Massachusetts, September 1990, pp. 699–705

[18] J. Mizia, K. Adamiak, A. R. Eastham, and G. E. Dawson, "Finite element force calculation: comparison of methods for electric machines," *IEEE Transactions on Magnetics*, Vol. 24, No. 1, January 1988, pp. 447–450.

[19] M. Marinescu and N. Marinescu, "Numerical computation of torques in permanent magnet motors by Maxwell stresses and energy method," *IEEE Transactions on Magnetics*, Vol. 24, No. 1, January 1988, pp. 463–466.

[20] D. Platt and S. Geetha, "Torque calculation of machines with permanent magnet materials," *Electric Machines and Power Systems*, Vol. 24, 1996, pp. 393–415.

[21] T. Kenjo, *Stepping motors and their microprocessor control*, Clarendon Press, Oxford Science Publications, First Edition, 1984.

[22] T. A. Lipo and Y. Li, "The CFM - a new family of electrical machines," *Proceedings of International Power Electronics Conference*, Yokohama, Japan, January 1995, pp. 1–9.

[23] D. Howe and Z. Q. Zhu, "The influence of finite element discretisation on the prediction of cogging torque in permanent magnet excited motors," *IEEE Transactions on Magnetics*, Vol. 28, No. 2, March 1992, pp. 1080–1083.

[24] Y. Kawase, T. Yamaguchi, and Y. Hayashi, "Analysis of cogging torque of permanent magnet motor by 3-D finite element method," *IEEE Transactions on Magnetics*, Vol. 31, No. 3, May 1995, pp. 2044–2047.

[25] B. Ackermann, J. H. H. Janssen, R. Sottek, and R. I. Van Steen, "New technique for reducing cogging torque in a class of brushless DC motors," *IEE Proceedings*, Vol. 139, Pt. B, No. 4, July 1992, pp. 315–320.

[26] Z. Q. Zhu and D. Howe, "Analytical prediction of the cogging torque in radial-field permanent magnet brushless motors," *IEEE Transactions on Magnetics*, Vol. 28, No. 2, March 1992, pp. 1371–1374.

[27] E. Favre, L. Cardoletti, and M. Jufer, "Permanent magnet synchronous motors : a comprehensive approach to cogging torque suppression," *IEEE Transactions on Industry Applications*, Vol. 29, No. 6, November/December 1993, pp. 1141–1149.

[28] T. Sebastian, G. R. Slemon, and M. A. Rahaman, "Design considerations for variable speed permanent magnet motors," *Proceedings of International Conference on Electrical Machines*, Vol. 3, München, Germany, September 1986, pp. 1099–1102.

[29] J. De La Ree and Jaime Latorre, "Permanent magnet machines torque considerations," *Conference Record of IEEE Industry Applications Society Annual Meeting*, Pittsburgh, Philadelphia, October 1988, pp. 32–37.

[30] J. Y. Hung and Z. Ding, "Design of currents to reduce torque ripple in brushless permanent magnet motors," *IEE Proceedings*, Vol. 140, Pt. B, No. 4, July 1993, pp. 260–266.

[31] C. Hanselman, *Brushless permanent-magnet motor design*, McGraw Hill, 1994.

[32] B. Nogarede and M. Lajoie-Mazenc, "Torque ripple minimization methods in sinusoidal fed synchronous permanent magnet machines," *Proceedings of International Conference on Electrical Machines & Drives*, London, United Kingdom, September 1991, pp. 41–45.

[33] H. Bolton and N. Mallinson, "Investigation into a class of brushless DC motor with quasisquare voltages and currents," *IEE Proceedings*, Vol. 133, Pt. B, No. 2, March 1986, pp. 103–111.

[34] J. A. Wagner, "Numerical analysis of cogging torque in a brushless DC motor," *Conference Record of IEEE Industry Applications Society Annual Meeting*, Vol. 75, CH0999-31A, Atlanta, Georgia, October 1975, pp. 669–674.

[35] A. Miraoui, L. De Fang, and J. Kauffman, "Performance analysis of permanent magnet brushless DC motor," *Proceedings of International Conference on Electrical Machines & Drives*, Oxford, United Kingdom, September 1993, pp. 371–375.

[36] E. Hamdi, A. Licariao-Nogueira, and P. Silvester, "Torque computation by mean and difference potentials," *IEE Proceedings*, Vol. 140, Pt. A, No. 2, March 1993, pp. 151–154.

[37] G. Jang and D. Lieu, "Vibration reduction in electric machine by magnet interlacing," *IEEE Transactions on Magnetics*, Vol. 28, No. 5, September 1992, pp. 3024–3026.

[38] T. Ishikawa and G. Slemon, "A method of reducing ripple torque in permanent magnet motors without skewing," *IEEE Transactions on Magnetics*, Vol. 29, No. 2, March 1993, pp. 2028–2031.

[39] C. Chan, J. Jiang, G. Chen, X. Wang, and K. Chau, "A novel polyphase multipole square-wave permanent magnet motor drive for electric vehicles", *IEEE Transactions on Industry Applications*, Vol. 30, No. 5, September/October 1994, pp. 1258–1266.

[40] A. Kaddouri and H. Le-Huy, "Analysis and design of a slotless NdFeB permanent-magnet synchronous motor for direct drive," *Conference Record of IEEE Industry Applications Society Annual Meeting*, Houston, Texas, October 1992, pp. 271–278.

[41] R. Hanitsch, R. Belmans, L. Walkoff, and W. Geysen, "Brushless DC motor with airgap windings - influence of back iron material on motor efficiency," *Proceedings of International Conference on Electrical Machines and Drives*, London, United Kingdom, September 1991, pp. 126–130.

[42] A. Murray, "Torque and EMF ripple reduction in brushless machines," *Proceedings of IEE Colloquium on PM Machines and Drives*, 1993, pp. 8/1–8/4.

[43] M. Lajoie-Mazenc, B. Nogarede, and J. C. Fagundes, "Analysis of torque ripple in electronically commutated permanent magnet machines and minimization methods," *Proceedings of International Conference on Electrical Machines and Drives*, London, United Kingdom, 1989, pp. 85–89.

[44] D. Jouve and D. Bui, "Torque ripple compensation in DSP-based brushless servo drive," *Proceedings of PCIM Conference*, Nürnberg, Germany, May 1993, pp. 28–37.

[45] M. Goto and K. Kobayashi, "An analysis of the cogging torque of a DC motor and a new technique of reducing the cogging torque," *Electrical Engineering in Japan*, Vol. 103, No. 5, 1983, pp. 113–120.

[46] K. Kobayashi and M. Goto, "A brushless DC motor of a new structure with reduced torque fluctuations," *Electrical Engineering in Japan*, Vol. 105, No. 3, 1985, pp. 104–112.

[47] D. A. Staton, W. L. Soong, and T. J. E. Miller, "Unified theory of torque production in switched reluctance and synchronous reluctance motors," *IEEE Transactions on Industry Applications*, Vol. 31, No. 2, March/April 1995, pp. 329–337.

[48] D. A. Staton, R. P. Deodhar, W. L. Soong, and T. J. E. Miller, "Torque calculation using the flux-MMF diagram in AC, DC and reluctance motors," *IEEE Transactions on Industry Applications*, Vol. 32, No. 1, January/February 1996, pp. 180–188.

[49] R. P. Deodhar, D. A. Staton, T. M. Jahns, and T. J. E. Miller, "Prediction of cogging torque using the flux-MMF diagram technique," *IEEE Transactions on Industry Applications*, Vol. 32, No. 3, May/June 1996, pp. 569–576.

[50] R. P. Deodhar, D. A. Staton, and T. J. E. Miller, "Variation of torque constant in brushless PM motors," *Proceedings of International Conference on Electrical Machines and Drives*, Durham, United Kingdom, September 1995, pp. 405–409.

[51] R. P. Deodhar, D. A. Staton, and T. J. E. Miller, "Modelling of skew using the flux-MMF diagram," *IEEE Transactions on Industry Applications*, Vol. 32, No. 6, November/December 1996, (in press).

[52] R. P. Deodhar, D. A. Staton, and T. J. E. Miller, "Flux-MMF diagram : a technique for analysis and comparative evaluation of electric machines," *Proceedings of Fourth International Conference on Electrical Rotating Machines*, Mumbai, India, January 1996, pp. 57–62.

[53] R. P. Deodhar, S. Andersson, I. Boldea, and T. J. E. Miller, "The flux-reversal machine : a new brushless doubly-salient permanent-magnet machine," *Conference Record of IEEE Industry Application Society Annual Meeting*, San Diego, California, October 1996, pp. 786–793.

[54] Y. Liao, F. Liang, and T. A. Lipo, "A novel permanent magnet motor with doubly salient structure," *IEEE Transactions on Industry Applications*, Vol. 31, No. 5, September/October 1995, pp. 1069–1078.

[55] A. E. Fitzgerald and C. Kingsley Jr., *Electric Machinery*, 2nd Edition, McGraw Hill, 1961.

[56] J. R. Hendershot and T. J. E. Miller, *Design of Brushless Permanent-Magnet Motors*, Clarendon Press, Oxford Science Publications and Magna Physics Publishing, 1994.

[57] T. J. E. Miller, *Switched Reluctance Motors and their Control*, Clarendon Press, Oxford Science Publications, 1993.

[58] T. J. E. Miller, *Brushless Permanent-Magnet and Reluctance Motor Drives*, Clarendon Press, Oxford Science Publications, 1989.

[59] H. H. Woodson and J. R. Melcher, *Electromechanical Dynamics Part I: Discrete Systems*, John Wiley, 1968.

[60] D. C. White and H. H. Woodson, *Dynamics of the Electromechanical Energy Conversion*, Wiley, 1963.

[61] D. A. Staton, *C.A.D. of Permanent-Magnet D.C. Motors for Industrial Drives*, PhD thesis, University of Sheffield, 1988.

[62] D. A. Staton and T. J. E. Miller, "Validation of PC-CAD using a precision dynamometer" *Proceedings of International Conference on Electrical Machines*, Vol. 3, Manchester, United Kingdom, September 1992, pp. 1221–1225.

[63] *Electro-Craft BRU-200 Servo Drives Instruction Manual*, Robbins & Myers / Electro-Craft, Minnesota, USA, July 1989.

[64] *HAUSER 3000 S Drive Installation and Commissioning Manual*, HAUSER Elektronik GmbH, Germany, December 1991.

[65] *Nicolet SYSTEM 500 Data Acquisition System Operations Manual*, Nicolet Instrument Corporation, Wisconsin, USA, October 1989.

[66] D. A. Lowther and P. P. Silvester, *Computer-Aided Design in Magnetics*, Springer-Verlag, 1st Edition, 1986.

[67] *OPERA-2d Reference Manual*, Vector Fields Ltd., 1995.

[68] M. Glinka, *Measurement and simulation of switched reluctance motors including the development of a software link between PC-SRD and MagNet*, Master's Degree Dissertation, July 1995

[69] C. Chwee, *Software Interface between PC-SRD and PC-OPERA*, SPEED Internal Report, September 1995.

[70] *MATLAB Reference Manual*, Math Works Inc., 1995.

[71] M. Liwschitz-Garik and C. C. Whipple, *Direct Current Machines*, Princeton, New Jersey USA, 2nd Edition, 1956.

[72] N. A. Demerdash, T. A. Nyamusa, and T. W. Nehl, "Comparison of effects of overload on parameters and performance of samarium-cobalt and strontium-ferrite radially oriented permanent magnet brushless DC motors," *IEEE Transactions on Power Apparatus and Systems*, Vol. PAS-104, No. 8, August 1985, pp. 2223–2231.

[73] T. Sebastian and G. R. Slemon, "Transient Modelling and Performance of Variable-Speed Permanent-Magnet Motors," *IEEE Transactions on Industry Applications*, Vol. 25, No. 1, January/February 1989, pp. 101–106.

[74] M. J. Shah, N. L. Kopp, and J. G. Vaidya, "Stall Torque Analysis of Brushless DC PM Motors," *PCIM Magazine*, February 1987, pp. 58–63.

[75] B. L. Theraja, *A Textbook of Electrical Technology : AC & DC Machines*, Vol. 2, Nirja Publications, New Delhi, 1986.

[76] T. J. E. Miller, "Definition of k_T and k_E for brushless DC motors," *Proceedings of 27th Annual Symposium on Incremental Motion Control Systems and Devices*, San Jose, California, 1992, pp. 87–96.

[77] W. L. Soong, *Design and Modelling of Axially-Laminated Interior Permanent-Magnet Motor Drives for Field Weakening Applications*, PhD Thesis, University of Glasgow, 1993.

[78] T. J. E. Miller and M. I. McGilp, "Non-linear theory of the switched reluctance motor for rapid computer-aided design," *IEE Proceedings*, Vol. 137, Pt. B, No. 6, November 1990, pp. 337–347.

[79] D. A. Staton, T. J. E. Miller, and S. E. Wood, "Maximising the saliency ratio of the synchronous reluctance motor," *IEE Proceedings*, Vol. 140, pt. B, No.4, July 1993, pp. 249–259.

[80] T. J. E. Miller and M. I. McGilp, "High-speed PC-based CAD for motor drives," *EPE Conference Proceedings* , Florence, Vol. 3, September 1991, pp. 435–439.

[81] D. A. Staton, M. I. McGilp, and T. J. E. Miller, "Interactive computer aided design of permanent magnet DC motors," *IEEE Transactions on Industry Applications*, Vol. 31, No. 4, July/August 1995, pp. 933–940.

[82] K. Binns, F. Chaaban, and A. Hameed, "Major design parameters of a solid canned permanent magnet motor with skewed magnets," *IEE Proceedings*, Vol. 140, Pt. B, No. 3, May 1993, pp. 161–165.

[83] K. H. Kim, D. J. Sim, and J. S. Won, "Analysis of skew effects on cogging torque and BEMF for BLDCM," *Conference Record of IEEE Industry Applications Society Annual Meeting*, Dearborn, Michigan, October 1991, pp. 191–197.

[84] R. Carlson, A. A. Tavares, J. P. Bastos, and M. Lajoie-Mazenc, "Torque ripple attenuation in permanent magnet synchronous motors," *Conference Record of IEEE Industry Applications Society Annual Meeting*, San Diego, California, October 1989, pp. 57–62.

[85] M. Jug, B. Hribernik, A. Hamler, M. Trlep, and B. Kreca, "Investigation of reluctance torque of brushless DC motor," *Proceedings of International Conference on Electrical Machines*, Boston, Massachusetts, September 1990, pp. 132–137.

[86] J. De La Ree and N. Boules, "Torque production in permanent magnet synchronous motors," *IEEE Transactions on Industry Applications*, Vol. 25, No. 1, January/February 1989, pp. 107–112.

[87] T. Li and G. Slemon, "Reduction of cogging torque in permanent magnet motors," *IEEE Transactions on Magnetics*, Vol. 24, No. 6, November 1988, pp. 2901–2903.

[88] T. Sebastian and V. Gangla, "Analysis of induced EMF and torque waveforms in a brushless permanent magnet machine," *IEEE Transactions on Industry Applications*, Vol. 32, No. 1, January/February 1996, pp. 195–200.

[89] S. Williamson, T. J. Flack, and A. F. Volschenk, "Representation of skew in time-stepped two-dimensional finite-element models of electrical machines," *Conference Record of IEEE Industry Applications Society Annual Meeting*, Denver, Colorado, October 1994, pp. 143–148.

[90] T. M. Jahns and W. L. Soong, "Pulsating torque minimization techniques for permanent magnet AC motor drives—a review," *IEEE Transactions on Industrial Electronics*, Vol. 43, No. 2, April 1996, pp. 321–330.

[91] M. Alhamadi and N. Demerdash, "Three dimensional magnetic field computation by a coupled vector-scalar potential method in brushless DC motors with skewed permanent magnet mounts - the no-load and load results," *IEEE Transactions on Energy Conversion*, Vol. 9, No. 1, March 1994, pp. 15–25.

[92] M. Alhamadi and N. Demerdash, "Modeling and experimental verification of the performance of a skewed mounted permanent magnet brushless DC motor drive with parameters computed from 3D-FE magnetic field solutions," *IEEE Transactions on Energy Conversion*, Vol. 9, No. 1, March 1994, pp. 26–35.

[93] M. Alhamadi and N. Demerdash, "Modeling of effects of skewing of rotor mounted permanent magnets on the performance of brushless DC motors," *IEEE Transactions on Energy Conversion*, Vol. 6, No. 4, December 1991, pp. 721–729.

[94] M. Naidu, N. Boules, and R. Henry, "A high-efficiency, high-power generation system for automobiles," *Conference Record of the IEEE Industry Application Society Annual Meeting*, Vol. 1, Orlando, Florida, Oct. 1995, pp. 709–716.

[95] R. Block and G. Henneberger, "Numerical calculation and simulation of a claw-pole alternator," *Proceedings of the International Conference on Electrical Machines*, Vol. 1, Manchester, UK, Sept. 1992, pp. 127–131.

[96] I. Boldea, E. Serban, and R. Babau, "Flux-reversal stator-permanent-magnet brushless generator with controlled DC output," *Conference Record of OPTIM-96*, Brasöv, Romania, May 1996.

[97] S. Andersson, *Flux-Reversal Machine*, Master Degree Dissertation, Lund Institute of Technology, Sweden, April 1996

[98] W. K. Kom, *Flux-Reversal Machine High Speed Generator*, Final Year Project Report, Department of Electronics and Electrical Engineering, University of Glasgow, April 1996.